Zvi Rosenberg · Erez Dekel

Terminal Ballistics

Springer

Terminal Ballistics

Zvi Rosenberg • Erez Dekel

Terminal Ballistics

Springer

Zvi Rosenberg
Ballistics Center
RAFAEL
Haifa
Israel
zvirosenberg@yahoo.com

Erez Dekel
Ballistics Center
RAFAEL
Haifa
Israel
erez.dekel@gmail.com

ISBN 978-3-642-25304-1 e-ISBN 978-3-642-25305-8
DOI 10.1007/978-3-642-25305-8
Springer Heidelberg Dordrecht London New York

Library of Congress Control Number: 2012930476

Printed on acid-free paper

Springer is part of Springer Science+Business Media (www.springer.com)

To the memory of our fathers,
Shmuel Rosenberg and Nisim Dekel.

Preface

The high velocity impact of solid bodies has attracted a large amount of research over the past century by both military and civil engineers. These impacts, at hundreds to thousands of meters per second, involve large deformations of the impacting bodies which can result in their total destruction around the impacted area. The impact of projectiles on armored vehicles (at 1–2 km/s) and the impact of meteorites at space stations at (10–20 km/s) are areas of much interest in this field. At impact velocities of a few meters per second, the structural response of the bodies is the relevant issue for safety engineers in the automotive industry. In order to study the effects of high velocity impacts, a special scientific discipline has been developed over the past 50 years, termed the dynamic response of solids to impulsive loading. This field involves several different disciplines such as: elasticity and plasticity theories, hydrodynamics, high pressure physics, material response to at high strain rates, fracture mechanics, and failure analysis. Several symposia dedicated to these issues were established during the last decades, such as the Hypervelocity Impact Symposia series, the International Symposia on Ballistics, the APS conferences on Shock Compression of Solids (in the US) and the DYMAT conferences in Europe. In addition, several journals specifically dedicated to this field were established, such as the International Journal of Impact Engineering, since 1983, and the International Journal of Protective Structures (launched in 2010). All of these activities are focused on the dynamic response of solids to impulsive loading, by developing new experimental facilities and diagnostics, as well as advancing numerical simulations and analytical modeling.

This book is focused on the subject of terminal ballistics which deals with the interaction between a moving object (the threat) and a protective structure (the target) at impact velocities in the range of a few hundreds to a few thousands of meters per second. At these velocities the damage induced in the target is local, extending laterally to several projectile diameters, but it is concentrated along the direction of projectile's motion. Thus, the target can be either perforated as is the case for thin targets, or deeply penetrated (for thick targets). These penetration/perforation issues are important for the armor engineer who looks for ways to

minimize the extent of damage to the protected structure. Similarly, the anti-armor designer is concerned with the improvements in the lethality of the threats by increasing their velocities, masses etc. The field of terminal ballistics covers a large range of scientific challenges and engineering applications, and we had to limit the number of the subjects which are discussed in this book. Naturally, most of the subjects we chose belong to armor issues, on which we worked for many years at the terminal ballistics laboratory in RAFAEL, a defense related research institute in Israel.

We wish to thank our colleagues for fruitful and exciting research during many years. In particular, we acknowledge the scientific collaborations with: Y. Yeshurun, D. Yaziv, M. Mayseless, Y. Ashuach, and Y. Partom from RAFAEL, S.J. Bless, M.J. Forrestal, and N.S. Brar from the US, and N.K. Bourne and J. F. Millett from England. We acknowledge the excellent work of: M. Siman, R. Kreif, M. Rozenfeld, Y. Reifen, D. Kanfer, N. Yadan, D. Mazar, I. Shaharabani and Y. Zidon, in performing many experiments in our lab for over 30 years. We thank C.E. Anderson, A.J. Piekutowski, K. Poormon, T.J. Holmquist, T. Borvik, S. Chocron and K. Thoma for helpful discussions during the preparation of this book, and for sharing some of their best shadowgraphs which add so much to this book.

Z. Rosenberg
E. Dekel

Introduction

The science and engineering of impacting bodies have a large range of applications depending on their type and their impact velocities. At very low velocities, these impacts can be limited to the elastic range of response, with practically no damage to the impacted bodies. In contrast, at very high impact velocities these bodies experience gross deformation, local melting, and even total disintegration upon impact. Various scientific and engineering disciplines are devoted to specific areas in this field such as: vehicle impacts, rain erosion, armor and anti-armor design, spacecraft protection against meteorites and the impact of planets by large meteors at extremely high velocities. In order to follow these different events the researcher has to be acquainted with diverse scientific fields which include: elasticity and plasticity of solids, fracture mechanics and the physics of materials at high pressures and temperatures. Terminal ballistics is the generic name for the science and engineering of impacts which are of interest to armor and anti-armor engineers. The relevant impact velocities usually range between 0.5 and 2.0 km/s, the so-called ordnance velocity range. These are the velocities at which projectiles are launched against personnel, armored vehicles and buildings, by rifles and guns. The impact velocities of shaped charge jets are within the hypervelocity range of 2.0–8.0 km/s, and their interaction with armor is also of major interest to both armor and anti-armor engineers. This book is devoted to the science of terminal ballistics, as it is defined here, through the various threats which operate in the battlefield.

The science of terminal ballistics started with the works of the great mathematician Leonard Euler (1745) and the British engineer Benjamin Robins (1742), who analyzed data for the penetration of steel cannonballs in soil as a function of their impact velocities. In the following two centuries, until the Second World War, the field of terminal ballistics was based on empirically derived relations between the penetration depth and the impact velocity of various projectiles into different targets. The reviews of Hermann and Jones (1961) and Backman and Goldsmith (1978), summarize many of these empirical formulas which were suggested over this period. During the years of WW-II, scientists in the US and UK have analyzed the penetration process of shaped charge jets and rigid steel projectiles into armor

plates, through analytical models which were based on physical considerations. These models identify the main force exerted on the projectile during penetration, which is then inserted in its equation of motion. The aim of these models is to reduce the mathematical description of a complicated three dimensional problem to a simple form which retains the essential physics of the penetration process. This simplification results in either a low dimensional system of ordinary differential equations or a few one-dimensional partial differential equations, which can be easily solved. The models can be tested by controlled experiments, in which the parameters are varied in a systematic way, in order to establish the non-dimensional parameters of the process. With these analytical models data correlation is made easy and extrapolations, to areas beyond the ability of experimental facilities, are possible. On the other hand, these analytical models require some compromise to be made, limiting their use to ideal cases where only a single mechanism is at work. Still, these models have been used successfully in order to account for the data and to reduce the number of the necessary experiments in terminal ballistics. Since the advancements in numerical simulations, the role of analytical models seems to decline as the codes are getting better and more efficient. However, these numerical simulations are often used just to account for experimental data, offering little physical insight for the process. Our strong belief is that analytical modeling is crucial for the field of terminal ballistics in order to understand the physics involved, and to highlight the important parameters which influence these processes.

Throughout this book we bring examples where physically based models play a major role in simplifying complex interactions. These models are derived either through experimental observations or through numerical simulations. Our approach is that numerical simulations can be viewed as the "perfect experiments," with which one can change a single parameter at a time and find its influence on the investigated process. We shall demonstrate the usefulness of these numerical studies for the construction of numerically-based models, and for the critical examination of existing models. Note that the term "model," as it is often used in the literature, is somewhat confusing since it is applied for both the description of material properties (material modeling) and for the analytical account of the process itself (the engineering model). For both applications these models should be physically based with parameters which can be calibrated by well-defined experiments. A valid material model should be applicable for a variety of experimental configurations, and an engineering model has to account for the behavior of many materials in a given experiment.

The book is divided into three parts. Part I includes a description of the terminal ballistics laboratory and the main diagnostic tools which are used in this field. It also summarizes several material models which are frequently used in numerical simulations. Part II is devoted to the field of penetration mechanics, dealing with the basic processes which take place upon the impact and penetration of various projectile/target combinations. Part III describes the working principles behind several armor concepts which are designed to defeat some of the more common threats.

Contents

Part I: Experimental and Numerical Techniques

Chapter 1
Experimental Techniques

Terminal ballistics is the general name for a large number of processes which take place during the high velocity impact of various projectiles/target combinations. There are two related disciplines which deal with launching these projectiles. Interior Ballistics concerns their acceleration to the desired velocity, and Exterior Ballistics deals with their flight dynamics from the launcher to the target. The present chapter describes, very briefly, some of the equipments and techniques which are used to launch a projectile to the desired velocity, as well as the relevant diagnostics which are used to follow its flight and its impact. The main experimental and theoretical techniques, which were developed in order to determine the relevant properties of the impacting materials, will also be described here.

1.1 The Terminal Ballistics Lab

1.1.1 Laboratory Guns

Most of the experimental work in terminal ballistics is performed through scaled experiments, within indoor laboratories, using the so-called laboratory guns. The obvious advantages of scaled experiments are their significantly higher ease and lower cost, as compared with full scale experiments. The most common scaling factors are the 1:3 and 1:4 scales, and the experiments are performed with guns of 20–40 mm in diameter. These guns can launch projectiles to velocities of up to 2.0 km/s with gun powder, and to 10 km/s by the two-stage light gas gun, which will be described here. Several reviews are devoted to the working principles and the design of these guns, such as Siegel (1955) and Stilp and Hohler (1990).

All the different launchers consist of a high pressure gas reservoir (the breech) attached to a long tube (the barrel) where the projectile is accelerated. The desired accelerating pressures are achieved either by burning a given amount of gun powder (the powder guns) or by the fast release of compressed gas (in gas guns).

Z. Rosenberg and E. Dekel, *Terminal Ballistics*,
DOI 10.1007/978-3-642-25305-8_1,

The acceleration process lasts as long as the projectile is in the barrel, but its velocity does not increase appreciably after a distance of about 120 diameters, which is the typical length of most guns. The basic equation for this acceleration process relates the final kinetic energy of the projectile to the work done by the high pressure pulse p(x), through:

$$\frac{1}{2}MV^2 = \frac{\pi}{4}D_g{}^2 \int p(x)dx \tag{1.1}$$

where M is the mass of the projectile and D_g is the inner diameter of the gun. Taking an average value of the pressure profile (p_{av}), which acts on the projectile, one can write for its exit velocity:

$$V = D_g \sqrt{\frac{\pi \cdot p_{av} L_g}{2M}} \tag{1.2}$$

where L_g is the length of the gun barrel. This equation gives the main ingredients which influence the performance of guns, as far as their ability to reach the desired velocity for a given mass. The science of Interior Ballistics deals with the exact determination of these pressure profiles and their average values, for different gases and gun powders. Every type of accelerating gas has a maximum velocity which it can impart to the projectile. This is the escape velocity (V_{esc}) with which the high pressure gas can move if it is allowed to expand freely (no mass to accelerate except its own), as given by:

$$V_{esc} = \frac{2c}{\zeta - 1} \tag{1.3}$$

where c is the sound speed in the gas at the high pressure condition, and ζ is its ratio of specific heats. The sound speed in a gas is inversely proportional to the square root of its molecular weight, which is the reason for using either helium or hydrogen in light gas guns. The escape velocity is also proportional to the temperature of the gas, which increases during its fast compression in light gas guns, enhancing their ability to reach higher velocities. These guns were developed in the 1950s in order to study the impact of meteorite-like projectiles on spacecraft bodies, at the hypervelocity regime of impact velocities ($\approx$10 km/s). The design principles of the light gas gun are described by Stilp and Hohler (1990), and its schematic description is shown in Fig. 1.1.

The first stage of this system includes a large chamber in which a gun powder is ignited and its products accelerate a large plastic piston along the pump tube, which is a long barrel with an inner diameter D_1. The piston has a conical section at its rear part in order to start its motion after some pressure buildup in the breech chamber. A predetermined amount of a light weight gas, usually helium, is inserted into the pump tube at pressures in the range of 20–30 atmospheres. As the plastic piston accelerates in the pump tube it compresses and heats the light gas to high pressures

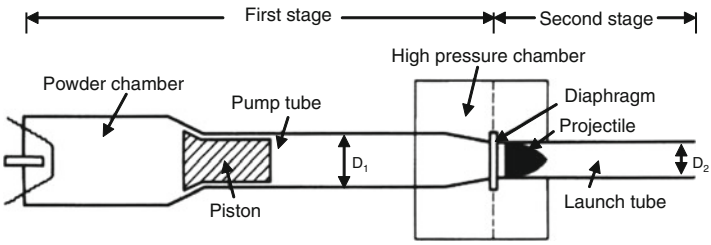

Fig. 1.1 A schematic description of the light gas gun

and temperatures. As seen in the figure, a conical steel section is leading the plastic piston from the pump tube (the first stage) to the launch tube (the second stage). This conical section is a very important feature of this gun design, as it has to stop the plastic piston and prevent it from extruding into the launch tube. The conical section is sealed at its far end with a steel diaphragm, which is designed to rupture at a certain predetermined pressure. The diaphragm divides the two parts of the system and the projectile itself is located in the launch tube, which has a smaller diameter (D_2). In most light gas gun systems the ratio between the diameters of the pump and launch tubes (D_1/D_2) is about 3–4, the diameters of the launch tubes are in the range of $D_2 = 20$–40 mm and the total lengths of these guns are 10–15 m. As stated by Hohler and Stilp (1990) the interior ballistics of the two stage gas gun is quite complex and its performance is determined by several factors such as the geometrical details of the two tubes, the conical section, and the weights of the plastic piston and the package to be launched. These details determine the exact values of the weight of the gun powder and the amount of light gas which have to be used in order to achieve the desired velocity.

1.1.2 Projectiles and Targets

The projectile is packaged within a plastic sabot, usually made of polycarbonate, in order to prevent metallic contact with the barrel. These sabots are made of several parts which are designed to separate as the package exits the gun barrel. Some gun systems have specially designed sabot strippers near the gun muzzle, which prevent the plastic sabots from reaching the target. Other systems are based on the sabots to open up by air drag, while the projectile is out of the gun. More details concerning sabot design and their separation before impact are given by Stilp and Hohler (1990). A metallic disc (the pusher plate), made of a high strength material, is placed behind the projectile in order to prevent the punching of the plastic sabot by the accelerating projectile. Since most laboratory guns are housed indoors, the targets are situated at a distance of about 1–5 m from the muzzle, in a specially designed target chamber which includes ports for high speed photography, pulsed X-ray shadowgraphy, velocity interferometry and other diagnostic devices.

After impact, all the debris from the target and projectile is collected in a large catcher tank, where the residuals are softly decelerated and recovered for further analysis.

The targets in terminal ballistics studies are classified according to their thickness as semi-infinite, intermediate, and thin. A semi-infinite target is large enough so that its lateral and back surfaces do not influence the penetration process. The measurements performed with semi-infinite targets are usually post-mortem determinations of the final penetration depth, the volume and the shape of the crater, and the characteristics of the residual projectile which is left at the crater bottom. Experiments with semi-infinite targets focus on the physics of the penetration process rather than simulating actual armor designs. The thickness of an intermediate target is enough to stop the projectile but it is not large enough to prevent damage at its back surface. The interactions of projectiles with targets of intermediate thickness are relevant for the armor designer, since they represent actual situations of projectile/armor encounters. This is a more complicated penetration process since it involves various failure mechanisms which can take place during the interaction. Some of these failure mechanisms are shown schematically in Fig. 1.2, from Backman (1976).

Thin targets are perforated by the projectile and their relevance for terminal ballistics is through the damage they can induce to the projectile. Targets which induce a considerable damage to the impacting threat, by a well-defined defeat

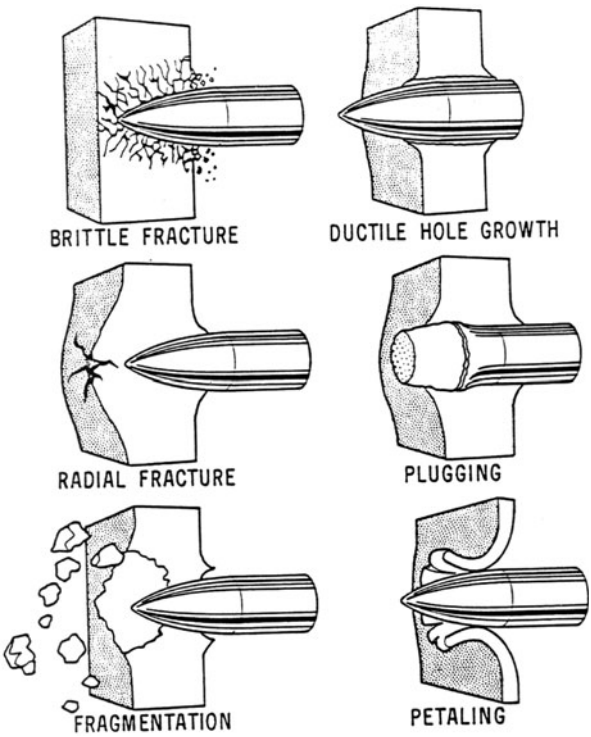

Fig. 1.2 Possible failure modes in different impact situations

mechanism, are considered as candidates for add-on armor designs. These mechanisms, which are of main interest to the armor designer, will be discussed in the third part of this book.

One of the most important properties of a given projectile/target combination is its ballistic limit velocity (V_{bl}), which marks the velocity threshold for target perforation. In principle, the value of V_{bl} for a given projectile/target configuration can be determined by two experiments at impact velocities which are close enough. The high velocity impact should result in a complete perforation of the target, while at the low velocity impact the projectile should be stopped in the target. However, due to experimental errors in velocity measurements, as well as variations in material properties, it is practically impossible to determine V_{bl} by a couple of experiments. Instead, a probabilistic approach was adopted according to which at least six experiments are performed at the estimated limit velocity. In half of these experiments the target should be perforated while for the other half it should stop the projectile. With the better statistics of this technique the limit velocity, which is termed the V_{50} velocity, is taken as the average of the highest velocity with no perforation and the lowest velocity with projectile perforation. The definition of perforation itself depends on the different standards which were adopted by various institutes. Thus, the US army criterion states that a complete penetration is achieved even if the projectile is still stuck in the target but light can pass through it. In contrast, according to the U.S. Navy's definition a complete perforation is achieved when the projectile fully emerges from the target.

1.1.3 Diagnostics for Terminal Ballistics

There are several measurements which have to be performed at each experiment in terminal ballistics. The most important one is the projectile's impact velocity, which has to be determined to an accuracy of about $\pm 0.5\%$, in order to have a meaningful result. This velocity is best determined by non-interfering optical techniques like laser beams (or screens) which are cut off by the flying projectile. Another useful technique is the pulsed X-ray shadowgraphy, which uses very short (about 30 ns) bursts of radiation from specially designed tubes. The short exposure time "freezes" the movement of the projectile, resulting in a sharp picture of its contour on specially designed films or screens. These flash X-rays are also used to follow the alignment of the projectile as it impacts the target, and for the determination of its shape and velocity after it exits the target. Thus, a terminal ballistic laboratory includes several pairs of flash X-ray tubes which follow the projectile during its free flight, its impact with the target, and its exit from the back surface, as shown schematically in Fig. 1.3. The use of two simultaneous flashes, at perpendicular orientations, is needed to follow the spatial orientation of the projectile at the impact moment (the pitch and yaw angles).

High speed photography techniques are also very useful to follow the interaction between the projectile and the target, as described by Stilp and Hohler (1990) and by

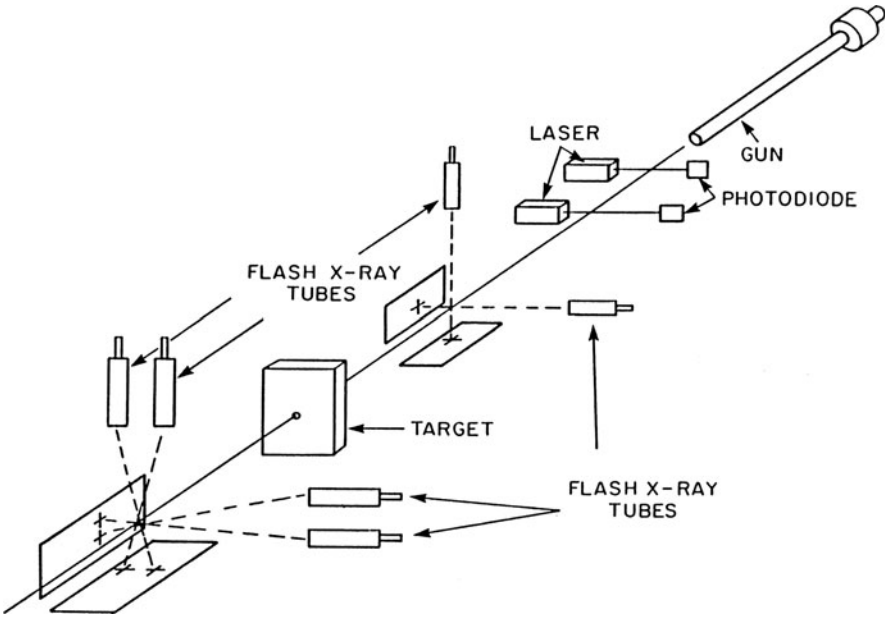

Fig. 1.3 Schematic description of the terminal ballistics experiment

Swift (1982). The basic objective of these cameras is to capture the projectile/target interaction at different times by projecting them at different places on a single film. This is done by using a rotating mirror which spins at an extremely high velocity by the action of an air turbine, as shown in Fig. 1.4. The projection of the impact event on the film is achieved by a series of projecting lenses as shown in the figure.

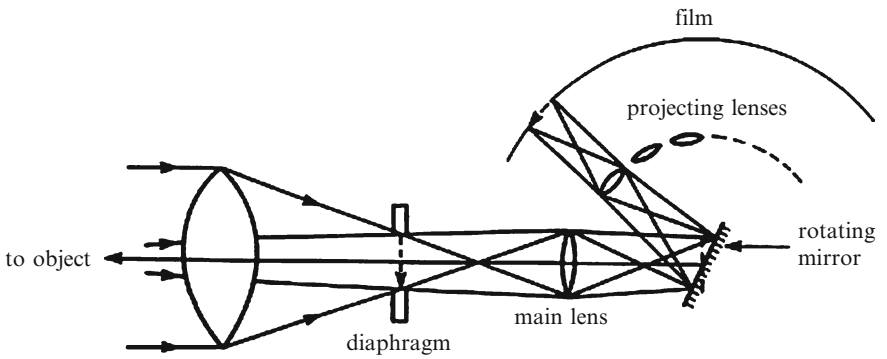

Fig. 1.4 Schematic description of the rotating-mirror camera

1.2 Determination of the Dynamic Properties

A high velocity impact induces high pressures and temperatures in the projectile and in the target, for very short times (high strain rates) which characterize the impulsive nature of this event. The term "dynamic properties" is referred to the physical and mechanical properties of the solid which are sensitive to high loading rates, as well as to high pressures and temperatures. Strain rates which are higher than about 10^2 s^{-1} fall in the category of high rates and pressures are considered to be high when their magnitude is larger than about 10 GPa. Temperature changes have to be considered when these are high enough to cause significant changes of material strength, by the so-called thermal softening process. The relevant temperatures are different for various materials depending on their melting temperatures. It is commonly accepted that the threshold temperature for thermal softening of a solid is about half its melting temperature.

The present chapter describes some techniques which are used to determine the influence of these parameters (strain rates, pressures and temperatures), on material properties which are relevant for terminal ballistics. These properties can be grouped in two classes, those which affect the material's equation of state and those which determine its constitutive relations. The equation of state of a solid relates its internal energy to the pressure and density which characterize its state. The constitutive relation accounts for the strength and failure characteristics of the solid under the high loading rates. As will be discussed in this book, the strength and failure of the solid are its most important properties, as far as terminal ballistics is concerned. Thus, a comprehensive account of their variation with loading rates, pressures and temperatures, is essential for the evaluation of a given material as a possible candidate for either armor or projectile design. Failure refers to situations where a given element in the structure reaches a critical state and its load capacity is reduced, either totally or partially. The failure of solids under dynamic loading conditions is one of the most important areas for terminal ballistics, and it has been the focus of much research.

1.2.1 Equation of State Measurements

A high velocity impact can induce very high pressures and temperatures for several microseconds, in the projectile and in the target, through fast moving shock waves. The irreversible increase in the temperature of shock loaded materials can reach their melting and even vaporization states. The study of materials response to shock wave loading is focused on their equations of state, which relate their densities to the high pressures and temperatures. Equations of state were determined for many solids in a systematic study, as described by Zeldovich and Raizer (1965), Al'tshuler (1965), McQueen et al. (1970), Chhabildas (1987) and Asay and Kerley (1987). These reviews also cover much of the experimental techniques which are

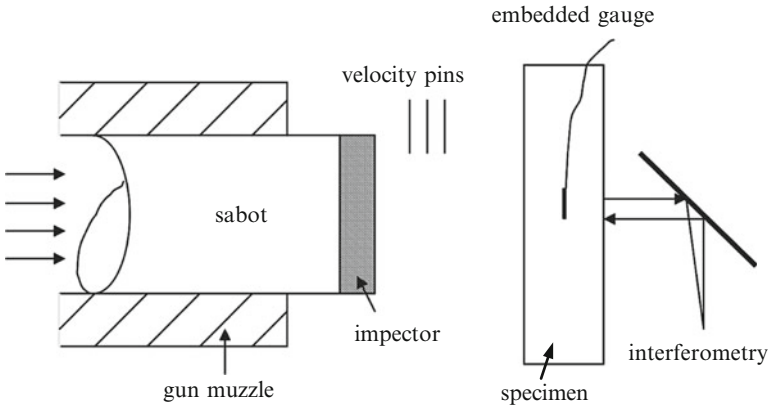

Fig. 1.5 The plate impact experiment

used in this field. The plate-impact experiment, as shown schematically in Fig. 1.5, is the most useful technique to obtain the important data for the shock equation of state of a given solid. This is a relatively simple experimental configuration, which is easy to analyze mathematically, as shown below.

Basically, a planar disc (the impactor) is accelerated by a large diameter gun towards a stationary disc (the target) which is made of the investigated material. The specimen disc is carefully aligned at the end of the gun in order to ensure maximum planarity of the impact. The impact velocity is measured by electrically shorting pins prior to impact, and the target is instrumented with various gauges and sensors, which follow the structure of the shock wave in the specimen, as described below. Upon impact, planar shock fronts, or waves as they are usually called, are initiated at the impact face and move into both the impactor and target plates. One can conceive of these shock waves as extremely thin fronts which sweep the material at a constant velocity. The material behind these fronts is compressed to a state of high pressure and density, which depend on the impact velocity and on the properties of the impacted materials. Since these waves are planar they are compressing the two plates in a uniaxial strain mode, by which the only non-zero strain in the specimen is along the impact direction. This special mode of compression is analyzed through the Rankine–Hugoniot (R–H) jump relations, which express the changes in density, pressure and internal energy of the shocked material. These relations are given in terms of two mechanical parameters which are measured in the experiment, the shock velocity (U_s) and the particle velocity (u_p) of the material behind the shock front. In fact, the R–H relations are the conservation equations for mass, momentum and energy under the special loading mode of uniaxial strain, and they are given by:

$$\text{Mass conservation}: \quad \rho_0 U_S = \rho\left(U_S - u_p\right) \tag{1.4a}$$

$$\text{Momentum conservation}: \quad p = \rho_0 U_S u_p \tag{1.4b}$$

$$\text{Energy conservation:} \quad \Delta e = \frac{p}{2} \cdot \left(\frac{1}{\rho_0} - \frac{1}{\rho} \right) \tag{1.4c}$$

where ρ, p and Δe are the density, pressure and change in internal energy of the shocked material, respectively. The subscript 0 stands for these parameters at ambient conditions. The shock velocity (U_s) and the particle velocity (u_p) are the measured parameters in each experiment. With several experiments at different impact velocities, one can determine the shock equation of state for the solid. One of the most useful ways to represent this equation of state, in a graphical display, is by plotting the relations between the pressure and the particle velocity behind the shock front. This $p = p(u_p)$ curve, called the "Hugoniot curve" of the solid, is the loci of all the points representing the possible states of the material which can be reached by a single shock wave. The Hugoniot curve is different than the isothermal compression curve of the solid, since each point on the Hugoniot is characterized by a different temperature (internal energy). Hugoniot curves, for several materials which are relevant to terminal ballistics, are given in Fig. 1.6.

For symmetric impacts, where the two impacting plates are made of the same material, the particle velocity behind the shock front is equal to half the impact velocity, since these are ideally plastic impacts. Thus, by accurately measuring the impact velocity one obtains the particle velocity behind the shock front in symmetric impacts. The shock velocity in the target plate is measured either by optical techniques or by electrical transducers which short-circuit upon the arrival of the shock front. For many materials, solids and liquids, the relation between shock and particle velocities has been found to be linear, according to:

$$U_S = C_0 + S u_p \tag{1.5}$$

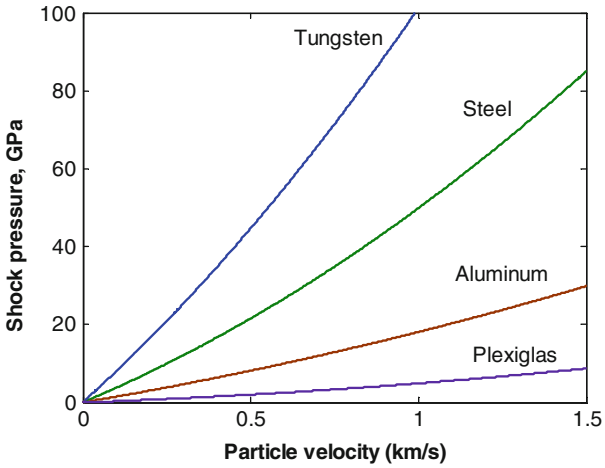

Fig. 1.6 Hugoniot curves for several materials

where C_0 is very close to the bulk sound speed of the solid at ambient conditions. The experimentally determined slope in this linear relation (S) has values in the range of S = 1.0–1.5 for most solids. The values for C_0 and S for many materials are listed in the data base of all the commercial codes which are used for numerical simulations of terminal ballistics experiments.

1.2.2 Dynamic Strength Measurements

The previous section gave a brief account for the behavior of materials under planar shock wave loading which is a one-dimensional strain configuration. The materials were assumed to behave as fluids in the sense that their strength was ignored in the analysis. Thus, the values of the principal stresses in the specimen are equal to each other, $\sigma_x = \sigma_y = \sigma_z = p$, where p is the pressure in the solid. This approximation is valid for intense shock waves where the pressure is much higher than the strength of the material (Y). When these pressures are less than about 10Y the analysis has to take into account the elasto-plastic properties of the material. The shock Hugoniot of a material with strength is shown schematically in Fig. 1.7. The addition of material strength means that the principal stresses in the shocked solid are not equal to each other. The stress along the shock propagation direction (σ_x) is higher by Y than the two stresses σ_y and σ_z, which are equal to each other. Note the distinction between the elastic and the so-called plastic regimes. The elastic response of the solid is represented by the straight line, which terminates at the Hugoniot elastic limit (HEL). The "plastic" response is given by the Hugoniot curve, which is superposed on the elastic straight line. This stress–strain curve is due to the fact that the material behind the shock front is compressed in a uniaxial straining mode, with $\varepsilon_x \neq 0$ and $\varepsilon_y = \varepsilon_z = 0$, where x is the shock propagation direction. Thus the strain along the shock propagation direction is, in fact, the volumetric strain of the material (ε_v), which is related to the density ratio (ρ/ρ_0) attained by the shock pressure. The value of the shock pressure is given as the average of the three principal stresses in the material, through $p = (\sigma_x + \sigma_y + \sigma_z)/3$.

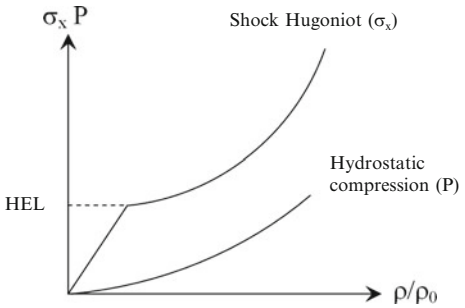

Fig. 1.7 A schematic description of the Hugoniot curve for a solid with strength

At very low impact velocities the solid behaves elastically and upon stress unloading it returns to its original state. The state of the solid within its elastic range is given by the longitudinal stress (σ_x) and the two lateral stresses ($\sigma_y = \sigma_z$) which, under the uniaxial straining mode, are given by:

$$\sigma_y = \sigma_z = \frac{v}{1-v}\sigma_x \tag{1.6}$$

where ν is the Poisson constant of the solid . The elastic regime terminates at the Hugoniot elastic limit (HEL), which marks the onset of material yielding under the uniaxial strain loading. At this point the difference between the principal stresses ($\sigma_x - \sigma_y$) reaches its maximal value which is equal to the dynamic strength of the solid (Y_d). This constraint is the result of the yield criteria of Tresca and von-Mises which limit the stress difference in the plastic range for metals. Using the yield condition, $\sigma_x - \sigma_y = Y_d$ together with Eq. 1.6, results in the following relation between the HEL of the solid and its dynamic strength:

$$HEL = \frac{1-v}{1-2v} \cdot Y_d \tag{1.7}$$

The dynamic strength (Y_d), as derived from its measured HEL value, can be very different than the static strength of the solid, especially for strain-rate sensitive materials.

The existence of two regimes in the response of a solid to shock waves, results in a discontinuity in the slope of the shock Hugoniot at the HEL, as shown in Fig. 1.7. This discontinuity leads to a splitting of the shock front into two waves, which propagate at different velocities in the solid. The precursor elastic wave, with amplitude which is equal to the HEL, is moving at the longitudinal wave velocity given by:

$$C_L = \sqrt{\frac{K + 4G/3}{\rho}} \tag{1.8}$$

where K and G are the bulk and shear moduli of the solid, respectively, and ρ is its density. The slower "plastic wave" is propagating at the shock velocity (U_s), as given by Eq. 1.5. By recording the amplitude of the elastic precursor one can determine the dynamic strength of the shocked material at the high strain rates which are of the order of (10^6–10^8) s^{-1}. With increasing shock amplitude the velocity of the plastic wave increases until it attains the value of C_L, and for higher shock amplitudes a single wave is propagating in the solid. The threshold amplitude, for the emergence of a single shock, depends on the properties of the solid varying between 10 and 100 GPa for most solids. For example, these threshold stresses are about 10 and 60 GPa, for aluminum and steel, respectively.

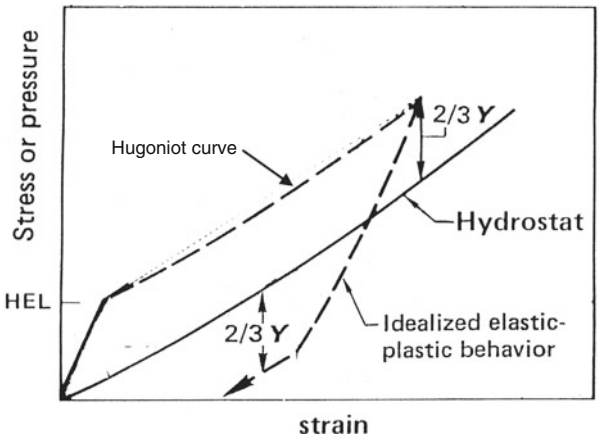

Fig. 1.8 Loading–unloading curves for a solid with strength

In a similar manner, one can follow the release process of the shocked solid by the release waves which emanate from free surfaces. The process takes place along the unloading path of the specimen in the stress–strain plane, as shown schematically in Fig. 1.8. The solid first unloads elastically along a straight line whose slope is related to the longitudinal wave velocity (C_L). At a certain point during the unloading process, this line meets the yield surface of the solid, below its hydrostatic compression curve. Further unloading is achieved along an isentrope, which is roughly parallel to the Hugoniot curve as shown in the figure. This part of the release, termed the "plastic release", lies at a distance of $2/3Y_d(p,T)$ below the hydrostatic compression curve. Since the shock Hugoniot is offset by the same distance above the hydrostatic compression curve, the vertical "distance" between the shock and release curves is equal to $4/3Y_d(p,T)$. The dynamic strength of the solid $Y_d(p,T)$ is related to its strength at the high pressure and temperature in the shocked state. This value can be much higher than the quasi static strength of the solid, due to pressure hardening effects. On the other hand, it can be lower than the quasi static value, if the temperature of the shocked material is high enough to induce its thermal softening. The discontinuity in the slopes of the elastic and "plastic" parts in the release curve, results in a structured release wave which can be monitored continuously by stress or particle velocity gauges. From the amplitude of the elastic release wave one can determine the strength of the solid at its shocked state, $Y_d(p,T)$, as will be discussed in the next section.

1.2.3 Diagnostics

The plate impact experiment is very useful for the determination of the important parameters in the constitutive relations of the solid. These relations account for the dependence of the material strength and its failure characteristics on the high rates,

pressures, and temperatures in the shocked state. Quantitative information about these variations are obtained by various in-situ measurements which record the shock wave profiles in plate impact experiments, as reviewed by Chhabildas (1987) and Asay (1997). The strain rates in these experiments can reach values of 10^8 s^{-1} and the pressures can range between few to several hundreds of GPa. The necessary information is obtained by embedding stress gauges in the target plate or monitoring its back surface velocity by interferometric techniques.

Embedded stress gauges are made of either piezoresistive materials, whose electrical resistivities are appreciably changing with pressure, or of piezoelectric materials which produce electric charge (current) when a pressure pulse is sweeping them. The most useful piezoresistive materials for both shock and static loading are manganin, Yitterbium and carbon. The most successful piezoelectric gauge is made of specifically poled foils of Polyvinyldifluoride (PVDF). The poling techniques of these gauges, as well as their calibration under shock loading, have been worked out by F. Bauer, as described in Bauer (1983), and in Bauer (1984).

The most common piezoresistance stress gauge for shock wave studies is made of manganin which is an alloy containing 84% copper, 12% manganese and 4% nickel. This material has an almost constant piezoresistive response up to pressures of about 100 GPa. In fact, the review article by Chhabildas (1987) cites measurements by P. de-Carli to shock pressures as high as 120 GPa. The electrical resistivity of manganin is practically insensitive to temperature changes, which makes it an ideal stress gauge for dynamic experiments. The Nobel laureate P.W. Bridgman installed manganin gauges in static high pressure cells, for his classical studies at the early years of the twentieth century. The first use of manganin as a pressure transducer in shock experiments was published by Fuller and Price (1964). They embedded thin foils of manganin between two planar discs, and monitored their resistance changes during the passage of shock waves through the assembly. With a pre-calibrated response curve, these profiles were translated to the pressure–time profiles in the shocked specimens. Calibration curves for foil and wire gauges have been obtained by Barsis et al. (1970), Kanel et al. (1978), Vantine et al. (1980), and Rosenberg et al. (1980). These calibrations agree with each other to within 2%, with an average piezoresistance coefficient of $\Delta R/R_0 = 2.4\%$ per GPa, where R_0 is the initial resistance of the gauge and ΔR is its resistance change. A typical gauge record from a plate impact experiment on a copper specimen is shown in Fig. 1.9. The figure also details the location of the gauge in this experimental set-up, the back surface configuration, which is specially suited for the determination of the dynamic compressive and tensile strengths of the specimen.

With this configuration the stress history is actually determined at the interface of the specimen and a Plexiglas backing plate. Several features in this record should be noted. The first one concerns the rising part of the signal, which clearly shows that the shock wave in the specimen has been split into the elastic precursor wave and the following "plastic wave". The elastic precursor, of amplitude which is equal to the HEL, serves to determine the strength of the solid at these high strain rates. The elastic and plastic waves are followed by a constant shock level which is subsequently unloaded, by a structured release wave. The unloading is followed

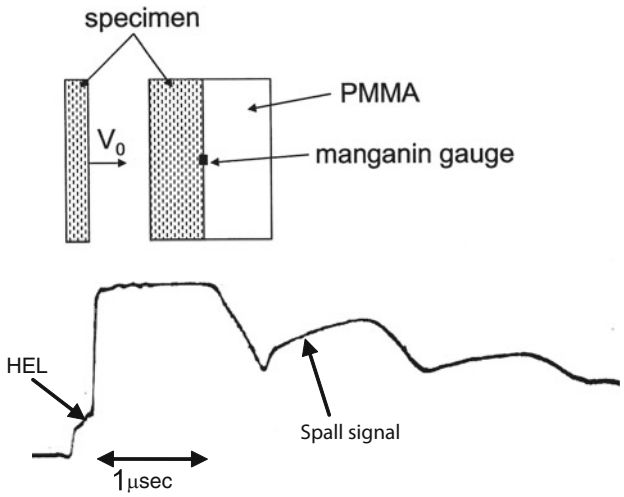

Fig. 1.9 The back-surface gauge setup (*top*) and the manganin gage record (*bottom*)

by several stress reverberations which are due to the spall failure inside the target plate. Spall is the onset of tensile failure which is due to the interaction between the two release waves inside the specimen. These release waves are initiated at the impactor's free surface and at the specimen/Plexiglas interface. The amplitude of the first reverberation in the spall signal is related to the failure strength of the specimen (the spall strength) under dynamic tensile conditions. Thus, with this simple experiment one derives the dynamic compressive strength of the specimen and its tensile failure threshold.

A direct technique to determine the compressive strength of the solid, at high shock pressures, is the lateral gauge technique, which was first suggested by Bernstein et al. (1967). Two stress gauges are embedded in the specimen at perpendicular planes, as shown in Fig. 1.10. The first gauge, which is embedded in a plane parallel to the shock front, measures the longitudinal stress in the

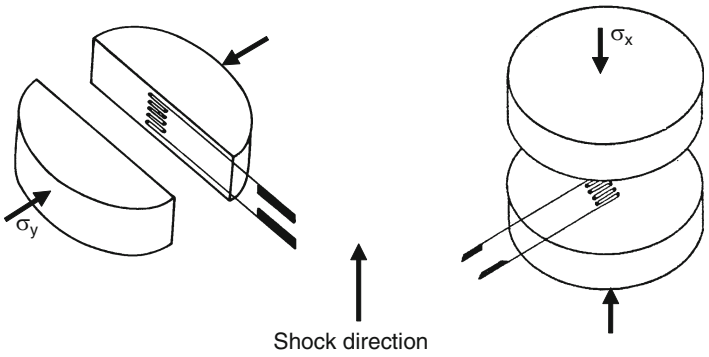

Fig. 1.10 The longitudinal (*right*) and lateral (*left*) gauge orientations

specimen (σ_x). The second gauge is embedded in a plane along the shock propagation direction, and it measures the lateral stress in the specimen (σ_y). The difference between the two measured stresses is equal to the strength of the specimen in its shocked state, hence $\sigma_x - \sigma_y = Y_d(p,T)$. The main difficulty with this technique stems from the fact that the two different gauge orientations result in different calibration curves for the gauge, as was shown by Rosenberg et al. (1981). With a proper calibration for the gauge at the lateral orientation, as determined for manganin gauges by Rosenberg and Partom (1985), this technique can be used to measure the strength of materials under high shock pressures. As we shall see in the third part of this book, the lateral gauge technique has been very useful in determining the strength of ceramic materials at high shock pressures.

The most accurate experimental techniques in shock wave research are the various interferometric devices which were reviewed by Chhabildas (1987). The basic idea behind these techniques is to follow the velocity of the specimen's back surface continuously, using the reflected light from a laser beam. The most popular of these optical interferometers are the VISAR (Velocity Interferometer System for Any Reflector) system, which was developed by Barker and Hollenbach (1964), and the Fabry–Perot interferometer which was first applied by Johnson and Burgess (1968). Both systems use Doppler-shifted light from the moving back surface, which is either specular or diffuse. The reflected light is split into two beams to form the different legs of a wide angle Michelson interferometer. The fringe sensitivity of the interferometer is dependent on the delay time between the two legs. With the VISAR system the delay is achieved by a glass etalon along the path of one of the legs, with a predetermined time delay. With the Fabry–Perot system the delay is achieved through a set of plates separated by a well defined distance. A superposition of the two beams results in a fringe system with a count which is proportional to the velocity of the back surface. Both systems have fast time response which enables one to follow small changes in the specimen's free surface velocity very accurately. However, these techniques suffer from several disadvantages which are related to the changes in the intensity of the reflected light (for the VISAR) and to the resolution of the recording film, with the Fabry–Perot system. A new technique, the heterodyne velocimeter, has been introduced by Strand et al. (2006). This technique overcomes the difficulties of both the VISAR and the Fabry–Perot systems while keeping their main advantages. The derived velocity–time history is directly related to the frequency of the beat wave form. Thus, there is no need for extra components to resolve the difficulties arising from the fringe jump ambiguities. In addition, the data is recorded on digitizers having long recording time, avoiding camera distortion.

With the high resolution of these techniques one can gain accurate values for the strength of shock compressed specimens by using the self consistent technique which was suggested by Asay and Lipkin (1977). A schematic diagram of this experimental setup together with the resulting VISAR records, are shown in Fig. 1.11. The technique is based on performing two similar experiments, which differ by the backing disc behind the impactor, having either higher or lower acoustic impedance than the impactor. The acoustic impedance of a material is defined by the product

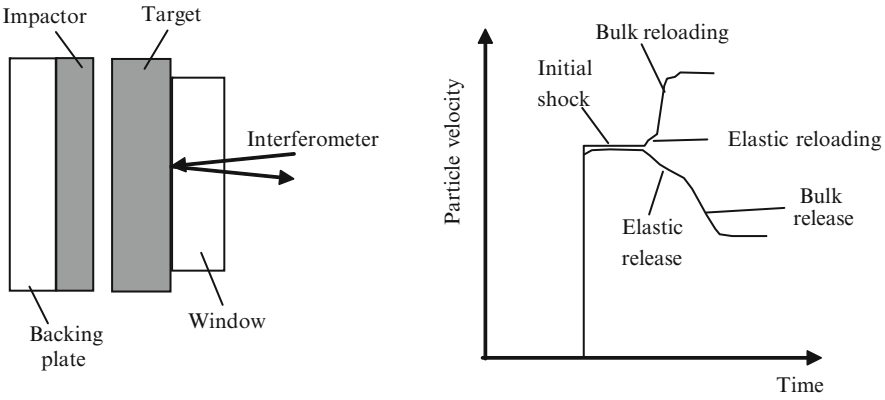

Fig. 1.11 The experimental setup and the resulting record from unloading and reloading experiments

$\rho_0 \cdot C_L$, where ρ_0 and C_L are the density and longitudinal sound velocity of the material, respectively. With the same impact velocity, the amplitudes of the initial shock waves in the two experiments are the same. The initial shock wave is followed either by a second shock, when the impactor is backed by a higher impedance material, or by a release wave, for a backing material with lower impedance. From the measured elastic parts of these reshock and release records, one can determine the dynamic strength of the specimen in its shocked state, namely, $Y_d = Y(p,T)$.

A concise summary of the results for various materials, from Asay and Kerley (1987), is shown in Fig. 1.12. The data is given for the normalized strengths, in

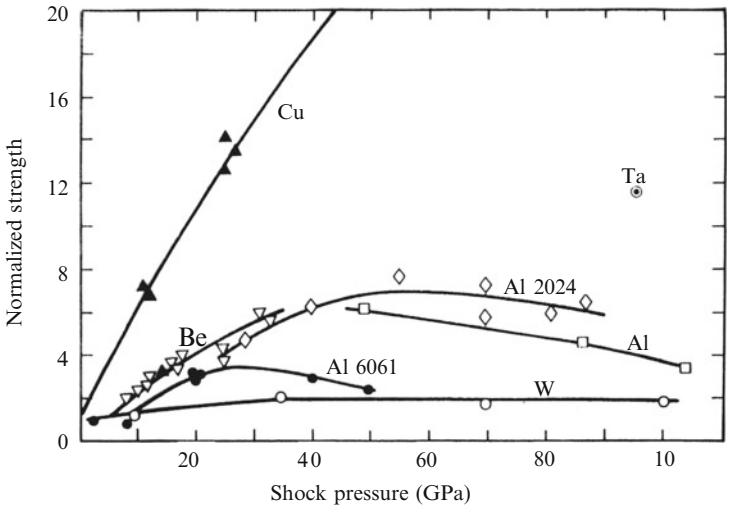

Fig. 1.12 The change in strength at high shock pressures for several materials

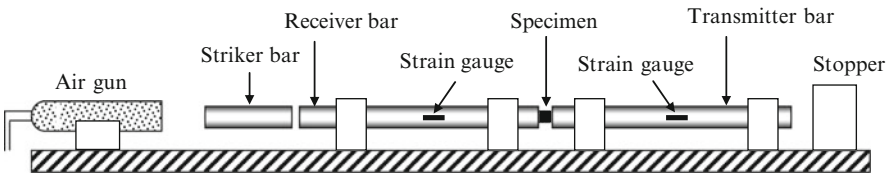

Fig. 1.13 A schematic description of the Kolsky bar system

relation with the static values, as a function of shock amplitude. The decreasing trend of the strength with shock pressures for some of these materials, is due to the competing effects of pressure hardening and temperature softening. Obviously, at high shock pressures the temperature of the specimen is high enough to induce its softening, as seen here for the aluminum alloys.

The Kolsky bar system which was introduced by Kolsky (1949), and is often referred to as the split Hopkinson bar, is the most useful technique to determine the dynamic stress–strain curves of solids under uniaxial stress conditions in the 10^2–10^4 s^{-1} range of strain rates. This is the relevant range of strain rates for the projectile and target materials around their interface during penetration. The Kolsky bar system consists of two long instrumented bars made of high strength steel, which hold the specimen as shown in Fig. 1.13. The diameter of these bars is usually in the range of 12–25 mm and their corresponding lengths are 3–5 m.

A short bar (the striker) is launched by an air gun towards the first bar (the receiver) at a velocity of 5–20 m/s, inducing a square shaped stress pulse in the receiver bar. The duration of this pulse is equal to twice the transit time of an elastic wave in the striker bar (typically 100–200 μs). This stress pulse is recorded by the first strain gauge, which is glued on the receiver bar at some distance from the bar/specimen interface. The incident strain-time history, $\varepsilon_i(t)$, is one of three strain signals which are necessary for the analysis. Upon reaching the specimen, the incident stress pulse is partly reflected back to the receiver bar and partly transmitted to the second bar (the transmitter). The reflected pulse, $\varepsilon_r(t)$, is recorded by the first strain gauge which recorded the incident wave. The transmitted pulse $\varepsilon_t(t)$ is recorded by a second strain gauge, which is glued to the transmitter bar at the same distance from the specimen as the first gauge. The diameter of the specimen disc should be smaller than the bar's diameter in order to achieve significant stress amplification in the specimen. With proper dimensions even strong materials can be compressed to large strains, well beyond their elastic range of response. Due to the early stress reverberations inside the specimen, the analysis of the Kolsky bar system cannot account for the elastic part of the specimen's response. The technique is considered to be accurate only for strains beyond several percent.

The variables which control the deformation of the specimen, are the velocities $V_1(t)$ and $V_2(t)$ of the two bars at their interfaces with the specimen. The strain rate of the specimen is simply given by:

$$\dot{\varepsilon} = \frac{d\varepsilon}{dt} = \frac{V_1(t) - V_2(t)}{h} \tag{1.9}$$

where h is the thickness of the specimen, which is also changing with time. The velocities $V_1(t)$ and $V_2(t)$ are derived from the measured strain-time histories by using the well-known relation for elastic waves in long bars, $V = C_b\varepsilon$, where C_b is the velocity of elastic waves in long bars. Thus, one can write for the two interface velocities:

$$V_1(t) = C_b[\varepsilon_i(t) - \varepsilon_r(t)] \quad , \quad V_2(t) = C_b\varepsilon_t(t) \tag{1.10}$$

The strain of the specimen is obtained by inserting these expressions for V_1 and V_2 in (1.9), and integrating it according to:

$$\varepsilon(t) = \frac{C_b}{h}\int [\varepsilon_i(t) - \varepsilon_r(t) - \varepsilon_t(t)]dt \tag{1.11}$$

Assuming stress equilibrium along the thickness of the specimen, the stress is derived by averaging the two stresses which act on the opposite sides of the specimen:

$$\sigma(t) = \frac{F_1(t) + F_2(t)}{2A_s} \tag{1.12}$$

where A_s is the cross section area of the specimen, which is also changing with time. The forces F_1 and F_2 are related to the strains in the bars, as measured by the two strain gauges, through:

$$F_1(t) = A_bE[\varepsilon_i(t) + \varepsilon_r(t)] \quad \text{and} \quad F_2(t) = A_bE\varepsilon_t(t) \tag{1.13}$$

where A_b is the cross section of the bar and E is its Young's modulus. With these stress and strain histories in the specimen, $\sigma(t)$ and $\varepsilon(t)$, one can easily derive its dynamic stress–strain relation, $\sigma = \sigma(\varepsilon)$, at the high strain rate under consideration. Changing the dimensions of the specimen or the impact velocity of the striker bar, results in different strain rates as well as different maximal strains for the specimen. When the analysis follows the transient values of the specimen's thickness, the resulting $\sigma(\varepsilon)$ curves are the so-called true stress–strain curves. If such a correction is not made they are referred to as the engineering stress–strain curves.

In order to plastically deform a high strength specimen in the Kolsky bar system their area ratio (A_b/A_s) should be large. This will result in considerable stress

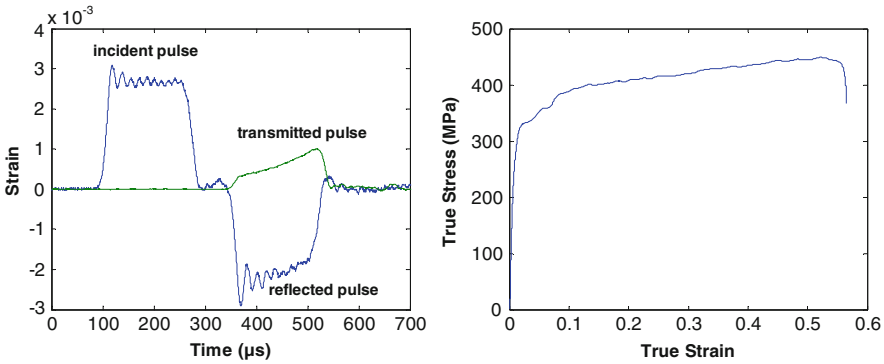

Fig. 1.14 The measured strain signals (*left*) and the resulting stress–strain response (*right*) for a specimen of the 6061-T651 aluminum alloy

amplification so that the stress in the specimen will be larger than its yield strength. It is very important to accurately measure the dimensions of the specimens before the experiment and to determine the elastic wave velocity (C_b) in the long bars. A typical set of strain signals in a Kolsky bar experiment, as measured in our laboratory for a specimen of the 6061-T651 aluminum alloy is shown in Fig. 1.14. The figure also shows the resulting true stress–strain curve which was derived from these strain histories.

The actual state of stress in the disc shaped specimens has been the subject of many works which analyzed the effects of specimen inertia, and the friction at the specimen/bar interfaces, on the stress uniformity in the specimen. One of the important conclusions, by Gorham et al. (1984), is that in order to minimize inertia effects the aspect ratio of the specimen, its thickness to diameter ratio, should be about 0.5. In order to minimize friction at the interfaces it is customary to apply some grease to the specimen faces before the experiment. The issue of inertia is significant for materials like concrete, as discussed by Li and Meng (2003). Their analysis shows that the apparent rate sensitivity of concrete and concrete-like materials, at strain rates of about 10^2 s^{-1}, is due to specimen's inertia rather than to an increased material strength at high strain rates. As far as metals are concerned these inertia effects are negligible, and the Kolsky bar system is the best experimental technique to derive dynamic stress–strain curves at strain rates which are relevant for terminal ballistics. In particular, the phenomenon of adiabatic shear banding can be easily identified by the shape of the stress–strain curve, as will be discussed in Chap. 2.

A new technique was recently developed by Avinadav et al. (2011) for the direct measurement of the bar velocities in the Kolsky system, instead of the traditional strain measurements. The new technique is based on the velocity interferometer technique of Strand et al. (2006), which has been termed the photonic Doppler

velocimeter (PDV), and is specifically adapted for low velocity measurements. The interferometers measure the velocities at the sides of the bars by using fiber focusers which illuminate them at an angle of about 30° and collect reflected Doppler-shifted light which is interfered with a reference beam. The new technique results in smooth velocity histories of the two bars, from which the stress and strain histories of the specimen are derived through the equations described above. This is a more direct and easy way to determine the dynamic stress–strain curves and, as shown by Avinadav et al. (2011), the results are identical to those obtained by the strain gauges.

The simple arrangement of the Kolsky bar system for the dynamic compression test, has been modified in order to load the specimen under dynamic tension or torsion. The basic principles of these devices are the same but the fixtures of the specimen are different. For example, tensile loading is achieved with the collar-technique where the specimen, having the shape of a standard tensile specimen, is screwed into the ends of the two bars and a collar made of high strength steel is placed over it. Upon loading, the compressive wave in the receiver bar is transmitted through the collar, while the specimen does not take a part in the compressive loading stage. At a later time, the stress waves reach the end of the bars and reflect back towards the specimen. The interaction of the two release waves loads the specimen in tension. At this stage the collar is detached from the bars and the tension acts only on the specimen. The same analysis of the strain gauge signals is used to derive the stress–strain response of the specimen under dynamic tension. This test configuration was used by Rosenberg et al. (1986) to heat the specimen in order to obtain high temperature dynamic stress–strain curves for several metals. The heating of the specimens has to be both localized and fast in order to avoid excessive heating of the bars. These requirements were met by using induction heating coils, as shown schematically in Fig. 1.15.

The collars in these tests were made of a high strength ceramic material in order to avoid their heating by the eddy currents which should flow only in the specimen. The heating times of the specimens with this system are typically less than a minute and their temperatures, as measured by a thermocouple inserted through a hole in the collar, can reach 1,000°C.

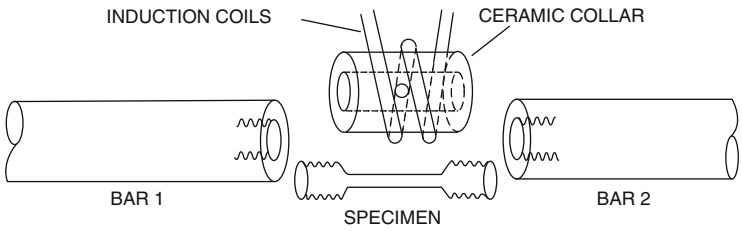

Fig. 1.15 The induction heating setup in a tensile Kolsky bar test

1.3 The Common Threats in Terminal Ballistics

This book is focused on the terminal ballistics of the more common threats which are encountered in the battlefield. These threats belong to the following four families (1) small arms projectiles, (2) fragment simulating projectiles (FSP), (3) long rods, (4) shaped charge jets and explosively formed projectiles (EFPs). The small arm projectiles, which are shot from rifles and machine guns, have either soft (usually lead) or hard cores made of steel or tungsten carbide. Their diameters range between 5 and 15 mm and their muzzle velocities are in the range of 600–1,000 m/s. The armor piercing (AP) projectiles has a high hardness core (around 60Rc), which is high enough to penetrate metallic target as a rigid body. A typical AP projectile, the 0.3″ APM2, with its different constituents, is shown in Fig. 1.16.

The ogive nose shape of these cores is the most effective nose shape as far as the penetration depth of a rigid projectile is concerned. This special shape is formed by sections of two spheres whose centers are outside the projectile, as shown schematically in Fig. 1.17. The radius of these spheres (s) is usually a multiple of

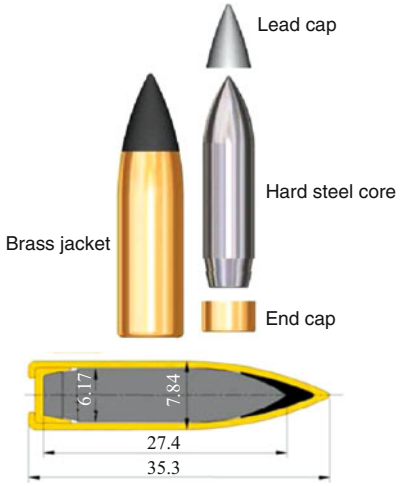

Fig. 1.16 The structure of the 0.3″ APM2 projectile. The dimensions are given in mm

Fig. 1.17 The ogive nose shape

Fig. 1.18 The fragment simulator

2–4 of the projectile's diameter, and it defines the ogival shape in terms of caliber-radius-heads (CRH). Thus, an ogive nose with s = 3D is termed 3CRH ogive.

Fragment simulators are steel cylinders with an aspect ratio of about 1.0, having diameters in the range of 5–20 mm and hardness of about 30Rc. These projectiles represent the shape of steel fragments from artillery shells, and their front face has a chiseled shape as shown in Fig. 1.18. They are usually used for testing new armor concepts which have to stop these fragments at impact velocities of about 1.0 km/s.

The shaped charge jet is formed by the collapse of a conical shell made of a ductile metal (usually copper), which is inserted in a conical cavity at the end of an explosive cylinder. Upon impact with the target the explosive cylinder is ignited and a detonation front is moving along its length. When this front reaches the copper cone it induces its symmetric collapse, which results in a long copper jet moving at velocities of several kilometers per second. In fact, these jets have a velocity gradient along their length which results in a continual stretching with time and distance. These long and thin jets (a few mm in diameter) can penetrate armor steel targets which are as thick as their length, making them a most lethal warhead against armored vehicles. Two consecutive shadowgraphs of such a jet, from Liden et al. (2008), are shown in Fig. 1.19. Note the shape of the leading portion of the jet, which is common for most shaped charge jets.

When a spherically shaped liner is inserted in the explosive cylinder, it collapses in a different way to form the so-called EFP. This is a spherically nosed rod with an aspect ratio of about 5 which moves at a velocity of about 2.0 km/s. The diameter of these EFPs, which are made of copper or tantalum, is much larger than that of shaped charge jets. Their high lethality is due to the large craters which they form in the target and the large number of debris which they

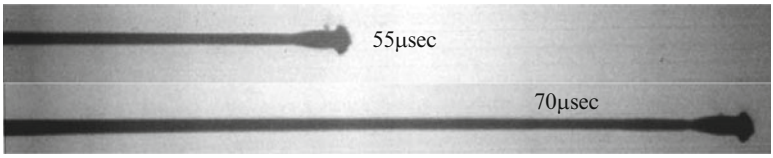

Fig. 1.19 The stretching of a shaped charge jets during its flight

propel into the inner compartment of the attacked vehicle. The debris includes the remnants of the EFP and the target material which is ejected from the crater at high velocities.

Long rod penetrators are made of high density materials, such as tungsten alloys or depleted uranium, with densities of about 17.5 g/cm^3. Their aspect ratios range between L/D = 20–30, and they are shot at velocities of about 1.7 km/s. Due to their pointed fronts they do not lose much of their velocity even after a flight distance of a couple of kilometers. These long rods replaced the older steel projectiles which had a much smaller aspect ratio, when it was realized that their depths of penetration are linearly dependent on their length. Since the compressive strength of these rods is only about 1.5 GPa, they are eroding during their impact and penetration in armor steel targets. A picture of such a rod in its early stages of flight is shown in Fig. 1.20. Note the three parts of the sabot which was used to launch the rod in the gun, as they are separated by the air drag.

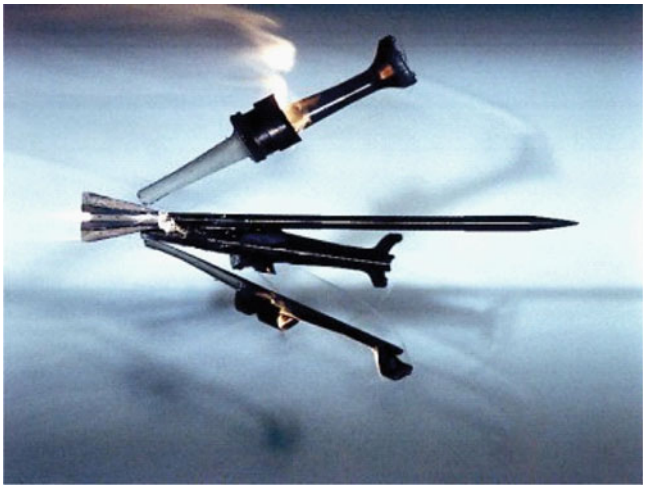

Fig. 1.20 A long rod penetrator in flight

Chapter 2
Material Models for Numerical Simulations

2.1 General Description

Numerical simulations of high velocity impact events are performed with large computer codes called hydrocodes, because their early use was for high pressure problems in which materials were treated as fluids. These codes can handle impulsive loadings which include shock waves with extremely high pressures and short rise times, as well as high temperatures and large deformations. Several review articles about hydrocodes and their use have been published over the past 30 years. As far as terminal ballistics is concerned, the reviews by Anderson (1987) and by Zukas (1990) are the most comprehensive and informative. The present chapter highlights some of the important issues concerning these codes for terminal ballistics studies. We follow Anderson's statement that "hydrocodes are the best instrumented experiment", since they can (and should) be used for sensitivity studies in terminal ballistics. These studies highlight the role of each parameter in the investigated process, and the physics behind the process is unveiled. Through the different issues presented in this book we shall demonstrate the construction and validation of analytical models with such sensitivity studies. As an example, consider the difficulty to determine experimentally the dependence of a projectile's penetration depth on the strength of the target. Any experimental attempt to vary only the strength of a target, within a large range of values, will result in some changes in its other properties as well. On the other hand, a series of simulations where only the strength of the target is varied systematically is easy to perform and it can offer the insight for this issue. Another important advantage of hydrocodes is that they can give information about events which are beyond any laboratory's performance. For example, the impact of meteors at velocities of 20–40 km/s, cannot be studied in the laboratory but it can be easily investigated with these codes.

Basically, the hydrocode is an efficient and accurate scheme for solving the set of conservation equations for mass, momentum, and energy under the initial and boundary conditions which characterize the physical event. In addition to these

Z. Rosenberg and E. Dekel, *Terminal Ballistics*,
DOI 10.1007/978-3-642-25305-8_2,

equations and problem constraints, there are two sets of data which have to be specified for all the materials involved. These are the equation of state of the material and its constitutive relations, which were discussed briefly in Chap. 1. The equations to be solved describe the behavior of a continuum, but the code is solving them by discretization techniques for both space and time, through finite difference or finite element forms. With the finite difference technique, a grid is generated to represent material points for the given geometry of the participating bodies. The continuous spatial derivatives in the equations, like df/dx, are replaced by difference equations like $\Delta f/\Delta x$, where the differences Δx are related to the cell dimensions in the grid. The same ideas are applied to the differentiation with respect with time. Values of the parameters at a certain time (t) are calculated by their values at an earlier time ($t - \Delta t$) and their corresponding time derivatives. With the finite element technique the actual differential equations are solved in small interconnected sub-regions (elements). Nodes are assigned to elements and an interpolation function is used to represent the variation of the variable over the element. Anderson (1987) discusses the four properties which have to be carefully considered in order to optimize these calculations, namely: consistency, accuracy, stability and efficiency.

The grids themselves are either Eulerian or Lagrangian and each type has its own merits and disadvantages. The Eulerian description has a spatial nature whereby the grid points and, consequently, the cell boundaries remain spatially fixed with time, while material can flow through the mesh. The net flow of material into this fixed cell volume determines its mass content, pressure, velocity etc. On the other hand, with the Lagrangian scheme, the grid is attached to the material and moves with it. With this scheme the grid points follow material paths, so it is more appropriate for cases where the material elements are less distorted. The Eulerian scheme is more useful for heavily distorted materials. An optimal combination for a situation where a rigid projectile is penetrating a soft target is obtained by using the Lagrange scheme for the projectile and the Euler scheme for the target.

One of the more important issues which have to be carefully considered is the issue of mesh size. Different results are obtained if the number of cells per unit length is not adequate. For example, it was found that for penetration studies with eroding long rods, the number of cells on the rod's radius should be at least eleven. The same density of cells should be kept in the target, at least for several projectile radii around its symmetry axis. In order to save computing time, the cell size at farther zones can be gradually increased according to their distance from the symmetry axis. The mesh cell size depends on the specific problem. As an example, a small cell size should be considered in cases where there is a fracture in the projectile or target. It is recommended that while preparing the code for its final runs, the numerical convergence with respect to mesh cell size should be checked. Another important issue, especially when material elements are expected to deform considerably, is the issue of erosion with Lagrangian codes. At large deformations the code may run into trouble when treating heavily deformed elements. The use of the erosion threshold condition is then necessary in order to eliminate elements at

a predetermined value of the plastic or geometric deformation. The erosion should be monitored constantly, and when it is too high one should replace the Lagrangian with an Eulerian code.

2.2 Material Properties

As was stated in Chap. 1, the relevant material properties for terminal ballistics belong either to their equations of state (EOS), which account for material compression at high pressures and temperatures, or to their constitutive relations, for the strength and failure characteristics. This chapter describes some of the equations of state and constitutive relations which are implemented in hydrocodes. These codes include a large data bank, which is continually updated, for the relevant parameters of the EOS and the constitutive properties for many materials.

2.2.1 The Equation of State

The equation of state (EOS) is a relation between the density of the material and the pressure and temperature which characterize its state. Usually it is given as $p = p(\rho,T)$ or $p = p(\rho,E)$, where E is the internal energy of the solid. One of the more useful EOS is the Mie-Gruneisen equation, given by:

$$p = p_H(\rho) + \Gamma\rho(E - E_H) \tag{2.1a}$$

The index H denotes the values of the parameters on the Hugoniot curve, as given by (1.4), and Γ is the Gruneisen parameter. The Mie-Gruneisen EOS is easy to apply for materials which have well-established Hugoniot curves in terms of $p_H = f(\rho)$ and $E_H = g(\rho)$. This EOS maps the off-Hugoniot states of the solid which account for its possible states after shock loading. There are several ways to present the Gruneisen parameter and one of them is through:

$$\Gamma = V_s\left(\frac{\partial P}{\partial E}\right)_{Vs} \tag{2.1b}$$

where $V_s = 1/\rho$ is the specific volume of the solid. It turns out that $\Gamma = 2.0$ for many solids at ambient conditions. Moreover, Γ is assumed to be independent on temperature and that $\Gamma\cdot\rho$ is constant for a given solid within a large range of pressures. Rosenberg and Partom (1982) demonstrated experimentally that this assumption holds for Plexiglas, by observing that a somewhat different definition of Γ can be used in conjunction with their measurements. This definition is given by:

$$\Gamma = -\left(\frac{\partial lnT}{\partial lnV_s}\right)_S \tag{2.1c}$$

This partial derivative is defined along the isentropic compression curve of the solid. Rosenberg and Partom (1982) performed direct measurements of the temperature rise and the volumetric strains of isentropically compressed Plexiglas, by using in-situ temperature and strain gauges. The isentropic loading of the specimen was achieved by a series of low amplitude shock reverberations in the specimen, and the gauges monitored its temperature and specific volume (strain) at each reverberation. Their main conclusion was that the product of $\Gamma \cdot \rho$ for Plexiglas is indeed constant within the range of their experiments.

Another EOS which is included in the libraries of most hydrocodes, is based on the Murnaghan equation for the isentropic compression of the solid, rather than on its Hugoniot, as follows:

$$p = p_S(\rho) + \gamma_m \rho (E - E_S) \tag{2.2}$$

where γ_m is the pressure derivative of the solid's bulk modulus. The Murnaghan EOS for the isentropic compression of the solid is given by:

$$p_S(\rho) = \frac{K}{\gamma_m}\left[\left(\frac{\rho}{\rho_0}\right)^{\gamma_m} - 1\right] \tag{2.3}$$

where K is the bulk modulus of the solid. As was shown by Ruoff (1967), the value of γ_m can be obtained by the relation $\gamma_m = 4S - 1$, where S is the slope of the linear relation between the shock and particle velocities in (1.5). Using a typical value of $S = 1.5$, the value for γ_m should be about 5.0, which is in accord with measured pressure derivatives of the bulk moduli for many solids.

2.2.2 The Constitutive Relations

The inclusion of the elastio-plastic behavior of solids into hydrocodes dates back to the early work of Wilkins (1964). His basic idea was to treat the elements of the stress tensor (σ_{ij}) as composed of two parts, the hydrostatic part (p) which is derived by the equation of state, and the deviatoric part (s_{ij}) which represents the geometric distortion of the material. Thus, according to this convention, the stress components are written as:

$$\sigma_{ij} = p \cdot \delta_{ij} + s_{ij} \tag{2.4a}$$

The rate of change in the deviatoric stresses is related to the strain rates through:

$$\dot{s}_{ij} = 2G\dot{\varepsilon}_{ij} \tag{2.4b}$$

where G is the shear modulus of the solid. These strain rates are decomposed to their elastic and plastic parts as follows:

$$\dot{\varepsilon}_{ij} = \dot{\varepsilon}^{e}_{ij} + \dot{\varepsilon}^{p}_{ij} \tag{2.4c}$$

Instead of working with tensors it is easier to define the equivalent (or effective) stress and strain measures, σ_{eq} and ε_{eq}, defined by:

$$\sigma_{eq} = \sqrt{\frac{3 s_{ij} s_{ij}}{2}} \tag{2.5a}$$

$$\varepsilon_{eq} = \sqrt{\frac{2 \varepsilon_{ij} \varepsilon_{ij}}{3}} \tag{2.5b}$$

with which the constitutive relations are written in the form: $\sigma_{eq} = \sigma\,(\varepsilon_{eq}, \dot{\varepsilon}, T)$.

Wilkins (1964) showed that it is easier to work within the stress space where the axes are along the principal stresses of the problem, denoted by σ_1, σ_2, and σ_3. The diagonal line in this three dimensional stress space, for which $\sigma_1 = \sigma_2 = \sigma_3$, denotes states on the hydrostatic pressure loading of the material. The equivalent stress is a measure for the distance of a given point in this space from the diagonal line. The various yield criteria define the maximum permissible value of this distance. Thus, in terms of the principal stresses the border between elastic and plastic states is a cylindrically shaped envelope around the diagonal line which corresponds to the hydrostatic loading conditions. All the states inside this yield envelope correspond to the solid's elastic range, while those on the envelope correspond to its plastic (yielded) states. By definition, the states which correspond to points outside this yield envelope are not permissible, and Wilkins (1964) suggested the procedure by which these states should be brought to the yield envelope in numerical simulations.

The equation for the yield surface in the principal stress space is given by:

$$(\sigma_1 - \sigma_2)^2 + (\sigma_2 - \sigma_3)^2 + (\sigma_3 - \sigma_1)^2 = 2Y^2 \tag{2.6a}$$

or, in its deviatoric form:

$$s_1^2 + s_2^2 + s_3^2 = \tfrac{2}{3} Y^2 \tag{2.6b}$$

The various yield criteria are, in fact, imposing a maximum value for this equivalent stress which has to be specified in the code. For example, the well-known von-Mises criterion states that the equivalent stress of the material cannot be higher than its yield strength under simple tension, $\sigma_{eq} \leq Y_0$. In terms of the yield surface in the stress space, this criterion is represented by the surface of a cylinder with a radius of Y_0, which surrounds the main diagonal ($\sigma_1 = \sigma_2 = \sigma_3$). The von-Mises criterion accounts for the yielding behavior of many metals and alloys which

exhibit elastic-perfectly-plastic characteristics. This is true for high strength materials, such as armor steels and the strong aluminum alloys. Softer metals often show an appreciable strain hardening behavior where the strength is a strong function of the strain. The stainless steel 304L is an example for a significantly hardening material, since its strength increases by a factor of 5 under plastic strains of 50%. On the other hand, steels which are referred to as rolled homogenous armor, show an almost ideal elastic-plastic behavior with no strain-hardening. One should note that the interaction between a penetrating projectile and a target is always accompanied by large strains in both materials. Thus, it is the stress at large strains, the so-called flow stress, which is the important strength property of the material for terminal ballistics. The relevant strain rates for impacts at ordnance velocities (up to about 2.0 km/s) are 10^3–10^4 s^{-1}. These are the rates covered by the Kolsky bar system which is the main reason for its extensive use. One has to consider the fact that the strength of most solids increases at high confining pressures, while high temperatures reduce their strength (thermal-softening). Thus, a complete constitutive relation for the strength of the solid should include all the data concerning the effects discussed here. Some of these constitutive models, which are implemented in hydrocodes, are described next.

The constitutive equation proposed by Johnson and Cook (1983) is one of the more popular in the field of terminal ballistics. This equation, which is referred to as the JC model, includes the effects of plastic strain, strain rate, pressure, and temperature on the material strength, as follows:

$$Y = \left[A_1 + A_2 \varepsilon_p^n\right] \cdot \left[1 + A_3 \ln\left(\dot{\varepsilon}_p^*\right)\right] \cdot \left[1 - T_H^m\right] \tag{2.7}$$

where A_1, A_2, A_3, n and m, are material constants. ε_p is the equivalent plastic strain, and $\dot{\varepsilon}_p{}^* = \dot{\varepsilon}_p/\dot{\varepsilon}_0$, is the normalized plastic strain rate with $\dot{\varepsilon}_0 = 1.0$ as the reference rate. The homologous temperature (T_H) is defined by the room and melting temperatures (T_{room} and T_m), according to:

$$T_H = \frac{T - T_{room}}{T_{melt} - T_{room}} \tag{2.8}$$

Another material model which is frequently used for high pressure impacts is the rate-independent model of Steinberg (1987). According to this model the changes in the flow stress (Y), with high pressures and temperatures, are equal to the corresponding changes in the shear modulus (G) of the material. The relations for Y(p,T) and G(p,T) are given by the following expressions:

$$Y(p,T) = Y_0 \cdot \frac{G(p,T)}{G_0}\left(1 + \beta_p \varepsilon\right)^n \tag{2.9a}$$

$$G(p,T) = G_0 \cdot \left[1 + \frac{G_p'}{G_0} \cdot \frac{p}{\eta^{1/3}} + \frac{G_T'}{G_0}(T - 300)\right] \tag{2.9b}$$

where β_p and n are material parameters, ε is the effective plastic strain and $\eta = \rho/\rho_0$ is the compression ratio of the solid. The primed parameters, with the subscripts p and T, are the derivatives of G with respect to pressure and temperature, respectively, at the reference state (T = 300 K, p = 0).

A third family of constitutive equations is due to Zerilli and Armstrong (1987), shortly termed the ZA model. Unlike the JC model, which is basically an empirical one, the constitutive equations of the ZA model are based on dislocation dynamics theory. They treat face centered (FCC) and cubic centered (BCC) metals differently, since the rate and temperature sensitivities are very different for these two families of materials. Their constitutive equations are given by:

$$\sigma_{eq} = \sigma_0 + kd^{-0.5} + C_2\varepsilon^{0.5}\exp[-C_3T + C_4T\ln\dot{\varepsilon}] \quad \text{For FCC materials} \quad (2.10a)$$

$$\sigma_{eq} = \sigma_0 + kd^{-0.5} + C_1\exp[-C_3T + C_4T\ln\dot{\varepsilon}] + C_5\varepsilon^n \quad \text{For BCC materials} \quad (2.10b)$$

where $C_1 \ldots C_5$ and n are material parameters. The Hall-Petch relation, between the strength of a metal and its average grain diameter (d), has been taken into account.

2.2.3 Failure of Ductile Materials

The models described above treat the changes in the material's effective strength through its hardening and softening mechanisms. The characterization of these changes is important for ductile materials which can withstand large plastic strains before they fail. Ductile materials fail either under tension or by shear when a certain threshold strain is reached. The failure of a specimen is defined by the loss of cohesion in its interior, leading to either its complete disintegration or to some inner damage which is manifested by the appearance of new free surfaces inside the specimen. Fracture under tension is the end result of the coalescence of small voids, forming macroscopic free surfaces inside the specimen. The processes of void nucleation and growth in ductile materials, under dynamic loading conditions, have been investigated by many workers and the review article of Curran (1982) gives a comprehensive account of this field. Fracture under shear is usually the end result of the appearance of shear bands in the specimen at the highest shear locations. These bands are very narrow zones in which voids are eventually developed, leading to failure by their coalescence when the shear strains in the bands exceed their limiting values. In contrast, brittle materials fail within their elastic response regime, with negligible straining, and their main mode of failure involves microcrack nucleation and coalescence, as discussed in the next section.

Johnson and Cook (1985) proposed a fracture criterion for ductile materials, which is especially suited for numerical codes. This criterion is based on the

maximum strain to fracture (ε_f) of an element, which depends on its strain path, strain-rate, and temperature. It also depends on the stress triaxiality, which is defined by $\sigma^* = \sigma_m/\sigma_{eq}$, where σ_m is the local pressure as calculated by the average of the three principal stresses in each element. This is a very important parameter, since the propensity of ductile materials to fail is strongly dependent on the pressure exerted on them. Compressive stresses tend to prevent failure by closing voids and microcracks, while tensile stresses enhance failure by further opening them. The influence of stress triaxiality according to various models is based on the void growth model of Rice and Tracey (1969). Different stress triaxialities are not easily achieved in well defined experiments, since it is difficult to accurately define the real state of a specimen, especially under complex loading situations. One of the more popular techniques for generating different stress triaxialities, was suggested by Bridgman (1952), and is based on varying the notch radius in the midsection of a tensile specimen. This is a relatively simple and straightforward technique which is easy to analyze through numerical simulations.

The dependence of fracture strain on the stress triaxiality for the structural steel Weldox 460E, as obtained by Hopperstad et al. (2003), is shown Fig. 2.1. Note that according to this representation, tensile and compressive stresses correspond to positive and negative triaxialities, respectively, while pure shear corresponds to zero triaxiality. Obviously, under compressive stresses the fracture strain increases markedly with stress triaxiality since high pressures oppose the opening of voids and cracks. In fact, there are some models according to which these graphs rise asymptotically to infinite fracture strains at a compressive triaxiality of $\sigma^* = -1/3$.

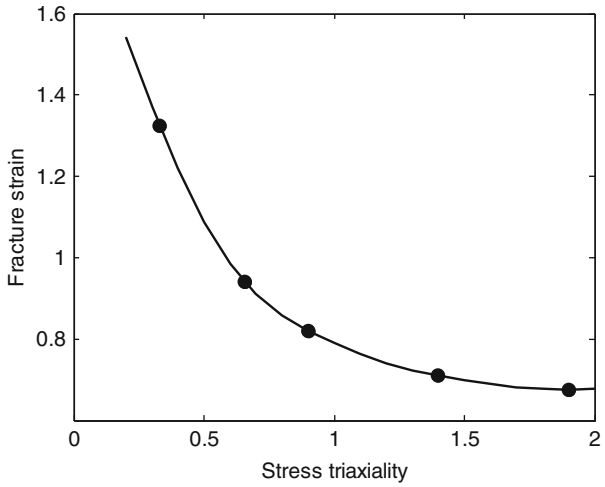

Fig. 2.1 The dependence of fracture strain on the stress triaxiality for Weldox 460E steel

The JC failure model defines a continuous degree of damage (D_f), in the element under consideration, which is given by:

$$D_f = \sum \frac{\Delta \varepsilon_{eq}}{\varepsilon_f} \tag{2.11a}$$

where $\Delta\varepsilon_{eq}$ is the increment of accumulated equivalent plastic strain during an integration cycle and ε_f is the equivalent plastic strain at fracture. This value is reached when the damage function (D_f) reaches the value of 1.0. The failure strain is given by the following functional form:

$$\varepsilon_f = [D_1 + D_2 \exp(D_3 \sigma^*)] \cdot \left[1 + D_4 \ln\left(\dot{\varepsilon}_p^*\right)\right] \cdot [1 + D_5 T_H] \tag{2.11b}$$

where $D_1 \ldots D_5$ are constants which have to be calibrated for each material.

The dynamic failure of metals and alloys under impulsive loading conditions is usually manifested by gross shearing at material interfaces, as a result of large velocity gradients at those locations. In many cases these large shear strains appear in very narrow bands which have been termed adiabatic shear bands (ASB). This failure mechanism, which is due to thermo-mechanical instabilities, is one of the more common failure modes under dynamic loading at strain rates of about $10^3\ s^{-1}$. The narrow shear bands often contain material which experienced a structural phase transformation, in which case they are referred to as transformation bands. The phenomenon of adiabatic shear banding received a lot of attention because of their importance for both military and industry applications. Bai and Dodd (1992) summarize much of the data and the analysis concerning this phenomenon. Important articles concerning the nature of ASBs are those of Staker (1981), Rogers (1983), Timothy and Hutchings (1985), and Giovanola (1988a, 1988b). Although many aspects of this issue have been highlighted in these studies, its physical picture is not complete because, in addition to the instabilities involved, the shear bands often include microcracks which initiate and grow during band growth. The work of Giovanola (1988a, 1988b) on 4340 steel under pure shear, highlights the interconnection between the thermo-mechanical shear instability, which acts at the first stage of the process, and the subsequent coalescence of microvoids which leads to fracture within the band at the subsequent stage.

The mechanism proposed by Zener and Hollomon (1944) accounts for the thermo-mechanical instability which initiates the adiabatic shear bands. The analysis starts by writing the differential for the shear stress, $\tau = \tau(T,\varepsilon,\dot{\varepsilon})$, which depends on the temperature, strain, and strain rate in the solid, in the following way:

$$d\tau = \left(\frac{\partial \tau}{\partial T}\right)_{\varepsilon,\dot{\varepsilon}} dT + \left(\frac{\partial \tau}{\partial \varepsilon}\right)_{\dot{\varepsilon},T} d\varepsilon + \left(\frac{\partial \tau}{\partial \dot{\varepsilon}}\right)_{\varepsilon,T} d\dot{\varepsilon} \tag{2.12a}$$

from which one obtains:

$$\frac{d\tau}{d\varepsilon} = \left(\frac{\partial \tau}{\partial T}\right)_{\varepsilon,\dot{\varepsilon}} \frac{dT}{d\varepsilon} + \left(\frac{\partial \tau}{\partial \varepsilon}\right)_{\dot{\varepsilon},T} + \left(\frac{\partial \tau}{\partial \dot{\varepsilon}}\right)_{\varepsilon,T} \frac{d\dot{\varepsilon}}{d\varepsilon} \tag{2.12b}$$

The instability condition is defined by $d\tau/d\varepsilon = 0$ which, for a constant strain rate experiment, occurs when:

$$\left(\frac{\partial \tau}{\partial \varepsilon}\right)_T = -\left(\frac{\partial \tau}{\partial T}\right)_\varepsilon \left(\frac{d\varepsilon}{dT}\right)^{-1} \tag{2.13}$$

Since these bands form under adiabatic conditions the generated heat cannot diffuse out of the bands themselves. Thus, one can write the following equation for the temperature rise in the bands, due to their plastic deformation:

$$\rho C_v dT = \tau d\varepsilon \tag{2.14a}$$

where ρ is the density of the specimen and C_v is its specific heat. From this relation one obtains:

$$d\varepsilon/dT = \rho C_v/\tau \tag{2.14b}$$

In order to predict the critical shear strain for adiabatic shearing from these equations, one needs to have the constitutive equation for the material. Assuming a power law dependence of the shear stress on shear strain, such as $\tau = N{\cdot}\varepsilon^n$, the threshold value of the strain (ε_i) which marks the onset of thermo-mechanical instability, is given by:

$$\varepsilon_i = n\rho C_v \left(\frac{\partial \tau}{\partial T}\right)_{\varepsilon,\dot{\varepsilon}} \tag{2.15}$$

This relation has been shown to account for the experimental results in many cases, but not for all of them, as discussed by Bai and Dodd (1992). Some confusion about the true nature of adiabatic shear bands arises from the fact that in many cases they appear in specimens with sharp corners, where a geometrically forced stress concentration is responsible for the shear failure. This issue will be further discussed in Chap. 4, where we discuss the importance of adiabatic shearing for plate perforation by blunt-nosed projectiles.

A dynamic stress–strain curve for a specimen of the titanium alloy Ti–6Al–4V, which was compressed by the Kolsky bar in our lab, is shown in Fig. 2.2. One can clearly see that at a compressive strain of about 20% the disc shaped specimen lost its load capacity. On the other hand, loading a disc of this titanium alloy in a static Instron machine resulted in its failure at a strain of about 50%. Thus, the adiabatic nature of the failure in this alloy is clearly manifested by the much lower value for the failure strain under dynamic loading, as compared to its value under quasi-static conditions.

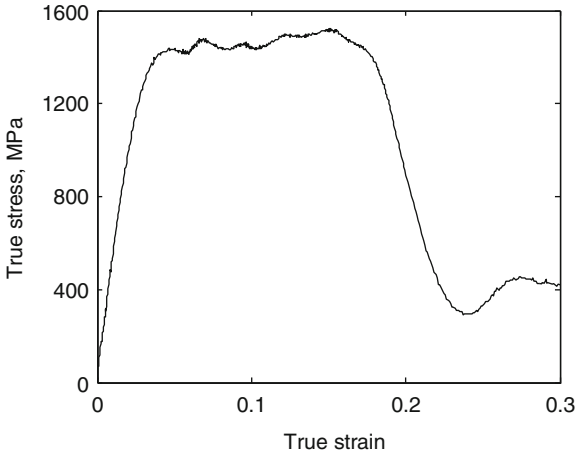

Fig. 2.2 The dynamic stress–strain curve for the Ti–6Al–4V alloy

2.2.4 Failure of Brittle Materials

The dynamic behavior of brittle materials, such as glass and ceramics, is quite different and more complicated than that of ductile metals and alloys. First, there is a large difference between the compressive and tensile strengths of a brittle solid, which can reach a factor of 10 and more. By definition, brittle solids fail within their elastic range of response, with practically no plastic straining. Their failure behavior is pressure dependent, with relatively very small (if any) strain rate sensitivity. Also, the damaged zone in a brittle material can spread from the impact point, through cracks which run in all directions, affecting the properties of a large volume in the brittle solid. The different constitutive equations which describe the failure thresholds of brittle materials are based on the classical work of Griffith (1920, 1924) who analyzed the stresses around an open elliptic flaw in a plate under biaxial stress loading. Griffith followed the analysis of Inglis (1913) who showed that even when the far end stresses are compressive, the stresses at the tips of the flaw are tensile. With increasing stress at the plate boundaries, these tensile stresses reach a critical value (σ_0), which is a material property, leading to uncontrolled crack growth. Denoting the two far-end stresses which act on the plate as σ_1 and σ_2, Griffith derived the following relations expressing the critical conditions for the brittle failure:

$$\sigma_2 = \sigma_0 \qquad \text{if:} \quad 3\sigma_2 + \sigma_1 > 0 \tag{2.16a}$$

$$(\sigma_1 - \sigma_2)^2 = 8\sigma_0 \cdot (\sigma_1 + \sigma_2) \qquad \text{if:} \quad 3\sigma_2 + \sigma_1 < 0 \tag{2.16b}$$

Note that tensile stresses are positive and compressive stresses are negative in this formulation. These equations give the failure envelope of a brittle solid in the

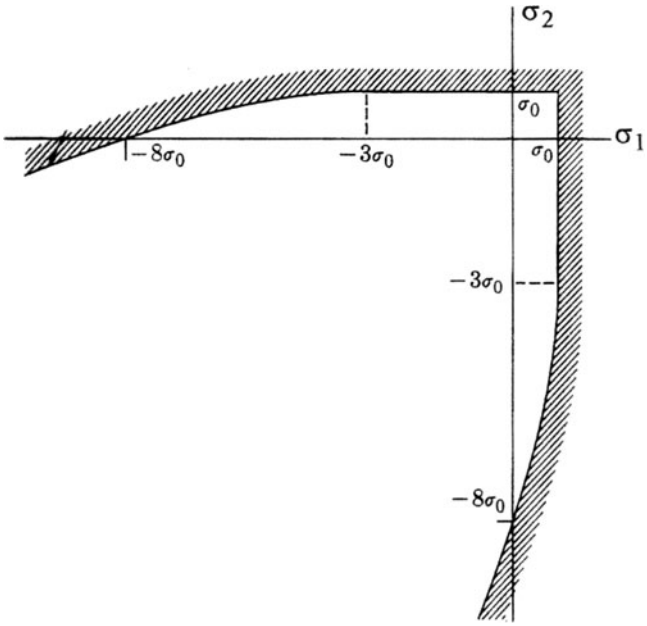

Fig. 2.3 The failure envelope for brittle materials, according to Griffith's theory

(σ_1,σ_2) plane, as shown in Fig. 2.3. All the states which are described by points inside the two curves correspond to intact material, while those outside the curves correspond to failure situations. Hydrostatic compressions, which correspond to the third quadrant in this figure, enhance the integrity of the brittle solid, as expected. According to Griffith's model the critical tensile strength (σ_0) of the solid is smaller by a factor of 8 than its compressive strength under uniaxial stress loading. Later works, by McClintock and Walsh (1962) for example, resulted in a factor of 10 between these two strength thresholds. Other refinements of these models, as well as data for concrete and ceramics, can be found in Paterson (1978).

The Griffith failure criterion which, in effect, defines the strength of a brittle solid under compression and tension, is very different from the yield criteria for ductile materials which were discussed above. Thus, the relation between the Hugoniot elastic limit (HEL) of a brittle solid and its dynamic strength (Y_d) should be different than the corresponding relation, (1.6), for ductile materials which follow the von-Mises yield criterion. The relation for brittle solids should be based on the Griffith criterion, 2.15, and Rosenberg (1993) derived the following relation by considering the Griffith criterion:

$$Y_d = \frac{(1-2\nu)^2}{1-\nu} \cdot HEL \tag{2.16}$$

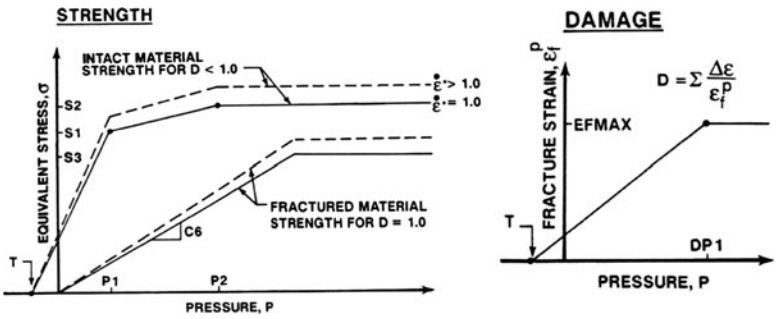

Fig. 2.4 The JH-I model for the constitutive equations of brittle materials

where ν is Poisson's ratio of the ceramic. Thus, according to the Griffith criterion, the dynamic strength of a brittle specimen is smaller by a factor of $(1-2\nu)$ than the strength deduced from (1.6) which is based on the von-Mises yield criterion.

The first numerical simulations for terminal ballistics applications involving ceramic tiles were performed in the late 1960s by M. L. Wilkins and his colleagues, as described by Wilkins (1978). This work will be described in the third part of this book, where we review the work on ceramic armor. The failure criterion in Wilkins' work was based on a maximum tensile strength, which was set at $\sigma_0 = 0.3$GPa in his simulations. The first implementation of the Griffith model itself, for ceramic tiles in terminal ballistics simulations, was by Mescall and Tracy (1986). Johnson and Holmquist (1990, 1993) further developed the Griffith model and included a damage function at every time step in the simulation. The various parameters in the first version of their model (JH-1) are shown in Fig. 2.4, for the strength and the damage functions of a brittle material. The model distinguishes between the tensile and compressive strengths which are denoted by T and S, respectively, in the figure. The compressive strength is linearly dependent on pressure at the low pressure range, and it reaches an asymptotic value which depends on the strain rate. The damage function is calculated continuously at each time step in the simulation, and it lowers the strength of the material to values which are determined by the curves denoting the strength of the fractured material. This model will be further discussed in Chap. 6 where we deal with ceramics for armor applications.

2.2.5 The Spall Failure

It was noted earlier that spalling is a unique failure phenomenon, which takes place under dynamic conditions when shock waves which are reflecting from free surfaces as release waves, induce high tensions in the solid. If the amplitude of these tensile waves is high enough, the material fails and a spall is created near its free surface. The relevance of this mode of failure for terminal ballistics can be seen

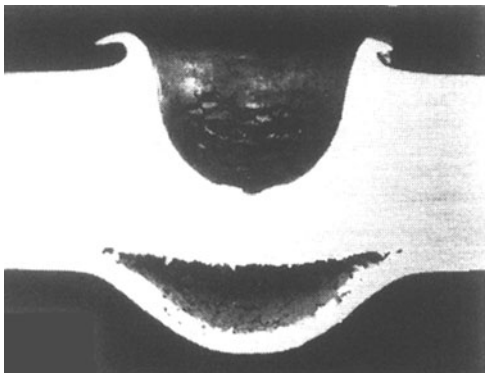

Fig. 2.5 Spall failure in an aluminum plate impacted by a glass sphere

in sectioned targets, which have been impacted by relatively blunt projectiles at high impact velocities. For example, the spall in an annealed 1100 aluminum plate impacted by a glass sphere, from the work of Horz et al. (1994), is clearly seen Fig. 2.5. The diameter of the sphere (3.18 mm) was about a quarter of the plate thickness, and its impact velocity was 6.0 km/s.

The study of spall failure in solids has been the focus of a large amount of research for over 50 years. The early models assigned a threshold tensile strength to the specimen, which was calibrated by one-dimensional shock wave experiments, as discussed in Chap. 1. Subsequent developments showed that even under these simple conditions the spall process is more complicated, and that its time dependence should be taken into account, as was noted by Tuler and Butcher (1968). Many models were developed in order to account for this type of failure and the article of Curran (1982) describes those which are based on the nucleation of defects and their growth (the so called NAG models). The time dependence of the spall process leads to scaling effects which were the focus of an intense research by Russian researchers, as summarized by Ogorodnikov et al. (1999). The dependence of the spall failure on the tensile impulse, rather than on a threshold stress, has been highlighted by the work of Gray et al. (2007). They showed that a square shaped tensile pulse and a triangular shaped pulse can cause the same amount of incipient spall if they induce a similar stress-time impulse at the spall plane in the specimen. Thus, according to Gray et al. (2007), the tensile impulse is the important factor for the spall phenomenon, rather than the amplitude of the tensile wave.

Grady (1988) proposed energy balance considerations to establish the loading conditions at which spall occurs. This approach accounts for the transition between brittle and ductile spall failures, which has been observed for several materials when the loading conditions are changed. As an example, consider the sectioned 6061-T6 aluminum targets from the plate-impact experiments of Christman et al. (1971), as shown in Fig. 2.6. A marked difference in the void shape is clearly seen in these plates, which were subject to tensile stresses of different durations and rates. The round shaped voids, in the specimen at the left side, suggest a ductile spall mechanism for the shorter pulse duration (higher rate). On the other hand, a brittle

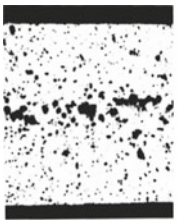

Fig. 2.6 Different void shapes in aluminum alloy plates subjected to tensile pulses of different durations

spall is evident in the cross section of the specimen on the right hand side, which was subjected to a tensile pulse of a longer duration (and lower rate). The different loading rates in the two experiments resulted in from the different thicknesses of the impactor and the target in these experiments. Note that in both cases the specimens are only partially spalled, a phenomenon which is termed "incipient spall". A full spall process is characterized by the complete coalescent of the voids, leading to a clear opening inside the specimen, as shown in Fig. 2.5.

The analysis of Grady (1988) is based on macroscopic material properties, such as the fracture toughness and the flow stress of the material, resulting in a predictive tool for the occurrence of spall under given loading conditions. This analysis leads to the following relations between the spall strengths for both ductile and brittle materials, and their relevant properties and loading conditions:

$$P_{spall} = \left(3\rho\, C_0 K_c^2 \dot{\varepsilon}\right)^{1/3} \quad \text{For brittle spall} \tag{2.17a}$$

$$P_{spall} = \left(2\rho\, C_0 Y \varepsilon_f\right)^{1/2} \quad \text{For ductile spall} \tag{2.17b}$$

where ρ and C_0 are the specimen's density and sound speed, respectively, Y is its flow stress and K_c is its fracture toughness. The strain rate ($\dot{\varepsilon}$) in the experiment is important for the brittle fracture, while the strain to failure (ε_f) plays an important role for the ductile failure mode.

Rosenberg (1993) analyzed the spall failure in brittle materials through the Griffith failure model and derived the following relation between the spall strength and the HEL:

$$\sigma_{spall} = \frac{(1-2\upsilon)^2}{8(1-\upsilon)} \cdot HEL \tag{2.18}$$

where ν is the Poisson ratio of the solid. This expression results in a factors of 15–25 between the HEL and the spall strength of brittle materials with Poisson's ratios in the range of ν = 0.15–0.25. Such factors are often measured for strong ceramics having spall strengths of 0.3–0.6GPa and HEL values in the range of 6.0–15.0 GPa.

A rather simple model for the spall strength of ductile materials was proposed by Rosenberg (1987). This model is based on the cavity expansion analysis of Bishop et al. (1945) for the minimal pressure which has to be applied on the walls of a small cavity, inside an elasto-plastic solid, in order to expand its volume. The cavity expansion process and its relevance to penetration mechanics will be discussed in Chap. 3. Assuming that spall is initiated by a process which is similar to the cavity expansion process, Rosenberg (1987) derived the following expression for the spall strength of ductile solids:

$$\sigma_{spall} = \frac{2Y}{3}\left[2 + \ln\left(\frac{E}{3(1-\upsilon)Y}\right)\right] \tag{2.19}$$

where E and Y are the Young modulus and strength of the solid, respectively. The predicted spall strengths of various materials, as calculated by this expression, were found to be close to their corresponding experimental results. For example, this expression results in: $\sigma_{spall} = 1.7$, 3.6 and 4.6 GPa, for an aluminum alloy with strength of $Y = 0.4$ GPa, steel with $Y = 0.8$ GPa and the titanium alloy Ti/6Al/4V with strength of $Y = 1.2$ GPa, respectively. These values are very close to the experimentally derived spall strengths of these materials.

Part II: Penetration Mechanics

This part of the book deals with the physical processes which take place during the penetration of various targets by different penetrators, a subject which has been termed Penetration Mechanics. The penetration processes in targets made of metals, ceramics, polymers or woven fabrics, are usually treated separately, because of their different properties. Projectiles are classified according to their mode of penetration as small arms bullets, long rods, shaped charge jets, and fragment simulators (FSPs). These threats are referred to as penetrators, a term which will be used frequently here. The large range of impact velocities results in different failure modes for both penetrators and targets, leading to further complexities with classification schemes in this field. The simplest velocity classification includes: the low velocity range (below 500 m/s), the ordnance velocity range (between 500 and 2,000 m/s) and the hypervelocity range (above 2,000 m/s). This part of the book is focused on the penetration into metallic target, due to their importance for armor applications. The penetration of rigid penetrators into semi-infinite targets is discussed in Chap. 3. Semi-infinite targets are defined as large enough so that their lateral and back surfaces do not influence the penetration process. The perforation of finite thickness plates is discussed in Chap. 4, and the penetration of eroding penetrators is summarized in Chap. 5. The interactions of various penetrators with ceramics, polymers and woven fabrics, are described in the third part of the book. The properties of these materials will be highlighted through their improved ballistic performance for armor applications.

Chapter 3
Rigid Penetrators

3.1 The Mechanics of Deep Penetration

The penetration of a very thick (semi-infinite) target by a rigid projectile has been the subject of intense research for over two centuries. A large number of empirical relations and engineering models have been proposed over these years, as reviewed Backman and Goldsmith (1978). These relations account for the penetration depth of a given projectile in terms of its impact velocity, and they differ by the basic assumptions concerning the retarding forces (stresses) on the projectile. With the recent advancements in the quality and reliability of numerical simulations, these analytical models can be further validated, as will be demonstrated in this chapter. We start the discussion with a short review of the more popular models which have been proposed over the years. This is followed by a careful examination of a certain set of experimental data, which will lead to the proper choice of an analytical model for the deep penetration by rigid penetrators. Numerical simulations are then used in order to enhance the validity of this model and to explore the role of its physical parameters.

The penetration process of a rigid penetrator is determined by the retarding force which the target exerts on it during penetration. Since, by definition, the mass (M) of the rigid penetrator does not change during penetration, the process is governed by its deceleration (a). Thus, the following discussion concentrates on the deceleration of a rigid penetrator. Replacing the time variable (dt) with the penetration increment (dx), the deceleration is given by:

$$a = \frac{dV}{dt} = V\frac{dV}{dx} \tag{3.1a}$$

which can be rewritten as:

$$dx = \frac{V}{a(V)}dV \tag{3.1b}$$

Z. Rosenberg and E. Dekel, *Terminal Ballistics*,
DOI 10.1007/978-3-642-25305-8_3,

The penetration depth (P) of the rigid penetrator is obtained by integrating this equation between the boundaries: V = V_0 at x = 0, and V = 0 at x = P. The only unknown in this equation is the actual dependence of the deceleration on penetration velocity, a = a(V). Various functional forms for a(V) have been suggested over the years for different projectile/target combinations, and all of them are special cases of the general expression:

$$a(V) = C + AV + BV^2 \tag{3.2}$$

where the constants A, B and C have been determined empirically for each set of experiments.

The most popular forms for a(V) are:

$$\text{Euler} - \text{Robins} \quad a = C = const \tag{3.3a}$$

$$\text{Poncelet} \quad a = C + BV^2 \tag{3.3b}$$

$$\text{Resal} \quad a = AV + BV^2 \tag{3.3c}$$

The first expression, with the constant deceleration, was suggested (independently) by the great mathematician Leonard Euler (1745) and the gun engineer Benjamin Robins (1742). The second and third equations are attributed to Poncelet (1835) and Resal (1895), respectively. Inserting these expressions for a(V) in (3.1b) and integrating between the boundary conditions, results in the following expressions for the final penetration depth (P) in terms of impact velocity (V_0):

$$P = \frac{V_0^2}{2C} \tag{3.4a}$$

$$P = \frac{1}{2B} \ln\left(1 + \frac{BV_0^2}{C}\right) \tag{3.4b}$$

$$P = \frac{1}{B} \ln\left(1 + \frac{BV_0}{A}\right) \tag{3.4c}$$

Clearly, the various expressions for a(V) result in different relations for the final penetration depth of a rigid penetrator. There are several ways by which the actual dependence of a(V), for a given projectile/target pair, can be determined. The most obvious one is to measure the deceleration history during penetration. Such measurements have been performed for projectiles penetrating soil and concrete, as in Forrestal et al. (1984). However, these measurements are not accurate enough and they are difficult to perform with other target materials. Another way to determine the functional form of a(V) is through theoretical models which are based on some physical principles, such as the conservation laws. Due to the complexity of

the process, this route did not result in a clear answer either. The third possibility, which is the one we adopt here, is based on analyzing experimental data of P = P (V_0) for a given rigid penetrator, in order to infer the actual dependence of its deceleration on velocity. The conclusions from this analysis will be further enhanced through numerical simulations.

In order to determine the functional dependence of a(V) one needs a reliable set of experiments where the values of P = P(V_0) are given for a large range of impact velocities. The extensive studies of M. Forrestal and his colleagues offer a wealth of such data, as in Forrestal et al. (1988), Forrestal et al. (1991), and Piekutowski et al. (1999), for example. These works include accurate measurements of impact velocities and penetration depths of hardened steel rods impacting thick aluminum targets. The aspect ratios of these rods were in the range of L/D = 10–15, where L and D are rod length and diameter, respectively. The rods had different nose shapes (conical, ogive and spherical) and the aluminum targets were of the 6061-T651 alloy. The largest range of impact velocities for which these rods remained rigid, was obtained by Piekutowski et al. (1999) for L/D = 10 ogive-nosed rods. Impact velocities in these experiments reached 1.82 km/s with no sign of rod deformation. The data from this set of experiments will be used now in order to construct the analytical model for the deep penetration of rigid long rods.

We start the analysis with the simplest assumption possible, namely, that the average deceleration of these ogive-nosed rods does not depend on their velocity. This is the assumption behind the Euler–Robins model which leads to the simplest penetration relation, (3.4a). The validity of this assumption can be easily checked by using the experimental data of Piekutowski et al. (1999), in order to calculate the average rod deceleration (a_{av}) in each experiment, through the expression:

$$a_{av} = \frac{V_0^2}{2P} \tag{3.5}$$

Table 3.1 presents the data from Piekutowski et al. (1999) in terms of the impact velocity and penetration depth for each experiment, together with the corresponding values for a_{av} as determined by (3.5).

Table 3.1 The data from Piekutowski et al. (1999), and the average decelerations of the ogive-nosed rods

V_0 (m/s)	P (mm)	a_{av} (10^{-3} mm/μs^2)
570	55	2.95
679	72	3.2
821	102	3.3
966	140	3.33
1,076	160	3.62
1,147	190	3.46
1,255	229	3.44
1,348	254	3.58
1,538	332	3.56
1,654	389	3.52
1,786	452	3.53
1,817	462	3.57

It is clear that, except for the low velocity experiments, this set of results strongly supports the Euler–Robins model since the average decelerations are practically independent on impact velocity. This independence over a wide range of impact velocities means that the deceleration of the rod was constant during each experiment, with an average value of: $a = 3.55 \cdot 10^{-3}$ mm/μs^2. Figure 3.1 demonstrates the agreement between the experimental results of Piekutowski et al. (1999) and the model's predictions through (3.4a) with this value for the constant deceleration. The rods in this set of experiments were made of two different steels, the VAR 4340 steel and the stronger AerMet 100, which remained rigid at higher impact velocities. As was demonstrated by Rosenberg and Dekel (2009a), the same conclusion about the constant deceleration of long rods at deep penetrations, is obtained by examining the data for rods with other nose shapes (conical, spherical). Thus, we conclude that the deep penetration of rigid rods in semi-infinite metallic targets is characterized by a constant deceleration process. This conclusion holds for impact velocities beyond the low velocity range where the decelerations are somewhat lower due to the target's free impact face, as discussed below.

The impact face of the target exerts a lower retarding force on the penetrator since the target material around the rod can flow backwards. In contrast, at deep penetration the target material is "pushed" forward or sideways by the advancing penetrator. This is the so called "entrance phase effect", which accounts for the relatively higher penetrations (lower decelerations) of rigid penetrators at the low impact velocity range. The low velocity experiments of Piekutowski et al. (1999) are within the influence range of the entrance phase, and they are underestimated by the constant deceleration model, as is clearly seen in Fig. 3.1. In the next sections we shall quantify the influence range of the impact face through a numerically-based model which accounts for the entrance phase effect.

The next step is to use numerical simulations in order to validate the conclusion concerning the constant deceleration of the rigid rod, and to determine the physical

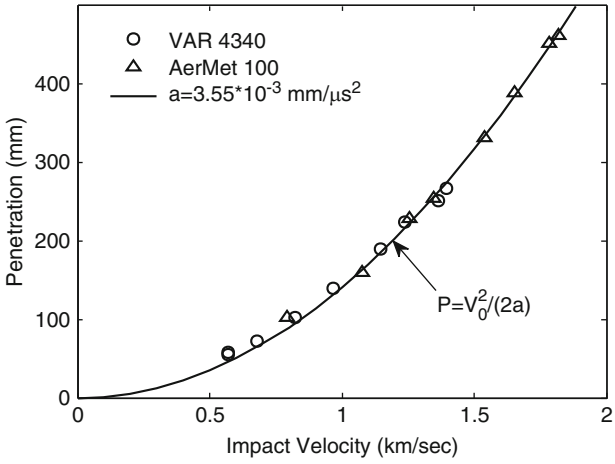

Fig. 3.1 Comparing the constant deceleration model with the data for ogive nosed steel rods

parameters which govern this deceleration. These numerical simulations, with the AUTODYN-2D code, were described in detail in Rosenberg and Dekel (2009a) and we summarize their findings here. The rigid rods were simulated with the Lagrange processor of the code, using a value of 50 GPa for their yield strength, in order to prevent their plastic deformation at all impact velocities. The Eulerian processor, which handles large deformations in a better way, was used for the targets in these simulations. The constitutive relations for the targets were based on the simple elasto-plastic model, using the von-Mises criterion with no strain hardening or strain rate effects in order to simplify the analysis.

Consider first the penetration and velocity histories of L/D $=$ 20 steel rods with different nose shapes, impacting a semi-infinite aluminum target with strength of 0.4 GPa, at $V_0 = 1.0$ km/s, as shown in Fig. 3.2. Clearly, the ogive-nosed rod is the

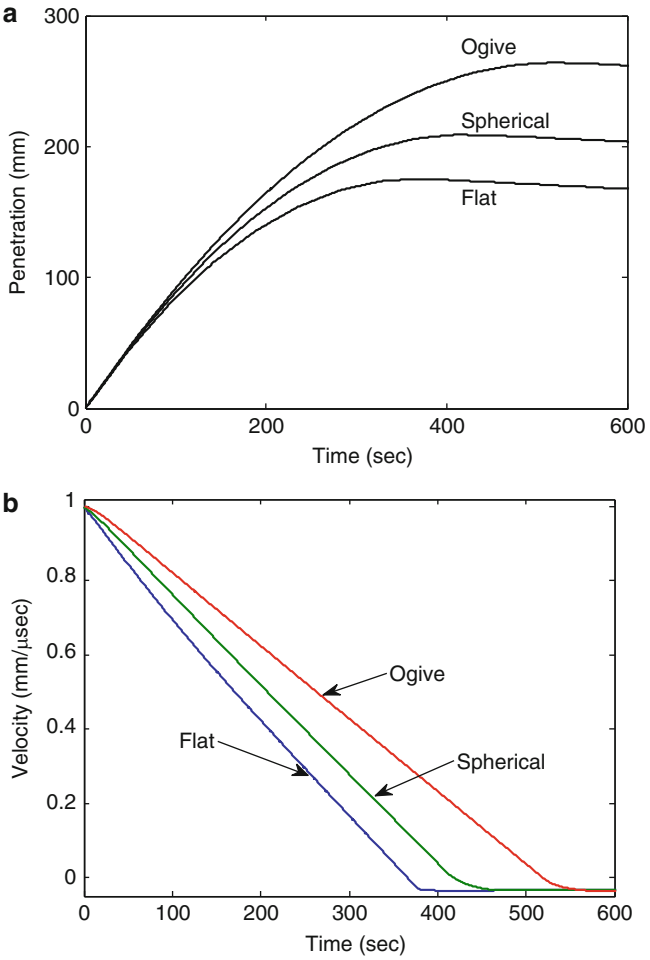

Fig. 3.2 Simulation results of penetration and velocity histories for different nose shaped rods

most efficient one since its final penetration depth is the highest, while the flat-nosed rod is the less efficient, as expected. The slight decrease in penetration depths seen at the later times of these penetration histories is due to the elastic rebound of the target, which pushes the projectile backwards at the end of the process. Final penetration depths should be determined by their maximal values in the simulations. Figure 3.2b shows the velocity histories of these rods and it is clear that their corresponding decelerations, as determined by the slopes of these histories, are practically constant. Moreover, the corresponding slopes of these velocity histories suggest that the least deceleration is obtained for the ogive-nosed rod and the highest for the flat ended rod. This relatively straightforward result needs further investigation because of its importance.

We now follow the actual mechanism which governs the velocity changes of a rigid rod during its deep penetration. Any change in the velocity of the rod's nose takes a certain time to reach its tail, since it must be transmitted by an elastic wave which travels along the rod. Upon reaching the rod's tail this elastic wave travels back towards the nose of the rod as a release wave. Thus, the actual process of rigid rod deceleration is achieved by a series of elastic waves reverberating along the rod length at the bar velocity, $C_b = (E/\rho)^{0.5}$, where E and ρ are the Young's modulus and density of the rod material, respectively. These reverberations are clearly seen in Fig. 3.3, from Rosenberg and Dekel (2009a), for the nose and tail velocities of a spherical-nosed steel rod impacting an aluminum target. The rod in this simulation was 120 mm long and 6 mm in diameter, the aluminum target had strength of $Y_t = 0.4$ GPa, and the impact velocity was 1.5 km/s. Note the constant amplitude of the steps in these velocity histories, and their corresponding time shift in Fig. 3.3b, which is equal to the transit time of an elastic wave through the length of the rod.

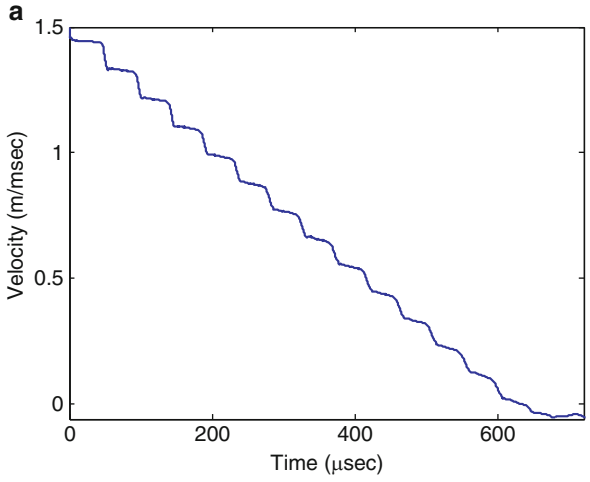

Fig. 3.3 (continued)

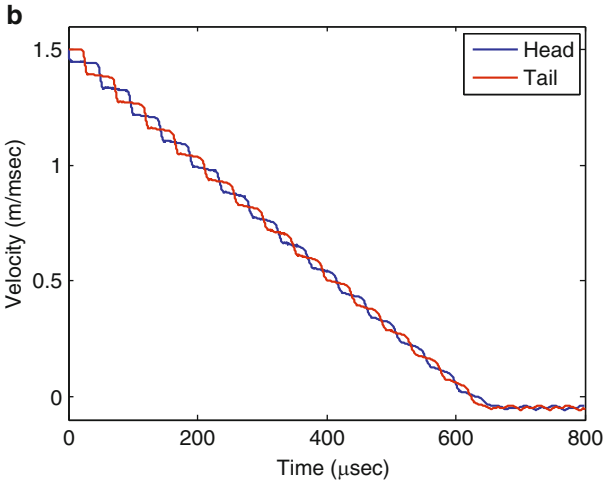

Fig. 3.3 (**a**) Simulation results for the nose velocity of a spherical-nosed steel rod impacting an aluminum target at 1.5 km/s and (**b**) Both nose and tail velocities for the same impact

Similar step-like velocity histories, for L/D = 20 rods with different nose shapes, impacting an 0.4 GPa aluminum target at 1.0 km/s, are shown in Fig. 3.4. The reverberating elastic waves have significantly different amplitudes, which depend on the nose shape of the rod. The low amplitude waves in the ogive-nosed rod result in the longest penetration time and, consequently, their low deceleration. In contrast, the high amplitude waves which reverberate in the flat-ended rod, result in the shortest penetration time and highest deceleration. Thus, the ogive nosed rod is expected to penetrate deeper than the others and the flat ended rod should result in the lowest penetration, in accord with the results shown in Fig. 3.2.

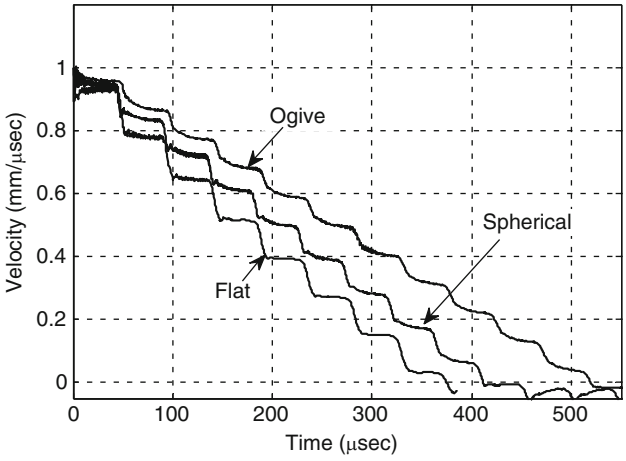

Fig. 3.4 Nose velocity histories for rods with different nose shapes

The stresses corresponding to these waves can be calculated by the well-known relation between stress (σ) and particle velocity (v) in a long elastic bar:

$$\sigma = \rho C_b v \tag{3.6a}$$

where ρ and C_b are the density and elastic wave velocity of the bar, respectively. In fact, the velocity steps of the rod's nose as seen in Fig. 3.4, are equal to twice the particle velocity (v) behind the reverberating wave fronts, since the particle velocity is doubled with each reflection from the rod's ends. Thus, the velocity steps in Fig. 3.4 have amplitudes of $\Delta v = 2v$, and the corresponding stresses (σ) should be calculated through:

$$\sigma = \rho C_b \Delta v/2 \tag{3.6b}$$

Using the corresponding values for the rod's density and its elastic wave velocity, one can have an estimate for the amplitudes of these reverberating stress waves: $\sigma = 1.9$, 2.2 and 2.5 GPa, for the ogive, spherical and flat-nosed rods, respectively. As we shall see later on, these stresses are equal to the resisting stresses which the target exerts on these rods. Note also that the first step in the velocity histories of the rod's nose has half the amplitude of the other steps. This velocity drop results in from the impact itself, while all the later velocity drops are subjected the doubling process discussed here.

The next step in this numerical study is to follow the deceleration of the rigid rod impacting a given target at different velocities. Such deceleration histories, for an ogive nosed rod impacting the 0.4 GPa aluminum target, are shown in Fig. 3.5. The constant deceleration of this rod for an impact velocity of 1.0 km/s is clearly seen in Fig. 3.5a, and the independence of the deceleration on impact velocity is demonstrated in Fig. 3.5b.

The deceleration of the rod at the early stages of penetration is lower than its value at deep penetration, as shown by the shaded area in Fig. 3.5a. This is due to the effect of the entrance phase, as discussed above. Rosenberg and Dekel (2009a) found through theses simulations that for ogive nosed rods the entrance phase dominates the process for a penetration depth of six rod diameters. Figure 3.5b clearly shows that higher impact velocities result in a shorter duration of the entrance phase, since it takes less time for the rod to reach this penetration depth. For spherical nosed rods the deceleration achieves a constant value at a depth of about three rod diameters. These values of $P = 6D$ and $P = 3D$ are the dominance ranges of the entrance phase for the ogive and spherical nosed rods, respectively. The influence range of the entrance phase extends to much larger penetration depths, as will be demonstrated by the numerically based model for the entrance phase effect. One should note that short rigid projectiles such as armor piercing (AP) projectiles, do not reach the constant deceleration phase since their penetration depths are of the order of a few projectile diameters. Thus, the whole penetration process of short projectiles is within the influence range of the entrance phase, and it should be analyzed differently, as will be discussed in Sect. 3.5.

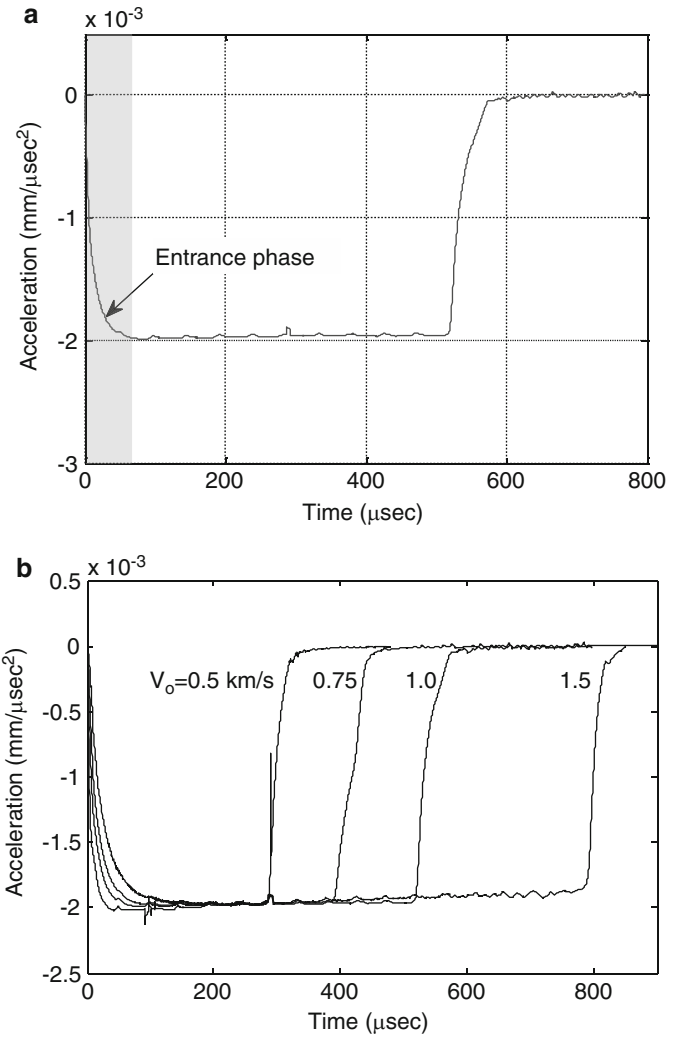

Fig. 3.5 (**a**) The deceleration histories of an ogive-nosed rod penetrating 0.4 GPa aluminum target, at an impact velocity of 1.0 km/s and (**b**) the decelerations for several impact velocities

The advantage of using numerical simulations in order to follow the physics of deep penetrations is demonstrated by the following sets of simulations, from Rosenberg and Dekel (2009a). Simulation results for the deceleration of the ogive nosed rods, as they penetrate aluminum targets with different strength (0.4 and 0.8 GPa), are shown in Fig. 3.6. As expected, the stronger target exerts a higher force (deceleration) on the rod. From these simulations it is clear that the constant decelerations do not follow a linear dependence on target strength, as will be further discussed in the next section.

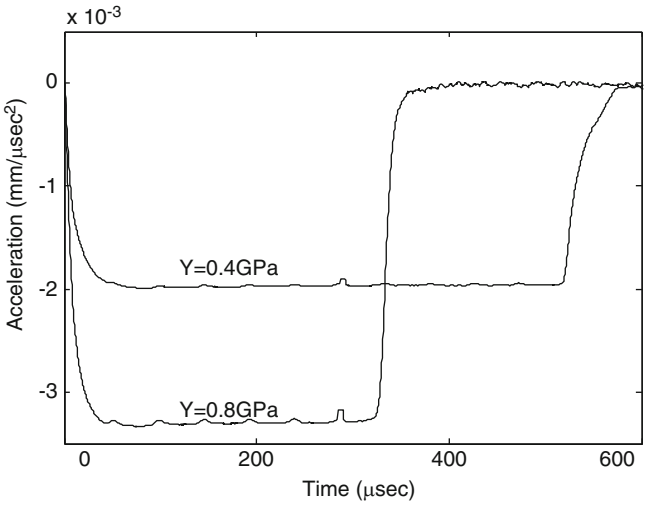

Fig. 3.6 The effect of target strength on the deceleration of an ogive-nosed rod

The role of rod density is highlighted in Fig. 3.7 which shows the nose velocities of L/D = 20 spherical nosed aluminum and steel rods, impacting the 0.4 GPa aluminum target at 1.4 km/s. The velocity steps in the aluminum rod are about three times higher than those of the steel rod. This is the expected result considering (3.6b) for the amplitude of the reverberating elastic stress waves. We have already mentioned that the amplitudes of these stress waves are equal to the resisting stress which the target exerts on the rod. For the same resisting stresses, the reverberating waves in these rods have to be of equal stress amplitude. This means that their velocity steps should be inversely proportional to the corresponding products ρc_b of

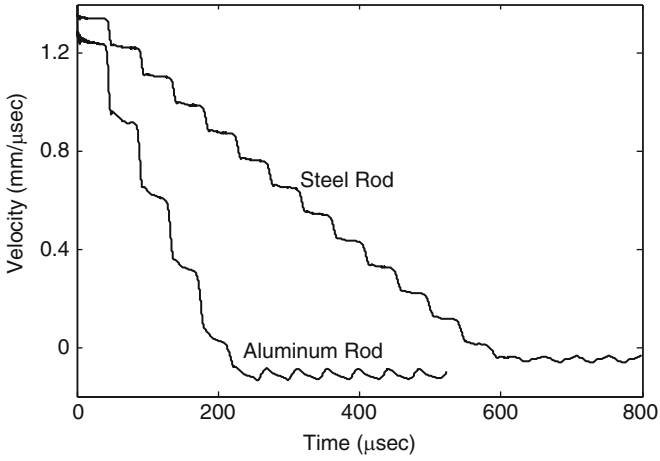

Fig. 3.7 Nose velocity histories of the spherical-nosed aluminum and steel rods, penetrating an aluminum target

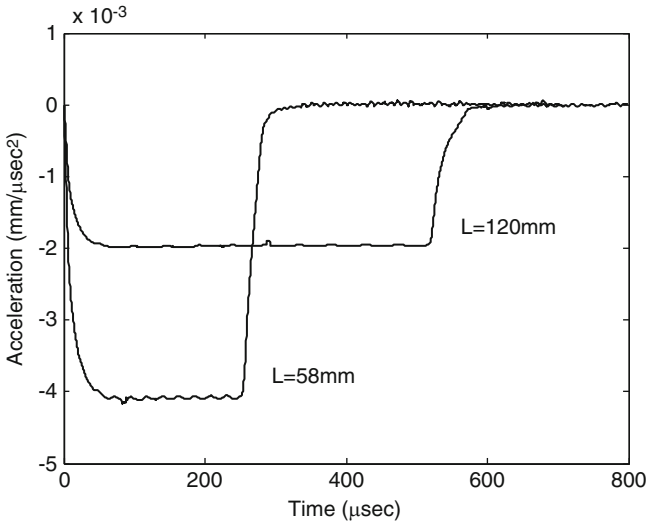

Fig. 3.8 Deceleration histories for rods of different length

the two rod materials. Since aluminum and steel have similar values for their wave speeds, the velocity steps should be inversely related to their density ratio, which is about three. This is exactly the result obtained in the simulations for the two rods, as seen in Fig. 3.7. Stated differently, this result indicates that the amplitudes of the reverberating stress waves in the two rods are equal. The larger velocity steps in the aluminum rod shorten its total penetration time and increase its deceleration, as compared with the steel rod.

The simulation results for the deceleration of ogive nosed steel rods of different lengths are shown in Fig. 3.8. These rods, with L = 58 mm and L = 120 mm and the same diameter (D = 6 mm), impacted the 0.4 GPa aluminum target at 1.0 km/s. The deceleration of the shorter rod is higher simply because it takes less time for the elastic waves to reverberate along its length.

In summary, the experimental results for rigid rod penetrations suggest that their deceleration is constant, beyond the dominance range of the entrance phase. The numerical simulations show that the constant deceleration of a rigid rod depends on its nose shape and on the strength of the target, and it is inversely proportional to the rod's density and its length.

3.2 The Penetration Model for Rigid Long Rods

We are now ready to present the analytical model for the penetration of rigid rods into semi-infinite targets. The model accounts for target materials which are characterized by well-defined flow stress and elastic moduli. Many metals and alloys show some

hardening effects at increased strain and strain rates, as well as thermal softening in regions which experience large deformations. These complicating effects are ignored in the following discussion in order to simplify the analysis. However, the model presented here is still applicable for materials which moderately harden (or soften) if an effective (average) flow stress is used for the strength of these materials. These flow stresses should be taken from the corresponding stress–strain curves at high strain values. As discussed in Chap. 1, the Kolsky bar test is most appropriate for the determination of these flow stresses at the relevant strain rates which the targets experience during penetration.

3.2.1 Impact at the Ordnance Velocity Range

With the observations discussed in Sect. 3.1, we can construct the analytical model for the deep penetration of rigid long rods in terms of their properties (density, length and nose shape), and those of the target (strength and elastic moduli). The model ignores the entrance phase effect and assumes that the deceleration of a rigid rod is constant throughout the whole penetration process. This means that the retarding force (F), which the target exerts on the rod, is also constant during its penetration. The retarding force can be expressed by the resisting stress (R_t), which the target exerts on the rod, multiplied by its cross section area (πr^2). Thus, for a rod with mass M, an effective length of L_{eff} and radius r, one can write:

$$F = Ma = \rho_p L_{eff} \cdot \pi\, r^2 a = const = \pi\, r^2 R_t \tag{3.7a}$$

where the effective length of the rod is defined by: $L_{eff} = M/\pi r^2 \rho_p$. The constant deceleration of the rod is related to the resisting stress (R_t) through:

$$a = \frac{R_t}{\rho_p L_{eff}} \tag{3.7b}$$

The inverse dependence of the rod's deceleration on its density and length has been already demonstrated by the simulations presented above. We have also seen that the rod's deceleration depends on its nose shape and on the strength of the target. Thus, we may assume that the resisting stress (R_t) depends on these parameters as well. Inserting the above relation for the constant deceleration in the corresponding expression for the penetration depth, (3.4a), results in the following penetration equation for the rigid long rod:

$$P = \frac{\rho_p L_{eff} V_0^2}{2R_t} \tag{3.8a}$$

and the normalized penetration is given by:

$$\frac{P}{L_{eff}} = \frac{\rho_p {V_0}^2}{2R_t} \tag{3.8b}$$

Several points should be noted here. According to this equation the penetration depth of a rigid rod does not depend on the density of the target. It is only the target strength which determines the penetration depth, through its resisting stress (R_t). In fact, its Young's modulus also plays an important role in determining the value of R_t, as will be shown below. The nose shape of the rod plays an important role in determining its deceleration and one may expect that R_t depends on the rod's nose shape as well. The influence of the entrance phase was ignored throughout the analysis. Thus, the predicted penetrations through (3.8) are expected to underestimate the experimental data for low impact velocities.

The simple penetration equation derived above is based on the target's resistance to penetration (R_t) which has to be determined for each rod/target combination. A well established theoretical model for R_t is still lacking, although several attempts were made over the years, as will be discussed below. The procedure which will be described now for the determination of R_t can be referred to as a "numerically based" model. With this approach the "data" is obtained through numerical simulations by varying each parameter at a time. For the present case consider the simulation results of Rosenberg and Dekel (2009a) for rods with different nose shapes. These simulations resulted in the rod's deceleration for different target materials and strengths. These decelerations were inserted into (3.7b) and the corresponding values of R_t were determined for the various rod/target combinations. Simulation results for R_t values are given in Table 3.2, for rigid rods with different nose shapes impacting aluminum and steel targets.

The simulations of Rosenberg and Dekel (2010b) were aimed at finding a general relation between R_t and the relevant parameters of the target (Y_t, E), for rods with different nose shapes. The strength of the aluminum and steel targets in these simulations was varied within a large range, $Y_t = 0.05$–0.8 GPa. The resulting R_t values were presented through the dependence of R_t/Y_t on $\ln(E/Y_t)$, for the different rod/target combinations, as shown in Fig. 3.9.

As is clearly seen, these R_t values follow a linear relation between the normalized values R_t/Y_t and the corresponding values for $\ln(E/Y_t)$, according to:

$$\frac{R_t}{Y_t} = 1.1 \ln\left(\frac{E}{Y_t}\right) - \phi \tag{3.9}$$

where ϕ depends on the nose shape of the rod, having the values of: $\phi = 1.15, 0.93$ and 0.2, for the 3CRH ogive, the conical and the spherical nosed rods, respectively. The values of Young's modulus for steel and aluminum in these simulations were

Table 3.2 Values of R_t (in GPa) for different targets and rod nose shapes

Nose shape	Aluminum targets		Steel targets	
	$Y_t = 0.4$ GPa	$Y_t = 0.8$ GPa	$Y_t = 0.4$ GPa	$Y_t = 0.8$ GPa
Ogive	1.87	3.12	2.28	3.96
Spherical	2.25	3.87	2.63	4.71
Conical	1.95	3.30	2.36	4.14

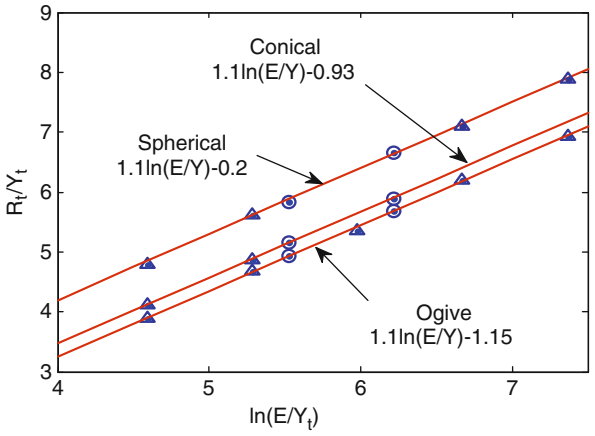

Fig. 3.9 Simulation results for the relation between R_t/Y_t and E/Y_t. *Triangles* and *circles* denote aluminum and steel targets, respectively

E = 200 and E = 73 GPa, respectively. The ogive nosed rods in these simulations were of 3CRH and the conical nosed rod had a nose length of three rod radii. Different cone lengths and ogive radii are expected to result in different R_t values, as will be shown in Sect. 3.4.

In order to asses the validity of this numerically-based model we compare its predictions with experimental data for rigid L/D = 10 steel rods, having different nose shapes, impacting 6061-T651 aluminum targets. These experiments are described in Forrestal et al. (1988) and in Piekutowski et al. (1999). The dynamic stress–strain curve of the 6061-T651 aluminum alloy, as obtained from the Kolsky bar system in our lab, is given in Fig. 1.14. It is clear that a flow stress of $Y_t = 0.42$ GPa represents an average value for the dynamic strength of this material at large strains. Inserting this value of Y_t in (3.9), together with E = 69 GPa for this alloy, results in the values of $R_t = 1.87$, 2.27 and 1.97 GPa for its resisting stresses against rods with ogive, spherical, and conical nose shapes, respectively. Inserting these R_t values in (3.8) results in the corresponding relations for the penetration depths of these rods into 6061-T651 aluminum targets. These relations, together with the data from Piekutowski et al. (1999) and Forrestal et al. (1988), are shown in Fig. 3.10.

The experiments of Piekutowski et al. (1999), with the ogive nosed rods, were described earlier and their results are given in Table 3.1 and Fig. 3.1. With the corresponding value of $R_t = 1.87$ GPa, we get from (3.8b) the predicted penetration relation for this rod/target pair: $P/L_{eff} = 2.12\ V_0^2$ (where V_0 is given in km/s). The excellent agreement between this relation and the experimental results of Piekutowski et al. (1999) is shown in Fig. 3.10a. The experiments of Forrestal et al. (1988) included both spherical and conical nosed rods. For the spherical nosed rods we find, from (3.8b) that the penetration equation is: $P/L_{eff} = 1.76\ V_0^2$, and the agreement with the experimental results of Forrestal et al. (1988) is shown in Fig. 3.10b. In a similar way, the penetration equation for the conical nosed rods, according to the model, is: $P/L_{eff} = 2.04\ V_0^2$ and its agreement with the data from Forrestal et al. (1988) is shown in Fig. 3.10c. The agreement between the predicted

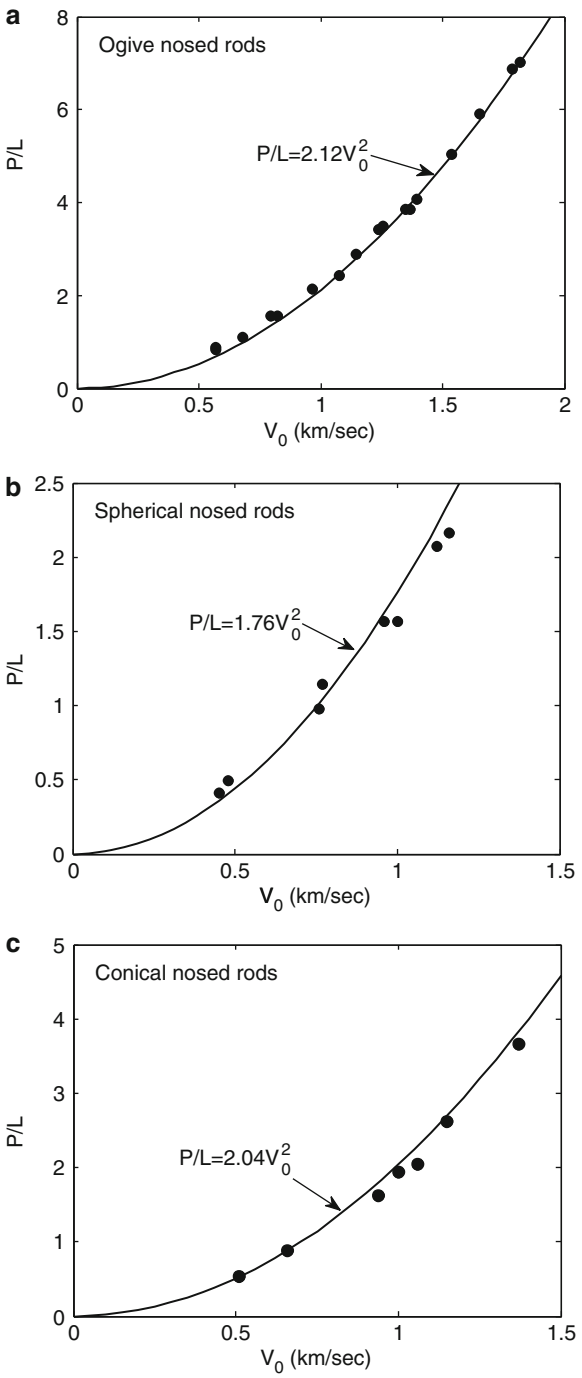

Fig. 3.10 The agreement between model's predictions and the experimental data for: (**a**) ogive nosed rods, (**b**) spherical nosed rods, and (**c**) conical nosed rods, impacting 6061-T651 aluminum targets

penetration formulas and the experimental data for these rods with the different nose shapes, strongly enhances the validity of the penetration model presented here.

The penetration capabilities of rigid rods with the different nose shapes are related to their corresponding R_t values as given by (3.9), which was derived through the numerical simulations of Rosenberg and Dekel (2010b). The specific choice for this relation was motivated by the fact that similar relations were obtained for the resisting stresses on rigid rods, by the models of Tate (1986) and Yarin et al. (1995). These models follow the flow field of the target material around a rigid projectile which has the shape of a Rankine ovoid. This particular shape for a body of revolution enables a closed analytical solution for the potential function which determines the velocity field around the body. The shape of the Rankine ovoid is shown in Fig. 3.11, together with the equation which describes its surface. The projectile's radius, at a large distance from its nose, is R.

The analysis by Tate (1986) resulted in the following expression for the resisting stress on the ovoid-shaped rod:

$$R_t = Y_t\left[\frac{2}{3} + ln\left(\frac{2E}{3Y_t}\right)\right] \tag{3.10a}$$

which can be rewritten as:

$$\frac{R_t}{Y_t} = ln\frac{E}{Y_t} + 0.26 \tag{3.10b}$$

The analysis of Yarin et al. (1995), for an incompressible elastic–plastic solid, resulted in the following expression for the resisting stress on the ovoid-shaped rod:

$$\frac{R_t}{Y_t} = \left[ln\left(\frac{3G}{4^{4/9}Y_t}\right)\right] = ln\frac{G}{Y_t} + 0.482 \tag{3.10c}$$

where G is the shear modulus of the target material.

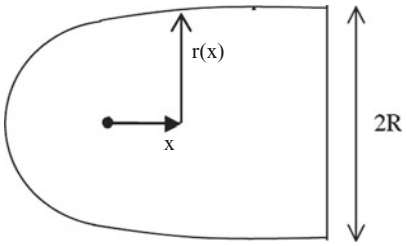

$$r(x) = [\frac{R^2 - x^2}{2} + \frac{x}{2}(x^2 + 2R^2)^{1/2}]^{1/2}$$

$$r(-\frac{R}{2}) = 0, \quad r(\infty) = R$$

Fig. 3.11 The shape of the Rankine ovoid

It is interesting to note that Tate's model, (3.10b), results in R_t values which are very close to those derived from (3.9) for the spherical nosed rod. For example, steel targets (E = 200 GPa) with compressive strengths of Y_t = 0.5, 1.0 and 1.5 GPa, result in the following values from Tate's model: R_t = 3.13, 5.56 and 7.73 GPa, respectively. The corresponding values, from (3.9) for the spherical nosed rod are: R_t = 3.2, 5.63, and 7.77 GPa, which are practically the same as those from Tate's model. This is the expected result since the ovoid shape is similar to the spherical nose. Using a value of G = 80 GPa for the shear modulus of steel, the analysis of Yarin et al. (1995) results in somewhat lower values for R_t, by about 12.5%, for these steel targets.

3.2.2 *High Velocity Impact: The Cavitation Phenomenon*

Up to this point we have analyzed experimental data and simulation results for rigid rods impacting semi-infinite targets at the ordnance range of impact velocities. We have seen that, except for the entrance phase, these rods experience a constant resisting stress (R_t) which depends on the target's strength and its Young's modulus, as well as on the nose shape of the rod. The simple expression, (3.8a and 3.8b), has been shown to account for penetration depths of rigid steel rods into aluminum targets. The question which we have to ask at this point is whether these conclusions hold for higher impact velocity as well. Before answering this question we have to introduce the concept of cavitation, which has an important role for high velocity impacts. In a short summary of his early work during WWII, Hill (1980) used the term cavitation, from fluid mechanics, to describe situations for which the diameter of the penetration channel is larger than the diameter of the projectile. His analysis is based on the assumption that the retarding force on the projectile should be expressed as the sum of two terms. The first term is related to the strength of the target and the second to its inertia. The main conclusion from Hill's analysis is that cavitation occurs at all impact velocities for both conical and spherical nosed projectiles. In contrast, for an ogive-nosed projectile, cavitation takes place only when its impact velocity is above a certain threshold (V_{cav}). The onset of cavitation means that the projectile "invests" some of its energy in expanding the channel's diameter. According to Hill's analysis the force on the ogive nosed projectile, at low impact velocities ($V_0 < V_{cav}$) should be constant, with no cavitation in the penetration channel. On the other hand, at higher impact velocities the resisting force on the projectile depends on its velocity through the target inertia term. At these velocities the diameter of the crater is larger than that of the projectile since cavitation takes place for $V_0 > V_{cav}$. This is an important observation since it relates the constant diameter of the penetration channel with a constant resisting stress which the target exerts on the projectile. In summary of Hill's assumptions, for ogive nosed projectiles the inertia of the target should be added to its resisting stress only at the high impact velocities ($V_0 > V_{cav}$). In contrast, for both spherical and conical nosed projectiles the inertia should be added at all impact velocities, resulting in the cavitation phenomenon at each shot. As we discuss below, this

assumption is in sharp contradiction with both experimental observations and numerical results. However, the notion of cavitation at high impact velocities is correct for all nose shapes, as will be demonstrated here.

Post-mortem pictures of the 6061-T6 aluminum targets, in the experiments of Forrestal and his colleagues, showed no cavitation for rods with either spherical or conical nose shapes, at impact velocities up to 1.2–1.4 km/s. At higher impact velocities the rods failed by plastically deforming or by breaking and eroding. For ogive–nosed rods, the penetration channels in the experiments of Piekutowski et al. (1999) showed no cavitation for velocities up to about 1.82 km/s. At impact velocities above 2.0 km/s these rods broke up as a result of the high impact pressures. Thus, there is no evidence for cavitation in the aluminum targets which were impacted by these rods with different nose shapes. Some of the post-mortem radiographs, from Forrestal et al. (1988) and Piekutowski et al. (1999), are shown in Fig. 3.12. Clearly, the channel diameters in these experiments were the same as the diameters of the rods. Moreover, the simulation results of Rosenberg and Dekel (2009a) for conical and spherical nosed rods did not show a cavitation phenomenon in aluminum targets for this range of impact velocities. Thus, the conclusion of Hill (1980) that cavitation is induced at all impact velocities for conical and spherical-nosed projectiles, has been refuted by both the experimental results of Forrestal and his colleagues and by the numerical simulations of Rosenberg and Dekel (2009a).

In order to investigate the issue of cavitation, Rosenberg and Dekel (2009a) performed 2D simulations for rigid steel rods, impacting steel and aluminum targets at high velocities. These simulations showed that a certain threshold velocity (V_{cav}) exists for every rod/target pair. For impact velocities below V_{cac}, the diameter of penetration channel was equal to the rod's diameter. On the other hand, for impact velocities above V_{cav} the diameter of the penetration

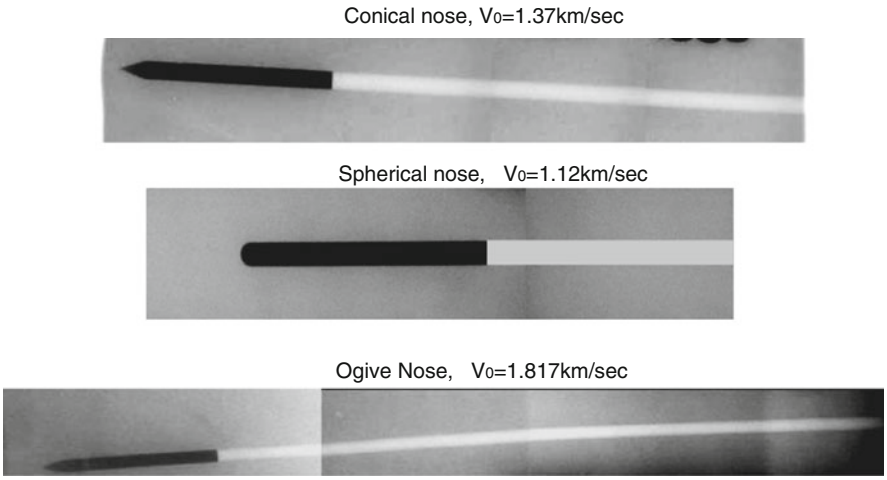

Fig. 3.12 Post mortem radiographs of conical, spherical and ogive nosed rods in aluminum targets

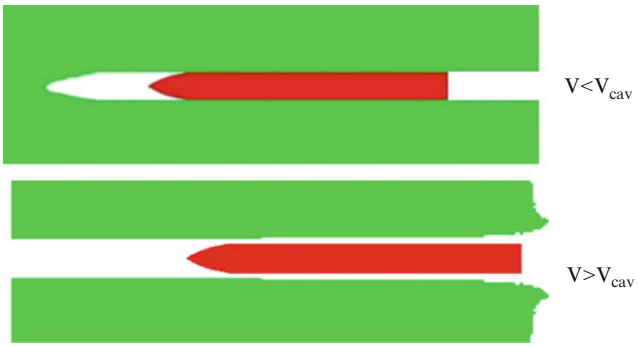

Fig. 3.13 The cavitation phenomenon

channel was larger than that of the rod. These cavitations take place at the initial part of the channel, which becomes narrower as the rod slows down at deeper penetrations. A close examination of the penetration and velocity histories in these simulations showed that when the velocity of the rod reaches the threshold value (V_{cav}), the diameter of the channel is exactly equal to that of the rod. Figure 3.13 shows the shape of the channel at low ($V < V_{cav}$) and high rod velocities ($V > V_{cav}$) in these simulations:

The simulations of Rosenberg and Dekel (2009a) showed that the threshold impact velocity (V_{cav}) depends on the nose shape of the rod and on the strength and density of the target, and it does not depend on the density of the rod. The highest values of V_{cav} were obtained for ogive nosed rods and the lowest for flat nosed rods. These simulations led to a simple relation for the value of V_{cav} in terms of the density of the target (ρ_t), its resistance to penetration (R_t), and the nose shape of the rod (b), which is given by:

$$b\rho_t V_{cav}^2 = R_t \tag{3.11}$$

The nose shape factor was found to have the following values: b = 0.15, 0.24, 0.5 and 1.25, for the 3CRH ogive, conical, spherical and flat nose shapes, respectively. The conical head of the rods in these simulations had a length which was three times the rod radius. Table 3.3 lists several values for V_{cav} which were obtained in these simulations for the various nose shapes and different targets. Note the high values of V_{cav} for the 0.4 GPa aluminum targets, which account for the absence of cavitation in all of the experiments by Forrestal and his colleagues with 6061-T651 aluminum targets, as discussed above

Rapoport and Rubin (2009) followed the analysis of Yarin et al. (1995) and showed that their model also predicts a cavitation threshold behavior, at $V_{cav} =$ 1.97 km/s, for the ovoid nosed projectile penetrating an aluminum target with strength of 0.4 GPa.

Table 3.3 Values for V_{cav}, (in km/s) for rods of different nose shapes and different targets

Nose shape	Aluminum (0.4 GPa)	Steel (0.4 GPa)
Ogive	2.17	1.385
Spherical	1.3	0.82
Conical	1.73	1.115
Flat	0.85	0.525

The qualitative explanation for these observations is relatively simple. As long as the velocity of the projectile is lower than V_{cav}, the lateral velocity imparted by the projectile to the target is not high enough to overcome its strength and the channel diameter remains the same as that of the projectile. At higher impact velocities, the lateral momentum is high enough to initiate the cavitation phenomenon in the target. As a result, the projectile invests an extra amount of energy in order to open the cavity, in addition to the energy needed for its advancement. In other words, the inertia of the target ($\rho_t V^2$) starts to play an important role at high impact velocities. The immediate consequence of these observations is that for $V_0 > V_{cav}$, the deceleration of the rod cannot be constant. This is clearly seen in Fig. 3.14, which shows the simulation result for the deceleration history of an L/D = 10 spherical-nosed steel rod, impacting a 0.4 GPa aluminum target at 2.5 km/s ($V_0 > V_{cav}$.). Note that at about 180 microseconds after impact, the deceleration reaches a constant level, since the velocity of the rod has reached the value of V_{cav} at this time. With these observations we can construct now the analytical model for the penetration depths of rigid rods at high impact velocities.

In order to derive an expression for the penetration depth of a rigid rod at impact velocities above V_{cav}, one has to divide the process into two parts. The first part starts with the impact at $V = V_0$ and ends when the rod slows down to $V = V_{cav}$.

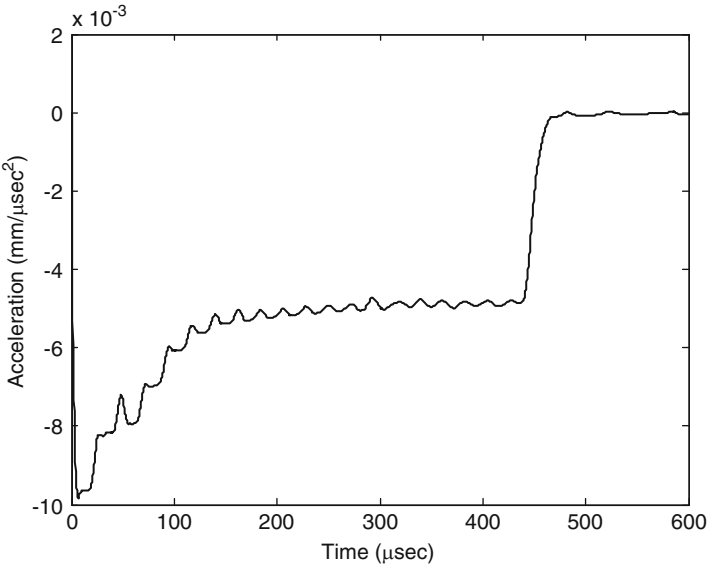

Fig. 3.14 The deceleration history for an impact of a spherical nosed projectile at $V_0 > V_{cav}$

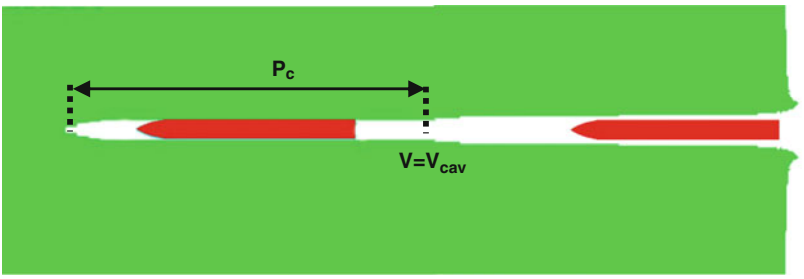

Fig. 3.15 The two penetration regimes for a high velocity impact

During this phase the inertia of the target has to be added to its strength related term (R_t), in order to account for its increased resistance to penetration due to cavitation. The second part of the process starts when $V = V_{cav}$ and ends at $V = 0$. The deceleration of the rod is constant during this phase, as discussed above, and the rod penetrates to a certain depth (P_c) which is derived below. The two penetration regimes are shown schematically in Fig. 3.15.

We start the analysis by considering the second penetration regime, with the constant deceleration of the rod. Inserting $V = V_{cav}$ in (3.8a), the penetration depth (P_c) in this regime is given by:

$$P_c = P(V_{cav}) = \frac{\rho_p L_{eff} V_{cav}^2}{2R_t} \tag{3.12a}$$

Using the expression for V_{cav} from (3.11), we get:

$$P_c = \frac{L_{eff}\rho_p}{2b\rho_t} \tag{3.12b}$$

or, in its normalized form:

$$\frac{P_c}{L_{eff}} = \frac{\rho_p}{2b\rho_t} \tag{3.12c}$$

This simple equation gives the maximal penetration depth (P_c), for a given rod/target pair, which can be achieved with no cavitation. The equation highlights the relevant parameters for P_c, namely, the density of the target and the rod, the effective length of the rod, and its nose shape factor (b). It is interesting to note that P_c does not depend on target strength. This result can be understood by realizing that the strength of the target is responsible for two opposing effects. On the one hand, the penetration depth of a given rod decreases with target strength. On the other hand, the cavitation threshold increases with target strength, and the no-cavitation range of impact velocities is larger for the stronger target. The fact that P_c in (3.12c) does not depend on target strength means that the two effects cancel each other.

In order to get an estimate for the values of P_c for some practical cases, consider a steel rod impacting an aluminum target, with a density ratio of $\rho_p/\rho_t = 2.85$. Since b = 0.5 for a spherical nosed rod, and b = 0.15, for ogive nosed rod, we get $P_c = 2.85L_{eff}$ and $P_c = 9.5L_{eff}$ for these rods, respectively. The large value of P_c for the ogive nose rod accounts for the fact that the penetration channels in the experiments of Piekutowski et al. (1999) showed no sign of cavitation even for an impact velocity of 1.82 km/s, with a penetration depth of nearly $7.0L_{eff}$. The value of $V_{cav} = 2.17$ km/s, from the simulations of the ogive nosed rod impacting the 0.4 GPa aluminum target, means that the rods in these experiments could penetrate without cavitation even at higher impact velocities. However, at an impact velocity of 2.0 km/s, these rods started to break and erode and the cavitation phenomenon could not be demonstrated in these experiments.

We now consider the first penetration stage, with impact velocities above the cavitation threshold. At these velocities the target's resistance to penetration has to include its inertia, as discussed above. Thus, the resisting stress (Σ) on the rod for these velocities should be given by the sum of two terms. The first term is the strength related resistance to penetration (R_t), and the second is a velocity dependent term which is due to the inertia of the target. A natural choice for the resistance to penetration would be:

$$\Sigma = R_t + B\rho_t\left(V^2 - {V_{cav}}^2\right) \tag{3.13a}$$

where B is a geometric factor which is related to the nose shape of the rod. A reasonable assumption is that the two shape factors, B and b, are related, and a possible choice would be that B = b/2. Inserting this relation in (3.13a), together with the definition of V_{cav} through (3.11), result in:

$$\Sigma = \frac{1}{2}R_t + \frac{1}{2}b\rho_t V^2, \quad \text{for:} \quad V \geq V_{cav} \tag{3.13b}$$

which results in the expected value of $\Sigma = R_t$ for $V_0 = V_{cav}$. This relation can be written in the form:

$$\Sigma = \frac{1}{2}R_t\left[1 + (V/V_{cav})^2\right] \tag{3.13c}$$

The resisting force on the rod is obtained by multiplying this expression for Σ by the cross section of the rod (πr^2). Inserting this force in the equation of motion, (3.7a), and integrating between $V = V_0$ and $V = V_{cav}$, results in the following relation for the penetration depth at the first stage of penetration, from $V = V_0$ to $V = V_{cav}$:

$$\frac{P}{L_{eff}} = \frac{\rho_p V_{cav}^2}{R_t} \cdot \ln\left(\frac{1+x}{2}\right) \tag{3.14a}$$

where the parameter x is defined by:

$$x = \left(\frac{V_0}{V_{cav}}\right)^2 \tag{3.14b}$$

Adding the penetration depth for the low velocity stage, as given by (3.12a), results in the following expression for the total penetration of a rigid projectile, at an impact velocity above the cavitation threshold:

$$\frac{P}{L_{eff}} = \frac{\rho_p V_{cav}^2}{2R_t} \cdot \left[1 + 2ln\left(\frac{1+x}{2}\right)\right] \quad \text{for:} \quad V_0 \geq V_{cav} \tag{3.15a}$$

With the definition of P_c in (3.12a), the total penetration depth can be written in a more compact form:

$$\frac{P}{P_c} = 1 + 2\ln\left(\frac{1+x}{2}\right) \quad \text{for:} \quad x \geq 1.0 \tag{3.15b}$$

Using the above expressions for P_c and R_t it is easy to show that the penetration depth in the low velocity range is given by:

$$P = \frac{\rho_p L_{eff}}{2b\rho_t} \cdot \left(\frac{V_0}{V_{cav}}\right)^2 \quad \text{for:} \quad V_0 \leq V_{cav} \tag{3.16a}$$

which, in its normalized form, is given by:

$$\frac{P}{P_c} = \left(\frac{V_0}{V_{cav}}\right)^2 = x \quad \text{for:} \quad x \leq 1.0 \tag{3.16b}$$

As was noted above, the values of V_{cav} are quite high for both ogive and conical nosed rods impacting aluminum and steel targets. At these impact velocities even high strength rods lose their rigidity by deforming or shattering. This is the reason for the absence of experimental data which show a clear cavitation thresholds and it is quite difficult to validate the analysis discussed above by using experimental data. Instead, Rosenberg and Dekel (2009a) compared the predictions from the model with numerical simulations for various rods, impacting both aluminum and steel targets at velocities above their corresponding values of V_{cav}. This comparison is shown in Fig. 3.16 demonstrating an excellent agreement between the model's predictions and the simulation results.

The penetration efficiency of rigid projectiles, at impact velocities above V_{cav}, is smaller than that for the low velocities, since the $P = P(V_0)$ curve is getting shallower with increased velocities. This is the expected result since an increasing amount of the projectile's energy is spent on enlarging the penetration channel laterally. In contrast, for impact velocities below V_{cav}, the kinetic energy of the

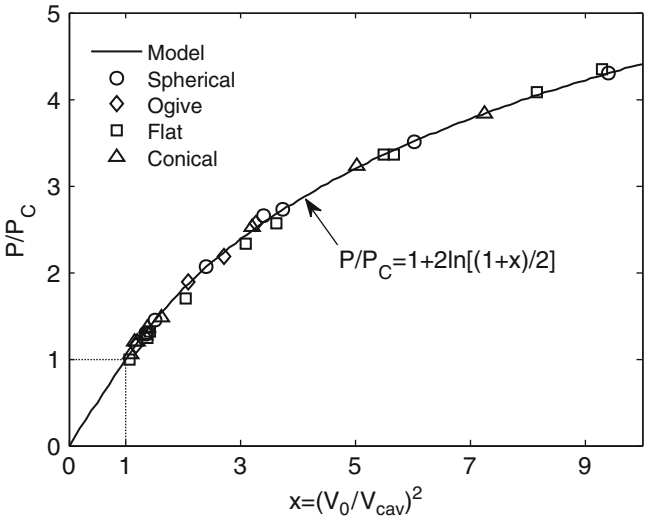

Fig. 3.16 Comparing the simulation results with the analytical predictions for $V_0 \geq V_{cav}$

projectile is spent only on forming the necessary channel for its passage. As discussed above, Hill (1980) noted that a penetration process with no cavitation must be achieved by a constant resisting stress, which depends on target strength. He defined this stress as "the mean work to form a unit volume of the resultant cavity by progressive penetration". In fact, Hill identified the constant resisting stress with the no-cavitation type of penetration. This is exactly what was found in the simulations of Rosenberg and Dekel (2009a) for impact velocities below the corresponding thresholds of all the rigid rods with different nose shapes. Both works conclude that the penetration process without cavitation is related to a constant resisting stress. The only difference between them is due to Hill's assumption that cavitation occurs at all impact velocities for both conical and spherical nosed projectiles. The numerical simulations of Rosenberg and Dekel (2009a) showed that a cavitation threshold exists for every nose shape. These simulation results are substantiated by the experimental results of Forrestal and his colleagues for rigid rods of spherical and conical nose shapes. No cavitation was observed in these experiments, which were performed at impact velocities as high as 1.2–1.4 km/s, in sharp contrast with Hill's prediction. It is important to note that Hill's prediction is based on the assumption that the resisting force on rods with these nose shpes, is dependent on target inertia for all impact velocities. This assumption has been a common practice by many workers who followed the penetration model of Goodier (1965), as discussed in the next section.

3.3 The Cavity Expansion Analysis

Several penetration models which are based on the work of Goodier (1965) have been suggested during the last decades. These models assume that the resistance to penetration of a rigid projectile should include the inertia of the target for all impact velocities, through an expression such as: $\Sigma = C + B\rho_t V^2$, where B is some nose shape factor. The strength related constant C in Goodier's model was determined by the threshold pressure which is needed to expand a small cavity in a large elasto-plastic body, as derived by the analysis of Bishop et al. (1945). Note that the third author of this classical work, the Nobel laureate Sir Neville Mott, worked for the war ministry in the UK during the years of World War II, and contributed important insights to the dynamic response of solids under impulsive loadings. The cavity expansion analysis of Bishop et al. (1945) was developed in order to account for the relatively high force which is needed to push a conical nosed rigid punch into a metallic block. This analysis resulted in threshold stresses in the range of 3–4 times the strength of the solid, which are needed to expand a small cavity against its resisting strength. These factors were in good agreement with indentation stresses of various metals, as measured by the sharp nosed hard punches. The use of this analysis, and the subsequent dynamic expansion analysis of Hill (1950), for terminal ballistics models was made for the first time by Goodier (1965). There are two issues in Goodier's model which have to be carefully reexamined, namely, the addition of target inertia to the resisting stress for all impact velocities, and the choice of the cavity expansion model for the value of the strength related term (C) in his expression for the resisting stress.

Goodier based his model on penetration data from Hermann and Jones (1961), for various metallic spheres impacting thick metallic targets at velocities up to about 1.5 km/s. Goodier found that the values for the strength term (C), as derived by the cavity expansion analysis, are too low in order to account for the penetration depths of these spheres, which were treated as rigid bodies in his analysis. Thus, he added the target's inertia term, in order to have a better agreement with the experimental data. However, the spheres in these experiments were made of copper, aluminum, soft steel and lead. Obviously, these materials are not strong enough to warrant their rigidity at this range of impact velocities. All of these spheres deformed heavily during impact and penetration, which was the main reason for their low penetration depths. Thus, the addition of target inertia to its penetration resistance, for all impact velocities, was based on a flawed interpretation by Goodier of the data he used for modeling. The second issue concerns the assumption that the strength related term for the target's resistance to penetration can be derived from the cavity expansion analysis of Bishop et al. (1945). As will be demonstrated below, the cavity expansion analysis results in much lower threshold pressures than the corresponding R_t values, which are obtained by experimental results and numerical simulations. They are also much lower than the values derived by analytical models such as those of Tate (1986) and Yarin et al. (1995), which follow the target's motion around the projectile's nose.

The cavity expansion analysis of Bishop et al. (1945) resulted in closed form expressions for the minimal pressures which are needed to expand a small cavity, either spherical or cylindrical, in a large elasto-plastic solid. The analysis showed that these threshold pressures depend on the Young's modulus (E), Poisson's ratio (ν) and the strength (Y) of the solid, through the following relations:

$$P_{sph} = \frac{2Y}{3}\left[1 + ln\frac{E}{(1+\nu)Y}\right] \qquad \text{For the spherical cavity} \tag{3.17a}$$

and

$$P_{cyl} = \frac{Y}{\sqrt{3}}\left[1 + ln\frac{\left(\sqrt{3}E\right)}{2(1+\nu)Y}\right] \qquad \text{For the cylindrical cavity} \tag{3.17b}$$

Both expressions were obtained for a solid which is incompressible in its plastic range. For a work-hardening material the threshold pressures have an additional term, related to the hardening modulus of the material, which is the slope of the stress–strain curve of the solid in its plastic range of response. Hill (1950) derived the corresponding expression for the spherical cavity in a solid which is compressible in both its elastic and plastic regions. The resulting expression from his analysis replaces the term (1 + ν) by the term 3(1−ν), in the logarithmic expression of (3.17a). Thus, according to Hill (1952), the critical (minimal) pressure which is needed to expand a spherical cavity in a large compressible solid, is given by:

$$P_{sph} = \frac{2Y}{3}\left[1 + \ln\frac{E}{3(1-\nu)Y}\right] \tag{3.18a}$$

Rosenberg and Dekel (2008) performed numerical simulations of the cylindrical cavity expansion process, from which they determined the threshold pressures which are needed to expand this cavity in compressible solids. These simulations showed that the term (1 + ν) in (3.17b) should be replaced by 3(1−ν) for the compressible solid, which is the same replacement as for spherical cavities. Thus, the threshold pressure to expand a cylindrical cavity in a compressible elasto-plastic solid, according to these simulations, is given by:

$$P_{cyl} = \frac{Y}{\sqrt{3}}\left[1 + \ln\frac{\left(\sqrt{3}E\right)}{6(1-\nu)Y}\right] \tag{3.18b}$$

These analytical expressions for the compressible solids result in threshold pressures which are much lower than the R_t values which are derived from the numerically based model of Rosenberg and Dekel (2009a), (3.9), for the spherical

and ogive nosed rigid rods. They are also lower than the threshold stresses obtained by the analytical models of Tate (1986) and Yarin et al. (1996), for the ovoid shaped rigid rod. As an example, consider the threshold pressures obtained by (3.18), $P_{sph} = 3.7$ GPa and $P_{cyl} = 3.12$ GPa, for a steel target ($E = 200$ GPa, $\nu = 0.29$) with strength of $Y = 1.0$ GPa. These values are, indeed, much lower than the corresponding value of $R_t = 5.6$ GPa, for a spherical nosed rod penetrating this steel target. Thus, the threshold pressures, as derived from the cavity expansion analysis, are bound to underestimate the resisting stresses which are exerted on rigid projectiles. These differences between the values of R_t for rigid rods and the threshold pressures from the cavity expansion analysis, are due to the different situations for which they are applied. The cavity expansion analysis accounts for cases where the material around the cavity is moving perpendicularly to the surface of the cavity. This is a one-dimensional problem where the material motion is very different than the complex motion along flow lines, which characterizes the penetration of rigid rods.

In all the models discussed here the functional dependence of the normalized threshold pressures (P_{thresh}/Y) on the relevant properties of the solid can be written as:

$$\frac{P_{thresh}}{Y} = K_1 ln \frac{E}{Y} + K_2 \tag{3.19}$$

where K_1 and K_2 have different values in these models. Thus, $K_1 = 2/3$ and 0.577, for the spherical and cylindrical cavity expansion models, respectively. On the other hand, $K_1 = 1.1$ according to the numerically based model of Rosenberg and Dekel (2009a), (3.9), and $K_1 = 1.0$ according to the analysis of Tate (1986). The values for K_2 depend on the nose shape of the rigid rod, according to the numerically based model presented above, and it depends on Poisson's ratio of the solid, according to both the cavity expansion models and Tate's model. The functional similarity of the expressions for P_{thresh}/Y is not surprising, since all the analyses presented here deal with the pressures which have to be applied inside the solid, in order to "push" it against a resisting stress which depends on its strength. The differences between the corresponding values of resisting stresses are related to the details concerning the actual flow of the material, as discussed above.

The numerical simulations of Rosenberg and Dekel (2008) were aimed at a better understanding of the cavity expansion process, in order to highlight the differences between this process and the penetration of rigid rods. They performed numerical simulations with small spherical cavities in large steel, aluminum and lead specimens, having strengths in the range of 0.5–1.5 GPa. In each simulation a certain pressure was applied inside the spherical cavity. The threshold value was defined as the pressure above which a steady-state velocity was imparted to the cavity wall. The values of these critical pressures for spherical cavities in

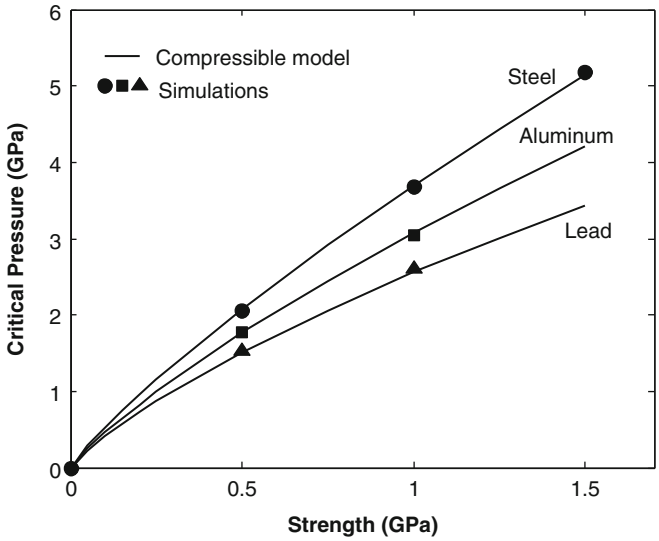

Fig. 3.17 The agreement between simulation results and the cavity expansion model for the critical pressures in compressible solids

aluminum, steel, and lead targets were in excellent agreement with those predicted by the analysis of Hill (1950), according to (3.18a). This agreement is shown in Fig. 3.17 and it demonstrates the usefulness of numerical simulations in verifying analytical models. On the other hand, the cavity expansion model has been well established for many years, and the agreement shown in Fig. 3.17 can be considered as a demonstration for the validity of these numerical simulations.

The numerical simulations of Rosenberg and Dekel (2008) were also used in order to find a relation between the velocity of the cavity's wall and the applied pressure (P_{dyn}) on the wall. These relations for steel, aluminum and lead, with strengths of 0.5, 1.0 and 1.5 GPa, are shown in Fig. 3.18a. The different curves shown in this figure can be normalized to a single curve, as shown in Fig. 3.18b.

The normalization presentation of these simulation results can be given by:

$$P_{dyn} = P_{spher} + 1.1875\rho V^2 \tag{3.20}$$

where P_{spher} is the threshold pressure which is needed to open the spherical cavity, as given by (3.18a). It is worth noting that this equation applies for very different metals which were used in these simulations, and it should be accounted for by a proper analytical model for the dynamic cavity expansion process. In fact, such a model for the dynamic expansion of a spherical cavity in an incompressible solid, was derived by Hopkins (1960). His result includes terms which are related to the expansion velocity of the cavity and to its acceleration. Assuming a constant

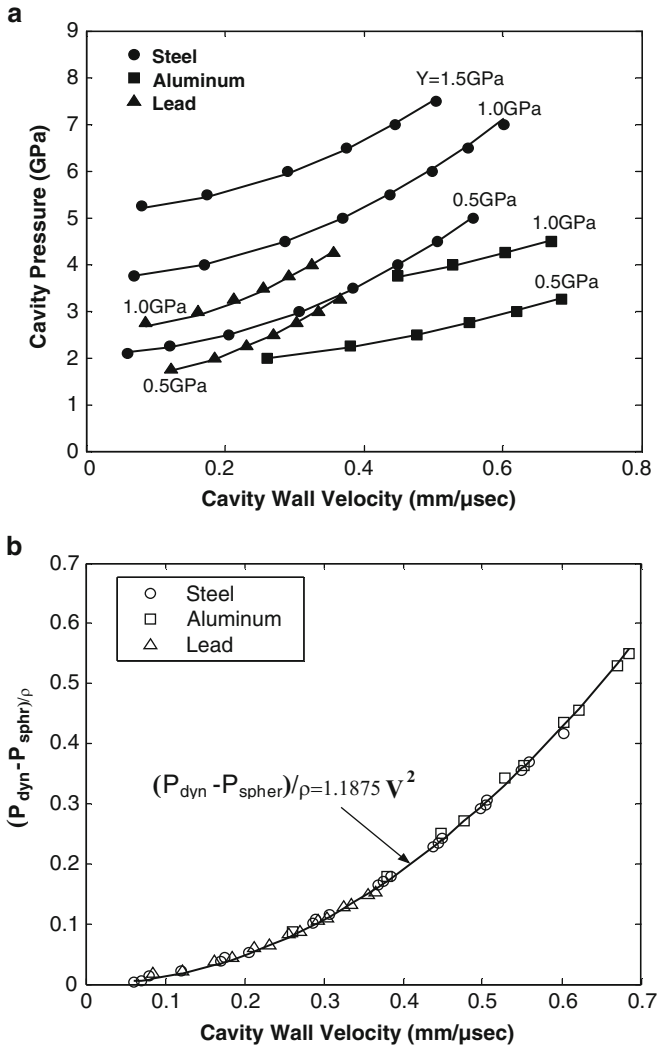

Fig. 3.18 (**a**) The relations between pressures and cavity wall velocities for the three materials, and (**b**) the normalized representation of these results

expansion velocity (V) the dynamic term, according to this analysis, is equal to 3/2 (ρV^2). The numerical factor in this expression is higher than the corresponding factor in (3.20), probably because the analysis of Hopkins (1960) was made for an incompressible solid, while the materials in the numerical simulations are inherently compressible. The analytical results of Masri and Durban (2005) show that this coefficient depends on the Poisson ratio of the solid (ν) and it is, indeed, smaller than 1.5 for every solid with a finite value of ν.

3.4 The Optimal Nose Shape

Several workers attempted to find an optimal nose shape for rigid projectiles which should result in maximal penetration depths. They start their analysis by writing an expression for the force on the projectile's nose, and minimize it with respect to the relevant parameter which describes the nose shape. This was done, for example, by Jones et al. (1998) who included the inertia of the target ($\rho_t V^2$) as well as its strength, for the resisting force. The conclusion from this analysis is that the optimal nose shape has a small blunt section at the tip of the nose which turns into a conical shape all the way to the cylindrical shank of the projectile. These nose shapes were not tested experimentally and, to our knowledge, no simulations were performed to enhance the claim that they are, indeed, optimal. It was shown above that the target's resisting stress is constant for impact velocities below the corresponding threshold (V_{cav}), and that the inertia term plays a role only for $V_0 > V_{cav}$. For a constant resisting stress there is no reason to expect an optimal nose shape, and one may assume that a sharper nose enhances the penetration capability of the rigid penetrator. The only question here is which of the sharp nose shapes, the cone or the ogive, is more efficient as far as rigid penetrations are concerned.

In order to answer this question we conducted a series of simulations for ogive and conical-nosed rigid steel rods, impacting aluminum targets with strength of 0.4 GPa. The sharpness of the rod's nose can be defined as the ratio of its length (ℓ) to its diameter (D). These ratios were varied in the range of $\ell/D = 0.25$–3, where $\ell/D = 0.5$ for an ogive nose is, in fact, the spherical nose shape. This ratio is equal to 2.95 for a 9CRH ogive nose and it compares with the ratio of $\ell/D = 3.0$ for the conical nose, which was the sharpest nose we simulated. The main output from these simulations was the constant deceleration of the rod (a), from which we derived the corresponding value of R_t, through the relation: $R_t = \rho_p L_{eff} a$. The simulations were performed with impact velocities in the range of 0.75–1.0 km/s. Figure 3.19 shows the resulting values of R_t, as a function of the nose sharpness

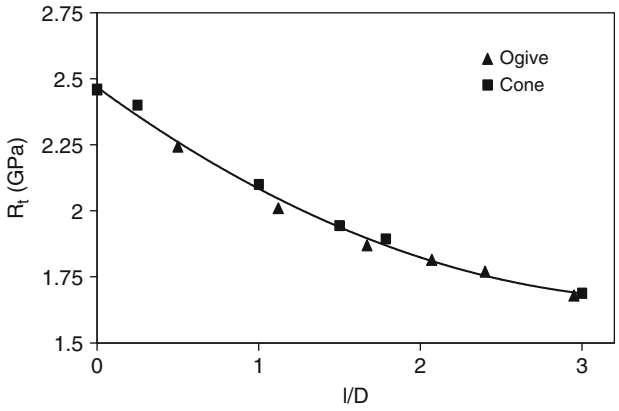

Fig. 3.19 The effect of nose sharpness on the target's resistance to penetration

(ℓ/D). We also added the point corresponding to a flat nosed rod (ℓ/D = 0), at R_t = 2.46 GPa, from our earlier simulations.

One can clearly see that the results for the two nose shapes practically fall on a single curve. The main conclusion from these simulations is that sharper noses experience less resistance and penetrate more, as expected, while the details of the nose shape (ogive or cone) are much less important. It is also clear that the benefit of sharper noses is decreasing with increased sharpness, and it seems that values of l/D > 3.0 will not add much to the penetration capability of rigid penetrators.

3.5 The Penetration of Short Projectiles

We have mentioned above that the penetration process of short projectiles is different than that of long rods, because of the enhanced effect of the impact face on the penetration depths of short projectiles. In fact, it was shown that the impact face dominates the penetration characteristics of ogive nosed rods for about six rod diameters. The effect is even more important for short projectiles impacting at velocities in the ordnance range, since they penetrate to depths of a few projectile diameters only. These projectiles are not expected to experience a constant deceleration during penetration. The present section deals with this issue in order to highlight the influence of the entrance phase. We shall present a numerically based model which accounts for the influence of the entrance phase. It will be shown that the predictions from this model are in good agreement with experimental data for short projectiles, demonstrating the usefulness of such numerically-based models.

3.5.1 The Influence of the Entrance Phase

Rosenberg and Dekel (2009b) followed the influence of the entrance phase in a more quantitative manner, through simulations for the penetration process of rigid projectiles with different nose shapes. Simulation results for the penetration histories of L/D = 3, D = 6 mm ogive-nosed projectile impacting a 0.4 GPa aluminum target are shown in Fig. 3.20a. Impact velocities of V_0 = 0.5, 1.0 and 1.5 km/s, resulted in penetration depths of: 17, 41.5, and 78.5 mm, respectively. A penetration depth of 17 mm is less than three projectile diameters, and is well within the dominance range of the entrance phase. Even for the 1.0 km/s impact, the penetration depth of 41.5 mm is very close to the six projectile diameters, which is the dominance range of the entrance phase. Thus, we do not expect a constant deceleration for these impacts, as is clearly manifested by the deceleration histories in Fig. 3.20b.

Figure 3.20b shows that a constant deceleration was obtained only for the highest impact velocity (1.5 km/s), at about 25 microseconds after impact. This

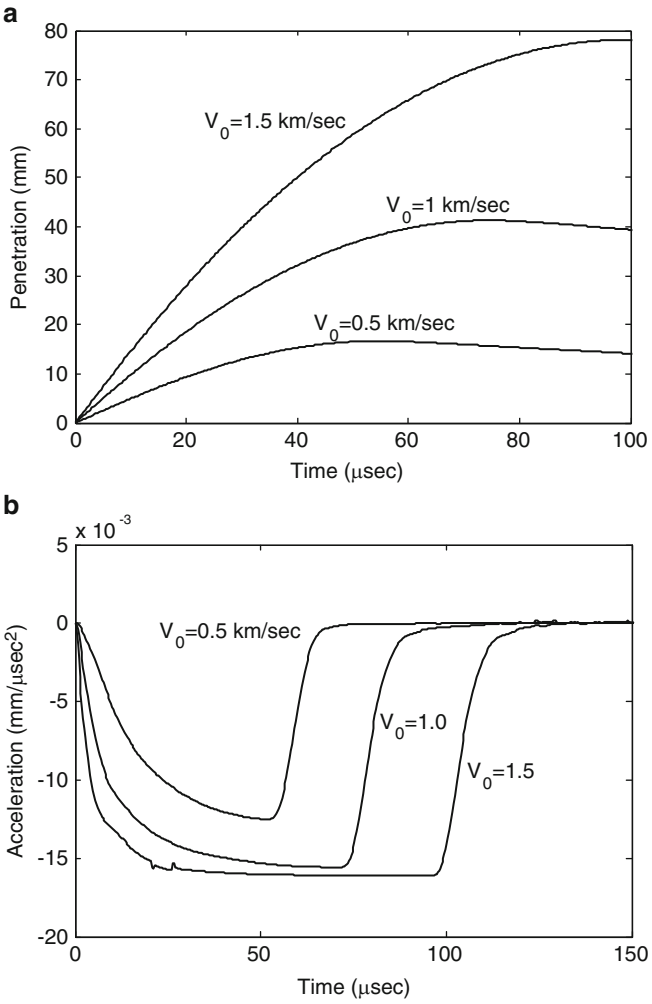

Fig. 3.20 (**a**) Penetration histories for the short projectiles and (**b**) their deceleration histories

time corresponds to a penetration depth of 36 mm in this simulation, which is exactly equal to six projectile diameters, the dominance range of the entrance phase. A close examination of the early part in the deceleration history, for the 1.5 km/s impact, shows that the entrance phase consists of two stages. During the first stage, up to about $t = 7$ μs, the projectile experiences a fast change in its deceleration, which is due to the embedment process of its nose in the target. The second stage, which lasts until $t = 25$ μs, is due to the entrance phase effect, as discussed above. The simulations of Rosenberg and Dekel (2009b) showed that the entrance phase takes less time for blunt projectile (either spherical or flat nosed), because their noses are shorter and their corresponding embedment times are

smaller. In fact, these simulations showed that the dominance range of the entrance phase for the spherical nosed projectile extends to about three projectile diameters only. However, its influence range extends to much larger depths, as is also the case with the ogive nosed projectiles. One may consider the influence range of the entrance phase as the range beyond which its dominance range plays a negligible part in the process. These issues will be further highlighted in the next sections.

In order to have a quantitative assessment for the influence of the entrance phase, one can use the penetration formula (3.8a) to derive an effective (average) resisting stress (R_{eff}), and an effective deceleration (a_{eff}) for the projectile, according to:

$$R_{eff} = \frac{\rho_p L_{eff} V_0^2}{2P} \tag{3.21a}$$

$$a_{eff} = \frac{V_0^2}{2P} \tag{3.21b}$$

Using the corresponding penetration depths in the simulations presented above and the effective length of the projectile $L_{eff} = 14.4$ mm, results in the following values for the effective resisting stresses: $R_{eff} = 0.84$, 1.37 and 1.63 GPa for the impacts at $V_0 = 0.5$, 1.0 and 1.5 km/s, respectively. These values are substantially smaller than the value of $R_t = 1.87$ GPa, which is the resisting stress exerted by a 0.4 GPa aluminum target on an ogive-nosed projectile at deep penetration. The increasing trend in R_{eff}, demonstrates the diminishing weight of the entrance phase with increasing impact velocities. However, even for the highest impact velocity the average deceleration is lower than the asymptotic value by 13%, because the penetration depth at this velocity is only twice the dominance range of the entrance phase.

In order to further demonstrate the strong effect of the entrance phase, Rosenberg and Dekel (2009b) performed several simulations with aluminum targets which have a cylindrical hole around their symmetry axis, as shown in Fig. 3.21. These holes were 50 mm deep (about eight times the projectile diameter) and their diameter was equal to the projectile's diameter (6 mm). The basic idea behind these simulations was to reduce the effect of the free impact surface by moving the impact area deep into the target. Thus, upon impact the projectile should experience a resisting stress (deceleration) which is much closer to that at deep penetrations.

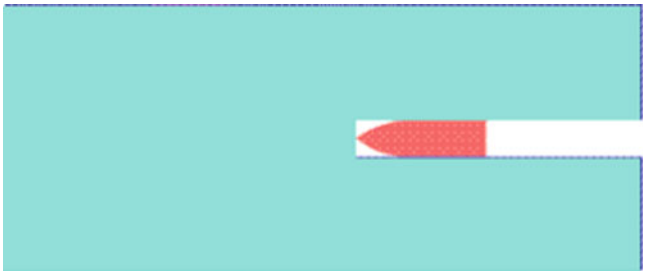

Fig. 3.21 The target with a central hole

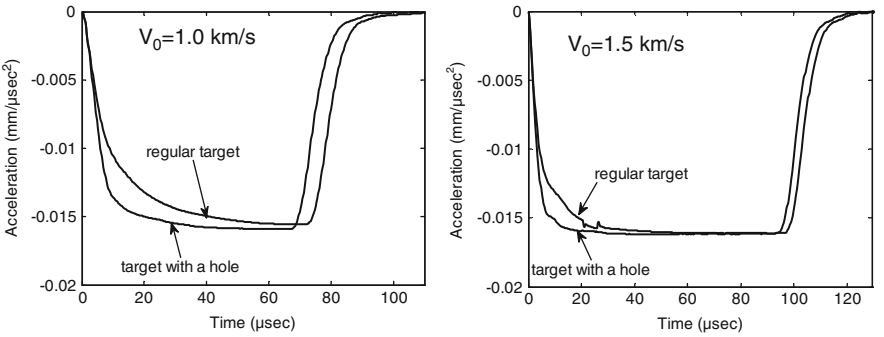

Fig. 3.22 Deceleration histories for the ogive-nosed projectile in a regular target and in a target with a hole

Deceleration histories of the ogive nosed projectile in both targets, with and without the hole, are shown in Fig. 3.22 for two impact velocities, $V_0 = 1.0$ and 1.5 km/s. One can clearly see that the effect of the entrance phase diminished by the addition of the hole, and the deceleration histories reach their asymptotic values shortly after impact. As expected, the penetration depths into the targets with the holes were lower than the corresponding depths in the flat targets. The differences diminished with increasing impact velocities, but even for the highest impact velocity (1.5 km/s) the depth of penetration into a regular target is higher by 5% than the corresponding depth in the target with the hole. The same trend was found in the simulations for the spherical nosed projectile. The corresponding differences between flat targets and those with a hole were much lower, due to the smaller dominance range of the entrance phase for these nose shapes.

A quantitative estimate for the strong effect of the entrance phase can be gained by analyzing the experimental results of Brooks and Erickson (1971). They shot ogive nosed tungsten carbide projectiles at 4340 steel targets with a Brinell hardness of 294BHN. These L/D = 4.92 projectiles, with a diameter of 8.86 mm, stayed rigid even at an impact velocity of 1.34 km/s. This set of experiments is particularly interesting since the high density of the projectiles (14.72 g/cm^3) resulted in relatively deep penetrations, well beyond the dominance range of the entrance phase. In order to asses the effect of the entrance phase we calculate the effective deceleration of the projectile for each experiment, through (3.21b). With increasing impact velocities these decelerations are expected to increase towards their asymptotic value at deep penetration. Table 3.4 lists the relevant data from the experiments of Brooks and Erickson (1971), together with the effective decelerations (a_{eff}), in units of 10^{-3} mm/μs^2, as calculated by (3.21b)

Table 3.4 The data from Brooks and Erickson (1971) and the effective decelerations

V_0 (m/s)	434	568	691	805	920	1,027	1,138	1,343
P (mm)	24.1	34.3	44	52	64	75.5	87	112
P/D	2.72	3.87	5.0	5.87	7.22	8.52	9.82	12.64
a_{eff}	3.91	4.7	5.43	6.23	6.61	7	7.44	8.05

Clearly, the effective decelerations increase with impact velocity but they do not reach a constant value, since the entrance phase is affecting the process in all of these experiments. This is the expected result since even the highest impact velocity resulted in a penetration depth of P = 12.6D, which is only twice the dominance range of the entrance phase. In order to have an estimate for the asymptotic deceleration of this projectile at deep penetrations, consider the target's flow stress of about $Y_t = 1.0$ GPa in these experiments. Inserting this value in (3.9) one obtains a value of $R_t = 4.68$ GPa for the resisting stress, which this target should exert on an ogive nosed projectile at deep penetration. From the dimensions of the projectile and its mass (30.9 g) one gets $L_{eff} = 34$ mm, for its effective length. Inserting the values for R_t, ρ_p and L_{eff} in (3.7b), results in a value of $a = 9.35 \cdot 10^{-3}$ mm/μs^2 for the asymptotic value of the deceleration for this projectile/target combination. This value is higher by 17% than the maximal value for the effective deceleration in these experiments, as given in Table 3.4. These examples demonstrate the significant effect of the entrance phase on the penetration process of short projectiles. It is clear that the entrance phase influences their penetration depths much beyond its dominance range. On the other hand, there are situations where the penetration depths are much higher than 6D, even for short projectiles, and the penetration formula (3.8a) should predict the correct penetration depths for these impacts. Obviously, such cases involve targets with low values of R_t, which can be penetrated to large depths, well beyond the influence range of the entrance phase.

In order to demonstrate this issue, consider the impact of a 0.5″AP projectile at a large Plexiglas block, with an impact velocity of $V_0 = 0.9$ km/s. Its penetration depth, as measured in our lab, was P = 190 mm which amounts to P = 17D for the D = 11 mm hard steel core of this projectile. This penetration depth is well beyond the dominance range of the entrance phase (P = 6D), and the model presented above should account for it. The values of Young's modulus for Plexiglas is about E = 5.5 GPa and its dynamic compressive strength is near $Y_t = 0.35$ GPa. Inserting these values in (3.9) and noting that the hard steel core of the 0.5″ projectile has an ogive shape, with $\phi = 1.15$ in (3.9), we obtain a value of $R_t = 0.66$ GPa for the resisting stress of Plexiglas. Inserting this value, together with $L_{eff} = 38.2$ mm for the hard steel core, in (3.8a) results in a predicted penetration of P = 185 mm, which is very close to the experimental result of P = 190 mm. The excellent agreement between model and experiment, for this L/D = 3.5 projectile, is the result of its deep penetration in the target, as discussed here. Note that the value of V_{cav} for this projectile/target pair as calculated by (3.11) is $V_{cav} = 1.55$ km/s, and no cavitation was expected for this shot (at $V_0 = 0.9$ km/s) as was, indeed, the case.

Another set of data which was affected by the entrance phase is given by Forrestal et al. (1991) for L/D = 5, 10 and 15 spherically nosed steel rods, impacting 6061-T651 targets at velocities in the range of $V_0 = 0.25$–1.0 km/s. The normalized penetration depths, for the three types of rods, are shown in Fig. 3.23 and it is clear that the results for the L/D = 10 and 15 rods fall around a single curve. In contrast, the L/D = 5 rods resulted in considerably higher values of P/L. Since their maximal penetration depth was only P = 9.5D, the entrance

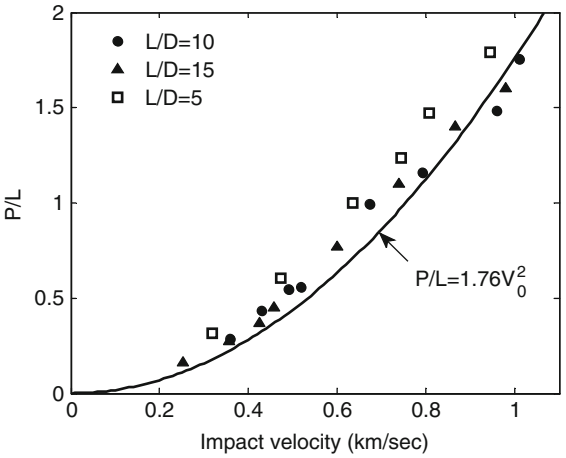

Fig. 3.23 Normalized penetrations for the spherical-nosed steel rods with different aspect ratios

phase is expected to influence all the penetrations of these short rods. On the other hand, the maximal penetrations for the L/D = 10 and 15 rods were P = 18D and P = 23D, respectively, which are well beyond the entrance phase dominance.

Figure 3.23 also includes the predicted penetration curve for the spherical nosed rod impacting the 6061-T651 aluminum targets, given by: P/L = 1.76 V_0^2, which was calculated for Fig. 3.10b. This curve accounts for the data of the L/D = 10 and 15 rods, while the data for the L/D = 5 rods lies significantly above this curve. This is a clear demonstration for the effect of the entrance phase, and we shall compare these results with the predictions of the numerically based model in the next section.

3.5.2 *A Numerically Based Model for the Entrance Phase Effect*

The influence of the entrance phase complicates the analysis to such a degree that it is very difficult to construct an analytical model for the penetration process of short projectiles. Thus, a different approach is suggested here which is based on numerical simulations. The recent improvements with hydrocodes enable one to construct numerically-based models for terminal ballistics. Obviously, the validity of these models should be checked by comparing their predictions with experimental results, as will be demonstrated in this case. The effect of the entrance phase will be quantified through an effective resisting stress (R_{eff}), as defined by (3.21a). We first rewrite this equation and obtain a general expression for the normalized penetration depth of a rigid projectile:

$$\frac{P}{L_{eff}} = \frac{\rho_p V_0^2}{2R_{eff}} \quad \text{with:} \quad R_{eff} \le R_t \tag{3.22a}$$

It is clear that R_{eff} should increase with impact velocity towards its value of R_t at deep penetrations. Rewriting (3.22a) we obtain:

$$\frac{P}{L_{eff}} = \frac{P}{D} \cdot \frac{D}{L_{eff}} = \frac{\rho_p V_0^2}{2R_t} \cdot \frac{R_t}{R_{eff}} \tag{3.22b}$$

which leads to the following relation:

$$\frac{P}{D} \cdot q = \frac{\rho_p V_0^2}{2R_t} \cdot \frac{L_{eff}}{D} \equiv I \quad \text{where:} \quad q \equiv \frac{R_{eff}}{R_t} \tag{3.23}$$

Up to this point we have only defined two new parameters, q and I. The parameter q, as defined by the ratio R_{eff}/R_t, expresses the effect of the entrance phase. Its value is always smaller than 1.0 and it is expected to approach this value at deep penetrations. The parameter I is a measure for the penetration power of the particular projectile into the given target. In fact, I is equal to the normalized penetration (P/D) of the projectile without the entrance phase effect, according to the constant deceleration model presented above. All the terms which determine the value of I are well defined for a given projectile/target pair and none of them depend on the details of the entrance phase.

Several workers have used similar parameters in order to account for their penetration data. Haldar and Hamieh (1984) presented penetration data for concrete targets using empirical relations between P/D and a parameter which they called the Impact Factor. This factor was defined through the mass (M), the diameter (D) of the projectile, and its impact velocity, according to:

$$\text{Impact Factor} = N\frac{MV_0^2}{D^3 f_c} \tag{3.24}$$

where f_c is the unconfined compressive strength of the concrete, and N is a nose shape factor. It is easy to see that the impact factor as defined by (3.24) is similar to the parameter I as defined by (3.23), since the term M/D^3 is equal to the term $\rho_p L_{eff}/D$. The two definitions differ by the expression for the target strength. Haldar and Hamieh (1984) use the target's compressive strength (f_c), while the resistance to penetration (R_t) is used in our definition. In addition, the target strength and the nose shape parameter appear separately in the definition of the impact factor through (3.24), while by our definition both of them are lumped together in R_t. Chen and Li (2002) also used an impact factor to account for the penetration depths of rigid rods in semi-infinite targets. Their impact factor includes a target strength term which is derived from the cavity expansion analysis. They also used a nose shape parameter in a similar way to that proposed by Haldar and Hamieh (1984). Thus, all the relevant parameters which influence the penetration depth of a given projectile are lumped into these closely related impact factors. As far as our approach is concerned, the impact factor is not a free parameter since it is the expected penetration efficiency (P/D) of the rigid projectile according to the constant deceleration model. The basic idea behind our approach is to account for the lower resisting stresses at the entrance phase through a universal relation between q and I. This will be achieved by a numerically-based model as described below.

The model is based on analyzing simulation results for the penetration depths of L/D = 3 projectiles, impacting a given target at several velocities. With these penetration depths, the corresponding values for R_{eff} and q can be calculated, in order to determine the influence range of the entrance phase. As a next step, general relations between P/D and the impact factor (I) will be constructed, for both ogive and spherical nosed projectiles. The main assumption behind the analysis is that these relations can be treated as universal for all the projectiles with similar nose shapes. This assumption will be validated by the close agreement between the model's predictions and experimental data.

The simulations were performed for D = 6 mm rigid steel projectiles, with ogive (3CRH) and spherical noses, having effective lengths of L_{eff} = 14.5 and 17.1 mm, respectively. These short projectiles impacted an aluminum target with strength of 0.4 GPa, at velocities in the range of V_0 = 0.1–2.0 km/s, for the ogive nosed projectile, and V_0 = 0.1–1.25 km/s, for the spherical nosed projectile. These velocity ranges were chosen in order to avoid the cavitation phenomenon, which complicates the analysis. Each simulation resulted in the corresponding value of P, from which R_{eff} values were determined through the relations given above. With the known values of R_t for both nose shapes, the curves for $q = R_{eff}/R_t$ vs. impact velocity, were constructed as shown in Fig. 3.24. As expected, the values for q increase asymptotically from q = 0 at V_0 = 0, towards a value of q = 1.0 for high impact velocities, as R_{eff} approaches its asymptotic value of R_t.

These simulation results are presented in Fig. 3.25 in terms of P/D as a function of qP/D = I, and as is clearly seen the two curves are very close to each other. This important result means that all the sharp nosed projectiles, conical and other ogives, should follow the curve derived here for the 3CRH ogive nosed projectile. These curves will be treated as universal relations which account for the entrance phase effect for sharp and spherical nosed projectiles.

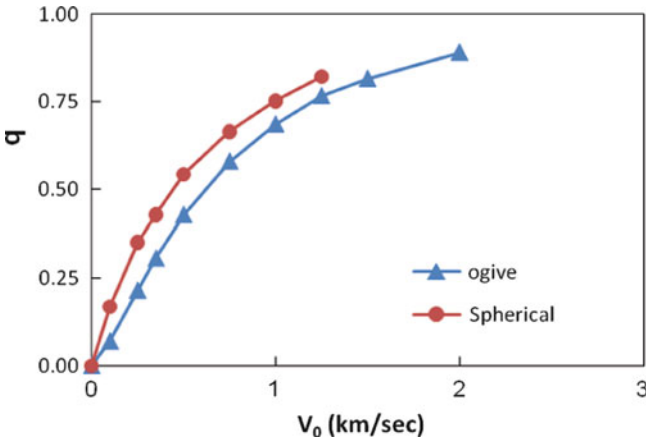

Fig. 3.24 Simulation results for the parameter q as a function of V_0 for both nose shapes

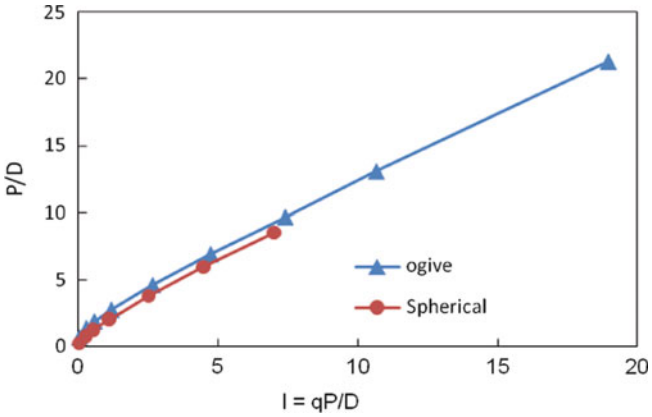

Fig. 3.25 Simulation results for the relation between P/D and I for the two nose shapes

In order to verify that these curves are not dependent on the density of the target, an additional set of simulations was performed, for the ogive-nosed projectile impacting a 0.4 GPa steel target. The results of these simulations are shown in Fig. 3.26, together with those for the 0.4 GPa aluminum target, and it is clear that both sets of simulations results fall on a single curve.

The two curves in Fig. 3.25 rise very sharply for low I values (up to about $I = 1.0$) and then increase more gradually for the higher values of I. These trends will be represented by different relations between P/D and I for the two regimes. For large values of I ($I > 1.0$) the following fits were chosen to represent the simulation results:

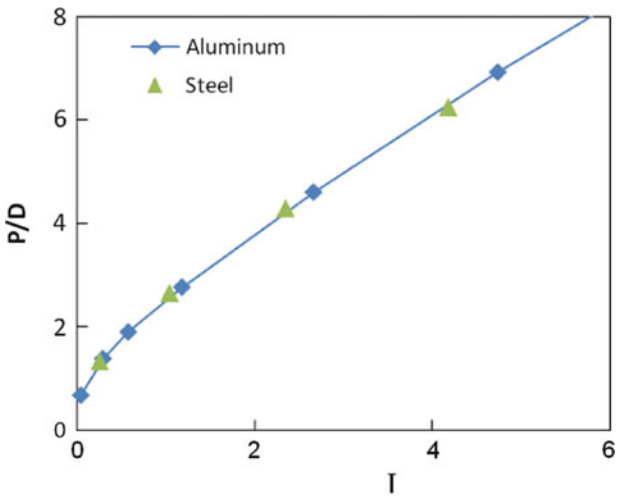

Fig. 3.26 Simulation results for ogive-nosed projectiles impacting 0.4 GPa steel and aluminum targets

$$\frac{P}{D} = 1.32 + 1.2\,I - 0.008\,I^2 \quad \text{For sharp nosed projectiles} \tag{3.25a}$$

$$\frac{P}{D} = 0.65 + 1.3\,I - 0.025\,I^2 \quad \text{For spherical nosed projectiles} \tag{3.25b}$$

It is interesting to note that the curves corresponding to these expressions meet the diagonal line P/D = I at I = 30 and I = 14, for the sharp and spherical nosed projectiles, respectively. These are the corresponding influence ranges of the entrance phase for these projectiles. The influence range for the sharp nosed projectile (P/D = 30) is about twice as large as that of the spherical nosed projectile (P/D = 14). The same factor was obtained for the dominance ranges of the entrance phase, P = 6D and P = 3D, for the ogive and spherical nosed projectiles, respectively. The values, of I = 30 and I = 14, define the applicability range of the numerically based model, which accounts for the entrance phase effect. For higher values of the impact factor (I) one should use the simple penetration relation of (3.8). In order to have a qualitative estimate for the influence of the entrance phase, consider the two intermediate cases where I = 20 for an ogive nosed projectile, and I = 10 for the spherical nosed projectile. Using (3.25) we find that P/D = 22.1 and P/D = 11.15, for the ogive and spherical nosed projectiles, respectively. These values are about 10% higher than their corresponding impact factors, demonstrating the significance of the entrance phase even for relatively high impact factors. The experimental penetration depths are expected to be higher than those calculated through (3.8) by 10% for ogive and spherical nosed projectiles having impact factors of I = 20 and I = 10, respectively.

The P/D = f(I) curves for the low values of I (I $\leq$ 1.0), are shown in Fig. 3.27. The fact that the curve for the ogive nosed projectiles is much higher than that of the spherical nosed ones is due to the larger dominance range of the entrance phase for the ogive nosed projectiles, as discussed above.

The following expressions were chosen to represent the relations between P/D and I, for the low values of I (I $\leq$ 1.0):

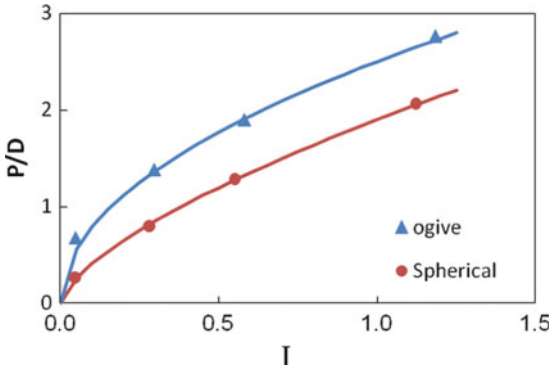

Fig. 3.27 Simulation results for the low values of the impact factor (I)

$$\frac{P}{D} = 2.5\, I^{0.5} \quad \text{For sharp nosed projectiles} \tag{3.26a}$$

$$\frac{P}{D} = 1.9\, I^{2/3} \quad \text{For spherical nosed projectiles} \tag{3.26b}$$

Inserting the definition of I, from (3.23), into these expressions results in the following relations between P/D and V_0, for the low range of impact factors ($I \leq 1.0$):

$$\frac{P}{D} = 1.77\left(\frac{\rho_p L_{eff}}{R_t D}\right)^{0.5} V_0 \quad \text{For sharp nosed projectiles} \tag{3.27a}$$

$$\frac{P}{D} = 1.2\left(\frac{\rho_p L_{eff}}{R_t D}\right)^{2/3} {V_0}^{4/3} \quad \text{For spherical nosed projectiles} \tag{3.27b}$$

These relations predict a linear dependence of P/D on impact velocity for the sharp nosed projectile and a ${V_0}^{4/3}$ dependence for the spherical nosed projectile, at low values of the impact factor ($I \leq 1.0$).

In order to demonstrate the validity of the equations derived above, we compare their predictions with experimental data for several projectile/target combinations. The data of Brooks and Erickson (1971), as given by Table 3.4 above, is a good case for such a validity check because both the projectile and the target are different from those used in the simulations presented above. These were ogive-nosed tungsten-carbide projectiles, with $\rho_p = 14.72$ g/cm^3, D = 8.86 mm and $L_{eff}/D = 3.84$, and the targets were 4340 steel with hardness of 294 Brinell, which corresponds to $R_t = 4.68$ GPa. Inserting these values of R_t, ρ_p and L_{eff}/D in (3.23), we get for this projectile/target pair: $I = 6.04 \cdot {V_0}^2$, where the velocity is given in km/s.. The values of I for each experiment in this set are listed in Table 3.5. These values were inserted in (3.25a) in order to obtain the corresponding values of P/D. The predicted penetration depths (in mm) are compared with the experimental data in Table 3.5. The good agreement between the two sets enhances the validity of the numerically-based model.

Consider the experimental results from Forrestal et al. (1991), for the L/D = 5 spherical-nosed steel rods impacting aluminum targets, which were presented in Fig. 3.23. Due to the entrance phase effect these short rods resulted in higher values for their normalized penetrations (P/L), as compared with the L/D = 10 and 15 rods. We wish to compare now the predictions from the numerically-based model

Table 3.5 Comparing the model's predictions with the data of Brooks and Erickson (1971)

V_0 (km/s)	0.434	0.568	0.691	0.805	0.920	1.027	1.138	1.343
I	1.14	1.95	2.88	3.91	5.11	6.37	7.82	10.89
P (calc)	23.7	32.2	41.7	52.2	64.2	76.5	90.5	119
P (exp)	24.1	34.3	44	52	64	75.5	87	112

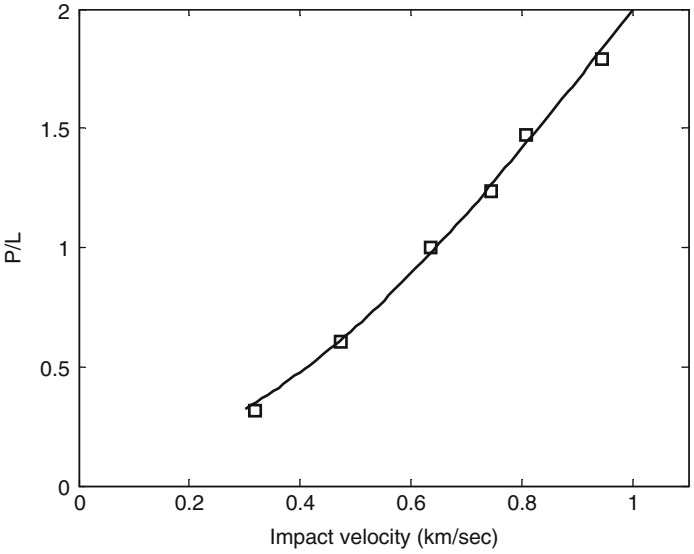

Fig. 3.28 Comparing the model's predictions (*curve*) with the data (*squares*) for the L/D = 5 spherical nosed rods impacting 6061-T651 aluminum targets

with the experimental results for these short rods. Using (3.23) with the following values: $\rho_p = 8.0$ g/cm^3, $L_{eff}/D = 5.34$, and $R_t = 2.27$ GPa for the 6061-T651 aluminum target (E = 69 GPa, $Y_t = 0.42$ GPa), we find that for this rod/target combination: $I = 9.39 \cdot V_0^2$. Using (3.25b), for spherical nosed projectiles, results in the predicted penetration curve shown in Fig. 3.28, together with the experimental results. The excellent agreement between the model's predictions and the experimental data strongly enhances the validity of the numerically-based model.

The penetration process of a long rod can be influenced by the entrance phase even at moderate impact velocities, when the target has a high strength, resulting in relatively low impact factors. This is the case with the experiments of Forrestal et al. (1992) for ogive nosed steel rods impacting 7075-T651 aluminum targets at velocities up to about 1.0 km/s. The dynamic flow stress of this aluminum alloy is about $Y_t = 0.7$ GPa, and with E = 73 GPa for its Young's modulus, a value of $R_t = 2.77$ GPa is obtained from (3.9), for this rod/target pair. Together with $\rho_p = 8.02$ g/cm^3, $L_{eff} = 77.8$ mm and D = 7.11 mm, (3.23) results in $I = 15.84\ V_0^2$ for the impact factor in this case. We have already seen that an impact factor of I = 20 for ogive nosed rods results in a correction of 10% in their penetration depth due to the entrance phase effect. The low velocity experiments of Forrestal et al. (1992) are expected to be significantly influenced by the entrance phase. The predicted penetration depths for these experiments are given in Table 3.6, together with the experimental results from Forrestal et al. (1992). We also added the calculated penetration depths from (3.8), ignoring the entrance phase effect. This equation results in very low penetration depths as compared with the

Table 3.6 Comparing calculated and measured penetration depths (in mm) for the 7075-T651 aluminum targets

V_0 (km/s)	0.372	0.695	0.978	1.067
P (exp)	26	70	127	147
P (from 3.25)	27.8	71.3	125.5	144.5
P (from 3.8)	15.6	54.4	107.7	128

experimental data, demonstrating the strong effect of the entrance phase. This effect is especially strong in this case where ogive nosed rods impacted high strength targets at low velocities. On the other hand, the agreement between the measured penetration depths and those predicted by (3.25a) is very good, demonstrating the validity of the numerically based model for the entrance phase effect.

Finally, we compare the predictions from the numerically based model with the penetration data for 0.3" APM2 projectiles, impacting 6061-T6 aluminum targets from Chocron et al. (1999). They used a modified projectile which consisted mainly of the hard steel core, with D = 6.17 mm and L_{eff} = 22.4 mm. For these aluminum targets (E = 69 GPa and Y_t = 0.42 GPa) and ogive-nosed projectiles, we have: R_t = 1.87 GPa, from (3.9). Inserting these values in (3.23) results in: I =7.6 V_0^2, for this projectile/target combination. With (3.25a) we calculate the penetration depths of these steel cores, as shown in Fig. 3.29, and find that the agreement between model and data is very good.

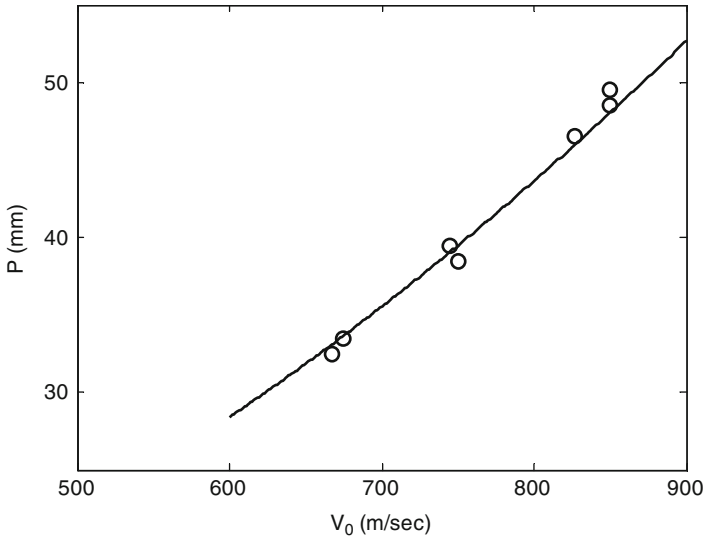

Fig. 3.29 The model's prediction (*curve*) and the data (*circles*), for the hard cores of 0.3"APM2 projectiles impacting 6061-T6 targets

3.6 The Impact of Spheres

The entrance phase regime introduces an inherent complexity to the analysis of the penetration data for compact rigid projectiles, such as spheres and L/D = 1 cylinders, since their penetration depths are well within the dominance range of the entrance phase. Another complicating issue concerns the role of target density. In the previous sections we have seen that, as far as rigid penetrators are concerned, the relevant target properties are its strength and Young's modulus, which determine its resistance to penetration. The density of the target does not play a role because the initial shock waves, which are generated upon impact, have negligible effect on the penetration process of rigid projectiles. Obviously, this assertion is much less accurate for short projectiles having a blunt nose shape, and the transient shock phase can have a non-negligible effect on their penetration process. In fact, the initial penetration velocity of a thin plate impacting a given target depends on the ratio of their acoustic impedances (the products of their density and sound velocity). Since sound velocities in most metals have similar values, we expect the density ratio to play an important role on the early deceleration of these projectiles. Indeed, experimental data for spherical projectiles impacting different metallic targets show a significant dependence of their penetration depths on their density ratio (ρ_p/ρ_t). These complicating factors are the main reason for the lack of analytical models for these cases. Instead, the experimental data has been presented through empirical relations for the dependence of the normalized penetration depth (P/D) on impact velocity and on the density ratio. Obviously, such relations can be used only as an interpolation tool. A comprehensive review of such studies for a large range of impact velocities is given in the survey of Hermann and Jones (1961). Most of the data in this review is concerned with the hypervelocity range where the spheres are heavily deforming. However, several sets of data include the impact of rigid spheres, which are presented empirically as $P/D = f(\rho_p/\rho_t, Y_t)\cdot V_0^n$, where the values for the exponent are around $n = 1.5$.

3.6.1 Rigid Sphere Impact

The complexity of the interaction between an impacting sphere and a semi-infinite target can be overcome by using numerical simulations, in order to estimate the dependence of the normalized penetration depths (P/D) on the relevant parameters. We performed several sets of simulations, for various rigid spheres impacting aluminum and steel targets of different strengths. The results of these simulations showed that, indeed, the density of the target plays an important role in determining the penetration depths of these spheres. However, it turned out that the dependence of the penetration depths on the density ratio is very complex. Even the exponent n, in the expression for P/D as a function of V_0, turned out to depend on the density ratio. Thus, it was practically impossible to derive simple relations to account for

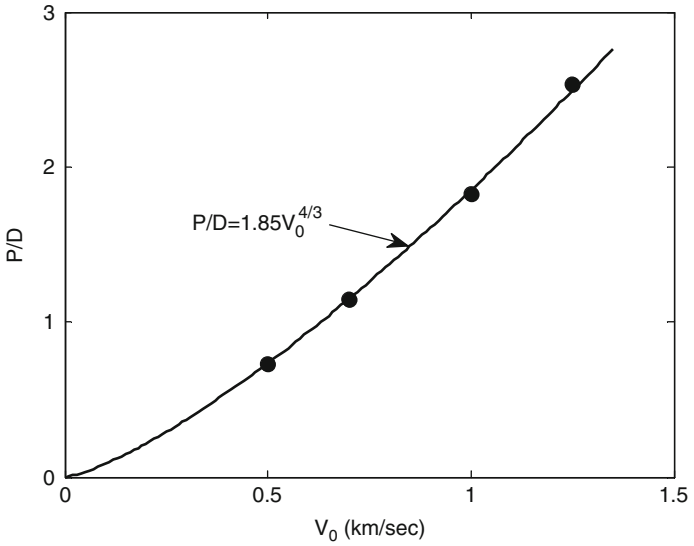

Fig. 3.30 Simulation results for rigid steel sphere impacting 0.4 GPa aluminum target

the penetration depths of rigid spheres, from these simulations. Still, for a limited set of experiments one can have some useful information, as we show next.

Consider the simulation results for a rigid steel sphere impacting an aluminum target with strength of 0.4 GPa, as shown in Fig. 3.30. The maximal impact velocity in this set of simulations was $V_0 = 1.25$ km/s, in order to limit the discussion to the no-cavitation range ($V_0 < V_{cav}$). The normalized penetration depths (P/D) seem to follow a relation of the sort: $P/D = kV_0^n$. A value of $n = 4/3$ for the exponent was chosen for the sake of consistency with (3.27b), which was derived from the numerically based model for spherically nosed projectiles, at low values of the impact factor (I). As shown in Fig. 3.30, the simulation results for steel spheres impacting the 0.4 GPa aluminum target, follow an empirical relation of the form:

$$\frac{P}{D} = k_1 {V_0}^{4/3} \tag{3.28}$$

where $k_1 = 1.85$ for this sphere/target combination, and V_0 is given in km/s.

The value of the multiplying constant (k_1) depends on the strength of the target and on the density ratio (ρ_p/ρ_t), as discussed above. At this stage we assume that the functional dependence of P/D on target strength should be similar to that given by (3.27b), as discussed above. We replace the term R_t in (3.27b) by Y_t, since the penetration resistance at very low penetration depths is expected to be governed by Y_t rather than by R_t. Thus, we write:

$$\frac{P}{D} = k_2 \left(\frac{{V_0}^2}{Y_t} \right)^{2/3} \tag{3.29}$$

with a new constant (k_2) which is assumed to depend on the densities of the sphere and the target. Inserting the value of $Y_t = 0.4$ GPa for the aluminum target in these simulations, we find that $k_2 = 1.0$ for the impact of rigid steel spheres at the 0.4 GPa aluminum target.

In order to check the validity of this result consider the experiments of Weimann (1974), who shot hard steel spheres at semi-infinite 2024-T351 aluminum targets. The diameter of these spheres ranged between 3 mm and–20 mm and their impact velocities reached 1.5 km/s. The flow stress of this aluminum alloy varies between 0.55 GPa and 0.65 GPa and an average value of $Y_t = 0.6$ GPa, results in the following expression for the normalized penetration in this case:

$$\frac{P}{D} = 1.4 V_0^{4/3} \tag{3.30}$$

where V_0 is given in units of km/s. The good agreement between this expression and the normalized penetrations of the rigid steel spheres of Weimann (1974) is shown in Fig. 3.31.

Another important result from Weimann's experiments concerns the crater's diameter, measured at the impact face, for rigid steel spheres with $D_0 = 12.7$ mm impacting the 2024-T3 aluminum targets. The crater diameter (D_c) should be equal to that of the sphere for impact velocities below the cavitation threshold (V_{cav}). For higher velocities the cavitation phenomenon should result in an increase of the crater

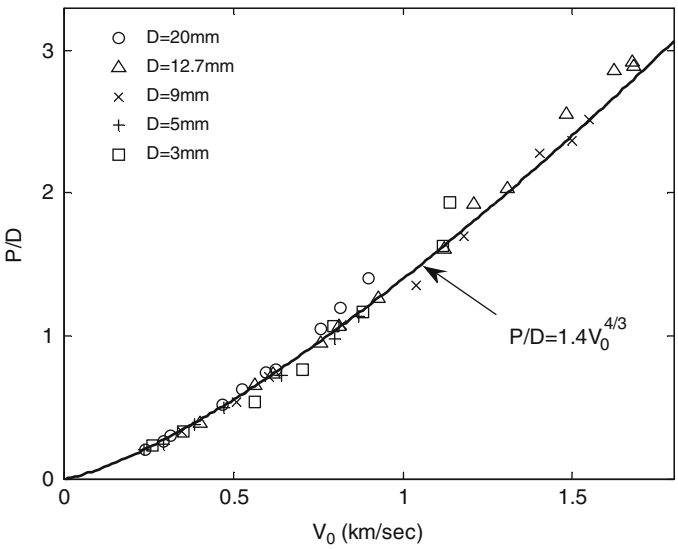

Fig. 3.31 Comparing the model's predictions with the data for hard steel spheres impacting 2024-T3 aluminum targets

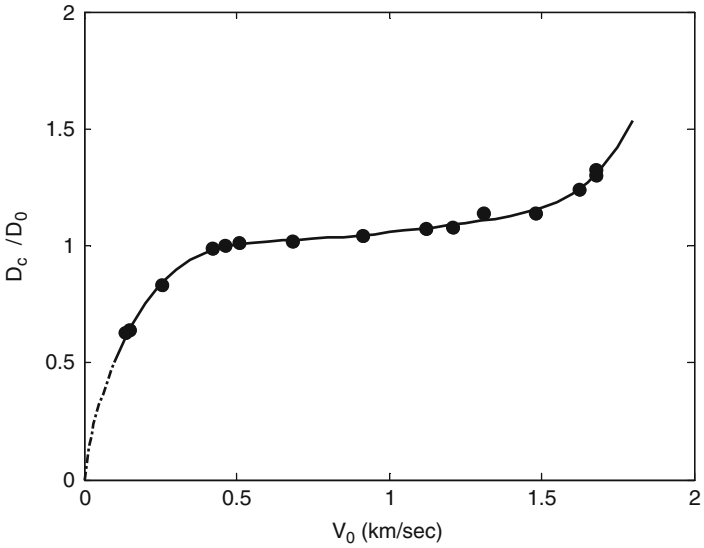

Fig. 3.32 The normalized diameters of the craters at the impact face for the 12.7 mm rigid spheres

diameter with impact velocity. Using (3.9) with $Y_t = 0.6$ GPa for the flow stress of the 2024 aluminum, results in a value of $R_t = 3.05$ GPa, for the resisting stress which this target exerts on rigid spheres. From (3.11) one gets an estimated value of $V_{cav} = 1.48$ km/s for a spherically nosed projectile ($b = 0.5$) impacting these aluminum targets. Thus, a plot of the experimental results for the crater diameters as a function of impact velocity, is expected to show a marked increase near this value of impact velocity. The experimental results of Weimann (1974) for the normalized crater diameters (D_c/D_0), at their impact face, are shown in Fig. 3.32. The crater diameters are relatively constant for impact velocities in the range of $V_0 = 0.5$–1.5 km/s, and they increase markedly for higher impact velocities. For impact velocities below 0.5 km/s these spheres did not penetrate more than half of their diameter and their crater diameter was less than that of the sphere.

The expected plateau at $D_c/D_0 = 1.0$ for impact velocities below V_{cav} is, in fact, increasing slightly, and the increase in D_c/D_0 for higher velocities is not an abrupt one as predicted by the model. These trends are probably due to effects which are not accounted by the model. Such an effect is the temperature increase of the target as a result of high velocity impacts. An impact at 1.5 km/s of a steel sphere on an aluminum target creates a shock wave which induces a temperature rise of about 200° in the target. This temperature change can lower the flow stress of the target material around the crater, resulting in a decrease in the value of its R_t value and, consequently, a lower value for V_{cav}. Still, the overall shape of the D_c/D_0 curve in this figure is in general agreement with the expected trend, according to the model presented in this chapter.

3.6.2 The Impact of Non-rigid Spheres

A large portion of the published data for the penetrations of spheres is actually given for deforming spheres. In order to have an estimate for the difference between the penetration capabilities of rigid and deforming spheres consider the data of Weimann (1974), who used 12.7 mm steel spheres which were hardened to different levels. These spheres impacted 2024-T351 aluminum targets at velocities up to 1.5 km/s. The results for the fully hardened and for the half-hardened spheres are shown in Fig. 3.33. Note the lower penetrations of the half hardened (soft) spheres, which flattened to various degrees with increasing impact velocity. Thus, the deformation of these spheres has a strong effect on their penetration capability. We also added the experimental results from the survey of Hermann and Jones (1961) for steel spheres impacting 2024-T3 aluminum targets. These experimental results were used by Goodier (1965) for his penetration model of rigid spheres, as described above. Obviously, the penetration depths of these spheres are significantly lower than those of the rigid spheres in the experiments of Weimann (1974). In fact, they are even lower than the data for the half hard spheres in Weimann's experiments.

The methodical study of Weimann (1974) resulted in another important observation which concerns the volumes of the craters formed by rigid and deforming spheres. The experiments with rigid spheres of diameters in the range of D = 3–20 mm, resulted in the following relation between crater volume (Vol) and impact velocity:

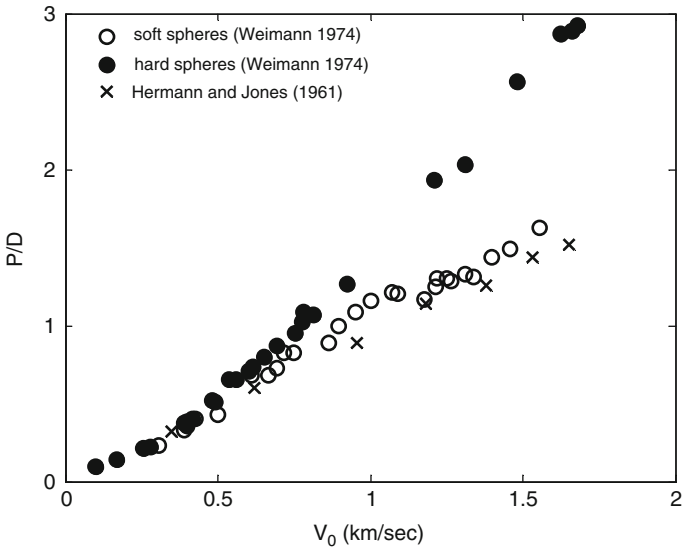

Fig. 3.33 The effect of sphere hardness on its penetration efficiency

$$\text{Vol}\left(\text{mm}^3\right) = 1.14\text{D}^3\text{V}_0{}^2 \tag{3.31}$$

where D is in mm and V_0 in km/s. This relation shows that the crater volume is proportional to the initial kinetic energy of the projectile, which is the expected result since no energy was dissipated in deforming or breaking the spheres. Weimann (1974) also measured the crater volumes in experiments with deforming steel spheres having different hardness. The crater diameters in these experiments were larger than those with the rigid spheres and their penetration depths were smaller, as expected. However, the data for all the different hardness spheres, including the rigid ones, followed the same linear relation between the volume of the crater (Vol) and the initial kinetic energy of the sphere (E_k), according to:

$$\text{Vol.}\left(\text{mm}^3\right) = 0.554\ \text{E}_\text{k}\left(\text{joules}\right) \tag{3.32}$$

This result means that the energy spent on plastically deforming the softer spheres is too small to have an appreciable influence on their penetration process.

The high velocity impact of very hard spheres results in their shattering, rather than their deformation, due to the low ductility of strong metals. One may expect that a hard sphere impacting a given target will shatter at a well defined velocity, with some loss of its penetration capability. Such reductions in penetration depth with impact velocity have been reviewed by Hermann and Jones (1961) for tungsten-carbide spheres impacting various targets. The data for these spheres impacting two types of aluminum targets is shown in Fig. 3.34. Note that the

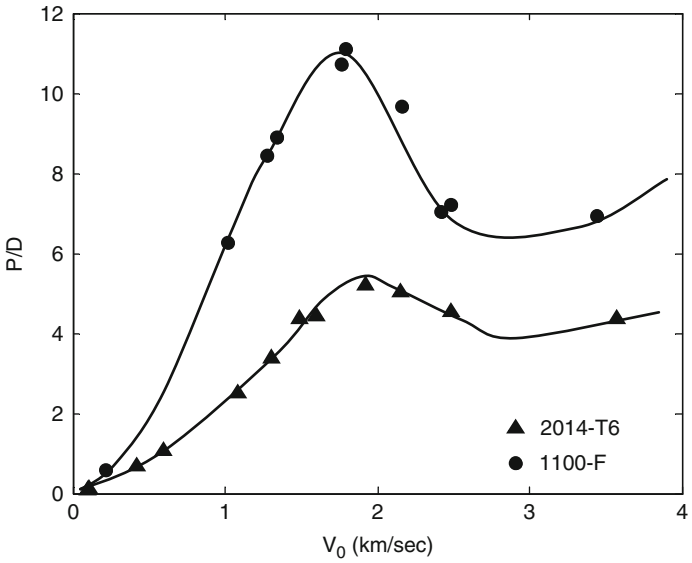

Fig. 3.34 The penetration depths of tungsten-carbide spheres in two aluminum targets

strength of the 2014-T6 alloy (0.5 GPa) is higher by an order of magnitude than the strength of the 1100 F aluminum targets, resulting in the significant difference between their corresponding penetration depths.

The threshold impact velocities for sphere shattering are practically the same for the two types of aluminum targets, and one may conclude that these thresholds depend on target density rather than on its strength. Indeed, the data for tungsten-carbide spheres impacting several targets, in Hermann and Jones (1961), shows a decreasing tendency of the shattering threshold velocity (V_{shatt}) with increasing target density. The range of velocities, from the onset of penetration decline to that where the penetration is as deep as that at the threshold, is known by the name of "shatter range" in the military literature.

The relation between the threshold velocity for shattering (V_{shatt}) and the density of the target was further investigated by Senf (1974), for hardened steel spheres. He found that these thresholds are related to the target's density by a simple equation :

$$\rho_t V_{shatt}^2 = const \tag{3.33}$$

The experimental results of Senf (1974) are shown in Fig. 3.35 for a large number of different targets, together with the curve which fits them, $\rho_t {V_{shatt}}^2 = 7.8$ GPa, as obtained by Senf (1974). One can use this value in order to define a threshold shattering pressure through a Bernoulli type of relation: $P_{shatt} = \rho_t {V_{shatt}}^2/2 = 3.9$ GPa. This value is higher by a factor of 2 than the compressive strength of the hard steel spheres which were used in this study ($Y_t = 1.9$ GPa).

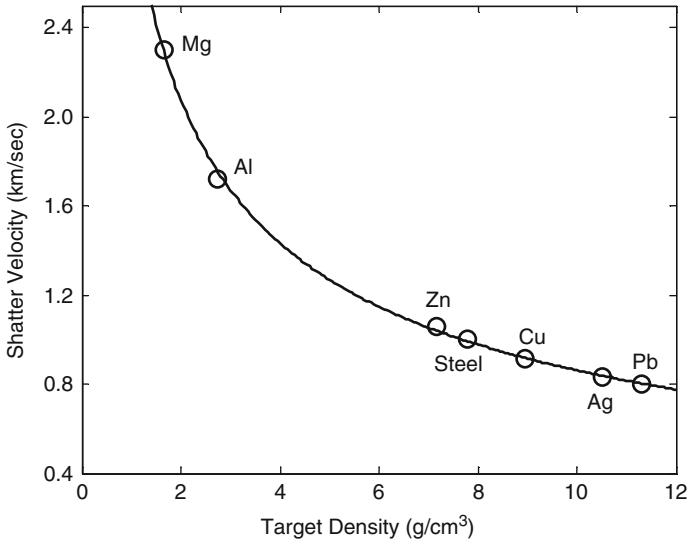

Fig. 3.35 The relation between shattering velocity and target density for hardened steel spheres

However, the shattering of these spheres should be related to their dynamic tensile strengths (spall), rather than their compressive strength. A spall strength of 3.9 GPa is a very reasonable value for steel with a compressive strength of 1.9 GPa. The shattering of high strength projectiles deserves further analysis due it is importance for both armor and anti-armor designs.

3.7 The Effect of Friction

One of the less understood issues in the field of terminal ballistics concerns the friction between the projectile and target surfaces, at the high sliding velocities which characterize the penetration process. It is usually assumed that friction effects are small, even negligible, which is the main reason for the scarcity of basic studies concerning this issue. Friction between the projectile and the target is manifested by the nose coloring of the recovered projectile which has often a snow-cap characteristic. The area of this snow-cap can be reduced by lubricating the projectile but its appearance is an indication for surface melting during penetration. Metallurgical examination of the target material near the crater surface shows that a thin layer has reached the melting point, which is also an indication for frictional forces.

One of the more interesting studies in this field is that of Kraft (1955) who measured the friction forces on a spinning conical-nosed projectile. He used a torsion-type Kolsky bar system in order to measure the torsional adhesion of the projectile during penetration. The system consisted of a long metallic bar with several strain gauges glued to its surface, at different locations and different orientations. Longitudinal strain gauges were glued near the impact point, while gauges oriented at 45^{o} to the bar's axis were glued farther along the bar. With this arrangement the longitudinal and shear waves in the bar could be separated easily and the effect of the torsional forces could be determined. The conical nosed hard steel projectiles were fired from a spirally rifled 0.3" gun. The strain gauge records which followed the torsion effects, showed a clear difference between spinning and non-spinning projectiles. The measured torque was compared with predictions from a theoretical model, which was based on the assumption that friction arises from molten surfaces. It turned out that the energy consumed by the torsional friction forces amounts to about 3% of the total energy consumption of the rigid projectile. These results agree with other experiments, where the projectiles had different surface finish and lubrications, resulting in friction-induced energy losses of three to four percent.

A closely related issue concerns the influence of friction on the projectile's cylindrical body (the shank) during its penetration process. In order to have an estimate for the effect of this frictional force Rosenberg and Forrestal (1988) performed a series of experiments with long conical-nosed steel rods having different shank designs (but the same mass) as shown in Fig. 3.36.

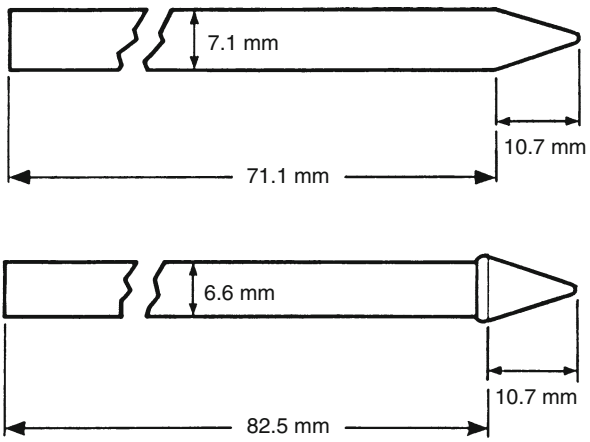

Fig. 3.36 The two rod designs for the friction study

These rods were shot at 25.4 mm thick 6061-T651 plates, and their residual velocities were determined. Clearly, the reduced-shank design avoids frictional forces on the shank, so that any difference between their residual velocities should be attributed to friction acting on the rod's shank. Residual velocities were determined for impact velocities in the range of 0.3–0.9 km/s and the results are shown in Fig. 3.37. The residual velocities of the reduced-shank rods were somewhat higher, indicating that friction on the regular rods was small but not negligible. For the same reason, the V_{bl} value for the reduced-shank (arrowhead) rod was somewhat lower, as seen in this figure.

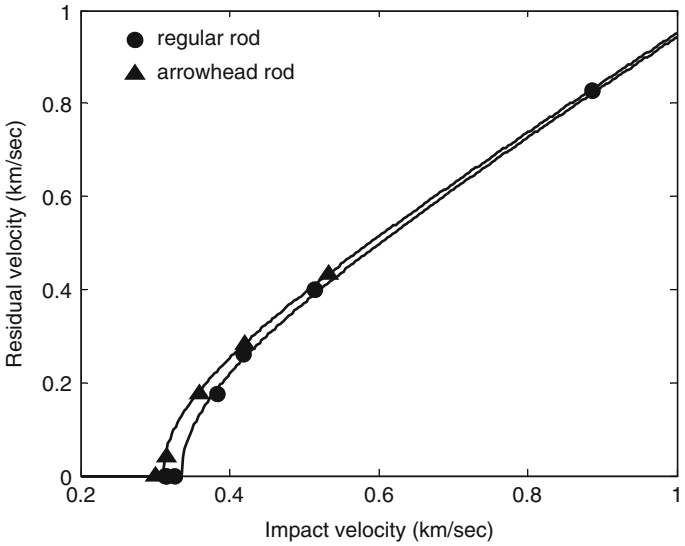

Fig. 3.37 Residual velocities for the rods with different shank design

A set of deep penetration experiments, with spherical nosed steel rods having cut-back shanks, was performed by Forrestal et al. (1988). The resulting penetration depths of these rods were very close to those for the regular rods, indicating that the friction on the rod's shank is very small in such experiments.

3.8 Concrete Targets

The penetration depths of rigid rods impacting semi-infinite concrete targets were analyzed by Rosenberg and Dekel (2010a). They arrived at the same conclusion as for metallic targets, namely, that the deceleration of these rods in semi-infinite concrete targets is constant, for penetration depths beyond the dominance range of the entrance phase. In order to demonstrate this finding, consider Table 3.7, which lists the relevant data from the experiments of Frew et al. (1998). In these experiments L/D = 10 ogive nosed steel rods impacted concrete targets, having a compressive strength of $f_c = 58.4$ MPa. The table lists the average decelerations (a_{av}) of these rods through the relation: $a_{av} = V_0^2/2P$. The inferred (average) decelerations in this set of experiments are clearly velocity independent, except for the low velocity shots which resulted in lower decelerations due to the entrance phase effect.

In order to calculate the resisting stress which these concrete targets exerted on the rods, we use their effective length $L_{eff} = 282.6$ mm and an average value of their inferred decelerations: $a = 2.53 \cdot 10^{-4}$ mm/μs^2. Inserting these values in the relation $R_t = \rho_p \cdot L_{eff} \cdot a$, we find that $R_t = 0.566$ GPa for these concrete targets.

It is interesting to check whether the numerically-based model presented above, for the effect of the entrance phase in metallic targets, accounts for the depths of penetration of the two low velocity shots in Table 3.7. We first calculate the relation: $I = 64.3\ V_0^2$, for this rod/target combination, using $\rho_p = 7.85$ g/cm^3 $L_{eff}/D = 9.27$, and $R_t = 0.566$ GPa, as derived above. With this relation for impact factor, we obtain $I = 12.73$ and 21.92 for the low velocity shots with $V_0 = 0.445$ and 0.584 km/s, respectively. Using these values of I in (3.25a), we obtain the

Table 3.7 The data from Frew et al. (1998), and the resulting inferred decelerations

V_0 (km/s)	P (mm)	a_{av} (10^{-4} mm/μs^2)
0.445	460	2.15
0.584	790	2.16
0.796	1,230	2.57
0.972	1,960	2.41
0.980	1,950	2.46
0.992	1,960	2.51
1.176	2,670	2.59
1.225	2,830	2.65

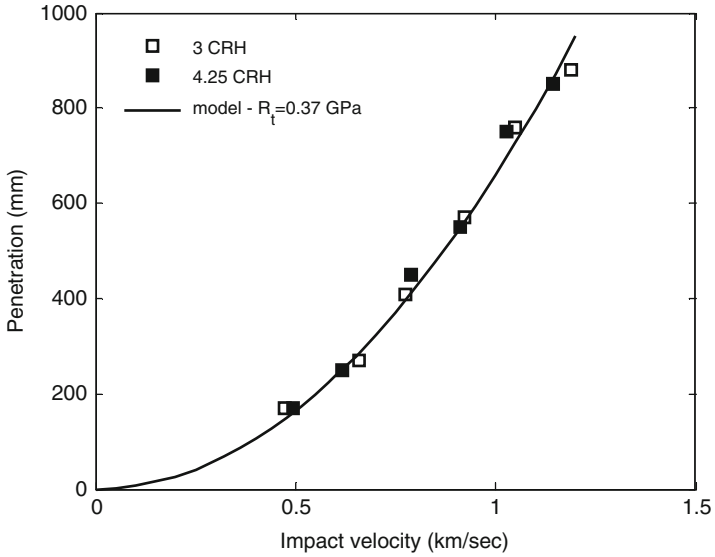

Fig. 3.38 Comparing model and data for penetration depths in $f_c = 21.6$ MPa grout targets

predicted values of P = 466.5 and P = 726 mm for these shots. For the $V_0 = 0.445$ km/s experiment the agreement is excellent (about 1%), while the model under predicts the data by 8% for the higher velocity shot. Based on this example, as well as on other low velocity impacts on concrete targets, we conclude that the numerically based model for the entrance phase effect accounts also for the data of concrete targets.

The experiments of Forrestal et al. (1996), with ogive nosed steel rods impacting grout targets with a compression strength of $f_c = 21.6$ GPa, resulted in a value of $R_t = 0.37$ GPa from the inferred decelerations of these rods. The agreement between the constant resisting stress model and the data for these targets is shown in Fig. 3.38.

This agreement enhances the claim that the deep penetration of rigid rods in concrete targets is achieved by a constant deceleration. Such agreements were demonstrated by Rosenberg and Dekel (2010a) for other concrete targets with higher compressive strengths. The values of R_t for the different concrete targets in the experiments of Forrestal et al. (1994, 1996) and Frew et al. (1998), were calculated by the same manner and were related to the concrete's unconfined compressive strength (f_c) through:

$$R_t = 0.22 \ln(f_c) - 0.285 \tag{3.34}$$

where R_t is given in GPa and f_c in MPa. This relation holds for concrete and grout targets, with unconfined compressive strengths in the range of $f_c = 13$–100 MPa, as shown in Fig. 3.39.

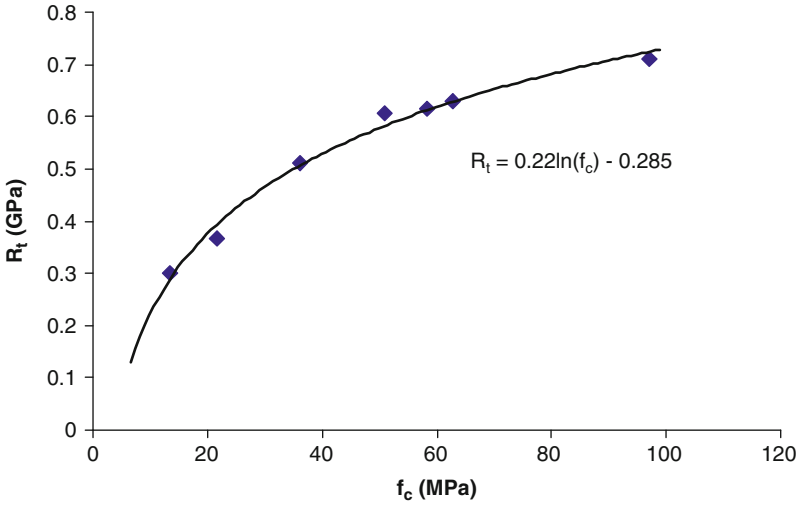

Fig. 3.39 The relation between R_t and f_c for different concrete and grout targets

It is interesting to note that concrete and concrete-like materials, have been considered by many workers to be strain rate sensitive, especially at rates of 10^2–10^3 s^{-1}, through dynamic strength measurements with the Kolsky bar system. In contrast, the analysis of Li and Meng (2003) showed that the apparent increase in concrete strength at these strain rates is due to inertia effects, rather than a real strengthening mechanism. This is the expected result since, according to Li and Meng (2003), there is no physical basis for the strain-rate sensitivity of concrete and concrete-like materials. The penetration experiments of Canfield and Clator (1966) support this claim, although in a non-direct way. In these experiments, ogive-nosed hard steel projectiles impacted reinforced concrete targets at velocities up to 820 m/s. The L/D = 2.16 ogive-nosed projectiles were of two different scales, the full scale with D = 76 mm and the 1:10 scale with D = 7.6 mm. A lot of care was put in manufacturing the scaled targets in order ensure that all the relevant parameters, such as the aggregate size and the diameter of the reinforcing bars, are properly scaled. The resulting normalized penetrations (P/D) from the two sets of experiments of Canfield and Clator (1966), are evenly scattered around a single curve, as shown in Fig. 3.40. Thus, according to these results, the process of deep penetration in concrete targets is geometrically scaled. This finding enhances the claim of Li and Meng (2003) that concrete is not a strain-rate sensitive material, since rate sensitivity is expected to result in a measurable size effect in experiments with these different scales. The most important issue here is that scaled experiments with concrete targets can be used in order to obtain relevant information about their terminal ballistics properties.

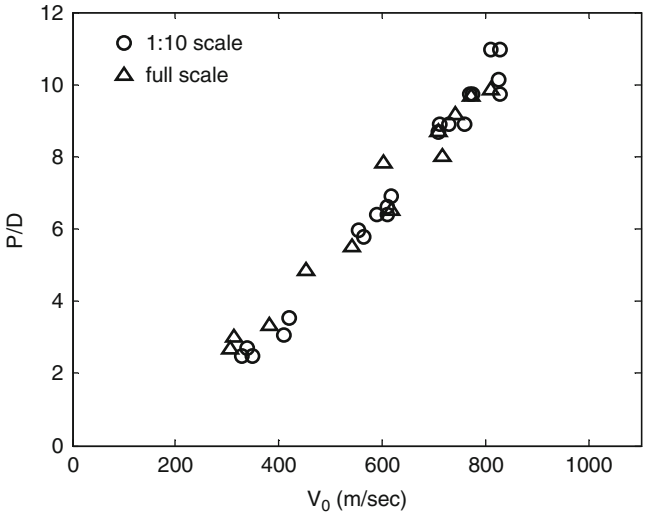

Fig. 3.40 Normalized penetrations for full scale and 1:10 scaled projectiles impacting concrete targets

3.9 The Deep Penetration of Deforming Rods

The deep penetration of rigid penetrators has a rather limited application since most of the practical cases involve eroding rods and shattering projectiles. Before we discuss the penetration of eroding rods we wish to explore the range where these rods deform rather than erode. Thus, we consider a rod which is rigid at low impact velocities, but at a certain threshold velocity (V_d) it deforms during penetration. For these impact velocities the length of the rod is shortening and the diameter of its front portion becomes larger than its original diameter. As a result, the rod loses its penetration capability and its penetration depths are decreasing with increasing impact velocities. This deformation phase takes place in a narrow range of impact velocities, as we shall see here. The threshold velocities depend on the properties of the rod (strength and nose shape) and on the strength of the target. At higher impact velocities, above another threshold velocity, rod erosion sets in and the penetration process becomes that of an eroding rod. This complex behavior was noted by Brooks (1974) in his work on short projectiles impacting steel targets. He termed the second threshold velocity, from deforming to eroding projectiles, as the hydrodynamic transition velocity (V_{HT}). The model of Tate (1977) for the hydrodynamic transition velocity in long rod, assumes that this transition occurs when the rod's erosion rate is equal to the velocity of the "plastic wave front" in the rod, which results in its gross plastic deformation.

The transition from rigid to deforming rods is analyzed here through experimental results and numerical simulations. These will be also used to construct an analytical model for the transition velocity. We shall consider rods of intermediate

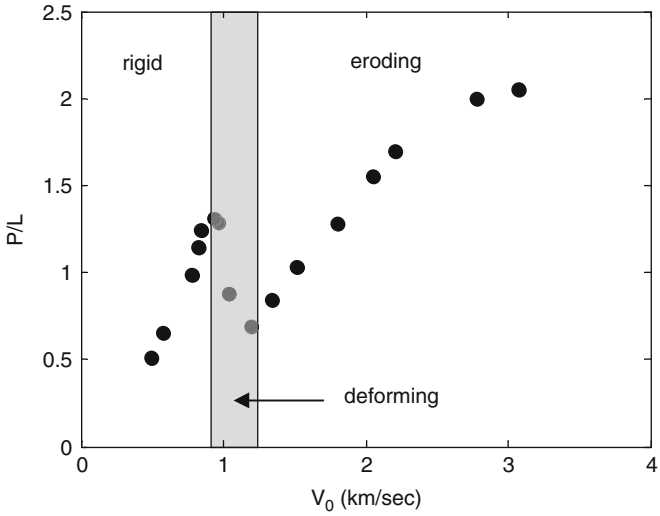

Fig. 3.41 The data for spherical-nosed steel rods impacting aluminum targets

strength (Y_p) which is somewhat lower than the resistance of the target to penetration (R_t). Consider first the results of Forrestal and Piekutowski (2000), for the penetration depths of spherically-nosed steel rods impacting 6061-T651 aluminum targets, as shown in Fig. 3.41. The general trend of the data shows that the transition from rigid to eroding rod behavior does not take place at a well-defined threshold velocity. Instead, there is a certain range of impact velocities between the two regimes, which corresponds to heavily deforming rods with no mass loss. The penetration depths in this regime, which is marked by the shaded area in the figure, decrease with increasing impact velocities. Thus, the actual sequence of impact events with increasing impact velocities, is as follows (1) at low impact velocities the rod penetrates as a rigid body up to a certain threshold velocity (V_d) which corresponds to the onset of its deformation, (2) for higher impact velocities the rod is deforming with no mass loss, resulting in reduced penetrations with increasing impact velocities, (3) at a certain impact velocity rod erosion sets in and for higher impact velocities the penetration depths are increasing again.

The post-mortem radiographs in Fig. 3.42, from Forrestal and Piekutowski (2000), show three residual steel rods which impacted the aluminum targets at velocities just below and above the onset of rod deformation and its erosion.

V_0=932m/s V_0=1037m/s V_0=1193m/s

Fig. 3.42 The post-mortem radiographs of the residual rods in the aluminum targets

The residual rod in the intermediate velocity shot, at $V_0 = 1{,}037$ m/s, is heavily deformed at its front part, with a diameter of about 1.5 times that of its undeformed back part. An impact velocity of 1,193 m/s resulted in an eroded rod with a much lower penetration depth, as is clearly seen in the radiograph at the right hand side.

These features were investigated by Rosenberg and Dekel (2010b) through numerical simulations for steel rods, with strengths between 1.2 GPa and 2.0 GPa, impacting semi-infinite aluminum targets with strengths in the range of 0.4–0.6 GPa. The simulations were carried out for impact velocities which correspond to the rigid and the deforming-rod phases, with the aim to better understand the deformation mechanism. These observations were used to construct an analytical model for the transition velocity from rigid to deforming rod behavior. The constitutive model for both rod and target materials was the simple von-Mises criterion, with well defined strength values and without strain hardening or strain rate effects. This choice of constitutive relation is in accord with the stress–strain relations of the high strength rods which were used by Forrestal and Piekutowski (2000), and with the stress–strain curve of the 6061-T651 aluminum targets. Figure 3.43 shows the deformation process of a 2.0 GPa steel rod as it penetrates the 0.4 GPa aluminum target, for an impact velocity of 1.2 km/s. One can clearly see that the deformation takes about 160 microseconds, after which the rod reaches its final shape, with a clear distinction between the deformed and undeformed parts. Note the similar shape of the deformed rod in this simulation and that of the residual rod in the experiment with $V_0 = 1.037$ km/s, as shown in Fig. 3.42.

A close examination of the nose deformation process in this simulation shows that after about 30 microseconds the diameter of the rod's nose reached its final

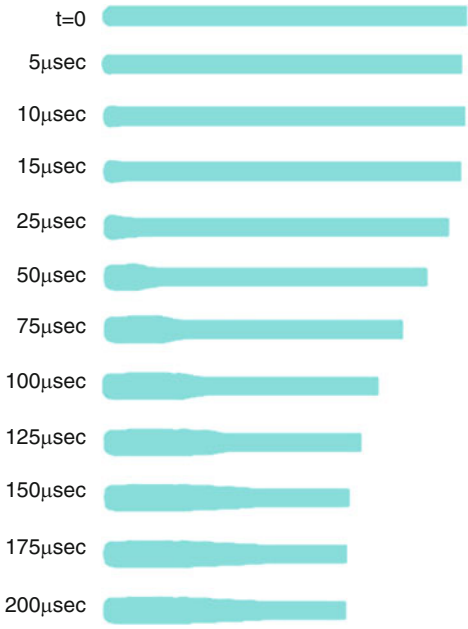

Fig. 3.43 Simulation results for the deformation of a 2.0 GPa steel rod impacting the 0.4 GPa aluminum target at 1.2 km/s

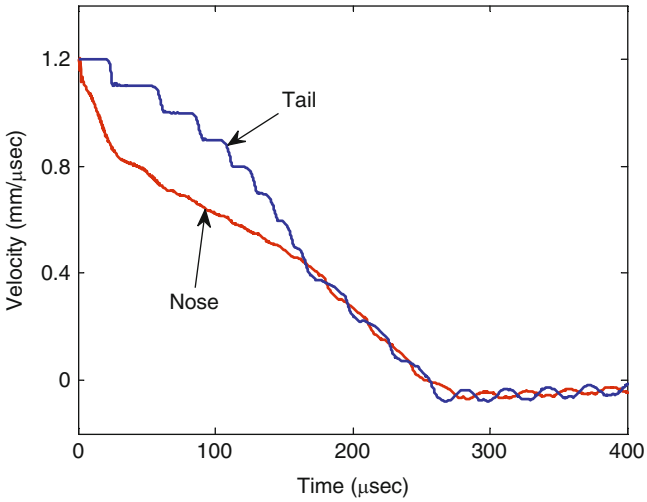

Fig. 3.44 The velocity histories of the deforming rod's nose and tail

value. This is, roughly, the time which is needed for the rod to penetrate through the dominance range of the entrance phase. Thus, the continued growth of the nose diameter is probably due to the increasing resisting stress which the target exerts in this range. As the rod penetrates deeper the length of its plastically deformed part continues to grow until about 160 microseconds after impact. At this time the velocities of its nose and tail attain similar values, as shown in Fig. 3.44.

The velocity of the rod's tail is decreasing through a series of steps, having a well defined amplitude, in a similar way to that of a rigid rod. The elastic waves which reverberate in the rigid and the deforming rods are different in two respects. The first difference is in their amplitude which, for a rigid rod, is equal to the target's resistance to penetration (R_t). For the impact discussed here the strength of the rod is $Y_p = 2.0$ GPa and the target's resistance to penetration is $R_t = 2.24$ GPa. Obviously, the rod cannot carry an elastic wave with amplitude which is higher than its strength. The amplitude of the velocity steps in Fig. 3.44 is $\Delta v = 0.1$ mm/μs which, according to (3.6b), corresponds to stress steps of $\sigma = 2.0$ GPa, exactly the strength of the rod (Y_p) in this simulation. Thus, the deceleration of the rigid part of a deforming rod is controlled by its strength, rather than by the target's resistance to penetration. Another issue concerns the time durations of these velocity steps, which are equal to the transit time of the elastic waves between the rod's tail and the propagating boundary of its deforming front. Obviously, these times are getting shorter at each reverberation due to the propagating plastic front.

The deceleration of the deforming rod is expected to be much higher than that of a rigid rod because of these shorter stress reverberations, as is clearly seen in Fig. 3.45. The deceleration achieved a constant value at about $t = 80$ μs, when its front and tail velocities are still varying in a very different manner, as seen in Fig. 3.44. The value of this constant deceleration is higher by a factor of two than

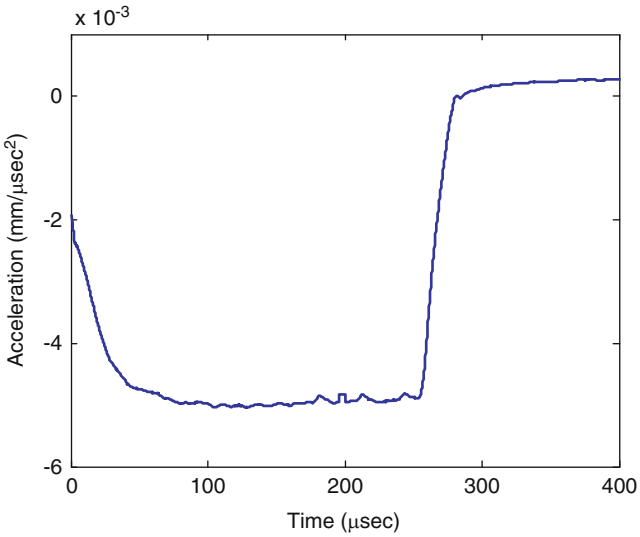

Fig. 3.45 The deceleration history of the deforming rod

the deceleration of a rigid rod with the same initial dimensions, since its effective length is smaller by the same factor.

The next sets of simulations were performed by Rosenberg and Dekel (2010b) in order to determine the threshold velocities for rod deformation. Figure 3.46 shows the simulation results for the penetration depths of both spherical and ogive nosed L/D = 20 steel rods, with strengths of 1.6 and 2.0 GPa, impacting aluminum targets with strength of 0.4 GPa. Note that the values for R_t of this aluminum target are: $R_t = 2.24$ and 1.87 GPa, for the spherical and ogive nosed rods, respectively. Thus, these simulations deal with cases where the rods' strengths are close to the resisting stresses of the target. The figures also include the penetration curves for the corresponding rigid rods, using the model presented above. These curves help in determining the onset for the gross deformation of the rods, as their penetration depths start to decrease with impact velocity.

The transition velocity from rigid to deforming rod increases with rod strength, as expected. Moreover, the transition velocities for the ogive nosed rod are higher, by a factor of about two, than those for the spherical nosed rod of the same strength, in agreement with the experimental results of Forrestal and Piekutowski (2000). In addition, the velocity range where rod deformation takes place is getting narrower with increasing rod strength, which was also found experimentally by Forrestal and Piekutowski (2000).

In order to construct an analytical model for the deformation threshold velocity (V_d) Rosenberg and Dekel (2010b) considered the effect of the confining stresses which the target exerts laterally on the rod's nose. Such stresses can prevent the deformation of the rod, or postpone it to higher impact velocities. This idea was suggested by Segletes (2007) in order to account for the deformation pattern of

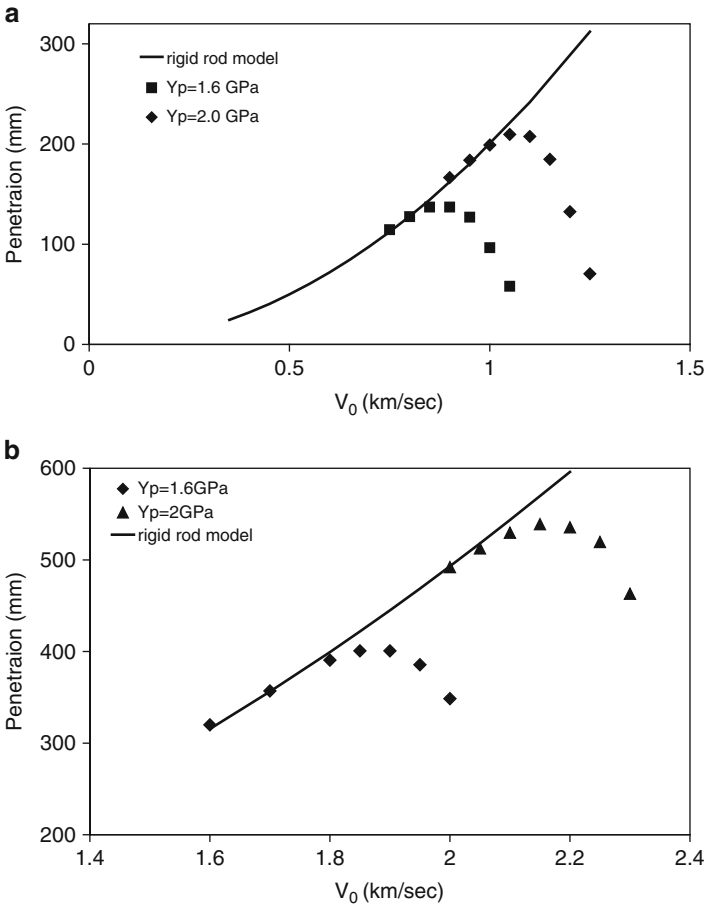

Fig. 3.46 Simulation results for steel rods impacting 0.4 GPa aluminum targets for: (**a**) spherical-nosed rods and (**b**) ogive-nosed rods

spherical nosed tungsten-alloy rods perforating aluminum plates. His basic assumption was that once the rod's nose is embedded in the target, its bulging is constrained by the surrounding material which exerts these lateral stresses. In order to validate the effect of these laterally confining stresses, Rosenberg and Dekel (2010b) performed several simulations for spherical nosed steel rods impacting aluminum targets which had a cylindrical hole around their symmetry axis. The diameter of these holes was 6 mm (as the rod's diameter) and their depths varied between 6 mm and 30 mm. The rods in these simulations had strength of 2.0 GPa and their impact velocity was 1.2 km/s. Table 3.8 lists the resulting penetration depths, as well as the final nose diameters of the rods in these simulations. The results from the reference simulation, with a flat-faced target, are added for the sake of comparison. It is evident that the lateral confinement of the rod's nose limits its mushrooming and enhances its penetration capability. This confining effect is significant even for the

Table 3.8 Simulation results for steel rods impacting aluminum targets with a hole

Hole depth (mm)	Final nose diameter (mm)	Penetration depth (mm)
0	8.65	213
6	6.91	213.2
12	6.82	222.4
18	6.78	225.3
24	6.76	226
30	6.74	228

6 mm hole (one rod diameter), since the final nose diameter in this simulation is considerably smaller than that for the impact on a flat target.

The penetration depths of the rod in these simulations should be compared with those for a rigid rod impacting targets with holes of different depths. As was shown above, such impacts should results in smaller penetration depths with increasing hole depths, due to the diminishing effect of the free impact face. The fact that the deforming rod penetrates deeper with increasing hole depth, strongly supports the assumption of Segletes (2007) concerning the role of the lateral stresses. Apparently, the effect of these stresses is strong enough to overcome the higher resisting stresses at the deeper depths.

The model of Rosenberg and Dekel (2010b) is based on the assumption that the onset of rod deformation takes place when the pressures on both sides of the rod/target interface are equal. On the rod side the pressure is equal to the effective strength of the rod Y_{eff}, which includes the lateral support from the target (H_{lat}). On the target side, the pressure at the interface is given by the target's effective resistance to penetration (R_{eff}) and the dynamic (inertia) contribution, $b\rho_t V^2$, where b is the nose shape factor which was defined above. Thus, the basic equation of this model is:

$$Y_{eff} = Y_p + H_{lat} = R_{eff} + b\rho_t V_d^2 \tag{3.35}$$

Rosenberg and Dekel (2010b) noted that since the deformation process starts right after impact, the target resistance term (R_{eff}) cannot assume its value at deep penetration (R_t). As will be shown in Chap. 5, the resistance of the target at the very early stage of penetration is equal to $3Y_t$. Thus, the effective resistance term (R_{eff}) was chosen as the average of these two resisting stresses, namely, $3Y_t$ and R_t. For the confining lateral stress they assumed a value of $H_{lat} = 3Y_t$ through some simplifying assumptions. These considerations led to the following expression for the threshold velocity (V_d) between rigid and deforming rod behavior:

$$V_d = \sqrt{\frac{Y_p - \Delta}{b\rho_t}} \tag{3.36}$$

The nose shape factors are b = 0.5 and b = 0.15 for the spherical and ogive nosed rods, respectively. The large difference between these values accounts for the much higher values of V_d for the ogive nosed rod as obtained in the simulations. This was also the case for several sets of experiments with rods having these nose shapes, as shown by Rosenberg and Dekel (2010b). The term Δ in (3.36) is due to the averaging scheme for the resisting stresses within the entrance phase. Since the range of influence of this phase is different for the ogive and spherical nosed rods, their corresponding expressions for Δ are somewhat different, as given by:

$$\Delta = (R_t - 3Y_t)/2 \quad \text{For spherical nosed rods} \tag{3.37a}$$

$$\Delta = (R_t - 4Y_t)/2 \quad \text{For ogive nosed rods} \tag{3.37b}$$

These simple relations were found to account for all the values of V_d obtained by the simulations of Rosenberg and Dekel (2010b), and for the experimental data of V_d from several studies, such as Piekutowski et al. (1999) and Scheffler (1997). For example, the ogive nosed rods used by Piekutowski et al. (1999) were of two types of steel, the VAR 4340 with strength of 1.14 GPa, and the AerMet 100 with strength of 1.72 GPa. These rods were shot at 6061-T651 aluminum targets, which have a dynamic flow stress of $Y_t = 0.42$ GPa. Inserting these values of Y_p in (3.36), together with the corresponding value of $R_t = 1.87$ GPa, results in $V_d = 1.57$ and 1.98 km/s for the two rods. These predicted values are in excellent agreement with the experimental results of $V_d = 1.58$ and 1.92 km/s for the $Y_p = 1.14$ and 1.72 GPa rods, respectively.

3.10 The Transition to Finite-Thickness Targets

As was stated above, the semi-infinite target has a tutorial role in the field of penetration mechanics. In most of the actual situations the targets are either perforated, or they are thick enough to stop the projectile near their back surface. In these cases the back surface of the target plays an important role through its interaction with the projectile, as we shall see in the next chapters. This interaction lowers the resisting stresses on the penetrator as it approaches the back surface of the target. Moreover, the interaction can induce various failure modes in the rear part of the target, which further lower the resisting forces on the penetrator. The immediate result of these back surface interactions is that the thickness of the plate which is needed to stop a given projectile, is always larger than the penetration depth of the projectile in a semi-infinite target. This issue was studied by Senf and Weimann (1973), with 12.7 mm rigid steel spheres impacting finite plates of 2024-T3 aluminum. They found that the ratios of the penetration depths into the semi-infinite targets (P_n), and the thicknesses of the finite plates which are needed to stop these spheres (H_{BL}), are about 0.73. One should note that the values of H_{BL} depend

on the specific criterion chosen for plate perforation. Thus, different values may appear in the literature for the P_n/H_{BL} ratio even for the same projectile/target combinations. This issue was pointed out by Dehn (1986) who reviewed a large number of projectile/target combinations and quotes values of $P_n/H_{BL} = 0.33–0.9$ for this ratio.

Kinard et al. (1958) investigated this issue at much higher impact velocities (1.2–4 km/s) by impacting aluminum spheres at aluminum targets and steel spheres at copper targets. These spheres perforated plates which were 1.5 times thicker than their penetration depth in semi-infinite targets (P_n). Thus, their experiments resulted in $P_n/H_{BL} = 0.67$. They also found that the penetration depth (P) at a given impact velocity is strongly dependent on the plate thickness (H). These experimental results were summarized, empirically, by the relation:

$$\frac{P}{H} = 1.3 \cdot \sqrt{\frac{P - P_n}{P_n}} \tag{3.38}$$

With this relation it is possible to predict the penetration depth of a spherical projectile in a given target, if its penetration into a semi-infinite target is known. The minimal plate thickness which is needed to stop a given projectile is obtained by setting $P/H = 1$ in (3.38), resulting in a ratio of $P_n/H_{BL} = 0.63$. Another set of experiments, with relatively soft $L/D = 1$ steel cylinders impacting armor steel targets, both finite and semi-infinite, is given by Hohler and Stilp (1990). Impact velocities reached 4.0 km/s and the semi-infinite penetrations were substantially smaller than the corresponding values for H_{BL}. The corresponding ratios (P_n/H_{BL}) increased gradually from about 0.33 to 0.68, for impact velocities in the range of 1.0–4.0 km/s.

Chapter 4
Plate Perforation

4.1 General Description

The process of plate perforation is the most important issue in terminal ballistics for armor engineers who seek to optimize the weight and cost of their protective designs. This subject has been the focus of a large number of studies which concentrate on two issues (1) the ballistic limit velocity for a given projectile/plate combination and (2) the projectile's residual velocity and mass, as a function of its impact velocity. The perforation process is influenced by the back surface of the target which, together with the impact face, results in a time-varying force on the projectile during perforation. Different modes of perforation are possible and their energy absorption capabilities have to be carefully analyzed, especially when the process involves more than a single mode. For example, when thin plates are perforated they tend to stretch and bend around the impact area, absorbing a significant part of the projectile's kinetic energy through these deformations. On the other hand, several failure modes can take place during perforation of thick plates such as spalling, petalling, discing, and plugging. These failure modes depend on several factors such as the impact velocity, the properties of the plate material, and the loading geometry (plate thickness, projectile diameter and its nose shape). These issues have been discussed by Wilkins (1978), Woodward (1990), Corbett et al. (1996), Liu and Stronge (2000) and others. These inherent complexities call for different analytical approaches to the process of perforation, as compared with the deep penetration of rigid penetrators which were discussed in Chap. 3.

Some of the failure modes in perforated plates are shown in Fig. 4.1, from Wingrove (1973), demonstrating the wealth of phenomena that take place by changing the nose shape of the projectile. In this work, 2014-T6 aluminum plates 10 mm thick were impacted by hard steel projectiles, 7 mm in diameter, with different nose shapes. This aluminum alloy is known to behave in a semi-brittle manner due to its high strength. The picture on the left side of the figure shows the plug formed through a shearing process, by the impact of a flat-ended projectile at

Z. Rosenberg and E. Dekel, *Terminal Ballistics*,
DOI 10.1007/978-3-642-25305-8_4,

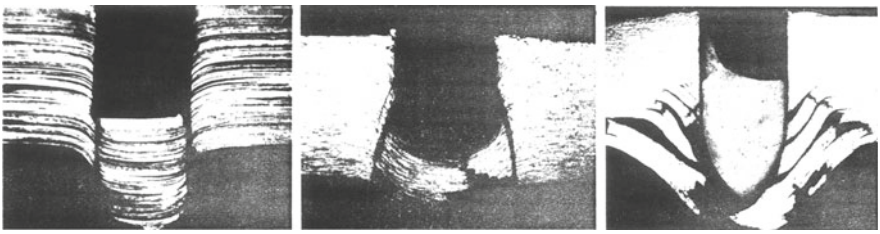

Fig. 4.1 Failure modes during plate perforation by rigid projectiles of different nose shapes

180 m/s. The diameter of the plug is equal to that of the projectile and its thickness is somewhat smaller than the plate's thickness. The spherical nosed projectile induced a cone-shaped plug with a thickness of about half the plate thickness, as seen in the middle picture. The ogive-nosed projectile induced a failure through the discing phenomenon, which is evidenced by the detached plates at the back of the target. Discing is a common failure mode for high strength materials, and it is due to the bending of the back part of the plate. This bending induces tensile failure along weak planes parallel to the face of the plate, as discussed by Woodward (1990).

Wingrove (1973) measured the resisting stress which the plate exerts on the flat ended projectile, during a quasi-static perforation process, by continuously monitoring the load in an Instron machine. He found that this force is increasing up to a point where the penetration is about 3.5 mm, after which it decreases gradually until the breakout of the projectile. This means that the process of plug formation is over by the time the projectile is at a distance of about one diameter from the back surface of the target. We shall discuss this issue when we analyze the perforation of plates by flat-ended projectiles. These pictures demonstrate the wealth of different failure modes which take place during perforation, complicating the analysis as far as engineering models are concerned. The present chapter deals with perforation processes for which a reasonable understanding exists through numerical simulations and analytical models. A comprehensive review of various analytical models for plate perforations has been given by Corbett et al. (1996). We shall focus on perforation processes of metallic plates by rigid projectiles of different nose shapes (sharp, spherical and blunt). The perforation of non rigid projectiles will be discussed in Chap. 5, where we deal with the penetration process of eroding penetrators.

The perforation of ductile metallic plates by sharp nosed projectiles is the simplest process for analytical modeling, since it is achieved by the so-called ductile hole enlargement mechanism. This interaction will be discussed in detail in the next section. The perforation of thin plates is characterized by the dishing process, through which the plate is heavily stretched and bent (globally deformed) in a large area around the impact point. At certain impact conditions the large bending of thin plates is followed by a petalling phenomenon, which results in a fracture of the deformed plate around the perforation hole. The petalling process was analyzed by Landkof and Goldsmith (1985), Atkins et al. (1998) and Wierzbicki (1999) by considering the energy involved in hoop stretching. Since

our main interest is focused on terminal ballistics for armor applications we shall not discuss the petalling process in thin plates, and the interested reader is referred to these articles. The perforation of plates by blunt projectiles is much more complex since several failure modes take place during this process, and the borderlines between the corresponding regimes are unclear. The specific type of failure depends on the normalized thickness of the plate (H/D), where D is the diameter of the projectile. This ratio is often used in order to classify a target as either thin or thick, as we shall see here.

4.2 The Perforation of Ductile Plates by Sharp Nosed Rigid Projectiles

The perforation of ductile plates by sharp nosed projectiles is considered as the simplest perforation process, since it does not involve a failure mechanism in the plate. The passage of the projectile through the plate is achieved by pushing the target material to the side, through the so-called ductile hole enlargement mechanism. Such a process, for a conical nosed steel projectile perforating an aluminum plate, is shown in Fig. 4.2 from Woodward (1978). One can see that a significant amount of target material has been pushed along the projectile's direction of motion, creating the front and back "lips" in the target. The aluminum plate shows no bending and there is no evidence for material failure inside the plate itself.

Rosenberg and Dekel (2009b, 2010c) followed the forces which act on the projectile during such perforations by using numerical simulations. In order to simplify the analysis the constitutive relations of the plate materials were based on the simple von-Mises yield criterion without the complicating effects of strain rate and strain hardening. Since most materials show a certain amount of strain hardening, we recommend that the strength of such materials, in the numerical simulations, will be taken as their dynamic flow stresses. These are the high strain values of their stress–strain curves as determined by Kolsky bar system. As discussed in Chap. 1, these tests are characterized by strain rates in the range of 10^3–10^4 s^{-1}, which are the relevant rates for impact velocities at the ordnance range.

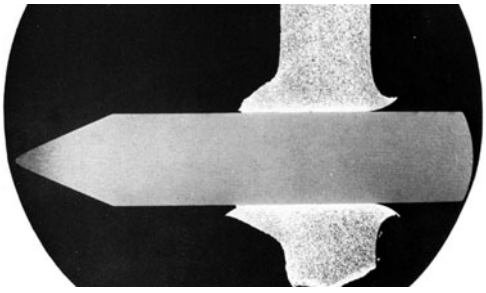

Fig. 4.2 A conical nosed projectile perforating a mild steel plate

We start the analysis by considering the deceleration characteristics of the rigid projectile as obtained by the numerical simulations of Rosenberg and Dekel (2009b). These simulations for a conical nosed tungsten projectile with D = 8.3 mm and L_{eff} = 25.6 mm, impacting aluminum plates with strength of 0.4 GPa, followed the experiments of Forrestal et al. (1990). The simulation results for the residual velocities of the projectiles were very close to the experimental data for all the plate thicknesses. Thus, they were used by Rosenberg and Dekel (2009b) in order to highlight the physics of the perforation process. The first issue which can be demonstrated with such simulations concerns the nature of the deceleration histories for these projectiles during perforation. The deceleration histories for the conical-nosed projectiles impacting plates of different thicknesses at V_0 = 800 m/s, are shown in Fig. 4.3a. It is clearly seen that, except for the H = 100 mm plate, these decelerations do not reach a constant level, due to the combined influence of the front and back free surfaces. Even for the 100 mm plate, with H/D = 12, a constant deceleration is achieved only for a very short time, which terminates at about t = 120 μs, as shown in Fig. 4.3a. This time marks the onset of the influence of the plate's back surface, and it is clear that even for the thickest plate the perforation is achieved mostly through a time-varying deceleration. In contrast, the deceleration of this projectile in a semi-infinite target reaches a constant value after about 100 μs, as shown in Fig. 4.3b. This is the time duration for a penetration depth of about 6D which is the dominance range of the entrance phase for sharp nosed penetrators, as discussed in Chap. 3.

Rosenberg and Dekel (2010c) found that the back surface starts to exert its influence on the projectile when it is about three diameters away from this surface. Since the dominance range of the impact phase is 6D, we may conclude that the thickness of a finite plate should be at least 10D, in order to exert its full resisting stress. Even for these large thicknesses most of the penetration process is achieved through a non constant deceleration, as shown in Fig. 4.3. Due to these time-varying decelerations, a simple analytical model for finite plate perforation is difficult to construct. This is the main reason for the fact that researchers use integral approaches, which are based on energy and momentum conservations, such as the model of Recht and Ipson (1963). This is a relatively simple model which accounts for a vast range of experimental data for both rigid projectiles and long rods. This model, which will be termed the RI model, is described below and its validity will be demonstrated through both experimental results and numerical simulations.

The RI model assumes that the reduction in the projectile's kinetic energy as a result of plate perforation is equal to the work invested in the target in order to open a hole for the passage of the projectile. The kinetic energy of the plate and the energy invested in its bending or stretching, are ignored by the RI model. Thus, the energy balance between the projectile's kinetic energy, before and after perforation, and the work invested in the target (W_p), is given by:

$$\frac{1}{2}MV_0^2 = \frac{1}{2}MV_r^2 + W_p \tag{4.1a}$$

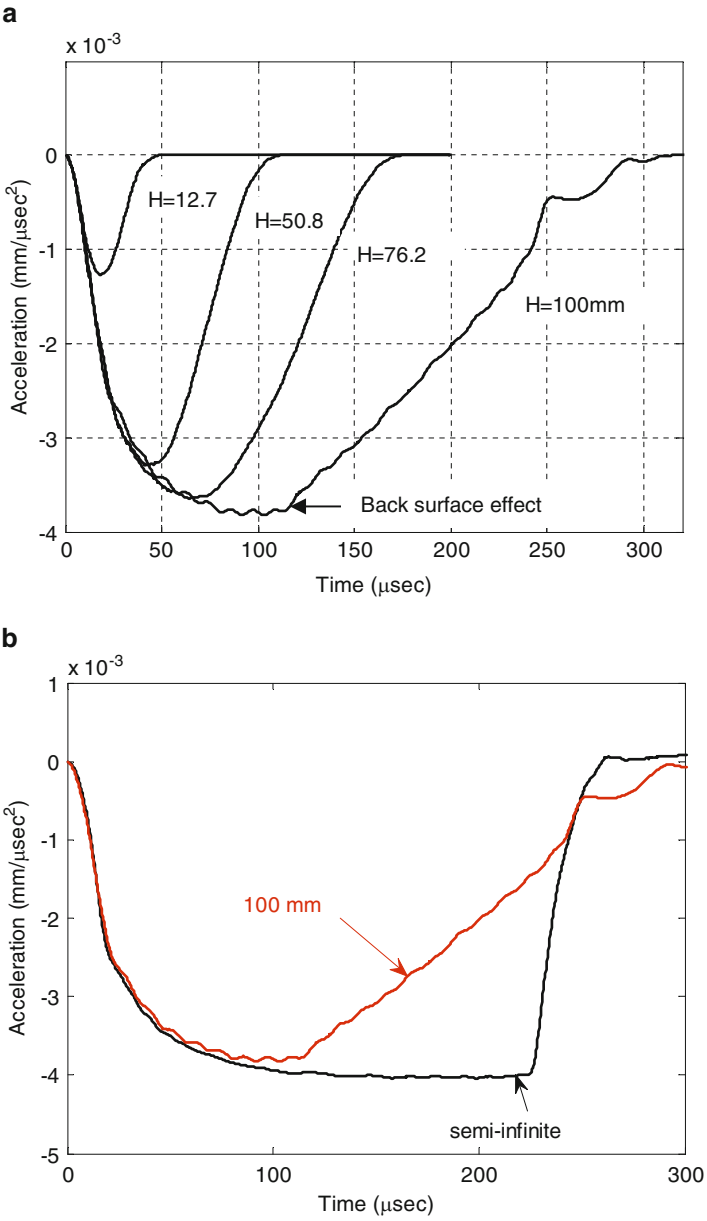

Fig. 4.3 The deceleration histories of a short projectile impacting several aluminum plates at 800 m/s

where V_0 and V_r are the impact and the residual velocities, respectively.

By definition, for an impact at the ballistic limit velocity the residual velocity is equal to zero, and one can write:

$$\frac{1}{2}MV_{bl}^2 = W_p \tag{4.1b}$$

Combining the two equations results in the following relation:

$$V_r^2 = V_0^2 - V_{bl}^2 \tag{4.2a}$$

and its normalized version:

$$\frac{V_r}{V_{bl}} = \sqrt{\left(\frac{V_0}{V_{bl}}\right)^2 - 1} \tag{4.2b}$$

This simple equation has been found to be extremely successful in accounting for the data concerning sharp nosed rigid penetrators perforating ductile plates, as was shown by Rosenberg and Dekel (2009b). Figure 4.4 summarizes experimental results from Forrestal et al. (1987, 1990) and Piekutowski et al. (1996), for ogive and conical nosed steel rods perforating aluminum plates. One can clearly see that the model's predictions are in excellent agreement with the data for a large range of impact velocities. The nature of (4.2b) leads to an asymptotic approach of V_r to V_0 with increasing impact velocities, since the work needed to perforate the target is getting much smaller than the kinetic energy of the projectile

The numerical simulations of Rosenberg and Dekel (2009b) for different projectiles, targets, and impact velocities support the basic assumption of the RI

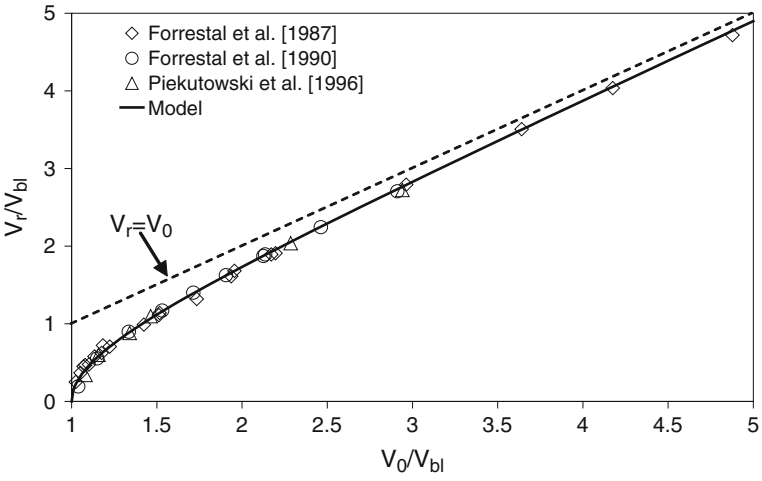

Fig. 4.4 The agreement between the RI model, (4.2), and data from several sources

model, that the energy spent on perforating a given plate, is practically independent on the impact velocity. In order to demonstrate this issue consider the simulation results for the conical nosed tungsten projectile perforating a 12.7 mm aluminum plate, with strength of 0.4 GPa. For impact velocities of $V_0 = 300$, 500 and 800 m/s, the simulations resulted in residual velocities of $V_r = 207$, 449 and 769 m/s, respectively. Using (4.2a) we get the inferred value of $V_{bl} = 217.1$, 220, and 220.5 m/s for these simulations, respectively. Thus, one can claim that the inferred ballistic limit of this projectile/target combination is $V_{bl} = 218.8 \pm 1.7$ m/s. The small variation in the value of V_{bl} enhances the claim that the work needed to perforate this plate, as inferred by (4.1b), is practically independent on impact velocity. Similar results were obtained with simulations for the other plate thicknesses, which resulted in small variations (less than 2%) in the inferred values of V_{bl} at different impact velocities. In conclusion, these simulation results support the main assumption behind the RI model, as manifested by (4.1a and 4.1b). They also demonstrate the usefulness of numerical simulations for the validation of basic assumptions behind analytical models.

The main significance of the RI model, as manifested by (4.2a and 4.2b), is that there is no need to perform many experiments in order to determine the $V_r(V_0)$ curve for a given projectile/plate combination, if the perforation is achieved by the ductile hole enlargement process. In fact, one has to determine the value of V_{bl}, accurately enough, and then use (4.2b) to derive the residual velocity for any impact velocity. Thus, the whole physics of this perforation process is manifested by the value of V_{bl} for the given projectile/plate pair. The value of V_{bl} can be determined by a single experiment in which the impact and residual velocities are measured to a great accuracy, by inserting these velocities in (4.2a). With this inferred value of V_{bl} the normalized curve of V_r/V_{bl} as a function of V_0/V_{bl} is obtained through (4.2b). It is important to note that the normalized equation has a very steep slope for impact velocities slightly above the ballistic limit velocity. In fact, the curve is practically perpendicular to the horizontal axis at $V_0 = V_{bl}$. Thus, small variations in material properties may cause a large scatter in the measured residual velocities at this range, as is often the case with the experimental results. By analyzing the various sources for experimental errors, Rosenberg and Dekel (2009b) recommended that the single experiment, for the determination of V_{bl}, should be performed at an impact velocity of about $1.5V_{bl}$. Such an impact velocity is beyond the steep rise of the $V_r(V_0)$ curve, and it is not high enough to be in the range where small errors in the measured residual velocity cause large variations in the inferred ballistic limit velocities.

In order to demonstrate the importance of these issues consider the data of Dey et al. (2004) concerning the perforation of 12 mm thick plates, of three different steels, by ogive nosed steel projectiles with $L_{eff} = 80$ mm and $D = 20$ mm. The plates were made of the Weldox 460E, 700E, and 900E steels. Four experiments were performed for each type of steel at impact velocities above the corresponding ballistic limits, and several experiments were performed below these limits. Dey et al. (2004) determined the values of V_{bl} by averaging the lowest impact velocity which resulted in plate perforation, and the highest velocity for which there was no perforation. This is the accepted technique to determine the value of the ballistic

limit velocity, as explained in Chap. 1. With these values of V_{bl} they fitted their data for V_r/V_{bl} through an empirical relation which is different than the physically based relation of the RI model, (4.2a). We wish to emphasize that such an empirical fit does not serve the science of terminal ballistics, even when it results in a better agreement with the data, as compared with the physically based model. The impact velocities in most of the experiments of Dey et al. (2004) were only slightly higher than the corresponding V_{bl} values, and repeated experiments with the same impact velocities did not result in the same residual velocities. These facts led to the result that the data did not adhere to the RI model, and Dey et al. (2004) used empirical fitting procedures. A physically-based approach to these experiments is suggested here.

The first step in the data analysis process is to determine the inferred value of V_{bl} for each experiment through (4.2a), and average these values in order to determine the value of V_{bl} for each plate. This procedure results in the following values: $V_{bl} = 282.0$, 317.6, and 312.5 m/s for the 460E, 700E, and 900E steel plates, respectively. These inferred ballistic limits are slightly different than those determined by Dey et al. (2004) which were $V_{bl} = 290.6$, 318.1, and 322.2 m/s, but they are consistent with the physically-based RI model. Moreover, these values for the inferred ballistic limits can highlight important issues concerning the perforation mechanisms of the different plates. As an example, consider the inferred values of V_{bl} for the 700E and the 900E steels which result in a non-monotonic change of V_{bl} with target strength. This trend indicates that the perforation process of the hardest steel plate cannot be described by the ductile hole enlargement process, probably because of some failure mechanism which took place during its perforation. The same non-monotonic trend was also observed for the conical nosed projectiles in this study, and it was even more pronounced in the experimental results for the flat ended projectiles. As we shall see below the perforation process by the ductile hole enlargement mechanism should result in a monotonic increase of V_{bl} with both plate thickness and its strength. In summary, by analyzing the data through the physically-based RI model one can follow such deviations from the ductile hole enlargement process, as described here. The following discussion concentrates on the ductile hole enlargement process in metallic plates, with the aim of establishing a relation between the compressive strength of the plate material and its resistance to peroration. Such a relation will lead to an analytical model for the ballistic limit velocity of a given projectile/plate pair, in terms of their relevant physical properties.

There have been several attempts at constructing analytic models for the ballistic limit velocity which are based on the work invested in the target during perforation. This issue has been thoroughly analyzed by the great physicists, the Nobel laureate Hans A. Bethe (1941) and G.I. Taylor (1948), who worked at the war ministries in the U.S and England during the second world war. Short summaries of their work can be found in Woodward (1978) and in Corbett et al. (1996), for the resisting stress which has to be overcome in order to open a hole in a metallic plate. In order to simplify their analysis, Bethe and Taylor assumed plane stress conditions in the plate and that the diameter of the hole is of the order of the plate thickness (H). The expressions which they obtained for this work (W_p) were similar to each other but differed by their numerical factors, according to:

$$W_p = \pi r^2 H \cdot 2Y_t \qquad \text{Bethe [1941]} \tag{4.3a}$$

$$W_p = \pi r^2 H \cdot 1.33Y_t \qquad \text{Taylor [1948]} \tag{4.3b}$$

where Y_t is the strength of the plate material and r is the radius of the hole which is, in fact, the radius of the perforating projectile.

One can interpret these equations as defining the effective stresses which resist the opening of the hole, which are equal to $2Y_t$ and $1.33Y_t$ according to the analyses of Bethe and Taylor, respectively. These values are lower than the threshold pressures which are needed to open a spherical or cylindrical cavity in a large elasto-plastic solid, as calculated (also during WW II) by Bishop et al. (1945). As described in Chap. 3, the cavity expansion analysis results in values of the order of $(3–4)Y_t$ for these threshold pressures. The values obtained from Eqs. 4.3 are much lower than the resisting stresses on a rigid projectile during its penetration in a semi-infinite target, which amount to $R_t = (5–6)Y_t$, as derived in Chap. 3. The low resisting stresses from (4.3) are due to the fact that the stress state in a finite thickness plate is close to a plane stress, where the stress normal to the plate is zero. On the other hand, the three dimensional state of stress in a semi-infinite target is closer to a plane strain situation, which results in much higher resisting stresses.

Rosenberg and Dekel (2010c) presented a numerically-based approach in order to derive the effective resisting stress on the perforating projectile, by using 2D numerical simulations. Their basic idea was to replace the actual time-varying stresses by a constant (effective) stress, which results in the same energy loss for the projectile. This effective resisting stress (σ_r) was defined through the equation of motion for the rigid projectile as it perforates a plate of thickness H:

$$F = M\frac{dV}{dt} = MV\frac{dV}{dx} = \pi r^2 \sigma_r = const. \tag{4.4}$$

where M is the projectile's mass and r is its radius. Integrating this equation between the boundaries: $V_0 = V_{bl}$ at $x = 0$, and $V = 0$ at $x = H$, results in:

$$\frac{MV_{bl}^2}{2} = \pi \cdot r^2 H \sigma_r \tag{4.5a}$$

Using the definition of L_{eff}, through $M = \rho_p \pi r^2 L_{eff}$, and rearranging (4.5a), lead to the following relation for V_{bl}:

$$V_{bl} = \sqrt{\frac{2H\sigma_r}{\rho_p L_{eff}}} \tag{4.5b}$$

This simple equation can be used in order to derive the ballistic limit velocity for any projectile/plate pair, if the corresponding value of σ_r is known. In principle, one can determine the value for V_{bl} even without performing a single experiment if a reliable model is constructed for σ_r, in terms of the relevant parameters for the projectile and the target plate. One of these parameters is, obviously, the thickness

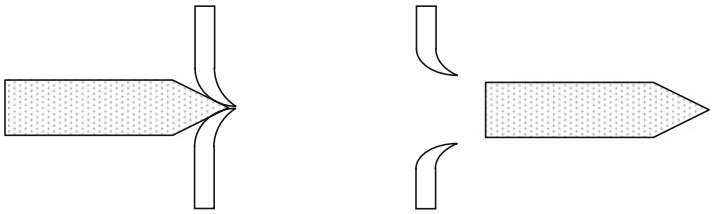

Fig. 4.5 Schematic description of the dishing process in thin plates

of the plate (H). The dependence of σ_r on H should be quite strong, considering the values which σ_r attains for the extreme cases of thin and thick plates, as discussed above. A plausible assumption is that the relevant measure for the plate thickness is the ratio H/D, where D is the diameter of the projectile. Thus, thin plates are those with $H/D \ll 1.0$, plates of intermediate have $H/D \approx 1$, and thick plates are those with $H/D \gg 1.0$.

The analytical model of Thomson (1955) for thin plates, gives the lower bound on σ_r by considering the perforation process through the dishing mechanism, which is shown schematically in Fig. 4.5. According to Thomson's model the resisting stress on the projectile approaches the value of $\sigma_r = Y_t/2$ for very thin plates. The dishing mode of perforation involves also plate stretching and bending, which have to be analyzed through further modeling, as in Woodward and Cimpoeru (1998).

We can summarize the analytical expressions for the resisting stresses from the models presented above. According to Thomson's model the limiting value of the resisting stress is equal to $\sigma_r = Y_t/2$ for very thin plates. For intermediate plate thicknesses, of the order of the projectile's diameter, the models of Bethe (1941) and Taylor (1948) result in values in the range of $\sigma_r = (1.33–2)Y_t$. As the thickness of the plate increases its free surfaces become less influential, and σ_r should approach values of $R_t = (5–6)Y_t$, as derived in Chap. 3. Thus, by moving from very thin plates to very thick ones, the effective resisting stresses (σ_r) are expected to increase by an order of magnitude. A reasonable assumption is that the proper measure of a plate's resistance to perforation is the normalized stress σ_r/Y_t, where Y_t is the compressive strength of the plate material. The following discussion of the perforation process by the hole enlargement process, is aimed at determining the relations between the normalized effective stress (σ_r/Y_t) and the normalized thickness of the plate (H/D).

The best way to perform a rigorous parametric study for these relations is through numerical simulations with well defined variations for each parameter. This was done by Rosenberg and Dekel (2010c) who constructed a numerically-based model for σ_r, through a large number of simulations with different projectile/plate combinations. With these simulations they were able to determine the dependence of σ_r on the plate's thickness and on the strength of the plate material. The results were analyzed in terms of the relation between the normalized parameters σ_r/Y_t and H/D, for steel and aluminum plates of different strengths and thicknesses in the range of $H/D = 0.026–15$. The nose shapes of the projectiles were either conical or ogival with various sharpness, in order to cover a large range of sharp nosed projectiles. The value of σ_r for each projectile/target combination was

determined through the following steps (1) Several simulations with impact velocities above V_{bl} resulted in the corresponding values for the residual velocities (V_r). (2) These values of V_r were inserted in (4.2a) and the inferred ballistic limit velocity was obtained. (3) This inferred V_{bl} was inserted in 4.5b, and the value of σ_r was determined for the particular projectile/plate pair. The normalized values of σ_r/Y_t as a function of H/D, for all the different projectile/plate combinations, are shown in Fig. 4.6.

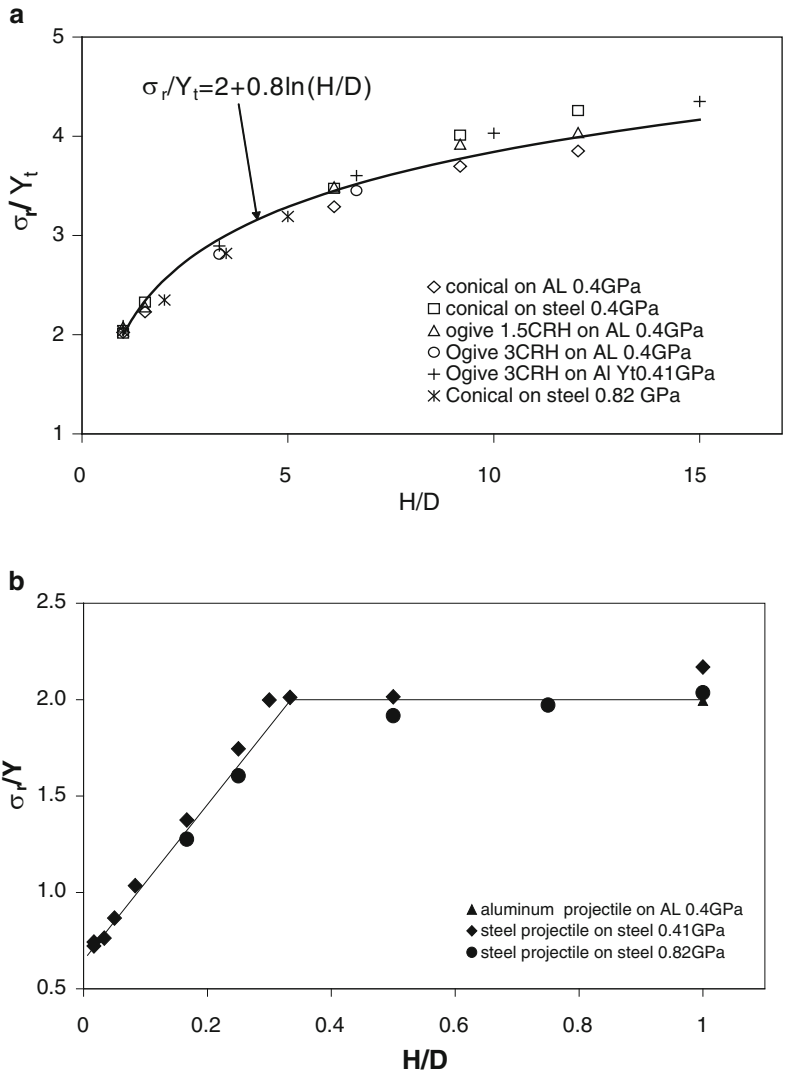

Fig. 4.6 The simulation results for σ_r/Y_t vs. H/D. (**a**) Thick plates with H/D $\geq$ 1.0 and (**b**) intermediate and thin plates with H/D $\leq$ 1.0

The simulation results can be grouped into three families according to their corresponding values for H/D. For thin plates (H/D ≤ 1/3), the results follow a straight line with a relatively steep slope, which is given by:

$$\frac{\sigma_r}{Y_t} = \frac{2}{3} + 4\left(\frac{H}{D}\right) \quad \text{for:}\ \frac{H}{D} \le \frac{1}{3} \tag{4.6}$$

For intermediate plate thicknesses (1/3≤H/D≤1.0), the results fall on a horizontal line, according to:

$$\frac{\sigma_r}{Y_t} = 2.0 \quad \text{for:}\ \frac{1}{3} \le \frac{H}{D} \le 1.0 \tag{4.7}$$

Since $\sigma_r = 2Y_t$ for this range of plate thicknesses, a simple relation is obtained for their V_{bl} values from (4.5b), as follows: $V_{bl} = 2(HY_t/\rho_p L_{eff})^{0.5}$.

For the thick plates with H/D≥1, the values of σ_r increase asymptotically towards their corresponding R_t values for semi-infinite targets. Rosenberg and Dekel (2010c) chose the following relation between (σ_r/Y_t) and (H/D), to represent their numerical results for these plates:

$$\frac{\sigma_r}{Y_t} = 2.0 + 0.8\ln\left(\frac{H}{D}\right) \quad \text{for:}\ \frac{H}{D} \ge 1.0 \tag{4.8}$$

Several points are worth noting here. The numerical results of σ_r for all the projectile/plate combinations are within ±5% of these expressions. Thus, the maximum error in determining V_{bl}, through (4.5b) should be ±2.5%, which can be considered as a reasonable agreement between model and data. Rosenberg and Dekel (2010c) showed that such an agreement is, indeed, obtained between the predicted V_{bl} values and several sets of experimental data, as will be demonstrated below. The constant value of $\sigma_r/Y_t = 2.0$, for the intermediate plate thicknesses with 1/3<H/D<1.0, is exactly the value calculated by Bethe (1941) as given by (4.3a). This agreement is very satisfying since Bethe's analysis deals with plates of intermediate thicknesses, where H ≈ D. The constant plateau in the values of σ_r/Y_t for the intermediate plate thicknesses is probably due to the plane stress conditions which characterize the stress state of these plates. The transition to the plane strain condition takes place, apparently, at a value of H/D = 1.0. Obviously, these observations need further analytical modeling. The asymptotic increase in σ_r/Y_t with H/D for thick plates is quite expected since the values of σ_r should approach the corresponding values of $R_t = (5–6)Y_t$, which were derived in Chap. 3. As was mentioned above, according to the model of Thomson (1955) the limiting value of σ_r, for diminishing plate thicknesses, is $Y_t/2$. This value is close to the limiting value of $2/3Y_t$ from these simulations, as given by (4.6). One may wonder about the

physics behind a mechanism which assigns a finite resisting stress to a plate whose thickness approaches zero. A qualitative explanation can be given by considering the fact that as the plate is getting thinner, a larger area is participating in the dishing process, resulting in a non vanishing value for the energy absorbed by the dishing process.

The simulations for thin plates ($H/D \leq 1/3$) showed that the plates were heavily bent and that a dishing process characterized the perforated area, as expected. In fact, for a normalized plate thickness of about $H/D = 1/3$, the perforation process changed from dishing to the ductile hole enlargement, as shown in Fig. 4.7. These simulations were performed for aluminum plates perforated by an ogive nosed projectile, with $D = 6$ mm. The plate thicknesses were $H = 1.5$, 1.8 and 3 mm, corresponding to normalized values of $H/D = 0.25$, 0.3 and 0.5, respectively. The ductile hole enlargement in the thicker plate ($H/D = 0.5$), is characterized by very small plate bending and by the appearance of front and back "lips" around the hole. The dishing process is clearly evident for the thinner plate ($H/D = 0.25$), and to a lesser extent for the $H/D = 0.3$ plate. Considering these simulation results, one may conclude that the value of $H/D = 1/3$ marks the transition in the perforation mechanism from dishing to ductile hole enlargement. Due to the scatter in the simulation results, as shown in Fig. 4.6b, this value should be viewed as an average value for different projectile/plate combinations.

In conclusion, the results from this numerically-based model are in agreement with the analytical models of Thomson (1955) and Bethe (1941), and with the expected increase of σ_r for very thick targets. The numerical simulations covered a large variety of projectiles and plates and the resulting relations for σ_r, as given by (4.6, 4.7 and 4.8), can be used for the derivation of V_{bl} values for many projectile/plate combinations, through (4.5b). In order to demonstrate the predictive capability of this numerically based model for V_{bl}, in conjunction with the RI model for

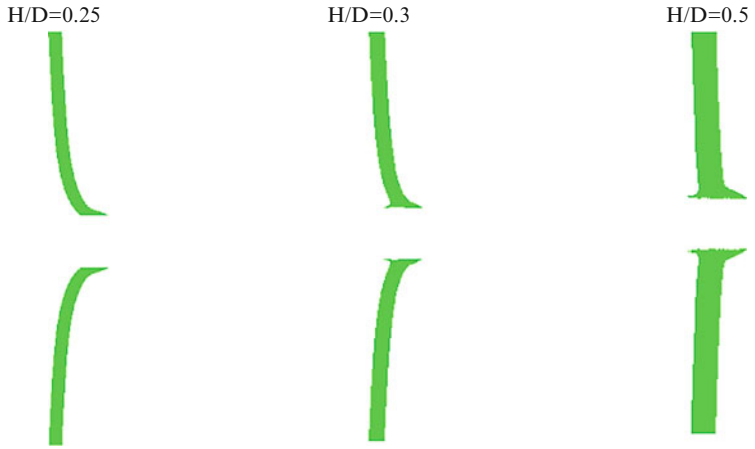

Fig. 4.7 The change from dishing to the hole enlargement process with increasing plate thickness

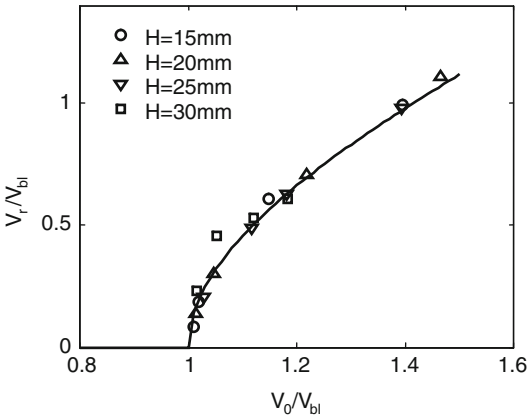

Fig. 4.8 The normalized residual velocities of the conical nosed projectiles perforating aluminum plates with the different thicknesses

V_r/V_{bl} we compare their predictions with several sets of experimental data from different sources, which cover a large range of H/D and Y_t values.

Consider first the experiments of Borvik et al. (2004) for conical nosed steel projectiles, with $L_{eff} = 80$ mm and $D = 20$ mm, perforating 5083-H116 aluminum plates with thicknesses in the range of $H = 15$–30 mm. The corresponding H/D ratios ranged between $H/D = 0.75$–1.5. The experimental data for the normalized velocities, V_r/V_{bl} vs. V_0/V_{bl} are given in Fig. 4.8. The ballistic limit velocities, as obtained by these experiments, were: $V_{bl} = 216.8$, 249, 256.6, and 314.4 m/s for the $H = 15$, 20, 25, and 30 mm plates, respectively. The predicted curve for V_r/V_{bl} in terms of V_0/V_{bl} from (4.2b) of the RI model is also shown in this figure, and it is clearly seen that this model accounts for the experimental results.

In order to check the ability of the numerically-based model to account for the experimental values of V_{bl}, the flow stress of the aluminum plates has to be known. The different plates which were used by Borvik et al. (2004) had different flow stresses, as depicted by their corresponding stress–strain curves in Borvik et al. (2009). Thus, the following values for Y_t were considered in the model: $Y_t = 0.48$ GPa for the 15 mm plate, $Y_t = 0.45$ GPa for the 20 mm and 30 mm plates, and $Y_t = 0.4$ GPa for the 25 mm plate. Inserting these values in (4.7) for the 15 mm and 20 mm plates, and in (4.8) for the 25 mm and the 30 mm plates, result in the following values for the effective resisting stresses: $\sigma_r = 0.96$, 0.9, 0.87 and 1.06 GPa, for the $H = 15$, 20, 25 and 30 mm plates, respectively. Inserting these values of σ_r in (4.5b) results in the predicted values of: $V_{bl} = 214$, 239.5, 263.2 and 318.2 m/s, for the 15, 20, 25 and 30 mm plates, respectively. These values are in excellent agreement with the corresponding experimental value of Borvik et al. (2004): $V_{bl} = 216.8$, 249, 256.6, and 314.4 m/s. As far as these experiments are concerned, the RI model for the residual velocities, and the numerically-based model for V_{bl} from Rosenberg and Dekel (2010c), successfully account for the data of sharp nosed projectiles perforating ductile metallic plates.

Cheeseman et al. (2008) determined V_{bl} values for relatively thick 2139-T8 aluminum plates, with compressive strength of $Y_t = 0.5$ GPa, which were impacted

Table 4.1 Comparing the model's predictions for V_{bl} (in m/s) with the data from Cheeseman et al. (2008)

0.3″ projectiles			0.5″ projectiles		
H (mm)	V_{50} (exp)	V_{bl} (pred)	H (mm)	V_{50} (exp)	V_{bl} (pred)
25.2	682.6	672	39	657.3	653
32.3	783.2	780	40	668	663.4
39	860.9	876	40.9	677.4	673
40.9	893	902	52.1	785.4	783.3
			57.2	819.5	830
			64.1	873.5	884.5

by 0.3″APM2 and 0.5″APM2 projectiles. The normalized thicknesses of the aluminum plates were in the range of: H/D = 3.6–6.6, for which (4.8) has to be used in order to determine the effective resisting stress (σ_r) for each plate. This value is then inserted in (4.5b) in order to derive V_{bl} for the specific projectile/plate pair. The model's predictions were calculated for the hard steel cores of these projectiles, with D = 6.2 mm, L_{eff} = 22.4 mm for the 0.3″ core, and D = 10.8 mm, L_{eff} = 34.8 mm for the 0.5″core. Table 4.1 shows the excellent agreement between the predicted V_{bl} values and the experimental V_{50} values from Cheeseman et al. (2008).

Gupta et al. (2007) used thin (0.5–3.0 mm) plates of 1100-H12 aluminum, with strength of Y_t = 0.28 GPa, which were perforated by ogive nosed hollowed steel projectiles, with D = 19 mm and L_{eff} = 23.6 mm. This is a case study for very low H/D values, ranging from 0.0263 to 0.158. The predicted values of σ_r were calculated by (4.6), which applies for normalized thicknesses in the range of H/D$\leq$1/3. Table 4.2 shows the agreement between the predicted V_{bl} values and the experimental data which were bounded by the highest impact velocity with no perforation (V_1), and the lowest impact velocity with perforation (V_2). The good agreement between model's predictions and experimental results enhances the validity of the numerically-based model for very low H/D values, where dishing is the main perforation mechanism.

Up to this point both the simulations and the experiments dealt with materials which behave in an ideal elastic-perfectly plastic manner, obeying the von-Mises yield criterion. Many metals and alloys experience a significant strain-hardening effect, without having a well-defined value for their flow stress. In order to investigate the effect of strain-hardening on the perforation process, Rosenberg and Dekel (2010c) performed a series of numerical simulations for conical nosed rigid steel

Table 4.2 Comparing the model's predictions for V_{bl} with the data from Gupta et al. (2007)

H (mm)	H/D	V_1 (m/s)	V_2 (m/s)	V_{bl} (pred)
3.0	0.158	90.4	96.9	108.4
2.5	0.1315	79.4	96.7	94.6
2.0	0.105	67.2	83.7	81
1.5	0.079	54.3	62.9	66.4
1.0	0.0526	45.3	51.3	51.5
0.71	0.03	38.4	44.3	41.4
0.5	0.0263	33.7	40.7	34.1

projectiles perforating stainless steel plates of the 304 alloy. This material exhibits a significant hardening effect with a strength increase from 0.34 GPa at yield, to about 2.5 GPa at failure. Material constants for these simulations were taken from Steinberg's model, as given in the code library, according to: $Y = Y_0(1 + \beta_p\varepsilon_p)^n$, with $Y_0 = 0.34$ GPa, $\beta_p = 43$, and $n = 0.35$. These simulations, for various plate thicknesses, were analyzed by the method described above. Namely, the impact and residual velocities were used to determine V_{bl} for each plate thickness, and this value was inserted in (4.5b) in order to derive the corresponding value of σ_r. The results of these simulations, in terms of σ_r as a function of H/D, are shown in Fig. 4.9. Obviously, the values for σ_r were not normalized in this presentation, since Y_t does not have a well defined value for this strain hardening steel. Figure 4.9a presents the simulation results for the whole range of plate thicknesses, and Fig. 4.9b is an expanded view of the results for plate thicknesses in the range of H/D≤1.5.

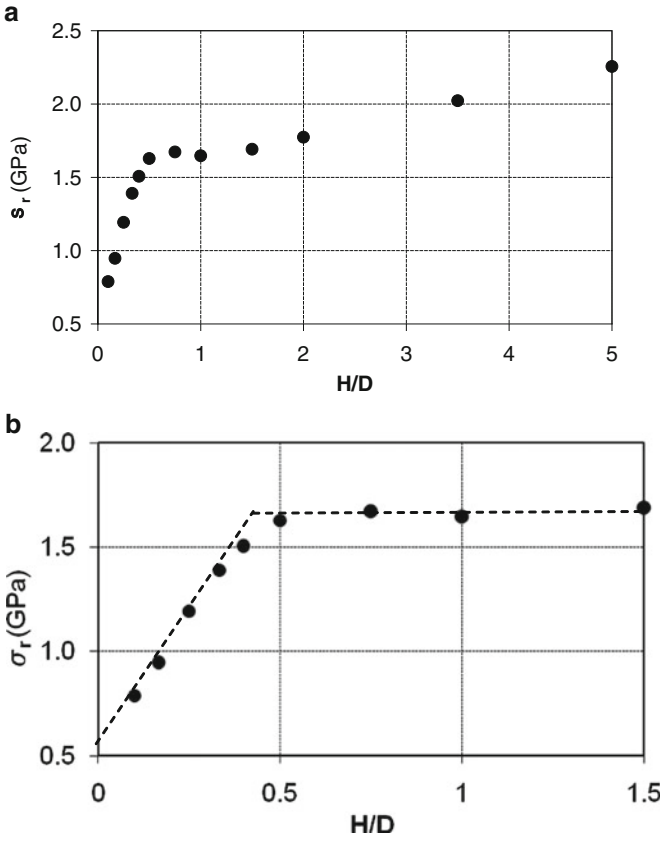

Fig. 4.9 Simulation results for 304 stainless steel plates perforated by conical-nosed rigid projectiles

All the features observed for the elastic-perfectly plastic solid are also evident for the strain-hardening 304 steel. These features include the fast rise of σ_r with H/D for low values of H/D, a constant plateau for H/D = 0.4–1.5, and the subsequent increase of σ_r for H/D>1.5. The fact that the transition from dishing to the hole enlargement process takes place at about H/D = 0.4, rather than at H/D = 1/3, is probably due to the strain hardening property of this steel. The same argument holds for the span of the plateau region which extends to H/D = 1.5, rather than to H/D = 1.0 for the elastic-perfectly plastic plates.

The simulations resulted in a value of $\sigma_r = 1.66$ GPa at the plateau between H/D = 0.4 and H/D = 1.5. Assuming that the same ratio of $\sigma_r/Y_t = 2.0$ also holds for strain hardening materials, we obtain an effective strength of $Y_{eff} = 0.83$ GPa for the 304 stainless steel. This is an intermediate value between the values of $Y_0 = 0.34$ GPa and $Y_{max} = 2.5$ GPa, representing an average strength for the different elements in the plate around the expanding hole. Extrapolating the straight line in the lower range of H/D, to the limit of H/D = 0, results in a value of $\sigma_r = 0.55$ GPa. This value corresponds to a ratio of $\sigma_r/Y_{eff} = 2/3$ for the limiting stress of very thin plates, which is the same ratio for the elastic-perfectly plastic plates.

A linear fit through the simulation results for H/D≤0.4, as shown in Fig. 4.9b, gives a slope of 3.33 which is somewhat lower than the corresponding slope of 4.0 for the von-Mises materials. One can conclude that these results account for the response of other strain-hardening materials, and that their σ_r/Y_{eff} values for thin plates are bounded between (4.6) and the corresponding relation for the 304 steel:

$$\frac{\sigma_r}{Y_{eff}} = \frac{2}{3} + 3.33\frac{H}{D} \qquad \text{for} \quad H/D \leq 0.4 \tag{4.9}$$

Obviously, the exact values for Y_{eff} depend on the parameters which describe the stress–strain curve of the plate material (Y_0, Y_{max}, β_p and n), and more work is needed through analytical modeling, in order to account for these numerically-derived relations.

The analysis presented here applies for ductile plates which experience no failure during the perforation process. When quasi-brittle plates, such as the strong aluminum alloys 2024-T351 or 7075-T651, are impacted by sharp nosed rigid projectiles they may experience significant failure, with large pieces of material sheared off their back sides through scabbing and discing. An example for such a discing process, in 2014-T6 aluminum plate impacted by an ogive nosed projectile, was shown in Fig. 4.1. Such a failure results in a reduced effective thickness of the target, which lowers its ballistic limit velocity. This was the case with the experiments of Borvik et al. (2010), who impacted ogive nosed projectiles with $L_{eff} = 80$ mm and D = 20 mm, at 20 mm thick 7075-T651 aluminum plates. Cross sections of these plates showed that a large volume from their back side was detached through this brittle failure. The resulting value for the ballistic limit velocity for this plate was $V_{bl} = 208.7$ mm. This value is much smaller than the corresponding value of $V_{bl} = 249$ mm for a 20 mm thick 5083-H116 aluminum plate perforated by a conical nosed projectile of similar dimensions, as determined

by Borvik et al. (2004). Thus, in spite of an increase by a factor of nearly two in their strength, the value of V_{bl} for the stronger 7075 alloy is lower (by about 15%) than that of the ductile 5083 plate, due to the back surface failure of the quasi-brittle aluminum.

The damaged volume at the back of a brittle plate is directly related to the diameter of the impacting projectile. Thus, the failure in the 7075-T651 aluminum plates is expected to be less important for perforation tests with smaller projectiles, and the results of these experiments are expected to follow the trends discussed above. In particular, the ballistic limit velocities of plates with large H/D values and different strengths, should be proportional to their corresponding strengths through (4.5b). This was, in fact, the result obtained by Forrestal et al. (2010) for 20 mm and 40 mm aluminum plates of 7075-T651 and 5083-H116 alloys, which were impacted by 0.3″ AP projectiles. For example, the experimental values of V_{bl} were 513 and 633 m/s, for the 20 mm plates of the 5083 and 7075 alloys, respectively. Thus, the stronger plate resulted in a higher value for V_{bl} against the hard steel cores of the 0.3″ AP projectile (D = 6.17 mm), as expected by the model. We can also compare the predictions from the numerically-based model, with these experimental results. Using (4.8) one obtains for these 20 mm plates (with H/D = 3.24) a value of $\sigma_r/Y_t = 2.94$ for the normalized resisting stress. The corresponding stress–strain curves for the two alloys show that their flow stresses are 0.4 and 0.68 GPa, for the 5083 and 7075 alloys, respectively. Thus, the resisting stresses of these projectile/plate pairs are $\sigma_r = 1.176$ and 1.716 GPa, and with (4.5b) we get the predicted values of $V_{bl} = 517.5$ and 639 m/s, for the 5083 and 7075 plates, respectively. These values are in excellent agreement with the experimental results, strongly enhancing the validity of the numerically-based model. Moreover, this agreement supports the claim that the quasi-brittle nature of thick plates does not affect their ballistic performance.

One of the practical questions in armor design is whether a laminated target is more efficient, as compared with a monolithic target of the same total thickness. In order to highlight this issue, for the case of sharp nosed projectiles perforating ductile targets, consider a set of N plates each of thickness h, separated so that the projectile exits each plate before impacting the subsequent one. The residual velocity of the projectile as it exits from each plate is equal to its impact velocity at the next one. Thus, one can write the energy balance, (4.2a), for each plate and obtain a set of N equations:

$$V_{ri}^2 = V_{0i}^2 - V_{bli}^2 \tag{4.10a}$$

where

$$V_{ri} = V_{0(i+1)} \tag{4.10b}$$

Summing up these equations and noting that identical plates (thickness and material) have the same V_{bl} values, we find that the final residual velocity is given by:

$$V_r^2 = V_0^2 - NV_{bl}^2(h) \tag{4.11a}$$

where $V_{bl}(h)$ is the value for a plate of thickness h. Thus, the ballistic limit velocity of this widely-spaced laminated target is given by:

$$V_{bl}(N \times h) = \sqrt{N} \cdot V_{bl}(h) \tag{4.11b}$$

One can estimate the efficiency of a laminated target by considering its V_{bl} value in comparison with that of a monolithic target of the same total thickness (H). This estimate can be made by comparing the terms $(\sigma_r H)^{0.5}$ and $(\sigma_r h)^{0.5}$ which appear in (4.5b) for V_{bl}. If σ_r has the same value for the monolithic plate (of thickness H) and for the single plate in the laminate (of thickness h), the two targets should have the same V_{bl} values. This situation occurs only when both H/D and h/D are in the plateau range for σ_r, with normalized thicknesses between1/3 and 1.0. For all the other cases $\sigma_r(H)$ is higher than $\sigma_r(h)$, and the monolithic target should have a higher value for V_{bl} than the laminated one. An intermediate case is obtained when the plates are closely packed and they support each other during perforation. Thus, one can write:

$$V_{bl}(H) \geq V_{bl}(N \times h)\,\text{closely packed} \geq V_{bl}(N \times h)\,\text{widely spaced} = \sqrt{N} V_{bl}(h) \tag{4.12}$$

A quantitative estimate for these inequalities can be obtained by considering an example for a plate of thickness H = 4D, which is split in several ways. For the monolithic plate, with H/D = 4, we find from (4.8) that $\sigma_r = 3.11Y$ which, by (4.5b), results in $V_{bl} = 5(YD/\rho_p L_{eff})^{0.5}$ for this plate. For the sake of simplicity let us define the term $V^* = (YD/\rho_p L_e)^{0.5}$, so that for the monolithic plate (with H = 4D) we obtain $V_{bl} = 5\ V^*$. The value of V_{bl} for a target composed of two plates, each of thickness 2D, should be $V_{bl} = 4.52\ V^*$, according to (4.11b). We have used (4.8) to calculate σ_r for the H = 2D plate, and inserted this value in (4.5b) to find that $V_{bl} = 3.2\ V^*$ for this plate. Repeating the same procedure for a target composed of two plates, of thickness D and 3D, results in $V_{bl} = 4.61\ V^*$ for this pair. Obviously, the same value is obtained for the two ordering possibilities. Finally, for a target consisting of four plates, each of thickness H = D, we find that $V_{bl} = 4\ V^*$. These examples give an estimate of the expected reductions in V_{bl} for different plate laminations, as compared with the value of V_{bl} for the monolithic plate. These estimates also show that the ordering of the plates plays no role, as far as their V_{bl} values are concerned. As mentioned above, these estimates are relevant for sharp nosed projectiles perforating ductile targets through the hole enlargement process. On the other hand, perforations by blunt projectiles may result in different ordering of the ballistic efficiency, as will be discussed in Sect. 4.4. Dey et al. (2007) reviewed much of the published data on laminated targets and concluded that they show contradicting results. These discrepancies can be explained, at least partly, by the fact that these works included projectiles of different nose shapes and targets with different H/D values.

In order to demonstrate the validity of the analysis presented here, consider the experiments of Dey et al. (2007). They shot ogive nosed steel projectiles, with D = 20 mm and $L_{eff} = 80$ mm, at plates of Weldox 700E steel, and determined the ballistic limit velocities for several plate configurations. The three different

setups, and their corresponding V_{bl} values, were (1) monolithic plates, 6 mm and 12 mm thick with $V_{bl} = 198$ m/s and 318 m/s, respectively, (2) two widely separated 6 mm plates with $V_{bl} = 280$ m/s, and (3) two closely packed 6 mm plates with $V_{bl} = 288$ m/s. The value of $V_{bl} = 280$ m/s for the two widely spaced 6 mm plates, is equal to exactly $\sqrt{2} = 1.414$ times the value of $V_{bl} = 198$ m/s for the single 6 mm plate, as predicted by (4.11b). For the closely packed 6 mm plates, the experimental value of $V_{bl} = 288$ m/s is somewhat higher than $V_{bl} = 280$ m/s for the widely spaced plates, as expected by the inequality 4.12.

Ben-Dor et al. (2006) summarized the results of several studies concerning the ballistic performance of monolithic and layered targets of the same total thickness. In general, these works support the observations discussed above as depicted by inequality 4.12. For example, Almohandes et al. (1996) impacted monolithic and layered mild steel targets having total thicknesses in the range of 8–14 mm, with a standard 0.3″ projectile. They found that monolithic plates were more effective than laminated targets, for all configurations. The difference in performance diminished with impact velocity and the effectiveness of the laminated targets, whether in contact or spaced, decreased with the number of plates comprising each target. Another set of experiments, with aluminum and steel targets, was performed by Gupta and Madhu (1997). They determined their ballistic efficiencies against 0.3″AP projectiles through residual velocities measurements. The experimental results showed that for plates with thicknesses of H/D>1.0, there is no significant change in the ballistic performance due to layering. For thinner plates they found that the layered targets resulted in higher residual velocities, thus, lower ballistic limits, as compared with the monolithic targets, in accord with the analysis presented above. In addition, spaced plates resulted in somewhat lower ballistic limits than the closely stacked targets. Similar results were obtained by Marom and Bodner (1979) for aluminum plates. The monolithic target performed better than the closely stacked one but its performance was somewhat lower than that of a widely spaced laminate. These results for widely spaced laminates can be explained by considering the fact that the projectile is deflected by the individual plates, and these deflections are further enhanced by successive impacts. In conclusion, the laminated targets should be less effective against sharp nosed projectile, as compared with monolithic targets of the same total thickness. In Sect. 4.4 we arrive at a different conclusion for the perforation of these targets by blunt nosed projectiles.

4.3 Plate Perforation by Spherical Nosed Projectiles

This is an intermediate case between the impacts of sharp and flat-nosed projectiles. It has been observed, empirically, that spherically nosed projectiles perforate a ductile plate in a similar way to that of a sharp nosed projectile, as long as the plate is not too thin. This was shown, for example, by Borvik et al. (2002) who shot hard steel projectiles, with D = 20 mm, at 12 mm plates of Weldox 460E steel, and found that the ballistic limit velocities for the conical and spherically nosed

projectiles were practically the same. A close examination of the sectioned plates indicates that their perforations were achieved through the ductile hole enlargement for both nose shapes. The only difference between the two sets of experiments was due to the ejection of a small plug from the target ahead of the spherical nosed projectile, which is a common feature for perforations by blunt projectiles. Thus, the perforation process by a spherical nosed projectile is, indeed, an intermediate case between blunt and sharp nosed projectiles. An important property of the experimental $V_r(V_0)$ curves for blunt projectiles is that they do not tend asymptotically towards the $V_r = V_0$ line, as is the case with sharp nosed projectiles. Instead, the data asymptotically approach a straight line below the $V_r = V_0$ line, with an offset which increases with plate thickness. This offset is due to the presence of the plug, and its magnitude is related to the kinetic energy of the plug, which has to be accounted for in the energy balance equation of these perforations.

In order to construct a simple model for the residual velocities of spherically nosed projectiles we follow the energy balance relation in a similar manner to that with sharp nosed projectiles, as given by (4.1a). The only difference is due to the kinetic energy of the plug which has to be accounted for, and one can write:

$$\frac{1}{2}MV_0^2 = \frac{1}{2}MV_r^2 + \frac{1}{2}mV_r^2 + W_p \tag{4.13}$$

where m is the mass of the plug, which is assumed to move at the same velocity as the exiting projectile (V_r). This is only a rough approximation since these plugs move ahead of the projectile at a higher velocity.

At the ballistic limit velocity we have $V_r = 0$ which results in $MV_{bl}^2/2 = W_p$ as in (4.1b), and we obtain:

$$\frac{V_r}{V_{bl}} = \sqrt{\frac{1}{1+m/M}} \cdot \sqrt{\left(\frac{V_0}{V_{bl}}\right)^2 - 1} \tag{4.14}$$

This equation accounts for the asymptotic approach of the experimental $V_r(V_0)$ curves to straight lines which are offset below the $V_r = V_0$ line. The magnitude of this offset depends on the mass ratio m/M, as is evident by (4.14).

For thin plates, with $H \leq D$, one may assume that the plug thickness is equal to that of the plate and that its diameter is close to that of the projectile. For this case the mass ratio is given by:

$$\frac{m}{M} = \frac{\rho_t H}{\rho_p L_{eff}} = \lambda \tag{4.15}$$

where L_{eff} is the effective length of the projectile.

Inserting this value in (4.15) results in the following expression for the residual velocity:

$$\frac{V_r}{V_{bl}} = \sqrt{\frac{1}{1+\lambda}} \cdot \sqrt{\left(\frac{V_0}{V_{bl}}\right)^2 - 1} \tag{4.16}$$

When the projectiles are rigid spheres, with an effective length of $L_{eff} = (2/3)D$, the equation takes the form:

$$\frac{V_r}{V_{bl}} = \sqrt{\frac{1}{1+\frac{3\rho_t H}{2\rho_p D}}} \cdot \sqrt{\left(\frac{V_0}{V_{bl}}\right)^2 - 1} \tag{4.17}$$

In order to demonstrate the validity of this analysis we show in Fig. 4.10 a comparison between measured and calculated values of $V_r(V_0)$ for the experiments of Senf and Weimann (1973). In these experiments hard steel spheres, with D = 12.7 mm, perforated 2024-T3 aluminum plates with thicknesses in the range of H = 3–25 mm. The following experimental values of V_{bl} were used in (4.17): V_{bl} = 0.2, 0.34, 0.5, 0.66 and 0.95 km/s, for the H = 3, 6, 10, 15 and 25 mm plates, respectively. Figure 4.10 shows that the predicted curves account for the experimental results and that they approach the straight lines which are offset from the $V_r = V_0$ line by the predicted distance.

Another set of measurements which can be used to demonstrate the applicability of this model, is given by Borvik et al. (2002) for hemi-spherical nosed steel projectiles, with L_{eff} = 80 mm and D = 20 mm, perforating 12 mm thick Weldox

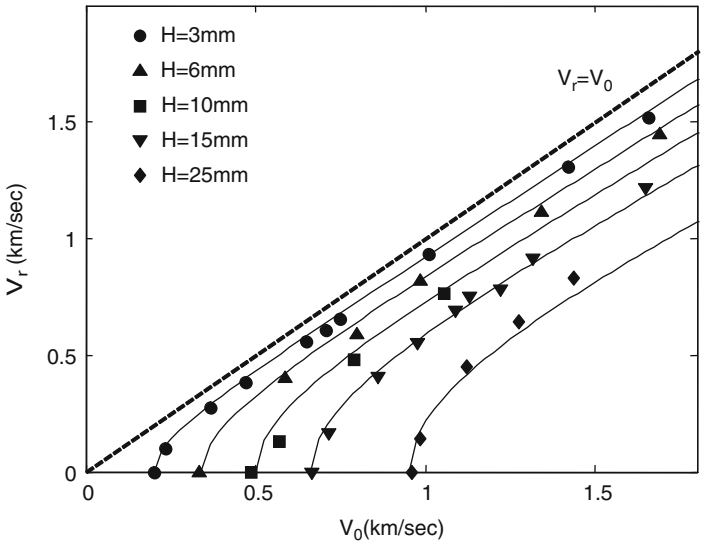

Fig. 4.10 Comparing predicted and measured residual velocities for hard steel spheres perforating aluminum plates

Table 4.3 Predicted and measured residual velocities (in m/s) for spherically nosed projectiles

V_0	300	326.7	362.9	420.6	452
Exp V_r	97.2	154.8	220.2	284.3	325.1
Calc V_r	88.2	148.9	209.5	287.7	327.1

460E steel plates. Choosing a value of $V_{bl} = 285$ m/s for this projectile/target combination, the comparison between the measured and calculated values of V_r, from (4.16), is given in Table 4.3.

The mass of the plug and its velocity which were measured in these experiments are different than those assumed by the model. In fact, the plugs were cup shaped rather than cylindrical, and their thicknesses ranged between (0.5–0.7)H, where H is the plate thickness. The smaller thickness of these plug indicate that the perforation process started with a ductile hole enlargement, and the plugs were formed when the projectiles reached depths of (0.3–0.5)H. The velocities of the plugs in these experiments were higher than the residual velocities of the projectiles by factors which ranged between 1.07 and 1.64. Thus, their kinetic energies were in the range of 0.6–1.8 times the values which are calculated by assuming that their thickness is H, and that their velocities are equal to V_r, as assumed by the model. The error introduced by these simplifying assumptions is not large since the mass of the plug was only 15% of the projectile's mass in these experiments.

In conclusion, the perforation model for spherical-nosed projectiles is similar to the RI model for sharp nosed projectiles, except for the presence of the plug. Once the value of V_{bl} is determined, the model accounts for the residual velocities of the projectile and the ejected plug, assuming that they move at the same velocity. An analytical model for the value of V_{bl} is still needed, and a numerically based model may be the easiest approach. Another issue which has to be resolved concerns the actual thickness of the plug ejected from plates which are perforated by spherically nosed projectiles. For very thin plates ($H/D << 1$), one may assume that the plate and plug thicknesses are the same, and that the plug's velocity is close the residual velocity of the projectile. The situation is more complicated for intermediate and thick plates ($H/D \geq 1.0$) since the plug's thickness can be much smaller than the thickness of the plate. The initial stage of perforation in these cases is achieved through the ductile hole enlargement process, while the final stage is due to shear plugging. Thus, an analytical model which accounts for these perforations should involve the two mechanisms. Such a model was proposed by Bai and Johnson (1982) for flat ended projectiles, and it will be described in the next section.

4.4 Plate Perforation by Blunt Projectiles

The perforation of plates by blunt projectiles is the most complicated perforation process due to the various failure mechanisms which can initiate in the plate, such as spalling, discing, and plugging by shear instabilities. In addition, stretching and

bending of thin plates should be taken into account since they absorb a significant amount of energy from the projectile. Several failure mechanisms can take place simultaneously during perforation, further complicating the analysis. These complexities were discussed by Awerbuch and Bodner (1974), Woodward and De-Morton (1976), Shadbolt et al. (1983), Liss et al. (1983), Ravid and Bodner (1983), Woodward (1987), Liu and Stronge (2000) and Woodward and Cimpoeru (1998). According to these studies, the perforation process consists of several stages which include initial compression and early penetration, bulge formation, plug formation, and its ejection. The transitions between consecutive stages were determined analytically in these models by applying basic principles from plasticity theory. A concise review of several models is given in Corbett et al. (1996). In the present section we focus on some of the more common failure mechanisms which affect the perforation process by flat nosed projectiles.

The spall failure which was described in Chap. 2, is due to the reflection of the impact shock wave from the back surface of the target. The size and velocity of the spalled layer depend on the intensity of the impact and on the spall strength of the target material. Usually, spalling is obtained by high velocity blunt projectiles impacting plates of intermediate thickness, as seen in Fig. 2.5. The process itself takes place while the projectile is still at the early stages of perforation, and its immediate consequence is to reduce the effective thickness of the plate ahead of the projectile. The discing failure mechanism is due to the bending and stretching of the plate, as explained by Woodward (1990). This bending can induce tensile failures at weak planes in the plate, which coalesce to form large discs or rings, as seen in the picture at the right side of Fig. 4.1.

Plugging takes place for plates of thin and intermediate thickness, which are easily sheared by the high strains in the plate around the periphery of the projectile. However, even for thick plates, with H/D>1, plugging occurs at the later stages of perforation when the projectile is at a distance of about D from the back surface of the plate. As discussed by Woodward (1990), a blunt projectile starts its perforation process through the ductile hole enlargement process and, at a certain depth, the penetration mode changes to the plugging mechanism which is less "costly" for the projectile. He analyzed a situation where the projectile is inside the target and the remaining thickness to be penetrated is h. In order to penetrate an extra depth of δh by the ductile hole enlargement process, the projectile has to invest an increment of work (δW) which is given by:

$$\delta W = \frac{\pi}{2} D^2 Y_t \delta h \tag{4.18}$$

Note that this expression is derived through the analysis of Bethe (1941) for the work which is needed to open a hole in the target, (4.3a). According to this approach the effective resisting stress which the target exerts on the projectile is equal to $2Y_t$. According to Woodward (1990), the incremental work which is needed to shear a plug of thickness h along a distance of δh, by overcoming a shear stress of $\tau = Y_t/\sqrt{3}$, is given by:

$$\delta W = \frac{\pi}{\sqrt{3}} Y_t D h \delta h \tag{4.19}$$

Equating the two expressions results in a threshold thickness of h = (√3/2)D where the penetration mode by plugging is more favorable. Thus, it is expected that a blunt projectile impacting a thick target (H/D>1) will first penetrate by the ductile hole enlargement process, pushing target material to the sides and compressing it in front of the projectile. At a distance of about 0.87D from the free surface of the target the process is expected to change to plug formation and its ejection. Plug formation is due to the large shear strains which develop in the target at the periphery of the projectile and extend to the target's back surface. In a later work Woodward and Cimpoeru (1998) assigned a value of $2.7Y_t$ to the resistive stress on the projectile during its early penetration. This value was adopted from the theory of Tabor (1951) for the indentation of plates by a flat ended punch, and it results in a transition from hole enlargement to plugging at distance of h = 1.17D from the back surface of the target. Thus, one may expect these transitions to occur at a distance of the order of h = D from the back surface, in accord with many experimental results, and a few examples are given below.

Figure 4.11, from Woodward et al. (1984), shows sectioned aluminum plates which were impacted by flat-ended rigid steel projectiles at different velocities. The diameter of the projectile was 4.76 mm and the thicknesses of these 7039-T6 aluminum plates were 9 mm. It is clearly seen that up to an impact velocity of about 260 m/s, the penetration is achieved through the ductile hole enlargement. The target material is compressed ahead of the projectile and pushed to the side, forming "lips" at the plate's front and a visible bulge at its back. At an impact velocity of 315 m/s, when the projectile is about one diameter from the target's back

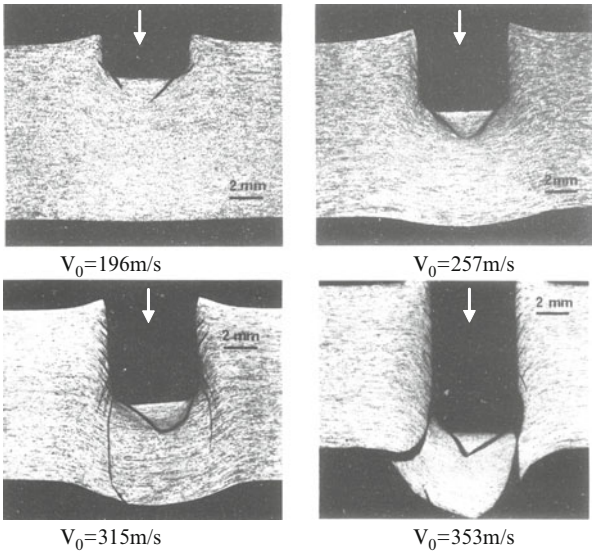

Fig. 4.11 Cross sections of aluminum plates impacted by blunt projectiles at different velocities

surface, the concentrated shearing develop to visible fractures around the plug, which is going to be ejected at higher impact velocities. Two plugs are formed in the plate at different locations and at different times. The upper plug with the conical shape is the so called "dead zone", which is formed early in the process, due to the large shear strains which develop directly below the projectile. The more familiar cylindrical plug is formed when the projectile is at a distance of about one diameter from the back surface of the target, and its thickness is close to the diameter of the projectile. This is the common perforation process for materials which have high strength and relatively high failure strains. In contrast, low strength plates deform considerably around their impacted area, avoiding the shear failure.

Numerical simulations were performed in order to follow the perforation process of steel plates having different thicknesses, by an L/D = 3 rigid cylindrical projectile with a diameter of 10 mm. The Johnson-Cook model was used for the constitutive relation of the plate with $Y_0 = 0.8$ GPa. These simulations were performed in order to follow the shearing process of these plates by flat-ended projectiles. In addition, they demonstrate the importance of the failure mechanisms of the plate by varying its maximal strain to failure (ε_f) and its spall strength (p_{min}). When the equivalent strain of a given element in the simulation reaches the threshold value (ε_f), its strength is reduced to zero at the subsequent time steps. In a similar way, the assignment of a threshold spall pressure (p_{min}) in the code leads to an immediate loss of strength in the element, if it experiences a tensile pressure which is larger than p_{min}.

Figure 4.12 shows simulation results for the perforation process of the 10 mm thick plate by the rigid steel cylinder, when the failure strain of the plate is $\varepsilon_f = 1.5$. The first stage of perforation is achieved through the ductile hole enlargement process as described above. A bulge is evident in the plate already after 10 μs, when the first sign of plate failure takes place, as observed for the aluminum plate in Fig. 4.11. At 20 μs after impact the shear failure in the plate is already evident through the cracks which move towards its back surface. These cracks form the plug whose thickness is about 8.6 mm in this case. This thickness amounts to 0.86D which is in excellent agreement with the predicted plug thickness by the model of Woodward (1990), as discussed above.

The velocity history of the projectile in this simulation is shown in Fig. 4.13 and it is clear that it contains new features which were not observed in the corresponding velocity histories of sharp nosed projectiles. Particularly, the flat levels in this velocity history are due to temporary detachments between the

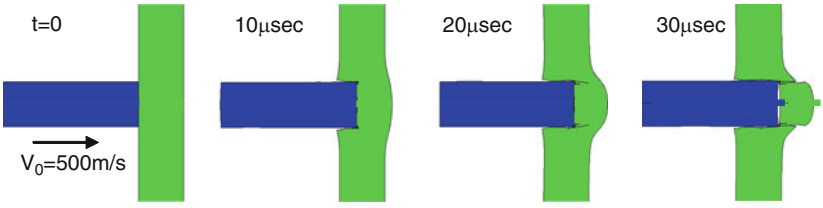

Fig. 4.12 Simulation results for the perforation of a plate with H = D

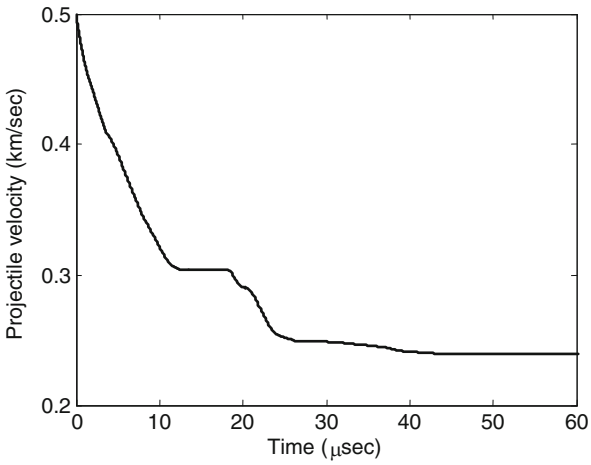

Fig. 4.13 The velocity history of the rigid steel projectile perforating the 10 mm thick plate

projectile and the plate and they are unique for this mode of perforation. The first plateau appears at about t = 10 μs, which corresponds to the initiation of the shear cracks in the plate around the projectile's periphery. These features mean that the deceleration history of the projectile is more complex than we have seen before, with sharp nosed penetrators. Thus, a simple model for plate perforation, which is based on its deceleration, should be much more difficult to construct.

Simulations results for other plate thicknesses are shown in Fig. 4.14. As is clearly seen the plug in the H = 5 mm plate is sheared off at an early time, and its thickness is somewhat smaller than the plate's thickness.

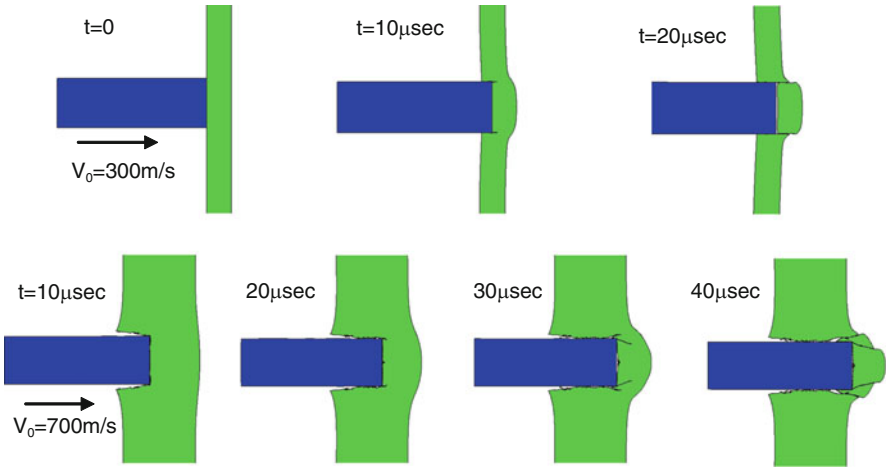

Fig. 4.14 Simulation results for perforation of a thin plate (H/D = 0.5) and a thick plate (H/D = 1.5)

The plug in the H = 15 mm plate is formed at about 30 μs after impact, and it seems to have sheared into a central plug and a surrounding ring. Similar features were obtained by Borvik et al. (2003) for the perforation of Weldox-460E steel plates, both experimentally and numerically. Their projectile's diameter was 20 mm and for plates of thickness up to about 16 mm the plug's thickness was equal to the plate's thickness. For thicker plates the plugs' thicknesses tended asymptotically to a value which was close to the diameter of the projectile, in general agreement with the model of Woodward (1990).

The perforation process is quite different for materials which have a high propensity for adiabatic shearing, such as the Ti/6Al/4V alloy. This was clearly demonstrated by Woodward et al. (1984) by impacting rigid steel cylinders, with D = 4.76 mm, at 6 mm thick plates of this alloy. The plates developed adiabatic shear failures even at low impact velocities, and the plugs were formed at the very early stages of perforation, as shown in Fig. 4.15. Thus, plugging by adiabatic shear is the expected mode of failure for materials with inherent tendency to localize their shear bands, such as carbon steels and titanium alloys. The localization itself weakens the material in and around the shear bands, due to the large temperature increase which develop inside the bands.

The propensity of this titanium alloy to fail by adiabatic shearing is clearly manifested by its dynamic stress–strain curve, as shown in Fig. 2.2. The failure takes place when the compressive strain of the specimen, in the Kolsky bar system, reaches a value of about 0.2. These early failures can be reproduced by numerical simulations which incorporate low failure strains (ε_f) for the plate material. In fact, these simulations can reproduce the basic features of adiabatic shear bands if the cell size is small enough. In the simulations presented here the cell size was 50 μm, which is close to the typical width of 20 μm for an adiabatic shear band.

Simulation results for the perforation of the 10 mm steel plate with strain to failure values of $\varepsilon_f = 0.2$, 0.5 and 1.0 are shown in Fig. 4.16. The L/D = 3 steel cylinder with D = 10 mm impacted these plates at $V_0 = 300$ m/s and the JC model with $Y_0 = 0.8$ GPa, was used for their constitutive relation, as above. One can clearly see the strong effect which the failure strain parameter has on the perforation process. In particular the low value of $\varepsilon_f = 0.2$ results in an early plug formation which is very similar to the plugging in the titanium alloy plate, as shown in

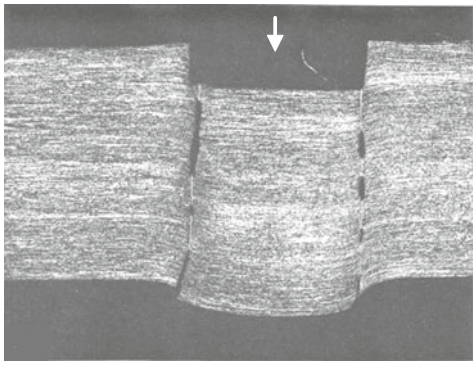

Fig. 4.15 Plugging in a Ti/6Al/4V plate impacted by a blunt projectile

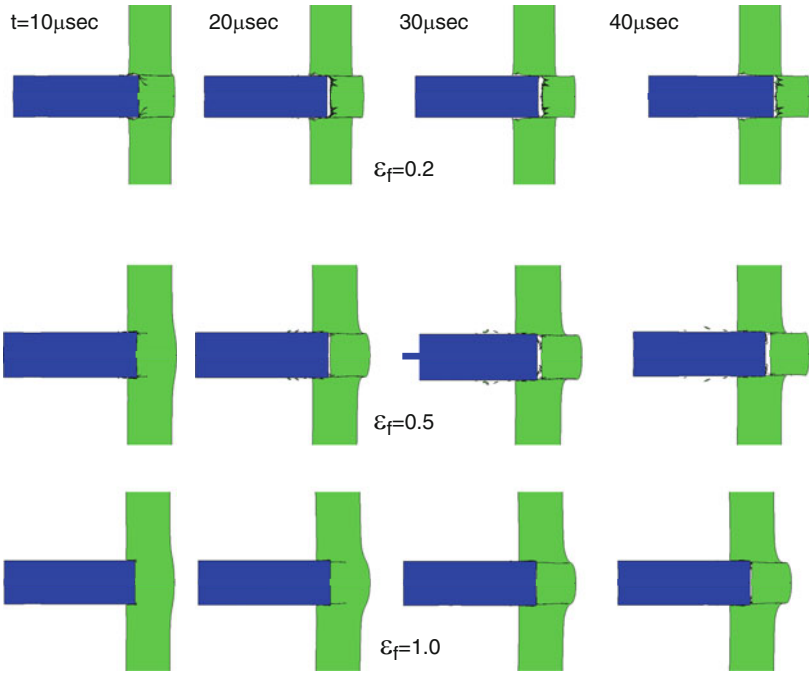

Fig. 4.16 Simulation results for the perforation of a steel plate having different strains to failure

Fig. 4.15. In fact, this simulation shows that the plug acquires a high enough velocity and it moves ahead of the projectile even before it is ejected from the plate. The residual velocities of the projectiles in these simulations decreased with increasing values of ε_f, as expected. Their resulting values were $V_r = 196$, 123, and 0 m/s for the cases of $\varepsilon_f = 0.2$, 0.5 and 1.0, respectively. The projectile did not perforate the plate in the simulation with εf = 1.0, but we can see that the plug was formed by the time of 30 μsec. The large differences between the values of V_r are due to the corresponding differences in the work which the projectile has to invest in the target in order to perforate it. This issue will be discussed below when we describe the analytical model of Recht and Ipson (1963) for V_r, and the model of Bai and Johnson (1982) for the perforation work.

Finally, we wish to demonstrate the ability of numerical simulations to reproduce other failure mechanisms which take place during the perforation of thin plates. The simulation results shown in Fig. 4.17 were obtained by using a different failure threshold for the target material. This is the p_{min} threshold according to which elements in the target fail when they experience a tensile strength which is equal to the value of p_{min}. For the particular simulation discussed here we used a value of $p_{min} = 0.8$ GPa, which is equal to the yield strength of this steel. One can clearly see the scabbing failure at the back of the plate as well as the cracks which develop around the penetration channel. These cracks can be developed to the

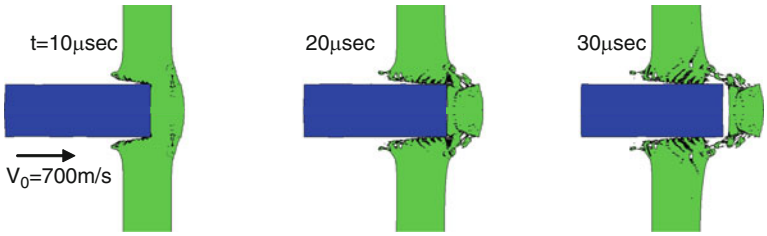

Fig. 4.17 The failure characteristics of a 10 mm steel plate with $p_{min} = 0.8$ GPa

discing rings which were discussed by Woodward (1990), and they are very similar to those in the 2014 aluminum plate which is shown at the right hand side of Fig. 4.1.

Considering the different failure modes which were described here, it is clear that a simple perforation model for blunt projectiles is not easy to construct. Moreover, in many cases the strength of these blunt projectiles is not high enough to guarantee their rigidity and they deform, erode or even shatter, at relatively low velocities adding more complications to the analysis. As mentioned above, several models were suggested over the years in order to account for the ballistic limit velocities and the residual velocities of blunt projectiles perforating metallic plates. However these multi-stage models are very complex since they rely on several parameters, which have to be calibrated for each stage in the perforation process. In contrast, the model of Recht and Ipson (1963) for the residual velocity of blunt projectiles treats the process in an integral manner, using only energy and momentum considerations. With this approach, the exact details of the failure modes are not important since they are lumped in the value for the plastic work (W_p) at the ballistic limit velocity. The basic assumptions of this model and its resulting expression for the residual velocities are outlined next.

The model starts with the notion that the impact between the projectile and the target is basically a plastic impact. As a first stage, the model considers the impact of the projectile with a free plug with mass m, surrounded by the rest of the target with no shearing processes. Conservation of momentum results in the loss of projectile's energy (E_{fn}) due to this plastic impact, according to:

$$E_{fn} = \frac{m}{M+m} \cdot \frac{1}{2} M V_0^2 \tag{4.20}$$

This "lost energy" is taken into account in the energy balance of the perforation process, which takes the form:

$$\frac{1}{2} M V_0^2 = \frac{1}{2} M V_r^2 + \frac{1}{2} m V_r^2 + E_{fn} + W_p \tag{4.21}$$

where W_p is the plastic work done on the target in order to push the plug out. For $V_0 = V_{bl}$ the residual velocity is zero and one can write:

$$\frac{1}{2}MV_{bl}^2 = E_{fn} + W_p \tag{4.22}$$

These equations lead to the following relation for the residual velocity:

$$V_r = \frac{M}{M+m} \cdot \sqrt{V_0^2 - V_{bl}^2} = \frac{1}{1+\lambda} \cdot \sqrt{V_0^2 - V_{bl}^2} \tag{4.23}$$

where $\lambda = m/M$ as defined by (4.15).

For the ballistic limit velocity one can write:

$$V_{bl} = \sqrt{\frac{2W_p(M+m)}{M^2}} \tag{4.24}$$

Equation 4.23 is similar to the corresponding relation for the spherical nosed projectile, (4.16), except for the fact that the square root of the mass ratio appears in (4.16). For $M \gg m$, the two expressions result in very close values, which is probably the main reason that (4.23) was used successfully for spherical nosed projectiles as well. This equation does not consider the physical properties of the target material such as its strength, hardening and rate sensitivities, and its failure strain. These properties determine the work needed to perforate the plate (W_p), and they are lumped into the value of V_{bl}, as is clearly evident by (4.24).

By writing (4.21) one assumes that the velocity of the plug is equal to the residual velocity of the projectile. This is seldom the case and the plugs often have much higher velocities than the projectiles. However, for relatively thin plates the predictions from (4.23) should be in good agreement with the data for V_r, since the difference between the actual and calculated kinetic energies of the plugs plays a minor role in the total energy balance. In order to account for the actual velocity of the plug (V_{pl}), we can define an effective plug mass (m^*) in the following way:

$$m^* = m\left(\frac{V_{pl}}{V_r}\right)^2 \tag{4.25}$$

This effective mass of the plug should be inserted in (4.23) instead of its actual mass (m), in order to have a better agreement with the data for V_r when the plug's velocity (V_{pl}) is significantly higher than the projectile's residual velocity (V_r).

In order to demonstrate the validity of this approach, one needs a set of experiments for which the velocities and the masses of the plugs were accurately determined. This was done by Borvik et al. (1999) who shot rigid steel cylinders, with L = 80 mm and D = 20 mm, at 12 mm thick Weldox 460E steel plate. The data shows that the ratio V_{pl}/V_r decreases from a value of about 1.5 for impact

Table 4.4 Comparing the predicted values for V_r (in m/s) with the data from Borvik et al. (1999)

V_0	303.5	285.4	244.2	224.7	200.4
V_r (exp.)	199.7	181.1	132.6	113.7	71.4
V_r (pred.)	202.4	182.3	134.4	107.7	65.7

velocities near the ballistic limit, to a value of about 1.2 for the highest velocity in this work. Thus, an average value of $V_{pl}/V_r = 1.35$ can be taken for this set of experiments. The mass of the plug is given in Borvik et al. (1999) for each experiment and their average value was m = 27.8 g. This value is somewhat lower than the value of m = 29.7 g for a plug whose diameter is exactly equal to that of the projectile, and its thickness is the same as that of the plate. Using a value of $V_{bl} = 184.5$ m/s for this set of experiments, as determined by Borvik et al. (1999), we find a good agreement between the data and the model's predictions for V_r, as shown in Table 4.4. This agreement enhances the validity of the model, as given by (4.23), with the correction for the effective plug mass as given by (4.25). It is clear that there is a real need for an analytical model to account for the higher velocities of these plugs which are ejected by flat ended projectiles.

Borvik et al. (2003) determined V_{bl} values and residual velocities for the same projectiles perforating Weldox 460E plates with thicknesses in the range of 6–20 mm. In all of these experiments the plug velocity was higher than that of the residual projectile by factors which were similar to those for the 12 mm plate, as described above. Using the same analysis for the plates of thicknesses in the range of 8–20 mm, shows that 4.23 and 4.25 account for all the data in Borvik et al. (2003) as far as $V_r = V_r(V_0)$ is concerned. On the other hand, the model does not account for the data concerning the H = 6 mm plates, because these thin plates experienced a large permanent deflection which is not accounted for by the model.

The various models which were presented in this chapter resulted in similar functional dependences of V_r on V_0. In fact, Lambert and Jonas (1976) reviewed a large number of perforation theories for non-deforming projectiles, and concluded that they adhere to a basic form which is given by:

$$\frac{V_r}{V_{bl}} = k\sqrt{\left(\frac{V_0}{V_{bl}}\right)^2 - 1} \tag{4.26}$$

where k is an empirical constant which depends on the plug/projectile mass ratio. We have seen that this equation can be derived by analytical considerations and that it applies for the different cases discussed above. Thus, with k = 1 (4.26) reduces to (4.2) of Recht and Ipson (1963), for sharp nosed projectiles. With $k = [M/(M + m)]^{0.5}$ this equation reduces to (4.16) for the spherical nosed projectile, and with k = M/(M + m) we get (4.23) for the flat-faced projectile.

In conclusion, the residual velocities of rigid projectiles can be accounted for by the energy and momentum conservation equations without specifying the actual failure modes of the plates. We emphasized the importance of using these physically-based equations in order to account for the experimental data, rather than using

empirical best-fitting procedures. The situation becomes more complex when the projectile loses mass through the process, in which case it is impossible to use such energy and momentum considerations. We shall discuss this issue in Chap. 5, where we deal with plate perforations by eroding rods. The next issue which has to be addressed now is that of determining the value of V_{bl} for blunt-nosed projectiles, through analytical models such as the RI model. The model resulted in a general expression for V_{bl} which is given by (4.24). The difficulty with this equation stems from the fact that the work needed to perforate the plate (W_p) is not easy to derive analytically, as will be discussed below.

We have shown in Sect. 4.2 that numerical simulations can be used to derive a numerically-based model for V_{bl} of sharp-nosed projectiles, perforating ductile metallic plates through the hole enlargement process. It is more difficult to construct such a model for the perforation process by blunt projectiles, because of the various failure modes involved. Several attempts at deriving analytical expressions for V_{bl} have been presented in the literature, for either thin or thick plates, as discussed above. Borvik et al. (2003) tried to account for their experimental results with some of these models. However, none of these models could account for the experimental values of V_{bl} of all the plate thicknesses which were used in this study. For thin plates, the values of V_{bl} could be accounted for by the model of Wen and Jones (1996), which takes global bending into account. On the other hand, the model of Bai and Johnson (1982) was more successful in accounting for the V_{bl} values of thick plates. This is a physically-based model for flat-nosed projectiles punching through plates of intermediate thickness, and it will be described next.

The model of Bai and Johnson (1982) addresses the work (W_p) needed to perforate a plate of thickness H by a rigid punch having a diameter which is close to the plate's thickness. The analysis starts with a general expression for the constitutive relation between the shear stress (τ) and shear strain (γ), of the plate material, according to:

$$\tau = \tau_0(1 - \alpha_T T)\gamma^n \tag{4.27}$$

where τ_0, α_T and the hardening coefficient (n) are material constants, and T is the temperature. The effect of strain rate is not taken into account in this analysis. The temperature is calculated according to the usual adiabatic assumption which converts the plastic work increment, $dW_p = \tau d\gamma$, to a temperature increase through $\rho C_v dT$, where C_v is the specific heat of the plate material. Using these relations and the definition of the instability strain (γ_i) as the strain for which $d\tau = 0$, Bai and Johnson (1982) obtained the following relation for the critical shear strain:

$$\gamma_i = \left(\frac{n\rho C_v}{\alpha_T \tau_0}\right)^{\left(\frac{1}{1+n}\right)} \tag{4.28}$$

and for the maximum shear stress (τ_m) they obtained:

$$\tau_m = \tau_0(1 - \alpha_T T_0){\gamma_i}^n \exp(\frac{-n}{1+n}) \tag{4.29}$$

where T_0 is the room temperature.

The analysis is based on the material parameters (n, γ_i, and τ_m) as well as on the thickness of the plate (H) and on the diameter of the punch (D), and it follows the plugging process via two consecutive stages. At first, the projectile is penetrating to a certain depth, as in the hole enlargement process. During this stage the shear stress in the target, around the periphery of the projectile, provides the main resistance to penetration. This stress increases according to the strain hardening rule, (4.27), until it reaches the value of τ_m, and the shear strain reaches its maximum value (γ_i). At this point the projectile has penetrated a certain distance (P_i), which has to be determined. The model assumes that beyond this point the target offers no further resistance as a result of its shear failure. Thus, the equation of motion for the first stage is:

$$(M+m)\frac{dV}{dt} = -\pi DH\tau_R \tag{4.30}$$

where M and m are the masses of the projectile and the plug, respectively, and τ_R is the shear stress in the target around the projectile's periphery. The value of τ_R is determined through the equations above and (4.30) is then integrated between $x = 0$ and $x = P_i$, which is the depth of penetration when instability sets in. In order to have an estimate of the strain distribution in the target around the punch's periphery, Bai and Johnson (1982) used the following expression for the shear strain (γ) in the plate at a distance r outside the punch radius (R):

$$\frac{\gamma}{\gamma_R} = \left(\frac{R}{r}\right)^{1/n} \qquad \text{for} \quad r \geq R \tag{4.31}$$

where γ_R is the target strain at $r = R$, which is assumed to be the maximum value of the shear strain. The resulting expression for the penetration depth (P_i), when the strain reaches its instability point, is:

$$\frac{P_i}{R} = \frac{n}{1+n}\gamma_R \tag{4.32}$$

This equation results in values for P_i of the order of 0.3R, since the value of γ_R is limited by the maximum strain (γ_i), which is around 1.0 for most ductile materials, and the values of n are usually bound in the range of $0.3<n<05$. Note that this value of P_i corresponds to a value of 0.15D, which means that the plug's thickness should be equal to about 0.85D. This is practically the same value derived by the simple approach of Woodward (1990), as discussed above. The second stage in the perforation process starts when the depth of penetration reaches the value of P_i and the shear strain has reached its maximal value (γ_i). High values of γ_i result in a

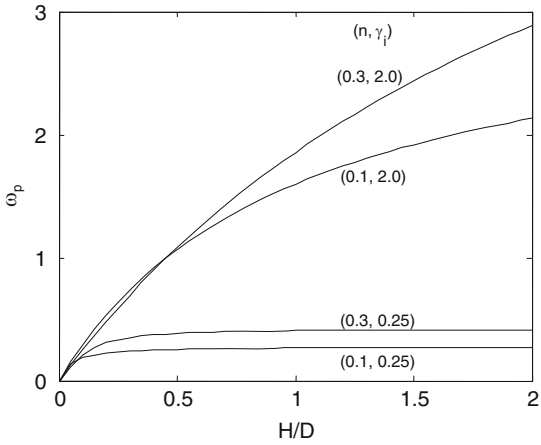

Fig. 4.18 The energy absorbed by the plate according to the model of Bai and Johnson (1982)

delay in the appearance of the instability, which is of major importance for the energy absorbed by the plate. Bai and Johnson (1982) derive equations for the energy absorbed in the plugging process, from which they can have an estimate for the ballistic limit velocities. The analysis results in two limiting cases for which V_{bl} is proportional either to $H(D/M)^{0.5}$ or to $D(H/M)^{0.5}$. As is often found in practical cases, the ballistic limit velocities do follow, empirically, one of these simple relations. The most important outcome of this dimensionless analysis is that the energy absorbed by the plate is dependent on n, γ_i and H/D. The end result is demonstrated in Fig. 4.18, where the normalized absorbed energy (ω_p) is plotted as a function of the normalized plate thickness (H/D) for several pairs of (n,γ_i) values. The normalized absorbed energy is defined by $\omega_p = 2W_p/\pi D^2 H\tau_m$.

As is clearly evident in this figure, in order to achieve a better resistance to plugging an increase of plate thickness is helpful only for materials with a high failure strain. The energy absorbed by materials with low γ_i values increases only linearly with the thickness of the plates. The expected ballistic limits for such plates will vary as $(H/\rho_p L_{eff})^{0.5}$. On the other hand, for materials with high values of γ_i, the perforation energy is related to H^2, and the ballistic limit velocities are expected to be related to $H(1/\rho_p L_{eff} D)^{0.5}$. These plates will absorb much more energy under this type of loading, which is the reason that materials with a high propensity for shear banding, like the Ti/6Al/4V alloy, do not perform as well as metals which exhibit high values of γ_i. These conclusions are substantiated by the numerical simulations presented above for the perforation process of steel plates having different values of the failure strain (ε_f). We have seen that this parameter plays a major role in determining the time for plug formation which, in turn, determines the amount of the projectile's energy absorbed by the plate and its residual velocity.

A simplified version of this model was suggested by Woodward (1990), for perforations through the plugging process. According to his model the work done by the projectile in shearing a plug of thickness H and diameter D is $W_p = \pi DH^2\tau$, where τ is the shear strength of the plate material. This expression is obtained by

assuming that a constant shear stress (τ) acts on the plug's cylindrical area (πDH), resisting the penetration for a distance of H, until the plug is ejected. In fact, this expression is a simplified version of the Bai and Johnson (1982) model for the case of high values of γ_i. Woodward (1990) recommends using the relation $\tau = Y/\sqrt{3}$ for the shear stress, where Y is the compressive strength of the target material. The plastic work to perforate the plate through this process is equated with the kinetic energy of the projectile at its ballistic limit velocity. Thus:

$$\frac{1}{2}MV_{bl}^2 = \pi DH^2\tau \tag{4.33a}$$

With $M = \pi D^2\rho_p L_{eff}/4$, this equation results in:

$$V_{bl} = 2H \cdot \sqrt{\frac{2\tau}{\rho_p L_{eff} D}} \tag{4.33b}$$

Thus, a linear relation between V_{bl} and plate thickness is expected by this simple plugging model. In order to check how well (4.33) predicts the experimental results of Borvik et al. (2003), we chose a value of $\tau = 0.35$ GPa for the Weldox 460E steel plates, using their flow stress of $Y = 0.6$ GPa. Inserting this value of τ together with $L_{eff} = 80$ mm $D = 20$ mm for the projectiles in (4.33b), results in the predicted values for V_{bl} which are listed in Table 4.5, together with the experimental results from Borvik et al. (2003). The close agreement between the model's predictions and the data, especially for the thicker plates, is due to the fact that the failure of these plates was mainly by a simple shearing mechanism. The agreement is getting worse for the thinner plates ($H \leq 10$ mm), due to the extra energy which the projectiles invested in the global deflection of these plates.

The different deformations of these plates are clearly evident in the pictures of the sectioned plates in Fig. 4.19, from Borvik et al. (2003). It is clear that the 6 mm thick plate, with $H/D = 0.3$, experienced a significant global deformation. The deformation is much smaller for the 8 mm plate, with $H/D = 0.4$, and it is negligible for the 12 mm plate with $H/D = 0.6$. The large deformations resulted in higher V_{bl} for the thin plates, as compared with the model of Woodward (1990), since the model does not include global deflections. These results suggest that the value of $H/D = 0.5$ marks the onset of global deflections for plates which are perforated by blunt projectiles.

In order to have a better estimate for the onset of global deflections consider the simulation results from Borvik et al. (2003) for plates with thicknesses between

Table 4.5 Comparing predicted and measured V_{bl} (in m/s) for the experiments of Borvik et al. (2003)

H (mm)	6	8	10	12	16	20
V_{bl} (exp.)	145.5	154	165.3	184.5	236.9	293.9
V_{bl} (pred.)	89.6	119.4	149.3	179.2	238.9	298.6

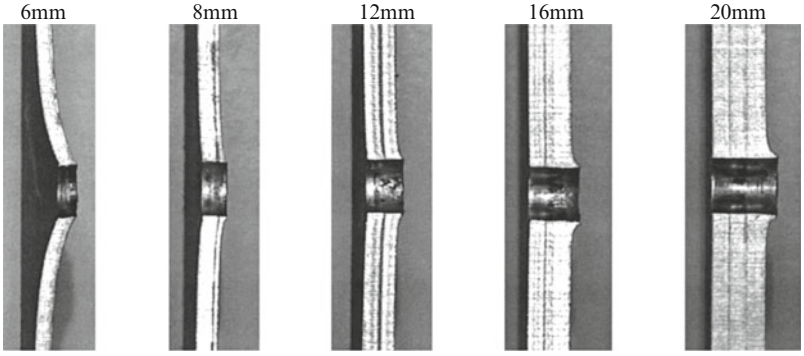

Fig. 4.19 Cross sections of perforated steel plates of different thickness

4 mm and 12 mm, as shown in Fig. 4.20. The simulations were performed for impact velocities which were higher by about 20% than the corresponding ballistic limit values of these plates. The global deflections are decreasing with plate thickness, as expected, and they are practically negligible for plates with $H \geq 10$ mm. Thus, a rough estimate for the transition can be set at $H/D = 0.5$. This transition is similar to the results presented in Sect. 4.2 for plate perforation by sharp-nosed projectiles, where the transition from dishing to ductile hole enlargement was found to be at about $H/D = 1/3$. The two processes are different in the sense that the perforation by blunt projectile does not involve a transition between penetration modes. The global deformation of the thin plates simply adds to the energy loss of the projectile. This addition plays a major role in the performance of laminated targets as compared with monolithic ones, as we show next.

The perforation process of laminated targets by blunt projectiles can be very different than their response to the impact of sharp-nosed projectiles. The difference is due to the fact that blunt projectiles have to invest more energy by perforating thin plates, through their global deflections. In addition, the plugs ejected from the first plates can influence the perforation of the subsequent plates, as noted by Gogolewski et al. (1996), Woodward and Cimpoeru (1998) and Dey et al. (2007).

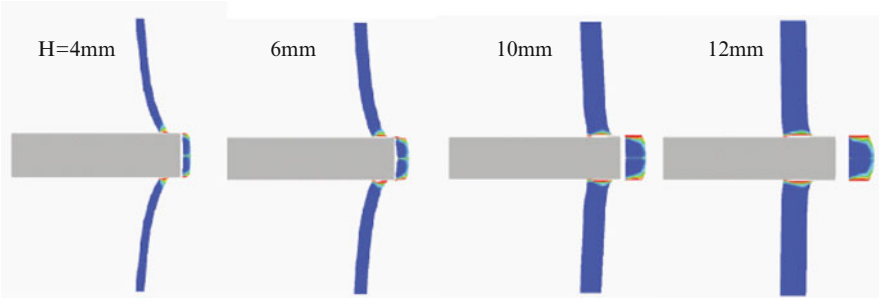

Fig. 4.20 Simulation results for different plate thicknesses perforated by flat nosed projectiles

These works compared ballistic limit velocities for cylindrical steel projectiles perforating monolithic and laminated targets, which were made of two or three closely stacked plates. The values of V_{bl} for the monolithic plates were considerably lower than those of the laminated plates, and we focus now on this enhanced performance of the laminates in these works.

Woodward and Cimpoeru (1998) performed V_{bl} tests for several double layered aluminum targets and compared them with the V_{bl} value for a monolithic plate of the same total thickness. All the double layered targets resulted in higher V_{bl} values as shown in Fig. 4.21, from Woodward and Cimpoeru (1998). The value of V_{bl} for the target with equal thickness plates was the highest and the improvement in V_{bl}, as compared with the monolithic plate, was by 13.5%. Moreover, the laminate with the thin back plate showed a better ballistic performance than the similar laminate with the thick back plate. This difference can be attributed to the pronounced global deflection in the back plate, as is clearly seen in the figure.

Let us consider now the improvement in V_{bl} values for the layered targets in the three works cited above in terms of the normalized thickness (h/D) of the corresponding back plates. Woodward and Cimpoeru (1998) used a cylindrical projectile with D = 6.35 mm, and obtained an improvement of only 13.5% in V_{bl} for the double-layered target of 2024-T351 aluminum plates, with h/D = 0.75. Gogolewski et al. (1996) used a D = 6.7 mm projectile and found an increase of 23% in V_{bl} for a laminated target consisting of three 2.235 mm thick 6061-T6 aluminum plates, for which h/D = 0.3. The experiments of Dey et al. (2007) were with monolithic and double layered targets of Weldox 700E steel plates with a total thickness of 12 mm. The resulting values for V_{bl} showed a significant increase (about 47%) for the laminated target, with h/D = 0.3, as compared with the monolithic target. Thus, it is already clear that both the strength of the plates and their normalized thickness (h/D) contribute to the improved ballistic performance of laminated targets.

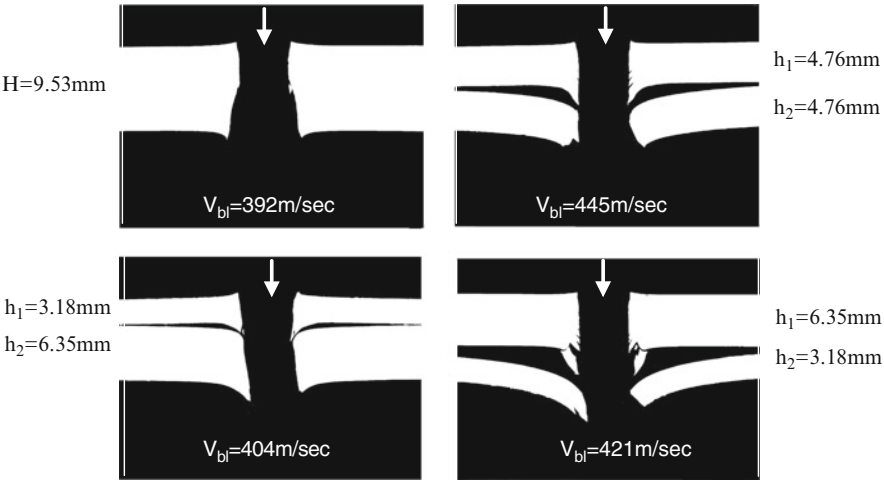

Fig. 4.21 Sectioned aluminum targets perforated by flat-ended projectiles

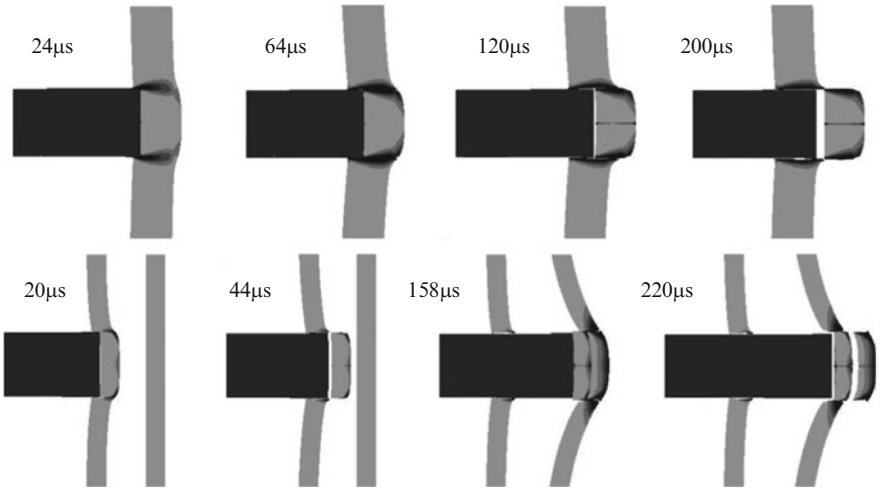

Fig. 4.22 Simulations results for monolithic and double layered targets of equal thicknesses

The deflection and stretching of the back plate is clearly evident in the simulations of Dey et al. (2007), for the widely spaced laminate shown in Fig. 4.22. We show these simulation results because they highlight the important features of the perforation process of laminated targets. These simulations were performed with impact velocities which were slightly higher than thee corresponding ballistic limits. The black colors in the targets correspond to high plastic strains in the plates around the projectile's periphery.

The simulations for the spaced target capture all the features which were seen in the experiments. In particular, they show that the ejected plug from the first pate prevents the shear localization in the second plate, which experiences a large deformation and membrane stretching. The plug itself is stopped at the second plate and adds an extra mass which has to be pushed by the projectile, leading to a further increase in the value of V_{bl}. The fact that the first plate does not experience a large deflection is due to the impact velocity which is much higher than the ballistic limit velocity corresponding to this plate. This is a well established result for high velocity impacts of thin plates by blunt projectiles, where a plug is sheared with no plate deflection. In fact, Goldsmith and Finnegan (1971) found that the amount of plate deflection is maximal at the ballistic limit velocity, and it decreases monotonically with impact velocity.

To summarize the experimental studies which were described above, the ballistic limit velocities of the laminated targets were significantly higher than the ballistic limits for monolithic plates of the same total thickness. The improvement depends on the corresponding h/D values of the laminated targets, where h is the thickness of the back plate. This is the plate which absorbs an extra amount of kinetic energy from the projectile through its large deflection. The two configurations with $h/D = 0.3$ resulted in much higher improvements than that with $h/D = 0.75$. This is the

expected result since thinner plates are more effective as energy absorbers, as is clearly shown in Fig. 4.21. Comparing the results of Dey et al. (2007) and Gogolewski et al. (1996), with h/D = 0.3 in both cases, we find that the strong steel plates of Weldox E700 resulted in a much higher improvement (by 47%), as compared with the improvement achieved (23%) with the 6061-T6 aluminum plates.

An estimate for the effect of h/D alone can be obtained through the simulation results of Teng et al. (2007) for two sizes of flat-nosed projectiles perforating the same targets. The ballistic limit of a 12 mm thick steel plate was compared with that of a double-layered target with 6 mm thick plates. The projectiles in these simulations were L/D = 4 steel cylinders with diameters of 20 mm and 7.6 mm. The properties of the plates in these simulations represented those of Weldox 460E steel, which has a lower strength than the Weldox 700E steel in the experiments of Dey et al. (2007). The ballistic limit velocities for the double-layered targets in these simulations were higher than those of the monolithic targets for both projectiles, as expected. The improvement in V_{bl} for the larger projectile, with h/D = 0.3, was about 25%, while for the smaller projectile, with h/D = 0.79, it amounted to only 7%. These simulations demonstrated the much larger deflection of the back plate in the double layered target which was impacted by the larger projectile. These results confirm the conjecture that the improved ballistic limits of laminated targets are due to the large deflections of their back plates, and it is more significant for plates with small h/D values, as obtained experimentally. Also, the improvement is strongly dependent on target strength, since it amounted to 25% in the simulations of Teng et al. (2007) for the Weldox 460E steel, while the experiments of Dey et al. (2007) resulted in an improvement of 47% for the stronger Weldox700E plates. Based on this rather limited information, we may conclude that the lamination and the strength of the plates play roughly equal roles, as far as the improvements in ballistic limits of laminated targets are concerned. The experimental data and the simulation results confirm the notion that the significant improvements in the values of V_{bl}, for laminated targets impacted by blunt projectiles, are due to the deflections of their back plates. These deflections are significant for plates with normalized thicknesses of about h/D = 0.3.

The simulations of Teng et al. (2007) for spaced laminates, impacted by the projectiles with the different sizes, D = 20 mm and D = 7.6 mm, resulted in a decrease of about 0.5–1.0% in their corresponding values of V_{bl}, as compared with the closely stacked laminates. These minor differences enhance the claim that the large improvements in V_{bl} which are often obtained experimentally for spaced laminates, are probably due to the deflection of the projectiles by the first plates, rather than to a physical effect. Teng et al. (2007) also performed numerical simulations for conical nosed projectiles with diameters of 20 and 7.6 mm, perforating the same monolithic and laminated steel targets. They found that for both projectiles the ballistic limit velocities were somewhat higher for the monolithic targets, as compared with the double layered target, which is the expected result by the analysis in Sect. 4.2. Also, for both cases the spaced plates resulted in a lower ballistic limit (by less than 1%), as compared with the closely stacked plates, which is also in agreement with the analysis presented there. These simulations

confirm the main conclusion derived in this chapter, that the effect of lamination is very different for the two types of projectile nose shapes.

4.5 Forced Shear Localization and Adiabatic Shear Failure

The issue of adiabatic shear in metals and alloys received a lot of attention for many years, as described in Chap. 2. The importance of this failure mode for terminal ballistics has been emphasized in the present chapter, particularly for the perforation of high strength plates by blunt projectiles. Traditionally, this mode of failure has been attributed to a shear instability which takes place under dynamic loading as a result of two opposing effects, the strain hardening of the material and its thermal softening. Various materials are often claimed to fail by adiabatic shear when, in fact, their failure under dynamic loading is very similar to that under static loading conditions. Rosenberg et al. (2010) made the distinction between materials which fail by shear instabilities, and those which fail by a distinctive adiabatic shear mechanism, such as the Ti/6Al/4V alloy. This titanium alloy fails at a strain of about 50% under static compression, while its failure strain is only 20% in a Kolsky bar experiment at strain rates of about 10^3 s^{-1}. In contrast, most of the strong alloys, such as the 2024-T3 and 7075-T651 aluminum alloys, fail at the same compressive strains under both static and dynamic loadings. The classification of dynamic failures as adiabatic should be free of geometrically-induced stress concentrations in the specimen. Materials are prone to fail at relatively low shear strains when such geometrical constraints are part of their testing configuration, and the measured failure strain should not be interpreted as a physical property of the material. Such stress concentrations appear in the hat-shaped specimen of Chen et al. (1999), the truncated cone specimen of Li et al. (2003), and the notched specimen used by Rittel et al. (2008), which are shown in Fig. 4.23. All of these geometries introduce well-defined locations of stress concentration, which mask the true nature of the adiabatic shear failure. For example, the shear failure is forced to occur along the dotted lines shown in the hat shaped specimen, and it will take place for all specimens at relatively low strain levels. The main conclusion of Rosenberg et al. (2010) is that the quest for a truly

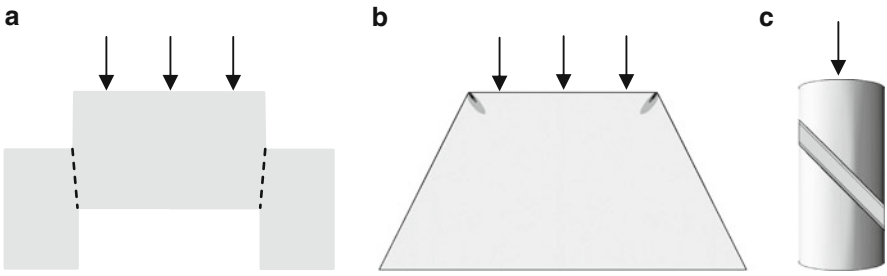

Fig. 4.23 Specimen geometries with inherent stress concentration zones, (**a**) the hat shaped specimen, (**b**) a truncated cone, and (**c**) the notched cylinder

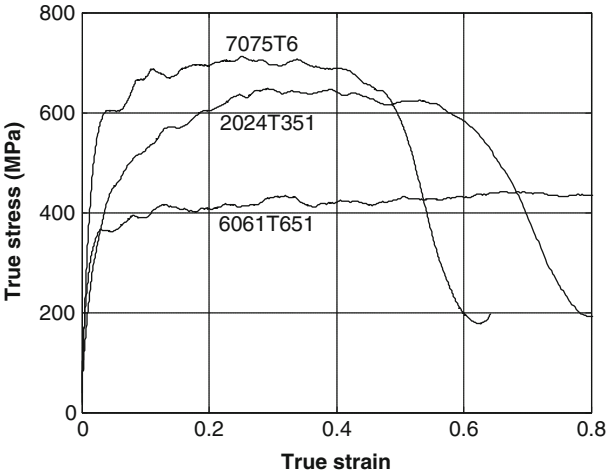

Fig. 4.24 Dynamic stress–strain curves for three aluminum alloys

physical account of the adiabatic shear phenomenon should be focused only on materials which have the inherent propensity for adiabatic shearing, such as the titanium alloy. These properties should be highlighted through experimental configurations which are free of stress concentrations, as discussed here.

The disc shaped specimen in the Kolsky bar test, with an aspect ratio of about H/D = 0.5, has the appropriate shape to derive such inherent material properties, since it is free of geometrical stress concentration zones. Typical examples of dynamic stress-train curves for three aluminum alloys are given in Fig. 4.24, as obtained by the Kolsky bar system in our laboratory. Note that the 6061-T6 alloy exhibits a truly ductile behavior where the specimen does not fail even at compressive strains as high as $\varepsilon = 0.8$. On the other hand the stronger alloys, 2024-T3 and 7075-T6, show a clear softening behavior at strains of about $\varepsilon = 0.5$ and 0.6, respectively. Such failure strains are also realized under static loading conditions, and they should not be classified as adiabatic shear failures. According to these tests, the flow stresses of these alloys at strain rates of about $10^3\ s^{-1}$, are: Y = 0.42, 0.62 and 0.7 GPa, for the 6061-T651, 2024-T351 and 7075-T6 alloys, respectively.

Flockhart et al. (1991) discussed the appearance of shear failure under various axisymmetric loading conditions, including indentation by a flat punch, perforation and deep penetration by blunt projectiles, and the compression of cylindrical specimens in the Kolsky bar system. They emphasize the difference between adiabatic shear failure by thermo-mechanical instabilities of the Zener and Hollomon (1944) model, which was described in Chap. 1, and failure by shear fractures through void nucleation, their growth and coalescence. The distinction between the two mechanisms is not clear, and in many actual cases the failure is by shear fracture within narrow bands of maximal shear strain, rather than by the adiabatic shear mechanism. They claim that in several actual situations the failure is not by an adiabatic shear mechanism, as in the appearance of a dead zone in brittle

materials and the occurrence of plugging in ductile materials. The numerical simulations of Flockhart et al. (1991) followed the velocity discontinuities in the specimens and confirmed their correspondence with shear failures, as identified by the shear strain rate maxima in the simulations. These maxima identify closely with the observed failures in compression tests, plugging during plate perforations, etc. We stress this issue here because there are many cases in the published literature where the term adiabatic shear is used very freely instead of referring to simple shear failure. The true nature of adiabatic shear is still an unresolved issue, and one should look for the physics behind this specific phenomenon.

The Ti/6Al/4V alloy is an excellent example for a material which fails by a true adiabatic shear mechanism, as mentioned above. Its compressive failure strain is about 20% under dynamic loading in the Kolsky bar, as was shown in Fig. 2.2. Obviously, this value of strain is too low to induce a significant uniform temperature increase in the specimen. Thus, its failure through shear banding cannot be simply related to a strain instability resulting from the two opposing mechanisms, strain hardening and thermal softening of the bulk specimen. Instead, one should consider the adiabatic shear failure as due to a significant heating within the localized shear band, and the simultaneous development of microvoids, or microcracks, which further raise the local temperatures and enhance the softening mechanism. Thus, a physically based model which accounts for adiabatic shear failure has to follow the temperature increase inside the shear bands, by the nucleation and growth of these imperfections. Rice and Levy (1969) adopted this approach and derived the following expression for the local temperature rise ahead of a microcrack which moves at a velocity V:

$$\Delta T = \frac{(1-\upsilon)^2 K_C Y}{E} \cdot \sqrt{\frac{2V}{\rho c \kappa}} \tag{4.34}$$

where ρ, E, ν and Y are the density, Young's modulus, Poisson's ratio and the strength of the material, respectively, K_c is its fracture toughness, c the sound speed, and κ is its thermal conductivity. The model is based on the following assumptions: (1) the material has no strain hardening features, (2) deformation takes place in a small zone ahead of the crack tip, and (3) there are no thermo-mechanical coupling effects. Equation 4.34 contains the relevant thermo-physical parameters which control the temperature rise ahead of a moving crack, and it can account for a large temperature increase inside a narrow band. Using published data for these variables Rice and Levy (1969) found that for a given crack velocity, the temperature rise in a Ti/6Al/4V specimen is an order of magnitude higher than the corresponding values for mild steel and the 2024 aluminum alloy. This difference can explain the propensity for adiabatic shearing in the titanium alloy.

4.6 Perforation of Thin Plates at the Hypervelocity Regime

The definition of the term "hypervelocity" has changed over the years, as noted in the review article by Swift (1982). Originally, the velocity of the projectile was used to determine this impact regime, but it is more customary now to consider the mechanisms which the impact invokes, in determining its nature. Thus, hypervelocity impacts are those which cause a complete pulverization of the materials, projectile and target, around the impact point. In this case both materials can be treated as fluids, neglecting their original strength, and the analysis becomes relatively easy. This definition results in different threshold velocities for the hypervelocity regime for materials which differ by their strength, melting and vaporization temperatures, and elastic moduli.

As summarized by Fair (1987), the early studies on hypervelocity impacts, during the 1950s, were motivated mainly by the need to protect the sensitive equipment in spacecrafts from accidental impacts of meteoroids. Whipple (1947) described his idea for a low weight shield which is based on a double wall system. This, so-called "Whipple Shield", consists of a thin sacrificial outer plate called the bumper shield, which is placed at some distance from the protected wall. Upon impact, both the meteoroid and the bumper completely disintegrate around the impact point, either by vaporization or melting. The resulting debris is dispersed through a cloud which expands behind the shield. The impact of this finely dispersed debris upon the wall of the spacecraft induces much less damage to the wall, thus saving the equipment inside the spacecraft. Obviously, the bumper plate should be made of a low melting material which has a high acoustic impedance, in order to induce high shock pressures (and temperatures) in the impacting meteoroid. It turned out, already in the early stages of the research, that cadmium has the optimal properties as a bumper shield. However, the research on hypervelocity impacts has been expanded for other materials, as reviewed by Hermann and Wilbeck (1987). A somewhat lighter design than the original bumper shield is based on two thin shields spaced apart, which further reduce the amount of debris and its spatial extent, when it hits the main wall of the spacecraft. All the experiments within this velocity regime were performed with light gas guns, described in Chap. 1, which were, in fact, developed for this space-oriented research.

The summary of Piekutowski (1996) is especially informative since it presents many flash X-ray shadowgraphs of the debris clouds formed by different projectiles (spheres and cylinders of various sizes) impacting thin plates at velocities up to about 7.0 km/s. These shadowgraphs reveal interesting details in the structure of the debris bubble, with which one can follow the trajectories of the debris particles from the projectile and the target. This is clearly seen in Fig. 4.25, which shows such a bubble at two different times after the impact of 12.7 mm aluminum sphere on a 2.03 mm thick aluminum plate at a velocity of 6.38 km/s. One can follow the complex structure of the bubble and determine the size and velocity of the different fragments comprising the debris cloud.

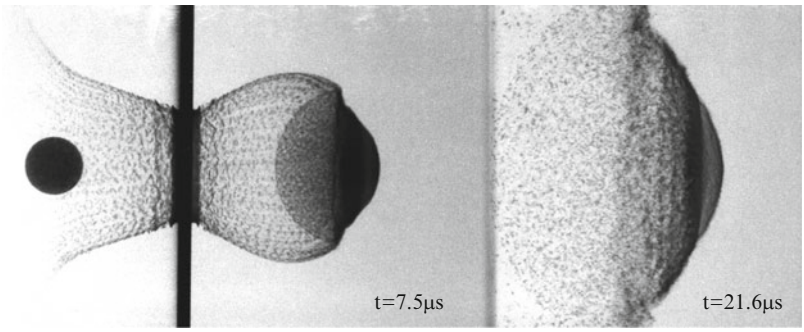

Fig. 4.25 The bubble formed by the impact of an aluminum sphere on an aluminum plate

The most interesting shadowgraphs are those which highlight the difference between materials which remain solid and those which melt upon impact or during the subsequent release process. This difference is clearly evident in the two shadowgraphs shown in Fig. 4.26, from Anderson and Mullin (1988). These debris clouds resulted in from the impact of a lead sphere on a lead plate, and a molybdenum sphere on a molybdenum plate. Both experiments were performed at an impact velocity of 6.58 km/s and the flashes were taken some 40 μs after impact. One should note that the densities of these materials are very close, $\rho = 10.21$ and 11.35 g/cc for molybdenum and lead, respectively. Thus, the shock pressures in the two impacts were practically the same. The significant difference in the shape of these bubbles is due the melting temperatures of the materials involved. The impact of the molybdenum sphere at the molybdenum plate resulted in the regular solid fragmentation, with no evidence for melting of either sphere or plate. On the other hand, the lead sphere and plate, having a much lower melting temperature, show a considerable amount of vapor in the debris cloud, as well as molten material.

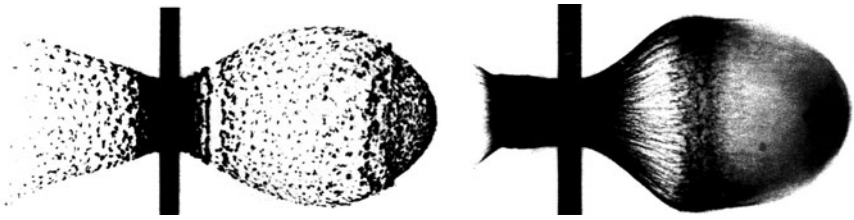

Fig. 4.26 Molybdenum impact (*left*) and lead impact (*right*) after about 40 μs

Chapter 5
Eroding Penetrators

This chapter deals with the penetration process of eroding penetrators, namely, long rods and shaped charge jets. The subject is of much interest for both warhead designers, who try to improve the penetration capabilities of these threats, and for armor engineers who try to defeat them with lighter and cheaper designs. As described in Chap. 1, a shaped charge jet is formed by the collapse of a thin walled conical liner, usually made of copper, which is inserted in a conical cavity at the end of a cylindrical explosive charge. Following the detonation of the explosive the copper liner is collapsing on itself, forming a long and thin jet, a few millimeters in diameter, which moves at extremely high velocities. In fact, the jet elements acquire different velocities during the collapse, and they move at a continuous velocity gradient from tip to tail. The head of the jet can reach velocities in excess of 8 km/s, while its tail is moving at about 3 km/s. A slower and much thicker part of the jet, called slug, is trailing behind at a velocity of about 2.0 km/s. Due to this velocity gradient, the jet can reach lengths of the order of 1 m, resulting in similar penetrations depths in armor steels. Long rod penetrators have aspect ratios in the range of L/D = 20–30 and diameters of about D = 20 mm. These rods are made of high density materials such as tungsten heavy alloys (WHA) or depleted uranium (DU), with densities of 17.0–18.0 g/cm^3. Long rods can penetrate armor steel targets of thicknesses which are equal to their lengths, at impact velocities in the range of 1.5–1.7 km/s.

The two types of penetrators are considered as the most lethal threats for armored vehicles. Thus, in order to design efficient armors against them one has to understand the various aspects of their penetration characteristics, which is the main subject of this chapter. We start with a short account of the so-called hydrodynamic theory of penetration, which was first applied for the penetration process of shaped charge jets, and was further developed for the penetration of eroding long rods. The analytical models which comprise the hydrodynamic theory are based on simple physical principles, which capture the important features of the experimental data as will be shown in this chapter.

Z. Rosenberg and E. Dekel, *Terminal Ballistics*,
DOI 10.1007/978-3-642-25305-8_5, © Springer-Verlag Berlin Heidelberg 2012

5.1 The Penetration of Shaped Charge Jets

During the years of the Second World War, groups in the U.S. and in England analyzed the structure of high velocity shaped charge jets and (independently) developed the so-called hydrodynamic theory, in order to account for their penetration depths in large metallic blocks. These works, which were published after the war by Birkhoff et al. (1948) and by Pack and Evans (1951), treated the metallic jet as a high velocity fluid which generates extremely high pressures upon impact, so that the strength of both jet and target could be ignored in the analysis. The penetration of the jet was treated as a steady state process and it was analyzed in terms of fluid mechanics. Figure 5.1 describes the essence of this process for a jet of length L and density ρ_j, impacting a large target of density ρ_t at a velocity V. Upon impact, the head of the jet is deformed to a mushroom-like shape, which penetrates the target at a constant velocity (U). It is simpler to view this process from a system of coordinates which moves with a velocity U, as shown in the lower part of Fig. 5.1

The model assumes that Bernoulli's equation, for the equality of pressures on both sides of the jet/target interface along their centerline, applies for this steady state process. Thus, one can write:

$$\frac{1}{2}\rho_j(V-U)^2 = \frac{1}{2}\rho_t U^2 \tag{5.1a}$$

The solution of this equation gives U in terms of V and the corresponding density ratio (ρ_t/ρ_j), according to:

$$U = \frac{V}{1+\mu} \quad \text{where:} \quad \mu = \sqrt{\frac{\rho_t}{\rho_j}} \tag{5.1b}$$

The erosion rate of the jet is given by (V−U) and it has a constant value for constant V and U. The final penetration depth is calculated via the total penetration time t = L/(V−U), when the jet is totally eroded, resulting in the following relation:

$$P = L \cdot \frac{U}{V-U} = L \cdot \sqrt{\frac{\rho_j}{\rho_t}} \tag{5.1c}$$

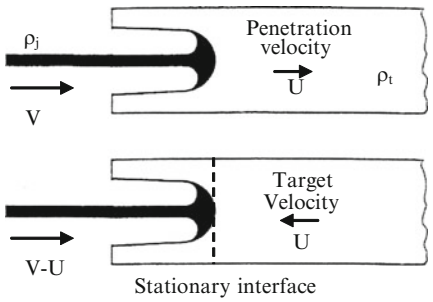

Fig. 5.1 The hydrodynamic picture of jet penetration

This elegant result means that the penetration depths of shaped charge jets are linearly dependent on their lengths, and they do not depend on their velocity. However, even in their early publications, both Birkhoff et al. (1948) and Pack and Evans (1951) noted that some modifications to the simple hydrodynamic theory are needed. For example, the penetration depths into very soft targets (such as lead) were much higher than those calculated by (5.1c). This extra penetration, which was termed the secondary penetration in those works, was attributed to the large momentum which the soft target acquires. This momentum overcomes the strength of the soft target and leads to the extra penetration after complete jet erosion, which was later referred to as the "third phase of penetration" by Orphal (1997). Another modification was made by Pack and Evans (1951) who realized the importance of target strength (Y_t), by observing the difference between jet penetrations into armor steel and soft steel. According to Pack and Evans (1951) the total penetration depth is the sum of two contributions, the primary penetration (P_{prim}) which depends on target strength (Y_t), and the secondary penetration P_{sec}, as follows:

$$P_{total} = P_{prim} + P_{\sec} = L\left(1 - \frac{\Omega Y_t}{\rho_j V^2}\right)\sqrt{\frac{\rho_j}{\rho_t}} + P_{\sec} \tag{5.2}$$

where Ω is an empirical constant which depends on the jet and target densities. According to Pack and Evans (1951), the second term in the brackets which is due to the strength of the target, can reduce the primary penetration by as much as 30%. The secondary penetration (P_{sec}) was taken by most workers as equal to half of the average crater diameter, which was also found to be dependent on the strength of the target material. A third modification to the simple hydrodynamic theory was due to the fact that jets are not moving at a constant velocity but have large velocity gradients along their length. This inherent jet property was noted by Birkhoff et al. (1948), who considered the particulation of the jet due to this velocity gradient. Eichelberger (1956) considered the combined effects of target strength and jet particulation. He added a strength term (σ) to the right hand side of (5.1a), which expressed the difference between the target and jet strengths. He also noted that the strength term (σ) should be important for the slower parts of the jet where the impact pressures are not too high. In order to account for jet particulation he multiplied the jet density in (5.1a) by a statistical factor (g), and suggested a modified Bernoulli equation, as follows:

$$\frac{1}{2} g\rho_j (V - U)^2 = \frac{1}{2}\rho_t U^2 + \sigma \tag{5.3}$$

In summary, many issues which are related to the non-ideal properties of the jet were already identified during the early stages of the research. Much of the historical developments concerning jet formation, its breakup, and its penetration process, were summarized by Dehn (1986), and by Chou and Flis (1986). An updated review of the research on this subject is given by Walters and Zukas (1989).

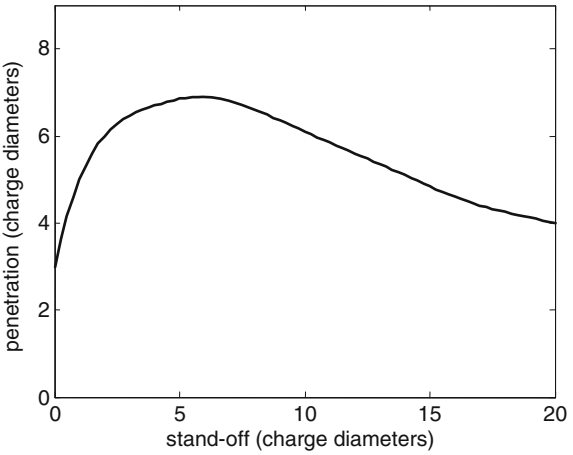

Fig. 5.2 A schematic description of the penetration depth of a shaped charge jet vs. its standoff distance

The velocity gradient of the jet elements is responsible for the observed shape of its penetration versus standoff-distance curve, as shown schematically in Fig. 5.2. The first part of this curve depicts the steep rise in penetration depths with increasing standoff, which is due to the stretching of the jet. With further standoff increase, jet particulation results in the more gradual change of the slope in this curve. At a certain standoff the jet elements deviate from their original flight direction and hit the crater wall, resulting in reduced penetration depths with increasing standoffs. This process is responsible for the maxima in the penetration vs. stand-off curve, as seen in Fig. 5.2. Obviously, in order to achieve large penetrations these shaped charge devices should be manufactured with high precision and symmetry to ensure their collinear motion even after jet breakup.

In order to account for the shape of these curves the concept of "virtual origin" was introduced by several authors during the early years of research. This concept states that all the jet elements can be considered as having a mutual origin in space and time, from which they start moving at different velocities. Allison and Vitali (1963) followed these ideas for the continuous jet, and were able to account for the increase of penetration with standoff distance up to its breakup. For larger standoffs, they introduced the concept of the cutoff impact velocity (V_{min}), below which a jet element does not penetrate the target. This concept was replaced with the penetration velocity cutoff (U_{min}) by DiPersio et al. (1965), who were able to account for the decreasing trend in penetration depths at large standoffs. The influence of jet breakup on its penetration capability has been also considered through its breakup time. These concepts provided useful penetration vs. standoff formulas for different jet/target combinations. For example, when the jet completes the penetration process before its breakup, the penetration depth (P) as a function of standoff distance (X) is given by:

$$P = X \cdot \left[\left(\frac{V_0}{V_{\min}} \right)^{1/\mu} - 1 \right] \tag{5.4a}$$

where V_0 is the velocity of the jet tip. A different approach, with U_{min} instead of V_{min}, resulted in the following relation between penetration depth and standoff distance:

$$P = X \cdot \left[\left(\frac{V_0}{(1+\mu)U_{\min}} \right)^{1/\mu} - 1 \right] \tag{5.4b}$$

These equations are very useful in accounting for the experimental data but they do not address the physical causes for jet breakup. This process was analyzed by several groups through the inclusion of viscosity and inertia, as reviewed by Walters and Zukas (1989).

5.2 The Penetration of Eroding Long Rods

The deep penetration of a long metallic rod into a semi-infinite target, has been studied intensively since the 1960s when such rods, made of dense materials, replaced the much shorter steel projectiles as tank ammunitions. By the term long-rods we mean penetrators with aspect ratios of at least ten, while short projectiles have aspect ratios of five or less. The deep penetration of long rods made of tungsten heavy alloys (WHA) or depleted uranium (DU), into armor steels, is accompanied by their continued erosion which terminates when the rod is totally consumed. Thus, the penetration process of long eroding rods is similar to that of shaped charge jets, and is very different from the penetration process of rigid long rods which was discussed in Chap. 3. The process itself has been envisioned by Christman and Gehring (1966) to be divided into four stages as shown schematically in Fig. 5.3, for the pressure at the rod/target interface.

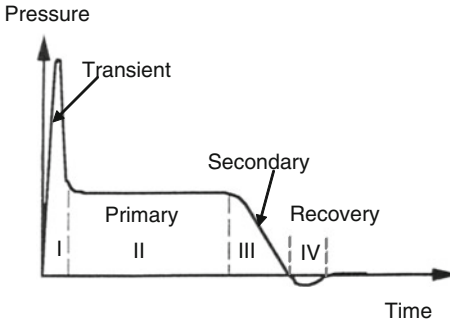

Fig. 5.3 The four penetration stages

The first stage in the process is the transient entrance phase which includes the high pressure shock waves generated in the rod and in the target, and the large deformation of the rod's nose. This phase lasts for a very short time by which the rod penetrates to a depth of a few rod diameters. The analytical description of this phase is very complex and a proper account for its contribution to the total penetration depth is still lacking. The second stage is the quasi-steady process of penetration which has been the focus of much research, both analytically and numerically, as will be described in this chapter. This is the dominant mode of penetration for high velocity rods of large aspect ratios. The third stage is called "secondary" by some researchers and "after flow" by others and it takes place after the rod is totally consumed. Orphal (1997) distinguishes between two different mechanisms which can operate at the end of the primary phase. The "secondary" penetration is related to the extra penetration which the inverted rod can achieve in certain cases. The "after flow" penetration is similar to that observed by Pack and Evans (1951) for shaped charge jets penetrating low strength targets. Namely, the momentum imparted to the target material is high enough to overcome its strength, and the crater continues to grow even after the rod has been completely eroded. We shall discuss these mechanisms later on and present some numerical results for these processes. The fourth stage is due to the target's recovery at the end of the penetration process by its rebound due to its strength. This process has a very small effect on the total penetration depth and it is usually ignored.

A "semi-infinite" target is large enough so that both its lateral dimensions and its thickness do not affect the penetration process. These free surfaces can influence both experimental and numerical results, and it is important to determine the minimal values of the target's dimensions in order to avoid their effects. This issue was investigated by Rosenberg and Dekel (1994a) through numerical simulations for L/D = 10 and 20 WHA rods, impacting steel targets at velocities in the range of 1.4–2.2 km/s. The Johnson-Cook constitutive model was used for the strength of the targets, with initial yield strength of either 0.8 GPa or 1.2 GPa in order to represent actual armor steels. The first set of simulations was performed for very large targets in order to determine the reference values of the penetration depths (P_0) in semi-infinite targets. The changes in the penetration depths with the target's diameter and thickness were then determined and the results are shown in Fig. 5.4. As is clearly seen in Fig. 5.4a the diameter of the target (D_t) should be at least 25 times larger than the rod diameter (D_p) in order to reduce the effect of lateral surfaces to within 1%. As far as the target thickness (H) is concerned, Fig. 5.4b shows that it should be about twice as thick as the penetration depth in order to be considered as a semi-infinite target. As stated above, these guidelines should be considered for both experiments and numerical simulations. Similar results were obtained by Littlefield et al. (1997) who performed both numerical simulations and experiments, with WHA rods impacting steel targets having different diameters, at a velocity of 1.5 km/s. They found that the ratio D_t/D_p has to be larger than about 15 in order to avoid lateral release effects, in general agreement with the findings of Rosenberg and Dekel (1994a).

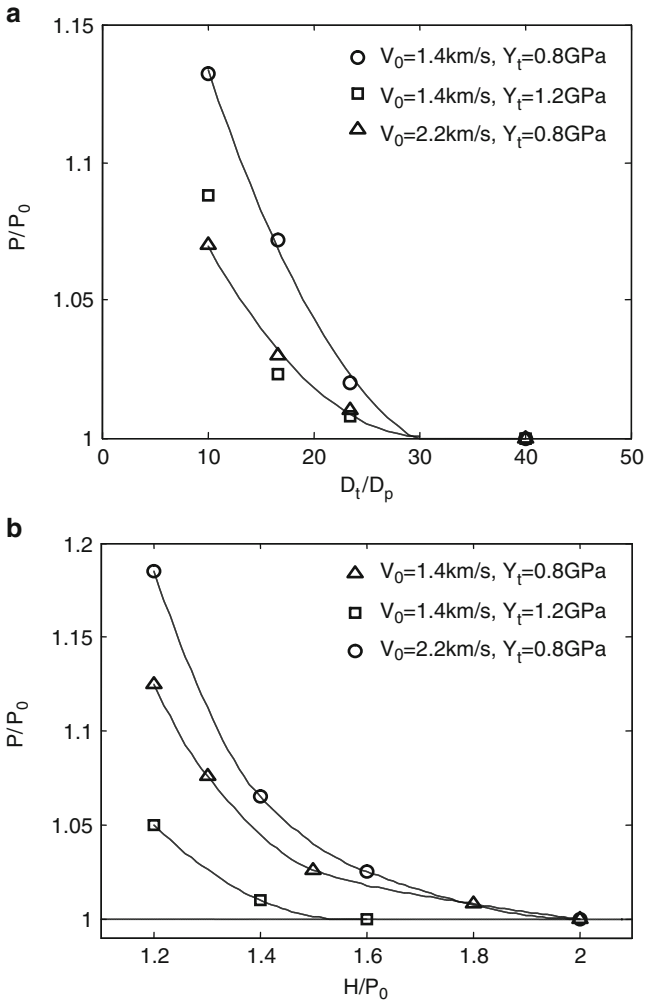

Fig. 5.4 Simulation results for the effects of target dimensions on the penetration depths of long rods: (**a**) the effect of target diameter and (**b**) the effect of target thickness

5.2.1 The Allen–Rogers Penetration Model

The first published account for the penetration of eroding long rods was by Allen and Rogers (1961). They used a two-stage light gas gun in order to launch 7075-T6 aluminum cylinders at very slender stationary rods, about 1 mm in diameter, which were made of different materials. This, so called "reverse ballistics" technique, is most suitable for high velocity impacts where the accelerations in the gun are too high for relatively soft and slender projectiles. The rods in these experiments were made of magnesium, aluminum, tin, copper, lead and gold, and their aspect ratios

were in the range of L/D = 6.3–12.2. The analysis of Allen and Rogers (1961) follows that of Eichelberger (1956) for shaped charge jets, setting g = 1.0 in (5.3) for the lack of velocity gradients in these rods. Since the rods were made of relatively soft materials the term σ in (5.3) was related to the target strength. Solving (5.3) for the penetration velocity U, results in the following expression:

$$U = \frac{V - \mu\sqrt{V^2 + Q}}{1 - \mu^2} \tag{5.5a}$$

where:

$$Q = 2\sigma \cdot \frac{1 - \mu^2}{\rho_t}\ ;\ \mu = \sqrt{\frac{\rho_t}{\rho_p}} \tag{5.5b}$$

and ρ_t/ρ_p is the target/rod density ratio.

Integrating over time, Allen and Rogers (1961) obtained the following expression for the normalized penetration depth (P/L) of these rods:

$$\frac{P}{L} = \frac{U}{V - U} = \frac{V - \mu\sqrt{V^2 + Q}}{\mu\sqrt{V^2 + Q} - \mu^2 V} \tag{5.6a}$$

For very high impact velocities the term Q in this equation can be neglected, and one obtains the so called "hydrodynamic limit" for the penetration of these rods, as given by:

$$\frac{P}{L} = \frac{1}{\mu} = \left(\frac{\rho_p}{\rho_t}\right)^{0.5} \tag{5.6b}$$

which is also the penetration depth of an ideal shaped charge jet, as given by (5.1c).

For the special case of $\rho_p = \rho_t = \rho$, (5.3) results in:

$$U = \frac{V}{2} - \frac{\sigma}{\rho_p V} \tag{5.6c}$$

leading to the following relation for the normalized penetration depth in this special case:

$$\frac{P}{L} = \frac{V^2 - 2\sigma/\rho_p}{V^2 + 2\sigma/\rho_p} \tag{5.6d}$$

The experimental results of Allen and Rogers (1961) are shown in Fig. 5.5, together with the P/L curves as calculated by (5.6a) and (5.6d). These curves were calculated with a value of σ = 1.95 GPa for the strength term of the 7075-T6 aluminum targets, as suggested by Allen and Rogers (1961).

One can clearly see that, except for the high velocity experiments with the gold rods, the simple hydrodynamic model is very successful in accounting for

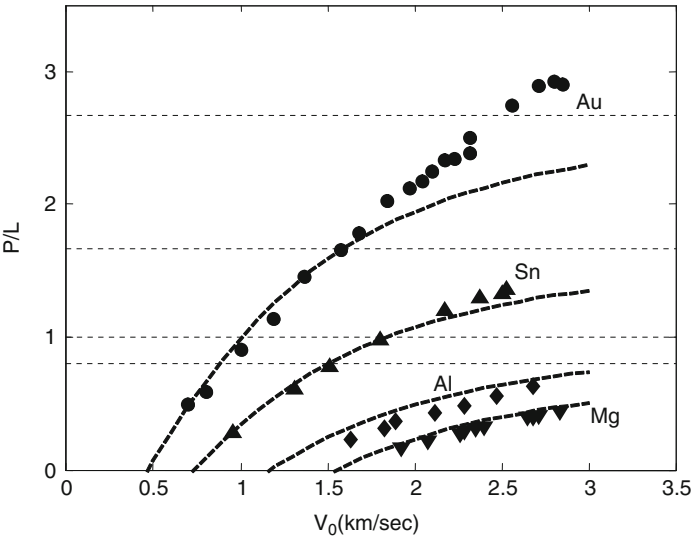

Fig. 5.5 The data of Allen and Rogers (1961) and the curves predicted by their model

the experimental results of these rods. The model predicts that the normalized penetration depths (P/L) should approach their corresponding hydrodynamic limits $(\rho_p/\rho_t)^{0.5}$ at high impact velocities, where the strength of the target is less important. This is clearly seen in Fig. 5.5, as the experimental results approach these limits for each rod material (the dotted horizontal lines in the figure). This asymptotic approach means that, as far as the penetration depths of eroding rods are concerned, there is no benefit in increasing their impact velocity beyond a certain value. This feature is in sharp contrast with the inherent property of rigid rods for higher penetrations with increasing velocities. In addition, rigid rods are much more efficient than eroding rods, as far as their corresponding values for P/L are concerned. In order to demonstrate this issue, consider the penetration depths of the ogive nosed steel rods into 6061-T651 aluminum targets, in the experiments of Piekutowski et al. (1999). These rods penetrated to depths of about seven times their length at an impact velocity of 1.8 km/s. In contrast, the maximal penetration depth of an eroding steel rod impacting an aluminum target is expected be only 1.7 times its length.

A very important observation from both the analysis and the experiments of Allen and Rogers (1961) is the existence of a threshold impact velocity (V_c), which marks the onset of penetration for a given rod. This threshold (critical) velocity is obtained by substituting $U = 0$ in (5.3), resulting in:

$$V_c = \sqrt{\frac{2\sigma_t}{\rho_p}} \tag{5.7}$$

The term σ_t, which is related to the target strength, expresses its resistance to penetration. In essence, the critical velocity is achieved when the dynamic impact pressure ($0.5\rho_p V^2$) is equal to the target resistance to penetration (σ_t). The experimental values of Allen and Rogers (1961) for the threshold velocities of the different rods, resulted in a value of $\sigma_t = 1.95 \pm 0.5$ GPa for the target's resistance to penetration. This value is about three times the dynamic compressive strength of the 7075-T6 alloy, which was used for the targets in this study. As noted by Allen and Rogers (1961), this is the expected result considering the indentation model of Tabor (1951). According to Tabor's analysis, the indentation pressure of a solid by a cylindrical punch should be equal to about three times its compressive strength. Thus, the minimum value for the dynamic pressure which the rod has to apply in order to achieve some penetration, should be equal to three times the dynamic compressive strength of the target.

With this definition of the critical velocity the normalized penetration of a rod into a target of the same density, through (5.6d), takes the form:

$$\frac{P}{L} = \frac{z^2 - 1}{z^2 + 1} \quad \text{where:} \quad z = \frac{V_0}{V_c} \tag{5.8}$$

The various relations discussed above have been derived through the assumption that the rod strength is negligible and the only strength which enters the analysis is that of the target, through its resistance to penetration (σ_t). Thus, according to the hydrodynamic model all the data for zero strength rods impacting targets of the same density should fall on a single curve which is given by (5.8).

In order to further highlight the role of these threshold velocities we performed numerical simulations with the AUTODYN-2D code, for L/D = 10 zero-strength steel rods impacting steel targets of different strengths. These strengths (von-Mises criterion) were: $Y_t = 0.4$, 0.8 and 1.2 GPa. Figure 5.6a shows the results for the three sets of simulations in terns of the normalized penetration depths vs. impact velocities. The results of these simulations enhance the validity of the hydrodynamic theory, through several aspects, as follows. Below a certain critical velocity the rod does not penetrate the target, and the critical velocities increase with target strength, as expected. In addition, the penetration depths approach the hydrodynamic limit (in this case P/L = 1) with increasing impact velocities, for all target strengths. A close examination of the simulation results shows that the critical velocities are: $V_c = 0.55$, 0.78 and 0.95 km/s for the $Y_t = 0.4$, 0.8 and 1.2 GPa targets, respectively. Using (5.7) we find that the corresponding values for σ_t for each target are exactly equal to $3Y_t$, in agreement with the results of Allen and Rogers (1961) and with the indentation analysis of Tabor (1951).

Once the threshold velocities are determined, one can construct the normalized penetration curve (P/L) in terms of the normalized velocities ($z = V_0/V_c$), as shown in Fig. 5.6b. It is clear that all the simulation results can be represented by a single normalized curve. However, this curve does not coincide with the curve predicted by the hydrodynamic model, (5.8), as is clearly evident in Fig. 5.6b. This comparison between a model's predictions and simulation results, is an excellent example

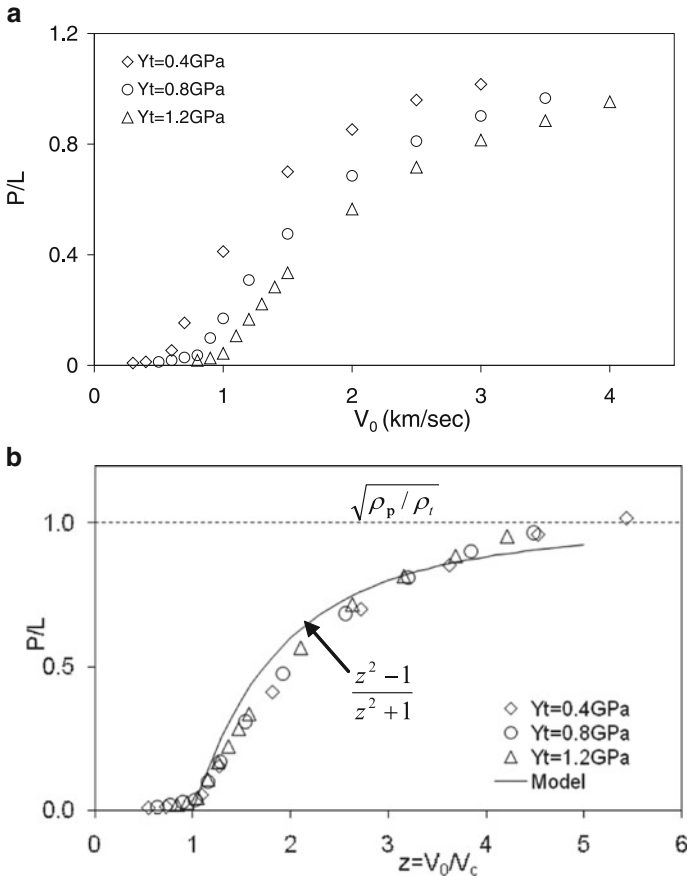

Fig. 5.6 (**a**) Simulation results for L/D = 10, zero strength steel rods, impacting steel targets of different strength. (**b**) The normalized presentation of these results, P/L vs. V_0/V_c

for the important role of numerical simulations for the validation of analytical models. For the present case we find that the general trends of the model and the simulation results are similar to each other. However, their slopes are quite different, and their corresponding values of P/L can be very different for certain values of z. In particular, at high impact velocities the numerical simulations result in higher penetration depths than the hydrodynamic limits which are predicted by the model. These higher values are often observed experimentally, as we shall see later on. Still, as far as a simplified 1D model is concerned, the hydrodynamic model can be considered as very successful in capturing the main features of the penetration process. An important result of this model is that the threshold velocity (V_c) does not depend on the density of the target. In order to check the validity of this issue we performed an additional set of simulations for the impact of zero-strength steel rods, at a semi-infinite aluminum target with strength of 0.4 GPa. These simulations resulted in a value of $V_c = 0.55$ km/s which is exactly the same value obtained for

the 0.4 GPa steel target. Thus, one may conclude that (5.7) can be used in order to predict threshold velocities for low strength rods and shaped charge jets.

We have noted in the Introduction that one of the main roles of numerical simulations is to validate the assumptions behind analytical models. We have already seen examples for such validity tests in the previous chapters, and from the analysis described here we learn about the validity limits of the hydrodynamic theory for penetration. A similar study was performed by Anderson and Orphal (2008), through numerical simulations for zero strength steel and WHA rods, impacting zero strength steel targets. They compared the penetration velocity histories from these simulations to those calculated by the hydrodynamic theory. Their main conclusion is that the differences between these velocity histories are related to material compressibility which is ignored in the hydrodynamic theory. With increasing impact velocities the compressibility effect increases and for an impact velocity of 6.0 km/s for the steel rod, the interface pressure is higher by about 10% than the corresponding value as calculated by the hydrodynamic theory.

The relatively deep penetrations of the high velocity gold rods in the work of Allen and Rogers (1961) were attributed by them to the "secondary penetration" process. According to their interpretation the inverted gold rods kept on penetrating the target after the primary phase ended. Their analysis showed that an inverted rod can penetrate the target if the rod/target density ratio (ρ_p/ρ_t) is large enough, and if the impact velocity is above a certain threshold. This issue has been reanalyzed by Rosenberg and Dekel (2000) who suggested a different explanation for the deep penetrations of these high velocity gold rods. According to their interpretation the cylindrical aluminum targets, which were launched at the stationary gold rods, were not thick enough to be considered as semi-infinite targets. Due to their high density, the gold rods penetrated to depths which were near the total length of these aluminum cylinders. The back surface of these cylinders lowered their resistance to penetration at the later stages of penetration, resulting in the extra penetration depths at the high-velocity impacts.

In order to enhance this explanation we performed numerical simulations for the impact of low strength (0.2 GPa) gold rods at semi-infinite 7075-T6 aluminum targets. The rods in these simulations had the same aspect ratio as those in the work of Allen and Rogers (1961), and the strength of the target in the simulation was set at $Y_t = 0.7$ GPa, using the von-Mises yield criterion. This value represents the flow stress of the 7075-T6 alloy, as discussed in Chap. 4. Impact velocities in these simulations were varied between 0.4 and 2.9 km/s, covering the range of impact velocities by Allen and Rogers (1961). The results of these simulations and the data from Allen and Rogers (1961) are shown in Fig. 5.7. The simulations follow the experimental results very closely for impact velocities up to 2.2 km/s. For higher impact velocities the experimental data fall above the simulation results, which showed no indication for a secondary penetration process through inverted rods. These simulations enhance the claim that the extra penetrations of the high velocity gold rods were due to some experimental artifact, rather than to a new penetration mechanism.

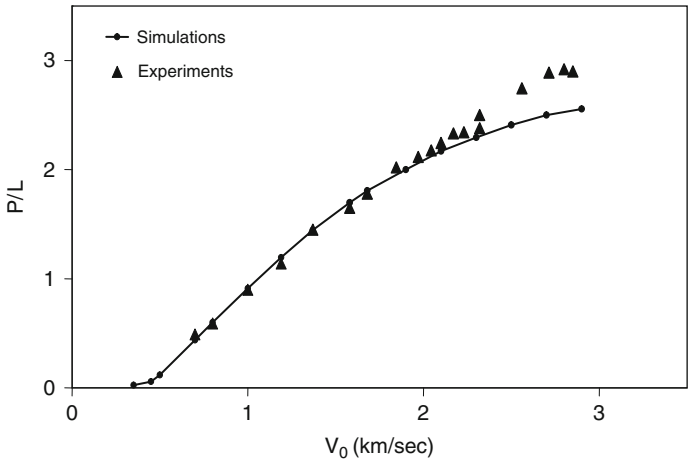

Fig. 5.7 Simulation results for gold rods impacting aluminum targets and the experimental data from Allen and Rogers (1961)

Christman and Gehring (1966) impacted aluminum and steel rods with aspect ratios of L/D = 0.17–25 at various targets, with velocities in the range of 0.3–6.7 km/s. Some of their experiments included flash radiographs which followed the rods during the penetration process. They analyzed the four penetration phases which are shown schematically in Fig. 5.3, and concluded that: "the secondary phase begins after the rod has been completely deformed and removed from the system as a source of energy. This phase lasts until the energy density behind the expanding shock wave becomes too small to overcome the intrinsic resistance of the target." They noted that both the primary and secondary phases may exist simultaneously during penetration. They also realized that at low impact velocities ($V_0 < 2$ km/s) these rods were not totally consumed, which implied that the back of the rod is decelerating during penetration. Thus, a steady state process was not achieved at the lower impact velocities. Christman and Gehring (1966) accounted for their results through a semi-empirical approach which was similar to the "after flow" concept, of Pack and Evans (1951), for shaped charge jets. According to their model, the primary penetration is achieved through a steady–state hydrodynamic process which lasts until the rod has a length of about L/D = 1. The remaining portion of the rod, with L/D = 1, adds an extra penetration which was found to be dependent on its velocity and on the strength of the target, as expressed by its Brinell hardness number (B_h). Their semi-empirical relation for the total penetration depth includes of the contributions from both phases, as follows:

$$P = (L - D)\left(\frac{\rho_p}{\rho_t}\right)^{\frac{1}{2}} + 2.42D\left(\frac{\rho_p}{\rho_t}\right)^{\frac{2}{3}}\left(\frac{\rho_t V^2}{B_h}\right)^{\frac{1}{3}} \tag{5.9a}$$

The secondary penetration term can be rewritten in a somewhat different form as:

$$\frac{P_{\text{sec}}}{D} = 2.42\left(\frac{\rho_p}{\rho_t}\right)^{\frac{1}{3}}\left(\frac{\rho_p V^2}{B_h}\right)^{\frac{1}{3}} \tag{5.9b}$$

This relation will be discussed in more detail when we deal with the hypervelocity impact of metallic spheres.

Rosenberg and Dekel (2001b) examined the issue of secondary penetration at high impact velocities, using numerical simulations for zero strength steel rods with aspect ratios of L/D = 3–30, impacting semi-infinite aluminum targets with strength of 0.4 GPa. The simulations showed a practically constant variation with time of rod length and its penetration depth, with a clear break towards the end of the penetration process. This is shown in Fig. 5.8a for an L/D = 10 rod impact at 7.0 km/s. Figure 5.8b shows the pressure time variation at the rod/target interface, and Fig. 5.8c shows the velocity-time histories of the rod's head and tail.

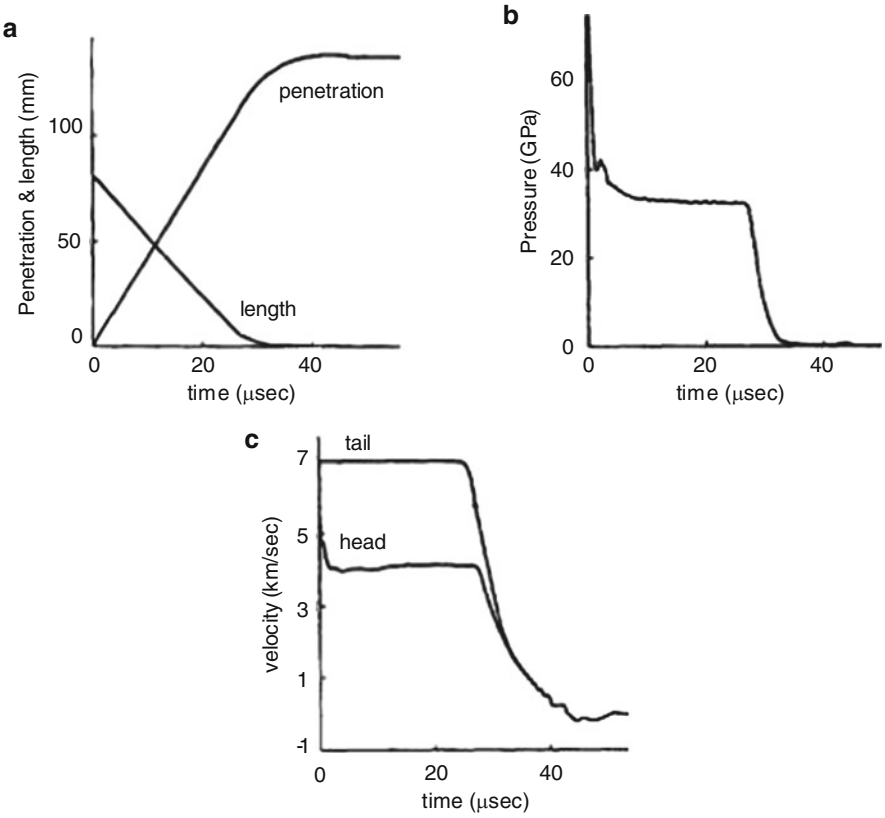

Fig. 5.8 Simulation results for an L/D = 10 steel rod impacting an aluminum target at 7.0 km/s. (**a**) penetration depth and rod length, (**b**) pressure at the interface, and (**c**) nose and tail velocities

The pressure and velocity histories show the expected behavior, with an initial transient phase which lasts for several microseconds. This is followed by the primary steady-state penetration with a constant interface pressure and constant head and tail velocities. The primary penetration phase is followed by a sharp decrease within a short time. This is the time duration of the secondary phase which adds the extra penetration to the steady-state primary phase. Rosenberg and Dekel (2001b) chose the break in the pressure–time history as the onset of the secondary phase, in order to distinguish between the penetration depths during the primary and the secondary phases. Their simulation results agreed with the general concepts of Christman and Gehring (1966), according to which the penetration at the end of the primary phase is very close to the hydrodynamic limit for a rod of length (L−D). They also found that the secondary penetrations of the L/D = 10–30 rods, are due to their last portion with L/D = 1. These secondary penetrations were found to be linearly dependent on impact velocity, in the range of V_0 = 3.0–7.0 km/s. Changing the strength of the aluminum targets in their simulations, they found that the secondary penetrations are proportional to the ratio $(V^2/Y_t)^{0.5}$. This result is not very different than the ratio of $(V^2/Y_t)^{1/3}$ in the empirical relation of Christman and Gehring (1966), as given by (5.9a). Similar results were obtained by Anderson and Orphal (2003) in their simulations for zero strength WHA rods impacting steel targets. They found that the length of the residual rod which is responsible for the extra penetration beyond the primary phase is about 1.25D, and that this last portion of the rod continues to penetrate until its length diminishes to zero.

In summary, these simulations showed that the last portion of the rod with L/D $\approx$ 1.0 is responsible for the extra penetrations beyond the hydrodynamic limits of long rods. These extra penetrations depend on the impact velocity of the rod and on target strength. No evidence was found in these simulations for the "after-flow" phenomenon, where the crater continues to grow after the rod is totally consumed. We should stress here that the situation is quite different for compact projectile, spheres or L/D = 1 cylinders, impacting semi-infinite targets at high velocities. As will be discussed later, these projectiles are consumed soon after impact, and the momentum which they impart to the target is responsible for the growth of a hemispherically shaped crater. As we shall see, the final size of this crater depends on the kinetic energy of the projectile and on the strength of the target even for impact velocities as high as 10.0 km/s.

5.2.2 The Alekseevskii-Tate Penetration Model

The next stage in the theoretical approach to the penetration of long eroding rods was made independently, and almost simultaneously, by Alekseevskii (1966) and Tate (1967, 1969). Their analysis has been considered as one of the more successful models in terminal ballistics. The AT model (after Alekseevskii and Tate), follows the penetration of an eroding long rod having a finite strength (Y_p), which is continuously decelerating during penetration. This model is also based on the

modified Bernoulli equation but it distinguishes between the dynamic strength of the rod (Y_p) and the target's resistance to penetration (R_t). The deceleration of the rigid part of the rod is achieved through elastic waves of amplitude Y_p, reverberating between its eroding front and its back surface. Thus, an equation for the deceleration of the back portion of the rod was added to the modified Bernoulli equation and to the relation for the erosion rate, which were used by Allen and Rogers (1961). The modified Bernoulli equation, with the two separate strength terms, takes the form:

$$\frac{1}{2}\rho_p(V-U)^2 + Y_p = \frac{1}{2}\rho_t U^2 + R_t \tag{5.10}$$

The other two equations of the AT model express the deceleration of the rigid part of the rod, of length ℓ, using Newton's second law:

$$\rho_p l \frac{dV}{dt} = -Y_p \tag{5.11}$$

and the kinematic equation for the rod's erosion rate:

$$\frac{dl}{dt} = -(V-U) \tag{5.12}$$

These equations have to be solved numerically in order to obtain the penetration depths of a given rod into a semi-infinite target for different impact velocities. The model distinguishes between two different situations concerning the rod and target strength parameters, either $Y_p > R_t$ or $Y_p < R_t$. Each case has its own solution and characteristic shape for the penetration vs. velocity curves, as follows:

1. $Y_p > R_t$—The strength of the rod is higher than the target's resistance to penetration and, at low impact velocities, the rod penetrates as a rigid body. The rigid penetration phase takes place until the impact velocity is high enough and the rod enters its eroding phase. Tate (1969) assumed that the retarding stress on the rigid rod is due to both the strength of the target (R_t) and its inertia ($\rho_t V^2/2$), so that the rod's equation of motion during its rigid penetration phase is:

$$\rho_p L \frac{dV}{dt} = -\left(\frac{1}{2}\rho_t V^2 + R_t\right) \tag{5.13}$$

It was shown in Chap. 3 that the deceleration of a rigid rod should be constant for all impact velocities below the cavitation threshold velocity (V_{cav}). Target inertia should be added only when $V_0 > V_{cav}$. Moreover, the resisting stress on a rigid rod depends on its nose shape, as shown in Chap. 3, an issue which is absent in the AT model. We have also seen that the transition from rigid to eroding rod penetration does not occur at a well defined threshold velocity, as suggested by Tate (1969). Rather, a certain range of impact velocities, where the rod is deforming without

losing mass, precedes the eroding rod phase. Due to these deficiencies, we shall not deal with this part of the AT model, and turn now to the second case, with $Y_p < R_t$, which is also the more relevant case for armor applications.

2. $Y_p < R_t$. The strength of the rod is lower than the target's resistance to penetration. This means that the rod does not penetrate the target unless its impact velocity is higher than a threshold value (V_c) which, from (5.10) with U = 0, is given by:

$$V_c = \sqrt{\frac{2(R_t - Y_p)}{\rho_p}} \tag{5.14}$$

For $V_0 > V_c$ the rod can penetrate the target and it starts to deform at the impact moment, achieving a mushroom-like shape within a short transient phase. Subsequently, the rod is continuously eroding while its back portion is decelerating. This is a quasi-steady penetration mode with a penetration velocity (U) which decreases with time. The modified Bernoulli equation, (5.10), results in the following relation between the penetration velocity (U) and the instantaneous velocity of the back part of the rod (V):

$$U = \frac{V - \sqrt{\mu^2 V^2 + (1 - \mu^2){V_c}^2}}{1 - \mu^2} \tag{5.15}$$

where $\mu = (\rho_t/\rho_p)^{0.5}$, as before, and V_c is the critical velocity defined by (5.14).

The rigid part of the rod is continuously decelerating by the reverberating elastic waves, as explained in Chap. 3, and it is continuously shortened by the erosion process. Penetration ceases either when the velocity of the rigid part reaches the value of V_c, or when the rod is completely consumed. Solving the three equations (5.10–5.12) numerically, results in an S-shaped penetration curve which starts at $V = V_c$ and approaches, asymptotically, the hydrodynamic limit $(\rho_p/\rho_t)^{0.5}$ at high impact velocities. This behavior is shown in Fig. 5.9 for WHA rods ($\rho_p = 17.3$ g/cc) impacting two steel targets ($\rho_t = 7.85$ g/cc) with different strengths. These curves were calculated for $Y_p = 1.0$ GPa for the WHA rod, and $R_t = 3.0$ and 5.0 GPa for the two steel targets.

The main features of these curves have been observed in many experimental studies with different rod/target combinations. These features include (1) the existence of a threshold velocity (V_c) below which the rod does not penetrate the target, (2) the fact that V_c increases with target strength according to (5.14), (3) the S-shape of the normalized curve and its steep rise at impact velocities in the ordnance range (1.0–2.0 km/s), and (4) the asymptotic approach, at higher velocities, to the hydrodynamic limit-$(\rho_p/\rho_t)^{0.5}$. Figure 5.10 shows the experimental results of Hohler and Stilp, from the database of Anderson et al. (1992), for L/D = 10 WHA rods impacting four steel targets with different hardness (strength) at velocities up to 4.0 km/s.

One can clearly see that all the features of the AT model, as discussed above, appear in these experimental curves, including their S-shape and their asymptotic

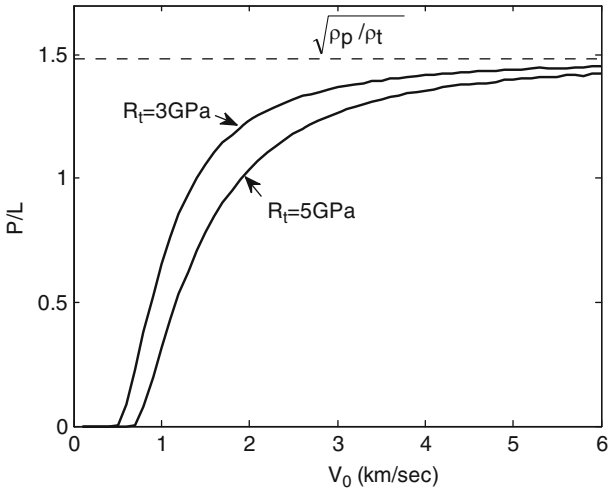

Fig. 5.9 The normalized penetration curves from the AT model for an eroding WHA rod impacting two steel targets of different strength

approach to the hydrodynamic limit, which is shown by the dotted line in the figure. Penetrations take place at velocities above a certain threshold (V_c), which is strongly dependent on the strength of the target, as expected. The most important issue, concerning both the AT model and the experimental data, is the significant

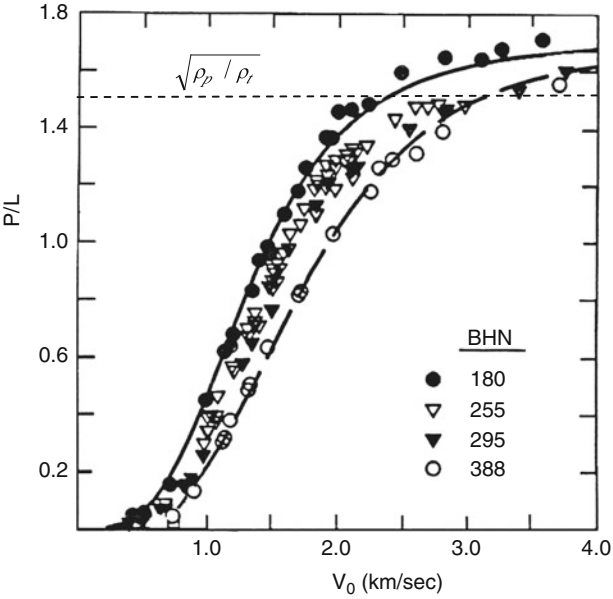

Fig. 5.10 Experimental result for L/D = 10 WHA rods impacting steel targets of different strength

dependence of the penetration depth on target strength, as shown in Fig. 5.10. For example, at an impact velocity of 1.5 km/s, an increase by a factor of two in target strength results in a reduction in penetration depth by a similar factor. At higher impact velocities the effect of target strength diminishes, as predicted by the AT model. Experimental results from other sources, with different rod/target combinations, as in Perez (1980), show the same features, strongly enhancing the validity of the AT model. On the other hand, at high impact velocities the data tend to cross the hydrodynamic limit, especially for low strength targets. These extra penetrations, beyond the hydrodynamic limit, are due to the later stages in the penetration process, as discussed above. It has been shown, both experimentally and numerically, that the strength of the rod has a much smaller effect on the penetration depth. This is partly due to the fact that higher rod strengths induce an increased deceleration of its rear part, which reduces its penetration capability. Thus, the possible gain in penetration depth by higher rod strengths is diminished by their enhanced decelerations. As we shall see later, the failure properties of the rod material are much more important than its compressive strength, as far as the penetration efficiency of the rod is concerned.

In order to compare the predictions from the AT model with actual penetration data, we chose two sets of experiments of Hohler and Stilp, which are given in the data base of Anderson et al. (1992). The steel targets in these experiments had hardness of 180 Brinell and the L/D = 10 rods were either steel or WHA rods. The results for the normalized penetration (P/L) vs. impact velocity, for the two sets of data, are shown in Fig. 5.11. Clearly, the higher density WHA rods penetrate more than the steel rods, and both penetration curves tend asymptotically to their

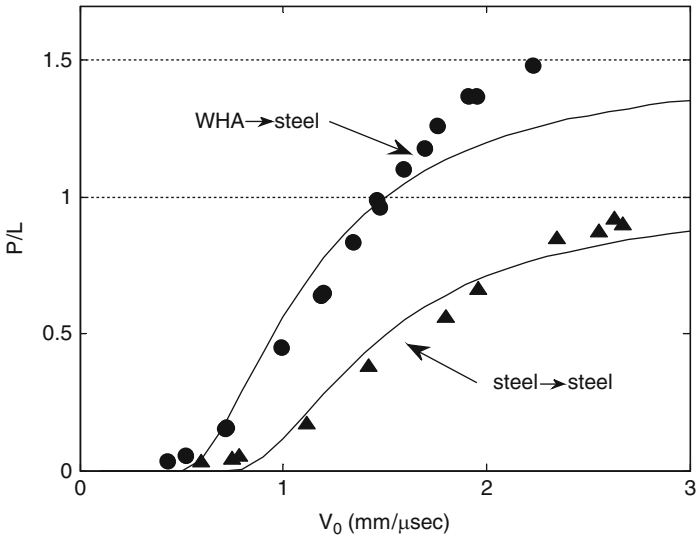

Fig. 5.11 Comparing model's predictions and data (symbols) for WHA and steel rods impacting a steel target

corresponding hydrodynamic limits of $(\rho_p/\rho_t)^{0.5} = 1.5$ and 1.0 for the WHA and the steel rods, respectively. These hydrodynamic limits are shown by the dotted horizontal lines in Fig. 5.11. In addition, the critical velocity (V_c) is higher for the steel rods, as predicted by (5.13). The figure also includes the predicted P/L curves from the AT model, using $R_t = 3.5$ GPa for the target and $Y_p = 1.2$ GPa for both the steel and WHA rods. Good agreement is evident for the steel on steel impact at all impact velocities. On the other hand, for the WHA rods the agreement is good only for the low velocity range. We have already mentioned a similar discrepancy between numerical simulations and the hydrodynamic model's predictions. The AT model results in lower penetration depths than those obtained by both experiments and simulations, which are in reasonable agreement with each other. As we noted above, these deviations are typical for low strength targets, and the agreement is getting better for targets of higher strength.

We turn now to the issue of similarity between different sets of rod/target combinations, as obtained by experimental data and their numerical simulations. Well established similarity relations can save a lot of experimental work, in addition to their importance in understanding the physics of a given process. In such a similarity study Rosenberg and Dekel (2001a) showed that different sets of data can be conveniently normalized by using the threshold velocity V_c as a normalization factor for the impact velocity. They suggested that experimental data should be presented as P/L vs. V_0/V_c. For example, the experiments with the WHA rods impacting two different steel targets which are shown in Fig. 5.12a, resulted in values of $V_c = 0.55$ and 0.75 km/s for the 180 and the 388 Brinell targets, respectively. Using the normalized values of V_0/V_c one finds that the two sets of data fall on a single normalized curve, as shown in Fig. 5.12b.

The numerical simulations of Rosenberg and Dekel (2001a) showed that all the penetration curves for a given rod, impacting targets which differ only by their strength, can be represented by a single normalized curve for P/L as a function of

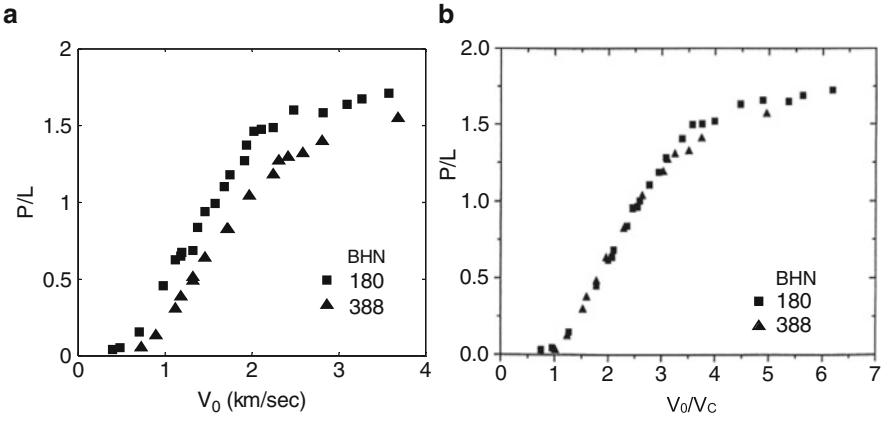

Fig. 5.12 (**a**) The data for WHA rods impacting steel targets with different hardness and (**b**) the normalized presentation of these experimental results

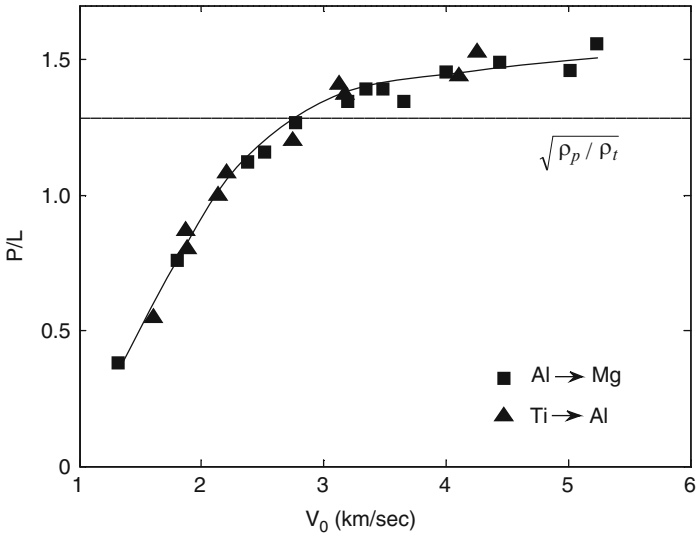

Fig. 5.13 The normalized penetrations of two rod/target combinations having the same density ratio

V_0/V_c. Also, multiplying the strengths of rod and target by the same factor, leads to the same normalized curve for both pairs. Moreover, the simulations showed that the same normalization scheme applies for different rod/target combinations if their corresponding density ratios are the same. In order to demonstrate that such normalization schemes are applicable for experimental data, consider Fig. 5.13. The data is taken from Perez (1980), who impacted L/D = 11 titanium alloy rods at aluminum targets and aluminum rods at magnesium targets. The density ratios of the two pairs are practically the same, $\rho_p/\rho_t = 1.66$ and 1.64, respectively. It is clear that the data points for the two sets of experiments fall on a single penetration curve for P/L vs. impact velocity. The excellent correlation between the two sets of data is also due to the fact that their strength ratios Y_t/Y_p have similar values. Note that the data points in both sets of experiments cross the hydrodynamic limit of $(\rho_p/\rho_t)^{0.5} = 1.28$, as for other targets of low strength.

5.2.3 The Validity of the AT Model

The validity of the one-dimensional AT model has been the subject of a large number of works over the years. The main incentive of these works was to account for several discrepancies between experimental results and the model's predictions, which were highlighted above. Anderson and Walker (1991) preformed numerical simulations which were specifically focused on the question whether the penetration process according to the AT model follows their simulations. Figure 5.14 shows the comparison between simulation results and the model's predictions, for the nose and tail velocities of an L/D = 10 WHA rod impacting an armor steel target at 1.5 km/s.

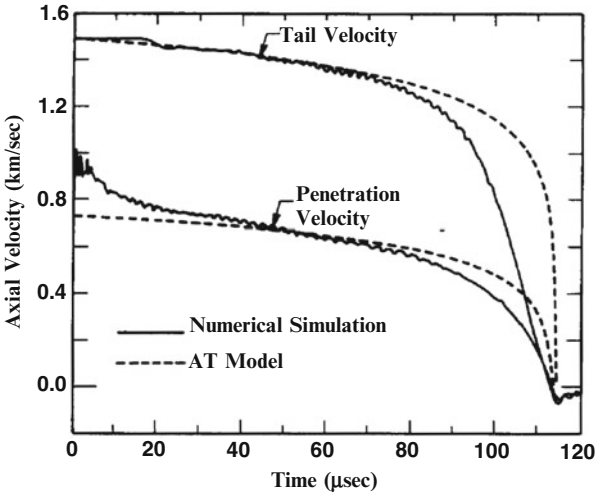

Fig. 5.14 Comparing simulation results with the AT model's predictions

The strong deceleration of the last portion of the rod, at the final stages of the process in the simulation, is not captured by the AT model. Also, the model predicts that the rod should be fully eroded at impact velocities in the range of 1.5–2.0 km/s, while both simulations and experiments show that a residual rod with L/D = 1 remains at the bottom of the crater. Additional simulations by Anderson et al. (1996c) showed that the difference $(R_t - Y_p)$ is velocity dependent. Thus, one may conclude that due to its simplicity, the AT model does not fully account for the complex process of eroding rod penetration.

The validity of the strength parameters of the AT model has been examined through numerical simulations by Rosenberg and Dekel (1994b), for the target's resistance to penetration (R_t), and in Rosenberg and Dekel (2000) for the rod strength (Y_p). In order to check the validity of R_t, they followed the penetration process of zero strength L/D = 20 rods made of different materials, such as steel, WHA, copper, and aluminum. The targets were of either steel or tungsten-alloy, with yield strengths (von-Mises criterion) which varied between 0.4 and 2.0 GPa. Such simulations, with zero strength rods have two advantages which are, in fact, related to each other. First, the term Y_p is eliminated from the modified Bernoulli relation, (5.10), and one can focus on the nature of the target strength parameter (R_t). In addition, with $Y_p = 0$ the rod is not decelerating during penetration, and both V and U are constant throughout the whole process. These issues simplify the analysis for the validity of R_t, as demonstrated by the following example.

The simulation results for the rod's tail and head histories for a zero strength L/D = 20 WHA rod, impacting a 0.8 GPa steel target at a velocity of 2.2 km/s, are shown in Fig. 5.15. It is clear that after a short transient phase, of about 20 microseconds, the penetration velocity reaches a constant value of U = 1.16 km/s. Inserting the values for V and U in (5.10), together with the corresponding densities of the rod and target, results in a value of $R_t = 3.9$ GPa for this target. Thus, the derivation of R_t values from simulations for zero strength rods, is a relatively

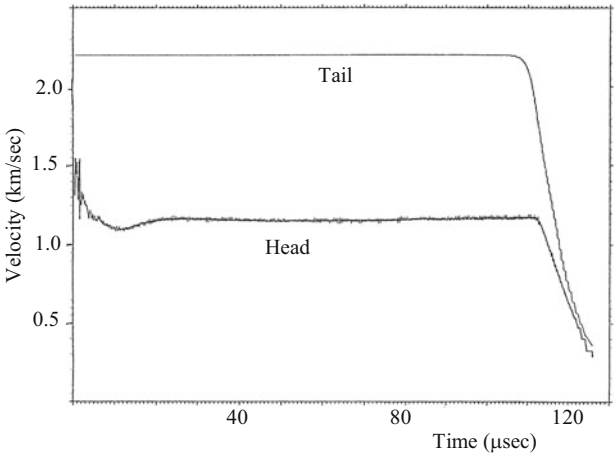

Fig. 5.15 Simulation results for a zero strength WHA rod penetrating a steel target

straightforward procedure. One should note that the transient phase in this simulation corresponds to a penetration depth of about three rod diameters, which is equal to the dominance range of the entrance phase for spherical nosed rigid rods, as discussed in Chap. 3.

Similar simulations were performed for several rod/target pairs where the strength of the target was varied in a large range, in order to derive relations between the target's resistance to penetration (R_t) and its strength (Y_t). The resulting relation between R_t/Y_t and $\ln(E/Y_t)$ for steel targets is shown in Fig. 5.16. These

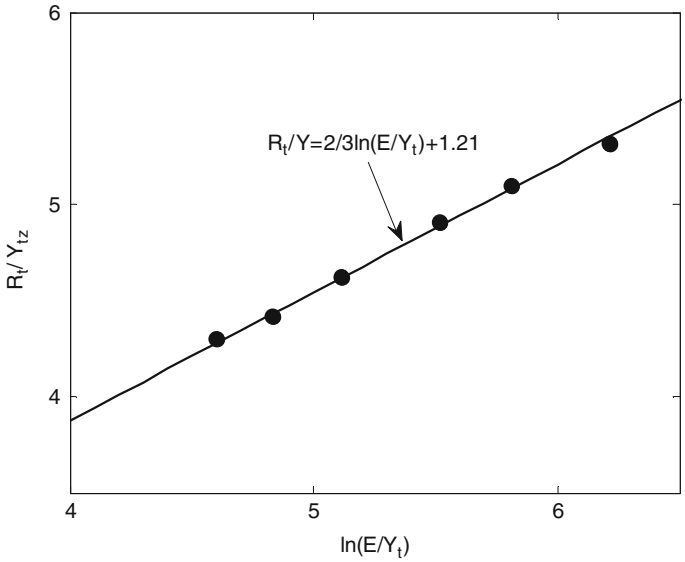

Fig. 5.16 Simulation results for the dependence of R_t on target strength

simulations were performed for L/D = 20 zero strength WHA rod, impacting steel targets of different strength at an impact velocity of $V_0 = 2.2$ km/s.

It is clear that the resulting values of R_t can be presented through a normalized form, with R_t/Y_t as a function of $\ln(E/Y_t)$, where E = 200 GPa is Young's modulus of the steel targets. This form of presentation is chosen in order to follow the numerical and analytical results for rigid rods, which were discussed in Chap. 3. With this choice of presentation, the normalized values of R_t/Y_t for different steel targets follow a similar dependence on $\ln(E/Y_t)$, according to:

$$\frac{R_t}{Y_t} = \frac{2}{3}\ln\left(\frac{E}{Y_t}\right) + 1.21 \tag{5.16}$$

The simulations of Rosenberg and Dekel (1994b) for different rod and target materials, showed that the parameter R_t depends on target strength, as expected, and that it is independent on either rod or target density. Moreover, for impact velocity up to about 3.0 km/s, the values of R_t were practically independent on impact velocity. The main conclusion from this study was that the parameter R_t can be considered as a valid physical property of the target, especially for the ordnance range of impact velocities (up to about 2.0 km/s). In contrast, the simulations presented by Rosenberg and Dekel (2000) for rods with finite strengths, showed that the rod strength parameter (Y_p), of the AT model, depends on both impact velocity and the rod's aspect ratio (L/D). Thus, the parameter Y_p in the AT model is its "weak" point, and it cannot be considered as a well defined physical parameter. In conclusion, the AT model was found to have several deficiencies, which are due to its simplicity. These deficiencies could have been overcome by additional corrections, if not for the so called "the L/D effect" which is its main problem, as discussed below. Before we turn to this issue we wish to highlight the difference between the resistance to penetration of a given target which is impacted by rigid and eroding rods.

It is clear that the values for R_t, as obtained from the simulations of zero strength rods through (5.16), are significantly lower than the corresponding R_t values for spherical-nosed rigid rods, as derived from (3.9). We can have an appreciation for these differences by comparing the corresponding R_t values for steel targets, of different strength, which are penetrated by these rods. Equation 5.16 results in: $R_t = 2.6$, 4.74, and 6.7 GPa for the eroding rod, and (3.9) gives: $R_t = 3.2$, 5.63, and 7.77 GPa for the rigid rod, penetrating steel targets with: $Y_t = 0.5$, 1.0 and 1.5 GPa, respectively. These differences, which amount to 16–23%, are due to the different flow fields of the target material in the two cases. Thus, the intuitive assumption that spherical nosed rigid rods experience the same resisting stresses as eroding rods is refuted by these simulation results.

In order to demonstrate the dependence of target resistance on the nature of its flow field, consider the simulation results of Rosenberg and Dekel (2008). These simulations followed the motion of spherical cavities inside a large elaso-plastic solid, which were partially loaded by an internal pressure, rather than on their whole surface. The partial

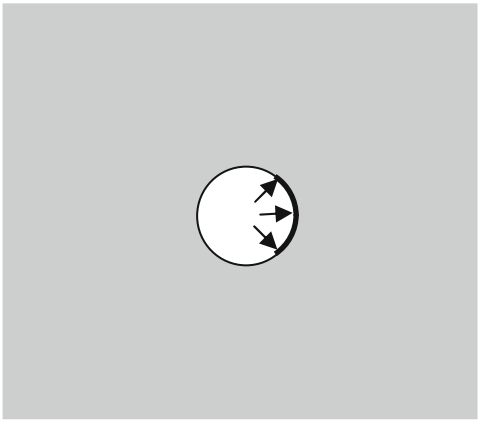

Fig. 5.17 A schematic description of the partially loaded cavity

loading was achieved by applying the pressure to a high strength thin shell (0.1 mm thick) at the cavity's wall, as shown schematically in Fig. 5.17.

The shells in these simulations extended to various angles around the symmetry axis of the 2D numerical scheme, which were: 13°, 27°, 54°, 90° and 180°. Due to the 2-D symmetry of these simulations, the 180° shell covers the whole area of the spherical cavity, while the 90° shell corresponds to the case where exactly half of the cavity area is loaded. The simulation results showed that the critical (threshold) pressures which are needed to expand these partially loaded cavities are strongly dependent on the area on which the pressure is applied. This dependence for a 1.0 GPa steel target is shown in Fig. 5.18. The critical pressures range from $P_{crit} = 3.63$ GPa for the fully loaded spherical cavity, to $P_{crit} = 5.64$ GPa when the

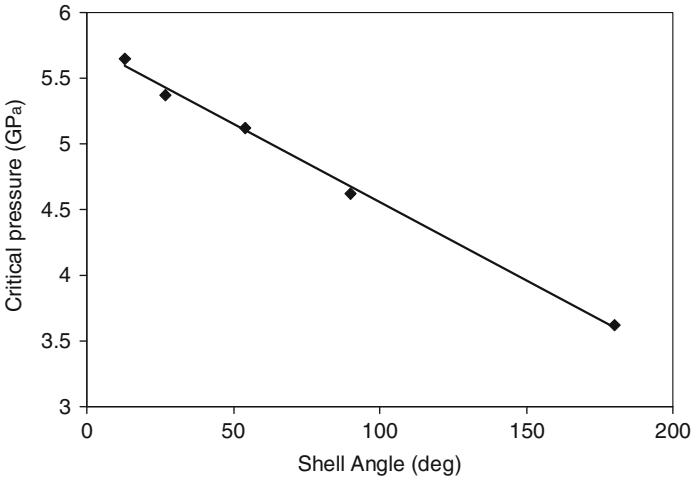

Fig. 5.18 The critical expansion pressures as a function of shell angle

cavity is loaded by the smallest shell (with an angle of 13°). These significantly different values are due to the different ways by which the material is flowing around the loaded area, much like the stream lines of the target around different nose shaped rods.

For the 180° case, where the whole cavity surface is loaded, the critical pressure is exactly equal to the value of P_{sph}, as derived from the spherical cavity expansion analysis for a compressible steel of strength 1.0 GPa. This is the expected result because the material in both cases is moving along radial directions, perpendicularly to the surface of the cavity. The most interesting result of these simulations concerns the 90° shell, which corresponds to a pressure applied on half of the cavity's area. The simulations resulted in a value of $P_{crit} = 4.7$ GPa for this case. This value is very close to the value of $R_t = 4.74$ GPa for the 1.0 GPa steel, as obtained by (5.16), from the numerical simulations for eroding rods. The agreement is due to the similarity in the flow fields of the target material in the two processes, namely, the deep penetration by an eroding rod and the expansion of a cavity by a constant pressure which is exerted on half of its area. This similarity is shown in Fig. 5.19 presenting the flow field of the 1.0 GPa steel target which was impacted by a copper rod at 2.2 km/s, and the field around an expanding cavity which was loaded at half of its surface (the 90° shell).The various colors in this figure correspond to different material velocities, and one can clearly see the similarity of the two flow fields.

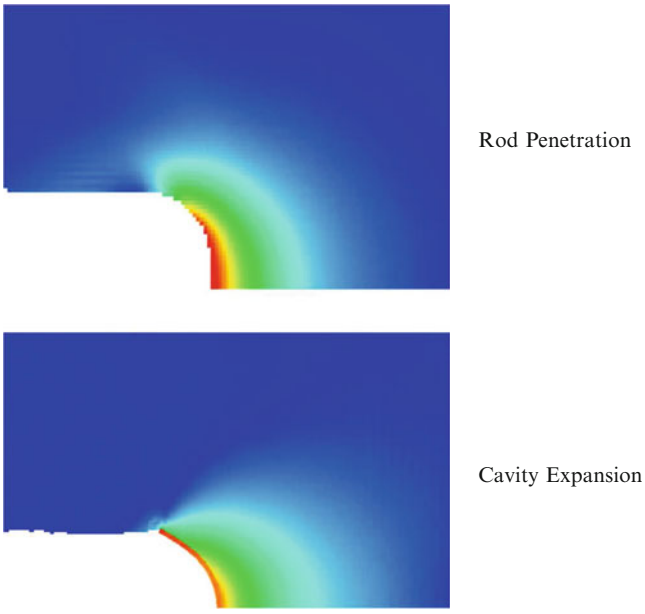

Fig. 5.19 Velocity fields around the crater during rod penetration and around the expanding cavity for the 90° shell

5.2.4 The L/D Effect

It has been a well-established fact that the penetration efficiency, as defined by the penetration depth per unit rod length (P/L), is lower for a long eroding than that of a short rod. In particular, an L/D = 1 cylinder has a higher efficiency than an L/D = 5 rod, and this rod has a higher efficiency than an L/D = 10 rod. This trend is clearly seen in Fig. 5.20, from Tate et al. (1978), for WHA rods impacting armor steel plates at the ordnance range of impact velocities. These rods had aspect ratios of L/D = 3, 6 and 12, and one can clearly see that the corresponding efficiencies, in terms of P/L, are decreasing with increasing aspect ratios.

The general assumption among researchers was that this decreasing trend saturates at about L/D = 10 and that all the data for L/D $\geq$ 10 rods should fall on a single curve of P/L vs. impact velocity. The independence of P/L on L/D is an inherent feature of the AT model for eroding long rods, and much of its success was attributed to this feature. However, the experimental data of Hohler and Stilp (1987), showed that the penetration efficiency of long rods decreases significantly even for L/D = 20 and 30 rods. Their results for steel and WHA rods impacting steel targets, revealed a strong dependence of P/L on L/D especially for impact velocities within the ordnance range. This dependence of P/L on L/D was termed "the L/D effect" and has been the subject of intense research during the 1990s. Figure 5.21 shows the data from Hohler and Stilp (1987), for WHA rods impacting armor steel targets (RHA). One can clearly see that the difference between the values of P/L, for L/D = 10 and 30 rods, reaches 50% at impact velocities around 1.5 km/s.

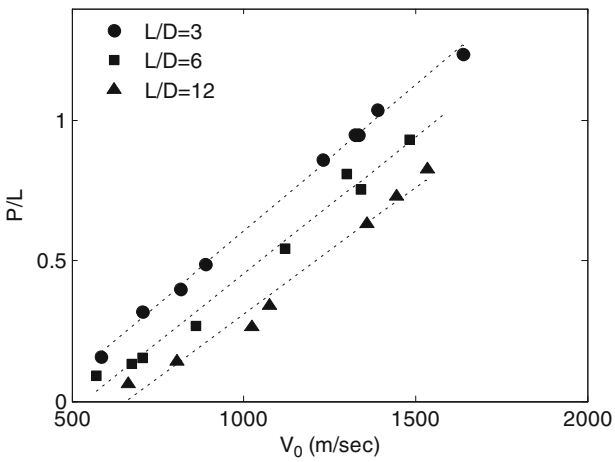

Fig. 5.20 The decreasing trend in P/L with increasing aspect ratio for WHA rods impacting armor steel targets

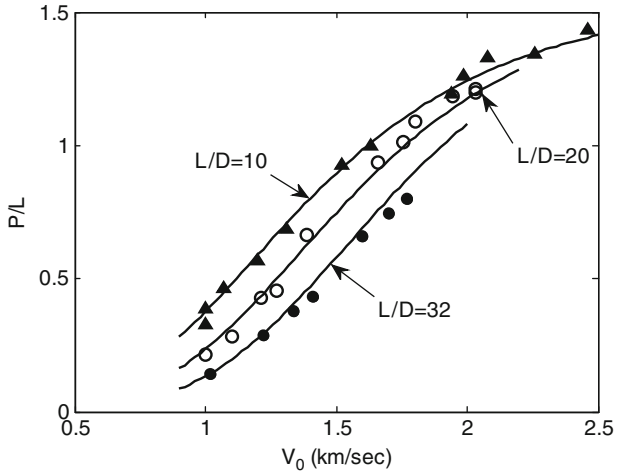

Fig. 5.21 Experimental results for WHA rods impacting RHA targets, demonstrating the L/D effect

The "L/D effect" became a major subject for further analysis by several workers, who used numerical simulations in order to find the mechanisms responsible for this effect. The simulations of Rosenberg and Dekel (1994c, 2001b) reproduced the L/D effect and showed that the differences in P/L are diminishing as the L/D ratios become larger. These simulations showed that even zero strength rods resulted in the same behavior, as is clearly seen in Fig. 5.22 for zero strength WHA rods impacting RHA targets at 1.4 km/s.

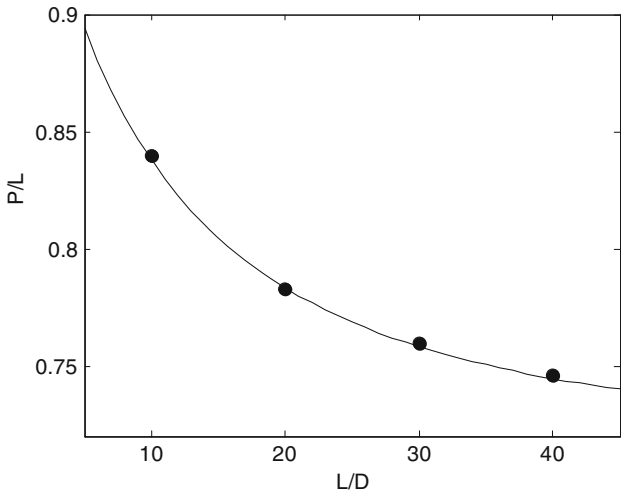

Fig. 5.22 Simulation results for zero strength WHA rods impacting RHA targets at 1.4 km/s

The numerical simulations of Anderson et al. (1995, 1996a) showed that several contributions are responsible for the "L/D effect" at different stages of the penetration process. For low impact velocities the non-steady nature of the process at the early stages is responsible for the effect. At the high velocity range, above 2.0 km/s, the terminal phase of penetration adds another contribution to the effect. Figure 5.23 summarizes experimental results from several sources for WHA rods impacting steel targets. These data were assembled by Anderson et al. (1995) in order to demonstrate that the L/D effect is practically independent on impact velocity within the ordnance range.

In conclusion, the one-dimensional penetration model of Alekseevskii and Tate has been found to be too simplistic to give a complete account for the penetration process of eroding rods, mainly because it does not deal with the transient phases at the start and at the end of the process. The steady state (primary) penetration phase, which is the main subject of the model, is established only after the rod penetrates to a depth of several rod diameters, as shown by the simulations of Anderson and Orphal (2008). The entrance phase for eroding rods includes the transition to the mushroomed-shaped nose, which also takes some time. With this transitory nature of the entrance phase one can have a qualitative estimate for the extent of the "L/D effect". As was shown above, eroding rods penetrate to depths of about 1.0–1.5 times their original length. Thus, for an L/D = 10 rod the total penetration depths are in the range of (10–15)D. Since the entrance phase may last for about five rod diameters, this means that the steady state process, for an L/D = 10 rod, accounts only for half of the penetration process. Thus, it is not surprising that such an "L/D

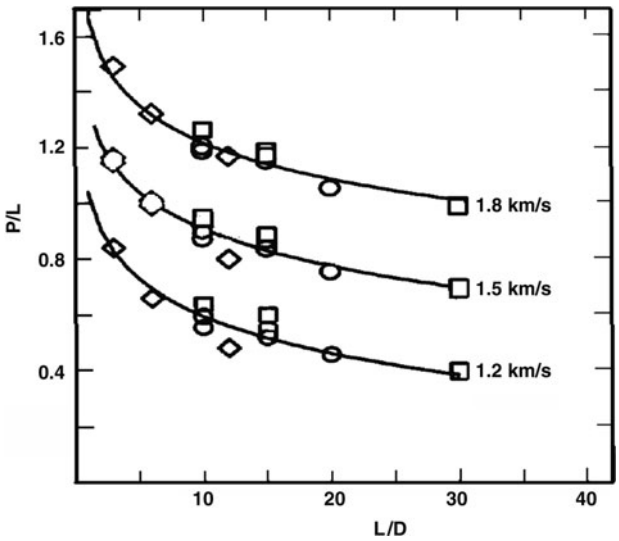

Fig. 5.23 The L/D effect for different impact velocities in the ordnance range

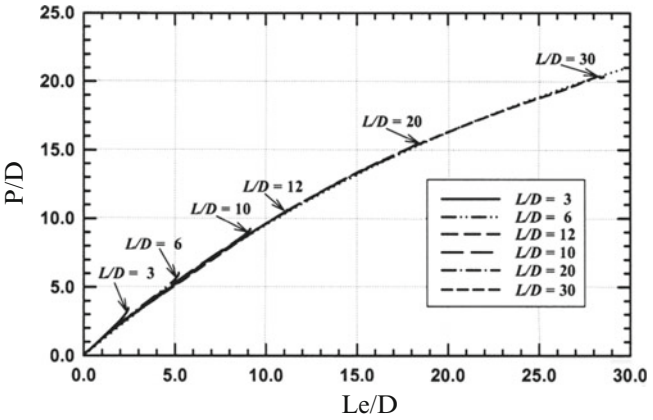

Fig. 5.24 The change of ballistic efficiency (P/D) with the eroded rod length for a 1.5 km/s impact of a WHA rod on an armor steel target

effect" is influencing the penetration depths of L/D = 10–30 rods. This point is demonstrated by the numerical simulations of Anderson (2003), as shown in Fig. 5.24. The figure summarizes simulation results for the penetration efficiency (in terms of P/D), as a function of the eroding part of the rod (L_e/D), for rods of different aspect ratios. The simulations were performed for WHA rods (L/D = 3–30) impacting armor steel targets at V_0 = 1.5 km/s. The different slopes of this curve are related to the ballistic efficiency of these rods, since they depict the change in the penetration depths as a function of the eroded rod length. It is clearly evident that the ballistic efficiency decreases with increasing rod length. The arrows in this figure point to the final penetration depths of the different rods in these simulations.

The large difference between the specific efficiency (P/L) for L/D = 1 and L/D = 10 or 20 rods motivated several workers to consider the idea of a segmented rod. This rod consists of ten or twenty L/D = 1 cylinders which are widely spaced. The basic idea is that this separation ensures that each segment completes its penetration before the subsequent segment impacts the crater. This way, the deceleration of the back part of the rod is avoided and the contribution of the back segments enhances the total penetration depth. Numerical simulations, by Orphal and Franzen (1989) for example, showed a promising gain with this arrangement, especially at high impact velocities. Tate (1990) reviewed the theory and the experimental data concerning this subject, as well as the practical issues involved with launching a segmented rod. He concluded that the relatively few trials which were published over the years did not reveal an appreciable improvement with segmented rods over continuous ones, for impact velocities within the ordnance range.

5.2.5 *Other Penetration Models*

The deficiencies of the one-dimensional AT model which were discussed above prompted several attempts to improve this model. These approaches consider the forces acting on the rod/target interface rather than the stresses along their centerline, as was suggested by Dehn (1987), Rosenberg et al. (1990), and Grace (1993). These models consider the area of the mushroomed nose as another free parameter and derive equations which are based on the resisting forces. The model of Dehn (1987) accounts for a large variety of penetrators (long and short, rigid and eroding), but it involves the knowledge of the projectile/target interface area, which has to be determined empirically for each penetrator/target combination. The non-steady penetration model of Grace (1993) is based on a new concept, by defining a finite target volume (thickness) which participates in the penetration process. An equation of motion for this volume has to be added to the deceleration and erosion equations for the rod.

A more rigorous treatment of the penetration process for an eroding long rod has been given by Wright and Frank (1988). They reduced the full balance laws for mass, momentum, and energy into a set of approximate penetration equations. They divided the rod material into two parts R and S as shown in Fig. 5.25, and treated the different parts accordingly. The target is specified by its density (ρ_t) and the cross section area of the crater (A_t).

In region R, the rigid part of the rod with density (ρ_p), length ℓ, and cross section (A_p), moves at a velocity (V). Region S is assumed to be constant in size and shape (steady state situation) and the material is assumed to flow plastically at the R-S boundary reversing its velocity direction (W) and attaining different values for its density of (ρ_d) and cross sectional area (A_d). The target material lies in region T and the cross section of the crater in the target is A_t. Both R-S and S-T boundaries simply translate horizontally with velocity U. Wright and Frank (1988) consider the conservation equations for the different parts of the rod and make several simplifying assumptions in order to reduce the number of free parameters. For part R they use the deceleration and erosion equations of the AT model, (5.11) and (5.12). For region

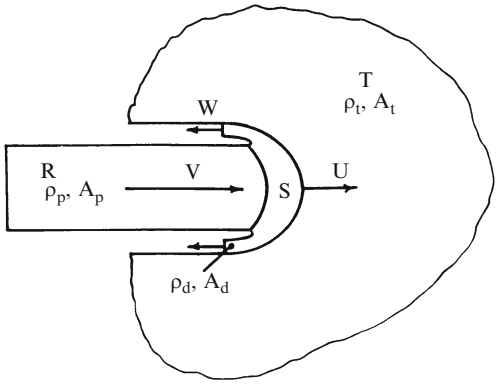

Fig. 5.25 The different regions in the Wright and Frank (1988) model

S, they consider the forces which act on the two interfaces R-S and S-T, using the different areas A_p, A_d and A_t.

Conservation of mass and momentum result in the following equations:

$$\text{mass:} \quad \rho_p A_p (V-U) = \rho_d A_d (U+W) \tag{5.17a}$$

$$\text{momentum:} \quad \rho_p A_p (V-U)^2 + \rho_d A_d (U+W)^2 = F_t - F_r - F_d = F \tag{5.17b}$$

The three forces in the momentum equation are: F_r—the axial force on the R-S boundary, F_d—the axial force on the rearward flow of the inverted rod, and F_t—the force on the S-T boundary. These forces have to be specified by some simplifying assumptions. For example, the compressive force on the S-T boundary for a steady state process has the form:

$$F_t = A_t \cdot \left(a_1 Y_t + b_1 \rho_t U^2\right) \tag{5.18}$$

where the constant b_1 plays the role of a shape factor. The most interesting result which emerges from this analysis is that the energy equation takes the form:

$$\frac{1}{2}\rho_p (V-U)^2 + Y_p = \frac{1}{4}\rho_t b_1 \cdot \frac{A_t}{A_p} U^2 + \left[\frac{A_t a_1 Y_t}{4A_p} + f\left(Y_p, \rho_p\right)\right] \tag{5.19a}$$

This equation can be re-written in a more concise way, which is very similar to the modified Bernoulli equation:

$$\frac{1}{2}\rho_p (V-U)^2 + Y_p = \frac{1}{2}\rho_t^* U^2 + R_t^* \tag{5.19b}$$

where R_t^* is the sum of the terms in the square brackets of (5.19a), and ρ_t^* is an effective target density defined by:

$$\rho_t^* = \frac{\rho_t b_1 A_t}{2A_p} \tag{5.19c}$$

With $b_1 = 0.5$ for the nose shape factor and assuming that $A_t/A_p = 4$, the true and effective target densities are equal. In addition, for $A_t/A_p = 4$ the first term in the square brackets of (5.19a), reduces to the well-known resistance to penetration, $R_t = a_1 Y_t$. The last term in the square brackets of (5.19a) is related to the rod, which means that the target resistance to penetration (R_t^*) includes the properties of the rod. However, one can move this term to the left side of the equation and add it to the rod strength (Y_p). This result may explain the difficulties discussed above, concerning the validity of the parameter Y_p of the AT model.

The time-dependent model of Walker and Anderson (1995) is based on a more elaborate description of the deformations in the rod and the target, around their

interface. This model starts with the momentum balance equation and uses numerical simulations in order to obtain the velocity gradients in the rod and in the target, away from their interface. The shape of the mushroomed end of the rod is similar to that of the Wright and Frank (1988) model, and the plastic zone in the rod extends to a certain distance (s) from the rod/target interface. The elastic waves which decelerate the rod reverberate between its free end and the plastic zone. A velocity profile for the material within the plastic zone is obtained from numerical simulations, and the velocity of the rod is gradually increasing from U to V within this zone. The velocity profile in the target is also taken from numerical simulations through another parameter (α_p) which determines the extent of the plastic zone in the target. The hemi-spherical plastic zone in the target extends to a distance of $\alpha_p D_c$, where D_c is the crater diameter. The parameter α_p is velocity dependent, thus it changes with time during penetration. The extent of the plastic zone in the projectile (s) is related to the parameter α_p through the relation:

$$s = \frac{D_c}{2}\left(\frac{V}{U} - 1\right)\left(1 - \frac{1}{{\alpha_p}^2}\right) \tag{5.20}$$

The extent of the plastic zone in the target (α_p) is obtained as the solution of the following transcendental equation:

$$\left(1 + \frac{\rho_t U^2}{Y_t}\right)\sqrt{K_t - \rho_t U^2 \alpha_p} = \left(1 + \frac{\rho_t U^2 {\alpha_p}^2}{2G_t}\right)\sqrt{K_t - \rho_t U^2} \tag{5.21}$$

where K_t is the pressure dependent bulk modulus of the target material, and G_t is its shear modulus.

The equations which have to be solved numerically are the equations for rod erosion, the deceleration of its rigid part and the stress balance across the rod/target interface. The rod erosion is given by the same equation as in the AT model, (5.11), while the equation for the deceleration of the rigid part is given by:

$$\frac{dV}{dt} = -\frac{Y_p}{\rho_p (L - s)} \cdot \left[1 + \frac{V - U}{c_b} + \frac{1}{c_b} \cdot \frac{ds}{dt}\right] \tag{5.22}$$

where c_b is the elastic wave speed in the rod. The third equation includes V and U, their time derivatives, and other terms which are related to s and α_p. Since α_p is both velocity and time dependent the main result of this model is that R_t is not constant during a given penetration process and that it depends on impact velocity. On the other hand, the time variation of α_p is not very large, as shown by Walker and Anderson (1995), and one can choose an average value to represent this parameter for a given penetration. The governing equations of this model reduce to those of the AT model if the three-dimensional terms are set to zero and the speed of the

elastic waves in the rod becomes very large. In fact, the expression for the target's resistance to penetration (R_t) reduces to:

$$R_t = \frac{7Y_t}{3} \ln \alpha_p \tag{5.23}$$

The model predicts, at the very minimum, that R_t varies with the extent of the plastic zone (α_p) and with the flow stress of the target (Y_t). Walker and Anderson (1995) suggested using the cavity expansion analysis from Bishop et al. (1945), in order to provide an a priori estimate for the value of α_p. They found that the expression for α_p from the cylindrical cavity expansion analysis provides a better agreement with the data, as compared with the spherical expansion analysis. This issue was further discussed by Chocron et al. (1998) who confirmed the better agreement with the cylindrical analysis.

The analysis of Bishop et al. (1945) gives the following expressions for the extent of the yielded material (r_y) around an expanding cavity of radius r, in an elasto-plastic material with Young's modulus (E), Poisson's ratio (ν), and strength (Y):

$$\left(\frac{r_y}{r}\right)_{sph} = \left[\frac{E}{(1+\upsilon)Y}\right]^{1/3} \quad \text{For the spherical cavity} \tag{5.24a}$$

$$\left(\frac{r_y}{r}\right)_{cyl} = \left(\frac{\sqrt{3}E}{2(1+\upsilon)Y}\right)^{0.5} \quad \text{For the cylindrical cavity} \tag{5.24b}$$

Using (5.24b) from the cylindrical cavity expansion, with $\alpha_p = (r_y/r)_{cyl}$, one gets from (5.23) the following relation for R_t according to Walker and Anderson (1995):

$$\frac{R_t}{Y} = \frac{7}{6} \ln \frac{E}{Y} + \frac{7}{6} \ln\left(\frac{\sqrt{3}}{2(1+\upsilon)}\right) \tag{5.25a}$$

which, for steel targets with $\nu = 0.29$, results in:

$$\frac{R_t}{Y} = 1.167 \ln \frac{E}{Y} - 0.465 \tag{5.25b}$$

The spherical expansion term for r_y/r, (5.24a), results in the following expressions for R_t/Y according to this model:

$$\frac{R_t}{Y} = \frac{7}{9} \ln \frac{E}{Y} + \frac{7}{9} \ln\left(\frac{1}{1+\upsilon}\right) \tag{5.26a}$$

which, for steel targets, gives:

$$\frac{R_t}{Y} = 0.778 \ln \frac{E}{Y} - 0.2 \tag{5.26b}$$

These expressions result in values of $R_t = 5.72$ GPa (cylindrical) and $R_t = 3.9$ GPa (spherical), for a steel target ($E = 200$ GPa) with strength of $Y = 1.0$ GPa. As was shown above, the numerical simulations of Rosenberg and Dekel (2000) resulted in an intermediate value of $R_t = 4.7$ GPa for this target. It is worth noting that the functional relations presented here, between R_t/Y and E/Y, are similar to the expression derived through the numerical simulations for the eroding rod, (5.16). They are also similar to the equations derived for the rigid rods, through the numerical simulations in Chap. 3 and the analytical models of Tate (1986) and Yarin et al. (1996).

5.3 Scaling Issues in Terminal Ballistics

Up to this point we did not encounter any scaling problems in terminal ballistics since all the penetration data, for both rigid and eroding penetrators, could be normalized through either P/D or P/L as a function of V_0. The scaling issue has an important practical aspect since most of the experimental work in terminal ballistics is done with scaled experiments using in-doors laboratory guns. Typical working scales are 1:3 and 1:4, and one should be aware of any non-scaling effect which may affect the conclusions from scaled experiments. This section deals with two closely related scaling issues which were highlighted by Magness and Farrand (1990) and Magness and Leonard (1993). In their work on depleted uranium (DU) and WHA rods, Magness and Farrand (1990) found that the penetration efficiency of DU rods is higher by an appreciable amount, although the densities and strengths of these rods are nearly the same. Their results for the corresponding penetrations in rolled homogenous armor (RHA) targets are shown in Fig. 5.26.

One can clearly see that the data points fall on two distinct lines, which are practically parallel within the ordnance range of impact velocities (around 1.5 km/s). This difference is a material scaling effect which must be due to some well defined difference between the properties of depleted uranium and the tungsten alloys. At higher impact velocities the data seem to merge into a single curve at about $V_0 = 2.0$ km/s. The different penetration efficiencies were attributed by Magness and Farrand (1990) to the "self sharpening" property of the DU rod, due the propensity of this material to fail by adiabatic shear. According to this interpretation, the nose shape of an eroding DU rod is more pointed than that of a WHA rod, since it fails at relatively lower strains by the adiabatic shear mode. The difference in nose shapes was evident by the flash shadowgraphs of residual rods in peroration experiments with finite thickness plates. Moreover, long rods made of uranium alloy which contains 6% niobium (U-6Nb) did not perform as well as the DU rods

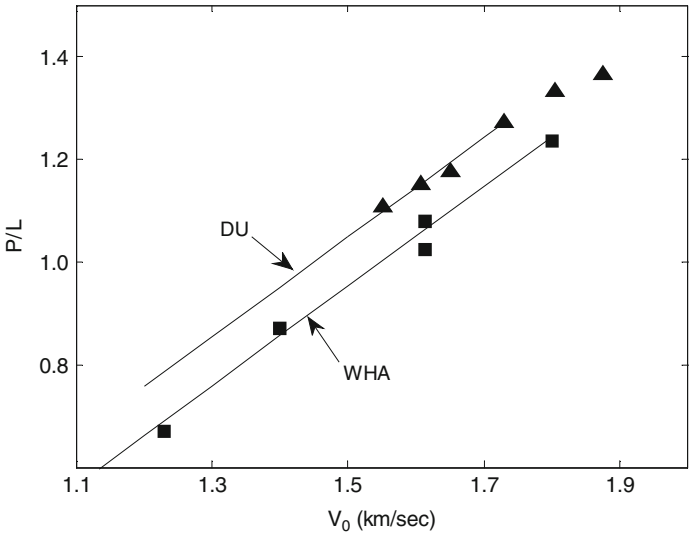

Fig. 5.26 The normalized penetration of DU and WHA rods into RHA targets

containing 0.75% titanium. The residual rods of the U-6Nb alloy showed no evidence for adiabatic shear failure, strongly enhancing the connection between the ballistic efficiency of long rods and their actual nose shape during penetration.

Magness and Leonard (1993) compared data from full scale experiments with data from 1:4 scaled experiments, for both DU and WHA rods impacting RHA targets. They found that for both materials the normalized penetrations of the full scale rods were substantially higher than those for the scaled rods, as seen in Fig. 5.27. This is a geometrical non-scaling effect which appears to be similar for both rod materials.

The geometrical non-scaling seems to be related to the different strain rates which the targets experience in these experiments. The strain rates in the smaller

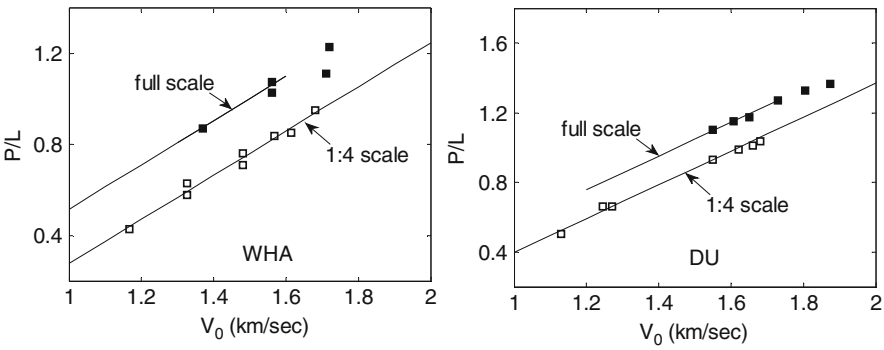

Fig. 5.27 Data for full scale and quarter scale experiments with DU and WHA rods

scale experiments are higher than those for the full scale experiments. This may lead to a higher strength of the smaller targets and, consequently, to lower penetration depths. In order to investigate this issue Anderson et al. (1993) performed a series of numerical simulations for WHA rods impacting armor steel targets at 1.5 km/s. The constitutive equation of their target included a strain rate term which allowed for a quantitative assessment of rate effects. A comparison of the penetration depths for the full scale and the 1:10 model in these simulations, resulted in a difference of only 5%, as far as the normalized penetration depths were concerned. This was also the magnitude of the strain rate effect for the residual velocities and rod lengths which perforated finite targets in these simulations. Thus, Anderson et al. (1993) concluded that the large scaling effects obtained for both tungsten alloy and depleted uranium, cannot be related with rate effects. Rather, they assumed that these scaling effects are due to the accumulated damage in the targets, which is a strong function of the absolute time rather than the scaled time.

These issues were further discussed by Rosenberg et al. (1997a) and Rosenberg and Dekel (1999a) and a possible mechanism was suggested for the two scaling issues described above. The basic idea in these works was that small changes in the nose shape of these rods can result in a significant difference in their penetration capability. This issue was demonstrated by numerical simulations for L/D = 6 rigid WHA rods with different nose shapes, impacting steel targets at 1.2 and 1.7 km/s. The results of these simulations are shown in Fig. 5.28, and it is clear that the nose shape of the rod dominates its penetration efficiency. Considering the large differences between the penetration depths of these rods, one may expect that even a small difference in the nose shape of the penetrating rod can lead to a significant change in its penetration depth.

Rosenberg et al. (1997a) performed several perforation experiments with rods of different materials, in order to examine their nose shapes. These L/D = 10 rods had the same dimensions and they were made of copper, WHA and the titanium alloy

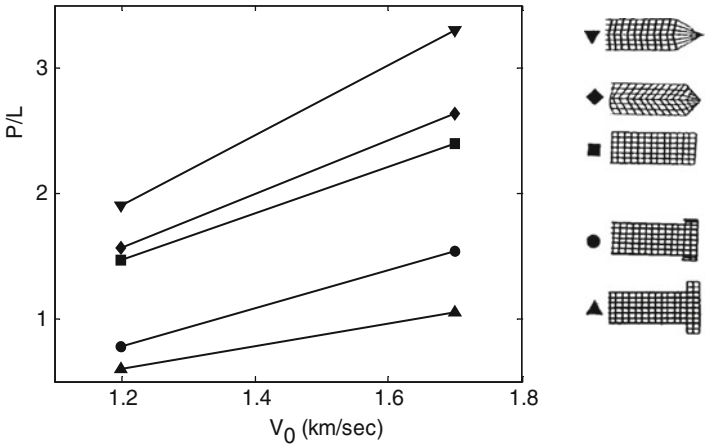

Fig. 5.28 The influence of nose shape on the penetration efficiency of rigid rods

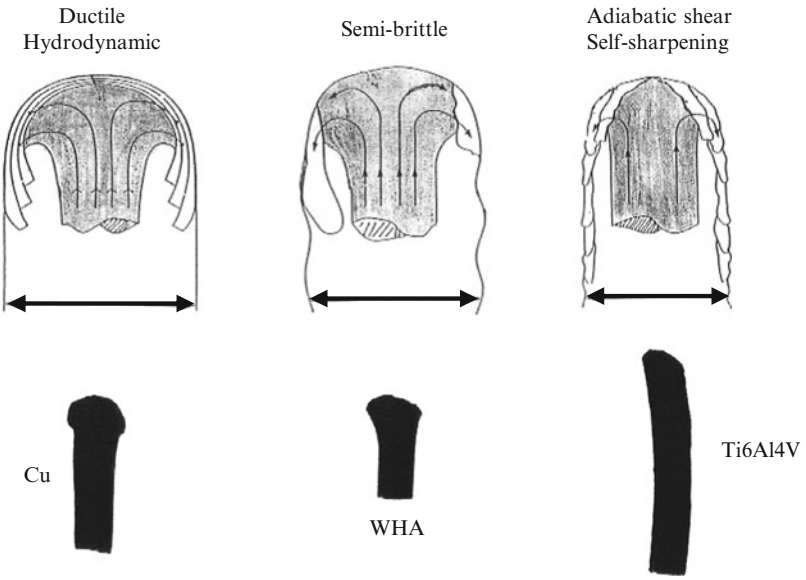

Fig. 5.29 Recovered residual projectiles of different materials

(Ti-6Al-4V), which is well-known for its tendency to fail by adiabatic shearing. This titanium alloy was used in order was to check the thesis that the failure by adiabatic shearing results in a much sharper nose shape. The recovered residuals of these rods, after perforating finite thickness plates, are shown in Fig. 5.29. One can clearly see the pointed shape of the titanium-alloy rod which failed by adiabatic shear, and the round nose of the copper rod which deformed in an ideal hydrodynamic manner. The nose shape of the tungsten alloy rod is intermediate between these two extremes. The figure also includes the schematic description with which Magness and Farrand (1990) describe the different failure mechanism in rods made of various materials. They refer to the three types of nose shapes as: early shear failure for DU-like rods which fail by adiabatic shearing, the late shear failure of the semi-brittle WHA rod, and the hydrodynamic mushrooming for very ductile materials, like copper. Figure 5.29 shows, schematically, that the different rods are expected to open craters of different diameters in a given target. Thus, a ductile rod should open the widest crater while the self-sharpening rod is expected to result in the narrowest crater, as shown by the arrows in the figure.

Rosenberg and Dekel (1999a) recovered the residuals of two L/D = 10 WHA rods with diameters of 8 and 16 mm, after perforating steel plates. As seen in Fig. 5.30 the nose shape of the larger rod is less "mushroomed," as compared with the small rod. The diameter of the smaller rod at its deformed head is 38% larger than the rod's diameter, while the larger rod's head is only 12% larger than its original diameter. Such a difference in the nose shape can account for the higher ballistic efficiency of the larger rod.

Fig. 5.30 The shape of the residual WHA rods of different size

These findings strongly support the thesis that both phenomena, the geometrical non-scaling and the superiority of DU over WHA rods, are related to the same effect, namely, the sharpening of the rod's nose. These rods experience considerable plastic strains around their nose area, much beyond their corresponding failure strains. Thus, the periphery of the nose is continuously failing by shear as they penetrate the target, leading to nose sharpening. The DU and the titanium alloy rods have lower values for their strain to failure, as compared with the WHA rod. Thus, they tend to form much sharper nose shapes resulting in the superiority of DU over WHA, as suggested by Magness and Farrand (1990). However, as shown in Fig. 5.30, the degree of sharpening is dependent on the rod's dimensions. Larger rods tend to sharpen more than smaller ones, leading to the geometrical non-scaling for both WHA and DU rods. On the other hand, copper is a very ductile material with a large strain to failure, resulting in the rounding of its nose shape. Thus, one may expect that the normalized penetrations for copper rods of different size will be independent on their dimensions. This was exactly the result obtained by Rosenberg et al. (1997a), for L/D = 10 copper rods which differed by a factor of two in their dimensions. Their normalized penetrations (P/L) for impact velocities in the range of 0.9–1.6 km/s were practically the same.

In order to explain these scaling issues Rosenberg et al. (1997a) considered the size of the plastic zone ahead of a crack (r_p), as defined by fracture mechanics. According to this theory, materials can behave as either ductile or brittle depending on their size, as compared with their corresponding r_p values. If the dimensions of a specimen are much smaller than its corresponding r_p value, it is expected to behave in a ductile manner under large deformations. On the other hand, specimens much larger than their corresponding r_p values will behave in a brittle manner. According to fracture mechanics, the size of the plastic zone ahead of a crack is given by:

$$r_p = \frac{1}{2\pi}\left(\frac{K_c}{\sigma_y}\right)^2 \tag{5.27}$$

where K_c is the fracture toughness of the material and σ_y is its yield strength. Using typical values of $K_c = 30$ and 150 MPa$\sqrt{m}$ for the fracture toughness of WHA and copper, respectively, with $\sigma_y = 1.2$ and 0.2 GPa for these materials, one obtained: $r_p = 0.4$ mm for the tungsten alloy and $r_p = 90$ mm for copper. The large value of

r_p for copper explain the fact that the copper rods behaved in a ductile manner at the two scales which were tested in the experiments described here. In contrast, WHA rods with a diameter of the order of a few millimeters are expected to behave in a quasi brittle mode, with different amounts of ductility for the two rod sizes, as described above. The issue of geometrical scaling in situations which involve both plastic flow and fracture received a lot of attention both experimentally and analytically. Such analyses have been summarized by Atkins (1988) and Ivanov (1994) for experimental configurations which are similar to the cases discussed here. In conclusion, the various experimental features of the non-scaling effects, which were highlighted by Magness and his colleagues, can be attributed to the strong dependence of the penetration depth on the exact shape of the rod's nose. This shape can be very different in rods of different size for quasi-brittle materials, which are characterized by plastic zones (r_p) of the order of the rod's diameter.

An important observation concerns the diminishing magnitude of the non-scaling effects, for both the superiority of DU rods and the geometric scaling, at impact velocities of about 2.0 km/s, as seen in Figs. 5.26 and 5.27. In order to explain this issue consider the numerical simulations of Rosenberg and Dekel (1998a) where a failure threshold was added to the constitutive equation of the rod. This is the maximum strain to failure (ε_f) which the material can sustain, and it is a common feature in the material models which are used in hydrocodes. We showed its influence on the perforation process of plates which are impacted by blunt-nosed projectiles, in Chap. 4. Once the strain in a computational element reaches this limiting value, its strength is reduced to zero in the following computational cycles. Rosenberg and Dekel (1998a) varied the value of ε_f for the WHA rods in their simulations, from $\varepsilon_f = 0.2$ to $\varepsilon_f = 5.0$, and obtained significant changes of their penetration depths into steel targets, as shown in Fig. 5.31. These simulations were performed for an L/D = 20 WHA rod impacting an RHA target at

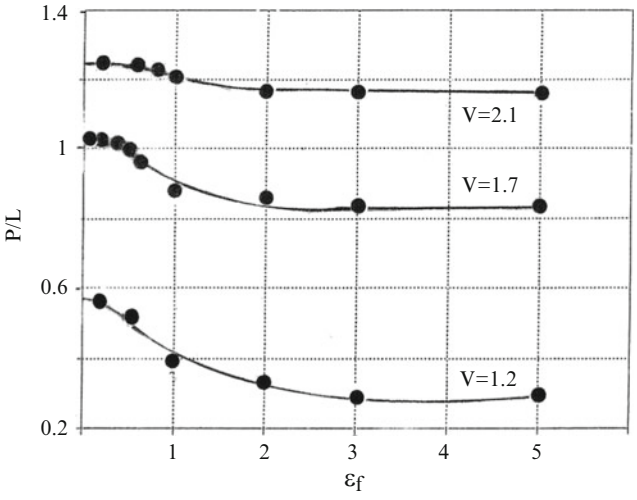

Fig. 5.31 Simulation results for the penetration depth dependence on the strain to failure (ε_f)

several velocities. As is clearly seen the sensitivity of the penetration depth to the value of ε_f is strongly dependent on impact velocity, and it decreases appreciably with increasing impact velocity.

The failure strain is a very effective parameter in numerical simulations, as far as its influence on the penetration depth is concerned, particularly in the range of $\varepsilon_f = 0.2–2.0$. With increasing ε_f the depth of penetration decreases by an amount which depends on impact velocity. This is also the trend seen in the data of Magness and Farrand (1990), as shown in Fig. 5.26. In fact, the data indicates that at a velocity of about 2.0 km/s, the penetration capabilities of DU and WHA penetrators should be practically the same. This experimental observation is accounted for by the simulation results shown in Fig. 5.31, since at an impact velocity of 2.1 km/s the penetration depths for different values of ε_f are very close to each other.

Anderson et al. (1999) showed that the addition of a failure strain parameter (ε_f) to the rod's constitutive relation, improves the agreement between simulation results and the experimental data for high strength steel rods, as far as their residual velocities and lengths are concerned. They assumed that the plastic work per unit volume, which can be absorbed by the projectile material before failure, is constant. Thus, the product $Y_p \cdot \varepsilon_f$, for the different steel rods which they used, was given a constant value of $1.5 GJ/mm^3$ in their simulations. This value corresponds to a failure strain of $\varepsilon_f = 1.0$ for a rod strength of $Y_p = 1.5$ GPa. Such a relation, between material strength and its maximum failure strain, is in accord with experimental results which show that stronger steels have lower elongations under tensile tests. In conclusion, the failure strain parameter (ε_f) in numerical simulations accounts for important features which have been observed experimentally. As suggested by Anderson et al. (1999), the values for ε_f in these simulations should be closely related to the real material property, namely, the maximum strain which it can tolerate under dynamic loadings.

The importance of attaching real material properties to the target and the projectile, in numerical simulations, was further demonstrated by Rosenberg and Dekel (1998a). In these simulations, for WHA rods impacting RHA targets, the strength of the rods (von Mises) was varied between 0.2 and 2.5 GPa. When the constitutive equations for the rods did not include a failure threshold, the simulations resulted in clear maxima in the penetration depth vs. rod strength curves, as shown in Fig. 5.32. The simulations for an impact velocity of 1.4 km/s showed that the deepest penetration was obtained for a rod strength of about 0.8 GPa. This unexpected result is due to two competing effects which are related to the rod strength. Clearly, a higher strength rod is expected to penetrate more into a given target. On the other hand, with increasing rod strength its deceleration during penetration is higher, which may lead to less penetration. Thus, for some rod strength the two contradicting effects balance each other, resulting in these maximal penetrations. When a thermal softening mechanism was added to the constitutive relation of the rod, these maxima disappeared, as is clearly seen in this figure. The addition of a failure mechanism to the target alone did not remove the maxima in the simulation results, and it only shifted the P/L curve to higher values, as expected, since the target became weaker with this addition.

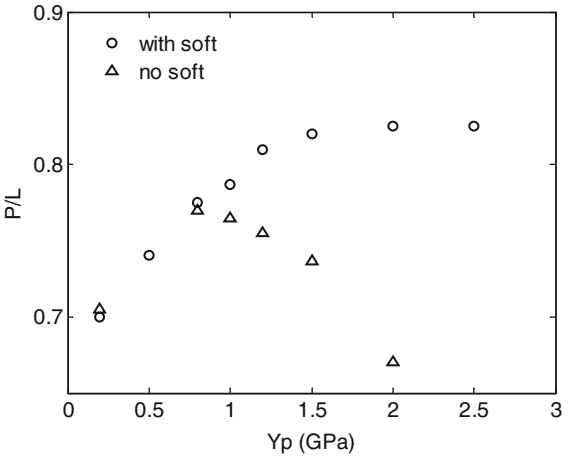

Fig. 5.32 Simulation results for the penetration efficiency of rods with and without their thermal softening

It is interesting to note that the simulations which included thermal softening of the rod show that its penetration efficiency (P/L) is very sensitive to its strength at low strength values. On the other hand, for rod strengths beyond about 1.2 GPa this sensitivity practically disappears. According to these simulations there is little gain by increasing the strength of the rod from 1.2 to 2.0 GPa. This saturation effect is probably the result of the compromise between the two opposing mechanisms which were discussed above, namely, the increased penetration capability of the rod and its higher deceleration with increasing strengths.

5.4 Penetration at the Hypervelocity Regime

The survey of Hermann and Jones (1961) includes many experimental results for the penetration depths of compact projectiles, impacting semi-infinite targets at the hypervelocity regime (2.0–10 km/s). These experiments were also reviewed by Hermann and Wilbeck (1987). The projectiles in these experiments were either spheres or short cylinders with an aspect ratio of about 1.0. The target craters at these high velocities had a hemispherical shape, which is the expected result when all the energy of the projectile is spent almost instantly upon impact. In fact, the crater in such an impact is formed by the radially expanding intense shock wave which is generated upon impact. In contrast, at low impact velocities the crater formed by a compact projectile is cylindrical, and its depth is either larger or smaller than its diameter, depending on the densities and strengths of the materials involved. With increasing impact velocities the craters become more hemispherical in shape. Several workers even used this observation in order to define the threshold impact velocity which marks the transition to the hypervelocity regime.

The ratio between the volume of these craters and the kinetic energy of the projectiles was found to be constant for impacts in the hypervelocity range. The value of this

ratio depends on the ultimate strength of the target material or, as summarized by Hermann and Wilbeck (1987), on its Brinell hardness (B_h), according to:

$$\frac{E_k}{Vol} = 27B_h \tag{5.28}$$

where the kinetic energy of the projectile (E_k) is given in joules, and the volume of the crater (Vol) in cm^3. It may be difficult to accept that such a relation can hold for velocities up to 10 km/s, where target strength is expected to play a minor role in the process. In fact, several works which were presented at the early hypervelocity symposia (from 1955 to 1965), tried to find the threshold velocity above which the strength of the target becomes negligible. In contrast with early conceptions, the resulting data showed that the effect of target strength is not diminishing even at impact velocities above 10 km/s. For example, Kineke and Richards (1963) extended the earlier work of Halperson and Atkins (1962), by impacting aluminum spheres at two types of aluminum targets. These were the 2014-T6 alloy, with strength of about 0.5 GPa, and the much softer 1100-F alloy with strength of about 0.05 GPa. Their results showed that the crater volumes in these materials had a constant ratio of about 0.37 even for impact velocities as high as 9.7 km/s. These 4.76 mm aluminum spheres resulted in a constant difference of about one projectile diameter, between the crater depths into the two aluminum targets, for impact velocities in the whole range of 3–9 km/s, as shown in Fig. 5.33. Thus, even at these extremely high velocities the strength of target plays a dominant role, as far as the crater dimensions are concerned.

The data for metallic spheres impacting semi-infinite targets, as summarized in Hermann and Jones (1961) and in Belyakov et al. (1964), show that the normalizing parameter which controls the penetration depths of these spheres, is the term $\rho_p V_0^2/B_h$, where B_h is the hardness of the target. This parameter is often termed the Best number, after the nineteenth century ballistician who investigated the

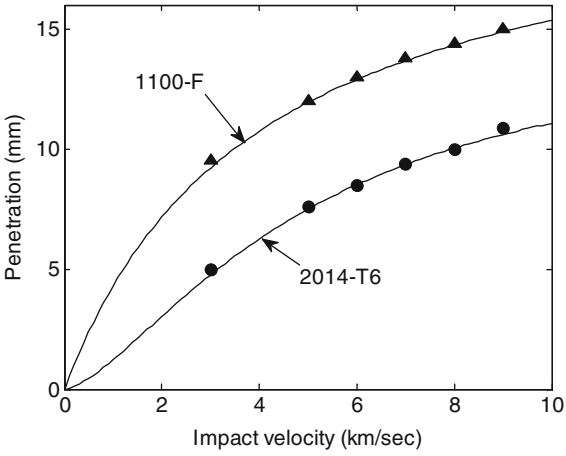

Fig. 5.33 Experimental results for aluminum spheres impacting two different aluminum targets

relation between the kinetic energy of projectiles and the volume of the craters which they produced in clay targets. Hermann and Jones (1961) present semi-empirical models for the penetration depths of high velocity spheres, which use the Best number as one of the non-dimensional parameters, and the projectile/target density ratio as a second parameter. Note that the empirical formula of Christman and Gehring (1966), (5.9b), for the secondary penetration of long rods at high impact velocities, also includes the Best number and the rod/target density ratio. According to Christman and Gehring (1966), the secondary penetration is due to the last segment of the rod, with L/D = 1. Thus, it is not surprising that its penetration depth is dependent on the Best number, as is the case with the high velocity impacts of compact projectiles.

In order to demonstrate the validity of this normalization scheme consider the data for the two aluminum alloys, 1100-F and 2014-T6, as shown in Fig. 5.33. The normalized presentation of the data with $B_h = 26$ and 137 BHN for these materials, is shown in Fig. 5.34, and one can clearly see that this is a viable normalization scheme. Belyakov et al. (1964) showed that the P/D data for symmetrical impacts, with spheres of iron, copper, aluminum and lead impacting targets of the same materials, fall on a single curve which extends to values of more than 400 for the Best number ($\rho_p V_0^2/B_h$).

Assuming a constant ratio between kinetic energy and crater volume, as given by (5.28), it is quite straightforward to derive the following relation for the normalized penetrations (P/D) of spherical craters:

$$\frac{P}{D} = k\left(\rho_p V_0^2\right)^{\frac{1}{3}} \tag{5.29}$$

where the constant k depends on the specific properties of projectile/target combination. One should note that the dependence of P on $V_0^{2/3}$ results in a curve which is very close to the curve of P as a function of $\ln(V_0)$. Thus, it is not surprising that many workers used this logarithmic relation for $P = P(V_0)$, in their semi-empirical

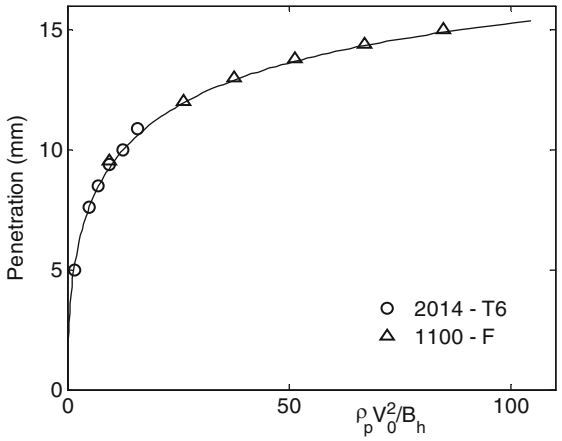

Fig. 5.34 The penetration depths of aluminum spheres as a function of the Best number for two aluminum targets

models for hypervelocity impacts (see Hermann and Jones (1961)). The particular dependence of P/D on ρ_p and V_0, as given by (5.29), has a physically-based justification through dimensional analyses which are based on the point source approximation, as was shown by Holsapple (1987). The basic assumption here is that the energy of the projectile which is delivered to the target is the same as that of a point source acting on its surface at the moment of impact. The point-source approach has been used successfully (since the 1940s) for gases and fluids. However, its application for solids was possible only after proving that a single scalar measure of the form $D(V_0)^{\delta 1}(\rho)^{\delta 2}$, is the general measure of all point source solutions. Here D and ρ are the projectile's diameter and density, respectively, and V_0 is its impact velocity. The exponents δ_1 and δ_2 determine the resulting scaling rules according to the initial assumptions of the theory. Holsapple (1987) showed that energy scaling leads to the result given by the above equation where $\delta_1 = 2/3$ and $\delta_2 = 1/3$. The interested reader is referred to the articles in Kinslow (1970) for more information concerning the theory of scaling rules and point source analyses, as well as numerical and experimental details concerning hypervelocity impacts.

There are several differences between the shapes of the craters produced by compact projectiles and long rods for impacts at the hypervelocity range. For compact projectiles these craters are roughly spherical, while long rods produce narrow and deep craters. Another difference is related to the limiting penetration depths at very high velocities. The penetration depths of long rods asymptotically approach the hydrodynamic limit of $(\rho_p/\rho_t)^{0.5}$, or to a somewhat higher value when strength effects are important. On the other hand, we have seen that for spherical projectiles the crater depth is practically unbounded, as it grows according to $V_0^{2/3}$. This is also the case for cylindrical projectiles with aspect ratios of about 1.0. It is interesting to find the threshold value of L/D which narks the transition from compact projectiles to long rods. In order to explore this issue, at least qualitatively, consider the simulation results of Rosenberg and Dekel (2001b) as shown in Fig. 5.35. These simulations, were performed for zero strength steel projectiles with L/D = 3–30, impacting 0.4 GPa aluminum targets at velocities up to 7.0 km/s. Note that the normalized penetration depths (P/L) are multiplied by $(\rho_t/\rho_p)^{0.5}$, in order to set the value of the asymptotic limit at 1.0. One can clearly see that the shortest projectiles, with L/D = 3 and 5, behave like the spherical projectiles shown above, resulting in a continued increase of penetration depths with impact velocity. On the other hand the L/D = 20 and 30 rods can be considered as long rods, since their penetration depths tend asymptotically to the hydrodynamic limit. The L/D = 10 rod shows an intermediate behavior and one may conclude that the threshold value of L/D, which marks the transition from a compact projectile to a long rod, is somewhere between L/D = 5 and L/D = 10.

In order to support this conclusion, consider the experimental results for the penetration depths of L/D = 5 tantalum and L/D = 10 WHA rods impacting 6061-T6 aluminum targets, as shown in Fig. 5.36. The data for the tantalum rods is taken from Bless et al. (1987). The experimental results of Hohler and Stilp for the WHA rods are tabulated in the data base of Anderson et al. (1992). Both sets of

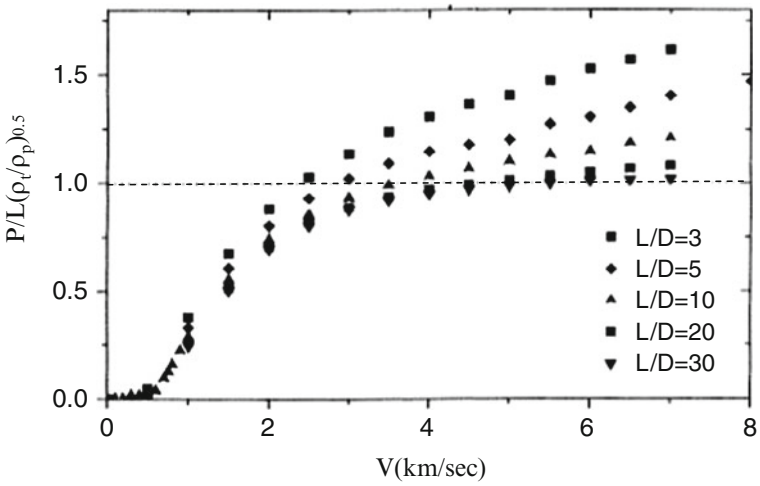

Fig. 5.35 Simulation results for zero strength steel projectiles impacting 0.4 GPa aluminum target

experiments cover a large range of impact velocities, and the normalized penetration (P/L) are multiplied by their corresponding density factors $(\rho_t/\rho_p)^{0.5}$ as in Fig. 5.35. It is clearly seen that the penetration depths of the L/D = 5 tantalum rods increase with impact velocity, while those for the L/D = 10 WHA rods reach an asymptotic value, in accord with the penetration theory for long rods. These

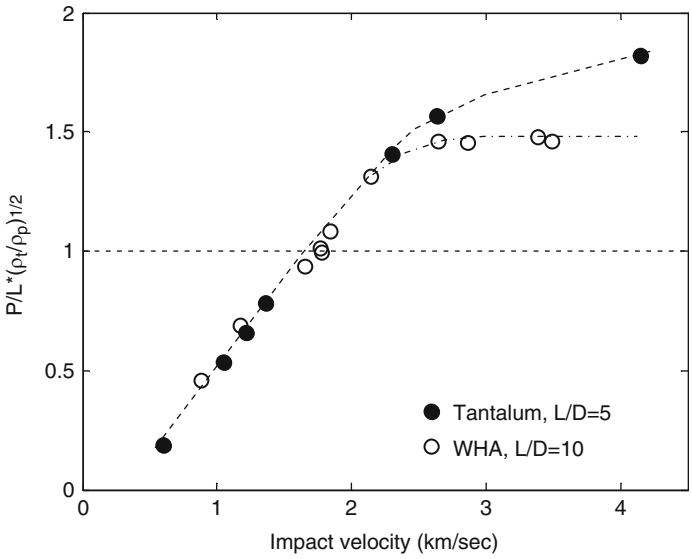

Fig. 5.36 Normalized penetrations in aluminum targets of L/D = 5 tantalum rods, and L/D = 10 WHA rods

different behaviors enhance the above statement that, as far as their aspect ratio is concerned, the division between short and long rods is somewhere between L/D = 5 and L/D = 10.

The normalized penetrations of the L/D = 10 WHA rods reach an asymptotic value which is considerably higher than the predicted value from the hydrodynamic penetration model, due to the high strength ratio for this rod/target pair, as was observed for other rod/target combinations. The normalized data for both sets of experiments, within the ordnance velocity range, fall on the same line although there is a large difference between their corresponding L/D values. This is due to several competing effects which are influencing the penetration process in different ways. On the one hand, the L/D effect should have resulted in higher normalized penetrations for the shorter tantalum rods. On the other hand, these rods have a much lower strength as compared with the strength of the WHA rods, resulting in their lower penetrations. In addition, tantalum is a ductile metal while the tungsten alloy has quasi-brittle properties. This difference can add to the deeper penetrations of the WHA rods, due to the material non-scaling effect which was discussed above. The three effects are influencing the penetration process of long rods especially at impact velocities in the ordnance range, and it seem that they cancel each other for the two sets of rod/target combinations.

5.5 Plate Perforation by Eroding Rods

The perforation of plates by eroding rods is by far the most important issue for the armor designer since this is the case encountered in most practical situations. At the same time, this is also the most complicated interaction between projectiles and targets, as it involves many issues which are difficult to describe analytically. These issues include the non-steady nature of the penetration and erosion processes, the reduction of the resisting stress by the target's back surface, and the various failure mechanisms which take place in the plate even before the projectile reaches its back surface. These complications are the main reason for the lack of simple analytical models which deal with ballistic limit velocity, residual velocity, and residual mass of the eroding penetrator. Several analytical models, such as those of Ravid and Bodner (1983) and Walker (1999), follow the penetration of eroding rods into finite plates, and account for the bulging of their back surface. The Ravid–Bodner model is based on plasticity theory while Walker's model considers the velocity field ahead of the penetrator and the influence of the target's back surface on this field. Chocron et al. (2003) combined these two perforation/bulging models and applied them for a case where an eroding rod is perforating a number of separated steel plate. However, all of these models are far from simple and they rely heavily on numerical simulations. The complexity of this interaction is demonstrated in Fig. 5.37, which shows the penetration crater in a steel plate impacted by an L/D = 10 steel rod at 2.03 km/s, from Stilp and Hohler (1990). The thin walled cylinder of the inverted rod is clearly seen in the figure as it lines up the crater wall.

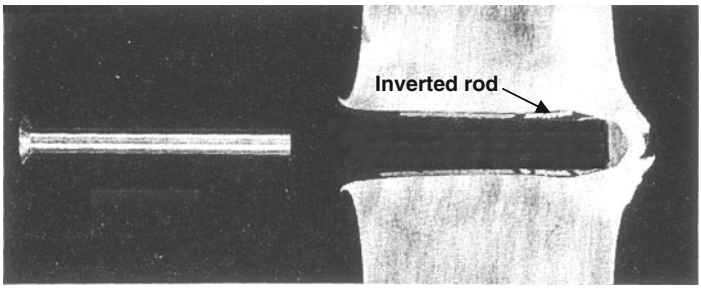

Fig. 5.37 The crater and the bulge in a steel target impacted by a steel rod

Note the bulging of the plate and the evidence for its tensile failure at the back surface. Also, the increased diameter of the crater near the back surface is an indication for the lower resistance of the target at the later stage of penetration.

Much of the work on finite plates has been aimed at determining the minimal impact velocity (V_{BL}) which is needed to perforate a given target of thickness (H). The data can be also interpreted as giving the minimal plate thickness (H_{BL}) which is needed to stop the rod at a given impact velocity. As expected, the limiting thicknesses of these plates are higher than the corresponding penetration depths into semi-infinite targets. The data compiled by Anderson et al. (1992) contains many results of such $H_{BL}(V_0)$ relations for various rods and plates. Figure 5.38 shows the data for $H_{BL}(V_0)$, by Hohler and Stilp, for L/D = 10 steel rods impacting steel plates with hardness of 180 Brinell. The normalized penetration depths (P/L), into semi-infinite steel targets of the same hardness, are

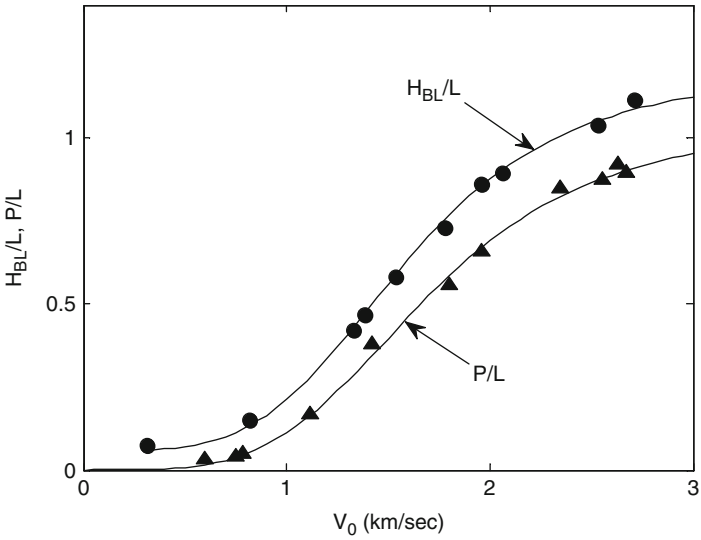

Fig. 5.38 The data for L/D = 10 steel rods impacting semi-infinite and finite steel targets

also shown in the figure. One can clearly see that the difference between the two sets of data is quite appreciable even at high impact velocities. In fact, the values of the ratio P/H_{BL} increase from 0.63, at an impact velocity of 1.0 km/s, to about 0.85 for a velocity of 3.0 km/s. Translating these differences to units of rod diameters, we find that H_{BL} is larger than P by one to two rod diameters in this velocity range. Similar results were obtained by Tate et al. (1978) for WHA rods impacting RHA targets. Thus, one can use these observations as a "rule of thumb," in order to asses H_{BL} values from the corresponding penetration depths into semi-infinite targets.

Hohler and Stilp (1975) performed a set of experiments with L/D = 10 steel rods impacting targets which consisted of two equal thickness steel plates separated by some distance. The shape of the craters in one of these experiments, from Stilp and Hohler (1995), are shown in Fig. 5.39. The shape of the residual rod as it emerges from the first plate is clearly seen in the figure. The impact velocity of the rod in this experiment was 2.63 km/s, and each plate was 25.2 mm thick.

The data from these experiments of Hohler and Stilp (1975) is plotted in Fig. 5.40. in terms of the combined thickness of the two plates (T_{12}) which is needed to stop these projectiles, as a function of their impact velocity. The curves $H_{BL}(V_0)$ and $P/L(V_0)$ from Fig. 5.38 are also shown in Fig. 5.40. At low impact velocities ($V_0 < 1.2$ km/s) the data for the double plate configuration (T_{12}/L) follows the curve for the finite-thickness plate (H_{BL}/L), and it shifts towards the curve for the semi-infinite target (P/L) at higher impact velocities.

The residual velocities of long eroding rods have been summarized by Grabarek (1971) for a large number of experiments with armor steel plates. He suggested the following empirical relation for the residual velocities:

$$\frac{V_r}{V_{bl}} = \frac{1.1y^2 + 0.8y + 2y^{0.5}}{1+y};\ y = \frac{V_0}{V_{bl}} - 1 \tag{5.30}$$

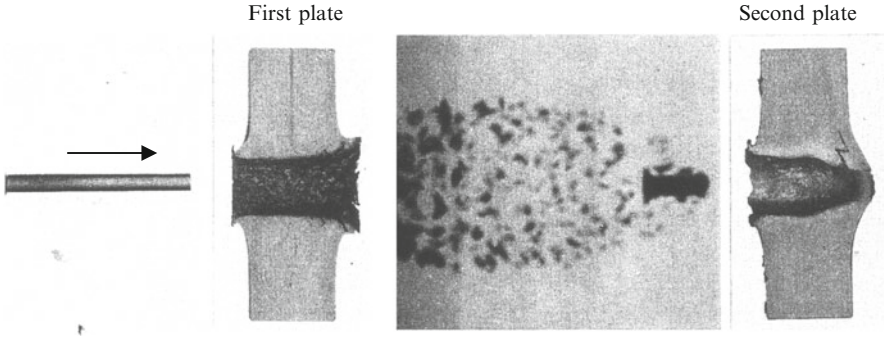

Fig. 5.39 The resulting craters and the exiting rod in an experiment with a double-plate target

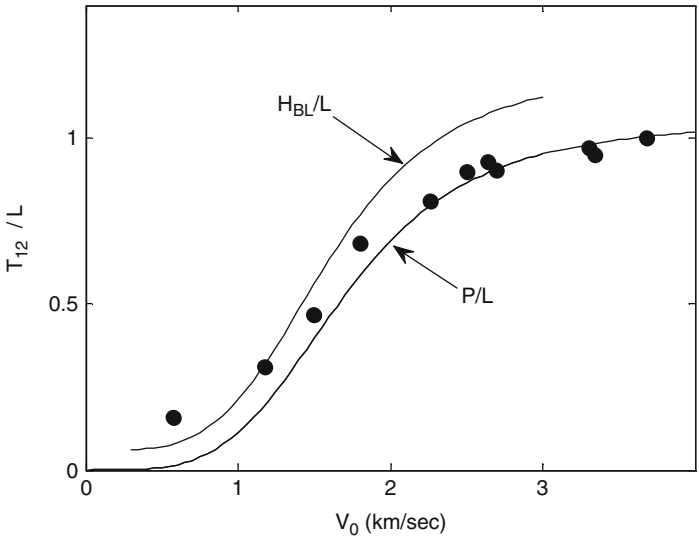

Fig. 5.40 The data for a double plate configuration (*circles*) compared with the curves for finite thickness and semi-infinite targets

This relation was found to hold for both normal and oblique impacts and it represents the data for impact velocities in the range $1.0 < V_0/V_{bl} < 2.5$. For impact velocities above $2.5V_{bl}$ the residual velocities are practically the same as the impact velocities. This result can be understood by noting that the deceleration of long eroding rods is relatively small for most of their penetration process, both in finite thickness and in semi-infinite targets. Only when the rod length is of the order of its diameter, the deceleration becomes appreciable, as was discussed above. Thus, when the impact velocity is much higher than the corresponding ballistic limit, the rod "spends" a relatively short time in the target with a negligible reduction of its velocity. This observation is clearly evident by the experimental results of Hohler et al. (1978) for L/D = 10 WHA rods, impacting steel plates of different thickness at 1.52 km/s. Figure 5.41 shows the results for both normal impacts and for an obliquity of $\beta = 60^o$, where β is the angle between the rod's axis and the normal to the plate. For a plate of thickness H which is inclined at an angle β, the relevant plate dimension is the line-of-sight thickness given by $H/\cos\beta$. Thus, the normalized thicknesses of these plates are $H/(L\cos\beta)$, as shown in the figure. The two curves enhance the features discussed above concerning the small reduction of the residual velocities, for targets which are much thinner than H_{BL}, and the large drop in V_r when the target thickness approaches H_{BL}. The values of H_{BL} are shown by the small arrows on the ordinate axis of Fig. 5.41. The value of H_{BL} for the inclined target is somewhat higher than that of the normal target, indicating that plate inclination improves its ballistic performance.

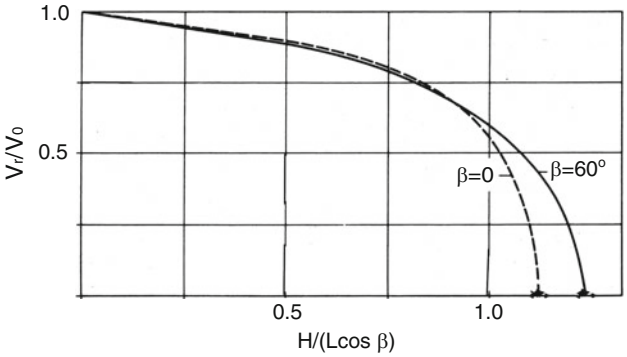

Fig. 5.41 The normalized residual velocity as a function of plate thickness for normal and oblique impacts

Anderson et al. (1996b) used Grabarek's functional dependence, (5.30), for their data on steel rods with different strengths perforating armor plates of two hardness values. Their best fit curve resulted in the following values for the numerical coefficients in (5.30): 0.9, 1.3 and 1.6 for the y^2, y and $y^{0.5}$ terms, respectively. These values are different than those given by Grabarek's empirical equation: 1.1, 0.8 and 2.0, respectively. It is clear that such empirical fits, which have no physical basis, are of little use if they do not account for a variety of experiments with the same set of empirical constants.

A different relation for the residual velocities of eroding long rods has been suggested by Lambert (1978). His semi-empirical approach is based on some analytical considerations, as described by Zukas (1982). The relation suggested by Lambert (1978), for the residual velocity of an eroding rod, is:

$$\frac{V_r}{V_{bl}} = k_0 \cdot \left[\left(\frac{V_0}{V_{bl}} \right)^m - 1 \right]^{1/m} \tag{5.31}$$

where k_0 and m are empirical constants which have to be determined for each projectile-target combination. This equation, with $k_0 = 1$ and $m = 2.5$, accounts for the data of Anderson et al. (1996b) very well, as shown in Fig. 5.42.

Burkins et al. (1996) measured the residual velocities of L/D = 10 WHA and DU rods perforating Ti/6Al/4V plates, and found that (5.31) with $k_0 = 1$ and $m = 2.6$, accounts for their data quite well. Considering the two empirical approaches which were discussed here, the Lambert relation, (5.31), is preferable to Grabarek's relation, (5.30), since it includes less parameters and it is based on some physical description of the process.

In order to further investigate this issue we performed a set of numerical simulations for L/D = 10, D = 6 mm steel rod impacting a 35 mm thick steel target. The strengths of the rod and the target in these simulations were 1.0 GPa and 0.8 GPa, respectively. Impact velocities ranged between 1.5 and 2.2 km/s and the resulting normalized values for V_r/V_{bl} as a function of V_0/V_{bl}, are shown in

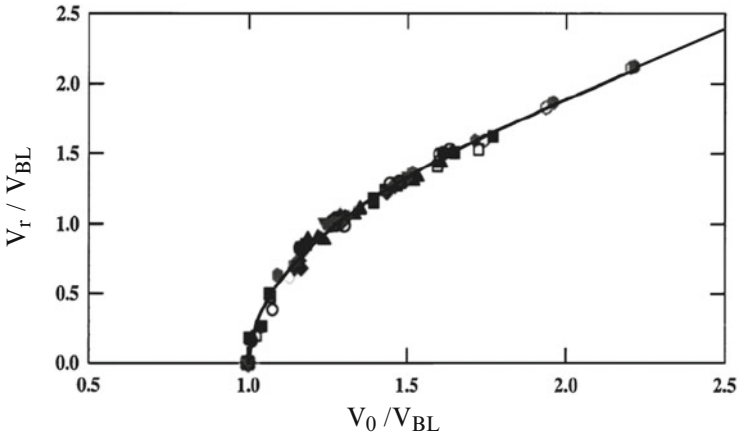

Fig. 5.42 Residual velocities for steel rods perforating RHA targets, and their fit to Lambert's equation with $k_0 = 1$ and $m = 2.5$

Fig. 5.43. The value for V_{bl} from these simulations was 1.55 km/s. The curve shown in Fig. 5.43 follows Lambert's relation, (5.31), with $k_0 = 1$ and $m = 2.5$, and it seems to follow the simulation results quite well. This agreement enhances the claim that the Lambert relation captures the essential features of the perforation process, as far as residual velocities are concerned. The parameter m in this relation determines the steepness of the curve at low values of V_0/V_{bl}. On the other hand, the high values of V_r/V_{bl} are less sensitive to this parameter. In order to demonstrate these points, consider the values of V_r/V_{bl} for $V_0/V_{bl} = 1.1$ from (5.31). The resulting values are $V_r/V_{bl} = 0.458$ and 0.69 for the $m = 2$ and $m = 3$, respectively. These values differ by about 50%, demonstrating the strong dependence of

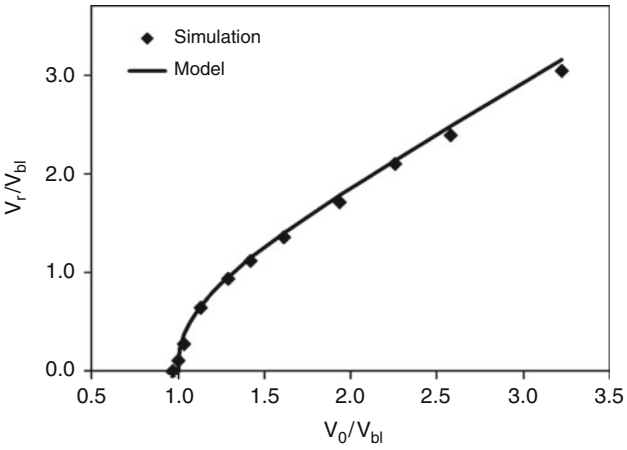

Fig. 5.43 The normalized residual velocities from numerical simulations

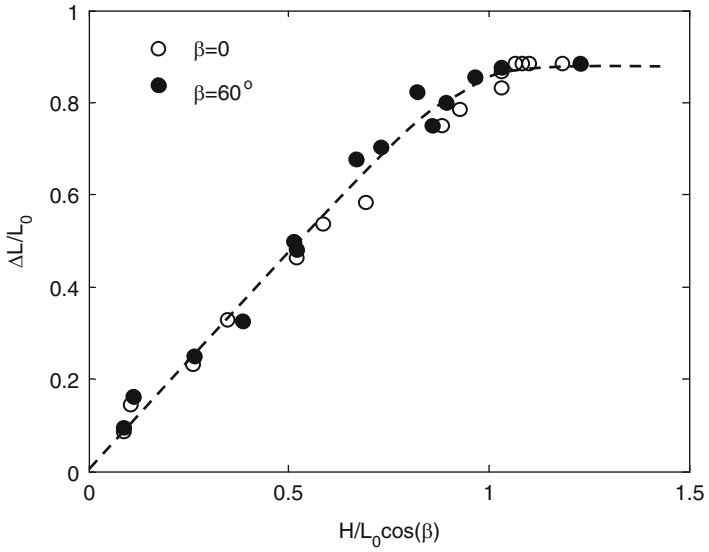

Fig. 5.44 The length reduction of long rods as a function of plate thickness

V_r/V_{bl} on the parameter m for impact velocities which are close to V_{bl}. On the other hand, for $V_0/V_{bl} = 3$ the Lambert relation results in $V_r/V_{bl} = 2.83$ and 2.96 for $m = 2$ and $m = 3$, respectively, which differ by only 4% from each other. It is also clear that the Lambert relation results in the fast approach of V_r to V_0 at impact velocities of $V_0 = 2.5V_{bl}$, which was observed by Grabarek (1971).

The residual length of an eroding long rod decreases proportionally with plate thickness, as expected. The experimental results of Hohler et al. (1978) for $L/D = 10$ WHA rods perforating armor steel plates at different impact velocities, are shown in Fig. 5.44 for both normal and oblique impacts. As discussed above, the normalized thickness of an inclined plate is given by $H/L_0\cos\beta$. Impact velocities in these experiments were about 1.52 km/s and the data from both sets of experiments, for the relative change in rod length ($\Delta L/L_0$), fall on a single curve. Note that the asymptotic value of the residual rod length in these experiments, is about $L_r = 0.1L_0$ (corresponding to $\Delta L/L_0 = 0.9$). This residual length amounts to one rod diameter for these $L/D = 10$ rods, in agreement with the results discussed above for the residual rod lengths at the ordnance range of impact velocities.

Part III: Defeat Mechanisms

The main goal of the armor designer is to prevent a given threat from penetrating the protected object with the lightest and simplest structure. This goal can be achieved by either optimizing the material properties of the protected object or by adding another structure, the so called add-on armor, in front of the object. In order to construct efficient add-on armors, the designer has to optimize some well-defined defeat mechanisms which will reduce the lethality of the impacting threat. This part of the book describes several defeat mechanisms of the three most common threats encountered in the battlefield. These threats are (1) the armor piercing (AP) projectiles with hard steel or tungsten-carbide cores, (2) long rod penetrators made of high-density materials (tungsten alloys or depleted uranium),and (3) shaped charge jets.

In order to reduce the lethality of these threats, the armor designer should maximize one, or more, of their defeat mechanisms, which are based on their deceleration, erosion, fragmentation, and deflection. These defeat mechanisms operate in various armor designs which are classified according to the following families: passive, reactive and active armors. Passive armors use high strength materials with special geometrical designs to defeat the threat. Reactive and active armors propel metallic plates towards the threat either upon impact (with reactive armor), or at some distance away from the vehicle (with active armor). A close examination of the main defeat mechanisms of these armor designs shows that they are based on two simple principles: (1) the use of high strength materials, preferably with low densities, in order to enhance their resistance to penetration, and (2) the use of asymmetry in of the interaction between the threat and the armor, through high obliquities. An informative account for the application of these defeat mechanisms in various combat vehicles is given by Ogorkiewicz (1995).

The present chapter is focused on defeat mechanisms at normal impact which are based on target strength. Oblique impacts and their inherent asymmetry will be discussed in the next chapter. Some of the better armor designs combine the two ingredients, the high strength of the target and its obliquity, in order to maximize the protective capability, as we shall see in Chap. 7.

Chapter 6
Defeat by High Strength Targets

6.1 Definitions

The protective capability of a structure against a given threat can be evaluated by several measures. One of them is the ballistic limit velocity (V_{bl}) of the specific armor/threat combination. Obviously, the aim of the armor designer is to increase the value of V_{bl} without increasing the weight of the structure. The relevant measure of the armor weight is its areal density (AD), given in units of kg/m^2, which is simply the density of the protective structure multiplied by its thickness. The ballistic efficiency of a given structure is defined by its areal density, as compared with that of a reference target, which is needed to defeat a given threat. Frank (1981) suggested several measures for the ballistic efficiency of improved structures, through their mass (E_m) and space (E_s) efficiency, according to:

$$E_m = \frac{(AD)_r}{(AD)_s} \tag{6.1a}$$

$$E_s = \frac{P_r}{P_s} \tag{6.1b}$$

where the indices (r) and (s) denote the reference target and the improved structure, respectively, and P is the minimal thickness of the target which is needed to defeat the threat. It is clear that the ballistic efficiency should be higher than 1.0 and the task of the armor designer is to increase these efficiencies to higher values. As mentioned above, one of the more practical ways to defeat a given threat is by adding a relatively lightweight structure in front of the protected object, as shown in Fig. 6.1. This add-on armor structure can significantly reduce the penetration capability of a given threat through an effective defeat mechanism, as will be demonstrated in this part of the book.

Z. Rosenberg and E. Dekel, *Terminal Ballistics*,
DOI 10.1007/978-3-642-25305-8_6,

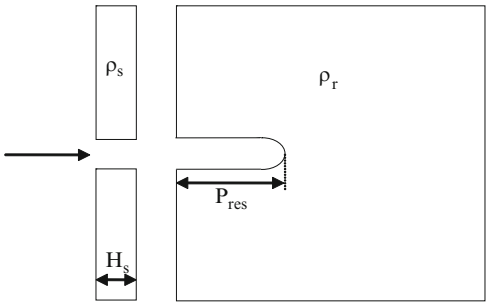

Fig. 6.1 The add-on armor and the relevant parameters for the differential ballistic efficiency

The most popular measure of the ballistic efficiency for add-on armors is the differential efficiency factor (DEF), as defined by Yaziv et al. (1986):

$$DEF = \frac{\rho_r \cdot (P_r - P_{res})}{\rho_s H_s} \tag{6.2}$$

where $\rho_s H_s$ is the areal density of the add-on armor. P_{res} and P_r are the penetration depths into the main structure, of density ρ_r, with and without the add-on armor, respectively.

6.2 Metallic Targets

The strength of the target is the most important physical parameter in determining the penetration depth of both rigid and eroding penetrators, as was demonstrated in Part II. The penetration efficiency (P/L) of rigid penetrators decreases with increasing values of the target's resistance to penetration (R_t), which depends on its compressive strength. In contrast, the density of the target was shown to play no role for impact velocities in the ordnance range (below the cavitation thresholds). This independence is demonstrated in Fig. 6.2, which summarizes the penetration depths of 0.5″APM2 projectiles impacting various targets at muzzle velocity. It is clear that their penetration depths depend on the strength of the target and not on its density.

As far as their areal densities are concerned, the aluminum targets are more efficient than the steel targets against these projectiles. This is obvious by comparing the corresponding products of density and penetration depth for the different targets. For example, the areal density of the 7075-T6 aluminum alloy is lower by a factor of 1.6 than that of the RHA steel. Thus, as far as these projectiles are concerned, it is much better to build the main body of the vehicle with high strength aluminum alloys. This was one of the considerations in using the 5083 aluminum alloy for some lightweight armored personnel carriers (APC's) with this aluminum alloy, instead of the traditional armor steel.

Similar conclusions hold for the penetration depths of shaped charge jets into monolithic armors, from the hydrodynamic theory for penetration. The theory predicts that the penetration depth of a jet is given by $L(\rho_j/\rho_t)^{0.5}$, where L is the jet length. Multiplying this expression by the target's density results in an areal

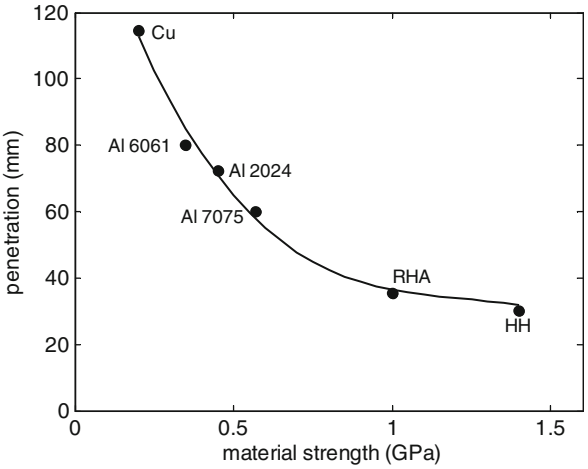

Fig. 6.2 Penetration depths of 0.5″APM2 projectiles into various targets

density of AD = $L(\rho_j \cdot \rho_t)^{0.5}$ which is needed to completely erode this jet. Thus, a low density target should defeat a given jet with a lower areal density, resulting in a higher ballistic efficiency. The effectiveness of a low-density target, as compared with a reference target, should be equal to the inverse square root of their corresponding densities. For example, an aluminum target should be more efficient than a steel target by a factor of $(7.85/2.75)^{0.5} = 1.69$. The addition of strength to the target improves its ballistic efficiency as discussed in Chap. 5, but it does not change the general trend, and for equal strengths the lower density target should be more efficient against shaped charge jets.

The same conclusion holds for eroding long rods although it is less obvious in this case. In order to demonstrate this fact, consider simulation results for eroding rods impacting two different targets which have the same strength. Figure 6.3 presents the

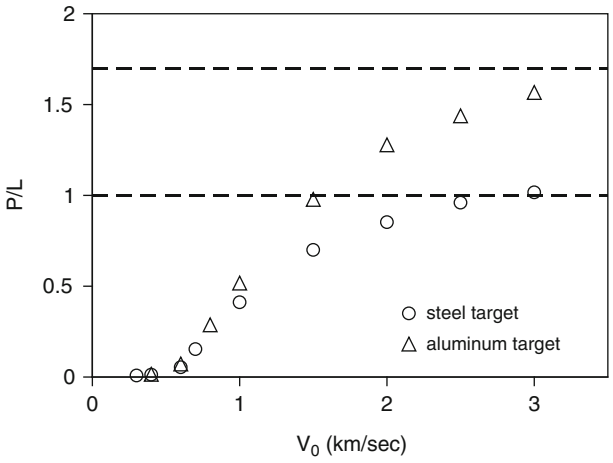

Fig. 6.3 Simulation results for zero strength steel rod impacting 0.4 GPa aluminum and steel targets

penetration depths of L/D = 10 zero strength steel rods impacting aluminum and steel targets having strength of 0.4 GPa.

The normalized penetrations asymptotically approach their corresponding hydrodynamic limits of $(\rho_p/\rho_t)^{0.5}$ at high impact velocities (marked by the dashed lines in the figure). These are also the penetration depths for shaped charge jets as discussed above. Thus, the lower density target is more efficient, by the same factor, against high velocity eroding rods. These simulation resulted in the same value of the critical velocity ($V_c = 0.55$ km/s) for both targets, in agreement with the AT model through (5.11). The most important result of the simulations is that at impact velocities which are slightly higher than the critical velocity, the penetration depths into the two targets are practically the same. Thus, the ballistic efficiency of the lower density target, as determined by its areal density, is higher by a factor which is equal to their inverse density ratio. Similar simulations for rods with finite strength show the same trend. In conclusion, for equal strength targets the ratio of their corresponding areal densities, which are needed to defeat an eroding rod, should change gradually from ρ_1/ρ_2 at low impact velocities to a value of $(\rho_1/\rho_2)^{0.5}$ for high velocities.

This is exactly the trend observed in the data of Gooch et al. (1995), who shot long rods of WHA and DU at semi-infinite steel (RHA) and Ti/6Al/4V targets. Their results for L/D = 10 WHA rods are given in Fig. 6.4 in terms of the areal densities, as calculated from the corresponding depths of penetration. Note that the areal density of the titanium-alloy targets is lower for the whole range of impact velocities. Moreover, their areal density ratio changes from a value of 1.75, at an impact velocity of 1.0 km/s, to a value of 1.45 at an impact velocity of 2.0 km/s. The steel/titanium density ratio is 1.76, and its square root is 1.33, which are very close to the experimental areal density ratios.

Consider now the perforation process of finite thickness plates by either rigid or eroding projectiles. We have seen in Chap. 4 that the resistance to penetration of

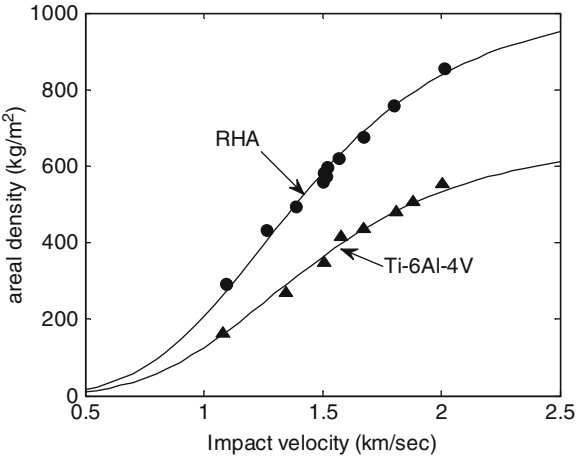

Fig. 6.4 Areal densities as calculated from the penetration depths of L/D = 10 WHA rods impacting RHA and Ti–6Al–4V targets

these plates is determined by their effective strength (σ_r), which was shown to be related to their compressive strength. Moreover, the density of the target enters into the expressions for their ballistic limit velocity, only through the mass of the ejected plugs. Thus, in order to improve the ballistic efficiency of add-on structures, which are based on relatively thin plates, one should use high strength materials having low densities. This conclusion prompted a large amount of research on low density materials of high strength, such as the strong aluminum and titanium alloys mentioned above. These materials are said to have a high specific strength, which is defined by their strength/density ratio.

Another alloy which has been recently considered for armor applications is the magnesium alloy AZ31B, which contains about 3% aluminum and 1% zinc as the main additive. This material has a very low density (1.75 g/cc) and its ultimate tensile strength is about 0.26 GPa. Its specific strength is close to that of the aluminum alloy 5083-H131, which is used for the construction of APC's. The work of Jones et al. (2007) showed that the ballistic performance of the magnesium alloy against 0.3″AP is comparable with that of the 5083 aluminum alloy, and even with that of armor steel plates. Van-Wegen and Carton (2008) tested several magnesium alloys against various projectiles. The measured V_{bl} for 14.5 mm AP projectiles impacting plates of Elektron 675, resulted in mass efficiencies of $E_m = 1.3–1.5$, and $E_m = 2.0$ against 20 mm fragment simulating projectiles (FSP). These efficiency measures were calculated with reference to the armor aluminum alloy 5083-H32, and they show that magnesium alloys have a real potential for armor applications. Note that the efficiency of new armor materials is also tested against FSP projectiles, which represent the general shape of an artillery shell fragment.

The increase in strength for all of these potentially improved armor materials, is accompanied by an inevitable reduction of their ductility. Thus, high strength materials are also more brittle, resulting in a large volume of shattered material around the impact point. Moreover, the onset of brittleness can change the perforation mode for a given target, which may lead to a significant reduction of the target's ballistic efficiency with increasing strength. This transition in the penetration mode is especially important for thin plates which tend to fail by adiabatic shear. A schematic description for the contradicting effects of strength and brittleness is shown in Fig. 6.5, for high strength steel plates perforated by AP projectiles.

The lower hardness steel plates are perforated by the ductile hole enlargement process, with negligible damage to the hard steel cores. Their ballistic efficiency increases monotonically up to a hardness of about 370 Brinell. This is the range of armor steels (RHA) which are used for the main body of battle tanks. As the hardness of the steel plate is increased further, it fails by adiabatic shear plugging and discing, resulting in a clear reduction of its ballistic efficiency. At hardness value of about 450 Brinell this trend is reversed and the ballistic efficiency increases again, since these high hardness steels (HHS) are strong enough to shatter the hard cored projectile upon impact. The high hardness plates are very brittle and they

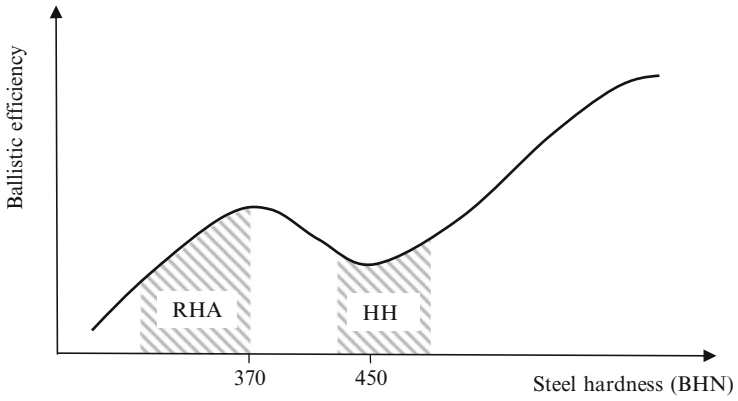

Fig. 6.5 The ballistic efficiency of steel plates, against hard cored projectiles, as a function of their hardness

experience a large damaged zone around the impact point, which reduces their multiple-hit capability.

In order to overcome the inherent deficiency of high hardness steels, armor designers came up with the idea of the dual-hardness target. This configuration is based on cladding a high-hardness front plate to a more ductile backing plate. The basic principle is that the first plate shatters the projectile while the second plate can deflect and arrest the debris of the projectile and the front plate. Moreover, the second plate minimizes the damage to the first plate by supporting it during perforation, resulting in a smaller comminuted volume in the high hardness plate. With an optimized ratio of the hardness and thickness of these plates, an increased ballistic efficiency can be achieved. The dual hardness concept was found to be quite effective against various AP projectiles. However, manufacturing problems in the welding process of these plates limit their application as add-on armor. Currently, dual hardness configurations have a front plate with hardness of 600–700 Brinell and a back plate of about 500 Brinell. Recent improvements in manufacturing techniques resulted in steel alloys which have high hardness without a loss of ductility. Such alloys have Brinell hardness of over 650, with tensile strengths of 2.0–2.25 GPa and elongations of about 8%. As shown by Showalter et al. (2008) these steels have 10–20% higher values of V_{50} against 0.3″ and 0.5″ AP projectiles, as compared with the standard high hardness plates. Obviously, the potential to improve the ballistic performance of these steels is the focus of research in many countries.

High strength steels are also very efficient against shaped charge jets as was demonstrated by Held (1993). His experimental results for the penetration depths of a given jet in different steel targets are listed in Table 6.1, in terms of charge diameters (CD). It is clear that significant improvements in the ballistic efficiency can be achieved by using very hard steels against shaped charge jets.

Table 6.1 Penetration depths of a shaped charge jet into steel targets of different strengths

Y_t(GPa)	0.3	0.45	0.7	2.05	2.9
P(CD)	5.9	5.25	4.8	3.25	2.2

6.3 Ceramics for Armor

A natural extension of the ideas presented above is to replace the hard steel front plate in the dual hardness target by a ceramic tile, and the backing steel plate by a lighter one, made of aluminum or a composite material. Ceramics have relatively low densities, in the range of 2.5–4.5 g/cc, and their compressive strengths are higher than those of high strength steels. Thus, it is not surprising that ceramic-based armors were found to be very effective against AP projectiles and long rods, as will be discussed in the following sections. A vast amount of research on this issue has been published during the last decades and the interested reader is referred to the articles presented in McCauley et al. (2002), which discuss various aspects of ceramic armor. In particular, the review article of Gooch (2002) outlines many of the ceramic-based designs for body armor, helicopter seats and armored personnel carriers. The following sections describe the interaction between different threats and ceramic tiles. Each section is devoted to a specific threat in order to highlight their different defeat mechanisms.

6.3.1 Ceramics Against AP Projectiles

The pioneering work of Mark Wilkins and his colleagues on ceramic armor is considered as one of the classical works in the field of terminal ballistics. This work, which was summarized in several internal reports (see Wilkins (1968) and Wilkins et al. (1970), for example), combined experiments and numerical simulations in order to follow the interaction of 0.3″ hard steel projectiles with targets composed of a front ceramic tile backed by a ductile metallic plate. The experiments included flash radiography which followed the interaction at different times, measurements of residual velocities, and the analysis of failure modes for both projectile and ceramic tile. The 2D numerical simulations, with the finite difference code HEMP, were the first of their kind in the field of terminal ballistics. Moreover, the model which was implemented in the code for the dynamic response of ceramics has been subsequently used by many researchers as the basis for their models. Short accounts of this work have been published by Wilkins (1978) and by Anderson (2002, 2006). The experimental work focused on the ballistic evaluation of various ceramics including alumina, boron-carbide, titanium-diboride, and silicon-carbide. The simulations incorporated the constitutive properties of the aluminum backing plates and the hard steel projectile, as determined by tensile stress–strain tests. The bulk and shear moduli of the ceramics were determined by ultrasonic measurements, and

their compressive strengths were derived from the corresponding Hugoniot elastic limits, as measured by plate impact experiments.

The failure model of these ceramics was based on the Griffith model for brittle materials, which was described in Chap. 2. The model incorporated the following features (1) Fracture initiates at a computational cell when one of the principal tensile stresses, in the plane of motion, exceeds a threshold value (which was set at 0.3 GPa). (2) There is a time delay to complete the fracture in a cell. (3) Fracture can initiate only at surfaces (including material interfaces) or at a neighboring cell which has been completely fractured. (4) A cell can fracture only after a certain time which depends on the velocity assigned to the fracture propagation, about half the shear wave velocity. (5) The strength of a fractured cell is reduced to zero in the following time step of the simulation. Anderson (2006) discussed these constraints and pointed out that the different models, which were developed in the 1990s, assigned some strength to the comminuted material, in order to have a better fit with more experimental data. In addition, he demonstrated that the crack velocity, or damage advancement velocity, should be much lower than half the shear wave velocity in order to get a better agreement with experiments. In spite of these modifications, the basic understanding for the sequence of events, from impact to perforation, has not changed since the early observations by Wilkins and his colleagues in the 1960s.

The initiation and development of fracture in the ceramic tile and the shortening of the projectile, from one of those early simulations, are shown in Fig. 6.6. In this simulation an 0.3″ conical-nosed hard steel projectile impacts a target which consists of an alumina tile backed by an aluminum plate, at 760 m/s. The thickness

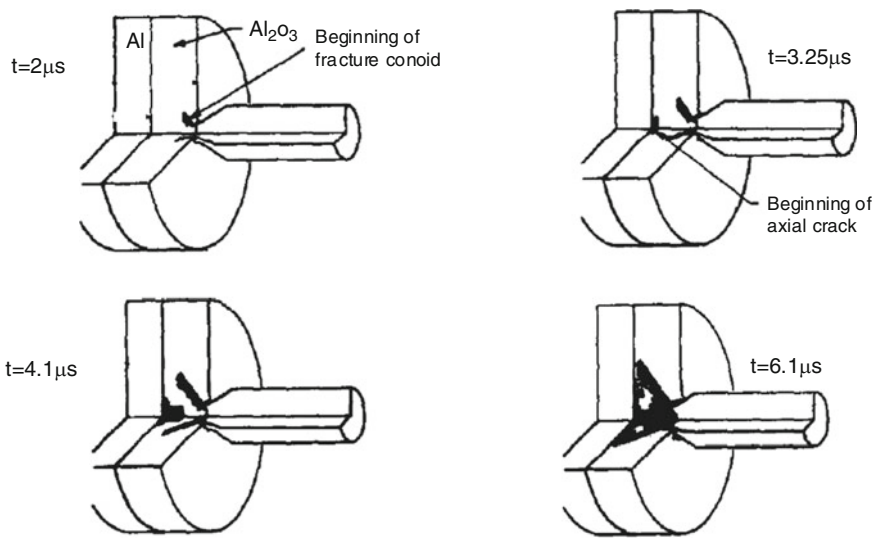

Fig. 6.6 Simulation results for the impact of a hard steel projectile on Al_2O_3/Al target

of the alumina tile in this simulation was 8.13 mm, and the thickness of the 6061-T6 aluminum backing plate was 6.35 mm.

Upon impact a fracture conoid initiates at the impact face, advancing into the ceramic tile at an angle and velocity which are very similar to those observed experimentally. At the same time the projectile's nose starts to break while its back part is slowing down. Thus, its kinetic energy is reduced by both the mass loss of its tip, and the deceleration of its back part. During this stage the projectile does not penetrate the ceramic target, a phenomenon which was called "dwell" some 30 years later when it was rediscovered through the research on long rods impacting thick ceramic tiles. The fracture conoid limits the amount of ceramic which takes place in transmitting the load to the back plate. The aluminum plate is compressed by the ceramic material inside the cone and starts to deflect at a certain time after the impact. This deflection relieves the high pressures at the ceramic/aluminum interface and the stress in the ceramic becomes tensile at this location. At this instant an axial crack is formed at the back of the tile and it propagates along its thickness, as shown by the dark areas in Fig. 6.6. Subsequently, all the ceramic material within the conoid breaks up and the remaining projectile can penetrate this comminuted material as a rigid body. Up to this time the projectile is continuosly losing mass and velocity while it is dwelling at the impact face. With these simulations Wilkins (1978) demonstrated that a stack of two alumina tiles, backed by an aluminum plate, is less efficient than a single tile of the same total thickness. The simulations showed that the first tile fails at its interface with the second tile at a relatively early time, resulting in a reduced ballistic efficiency for this double-tile arrangement. From this series of events it is clear that the most important issue is the dwell time by which all the material within the conoid is fractured. Thus, in order to maximize the ballistic performance of these targets it is essential to prolong their dwelling process as much as possible.

One can have an appreciation for the methodical work of Wilkins and his colleagues, by considering the amount of work (and its precision) which was needed to collect the data presented in Fig. 6.7. Here, the ballistic limit velocities, to within ± 15 m/s, are given for targets made of AD85 alumina tiles backed by 6061-T6 aluminum plates. This ceramic includes about 85% alumina and 15% silica, and its density is about 3.4 g/cm^3. This density is significantly lower than that of pure alumina (near 4.0 g/cm^3), but the low cost of these alumina tiles make them ideal for parametric studies which involve a large amount of experiments. One should note that each value of V_{bl} in Fig. 6.7 was obtained by several shots at different velocities. In addition, at least six shots had to be performed at $V_0 = V_{bl}$, half of them resulting in projectile penetration. A linear change in V_{bl} with the thickness of the backing plate (δ) was obtained for several tile thicknesses (Δ), as shown in Fig. 6.7. The distinctive breaks in these curves at $\delta = 5$–6 mm, are due to a change in the failure mode of the aluminum plate from dishing and petalling, for the low thicknesses, to shear plugging for the thicker plates, as noted by Wilkins (1978).

One of the main conclusions of Wilkins and his colleagues was that the ballistic performance of a given ceramic could be improved if its ductility is enhanced.

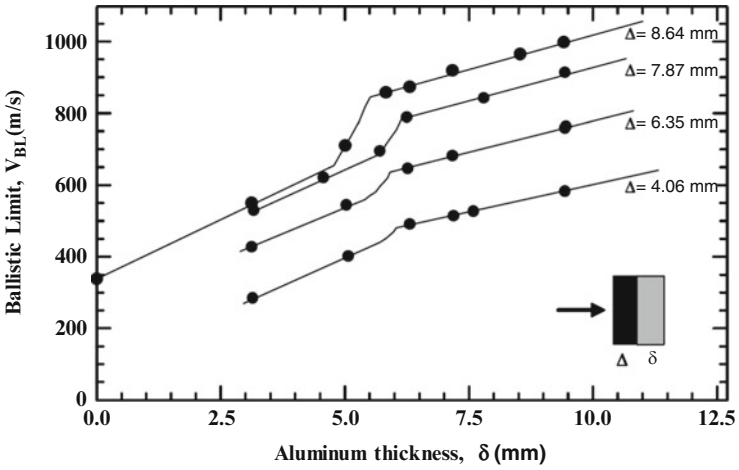

Fig. 6.7 The ballistic limit velocities of AD85 alumina tiles backed by 6061 aluminum plates

This prompted an intense research which lasted for several decades, and was aimed at adding a few percent of soft metal to the ceramic in order to improve its ductility. These materials, called cermets, perform better than their pure ceramic counterparts, but the improvements were not dramatic and did not justify their manufacturing cost. Another innovation which was initiated by Wilkins and his colleagues was that of graded ceramics. The realization that the ceramic failure starts at its interface with the metallic backing, led researchers to manufacture cermets in which the ceramic-metal proportions change gradually from a pure ceramic, at the impact face, to a pure metal at their back. Graded materials have also received a lot of attention but their manufacturing problems have yet to be solved.

Anderson (2002, 2006) further analyzed the defeat mechanisms which were described by Wilkins (1978), namely, the erosion of the projectile and its deceleration during the dwell phase. He showed that these processes contribute roughly equal parts to the loss of the projectile's kinetic energy, which can be reduced by as much as 50% at the end of the dwell phase. An excellent set of flash radiographs, from Anderson (2006), is shown in Fig. 6.8. One can clearly follow the dwell phase of the 0.3″ APM2 projectile at the interface of a 7.62 mm boron carbide tile, which was glued to a 6.6 mm thick 6061-T6 aluminum plate. Impact velocities in these shots were around 820 m/s and the radiographs were obtained by 1 MeV X-ray pulsers. Several features are clearly seen in this figure: the conoid fracture of the ceramic tile, the breakup of the projectile's nose during the dwell phase, which lasts for about twenty microseconds, and the subsequent penetration of the residual projectile (as a rigid body) into the comminuted ceramic.

In order to simulate these experiments with the CTH code, Anderson and Walker (1999) modified the original failure model of Wilkins, which was described above. Their model has five material parameters which describe the failure of the ceramic tile: the compressive strength of the intact material, the slope and cap of a

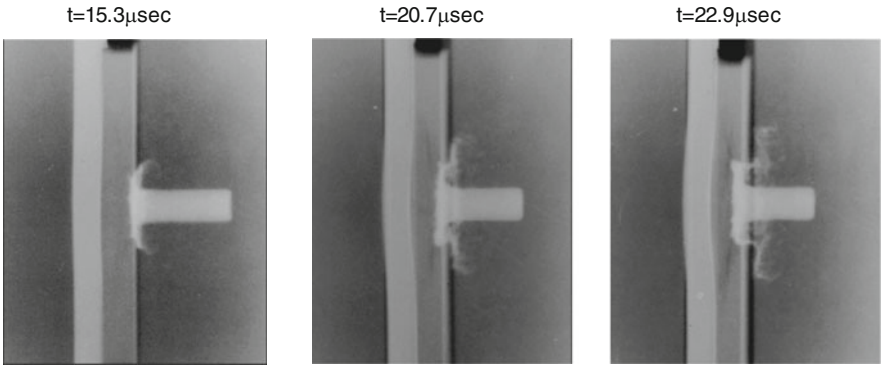

Fig. 6.8 Flash X-ray radiographs of a 0.3″ APM2 projectile impacting a B_4C tile backed by an aluminum plate

Drucker–Prager yield surface for the damaged ceramic, and a constant which governs the propagation speed of the damage in the ceramic tile. They found that in order to account for the experimental results, this speed should be about 0.025 times the shear wave velocity of the ceramic, rather than half the shear velocity which was used by Wilkins in his simulations. In addition, Anderson and Walker (1999) assigned a finite strength to the comminuted material, in contrast with the zero strength in Wilkins' model. These modifications resulted in an excellent agreement between the simulations and the experimental radiographs for the positions of the projectile's nose and tail. Such an agreement is shown in Fig. 6.9, from Anderson (2006), for the simulation of the experiment shown in Fig. 6.8.

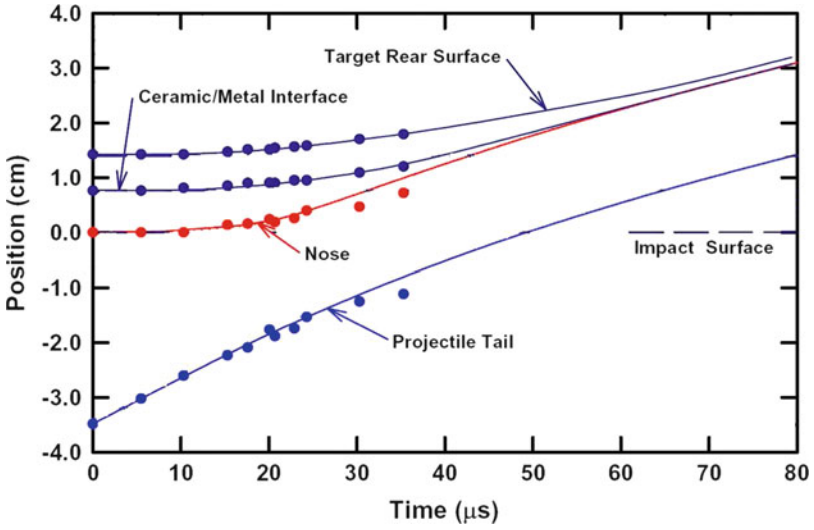

Fig. 6.9 The agreement between simulation results (*lines*) and experiments (*circles*) for the 0.3″ steel projectile impacting the B_4C/Al target

The data collected by Wilkins and his coworkers for the different ceramic tiles backed by a 6.35 mm aluminum plate, resulted in a hierarchy according to which the best performance was obtained by the lowest density ceramic beryllium-boride, while the poorest performance was obtained for the high density ceramics titanium-diboride and titanium-carbide. This hierarchy in the ballistic performance has been explained by Rosenberg et al. (2009), who plotted the figures of merit of these ceramics as a function of their density, as shown in Fig. 6.10. The different ceramics are compared with the boron-carbide tile which was given a figure of merit of 1.0. The other tiles obtained their figure of merit (relative efficiency) according to their ballistic limit velocity, as compared with that of boron-carbide. A clear correlation is obtained between the relative ballistic efficiency of these tiles and their density, as shown in the figure. The alumina tiles are marked by squares, the beryllium compounds by crosses, and the titanium compounds are marked by triangles.

The decreasing trend of tile efficiency with its density has to be due to a real physical phenomenon since the two different ceramics B_4C and BeO + B, which have practically the same density of 2.5 g/cm^3, resulted in exactly the same ballistic efficiency. In addition, the lighter titanium compound $TiBe_{12}$ is much more effective than the denser titanium compounds, TiB_2 and TiC. Thus, it is clear that the density of the tile, rather than its constituents or strength properties, is responsible for the trend we see in Fig. 6.10. In order to understand this trend one has to realize that these ceramics were graded by their corresponding values of V_{bl}, while keeping a constant weight for all the different tile/plate combinations. Since the aluminum plates in these targets were of the same thickness, the only changing parameter was the thickness of the tile which, obviously, varied with its density in order to keep a

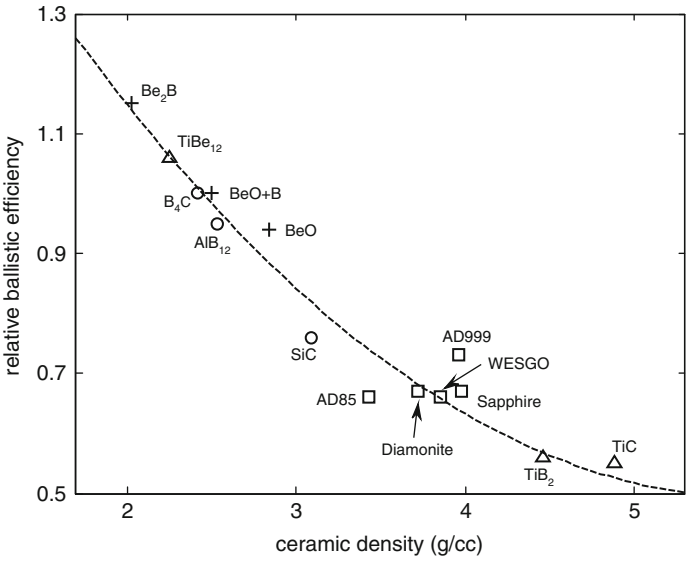

Fig. 6.10 The relative ballistic efficiencies as a function of the ceramic density

constant weight for the target. Thus, the Be_2B tile with the lowest density (2.0 g/cm^3) was the thickest tile in these tests, while the TiB_2 and TiC tiles with densities of 4.5 and 4.9 g/cm^3, were the thinnest. All of these ceramics are graded as armor materials, having minimal porosities and compressive strengths which are higher than that of the steel projectile. Thus, one may assume that all of them failed by the same mechanism which was described above. It was emphasized earlier that the dwell time is the most important parameter for the defeat process of these projectiles. Thus, one should look for differences in the dwelling times of these tiles, in order to account for their different ballistic efficiencies. Clearly, a thicker tile will result in a longer dwelling time since both the conoid formation and the comminuting of the material inside the conoid, are bound to take more time. Thus, a better performance is expected for the thicker tiles with longer dwell times, and these tiles had the lower densities in the experiments. This simple explanation accounts, at least qualitatively, for the decreasing trend in the relative ballistic efficiencies of the denser ceramics, as shown in Fig. 6.10.

In order to demonstrate that the compressive strength of these ceramics are high enough to defeat AP projectiles, Rosenberg et al. (2009) impacted a 0.5″AP projectile at a large block of alumina, 300 mm on each side. The projectile shattered upon impact and was completely stopped at the impact face, hardly scratching the block. This experiment also supports the thesis that the failure of thin tiles is due to tensile stresses which originate at their free surfaces or at their interfaces with other plates. Such a failure was avoided in the test with the large ceramic block, since its free surfaces were too far from the impact point to have a significant influence on the process. In conclusion, the different ballistic efficiencies of the ceramic tiles, in the experiments of Wilkins and his colleagues, are a direct consequence of their test configuration, namely, the V_{bl} test for constant-weight targets. The V_{bl} test is a design-specific test which gives a measure for the ballistic performance of a certain configuration. It includes various details, such as the properties of the backing plate, which are not related to the ceramic tile. The compressive strength of the ceramic tile did not manifest itself upon the resulting value of its V_{bl}, as shown by the results of Wilkins and his colleagues. In addition the V_{bl} test is a rather expensive one, since it demands several shots at different velocities around the value of V_{bl}.

A new test configuration was suggested by Rosenberg et al. (1987a) in order to overcome these deficiencies of the V_{bl} test. This is the thick-backing technique, shown schematically in Fig. 6.11, which has been later termed the depth of penetration test (DOP). This simple configuration has been widely used as a standard ranking method for ceramic tiles. The new configuration also provides relevant information concerning the performance of ceramics under realistic armor designs against long rods, as we shall see in the next section.

With the DOP test, the ceramic tile of thickness h_c and density ρ_c, is glued to a thick metallic block of a reference material, such as aluminum or steel. The residual penetration (P_{res}) of the projectile into the thick backing determines the ballistic efficiency of the ceramic tile, as compared with the backing material. In their work with different AP projectiles, Rosenberg et al. (1987a) and Rosenberg and Yeshurun (1988) used 2024-T351 aluminum blocks as their reference

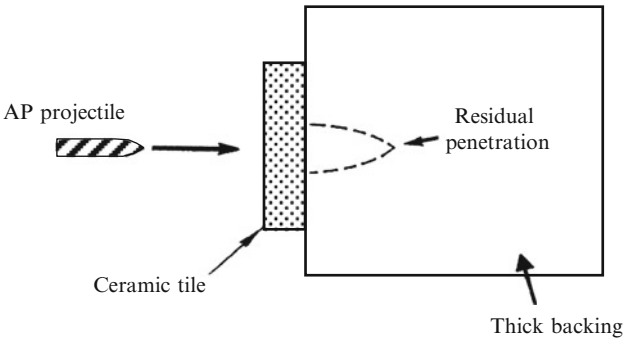

Fig. 6.11 The DOP test

materials. They applied the DEF measure, as defined by (6.2), to obtain the ballistic efficiency (η) of the ceramic tile through:

$$\eta = \frac{\rho_{Al}(P_{Al} - P_{res})}{\rho_c h_c} \tag{6.3}$$

where P_{Al} is the penetration depth of the projectile into the bare aluminum block, and $\rho_c h_c$ is the areal density of the tested tile. One of the main advantages of this configuration is due to the support which the thick backing supplies to the ceramic tile, preventing its early failure by tensile stresses or, at least, postponing this failure to much later times. More importantly, this configuration results in an efficiency measure for the ceramic through a single test, as will be shown below, simplifying the evaluation process as compared with the ballistic limit test.

In order to check whether this technique can be based on a single experiment for a given ceramic, Rosenberg et al. (1987a) performed several experiments with various AP projectiles, impacting AD85 alumina tiles of different thicknesses which were backed by thick blocks of 2024-T351 aluminum. The residual penetrations in these shots are given in Fig. 6.12, and it is clearly seen that they fall on well defined straight lines.

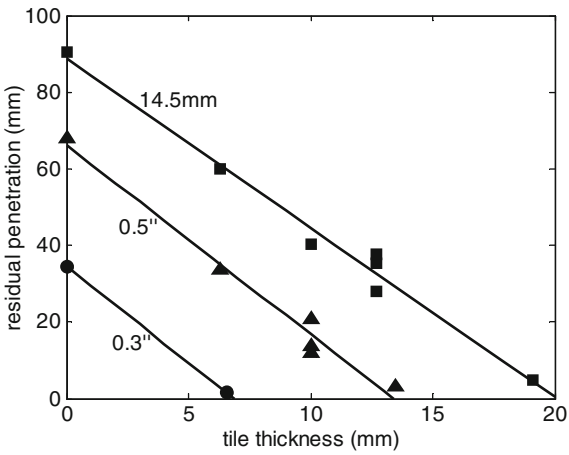

Fig. 6.12 The DOP test results for 0,3″, 0.5″, and 14.5 mm AP projectiles

The fact that the results for different tile thicknesses fall on a single line means that their ballistic efficiency is independent on tile thickness, and it can be determined by a single test using (6.3). The three AP projectiles in this study have similar ogive-nosed steel cores, which differ only by their size. Also, their muzzle velocities, in the range of 830–970 m/s, are close enough to obscure any velocity dependent effect. These similarities are the main reasons for the fact that the lines in Fig. 6.12 are very nearly parallel to each other. Once the data points were found to fall on straight lines, a somewhat different expression for the ballistic efficiency can be written. This expression is based on the extrapolation of these lines to a residual penetration of $P_{res} = 0$, according to the following ratio of the areal densities:

$$\eta = \frac{\rho_{Al} P_{Al}}{\rho_c h_c^*} \tag{6.4a}$$

where h_c^* is the minimal tile thickness for which the residual penetration is zero. If we plot the results of these tests in terms of areal densities rather than penetration depths, we find that the ballistic efficiency (η) is equal to the slope of the straight line through the experimental points. Thus, one can rewrite (6.4a) in terms of the angle (θ^*) which these straight lines form with the ordinate, as follows:

$$\eta = tg(\theta^*) \tag{6.4b}$$

This display of the ballistic efficiencies is shown in Fig. 6.13 for several ceramics which were impacted by 0.5″APM2 projectiles, as given by Rosenberg

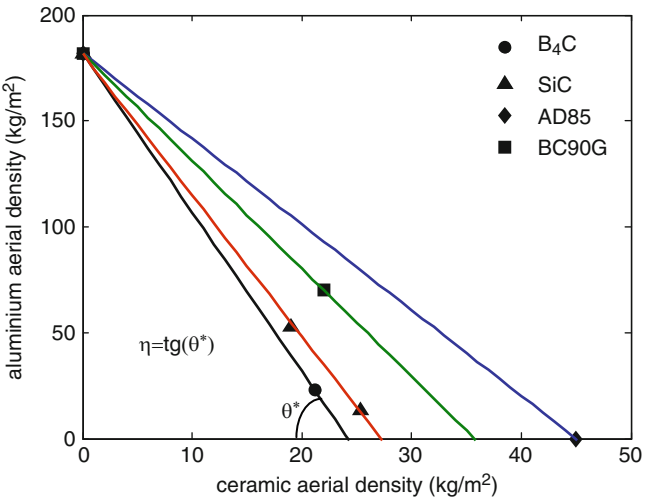

Fig. 6.13 The ballistic efficiencies for different ceramics, defined by the slope of the experimental lines

and Yeshurun (1988). These ceramics included silicon-carbide, boron-carbide, and two types of alumina ceramics (AD85 and the somewhat denser BC90G).

The resulting efficiencies are clearly dependent on both the density and the strength of the tile, in contrast with the results obtained by the V_{bl} tests which were summarized in Fig. 6.10. For example, the two alumina ceramics, AD85 and BC90G, have densities of 3.42 and 3.56 g/cc, respectively. Their Hugoniot elastic limits, as measured by plate impact experiments are 6.0 GPa and 7.0 GPa, for the AD85 and the BC90G, respectively. The higher strength BC90G alumina resulted in a ballistic efficiency of $\eta = 4.9$ as compared with a value of $\eta = 4.0$ for the AD85 alumina, in accord with the higher strength of the BC90G alumina. In fact, Rosenberg and Yeshurun (1988) showed that the ballistic efficiencies of different ceramics, as determined by the DOP test, are related to their specific strength which is defined by their strength to density ratio. It is also worth noting that the ballistic efficiencies of these ceramics can reach relatively high values, such as $\eta = 7.7$ which was obtained for the boron carbide tile in these tests. The high efficiency values are due to the thick aluminum backings, preventing the early failure of the tile by tensile stresses, as explained above. Such high efficiencies should motivate the armor designer to attach the ceramic tiles directly to the main body of their vehicle. In fact, this idea was implemented for several armored vehicles, as reviewed by Gooch (2002).

One should be aware of the main causes for the possible scatter in the results of these DOP tests, which is responsible for inconsistencies between different sources. The reproducibility of the same material properties for different tile thicknesses is one of the issues which can lead to a thickness dependent ballistic efficiency. Also, relatively thick tiles result in small residual penetrations, often with a large scatter between repeated tests. On the other hand, very thin tiles can cause some ambiguity in the results because of their small effect on the process. In order to avoid these difficulties one should use tile thicknesses which result in a residual penetration of about half the penetration into the bare metallic block. It has been found that the lateral dimensions of the tiles should be about ten times larger than the diameter of the projectile, in order to avoid the early failure by release waves from their lateral surfaces. The tiles can have smaller lateral dimensions if they are embedded in the metallic backing itself, with a close fitting between tile and backing.

The ballistic efficiency values cited above are related to the 2024-T351 aluminum backing, which was used by Rosenberg et al. (1987a) and Rosenberg and Yeshurun (1988). Other backing materials or different projectiles can result in different values for the ballistic efficiencies of the same ceramics, but their ranking order is not supposed to change. In fact, with 0.3″ projectiles made of sintered tungsten (Kennametal W-2), Rosenberg et al. (1987a) obtained a value around $\eta = 8.0$ for the ballistic efficiency of AD85 tiles backed by aluminum blocks. This value is higher by a factor of two than the value obtained for these tiles impacted by the 0.3″ AP projectiles. Vural et al. (2002) used the much softer 6061-T0 aluminum as the backing material for their tests on alumina tiles against 0.3″AP projectiles. Their efficiency merits were very high ($\eta = 8$–10), which is a clear demonstration for the effect of the strength of the backing material. Finally,

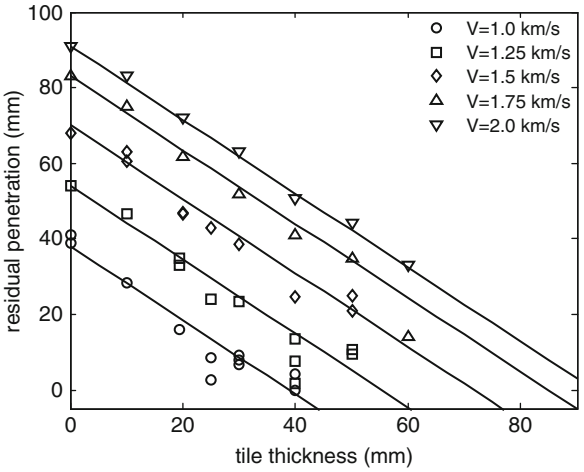

Fig. 6.14 DOP results for alumina/steel targets impacted by short WHA projectiles

Senf et al. (1998) used armor steel as a backing material for their AD995 alumina tiles, of density of 3.95 g/cc. The L/D = 3.2 spherical nosed tungsten-alloy projectiles, with a diameter of 10 mm, impacted the targets at velocities of 1.0–2.0 km/s. The efficiency measure for these tiles, against the tungsten alloy projectile was about 2.0 as compared with the steel backing. The residual penetrations vs. tile thickness from Senf et al. (1998) are shown in Fig. 6.14. At a given impact velocity, the data for different tile thicknesses fall on a straight line, as in the case of AP projectiles. This important result enhances the claim that the DOP test can give an efficiency measure for a given tile through a single experiment. Moreover, the data for different impact velocities fall on parallel lines, indicating that the ballistic efficiency of this alumina does not depend on impact velocity, at least for this range of velocities. The relatively large scatter in the data for the thicker tiles is due to the factors discussed above.

In conclusion, the examples presented here show that the efficiency merits of a given ceramic are strongly dependent on all the above mentioned parameters. Thus, the DOP test should be regarded as a convenient screening test for the relative ranking of ceramic tiles through a simple and cheap experiment.

6.3.2 The Interaction of Ceramics with Long Rods

The interaction of long rods with ceramic tiles and their defeat mechanisms are very different from those for hard cored AP projectiles. Long rods are made of heavy alloys which have much lower strengths than the hard steel cores of the AP projectiles. Thus, their defeat mechanism has to be based on the continued erosion of the rod rather than on its shattering. The thickness of a ceramic tile which is needed to completely erode a long rod has to be correspondingly large. This fact imposes several difficult-to-achieve constraints for the armor designer and, as

a result, the concept of ceramics against long rods is still in its early stages of implementation. Still, much work has been done on this subject since the 1980s, when hydrocodes became available. Numerical simulations are heavily used to follow the specific details in the rod/ceramic interaction, as will be reviewed here.

The use of the DOP test for the screening of ceramic tiles against eroding rods, was first reported by Bless et al. (1987) who impacted AD85 alumina tiles, glued to thick aluminum backings, with L/D = 5 tantalum rods. Mellgrad et al. (1989) and Woolsey et al. (1989) suggested the use of armor steel as backing materials, in order to reduce the residual penetrations of the rods, and to obtain information about the possible use of ceramics for real armor applications. The DOP configuration with the armor steel backing is being used by most researchers, with tiles which are either bare or have a thin cover plate at their front. Some works were aimed at providing a better lateral confinement to the tile by embedding them in the steel backing, in order to achieve optimal confinement conditions, as described by Hauver et al. (1992).

The experimental results of Hohler et al. (1995), with alumina tiles (density of 3.8 g/cm^3) backed by hard steel blocks, are shown in Fig. 6.15. The thickness of the tiles ranged between 10 mm and 80 mm, and the impact velocities of the L/D = 12 WHA rods were: 1.25, 1.7 and 3.0 km/s. As shown in Fig. 6.15, the residual penetrations fall on nearly parallel straight lines. Thus, the efficiency of these tiles against long rods was found to be independent on their impact velocity within a large range of these velocities. The ballistic efficiency of these alumina tiles against the long rods is $\eta = 1.7$ which is somewhat smaller than the value of $\eta = 2.0$ obtained by Senf et al. (1998) for similar tiles which were impacted by the

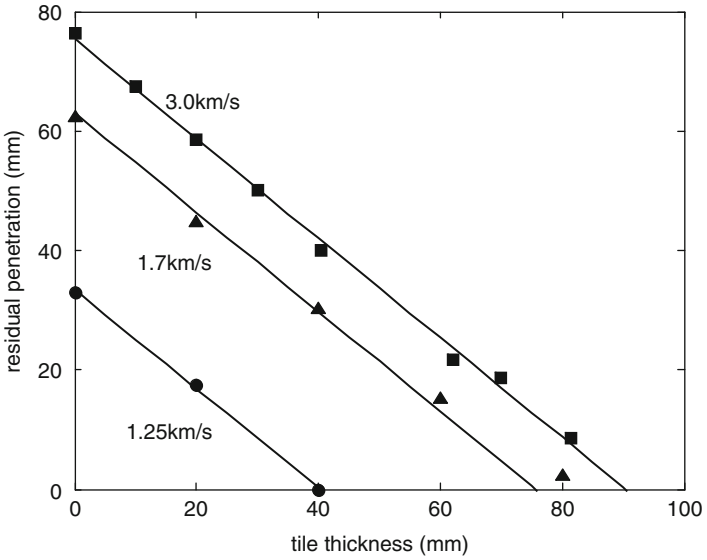

Fig. 6.15 DOP results for L/D = 12 WHA rods impacting alumina/steel targets at various velocities

shorter projectiles. The difference is due to the different strength of the steel backings used in the two sets of experiments, which was higher for the long rod experiments of Hohler et al. (1995). We have seen above that a backing material with a higher strength results in a lower ballistic efficiency for a given ceramic, since the tile's efficiency is related to the backing material.

Another set of experiments with various ceramics backed by high hardness steel blocks, is described by Rosenberg et al. (1998). The ceramics tiles were 20–80 mm thick and their lateral dimensions ranged between 75 mm and 150 mm. The tiles were impacted by an L/D = 12.5 WHA rods (with D = 5.8 mm) at 1.7 km/s. This set of experiments included silicon and boron carbides, titanium-diboride and aluminum-nitride ceramics. The resulting depths of penetrations as a function of the areal density of the tiles are shown in Fig. 6.16. The residual penetrations for the tiles with small lateral dimensions resulted in lower values of η. This is a clear indication of the effect of lateral release waves which reduce the high pressures around the rod/tile interface. Various experiments indicated that in order to avoid the interfering effects of lateral boundaries, the width of the tiles should be at least five times larger than their thickness. Another way to overcome lateral release effects is to embed the tile in the backing, or to apply a metallic frame around the tile. Improvements in the ballistic efficiency have been achieved by close fitting the tile into a cavity in the backing block. Several researchers have even used special glue around the tile which included metallic powder, in order to have a better acoustic match between the tile and its backing.

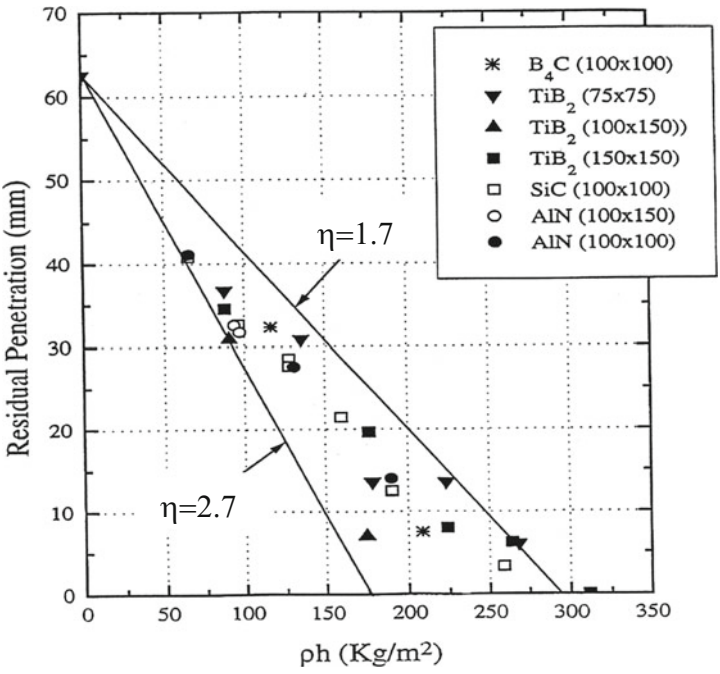

Fig. 6.16 DOP results for various ceramics

The ballistic efficiencies of the ceramics presented above are bounded between $\eta = 1.7$ and $\eta = 2.7$, as shown by the two lines in Fig. 6.16. These are typical values for the efficiency of strong ceramics as compared with high hardness steel backings, as was also shown by Reaugh et al. (1999). They shot L/D = 4 WHA rods at various ceramic tiles which were backed by high strength steel backings. The ballistic efficiencies for the different tiles, at an impact velocity of 1.7 km/s, were: $\eta = 2.0$ for alumina, $\eta = 2.5$ for both AlN and SiC, and $\eta = 3.1$ for the TiB_2 tiles.

The experiments of Hohler et al. (1995) with alumina tiles were performed with flash X-ray radiographs which followed the penetrating rod in the ceramic tiles, as shown in Fig. 6.17. It is clearly seen that the rod is eroding during its penetration in the ceramic in a similar way to its erosion in a thick metallic target. In particular, the quasi steady-state mode of penetration and the rod's erosion rate were found to be similar to those in metals. Thus, one may conclude that the penetration model of Alekseevskii and Tate (the AT model) can also account for the penetration of rods into thick ceramic tiles.

The applicability of the AT penetration model for the interaction of long rods with thick ceramic tiles, has been demonstrated by Rosenberg and Tsaliah (1990). Their first step was to check whether a penetration threshold velocity (V_c) can be defined for ceramics, in the same way as for semi-infinite metallic targets. They shot L/D = 10 rods of different materials and strengths (copper, steel and WHA), at large alumina blocks of two different types, AD85 and BC90G, having densities of 3.42 and 3.56 g/cc, respectively. By varying the impact velocity of these rods Rosenberg and Tsaliah (1990) found that below a certain threshold velocity these blocks were not penetrated, with only a small indentation shown around the impact point. The threshold velocities of the different rods impacting the AD85 alumina

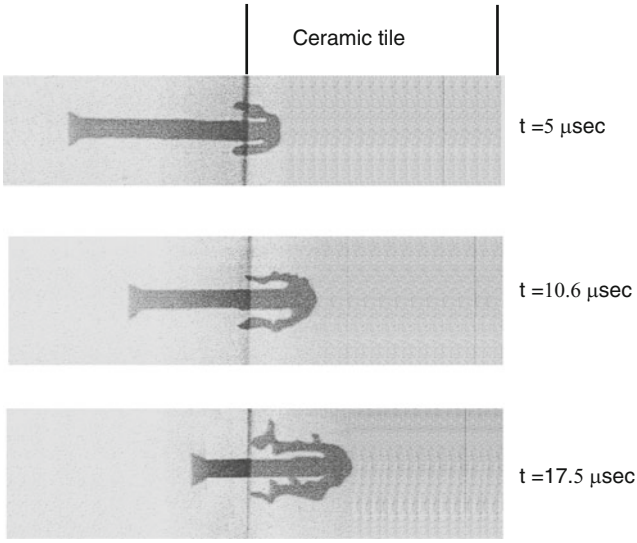

Fig. 6.17 The penetration and erosion of a WHA rod impacting an alumina tile at $V_0 = 2.5$ km/s

blocks were: $V_c = 1.15$, 0.99 and 0.66 km/s for the copper, steel and WHA rods, respectively. Using the strengths of these rods (Y_p), and the relation $V_c = [2(R_t - Y_p)/\rho_p]^{0.5}$ for the threshold velocity, a value of $R_t = 5.5 \pm 0.5$ GPa was obtained for the AD85 alumina. A similar set of experiments on the stronger alumina (BC90G), resulted in a value of $R_t = 7.0$ GPa for this alumina. These values of R_t for the two types of alumina, are very close to their Hugoniot elastic limits (HEL), as measured by plate impact experiments. In addition, Rosenberg and Tsaliah (1990) showed that these values for R_t account for the residual penetration in the steel backing, in several experiments with alumina tiles backed by steel blocks. Thus, they concluded that the assignment of $R_t \approx$ HEL for a given ceramic accounts for its resistance to penetration by long eroding rods. The threshold behavior which was demonstrated by the experiments of Rosenberg and Tsaliah (1990), was later termed "the interface defeat" phenomenon and it became the focus of intense research, as will be described below.

The experiments of Subramanian and Bless (1995) with L/D = 20 tungsten rods impacting large AD995 alumina tiles, resulted in a value of $R_t = 8.0 \pm 1.0$ GPa, which is close to the value of HEL for this alumina. This value was obtained by analyzing the measured penetration velocities of the rods, through flash x-ray radiographs. On the other hand, the experiments by Behner et al. (2008), with gold rods impacting thick SiC tiles, resulted in a threshold impact velocity of about 0.9 km/s. The corresponding stagnation pressure at this velocity is about 7.8 GPa, which is significantly lower than the value of HEL = 11 GPa for this ceramic. Obviously, a theoretical account of the threshold velocity for ceramics is very much in need. Since high-grade ceramics can have HEL values of 8–12 GPa, a rough estimate results in values of $V_c = 0.85$–1.1 km/s, for the threshold velocities of WHA rods (with $\rho_p = 17.5$ g/cc and $Y_p = 1.5$ GPa) impacting large ceramic blocks.

As mentioned above, Subramanian and Bless (1995) used flash x-ray radiography, in order to follow the eroding tungsten rod as it penetrated into thick AD995 alumina targets. Their experimental results showed that the penetration velocity (U) of the rod is linearly dependent on its impact velocity (V_0), as shown in Fig. 6.18. The open circles in this figure were obtained by linear fits to the data from each experiment, while the filled circles were obtained by fits to the combined data of six shots at the nominal velocity. The solid line is a linear fit to the data, and the broken line is the predicted relation according to the hydrodynamic model (no strength) through the relation:

$$U_{hyd} = \frac{V}{1 + \sqrt{\rho_t/\rho_p}} = 0.69V \tag{6.5}$$

These experiments resulted in the following relation between penetration velocities (U) and impact velocities (V_0), for $V_0 \geq 1.5$ km/s:

$$U = 0.836V_0 - 0.742 \quad \text{for AD995 alumina} \tag{6.6a}$$

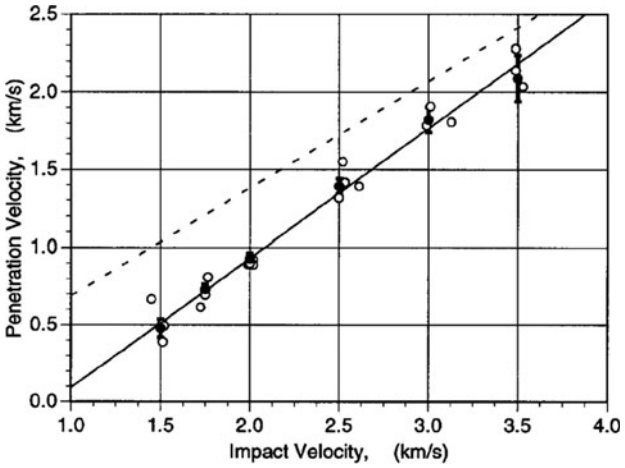

Fig. 6.18 The results for penetration velocities of tungsten rods into AD995 alumina tiles

where U and V_0 are given in km/s. A linear relation between penetration velocity and impact velocity was also obtained by Subramanian et al. (1995), for tungsten rods impacting 6061-T651 aluminum targets at velocities in the range of 1.5–4.2 km/s.

Similar results were obtained for other ceramics penetrated by WHA rods, for impact velocities between 1.5 and 5.0 km/s. These experiments were summarized by Orphal et al. (1996) for aluminum-nitride, Orphal et al. (1997) for boron-carbide, and Orphal and Franzen (1997) for silicon-carbide. The linear fits for the data in these works are:

$$U = 0.575V_0 - 0.406 \quad \text{for } B_4C \tag{6.6b}$$

$$U = 0.781V_0 - 0.51 \quad \text{for SiC} \tag{6.6c}$$

$$U = 0.792V_0 - 0.524 \quad \text{for AlN} \tag{6.6d}$$

These linear relations may seem to contradict the predictions of the AT penetration model, as discussed by Orphal and Anderson (2006). They conclude that this discrepancy highlights the shortcomings of the AT model, since similar relations were obtained for metallic targets as well. However, a close examination of the AT model shows that it predicts an effectively linear relationship between U and V_0 for high density rods and low density targets, especially at high impact velocities. Note also that at high impact velocities these rods do not decelerate appreciably during most of the penetration process. Thus, the velocity of their uneroded parts (V) is expected to be close to their impact velocity (V_0). An effectively linear relation between U and V_0 (or V) is obtained from the AT model, by considering the expression for U = U(V), as derived from the modified Bernoulli relation, (5.10):

$$U = \frac{V - \mu\sqrt{V^2 + A_0}}{(1 - \mu^2)} \tag{6.7a}$$

where A and μ are given by:

$$A_0 = \frac{2(R_t - Y_p)(1 - \mu^2)}{\rho_t};\ \mu = \sqrt{\frac{\rho_t}{\rho_p}} \tag{6.7b}$$

Using representative values for the densities of the materials involved in these experiments, $\rho_t = 3.0$ g/cc and $\rho_p = 17.5$ g/cc, together with typical values of $R_t = 10.0$ GPa and $Y_p = 1.0$ GPa, result in: $A_0 = 5$ and $\mu = 0.414$ for this case. Inserting these values in (6.7a), it is easy to show that the following relation accounts for the calculated values of U for impact velocities in the range of $V_0 = 1.5$–5.0 km/s:

$$U = 0.8V_0 - 0.7 \tag{6.8}$$

This relation is similar to the linear relations obtained experimentally for the various ceramics, as given by (6.6a–6.6d). In conclusion, the data for ceramic penetration by long rods can be analyzed by the AT model and the ballistic efficiencies of different ceramics can be related to their corresponding R_t values, as derived from the measured penetration velocities of eroding rods into these tiles.

The next step in this line of research was achieved by Bless et al. (1992) who showed that by properly encapsulating the ceramic tile, a much higher impact velocity is obtained for the onset of rod penetration into a large ceramic block. This issue has been the focus of intensive research due to its potential benefit for ceramic armor against long rods. The works of Hauver et al. (1993, 1994), Subramanian and Bless (1995), Lundberg et al. (1998, 2000) and Westerling et al. (2001) demonstrated that the penetration of high density rods can be prevented even at impact velocities as high as 1.6 km/s. Most of these experiments were performed with the reverse ballistics technique, where the rods are stationary and the ceramic target is launched by a light gas gun. This configuration is especially suited for high velocity impacts, which are impossible to achieve by accelerating these slender rods with either powder or gas guns. On the other hand, it is quite simple to accelerate a thick ceramic cylinder, confined in a metallic sabot, to velocities of 5.0 km/s with light gas guns. Since these guns have a diameter of about 40 mm, the experiments have to be highly scaled and the diameter of the stationary rod is limited to D = 1–2 mm. Thus, scaling issues had to be considered and Hauver et al. (2005) noted that larger scale experiments reproduced the main findings of the earlier studies. Scaled experiments have another advantage concerned with flash X-ray radiography. Due to the small size of the targets, the X-ray flashes can easily penetrate the small ceramic cylinders, and follow the shape and advancement of the rod during penetration. This is clearly shown in Fig. 6.19, from Holmquist et al. (2008), who shot silicon-carbide cylinders at slender gold rods (D = 1 mm, L = 70 mm).

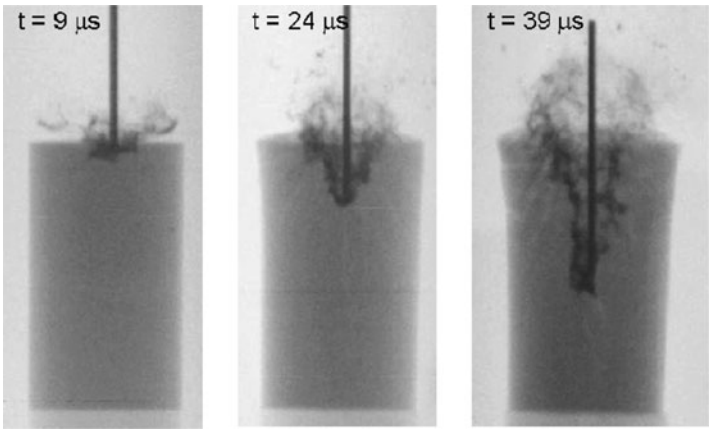

Fig. 6.19 X-ray radiographs in a reverse ballistics test of a SiC cylinder impacting a stationary gold rod at $V_0 = 1.38$ km/s

The analysis of such X-ray pictures led Lundberg et al. (1998) to the realization that the interface defeat mechanism is followed by a narrow range of impact velocities where the rod is actually "dwelling" at the interface for a certain amount of time before it starts penetrating. Note that such a dwell phenomenon was first observed by Wilkins and his colleagues in their classical work with AP projectiles, as described above. When the dwelling phase is over, the rod penetrates the ceramic target at a relatively low penetration velocity. For higher impact velocities the dwell phase is diminished, and penetration proceeds at a high velocity practically right after impact. The results of Lundberg et al. (1998) for boron carbide tiles impacting stationary WHA rods are shown in Fig. 6.20. One can clearly see the range of impact velocities around $V_0 = 1.5$ km/s which corresponds to the dwell mechanism (the shaded range in the figure). This is the transition range between the interface defeat of the rod and its regular penetration process.

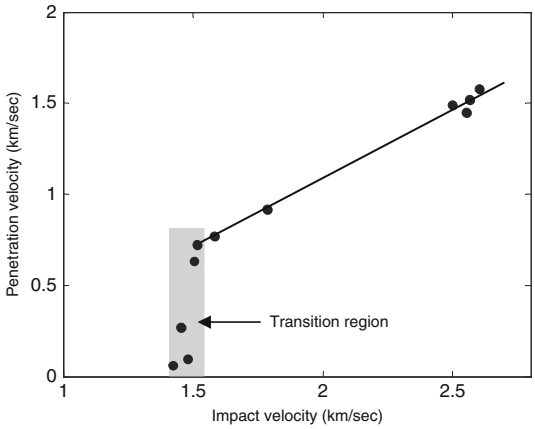

Fig. 6.20 The interface defeat and dwell regions for boron carbide tiles

The experiments of Bless et al. (1992), Hauver et al. (1993), Lundberg et al. (1998, 2000), and Hauver et al (2005), showed that much higher values of the impact velocities are obtained for the interface defeat velocity by a proper use of cover plates. These plates contain the rod material, around the impact point, which applies a continuous pressure on the tile for a relatively long time. This dynamic confinement prevents the early failure of the tile by tensile stresses which initiate at free impact surfaces. The second role of the cover plate is to spread the initial load of the rod as it impacts the ceramic tile, by enlarging its nose area. Lundberg et al. (1998) used a steel cover plate with a central protrusion having diameter and height of several rod diameters. Numerical simulations by Holmquist and Johnson (2002) showed that a small copper disc glued to the tile, is enough to result in a significant increase of the interface defeat velocities. The diameter and the thickness of the copper buffer in these simulations were equal to 2D and 4D, respectively, where D is the diameter of the rod. The role of the copper buffer will be discussed in the next section where we review the simulations concerning the impact of long rods on ceramic tiles. Lundberg et al. (2001) showed that the dwell process can last for long times (300 μs), by using very long rods (over 770 mm long), which were composed several welded rods. The aim of these experiments was to show that with the proper design, the interface defeat mechanism should be viable also against full scale rods.

6.3.3 Numerical Simulations

A large amount of research has been focused on numerically simulating the various phenomena described above, in order to highlight the physical parameters which control the response of ceramics to impact and penetration. Several material models for ceramics were implemented in commercial hydrocodes and all of them have the various features of the model developed by M. Wilkins, as described in Sect. 6.3.1. The most elaborate one is the JH-1 model of Johnson and Holmquist (1990), which was described in Chap. 2. Other models for brittle materials include those of Curran et al. (1993), Rosenberg et al. (1995), Rajendran and Grove (1996), Walker and Anderson (1996) and Walker (2003). The models are based on the realization that upon impact, high amplitude stress waves are generated in the ceramic tile inducing its fracture and comminuting in a large volume ahead of the penetrating projectile. Thus, in order to simulate the behavior of the ceramic tile it is necessary to account for the properties of both the intact and the fractured material. This unique feature of brittle materials was convincingly demonstrated by Shockey et al. (1990), who impacted small spheres at steel covered silicon-nitride tiles. The impact velocities in these experiments were relatively low and the impacting spheres did not penetrate the steel covers. However, a cross section of the tiles after impact revealed a wealth of different cracks and comminuted material below the impact point, as

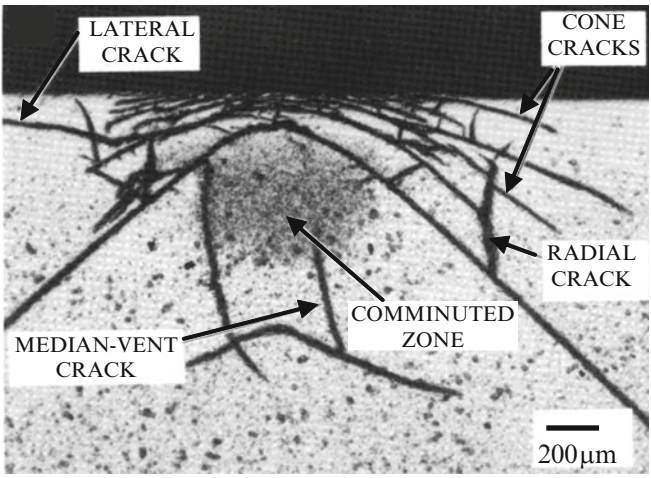

Fig. 6.21 Damage to a ceramic tile from a non-penetrating sphere impact

shown in Fig. 6.21. The extensive damage in this tile was due to the impact of a tungsten-carbide sphere at 231 m/s. Since the sphere did not penetrate the steel cover plate, the damage in the tile has to be attributed to the strong stress waves, compressive and tensile, which were initiated by the impact itself. Thus, a penetrating projectile is due to encounter a severely damaged tile, and it is evident that the properties of the damaged ceramic control the penetration process.

The modeling of these failures is even more complex because the cracked material has different properties than the comminuted one. These differences should be accounted for, especially for well confined tiles, since the confinement tends to keep the high pressures in the tile for a certain time. A cracked tile under high confining pressures is not expected to lose its resistance to penetration. Thus, the potential damage induced by tensile stresses can be prevented or delayed to much later times, by properly confining the ceramic. Much of the experimental work on the constitutive relations of ceramics has been devoted to the constitutive properties of fractured and comminuted ceramics. In fact, the main differences between the various models cited above, are due to the different values which they assign to the strength of the damaged material, as reviewed by Anderson (2006). For example, the different strength values for silicon carbide which are used by the JH-1 model and the model of Walker (2003), are shown in Fig. 6.22, from Anderson (2006). The strength of the fractured ceramic is 1.3 GPa in the JH-1 model and 3.7 GPa in Walker's model. These very different values were obtained by adjusting the models to different sets of experimental results, enhancing the need for well calibrated properties of failed ceramics. The data points for the strength of the intact ceramic, from several sources, are also shown in the figure.

In order to demonstrate the predictive capability of these models, consider the simulation results from Holmquist et al. (2008) for a SiC tile impacted by a gold rod

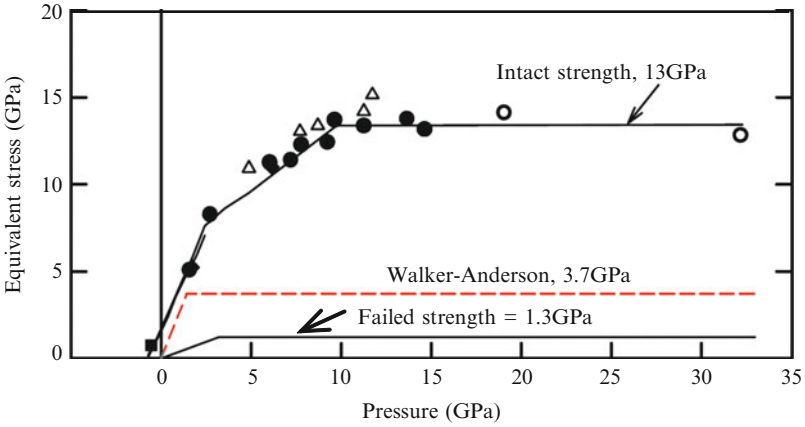

Fig. 6.22 The JH-1 model for SiC and the Walker–Anderson failure surface

at a velocity of 1.38 km/s, as shown in Fig. 6.23. The radiographs of the corresponding experiment are shown in Fig. 6.19. One can clearly see the excellent agreement between the simulation and the experiment concerning the advancement of the penetration process and the damage around the crater. Such an agreement strongly enhances the validity of the material model which was used for this ceramic.

The effect of the buffer discs has been investigated through numerical simulations by Holmquist and Johnson (2002), and Holmquist et al. (2005, 2008). A comparison between the simulation results and the experimental radiographs from Holmquist et al. (2008), for a buffered SiC tile impacting a gold rod at 1.484 km/s, is shown in Fig. 6.24. The copper buffer in this experiment and in the

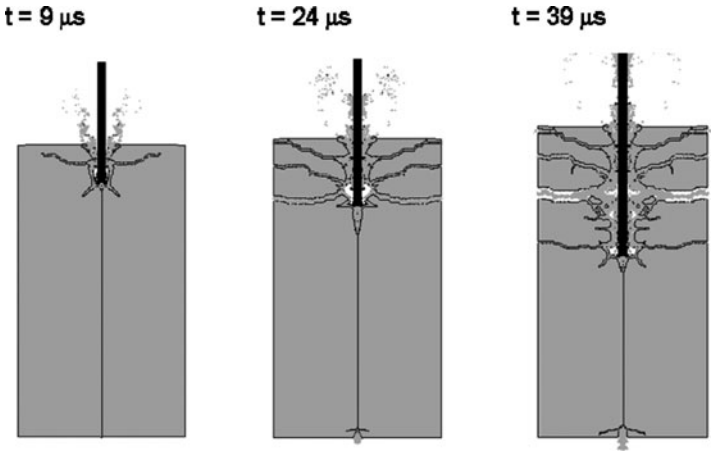

Fig. 6.23 Simulation results for the impact of a gold rod at a SiC cylinder

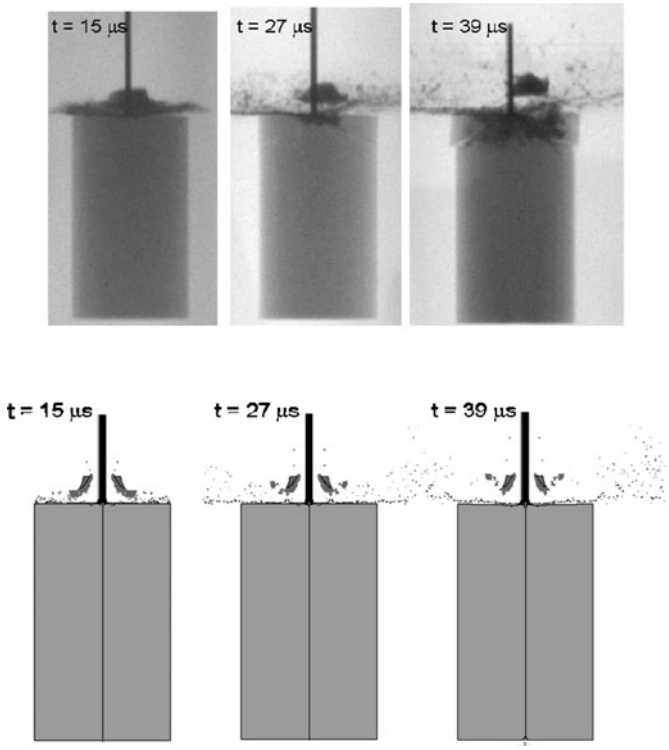

Fig. 6.24 Experimental and simulation results for a buffered SiC cylinder impacted by a gold rod at 1.484 km/s

simulation was 5 mm in diameter and 4 mm thick. The diameter of the rod was 1.0 mm and its length 70 mm, as in the impact on the bare tile at 1.38 km/s which was shown in Figs. 6.19 and 6.23. Clearly, the copper buffer prevented the penetration of the tile at the higher impact velocity, while the bare tile was easily penetrated by this rod at the lower velocity. Thus, both experiments and numerical simulations demonstrate that the addition of a small copper buffer leads to a significant increase in the range of impact velocities for the interface defeat phenomenon.

In order to demonstrate the effect of the copper buffer consider the simulation results of Holmquist et al. (2005), as shown in Fig. 6.25. These simulations were performed for bare and buffered silicon carbide tiles, impacted by a D = 0.75 mm L = 30 mm gold rod, at various velocities. The results of these simulations agree with the experimental data, as far as the interface defeat velocities and the corresponding dwell times are concerned.

Both experiments and simulations show that a bare SiC tile defeats these gold rods at impact velocities up to about $V_0 = 0.9$ km/s, which can be defined as the threshold velocity (V_c) for penetration. The stagnation (Bernoulli) pressure which corresponds to this impact velocity is: $P = 0.5\rho_p V_c^2 = 7.8$ GPa. On the other hand, the buffered SiC tile was shown, both experimentally and numerically, to defeat

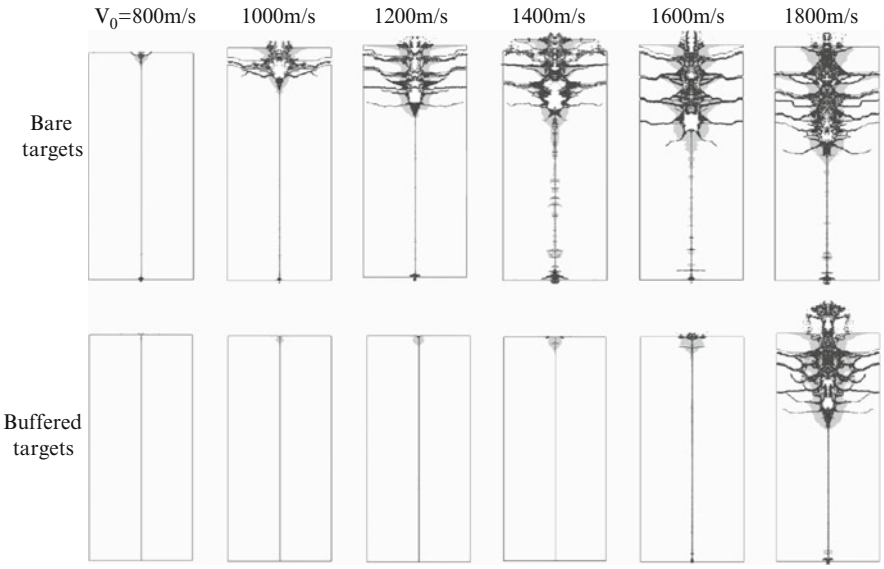

Fig. 6.25 Simulation results for bare and buffered SiC tiles impacted by gold rods at different velocities

the gold rods even at an impact velocity of $V_0 = 1.65$ km/s, corresponding to a stagnation pressure of about 26 GPa. Thus, the addition of a copper buffer increased the threshold pressure by a factor of 3.3. Such enhancements of the ballistic resistance draw much interest among armor designers for the practical application of ceramics tiles.

According to Holmquist et al. (2005) the buffer should be large enough to attenuate the impact shock which is delivered to the tile, and to induce a mushroom shape to the rod's nose in order to spread its load over a larger area. The buffer also applies some compressive pressure over the impacted area for a short time, which is enough to prevent the early failure of the tile by tensile stresses around the impact zone. The buffer material should have a high density to reduce the loading stress on the ceramic face. Simulations with a polycarbonate buffer resulted in a higher and steeper loading profile at the surface of the tile, as compared with those induced by either copper or tungsten buffers. These simulations were performed for a gold rod impacting the buffered silicon carbide tile at 1.6 km/s, and the impact stresses at the symmetry axis, for the three different buffers, are shown in Fig. 6.26, from Holmquist et al. (2005). The estimated impact shock which the gold rod imparts to the bare silicon carbide at $V_0 = 1.6$ km/s, is 38 GPa. The addition of copper or tungsten buffers reduces the amplitude of this shock to a level of 26.3 GPa, and spreads its rise time considerably, as is clearly seen in the figure. With the material parameters which were used in these simulations, the transition from interface defeat to the dwelling phase takes place at a stress level of about 26 GPa.

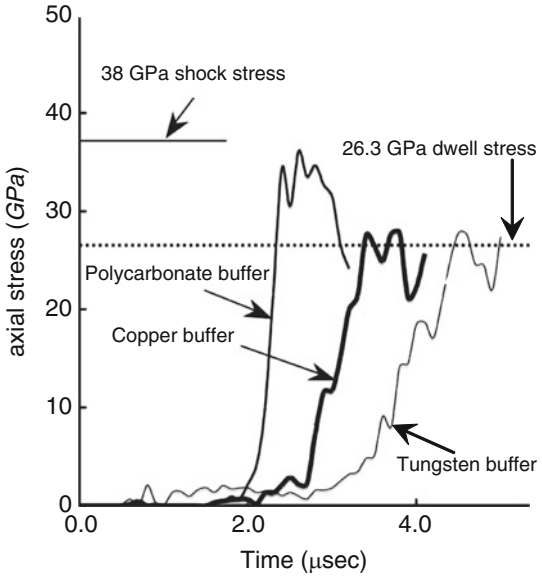

Fig. 6.26 Simulation results of the loading stresses for different buffer materials

Malaise et al. (2000) also obtained a significant increase in the interface threshold velocity by using a different experimental setup. They compared the penetration performance of L/D = 10, D = 5 mm WHA rods, which were encased by a large polycarbonate cylinder, with the penetration characteristics of a free flying rod. These rods impacted 30 mm thick SiC tiles which were backed by large steel blocks, at impact velocities of about 1.45 km/s. The free flying rod perforated the whole ceramic tile and left a residual penetration of 4.5 mm in the steel backing. On the other hand, the impact of the encased rod resulted in a dent of only 3 mm at the impact face of the tile, demonstrating the strong effect of the plastic encasement. The effect was attributed to the mushrooming of the plastic cylinder around the rod for a relatively long time. Thus, the impact of the plastic cylinder, and its subsequent mushrooming, applied high compressive stresses on the impact face of the ceramic tile and prevented its early failure by tensile stresses, as in the case of the copper buffer.

In conclusion, the role of the various buffers which were described here is to reduce the amplitude of the initial shock pressure to a value below the threshold for damage initiation, to prolong the compressive loading of the impact face, and to spread the load over a large area through the mushroomed shape of the rod. We should emphasize that the material parameters for the damaged ceramics, in all the simulations described above, are actually calibrated by experimental results. Thus, the fact that the simulation results agree with experimental data does not mean that a full understanding of the damage process has been achieved. Clearly, a theoretically based model for damage initiation and its evolution in impacted ceramics is needed in order to understand these empirical observations.

A simplified version of the JH-1 model was suggested by Rosenberg et al. (1995). This model accounts for much of the penetration data for long rods impacting ceramic tiles which are backed by thick metallic blocks. The model is based on experimental data for the constitutive properties of the intact material, which include its compressive strength (Y_c) under uniaxial stress conditions, its tensile strength (spall), and its compressive strength under high shock pressures (Y_{max}). The values of Y_{max} are measured by the lateral gauge technique which was described in Chap. 1. For materials which exhibit a constant strength at high pressures, the failure curve of the intact material is a bilinear line, as shown schematically in Fig. 6.27. The figure shows the constitutive relations for the intact and the failed material. When the stress state in an element of the numerical scheme reaches the upper curve, its strength is reduced to the lower curve which accounts for the properties of the failed material. This curve starts from the origin (no tensile strength) and it increases linearly with a certain slope up to the maximal strength of the failed material. This slope and the maximal strength level of the failed material are obtained by multiplying the corresponding slope and the maximal value (Y_{max}) of the intact material, by the failure parameter ($f < 1.0$), which is the only free parameter in the model.

The value of the failure parameter (f) for a given ceramic is obtained by the following procedure. Given a set of penetration experiments, choose one of them as the calibration experiment, and vary the value of the failure parameter (f) in the corresponding simulations until a match is obtained with the experimental penetration depth. All the other experimental results should be accounted for by simulations with the same value of the failure parameter (f). This technique resulted in a value of $f = 0.3$ for the AD85 alumina tiles which were analyzed by Rosenberg et al. (1995), and a value of $f = 0.45$ for the AD995 alumina in Rosenberg et al. (1997b).

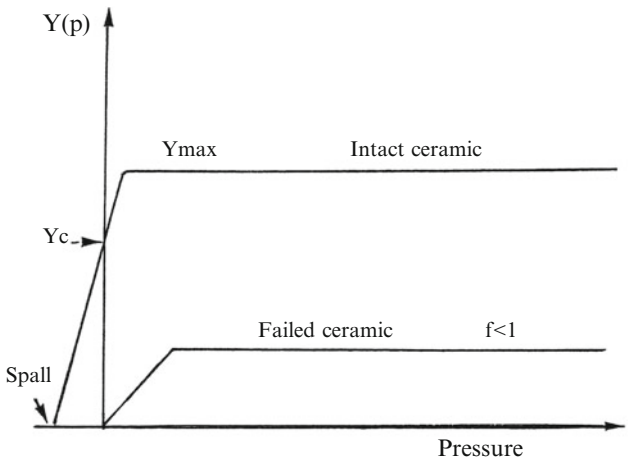

Fig. 6.27 The simplified model for ceramics

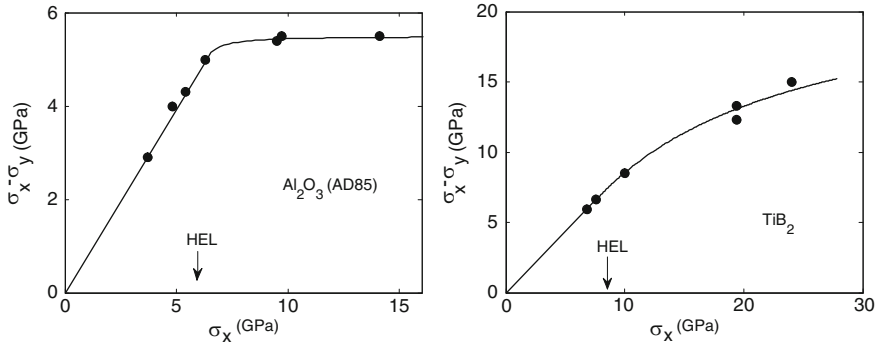

Fig. 6.28 The principal stress difference of AD85 alumina and TiB_2 as determined by longitudinal and lateral stress gauges in plate impact experiments

The value for the high pressure strength (Y_{max}) of the intact ceramic (Y_{max}) is obtained by using longitudinal and lateral stress gauges in plate impact experiments, as described in Chap. 1. These gauges determine the two principal stresses (σ_x and σ_y) in the shocked specimen, and its strength under high pressures is derived through a proper yield criterion. Using the von-Mises criterion results in: $Y_{max} = \sigma_x - \sigma_y$. The results for AD85 alumina from Rosenberg et al. (1987a), and for titanium-diboride from Rosenberg et al. (1991a), are shown in Fig. 6.28. It is clearly seen that the alumina specimens exhibit a constant strength at high pressures, which was also the case for aluminum-nitride as measured by Rosenberg et al. (1991b). On the other hand, the TiB_2 ceramic showed a pressure hardening effect, with a significant increase in strength with increasing shock pressures.

6.3.4 Ceramics Against Shaped Charge Jets

We have seen that the ballistic efficiency of various ceramics against high-density long rods is of the order of $\eta = 2.0$–3.0, as compared with armor steel targets. These relatively high efficiencies of the ceramic tiles are due to their high compressive strength and their low densities. Experimental results for both ceramic and glass blocks showed that they are even more efficient against shaped charge jets, resulting in values in the range of $\eta = 4.0$–5.0, as compared with armor steels. This fact was demonstrated for glasses by Hornemann (1989), Solve and Cagnoux (1990), Finch (1990), Moran et al. (1991) and Kozhushko and Rykova (1994), and for several ceramics by Kozhushko et al. (1992). It may seem that the high strength of these materials is more effective against the high speed jets, in contrast with the accepted knowledge that at high impact velocities the strength of the target becomes less important. High speed pictures and x-ray radiographs showed that the penetrating jet elements are significantly deflected from their original line of flight during penetration, by the action of some lateral forces. Thus, it was concluded that

the high efficiency of these materials against shaped charge jets is due to a lateral action, rather than to their high strength. These lateral disturbances were related to the dilatancy phenomenon in brittle materials. This term refers to the extra expansion of their volume after stress unloading, as a result of crack initiation and growth during the loading phase. Specifically, the enhanced efficiency of glass targets against shaped charge jets was attributed to the lateral impact of glass debris with the penetrating jet elements.

This issue has been investigated by Rosenberg et al. (1995) using numerical simulations for high velocity L/D = 10 zero strength rods impacting ceramic tiles which were backed by thick steel blocks. An impact velocity of 5.0 km/s was chosen for these simulations in order to represent the average velocity of the different jet elements. A 10 mm steel plate was place in front of the 40 mm alumina tile in these simulations. The failure model of the ceramic tile was the one described in the previous section with f = 1.0, in order to avoid the complications resulting from early failure. The simulations showed that the final crater depths in the steel backings are practically the same for ceramic strengths in the range of 3.0–9.0 GPa, confirming the notion that at these impact velocities the strength of the target plays a minor role on its resistance to penetration. However, the diameter of the crater in the tile decreased appreciably with increasing tile strength. More importantly, the crater walls in these simulations were collapsing laterally on the jet, and more material was launched towards the axis with increasing tile strength. The laterally moving material included both ceramic debris from the crater walls, and the inverted jet elements which lined the wall after penetration. This lateral motion for the 6.0 GPa alumina is shown in Fig. 6.29. One can clearly see that sometime

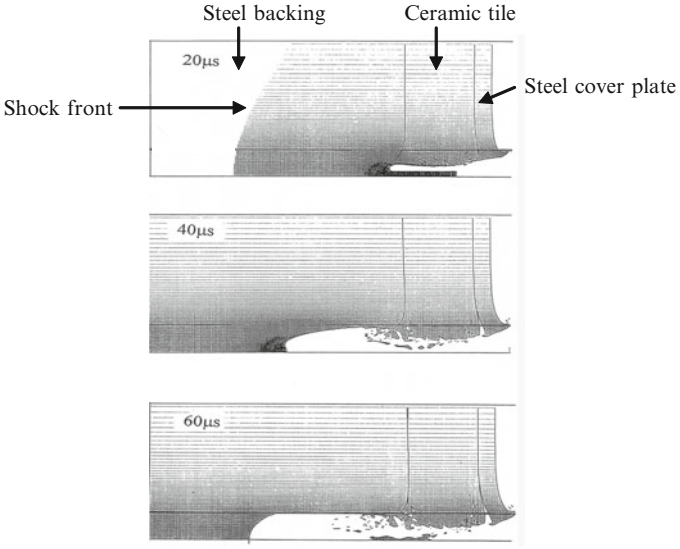

Fig. 6.29 Simulation results for the jet debris and inverted rod motion towards the symmetry axis

between 40 and 60 μs after impact, a large portion of the inverted rod material reached the symmetry axis with a significant lateral velocity. This laterally moving material can deflect the slower parts of a long jet, resulting in the enhanced ballistic efficiency of ceramics and glasses against shaped charge jets.

The numerical simulations of Rosenberg et al. (1995) highlighted the relation between the strength of the tile and the degree of these lateral disturbances, through the amount of material which is launched laterally towards the axis, as shown in Fig. 6.30. The figure shows the state of the tiles and the debris along the penetration axis at relatively late times, in order to emphasize the differences between the three cases. The simulation for the 3.0 GPa tile showed that no material was propelled towards the axis. On the other hand, the 9.0 GPa tile propelled more material, and at much earlier times, as compared with the 6.0 GPa tile. As is clearly seen here, the residual penetrations of the rods were practically the same for the different strength tiles, because their penetration process was over before the arrival of the lateral debris at the axis. With much longer jets, this debris is bound to impact their slower elements and reduce their penetration capability. Thus, the increased

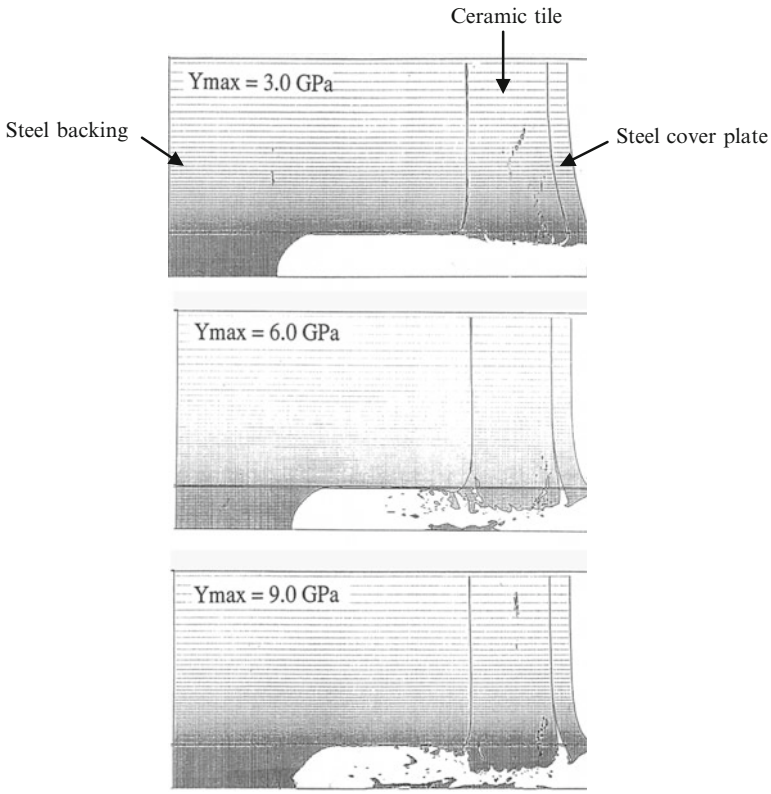

Fig. 6.30 The effect of ceramic strength on the lateral motion of the debris

efficiency of high strength ceramics and glasses against shaped charge jets has to do with the lateral impacts of the inverted jet debris, as depicted by these simulations.

6.4 Woven Fabrics as Armor Materials

We have seen that the optimal design for add-on armors is based on layered targets with low density materials, where the first layer has a high compressive strength (such as a ceramic tile) and the back plate has a high tensile strength, in order to absorb the debris from the projectile and the front plate. Composite materials which are based on woven fabrics have been found to be very efficient as the backing materials for ceramics and hard metallic plates, due to their improved specific strengths (the strength/density ratios). The first composites were introduced in the 1960s and they included glass fibers which reinforced various plastics (GFRP). More efficient materials are based on aramide fibers (trade name of Kevlar®), the ultra-high molecular weight polyethylene fibers (trade named Spectra® and Dyneema®), and the PBO fiber which was first marketed by the name Zylon®. The low density of these organic fibers, in the range of 1.0–1.4 g/cm^3, and their high tensile strength (around 3.0 GPa) led to their extensive use for various ballistics applications, from the protection of space stations to body armor vests. These fibers have high initial elastic moduli (around 100 GPa) and tensile failure strains of 3–5%, resulting in excellent energy absorption capabilities which surpass the energy absorption by metals. The fibers are bundled into yarns and these are woven into layers which are then stacked together, with or without impregnation, in order to produce the armor structure. The fibers are woven into 2D or 3D structures through different weaving techniques, as described by Zaera (2011). Comprehensive accounts of the properties and manufacturing processes of fibers, yarns, and woven fabrics, as well as their use in different armor systems, are given in Bhatanagar (2006) and in Abrate (2011). The most extensive use of fabrics is for vests which are manufactured either with fabric laminates alone, or with ceramic tiles attached to their front. Fabric laminates are also attached to the inner walls of armored vehicles as "spall liners", in order to stop the behind armor debris (BAD) which is generated by the penetrating threat. The fabrics themselves are used as either "dry" sheets sewn together, or impregnated with resins such as polyester or epoxy.

In order to follow the ballistic response of a panel made of several sheets of woven fabrics, researchers usually start with the response of a single yarn to the lateral impulse of a ballistic impact. The woven sheet is then considered with some assumptions concerning the cross joints of the fibers. Finally, the response of a bundle of sheets, either with or without the resin, has to be considered. Cheeseman and Bogetti (2003) review the important factors which control the perforation process of fabrics and compliant composites. These factors include the material properties of the yarns, the fabric structure, the shape and impact velocity of the

projectile, the interaction of multiple plies, the far-field boundary conditions, and the friction between the yarns and the projectile. This variety of different factors complicates the analysis of the penetration and perforation processes, and the conclusions from a given set of experiments cannot be generalized for other cases. For example, Jacobs and Van Dingenen (2001) observed that uniderctional layers of Dyneema fibers placed at $0^o/90^o$ orientation on top of each other perform much better than woven fabrics under the impact of blunt projectiles. They claim that this result is due to the fact that the $0°/90°$ arrangement allows for a much wider area of the structure to take part in the interaction. This conclusion holds only for blunt-nosed projectiles and, probably, for these fibers alone. Obviously, these complex factors are the main reason for the scarcity of analytical approaches to these projectile/composite interactions, although much progress has been made through empirical studies and numerical simulations.

The complexity of the interaction between projectiles and textiles can be appreciated by the post mortem pictures from Irenmonger (1999), as shown in Fig. 6.31. These are sectioned targets of Dyneema® which were impacted by 5.56 mm projectiles having a lead core and a hard steel tip. Note the shearing process of the thin target (H = 11 mm) which was easily perforated by the projectile, resulting in a crater diameter which is close to that of the projectile. This is the typical failure mode of relatively thin targets which are perforated by sharp-nosed projectiles at high impact velocities. The right hand side of the figure shows the more complex interaction for the H = 22 mm target, which was thick enough to defeat this projectile. The sectioned target shows that a shearing action by the projectile took place during the first stages of its penetration. At the later stages, the target exerted its high tensile strength on the projectile, as is evident by the extensive deflection and delamination of the back plies. This is the more common mode of operation for fabrics when they are used as backing layers in composite targets. With these configurations the fabrics exhibit their superior tensile properties in stopping debris, leading to their high ballistic efficiency. The large crater diameter at the later stage of penetration is due to the gross deformation

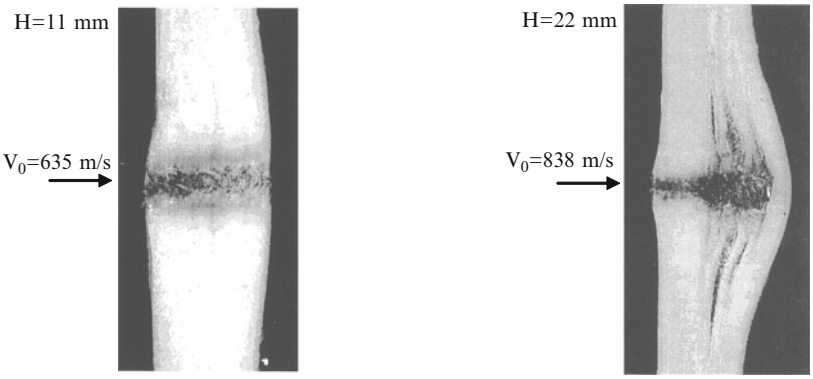

Fig. 6.31 Cross sections of Dyneema targets impacted by 5.56 mm projectiles

of the projectile during this stage. This deformation resulted in a much larger volume of fabric which participated in the process, as seen in the picture.

The geometry of the projectile and its impact velocity determine the failure mode of the fabric, and it is obvious that sharp-nosed projectiles actually wedge through the fabric with relatively low resistance to their motion. With higher impact velocities the yarns are sheared by the projectile, as shown above, and they can even rupture upon impact, as described by Cheeseman and Bogetti (2003). Thus, the best performance of these composites is achieved against low velocity blunt projectiles, where the yarns absorb a large part of the projectile's kinetic energy through large transverse deflections. It should be noted that for ballistic applications the resin content in the composite should be around 20% in order to enable large deflections of the plies. For the same reason, the fiber-matrix adhesion should not be too strong. When a multiple-ply target is impacted by the projectile the first few layers are sheared, as shown on the right hand side of Fig. 6.31. The remaining layers behave as a membrane and they absorb the projectile's energy through their deflection, exerting their optimal properties and high efficiencies. These features are clearly demonstrated by the experiments and numerical simulations of Gama and Guillespie (2011) with thick S-2 glass/SC15 laminates, which were impacted by L/D = 1 steel cylinders. In order to follow the relevant material properties for these projectile/fabric interactions we summarize some of the important issues concerning these interactions.

The early work on single yarn impact is considered as the basic theory for transverse loading of a woven sheet, as reviewed by Rakhmatulin (1966). The salient features of this theory, as developed by Smith et al. (1958), can be stated with reference to Fig. 6.32, which describes a transversely impacted yarn. The figure describes the shape of the loaded yarn as obtained by high speed photography, which show that the yarn takes a triangular shape which increases with time until failure takes place.

The mathematical treatment of this developing triangular shape assumes that upon impact, longitudinal and transverse strain waves are propagated outward from the impact point at different velocities. The longitudinal wave, which moves at the elastic wave velocity $c_0 = (E/\rho)^{0.5}$, puts the material under certain tensile stress (σ_0) and strain (ε_0). The high elastic moduli of these fabrics, together with their low densities, result in very high values of c_0. This means that a large portion of the

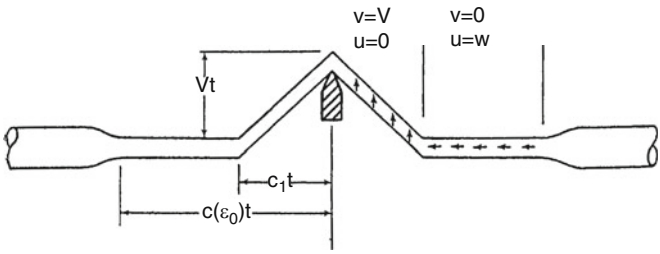

Fig. 6.32 Schematic description of a textile yarn impacted by a rigid projectile

target is engaged in the interaction with the projectile, enhancing its energy absorption capability. The material behind this wave front moves at a certain velocity (w) towards the impact point. The transverse wave, which propagates behind the longitudinal wave at a velocity of c_1, changes the direction of material motion towards that of the projectile. Behind the transverse wave front all particle velocities are equal to the velocity of the projectile (V), and the constant-angle triangle continues to grow with time. For a material with a constant modulus (E) the following relation was derived between the strain in the fiber (ε_0) and the projectile's velocity (V), as described by Roylance (1977):

$$V^2 = \frac{E\varepsilon_0\left(2\sqrt{\varepsilon_0 + \varepsilon_0^2} - \varepsilon_0\right)}{\rho} = c_0^2 f(\varepsilon_0) \tag{6.9}$$

This relation can be solved numerically in order to compute ε_0 in terms of V, for the purpose of design curves of a given fabric. Once ε_0 is known, all the other parameters of the problem such as σ_0, c_1 and w, can be determined for a given impact velocity. For example, the transverse wave velocity is given by:

$$c_1 = c_0\left(\sqrt{\varepsilon_0 + {\varepsilon_0}^2} - \varepsilon_0\right) \tag{6.10}$$

With this simplified analysis one can calculate the strain energy $\sigma_0\varepsilon_0/2$ and correlate it with the energy absorption rate of the fiber. When the maximal values for the tensile stress and strain are inserted in (6.9), the maximal value for V which marks the onset of fiber failure, is obtained. These critical velocities are seldom realized in the experiments and, in fact, the actual critical velocities are lower by a factor of two than the theoretical values. Several explanations have been suggested for this discrepancy, as in Bazhenov et al. (2001), but the issue is still unresolved. The work of Tan et al. (2003) examined the influence of the projectile's nose shape on the ballistic limits, the energy absorption behavior, and the perforation mechanisms of a single ply of plain woven aramide target. The experiments showed that the same trends were obtained for all the different projectiles shapes, namely, an increase in energy absorption up to a critical velocity and a subsequent decrease at higher velocities.

In order to demonstrate the high tensile elongations which can be achieved by a single yarn, consider the high speed pictures of a blunt nosed projectile on a nylon yarn, from Jameson et al. (1962), as shown in Fig. 6.33. The images in this figure are slightly displaced in order to highlight the fiber's extension in the way depicted by Fig. 6.32.

One should note that the ballistic efficiency cannot be increased indefinitely by increasing fiber stiffness as this is accompanied by a decrease in failure (breaking) strain. Thus, a complete model should have a relation between the two parameters in order to determine the optimal stiffness of the fabric. Considering the ballistic performance of a textile structure which consists of several plies, one has to take into account some conflicting trends which will adversely affect the

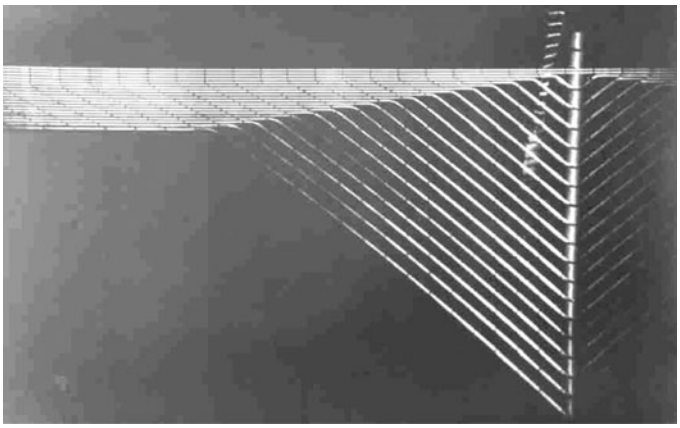

Fig. 6.33 High speed pictures of a nylon yarn impacted by a projectile

performance of the system, as described by Cunniff (1992). Adding plies may constrain the transverse deflection of the first plies, amplify the concentration of tensile stresses, and reduce the ballistic efficiency of the structure. Cunniff (1992) analyzed several aspects of the structure performance, such as the aperture size of the frame fixture which constrains the fabric. As expected, a larger aperture resulted in a higher ballistic limit velocity, since the plies could undergo larger deflections.

A large amount of data concerning the ballistic behavior of different fabrics has been summarized by Cunniff (1996) and in several papers which he presented at the 18th International Symposium on Ballistics (1999). Most of the data relates to right circular cylinders of an aspect ratio of L/D = 1, made of either steel or tungsten alloy. The textiles he analyzed included different Kevlar and Spectra fabrics as well as nylon (6,6), E-glass and others. As with metallic plates there are two issues which concern the armor designer, namely, the ballistic limit velocity (V_{bl}) of a given projectile/fabric combination, and the residual velocity (V_r) as a function of impact velocity for $V_0 > V_{bl}$. The general behavior of V_r as a function of V_0 is demonstrated in Fig. 6.34 from Cunniff (1996), for an 8-ply Kevlar 29 target impacted by steel cylinders of different mass: M = 0.13, 0.26, 1.04 and 4.16 g. One can see that the data follow similar trends as for metallic plates, with a steep rise of V_r for impact velocities just above the corresponding ballistic limits, and an asymptotic approach to a straight line which is parallel to the $V_r = V_0$ line (denoted by the dotted lines in the figure). With increased projectile mass the ballistic limit velocities decrease and the straight asymptotes approach the $V_r = V_0$ line, as for metallic targets.

The actual values for the ballistic limit velocities, as shown by Cunniff (1999a, 1999b) for a large number of projectile/target pairs, can be simply related to their areal density ratio. He showed that the values of V_{bl} can be scaled through a normalizing velocity (U*) which is typical for each fabric. This velocity is given

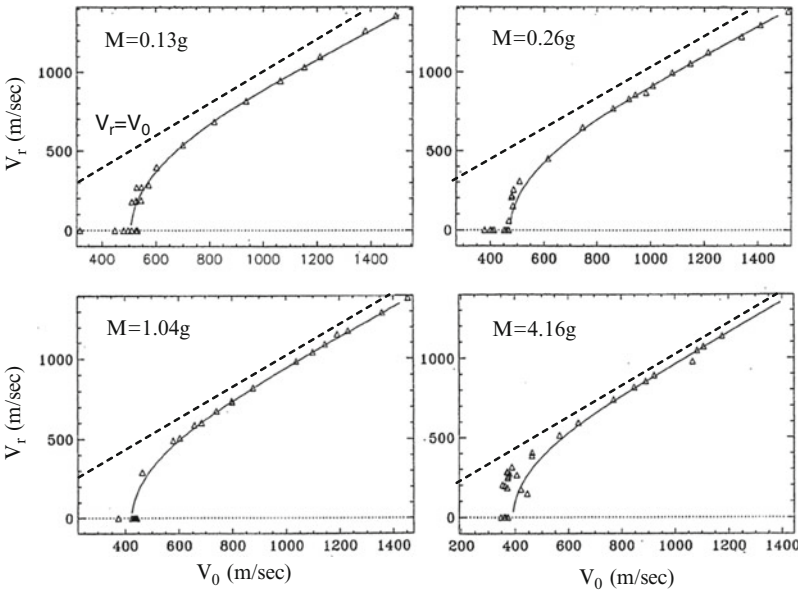

Fig. 6.34 The residual velocities of steel fragments perforating an 8-ply Kevlar 29 target

in terms of the strain energy $\sigma_f\varepsilon_f$ of the fabric, where σ_f and ε_f are its tensile failure strength and strain, respectively, and by its sound velocity (c_0), according to:

$$U^* = \left(\frac{\sigma_f \varepsilon_f c_0}{2\rho}\right)^{1/3} \tag{6.11}$$

With this velocity Cunniff (1999b) showed that the results for V_{bl}/U^*, for a large number of projectile/fabric combinations, are correlated with their areal density ratios. Thus, his empirical observations reduce to a universal relation between V_{bl}/U^* and the areal density ratio AD_t/AD_p:

$$\Phi\left(\frac{V_{bl}}{U^*}, \frac{AD_t}{AD_p}\right) = 0 \tag{6.12}$$

where the subscripts (t) and (p) relate to the target (the fabric) and the projectile, respectively. The tensile failure stresses (σ_f) for the various fabrics which were analyzed by Cunniff (1999b), are in the range of 3.0–5.0 GPa, and their failure strains are in the range of $\varepsilon_f = 3$–4%.

The same trends were found by Van-Gorp et al. (1993) who analyzed V_{bl} data for several fabrics impacted by rigid FSPs of different size. They showed that the data can be represented through a linear relation between the energy absorbed by the

fabric and the areal density ratio. Thus, their results for the ballistic limit velocity of a given projectile/fabric pair can be written as:

$$V_{bl}{}^2 = C\frac{AD_t}{AD_p} \tag{6.13}$$

where the slope (C) depends on the fabric type.

Walker (2001) offered a simple analysis for the perforation process of composites, and derived an expression for V_{bl} of a given projectile/fabric combination. Through momentum conservation, the following relation is obtained between the impact velocity (V_0) and the velocity of the projectile and the fabric right after impact (V):

$$V = \frac{MV_0}{M + \psi A_p \rho_f} \tag{6.14}$$

where M and A_p are the mass and the projected areas of the projectile, respectively, and ρ_f is the density of the fabric. The factor ψ denotes the actual area of the fabric under the projectile which takes part in the interaction, and Walker (2001) chose a value of $\psi = 2.5$ for his model. Realizing that the fabric can be stretched to a maximum value of ε_f, he arrived at the following relation for the ballistic limit velocity:

$$V_{bl} = 1.8\left(1 + \psi X_f\right) c_0 \varepsilon_f \tag{6.15}$$

where X_f is the corresponding projectile/fabric areal density ratio. This simple relation accounts for much of the data for the different fabrics which were impacted by L/D = 1 steel cylinders. Typical values for ε_f range between 3% and 4% for the different fabrics, as summarized by Cunniff (1999b).

The addition of resin to the fabrics results in a complex behavior which was further analyzed by Walker (2001). For a few sheets of fabrics this addition degrades the ballistic performance of the target. On the other hand, as the areal density of the fabric increases the fabric/resin panel outperforms the equivalent areal density dry fabric. It was found experimentally that the crossover in their ballistic performance is in the region where the amount of fabric involved in the momentum balance is equal to the mass of the projectile. In order to account for this complex behavior Walker (2001) considered the two contradicting effects of the resin. On the one hand, this addition is at the expense of fabric material, for equal areal density targets, and it is expected to lower the ballistic limit of the fabric /resin panel. On the other hand the addition of resin improves the bending resistance of the composite, increasing its ballistic limit velocity. He derived the following relation for $V_{bl}(X_f,r_f)$, where r_f is the mass fraction of the resin, in terms of the ballistic limit velocity of the dry fabric $V_{bl}(X_f,0)$:

$$V_{bl}\left(X_f, r_f\right) = \sqrt{1 - r_f + r_f\left(\psi X_f\right)^3} V_{bl}(X_f, 0) \tag{6.16}$$

This equation accounts for the ballistic limits of "dry" and "wet" Kevlar 29 panels, and for the crossover value of X_f, which was observed experimentally.

The published literature on numerical simulations for the impact on fabrics is very extensive, and they can be classified as either discreet or continuum simulations, as summarized by Chocron et al. (2011). The discreet simulations started with a 1D bar element which was pin-jointed to other elements in order to simulate the woven fabric, as in Shim et al. (1995). The 2D discreet approach uses shell elements which provide a more realistic interaction between the yarns, as well as between the layers. The 3D discreet approaches, where the fabric is described by solid elements which represent the yarns, are very popular since the availability of fast and powerful computers. Duan et al. (2006) and Rao et al. (2009) studied the effect of friction and performed sensitivity studies of various parameters. The continuum approach avoids the need to describe the yarns individually. Tensile and shear tests on the fabrics are used to evaluate the unit cell properties, and they are then tested against the data from ballistic tests. Chocron et al. (2011) used a mixed mode in the sense that the fabric was simulated in a discreet yarn level, and the yarns are composed of solid elements, as was first done by Shockey et al. (1999). The numerical models used by Chocron et al. (2011) for Kevlar KM2, Dyneema and PBO, were thoroughly checked against various experiments. These experiments included single yarn and single layer impacts, as well as multilayer and ballistic limit determinations. Good agreement between the simulation results and the experiments were obtained (of the order of 10%) and one can use such simulations as a design tool and save a lot of experimental work. An example for the capabilities of such simulations is given in Fig. 6.35, from Chocron et al. (2011). This is a perspective view of the pyramidal development in a Dyneema target composed of ten layers, which was impacted by a fragment simulating projectile (FSP).

As was mentioned above, the main advantage of fabric materials stems from their high specific strength, as defined by their tensile strength/density ratio. Their

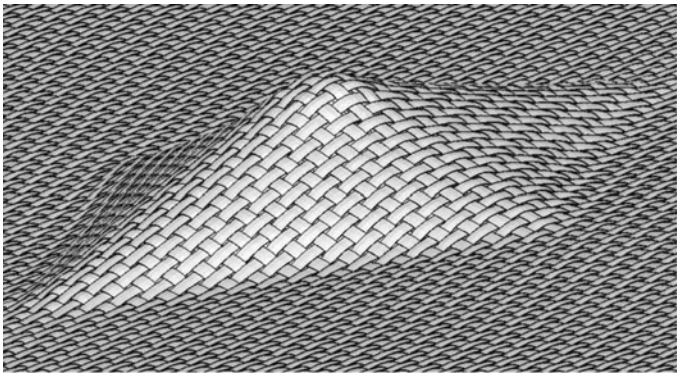

Fig. 6.35 The simulation result for the evolving deflection of a composite target, at 35 μs after impact of an FSP

high ballistic efficiency against blunt-nosed fragments makes them ideal as backing materials for either ceramic tiles or metallic plates. Basically, the hard facing material shatters the projectile, while the fabrics stop the fragments by applying their improved tensile properties. Obviously, the fabrics do not perform as well when they are directly impacted by sharp-nosed rigid projectile. This is the main reason for the fact that only a few experimental studies were devoted to the direct impact of these projectiles on textile targets. Zhu et al. (1992a, 1992b) impacted conical nosed hard steel projectiles at targets of Kevlar 29 plies which were impregnated by a thermosetting polyester resin. They determined V_{bl} values for two types of projectiles and for target thicknesses in the range of 3.1–12.7 mm. We wish to demonstrate now that their experimental results can be accounted for by the models which apply for metallic targets, as discussed in Chap. 4.

The projectiles in the works of Zhu et al. (1992a, 1992b) had diameters of 12.7 and 9.525 mm and masses of 28.5 and 12.5 g, respectively. The measured residual velocities, as a function of impact velocities, for the larger projectile (D = 12.7 mm) impacting the 6.35 and 12.7 mm targets, are shown in Fig. 6.36. The figure also shows the corresponding curves from the model of Recht and Ipson (1963), through the expression $V_r = (V_0^2 - V_{bl}^2)^{0.5}$, with V_{bl} values which were determined by the experiments. The good agreement between the model and the experimental results enhances the assertion that sharp nosed projectiles perforate the fabrics in a similar way to the perforation of a metallic plate.

The measured values of V_{bl} are given in Table 6.2 for the two types of projectiles perforating the Kevlar targets with different thicknesses. These values for V_{bl} show a similar dependence on target thickness as obtained for sharp nosed projectiles perforating metallic plates. In order to demonstrate this point, consider the effective

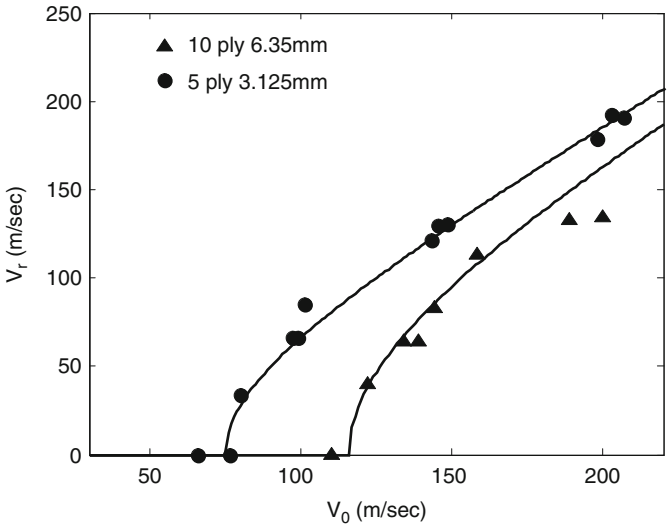

Fig. 6.36 The residual velocities for the 12.7 mm projectiles perforating the two Kevlar 29 targets

Table 6.2 The values for V_{bl} (in m/s) from Zhu et al. (1992a)

H (mm)	3.125	6.35	9.525	12.7
V_{bl} (D = 12.7 mm)	78	116	143	170
V_{bl} (D = 9.5 mm)	97	135	168	210

stresses (σ_r) which the target exerts on the projectile, as defined by (4.5): $\sigma_r = \rho_p L_{eff} V_{bl}^2/2H$, where H is the thickness of the target. The effective lengths of the D = 12.7 and 9.5 mm projectiles in this study were: L_{eff} = 28.7 and 22.4 mm, respectively. The calculated values of σ_r, as a function of the ratio H/D, are shown in Fig. 6.37. One can clearly see that the same features which were found for metallic targets perforated by sharp nosed projectiles are also evident here. Namely, there is a certain range of H/D values, between about 0.3 and 1.0, where σ_r is practically constant, while for target thicknesses outside this range, H/D < 0.3 and H/D > 1.0, the values of σ_r increase with H/D. Obviously, the few experimental results in this work are not enough to prove these similarities, and the subject deserves further experiments and analysis.

One of the applications of these composites for armor configurations is as liners behind the walls of the protected vehicle. These liners have been found to be very effective in reducing the number of fragments which penetrate the target, as well as their spatial extent. The damage to the interior of the vehicle can be reduced significantly by adding a relatively low-weight liner, as demonstrated by Lampert and Jeanquartier (1999) who shot L/D = 1 WHA cylinders at 13.7 mm steel plates, with and without Kevlar liners. The liners thicknesses ranged between 5 mm and 20 mm and the ballistic limit velocities were determined for each target. For the bare steel plates they obtained V_{bl} = 970 m/s, while for the steel plate with liners of

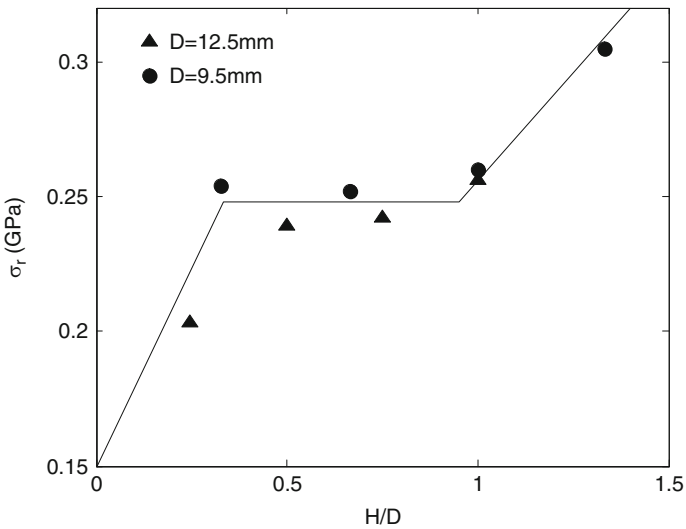

Fig. 6.37 The relation between σ_r and H/D for Kevlar 29 targets perforated by sharp-nosed projectiles

5, 10 and 20 mm they obtained $V_{bl} = 1350$, 1630 and 1900 m/s, respectively. These significant improvements in the stopping power of the steel/liner targets were accompanied by a substantial reduction in the number of fragments and their spatial extent, at impact velocities above the corresponding V_{bl} values.

Finally, consider the ballistic efficiency of thick targets made of composite materials, against long rod penetrators. The published data on this subject is very scarce, and the study of Ernst et al. (2003) is one of the very few publications. They determined the ballistic efficiency of glass reinforced plastics (GFRP) against L/D = 20, D = 7.25 mm WHA rods. The DOP configuration with a thick RHA backing was used in these tests. The thickness of the GFRP layers varied between 22 mm and 116 mm and impact velocities were around 1.8 km/s. The most interesting result from these tests concerns the increasing trend of the ballistic efficiency with the thickness of the fabric, reaching a value of about $\eta = 1.9$ as compared with RHA, for the large thicknesses. This is a relatively high value for the ballistic efficiency against long rods and, as recommended by Ernst et al. (2003), these materials should be considered as possible candidates for passive armor designs against long rods.

Chapter 7
Asymmetric Interactions

This chapter deals with defeat mechanisms which are due to asymmetrical interactions between the threat and the target, and their possible applications for armor systems. A major advancement in understanding and optimizing such defeat mechanisms is due to the continual improvements of three dimensional codes, which can follow these interactions accurately and efficiently. The basic asymmetry is obtained by inclining the target at a certain angle to the projectile's line of flight. There are two ways to define the impact angle of the projectile, as shown in Fig. 7.1a, and we shall use both of them throughout this chapter. These are the inclination angle (α) between the velocity vector of the projectile and the target's face, and the obliquity (β) between the projectile's velocity vector and the normal to the plate. The asymmetry of the impact at inclined plates induces a net force on the projectile, which is perpendicular to the target's surface. This force induces a torque on the projectile, which can result in its ricochet at obliquities beyond a certain threshold. Such an asymmetric interaction was demonstrated by Warren and Poormon (2001), for ogive-nosed steel rods impacting thick aluminum targets at different obliquities. The trajectory of the rod for an impact velocity of 1.184 km/s and an obliquity of 45° is shown in Fig. 7.1b. The asymmetry of the force on the projectile, at the early stages of its penetration, results in from the strong changes in the resisting stresses at the entrance phase. The asymmetric force on this rod's nose result in its curved trajectory in the target and its pronounced bending, which

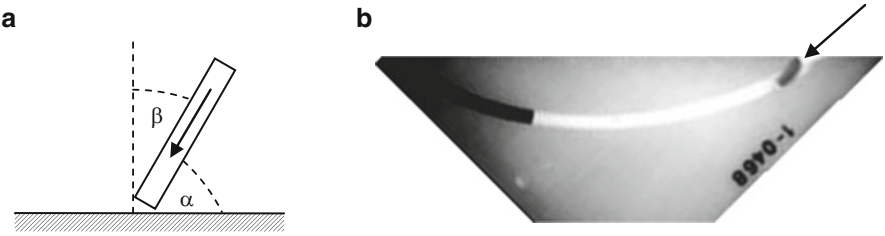

Fig. 7.1 (**a**) The definition of impact angles and (**b**) the curved trajectory of a long steel rod impacting an aluminum target at an obliquity of 45°

Z. Rosenberg and E. Dekel, *Terminal Ballistics*,
DOI 10.1007/978-3-642-25305-8_7, © Springer-Verlag Berlin Heidelberg 2012

enhanced its curved trajectory. As shown by the numerical simulations of Warren and Poormon (2001), rod bending and its subsequent ricochet was much less pronounced when the rod strength was increased by only 0.1 GPa.

For finite thickness plates the asymmetric forces on the projectile's nose act at both impact and back faces. These coupled forces result in a change in the flight direction of the projectile towards the normal to the plate, as shown schematically in Fig. 7.2a. An actual example for such a deflection of steel projectiles perforating aluminum plates is shown in Fig. 7.2b. The left side of this figure shows high speed pictures, from Piekutowski et al. (1996), of an ogive nosed steel projectile perforating an aluminum plate at an impact inclination of $\alpha = 60°$. The corresponding simulation results by Coleau et al. (1998) are shown on the right hand side of the figure. The influence of the asymmetric interaction is clearly evident by the strong deviation in the projectile's line of flight. One can also follow the appreciable bending of this projectile in the experiment which is reproduced by the numerical simulations. These bending moments can induce projectile breakup and even its total shattering, as will be demonstrate in this chapter.

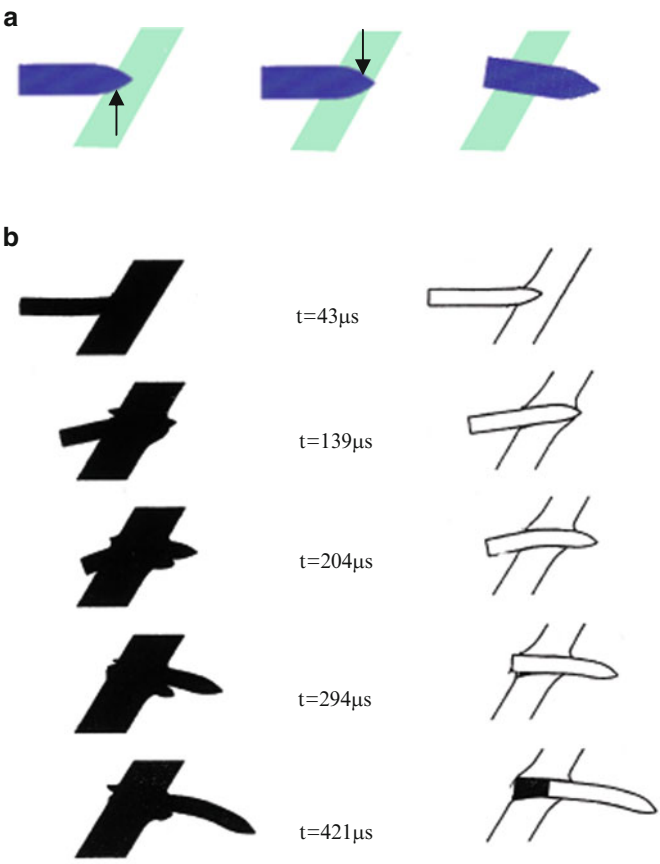

Fig. 7.2 (**a**) The asymmetric forces exerted by an inclined plate. (**b**) Experimental and numerical results for an ogive nosed steel projectile perforating an aluminum plate

These asymmetric forces can induce several defeat mechanisms which have to be well understood in order to optimize their effects for armor designs. Thick inclined plates can induce ricochet of long rods while thin plates of high hardness steel can totally shatter the hard cores of AP projectiles. The reactive and active armor concepts enhance these defeat mechanisms by adding velocity to the inclined plates, which prolongs the asymmetric interaction and increases the protective effectiveness of these devices. Much of the published work on asymmetric interactions was reviewed by Goldsmith (1999) and additional examples are given in Held (2005) and in Rosenberg et al. (2009).

There are two armor configurations which induce asymmetric interactions even though the armor itself is not inclined to the projectile's trajectory. The perforated armor plate, which was suggested by Ben-Moshe et al. (1986), is based on evenly drilled holes in a high hardness steel plate. The diameter of the holes and their spacing are so designed that the projectile always impacts an area which includes some part of a hole. The asymmetric forces on the AP projectile either break its hard core or deflect its path considerably. These perforated plates are very effective in reducing the penetration capability of the AP projectile, as demonstrated by Heritier et al. (2010) for example. They used steel plates with hardness of 600 Brinell, which were perforated to about 50% of their area, in order to stop AP projectiles up to 14.5 mm in diameter. In addition to the high ballistic efficiency of these plates they demonstrated an excellent multiple-hit capability, with plates which were impacted by twenty shots with no loss of their performances.

The second armor concept is based on ceramic spheres which induce a significant asymmetric interaction with AP projectiles except for impacts at their exact center, as was first suggested by Yeshurun and Ziv (1992). Other workers replaced the ceramic spheres with L/D = 1 cylinders having a hexagonal cross section and a spherical cap. These closely packed cylinders have a better coverage of the area, with no holes around their contact points. Both designs have an improved multiple hit capability since only a small area of the target around the impact point is destroyed at each shot. These innovations were designed for personnel protections when the ceramics are backed by woven fabrics made of aramide (Kevlar®) or the high-strength polyethylene laminates (Spectra® and Dyneema®). Rosenberg et al. (1996) demonstrated the effect of impacting a spherical surface, by using L/D = 10 ceramic rods (D = 10 mm) which were glued together side by side**.** The front parts of the impacting 0.3″ AP steel cores were shattered and their unbroken residuals acquired a significant angular velocity. These experiments demonstrated that spherical surfaces of hard ceramics are very effective in defeating AP projectiles. Obviously, the diameter of the ceramic spheres (or the cylinders), should correspond to the size of the AP projectile in a practical armor design.

The following sections discuss the main defeat mechanisms which are due to inclined plates, both static and moving. Each section deals with specific threats according to their classification as AP projectiles, long rods, and shaped charge jets. Some of the issues will be presented in a more detailed manner because they have an added tutorial value. These examples emphasize the benefits from combining experiments, numerical simulations, and analytical models in order to highlight the physics behind these interactions.

7.1 Defeating AP Projectiles

The asymmetric bending forces exerted by inclined high strength plates on AP projectile can cause their total shattering, as was shown by Yeshurun and Rosenberg (1993). They found that a relatively thin high hardness steel plate, inclined at about $\alpha = 45^{\circ}$, can totally shatter the hard steel cores of 0.5″ and 14.5 mm AP projectiles. These brittle cores are made of steel or tungsten-carbide and they shatter at a certain threshold obliquity, which depends on plate hardness and its thickness. A series of X-ray shadowgraphs, for impacts of 0.5″ AP projectiles on a 4.4 mm hard steel plate, is shown in Fig. 7.3.

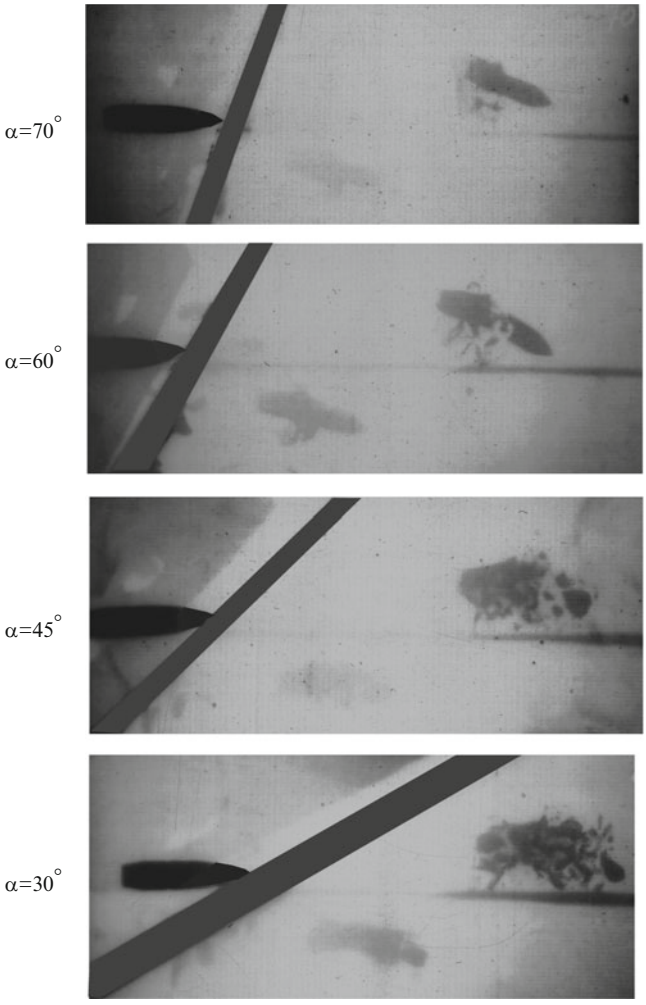

Fig. 7.3 The defeat of 0.5″ AP projectile by an inclined high strength plate

The hard steel core emerges intact for an impact inclination of $\alpha = 70°$ and its axis is diverted towards the normal to the plate, as expected. For an impact at $\alpha = 60°$ the core broke up into two large pieces in addition to its deflection. The most interesting results are shown in the lower shadowgraphs, for $\alpha = 45°$ and $\alpha = 30°$, where the core emerged totally shattered. Note that the symmetry axis of the shattered projectiles retained its original line of flight, indicating that the shattering process occurred during the early stages of perforation. Yeshurun and Rosenberg (1993) found that a high hardness steel plate, 4.4 mm thick, induces this shattering effects at a threshold angle of about $\alpha = 40°$ for 14.5 mm projectiles (both steel and WC cores) and at $\alpha = 50°$ for the 0.5″ steel core. The residual penetrations of these shattered projectiles into thick witness blocks, which were placed some distance away, were reduced by 80% as compared with the penetration depths of intact projectiles. Plates made of softer steel did not induce shattering to these cores at all inclination angles, as expected. Also, projectiles which have soft cores do not experience these shattering effects and the inclined plates are much less effective against them.

In order to gain more insight into these effects Rosenberg et al. (2009) performed numerical simulations with the AUTODYN 3D code. Such simulations can save much experimental effort for practical design purposes, by changing the values of the relevant parameters over a large range. In order to reproduce the experimental values for the threshold obliquities, the tensile strength of the projectile material in these simulations had to be much lower than its compressive strength. This brittle behavior is in accord with the actual properties of the hard cores of these projectiles, having hardness of about $60R_C$. Figure 7.4 shows simulation results for a 14.5 mm core impacting a 4 mm HH plate at two obliquities. One can clearly see that the basic features in the experimental shadowgraphs are reproduced in these simulations, namely, the total shattering at an inclination of $\alpha = 30°$ and the moderate core breaking at $\alpha = 60°$.

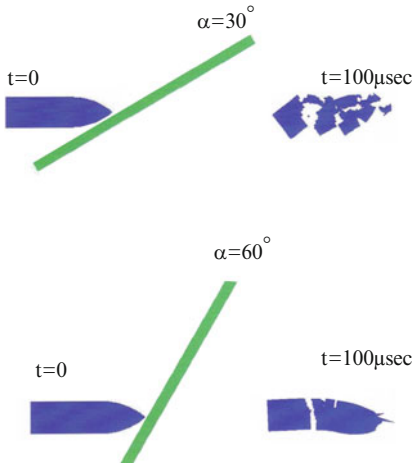

Fig. 7.4 Simulation results for a hard steel core impacting a high hardness steel plate

Various defeat mechanisms of AP projectiles impacting inclined metallic plates have been identified by the systematic work of Recht and Ipson (1962). They varied the impact velocity and the obliquity for several projectile/plate combinations, and summarized the results in graphical representations such as the one shown in Fig. 7.5. The different areas in this "configuration map" and their corresponding borders, identify the conditions for a given defeat mechanism which can aide the armor designer. One should note that in order to derive this configuration map, Recht and Ipson (1962) had to perform a large number of experiments, measure impact velocities very accurately, and recover the residual projectiles after each shot. This is a very costly and ineffective way to follow these interactions and 3D simulations should be used, after a proper calibration, in order to reduce the number of experiments which are needed to draw such maps.

A ricocheting projectile exits the inclined plate at an angle which is very close to its incidence angle, creating a rather long and shallow crater on the surface of the plate. The strength of the target is its most important property for the ricochet process of AP projectiles, as reviewed by Goldsmith (1999). In a series of experiments with inclined polymeric plates Yeshurun et al. (2001) found that Plexiglas plates can induce both ricochet and an appreciable deflection to 0.3″ AP projectiles at obliquities which can be used for practical armor designs. Other polymeric materials were tested in this study such as polycarbonate, PVC and an epoxy resin. However, only Plexiglas plates induced the enhanced ricochet which is

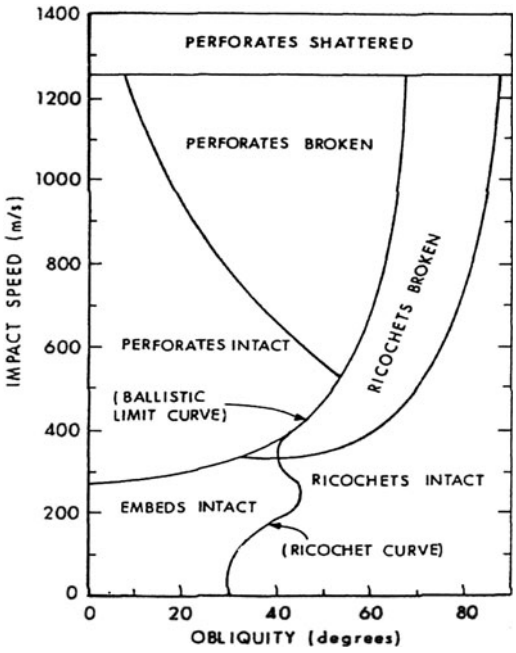

Fig. 7.5 The configuration map for 0.3″ AP projectiles impacting a 6.35 mm thick 2,024 aluminum plate

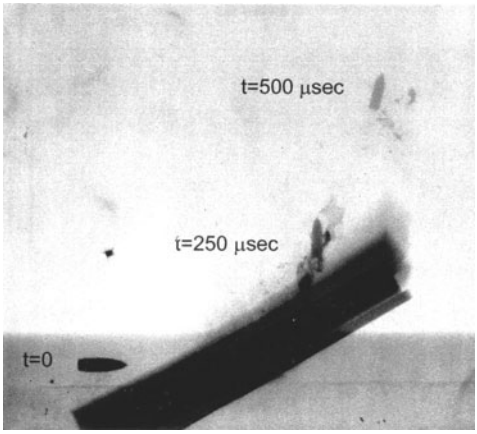

Fig. 7.6 The enhanced ricochet of a 0.3″ AP projectile from an inclined Plexiglas target

shown in Fig. 7.6. These shadowgraphs follow an 0.3″ AP projectile impacting a 20 mm thick Plexiglas plate at an inclination of $\alpha = 30°$, and emerging perpendicularly to its original line of flight.

This enhanced deflection was reproduced with 3D simulations by Rosenberg et al. (2005), who performed a parametric study of this interaction by varying the relevant properties of the polymeric plate. The simulations showed that this enhanced ricochet is due to the combination of high compressive strength and low tensile strength of the brittle Plexiglas plate. The compressive strength of Plexiglas under high strain rates can reach a value of 0.4 GPa, while its dynamic tensile strength (spall) is an order of magnitude lower. By assigning these values to the Plexiglas plates in their simulations, Rosenberg et al. (2005) reproduced the main features observed in the experiments. The basic mechanism which operates during this interaction can be understood by following the state of the plate material surrounding the projectile, as shown in Fig. 7.7.

Fig. 7.7 Simulation results for the ricochet process

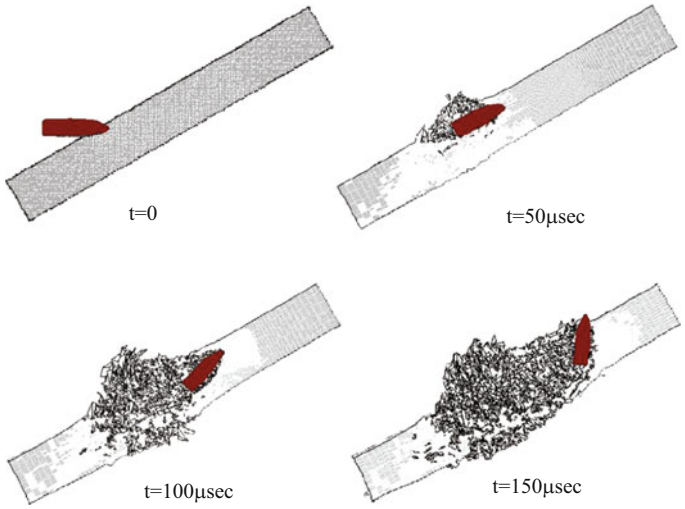

Fig. 7.8 The asymmetric force on the projectile during its penetration in the inclined Plexiglas target

During the early stages of penetration the target material above the projectile's trajectory is failing due to the tensile stresses, which are induced by the expansion of the free impact surface. On the other hand, the target material below the projectile's trajectory fails to a much less extent, since it is under compression during these stages. Obviously, the failed material cannot exert a resistive force on the projectile and it is only the material below the projectile which can affect its trajectory, as shown in Fig. 7.8. Thus, the upturning of the projectile inside the target is the result of the different states which the brittle Plexiglas attains, above and below the projectile's trajectory.

In order to appreciate the importance of the material properties for this interaction, consider the experimental result and the numerical simulations, from Rosenberg et al. (2005), for an impact at a polycarbonate (PC) plate at the same inclination of $\alpha = 30°$, as shown in Fig. 7.9. The 0.3″ AP projectile perforated the PC plate with the expected change in its flight direction. In the corresponding

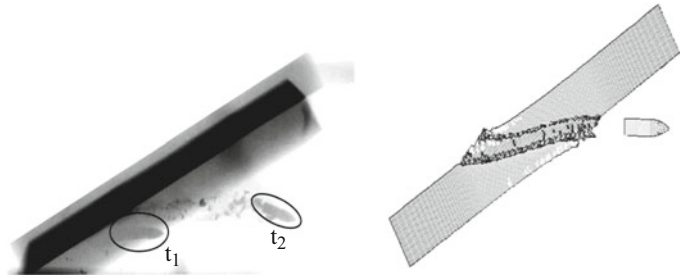

Fig. 7.9 Experimental shadowgraphs (*left*) and the simulation result (*right*), for an inclined impact of 0.3″ AP projectile at a polycarbonate plate

simulation both the compressive and tensile strengths were set at 0.1 GPa, which are typical values for polycarbonate.

In order to validate their interpretation for the enhanced ricochet, Rosenberg et al. (2005) performed a special experiment and a corresponding numerical simulation. A rectangular slot, 20 mm deep, was cut along the front face of a 40 mm thick Plexiglas target for about half of its length. The slot was wider than the projectile's diameter in order to avoid its impact with the walls of the slot, as shown in Fig. 7.10a. The projectile impacted at the end of this slot, so that its penetration path was totally encapsulated by the target. The free impact surface was actually removed from the process and the forces on the projectile were more symmetric.

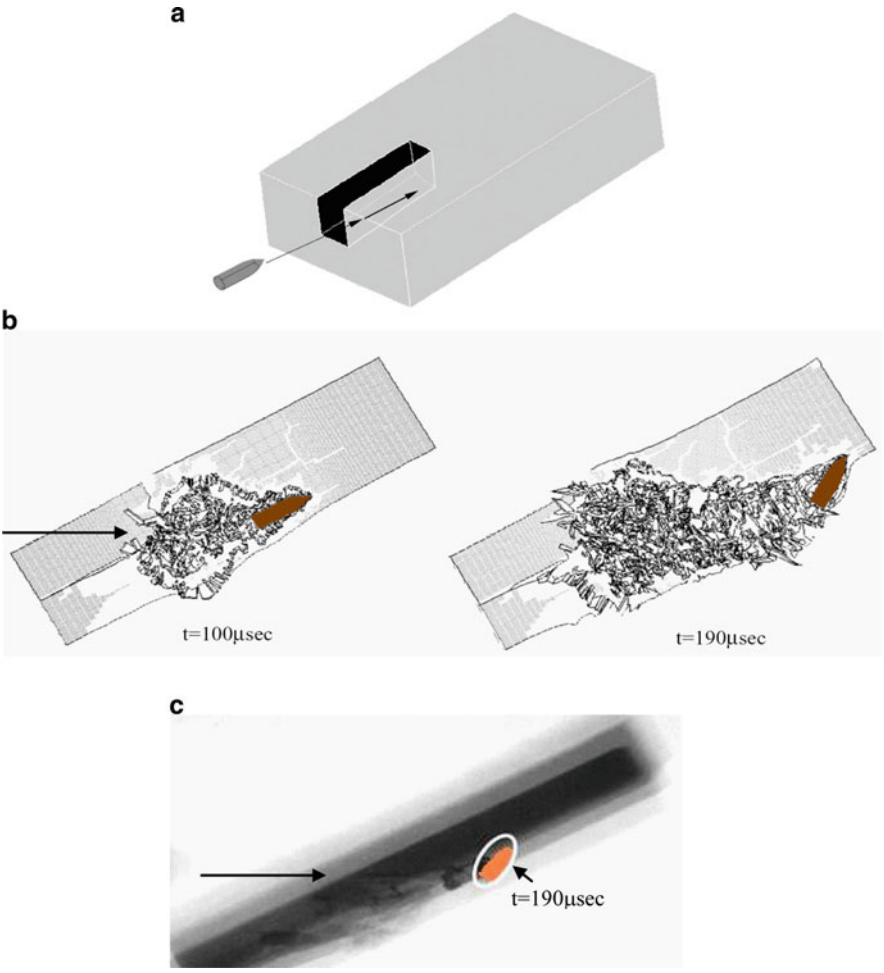

Fig. 7.10 (**a**) The slotted target experiment, (**b**) the corresponding simulations, and (**c**) the experimental shadowgraph

This impact was expected to result in a complete perforation of the Plexiglas plate which was, indeed, the case in both the experiment and the corresponding numerical simulation, as shown in Fig. 7.10. The simulation shows that the damaged volume in the Plexiglas around the penetrating projectile is much more symmetric, as compared to the shape of the damaged material in Fig. 7.8. The position and orientation of the projectile in the experiment and in the simulation, some 190 μs after impact, are very similar to each other. The resulting perforation of the plate strongly enhances the interpretation for the enhanced ricochet, as described above. We wish to emphasize the importance of such experiments and numerical simulations as validity tests. These tests should be performed in order to enhance the validity of the physical interpretation for a given phenomenon. We recommend that such validity tests be performed outside the range of the experiments which were performed during the course of the study, and they should be "critical" in the sense that their result either enhance or negate the proposed model.

7.2 Defeating Long Rods

7.2.1 Perforation of Inclined Plates

The effects of the asymmetrical forces which are exerted by an inclined plate on an eroding long rod are similar to those discussed above for rigid projectiles. This is clearly seen in Fig. 7.11, from Hohler et al. (1978), which shows three shadowgraph of an L/D = 10, D = 5.8 mm WHA rod, impacting an inclined steel plate, 8 mm thick.

The nose of the emerging rod is significantly bent, as seen here, and often it is broken into several pieces. Rods which do not break at their front end experience a larger deflection due to the prolonged action of the asymmetric forces, as seen in the Fig. 7.11. A deflected rod will subsequently impact a second target at a large yaw angle, resulting in a significant reduction of its penetration capability.

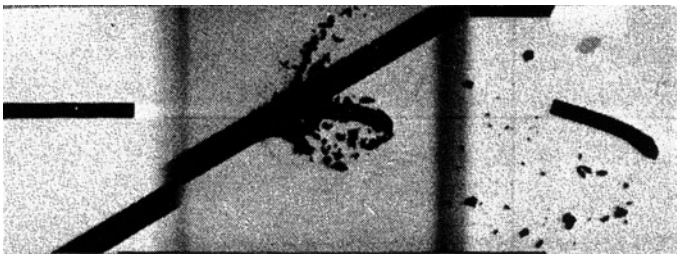

Fig. 7.11 Shadowgraphs of a WHA rod perforating an inclined steel plate

This is the main defeat mechanism achieved by inclined stationary plates against eroding long rods. As discussed in Chap. 5, the residual lengths and velocities of eroding rods perforating inclined plates follow the same variations with plate thickness as for normal impacts. Thus, as far as these parameters are concerned, obliquities do not enhance the ballistic efficiency of inclined plates. On the other hand, the asymmetry of the forces results in rod rotation, as well as its nose bending and breaking, which enhance the ballistic efficiency of inclined plates.

7.2.2 Ricochet of Long Rods

The thick and highly sloped fronts of main battle tanks are designed to offer maximal protection for the crew by exerting asymmetrical forces on the penetrators, in order to induce their ricochet. The ricochet of compact projectiles has been investigated by many workers, as reviewed by Goldsmith (1999), while the issue of long-rod ricochet received much less attention. Tate (1979) treated the ricochet process of a rigid rod which is rotated around its center of mass, by the asymmetrical forces on its nose at the impact face. While the rod tip is locally deformed according to the model, ricochet occurs only if the rod is rigidly rotated so as to produce a net velocity of the rod tip parallel to the surface of the target. The geometry of the deformed rod tip and the asymmetric force acting on its nose are shown in Fig. 7.12. Note that the obliquity angle (β) is defined as the angle between the rod's axis and the normal to the target.

Tate's ricochet model is based on the modified Bernoulli equation from the AT model, which relates the penetration velocity (U) with the impact velocity (V) and the strength parameters of the rod (Y_p) and the target (R_t). The force (F) which the target exerts on the rod is calculated through multiplying Y_p by the tip area on

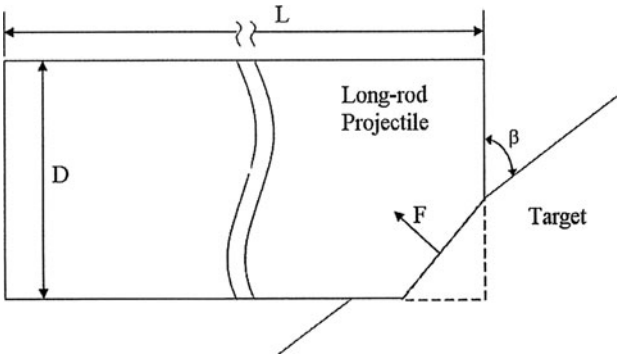

Fig. 7.12 The asymmetric force on the rod tip, according to Tate's model

which it is applied (the eroded area of the rod). The component of this force which is perpendicular to the axis of the rod is multiplied by half the length of the rod, in order to obtain the moment of this force about its centre of gravity. This moment induces a rotation rate which results in the following ricochet condition for the obliquity angle (β):

$$\tan^3\beta > \frac{2\rho_p V^2}{3Y_p} \cdot \left(\frac{L}{D} + \frac{D}{L}\right) \cdot \frac{V}{V-U} \tag{7.1}$$

The main difficulty with this model is that it treats the rod as a rigid body. Experimental observations showed that long rods are considerably deformed during inclined impacts, forming a plastic hinge around their contact area with the target. The existence of such a plastic hinge was observed by Senf et al. (1981), with L/D = 10 mild steel rods ricocheting from RHA plates. Figure 7.13 shows such a ricochet at an impact velocity of 968 m/s and an obliquity of β = 75°. The plastic hinge at the interaction area is clearly seen in the high speed pictures and in the numerical simulations performed by Senf et al. (1981).

In the ricochet model of Rosenberg et al. (1989) the asymmetric force (F), from Tate's model, acts only upon the mass of the rod which is engaged by the target. This alteration was made in order to account for the plastic hinge observed during rod ricochet. The analysis resulted in the following ricochet criterion for the minimum obliquity angle:

$$\tan^2\beta > \frac{\rho_p V^2}{R_t}\left(\frac{V+U}{V-U}\right) \tag{7.2}$$

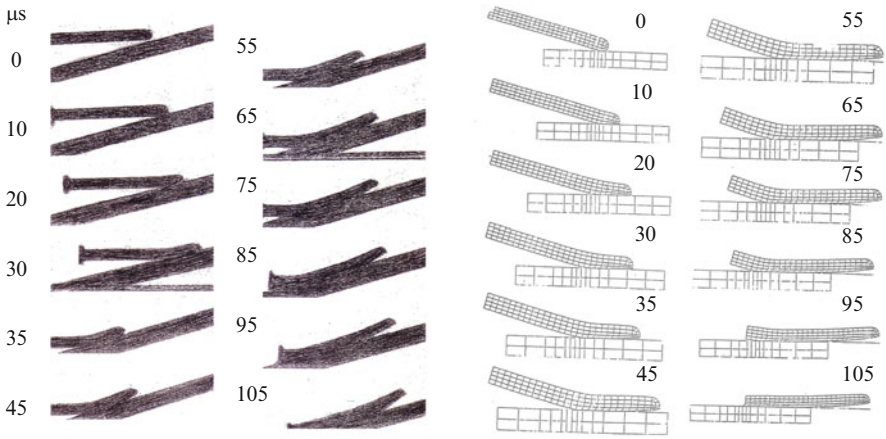

Fig. 7.13 Experimental and simulation results for the ricochet of a mild steel rod

This result is basically different than the ricochet condition of Tate's model since it includes the target resistance (R_t) as the controlling strength parameter, rather than the rod strength (Y_p). Also, the length of the rod does not appear in this model since it concentrates on the plastic hinge rather than on the rod's moment of inertia. One can define the critical angle for ricochet β_c as the value of β which is obtained when the inequality (7.2) is replaced by the corresponding equality. Thus, the ricochet condition of this model can be described by the following curve in the (β,V) plane:

$$\tan^2\beta_c = \frac{\rho_p V^2}{R_t}\left(\frac{V+U}{V-U}\right) \tag{7.3}$$

The model of Rosenberg et al. (1989) was shown to account for their experimental results with L/D = 10 WHA rods impacting armor steel targets, at velocities in the range of 0.65–1.3 km/s and for target obliquities of $\beta = 55°$–$75°$, as shown in Fig. 7.14.

Rosenberg et al. (2007) further developed these ideas, and found that an interesting situation arises when the impact velocity is lowered until it reaches the critical impact velocity (V_c) for the penetration of a given rod/target combination. At this impact velocity the rod does not penetrate the target (U = 0), and the following expression is obtained for the minimal value of the ricochet threshold obliquity (β_c^{min}) from (7.3):

$$\tan^2\beta_c^{\min} = \frac{\rho_p {V_c}^2}{R_t} = 2\left(1 - \frac{Y_p}{R_t}\right) \quad \text{at} \quad V_0 = V_c \tag{7.4}$$

where use was made of the relation $V_c = [2(R_t\text{-}Y_p)/\rho_p]^{0.5}$ according to the AT model. This result means that for every rod/target combination there is a minimum obliquity angle (β_c^{min}), which corresponds to the case of no penetration ($V_0 = V_c$

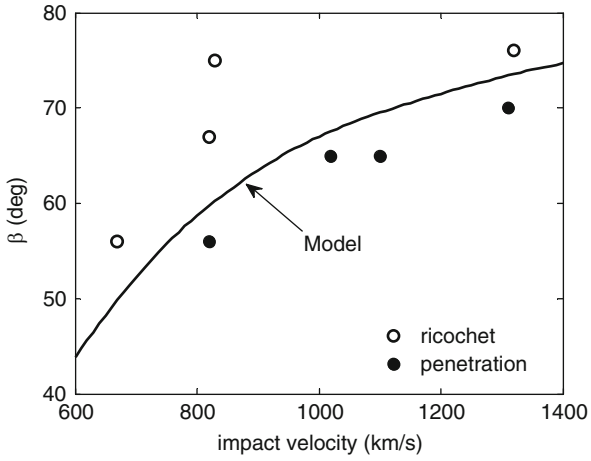

Fig. 7.14 The agreement between the ricochet model with the experimental results for the ricochet of WHA rods from steel targets

or U = 0). Thus, the ricochet curve in the (β,V) plane should start at the point (β_c^{min}, V_c). This minimal obliquity depends only on the rod/target strength ratio which, for typical values of Y_p and R_t, is equal to about 1/3 resulting in a minimal obliquity of $\beta_c^{min} = 49°$. Another interesting result is obtained for the case of $\rho_p = \rho_t$, which results in the following ricochet curve:

$$\tan^2\beta_c = 2z^2 \cdot \frac{3z^2 - 1}{z^2 + 1} \cdot \left(1 - \frac{Y_p}{R_t}\right) \quad \text{where} \quad z = V_0/V_c \tag{7.5}$$

This ricochet criterion accounts for the data of Johnson et al. (1982) with plasticine rods impacting plasticine targets, as shown in Fig. 7.15. The relevant material parameters were taken from Johnson et al. (1982), together with the value of $V_c = 45$ m/s for the critical velocity of this rod/target combination.

The aim of Johnson et al. (1982) was to demonstrate that soft materials with low densities, such as plasticine, behave in a similar way to metals when their corresponding damage number (J) is kept the same. The damage number was defined by Johnson (1972) as:

$$J = \frac{\rho_t {V_0}^2}{Y_d} \tag{7.6}$$

where ρ_t and Y_d are the density and the dynamic strength of the target, respectively, and V_0 is the impact velocity. This non-dimensional number is commonly used to classify the different regimes of projectile impacts and their severity, as far as the damage to the target and the projectile is concerned. The work of Johnson et al. (1982) on plasticine rods and targets demonstrated the validity of using this non-dimensional parameter, as far as rod deformation and their penetration depths are concerned.

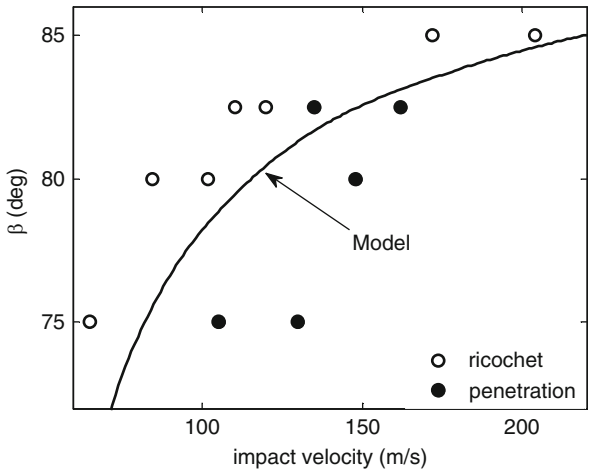

Fig. 7.15 Comparing the ricochet model with experimental results for plasticine rods impacting plasticine targets

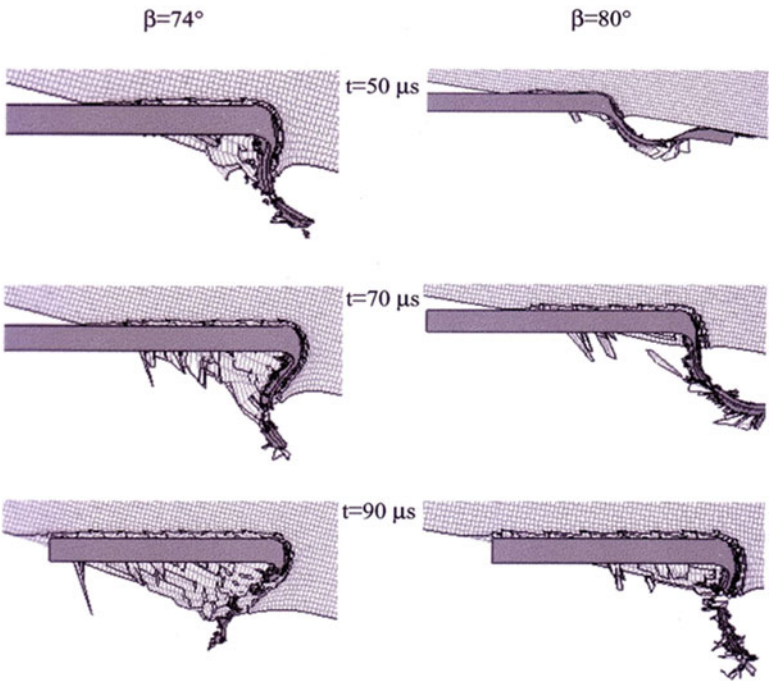

Fig. 7.16 Simulation results for long rod ricochet

The 3D numerical simulations of Rosenberg et al. (2007) resulted in ricochet thresholds for WHA rods impacting armor steel targets, at obliquities which agreed with the model's predictions. Figure 7.16 shows two of these simulation results for an L/D = 20 rod with strength of 1.2 GPa, impacting armor steel targets at a velocity of 1.45 km/s and obliquities of $\beta = 74^\circ$ and 80°. The difference between the two cases is clearly manifested as the rod penetrates the target for an impact obliquity of $\beta = 74^\circ$, while it is only gouging its surface for the $\beta = 80^\circ$ impact.

Up to this point, the analysis and the experiments dealt with very thick targets ignoring back surface effects. These effects, which are important for the interaction with thin plates, were investigated by Lee et al. (2002) both experimentally and numerically. They found good agreement between their simulations and experiments for L/D = 10.7 WHA rods, with D = 7 mm, impacting 6.25 mm thick plates of armor steel at velocities in the range of 1.0–2.0 km/s. Figure 7.17 shows simulation results for an impact velocity of 1.0 km/s and obliquities of $\beta = 76^\circ$ and 80°. The impact at $\beta = 80^\circ$ shows all the features of a ricochet, with a plastic hinge in the rod and little damage to the target. In contrast, for the $\beta = 76^\circ$ impact the rod seems to ricochet at the early stages of the interaction, but it penetrates the target at later times due to the effect of the back surface.

Obviously, the back surfaces of thin plates affect their threshold ricochet obliquities (β_c), which are expected to be larger than those for a semi-infinite target. Lee et al. (2002) compared their simulation results for β_c with those predicted from

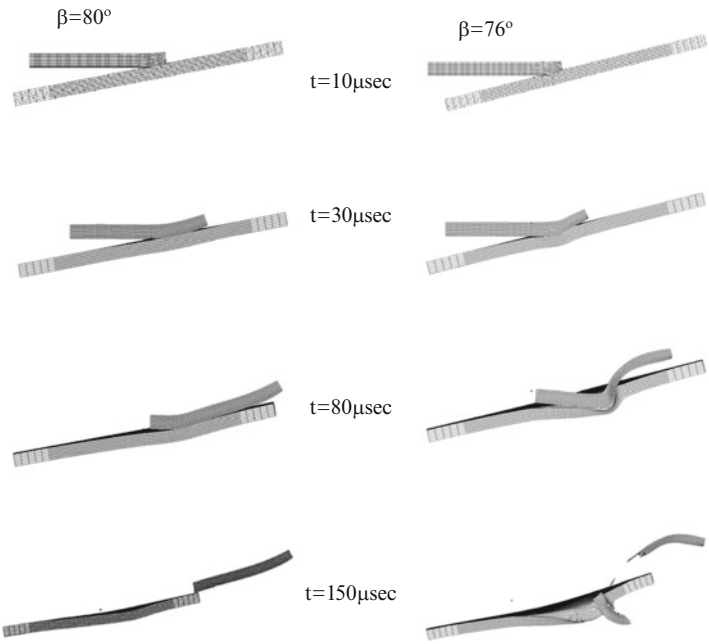

Fig. 7.17 Simulation results for a long WHA rod impacting a steel plate at $V_0 = 1.0$ km/s

the model of Rosenberg et al. (1989), as shown in Fig. 7.18. The two curves have a similar shape throughout the whole velocity range in this study, and the values of β_c for the thin plates are higher than those predicted by the model, as expected. However, the differences in the threshold obliquities amount to 3° only.

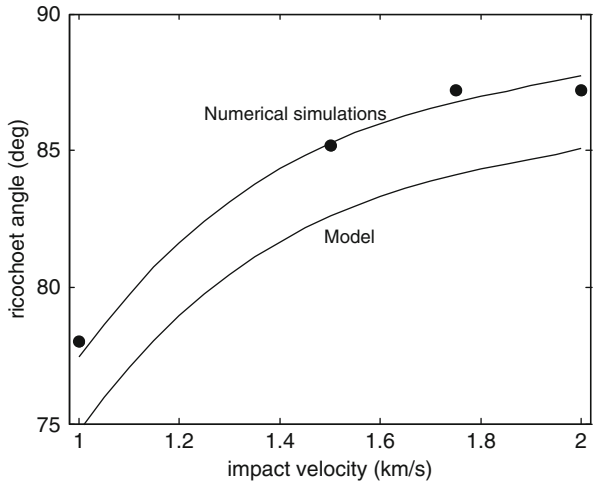

Fig. 7.18 Comparing simulation results for the ricochet thresholds from thin plates, with the analytical model for semi-infinite targets

7.2.3 The Interaction of Long Rods with Moving Plates

The work described above demonstrated the strong dependence of the threshold obliquities for ricochet on the impact velocity of the rod. Obviously it is easier to induce these ricochets if the plate is propelled in the direction of rod's velocity, as a result of their reduced relative velocity. This is one of the basic mechanisms by which a reactive armor design can be used in order to defeat long rod penetrators. These add-on armor configurations, which will be further discussed in Sect. 7.3, are based on two metallic plates with a layer of explosive between them. The explosive layer is initiated by the impact of the rod and the explosive products propel the two plates in opposite directions. The back plate, which moves in the same direction as the rod, can induce its ricochet for a larger range of inclinations, due to their low relative velocity. This effect was demonstrated by Rosenberg et al. (2009) who used an explosive layer to propel an armor steel plate to a velocity of 270 m/s. The impact of a WHA rod at 1.0 km/s and obliquity of $\beta = 63°$, resulted in its ricochet as shown in Fig. 7.19. Such an impact would have resulted in a complete penetration of a stationary plate. Add-on armor designs which are based on these moving plates can reduce their lethality.

The potential to defeat long rods with moving plates was demonstrated by Rosenberg and Dekel (2004). They presented results from a series of experiments and numerical simulations with WHA rods impacting inclined moving steel plates, as shown schematically in Fig. 7.20. The inclination angles were varied between $\alpha = 25°$ and $\alpha = 40°$, and the nominal velocity of the rods was $V_p = 1.4$ km/s. The 4.3 mm thick armor steel plates had a nominal velocity of $V_t = 430$ m/s in this study. We describe this work in detail because it is an excellent example for a study where experiments, numerical simulations, and an analytical model are combined in order to understand the basic physics of a given defeat mechanism.

In each experiment the rod/plate interaction was followed by three X-ray shadowgraphs at $t = 30$, 170 and 310 μs after impact. These times were chosen to follow the rod closely after impact, at about the middle of the interaction process and near its end, respectively. This set of experiments resulted in rod disruptions which were either mild or very severe. The most important observation was that all the severe disruptions took place in experiments with inclination angles of $\alpha \leq 35°$,

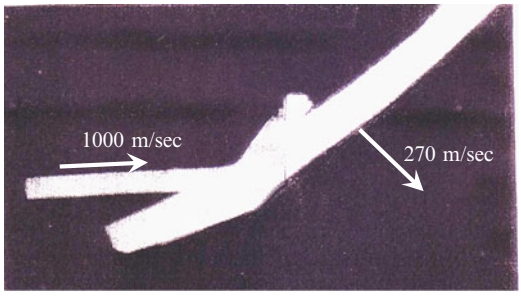

Fig. 7.19 The ricochet of a long WHA rod from a moving steel plate

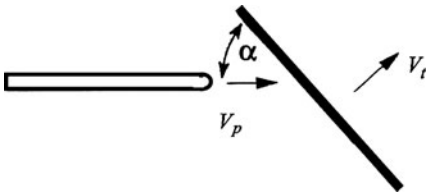

Fig. 7.20 The experimental set up for the interaction of a long rod with a moving plate

while for all the experiments with $\alpha \geq 40^\circ$ the rods experienced only a mild disruption. The different modes of rod disruption are clearly seen in Fig. 7.21, through the three shadowgraphs of experiments which resulted in the severe disruption at $\alpha = 35^\circ$, and the mild disruption at $\alpha = 40^\circ$. The plates in these shadowgraphs seem to be rather thick because of the parallax effect which takes place when the x-ray tube is not aligned optimally with the plate. The mild disruption resulted in a residual rod which was broken into several pieces, but its penetration capability was very close to that of an intact rod. In contrat, the penetration capability of the severely disrupted rod was very small. Clearly, a very efficient disruption mechanism is initiated at a certain impact angle, somewhere between $\alpha = 35^\circ$ and $\alpha = 40^\circ$.

In order to understand this result, Rosenberg and Dekel (2004) performed 3D numerical simulations of these impacts for plate inclinations of $\alpha = 30^\circ$ and $\alpha = 40^\circ$. These simulations reproduced the experimental results quite successfully, as shown in Fig. 7.22, enhancing the claim that the onset of severe disruption has a real physical basis.

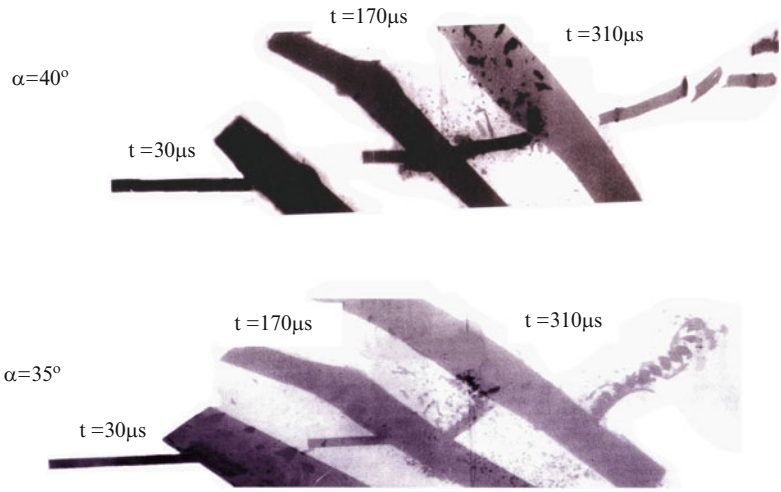

Fig. 7.21 Rod/plate interaction at $\alpha = 40^\circ$ (mild disruption) and $\alpha = 35^\circ$ (severe disruption)

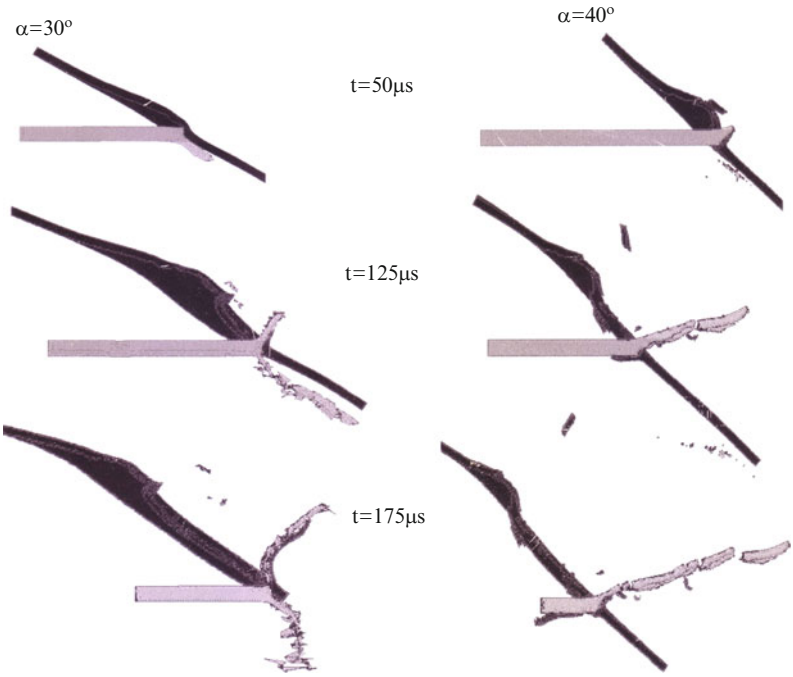

Fig. 7.22 Simulation results for the impacts at $\alpha = 30°$ (*left*), and at $\alpha = 40°$ (*right*)

In order to emphasize the excellent agreement between simulations and experimental results, consider the latest "snapshots" for the two cases discussed above, as shown in Fig. 7.23. One can see that the simulations reproduce all the fine details which have been observed experimentally. This is an important issue if one wishes to draw practical conclusions from such simulations, as will be described next.

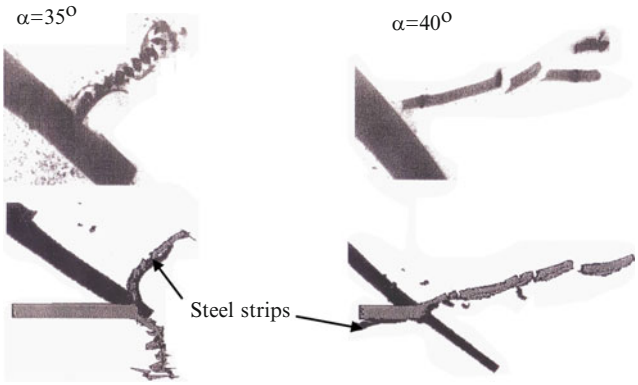

Fig. 7.23 The latest snapshots comparing experiments (*top*) and simulations (*bottom*), for the two impacts at different obliquities

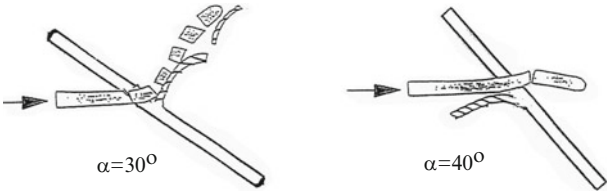

Fig. 7.24 The different orientations of the steel strips for the two inclinations

A close examination of the simulation results in Fig. 7.23, reveals a basic difference in the rod/plate interaction between the two impacts. This difference is manifested by the orientation of the steel strip which is sheared off the moving plate by its continuous interaction with the rod. The simulation "snapshots" in Fig. 7.23 show that this strip is either pushed in the direction of plate movement or forced down towards the rod. This important observation is shown schematically in Fig. 7.24, in order to highlight the main cause for the difference between the two interactions. The severe disruption of the rod is caused for by a strip which is being pushed backwards, as in the left side of the figure, while the minor disruption is caused by a strip which is pushed downwards, as shown in the right side of the figure. Both the experimental shadowgraphs and the simulation results for the $\alpha = 30°$ impact, show that the rod material is dispersed around its interaction point as it continuously shears the strip. In fact, the rod does not penetrate the moving plate in the sense that its debris remain on the same side of the strip throughout the interaction. On the other hand, for an impact at $\alpha = 40°$ the rod penetrates the plate as it pushes the strip downwards. Thus, the substantial disruption of the rod is related to the issue of rod/target penetration threshold. The difference in the direction of these strips could not be seen in the X-ray shadowgraphs because of the parallax mentioned above. Thus, we have an excellent example where the most important issue concerning the source of this disruption mechanism, was actually highlighted by the numerical simulations.

The analytical model presented by Rosenberg and Dekel (2004) considers the relative motion of the rod and the plate, as depicted schematically in Fig. 7.25. The plate is assumed to move in a perpendicular direction to its face at a velocity V_t.

The relevant velocity for this interaction is the relative velocity between the rod and the moving interaction point, as given by:

$$V_{rel} = V_p - \frac{V_t}{\sin\alpha} \tag{7.7}$$

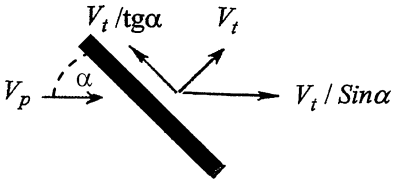

Fig. 7.25 A schematic description of the relative rod/plate velocity

In order to achieve a substantial disruption to the rod this velocity has to be smaller than the threshold velocity for penetration (V_c) of the given rod/target pair. Thus, the condition $V_{rel} < V_c$ for severe rod disruption leads to the following inequality:

$$\frac{V_t}{V_p} > \left(1 - \frac{V_c}{V_p}\right) \cdot \sin\alpha \tag{7.8a}$$

A second constraint on the relative velocity is that it should be positive, $V_{rel} > 0$, in order to obtain a continued interaction between the rod and the target. This is a purely geometrical constraint which leads to:

$$\frac{V_t}{V_p} < \sin\alpha \tag{7.8b}$$

Combining the two constraints results in the following conditions for the strong disruption process described above:

$$\sin\alpha > \frac{V_t}{V_p} > \left(1 - \frac{V_c}{V_p}\right) \cdot \sin\alpha \tag{7.9}$$

where the critical velocity is given by the AT model as $V_c = [2(R_t\text{-}Y_p)/\rho_p]^{0.5}$.

It is convenient to present these constraints as two curves in the "disruption plane," with axes which correspond to V_t/V_p and α, as defined by Rosenberg and Dekel (2004). The two inequalities (7.9) define the "disruption zone" which includes all the experiments resulting in severe disruption for the rod. The experimental results in Chap. 5, for WHA rods impacting RHA targets, show that $V_c = 640$ m/s for this rod/target combination. For the experiments described here, with a rod velocity of $V_p = 1.4$ km/s, one obtains $(1\text{-}V_c/V_p) = 0.54$, which should be inserted in the right hand side of inequality (7.9). The graphical representation of these inequalities is shown in Fig. 7.26, which includes the experimental results of Rosenberg and Dekel (2004) in terms of severe rod disruption (filled circles) and minor disruptions (open circles). The borderline between the two disruption modes, as predicted by the model, passes between the two sets of experiments. Considering the simple assumptions behind the model, this is an excellent agreement between a model and the experimental results. The shaded area in this figure, the "disruption zone," is of high important to the armor designer. Clearly, larger disruption zones result in severe rod disruptions at lower plate velocities, and for a wider range of plate inclinations.

A larger disruption zone is obtained by using high strength plates, with higher critical velocities (V_c), resulting in lower values for the term $(1\text{-}V_c/V_p)$ on the right hand side of inequality (7.9). Thus, the second curve in Fig. 7.26 is expected to be lower for a high strength plate, resulting in a larger disruption zone. In order to demonstrate this issue Rosenberg and Dekel (2004) repeated the experiment with the $\alpha = 40°$ inclination, using a high hardness (HH) steel plate. Note that this inclination with the RHA plate resulted in a minor disruption to the rod, as shown

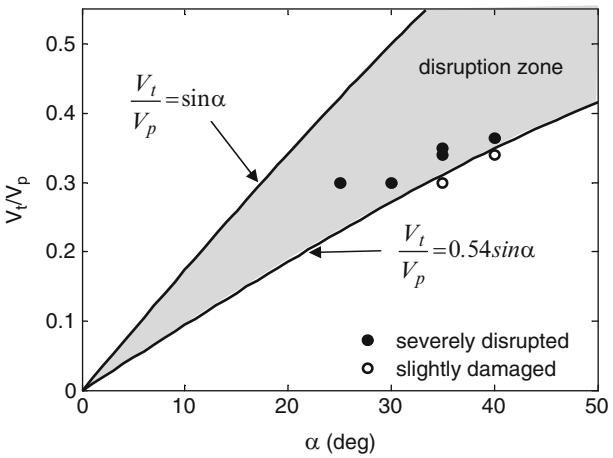

Fig. 7.26 The disruption zone and the experimental results for rod interaction with a moving plate

above. The critical penetration velocity for the WHA rod impacting an HH steel target, is estimated as $V_c = 720$ m/s, from the experimental data presented in Chap. 5. This increase of V_c lowers the border of the disruption zone to the curve $V_t/V_p = 0.486\sin\alpha$. The larger disruption zone was expected to encompass the two experiments which resulted in a minor disruption, marked by the open circles in Fig. 7.26. A significant disruption was expected for the $\alpha = 40°$ experiment with this high hardness steel plate, which was, in fact, the result obtained in this experiment, as is clearly seen in Fig. 7.27. Thus, with stronger steel plates the disruption zone can be expanded to include a larger range of impact velocities and inclination angles.

The critical velocity for penetration (V_c) was defined by the AT model for long rods impacting semi-infinite targets. It is unclear whether one can use the same values of V_c for the process of rod disruption by finite thickness plates. This issue was explored by Rosenberg and Dekel (2005), through numerical simulations in which the thickness and the velocity of the plate were systematically varied. The simulations resulted in either a strong disruption or a mild one, as observed before, but the border line between the two cases shifted systematically with plate

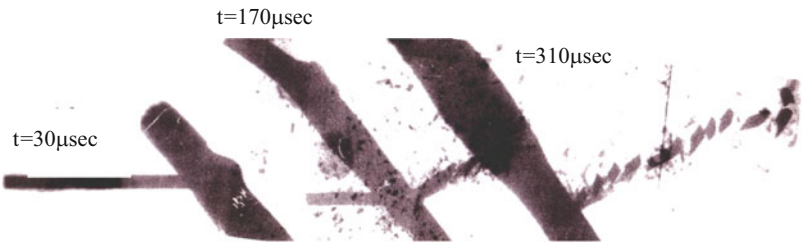

Fig. 7.27 Rod disruption by the HH steel plate at an inclination of $\alpha = 40°$

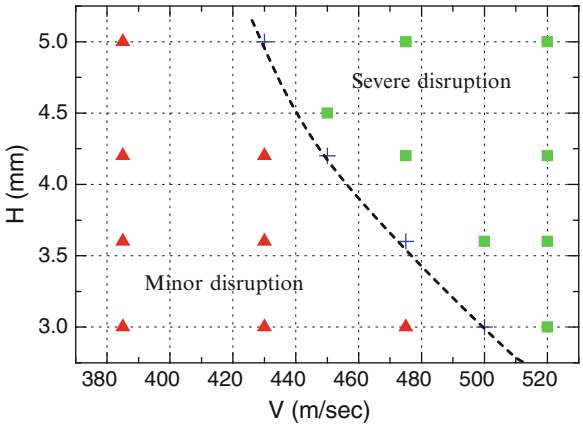

Fig. 7.28 Simulation results for rod disruption as a function of plate velocity and thickness

thickness. Simulation results for WHA rods impacting armor steel plates of different thickness, at an inclination of $\alpha = 35°$, are shown in Fig. 7.28. The rod's velocity in these simulations was 1.4 km/s and the velocity of the plates ranged between 390 and 520 m/s. The triangles in this figure correspond to minor rod disruptions, the squares to severe disruptions, and the crosses represent borderline cases.

The plate velocities which are needed to induce a meaningful disruption to the rod are higher for thinner plates, as expected, due to the enhanced influence of their back surface. For example, in order to induce a severe disruption, the velocity of a 3.0 mm thick plate should be at least 500 m/s according to these simulations. In order to validate these results Rosenberg and Dekel (2005) performed an additional experiment, with a WHA rod impacting a 3.0 mm RHA plate at $V_0 = 1.4$ km/s, and at an inclination of $\alpha = 35^{\circ}$. The velocity of the plate was 530 m/s which, according to these simulations, should have resulted in a strong disruption to the rod. This was, in fact, the result of this validation experiment, as shown in Fig. 7.29.

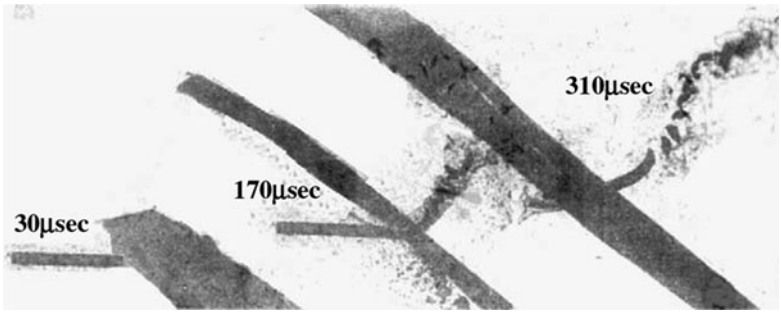

Fig. 7.29 The three shadowgraphs in the experiment with the 3.0 mm plate

We elaborated on this issue of rod disruption by a moving plate because it is an excellent example for the benefits gained by combining all the available tools for a given problem in terminal ballistics. At first, a rather surprising difference in rod disruption was found in two experiments which differed by only 5° in plate inclinations. The 3D numerical simulations revealed that this difference is due to the different directions by which the steel strips, which interact with the rod, are sheared off the plates. This realization led to a simple model for the interaction of rods with moving plates, which is based on the critical velocity for penetration (V_c) of the given rod/target combination. The model was able to account for all the experimental data and its validity was enhanced by additional experiments which were performed as validation tests.

These rod/plate interactions are important elements for the design of reactive armors, based on plates which are propelled by an explosive layer. As will be discussed in Sect. 7.3, the explosive reactive armor configuration (ERA) is very effective against shaped charge jets and it has been applied as add-on armor to various armored vehicles. On the other hand, reactive armors are still in their early stage of research as far as long rods are concerned. Held (2005) analyzed the various defeat mechanisms which can take place by the combined effects of the front and rear plates in a heavy ERA configuration. According to his results, with a proper design of the ERA cassette, the penetration capability of the rod can be reduced significantly.

The difference between the disruption potential of the two plates, which move in opposite directions in a reactive armor design, has been highlighted by Shin and Yoo (2003). They studied the impact of L/D = 15, D = 5 mm WHA rods with inclined steel plate, 5 mm thick, moving at different velocities, either towards the rod or away from it. Impact velocities of the rods, in these simulations, were 1.5 and 2.5 km/s and the inclination angle was $\alpha = 30^{\circ}$. The simulations clearly showed that the disruption by the plate which moves towards the rod is very small and is, in fact, similar to that caused by a stationary plate. On the other hand, plates which move away from the rod can induce a significant disruption, even when their velocities are as low as 200 m/s. A similar numerical study was performed by Paik et al. (2007) for L/D = 15 and 30, D = 5 mm WHA rods interacting with 2.5 mm thick steel plates of a reactive cassette. The impact velocities were 1.5 and 2.5 km/s in these simulations, the inclination angle $\alpha = 30^{\circ}$, and the plate velocities were varied between 0.2 and 0.5 km/s. The differential efficiencies of these cassettes, as calculated by the residual penetrations into a thick steel witness block, increased with plate velocity and were significantly higher against the longer rod. At plate velocities of 0.3–0.5 km/s, these efficiencies attained values in the range of $\eta = 3$–6, and the higher efficiencies were obtained for the lower velocity rods. The shapes of the disrupted rods in these simulations are similar to those observed in the experiments of Held (2005), enhancing his observations for the various defeat mechanisms which take place during these interactions.

7.2.4 The Impact of Yawed Rods

One of the more complex issues in the terminal ballistics of long rods concerns the penetration process of a yawed rod, especially at large obliquities. We shall first discuss the impact of yawed rods at normal incidence and then consider oblique impacts. The yaw of a rod is defined by the angle between its longitudinal axis and the velocity vector of its center of mass, as shown schematically in Fig. 7.30. There are two orthogonal attitudes which define the flight characteristics of the rod, the pitch (θ_1) and the yaw (θ_2). The total yaw angle (θ) is defined by the simple relation: $\tan^2\theta = \tan^2\theta_1 + \tan^2\theta_2$.

The data gathered on the impact of yawed rods shows that there is a narrow range for which their penetration depths are not affected significantly by the yaw angle, and that this range is smaller for rods with larger aspect ratios (L/D). Silsby et al. (1983) realized that the penetration capability of a long rod is not affected by yaw as long as its rear portion does not impact the wall of the crater. This geometrical constraint defines a threshold value, commonly referred to as the critical yaw (θ_c), according to:

$$\sin\theta_c = \frac{D_c - D_p}{2L} \tag{7.10}$$

where D_c and D_p are the diameters of the crater and the rod, respectively. The values of θ_c for L/D = 10–20 rods fall in the range of 1.5°–3°. Thus, an add-on armor system which induces yaw angles of several degrees to the impacting rod can be a very effective design. It is clear that the crater diameter plays an important role in this issue and, as described by Bierke et al. (1992), there is a wealth of different interactions between the rod and the crater walls, for impacts at increasing yaw

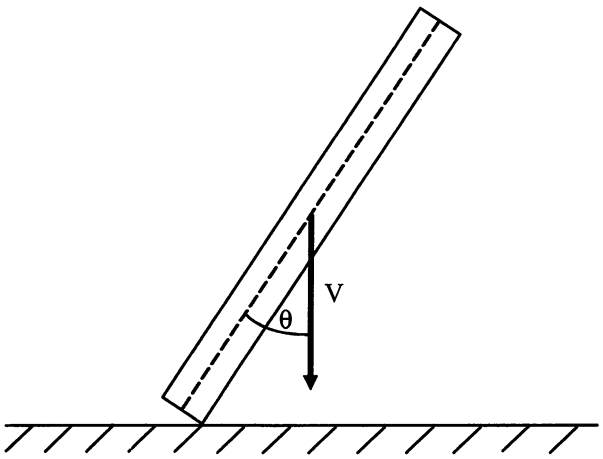

Fig. 7.30 Schematics of a yawed rod impact

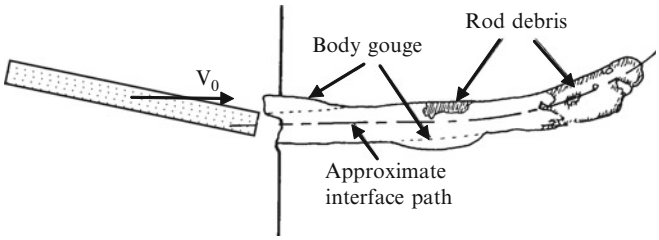

Fig. 7.31 The crater shape and rod debris for a moderate yaw impact

angles. For example, at striking yaws just above θ_c there is evidence for the gouging of the rod, through the depressions on one side of the crater wall. With increasing yaw angles there is evidence for a rebound of the rod's rear part, through the depressions on the opposite side of the wall. Thus, the rod's rear portion is bouncing from side to side during its penetration, resulting in an enhanced crater diameter which leads to a marked reduction in penetration depths. A typical shape of the crater at moderate yaw angles is shown in Fig. 7.31, from Bierke et al. (1992).

Gee and Littlefield (2001) performed a series of 3D numerical simulations in which they investigated the penetration process of L/D = 10 and 30 WHA rods, impacting armor steel targets at velocities of 1.4, 2.1 and 2.6 km/s. They observed the gouging phenomenon of the rod's tail and its subsequent realignment, following the interaction with the crater walls. They checked the possibility to normalize the numerical results by presenting them in terms of P/P_n as a function of θ/θ_c, where P_n is the penetration depth at normal incidence. The need for a normalized presentation is evident when one compares simulation results for L/D = 10 and 30 rods, impacting a steel targets at 2.1 km/s and at a yaw angle of $\theta = 30^\circ$, as seen in Fig. 7.32. Obviously, the crater shapes are very different for these impacts which, according to Gee and Littlefield (2001), is the result of the different values for the normalized yaw angles: $\theta/\theta_c = 8.8$ and 30, for the L/D = 10 and 30 rods, respectively. The normalization scheme was successful for yaw angles in the range of $\theta/\theta_c < 10$, while for higher yaw angles the normalized results for the L/D = 10 and 30 rods differed by a considerable amount.

The experimental works of Bless et al. (1978), Yaziv et al. (1992), Bukharev and Zhurkov (1995) and Hohler and Behner (1999) showed that the penetration depths of yawed rods decrease drastically with yaw angles when these are greater than the corresponding critical values. Several phenomenological models were suggested in these works which account for the data quite well, as far as the strong dependence of penetration on yaw is concerned. However, these models are applicable only for the specific ranges of materials, impact velocities, and rod aspect ratios for which they were calibrated. These models realize that for yawed impacts near the critical angle the penetration depth decreases according to the change in the effective rod length, which is proportional to $L\cos\theta$. On the other hand, for large yaw angles the penetration depth is influenced by the rod diameter and it is proportional to $D_p/\sin\theta$.

A different approach was taken by Lee and Bless (1998) who considered the yawed rod as comprised of a series of cylindrical disks. They assumed that the degradation in the penetration capability of such a disk is proportional to the portion

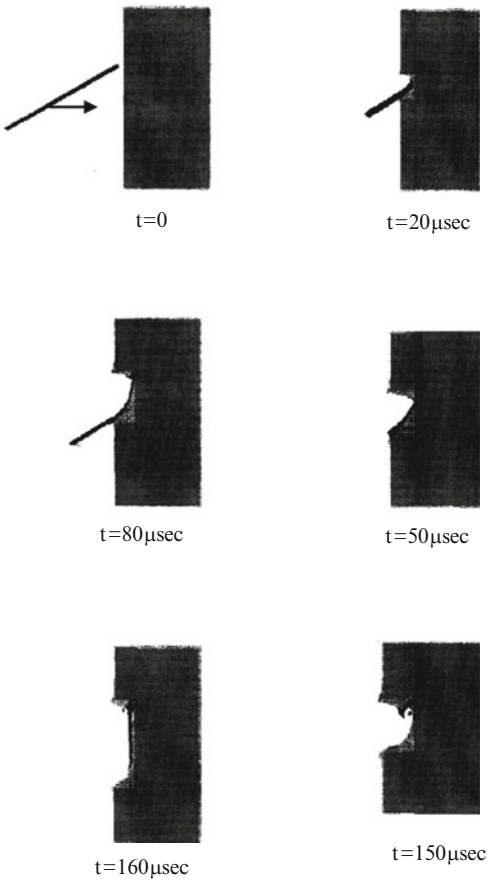

Fig. 7.32 Simulations for L/D = 10 (*right*) and L/D = 30 (*left*) rods, impacting at $V_0 = 2.1$ km/s and $\theta = 30°$

of its diameter which overlapps the crater edge. The diameter of the crater in this model was determined by a momentum balance principle, which was derived by Lee and Bless (1996). They used the AT model to calculate the penetration depth of the rod's front part until sidewall grazing occurs. Good agreement was found between the model's prediction and the experimental results of Yaziv et al. (1992), for L/D = 10 WHA rods impacting armor steel targets at 1.4 km/s, for a large range of yaw angles. Rosenberg et al. (2006) used a similar approach which was based on dividing the rod into n segments, each of length ℓ. They treated separately the segments which penetrate without gouging the crater wall, and those which impact the wall. The geometry of the model is described in Fig. 7.33.

The crater diameter (D_c) in terms of rod diameter (D_p) was taken from the empirical fit by Walker et al. (2001), for a large amount of data of WHA rods impacting armor steel targets, as given by:

$$D_c = D_p \cdot (1 + 0.7V_0) \tag{7.11}$$

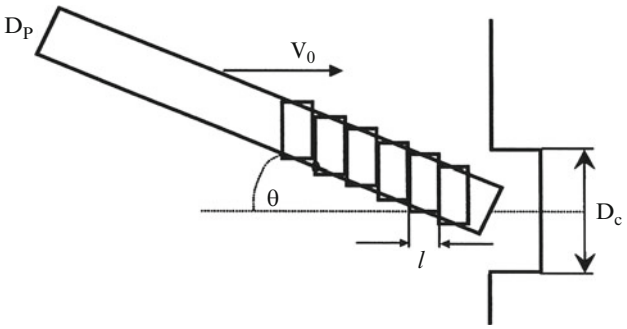

Fig. 7.33 The geometric model for yawed penetration

where the impact velocity (V_0) is given in km/s. Another empirical fit by Walker et al. (2001), for the normalized penetrations of these rods, was used in the model in order to account for the L/D effect:

$$\frac{P}{L} = 0.65 + 1.06 \ln V_0 - 0.055 \ln \frac{L}{D} \tag{7.12}$$

where V_0 is given in km/s. This equation accounts for a large range of penetration data, for WHA rods of different L/D values and impact velocities in the range of $V_0 = 0.75$–1.9 km/s.

The next step was to calculate, geometrically, the effective diameters of the elements which do not impact the crater wall. The effective diameter of the nth element can be written as:

$$D_{eff}(n) = \begin{cases} D_p/\cos\theta & \text{if} \quad nl\tan\theta + D_p/(2\cos\theta) \le D_c/2 \\ D_c/2 + D_p/(2\cos\theta) - nl\tan\theta & \text{otherwise} \end{cases} \tag{7.13}$$

The maximal number of segments is obtained when the lower corner of the nth segment aligns with the crater side. Thus, N_{eff} is limited by the projectile's length or diameter, according to:

$$N_{eff} = \begin{cases} \dfrac{L}{l\cos\theta} & \text{if} \quad \dfrac{D_c + D_p/\cos\theta}{2\tan\theta} \ge \dfrac{L}{\cos\theta} \\ \dfrac{D_c + D_p/\cos\theta}{2l\tan\theta} & \text{if} \quad \dfrac{D_p/\cos\theta}{\sin\theta} < \dfrac{D_c + D_p/\cos\theta}{2\tan\theta} < \dfrac{L}{\cos\theta}. \end{cases} \tag{7.14}$$

The last element to contribute is the one for which its edge hits the crater sidewall. For simplicity, the above equations do not include cases where the rod hits the target nearly sideways ($tg\theta > L/D_p$). These angles are larger than 80° even

for short rods with L/D = 5. The effective projectile diameter is obtained by averaging the $D_{eff}(n)$values, from (7.13), up to $n = N_{eff}$:

$$D_{eff} = \frac{1}{N_{eff}} \sum_{n} D_{eff}(n) \tag{7.15}$$

In a similar way the effective length of the rod is defined by:

$$L_{eff} = N_{eff} \cdot l \tag{7.16}$$

These equations for D_{eff} and L_{eff} are then inserted in (7.12), in order to obtain the penetration depth of the yawed rod with its effective aspect ratio of L_{eff}/D_{eff}.

Applying this model to WHA rods of different aspect ratios, impacting RHA targets at 2.1 km/s resulted in the normalized penetration curves shown in Fig. 7.34. Note that the results in this figure are presented in terms of P/D vs. yaw angle. Each curve has a flat top which means that there is a certain range of yaw angles with no reduction in the rod's penetration capability, and this range decreases with increasing L/D, as observed in the experiments. The common asymptote of P/D for large yaw values means that at these angles it is the rod diameter, rather than its length, which determines its penetration depth.

Rosenberg et al. (2006) also performed 3D numerical simulations for various sets of published data, in order to check whether a good agreement is obtained between these simulations, their analytical model and the experimental results. Figure 7.35 shows a series of "snapshots" from a simulation for a WHA rod impacting RHA target at $V_0 = 1.8$ km/s, with a yaw angle of $\theta = 60^{\circ}$. It is clear that for this yaw angle the rod is penetrating sideways rather than along its axis.

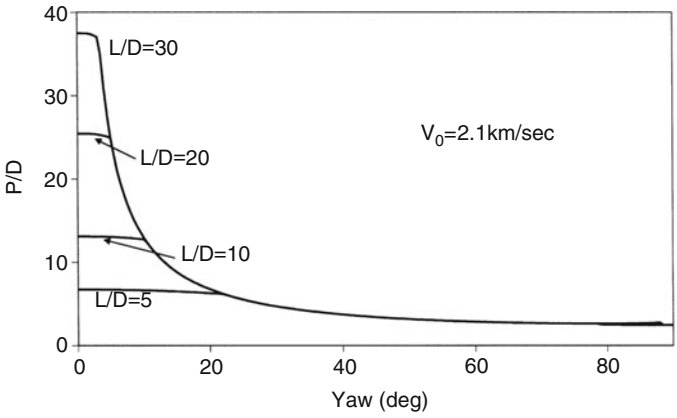

Fig. 7.34 Model's predictions for the effect of yaw on rods with different aspect ratios

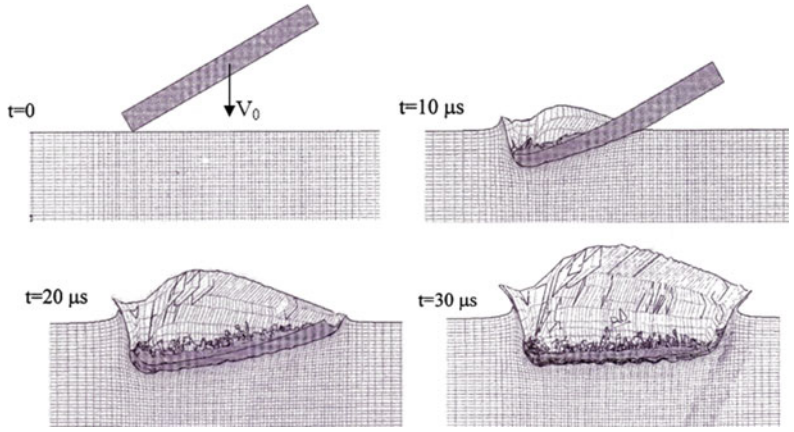

Fig. 7.35 3D numerical simulation for a yawed WHA rod impact at $V_0 = 1.8$ km/s and $\theta = 60°$

The agreement between the model and these 3D simulations for WHA rods of different L/D values impacting RHA targets at 1.8 km/s, is shown in Fig. 7.36. The agreement is satisfactory considering the simple assumptions behind the analytical model presented above.

The agreement between the model and experimental data for WHA rods impacting RHA targets is shown in Fig. 7.37. The data from Bukharev and Zhurkov (1995) for impacts at 2.1 km/s, is shown in the upper part of the figure, and the data from Yaziv et al. (1992), for L/D = 10 rods impacting at 1.4 km/s, is shown in the lower part.

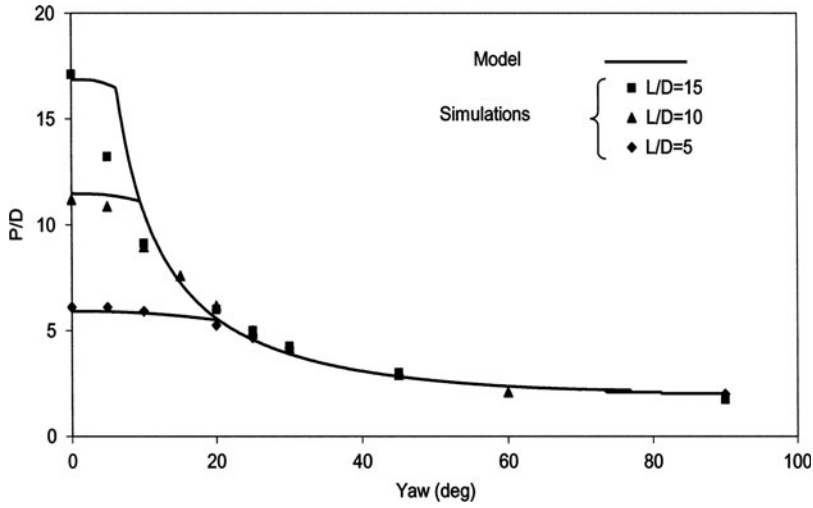

Fig. 7.36 Comparison between model predictions and simulation results for WHA rods impacting RHA targets at 1.8 km/s

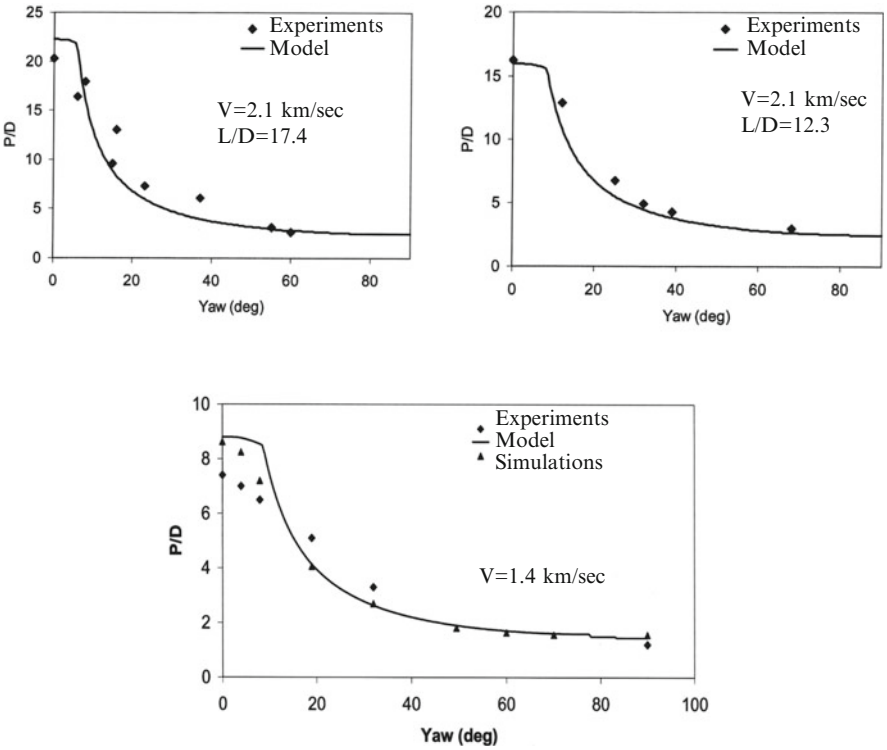

Fig. 7.37 Comparing the model with the data for WHA rods impacting RHA targets

So far, we discussed the impact of yawed rods on semi-infinite targets where the rod velocity vector is normal to the target face. A much more complex interaction takes place when the target is inclined to this vector, involving both yaw and obliquity. Relatively few works have been performed with thick targets impacted obliquely by yawed rods, and the work of Behner et al. (2002) is the most elaborate of these studies. They impacted L/D = 20 (D = 6.3 mm) blunt nosed WHA rods, on thick RHA targets which were inclined at $\alpha = \pm 30^{\circ}$, as shown in Fig. 7.38. The impact velocity was 1.65 km/s, yaw angles ranged between 0° and 90°, and the different techniques which were used to reach these yaw angles, are also described by Behner et al. (2002).

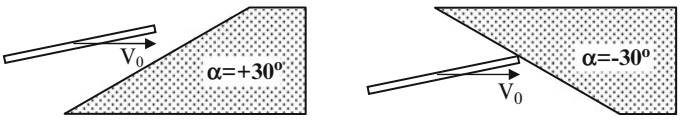

Fig. 7.38 Yawed rod impact on inclined surfaces

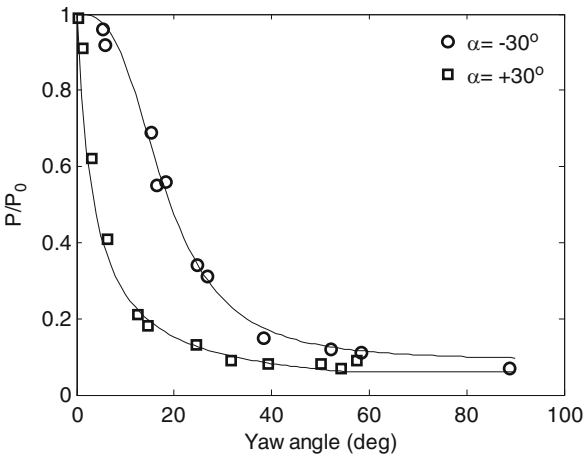

Fig. 7.39 The effect of combined yaw and obliquity on the penetration depths of long rods

The results of these experiments in terms of P/P_0 as a function of yaw angle are shown in Fig. 7.39, where P_0 is the penetration depth for zero yaw impact. The difference between the two sets of experiments, with the $\alpha = +30^\circ$ and $\alpha = -30^\circ$ obliquities, is clearly evident here.

As mentioned above, an add-on armor which induces a yaw of several degrees to an $L/D = 20$ rod can be a very effective design. However, the high density long rods which are used in military applications have high moments of inertia and it is not simple to induce a significant yaw in these rods. One of the more efficient techniques to achieve this goal is to launch a flying plate towards the rod, so that the impact takes place at a distance of several meters away from the protected vehicle. With a proper impulse delivered to the rod a significant yaw rate can be induced, resulting in its impact at a high enough yaw angles. This is the basic principle behind the active armor concept, as discussed by Wollmann et al. (1996), Ernst et al. (1999), and Sterzelmeier et al. (2002) who presented various techniques to launch these plates towards the oncoming rod. Obviously, in order to obtain a significant deflection of the rod the flying plate should be thick enough and its velocity vector should be inclined to the axis of the rod. The continued action of this plate as it sweeps across the rod can induce a significant rotation of the rod and even its breakup to several pieces.

Cagliostro et al. (1990) realized that a similar grazing action along the rod's shank is obtained by its oblique impact on a stationary plate, at a certain yaw angle. Bless et al. (1999) and Liden et al. (2006) used this technique in order to induce a continuous "grazing interaction" between the inclined plate and the yawed rod. In order to follow these interactions, consider the three situations described in Fig. 7.40, from Cagliostro et al. (1990), which define the positive and negative yaw angles. The yaw angle (θ) is given by $\theta = \gamma_0$-β, where γ_0 is the angle between the velocity direction of the rod and the normal to the plate, and β is the obliquity angle between the rod's axis and the normal to the plate, as shown in the figure. It is easy to show that, as far as the rod/plate interaction is concerned, the cases of positive and negative yaw are equivalent to the cases of plates moving away and towards the rod, respectively, as shown in lower part of the figure.

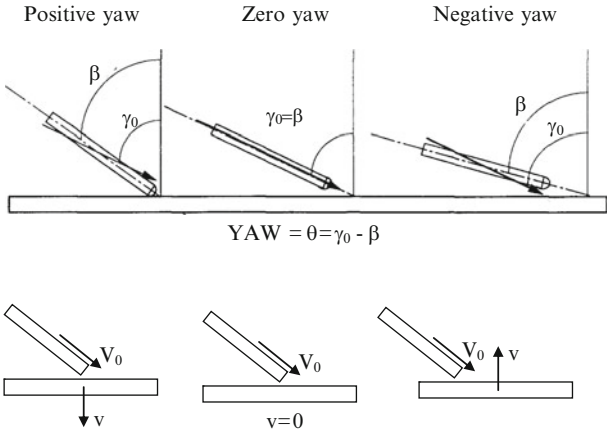

Fig. 7.40 The equivalence of inclined yawed impact and the impact with moving plates

For a rod velocity of $V_{0,}$ an obliquity of β, and a plate velocity of v, the equivalent yaw (θ) according to Liden et al. (2006) is given by:

$$\tan\theta = \frac{v\sin\beta}{V_0 \pm v\cos\beta} \tag{7.17}$$

where the (+) and (–) signs relate to plates moving towards and away from the rod, respectively. This analysis considers the relative velocity between the rod and the plate as $V_{rel} = V_0 \pm v\cos\beta$, which is different than the expression used by Rosenberg et al. (2004) in (7.7). This difference is due to the fact that (7.7) considers the rod/plate relative velocity in relation to their interaction point, while in the present case the interaction point is moving along the whole length of the rod (the grazing process).

Cagliostro et al. (1990) performed 3D numerical simulations in order to analyze experimental results for L/D = 10 spherical nosed rods, of the U-0.75%Ti uranium alloy, which impacted moving RHA plates. These experiments are described schematically in Fig. 7.41. The second experiment is the reference one where the rod impacts a stationary plate at an impact velocity of 1.29 km/s and obliquity of $\beta = 65^{\circ}$. The two other experiments were performed with moving plates, at different velocities and plate obliquities. These experiments are equivalent to impacts on stationary targets, with a velocity of 1.29 km/s and obliquity $\beta = 65^{\circ}$, at yaw angles of $\theta = -9.3^{\circ}$, and $\theta = +10.3^{\circ}$.

The difficulties encountered in performing well-controlled experiments with the desired velocity of the moving plate, prompted the use of the reverse ballistics technique. With this technique, an inclined plate is launched at a stationary rod which is aligned at a certain yaw with respect to the plate's velocity direction. The usefulness of this technique was demonstrated by Bless et al. (1999) who launched inclined steel plates towards stationary WHA rods. These L/D = 36 rods

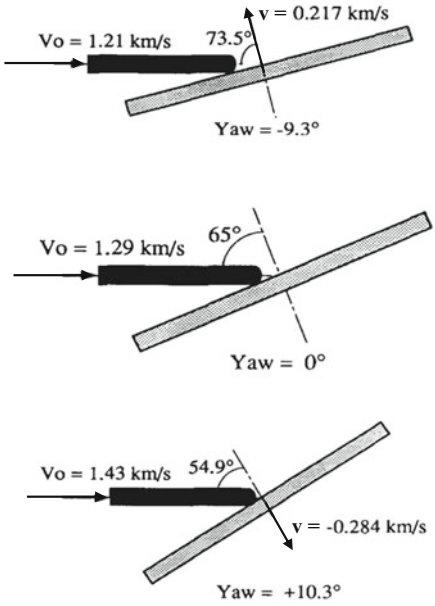

Fig. 7.41 The experiments with moving plates and the equivalent impacts on stationary targets with the corresponding yaw angles

were inclined to the plate's line of flight at the desired yaw angle. The combined yaw and inclination resulted in a significant rotation of the rods, which also broke up into several pieces during the grazing interaction.

Liden et al. (2006) used the same technique to follow the interaction of a moving plate with a long rod. They used 2 mm thick steel plates which constituted an integral part of their sabots, and obliquities of: $\beta = 20°$, 30° and 60°. The plates were launched by a two-stage gas gun to velocities in the range of 1.83–2.18 km/s towards WHA rods with L/D = 15, D = 2 mm. The rods were positioned at yaw angles of $\theta = 2.5°$–8° in order to achieve equivalent plate velocities of 100, 200 and 300 m/s, for a relative rod/plate velocity of 2.0 km/s. Figure 7.42 shows two sets of x-ray shadowgraphs from experiments with $\beta = 30°$ and yaw angles of $\theta = +2.6°$ and $\theta = -3.1°$, which correspond to effective plate velocities of +200 m/s and −200 m/s, respectively. The shadowgraphs show the stationary

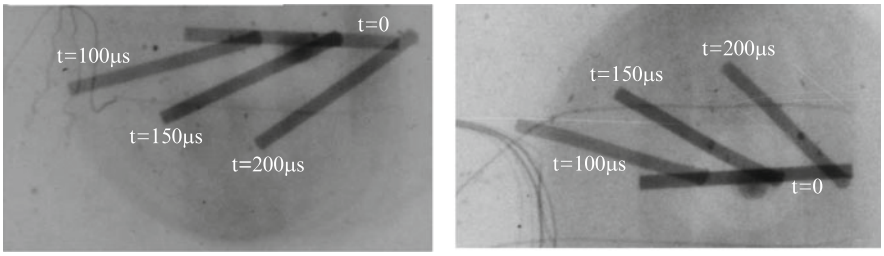

Fig. 7.42 Shadowgraphs from impacts at $\beta = 30°$. *Left*: positive yaw $\theta = 2.6°$, and *right*: negative yaw $\theta = -3.1°$

rods before impact, and the rotating rods at 100, 150 and 200 μs after impact. It is clear that the continued grazing interaction with the plates induces a significant rotation to these rods. At a larger yaw angle of $\theta = 7^\circ$ rod breakup was observed for the case where the plate was, effectively, moving away from the rod.

In order to follow these interactions Rosenberg et al. (2009) presented 3D numerical simulations for two cases in which the plates are moving at 2.0 km/s towards rods which are tilted at $\theta = +7^\circ$ and -7°, representing the experiments performed by Liden et al. (2006). The resulting yaw rates from such simulations should be taken into consideration for an active armor design, in order to determine the necessary distance to the protected vehicle. The interaction described on the left side of Fig. 7.43 corresponds to a plate moving away from the rod (positive yaw). This interaction resulted in a much higher yaw rate, as compared with the rate induced by the plate moving towards the rod (negative yaw), which is shown on the right hand side of this figure.

Liden (2008) added a fracture model to the Johnson-Cook strength model of the WHA rods in their simulations. Good agreement was obtained between these simulations and the experimental results for the number of rod fragments and their positions along the rod, as shown on the right hand side of Fig. 7.44. The simulations also reproduced the experimental results where the rods were significantly bent but did not fracture, as shown on the left side of Fig. 7.44.

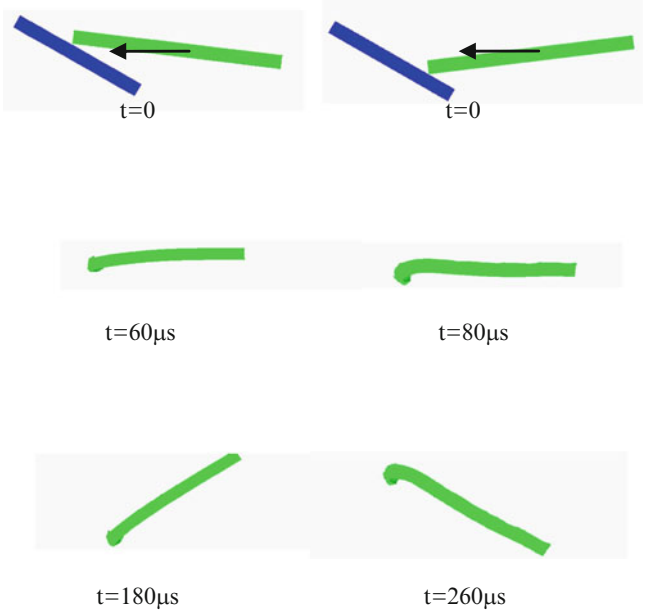

Fig. 7.43 Simulation results for impacts at inclined plates with positive yaw (*left*) and negative yaw (*right*)

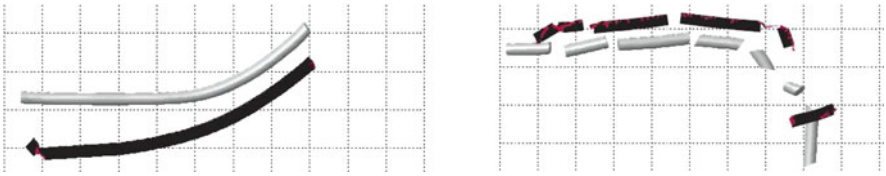

Fig. 7.44 Comparing simulations results (*grey*) with experiments (*black*) of yawed impacts, for plates moving towards the rod (*left*) and away from it (*right*)

7.3 Defeating Shaped Charge Jets

7.3.1 The Explosive Reactive Armor (ERA)

Shaped charge jets are the most lethal threats on battle tanks since their penetration capabilities exceed the wall thicknesses of these vehicles. Thus, armor designers were concentrating for many years on finding defeat mechanisms which will reduce the lethality of these jets. The invention of the explosive reactive armor (ERA) by Manfred Held (1970) is, undoubtedly, the most successful breakthrough in this field. Much of the published data on ERA as well as their interpretation, were summarized by Held et al. (1998) and by Mayseless (2010). The basic principle behind the ERA is very simple and its protective capability is so impressive that it is considered as the most efficient add-on armor technology, for both battle tanks and armored personnel carriers. The ERA cassette includes two, relatively thin, steel plates with an explosive interlayer between them. Typically, the thickness of each one these layers is 2–3 mm. The cassette is placed at an inclination angle of about 30° to the horizon, at a certain distance from the wall of the protected vehicle. The explosive layer is initiated upon jet impact and it propels the two plates at opposite directions to velocities of about 1.0 km/s. The moving plates interact with the jet for a long time, eroding and deflecting its elements and reducing their penetration capability. The significant disruption to the jet is evident in the shadowgraph shown in Fig. 7.45, from Mayseless et al. (1984). The jet is moving from left to right in this shadowgraph, and it is clearly seen that its fast parts are severely disturbed as they emerge from the moving plates. One can also observe the damage induced to the slower parts of the jet by the front plate before they reach the rear plate.

Fig. 7.45 Jet disruption by a reactive cassette

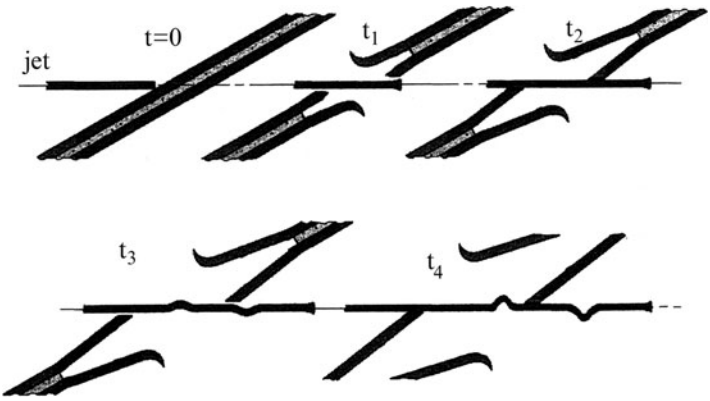

Fig. 7.46 A schematic description of the interaction between the jet and the moving plates

Upon impact, the jet initiates the explosive layer and opens a hole in both the front and back plates. The leading part of the jet, termed "the precursor," escapes the interaction without being disrupted. The size of this hole depends on the strength of the steel plates and on the diameter of the jet tip which is usually larger than the diameter of the rest of the jet, as seen in Fig. 1.19. As the plates are propelled by the explosive products they interact with the jet in a grazing mode, inducing small disturbances which grow with time as discussed by Held (2005), and shown schematically in Fig. 7.46. These disturbances are directed in opposite directions, depending on which plate interacts with the jet. The fact that some parts of the jet are missing in the shadowgraph is due, according to Held (2005), to the rear plate's interaction with the disturbances which were produced by the front plate.

As stated above, due to their high effectiveness against shaped charge jet, these ERA cassettes have been applied to various armored vehicles. However, there are very few publications which detail information concerning their performance as a function of the relevant parameters, such as plate thicknesses and their velocities. Held (2006) summarized some of his results and those of Ismail et al. (2004), while Mayseless (2010) analyzed these results by applying an analytical approach. In both sets of experiments, the residual penetrations (P_{res}) of the jets into steel witness blocks were determined as a function of explosive layer thickness (h) in a symmetric cassette b/h/b. The plate thicknesses (b) were 1 and 3 mm, in the works of Held (2006) and Ismail et al. (2004), respectively. The penetration depths (P_0) of these jets into a thick steel target (without the cassette), were used to evaluate the effectiveness of these cassettes. Thus, the efficiency of a given cassette is inversely proportional to the ratio P_{res}/P_0. Although the two sets of experiments were performed with different explosives they seem to fall on a single curve, for the ratio P_{res}/P_0 as a function of explosive thickness (h), as shown in Fig. 7.47.

The coincidence of these two sets of data is probably fortuitous as argued by Held (2006), who reasoned that the velocity of the plates should be the controlling parameter, rather than the thickness of the explosive. Plate velocities can be

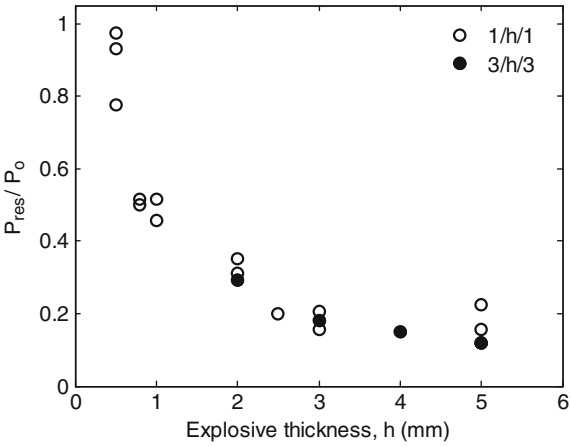

Fig. 7.47 The effect of explosive thickness on cassette efficiency for two types of cassettes

calculated by the analysis of Gurney (1943), for the velocity of metallic plates which are propelled by explosive layers. Detailed descriptions of Gurney's analysis for spherical, cylindrical, and planar configurations are given in Walters (1990) and in Meyers (1994). According to this analysis the velocity of the plates in a symmetric cassette which consists of two equal mass (M) plates, and an explosive interlayer of mass C_{exp}, is given by:

$$V = \frac{\sqrt{2E_{\exp}}}{2M/C_{\exp} + 1/3} \tag{7.18}$$

where the term $(2E_{exp})^{0.5}$ is given in units of velocity, and E_{exp} is related to the chemical energy of the specific explosive being used.

Using this equation, Held (2006) derived the velocities of the plates for the 1/h/1 and the 3/h/3 cassettes, and plotted the corresponding P_{res}/P_0 ratios in terms of plate velocities, as shown in Fig. 7.48.

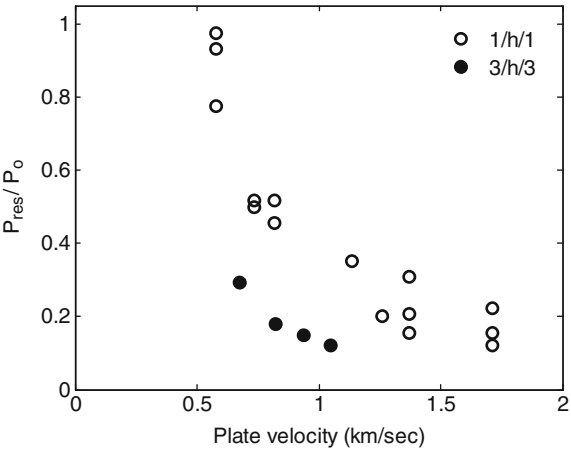

Fig. 7.48 The relation between cassette efficiency and plate velocity for the two types of cassettes

This display of the experimental results shows that the efficiency of a given cassette depends on the velocity of the plates (V_p) and on their thickness (b). A close examination of the data points in this figure shows that for a given value of P_{res}/P_0, the two cassettes have equal values of the product bV_p^2. This means that the data for the two cassettes should fall on a single curve of P_{res}/P_0 as a function of the kinetic energy of the plates. In fact, this is the expected result from Fig. 7.47 where the explosive thickness is the free parameter since, according to the Gurney relation, the plate's energy is directly related to the explosive thickness. Thus, it seems that an energy-based interaction may account for the efficiency of reactive cassettes against shaped charges.

Koch and Bianchi (2010) performed a parametric study by varying the thicknesses of the plates and the explosive layers. They also tested cassettes with different steel plates in order to study the effect of plate strength on cassette efficiency. Their 50 mm charge was placed at a distance of 250 mm from the reactive cassette, and a thick witness block was placed at a distance of 220 mm from the cassette, in order to determine residual penetrations. The thicknesses of the plates were b = 1.0, 3.0 and 6.0 mm and the thicknesses of the PETN-based explosive layers, with density of 1.4 g/cm^3, were in the range of h = 1.0–7.0 mm. In all of these tests the inclination angle of the cassettes was $\alpha = 45^{\circ}$. As expected, plates with higher strength resulted in a higher efficiency, due to the smaller holes which the jet opened in these plates. The resulting mass efficiencies (E_m) of these cassettes were E_m = 2.85, 3.0, and 4.03 for steel plates with compressive strengths of: Y = 0.4, 0.6 and 2.0 GPa, respectively, enhancing the assumption that stronger plates result in higher efficiencies.

The results of Koch and Bianchi (2010) for three types of symmetrical cassettes, in terms of their mass efficiency as a function of explosive thickness, are shown in Fig. 7.49. The mass efficiency increases with explosive thickness due to the higher velocities imparted to the plates, in accord with the other cassette designs which were described above.

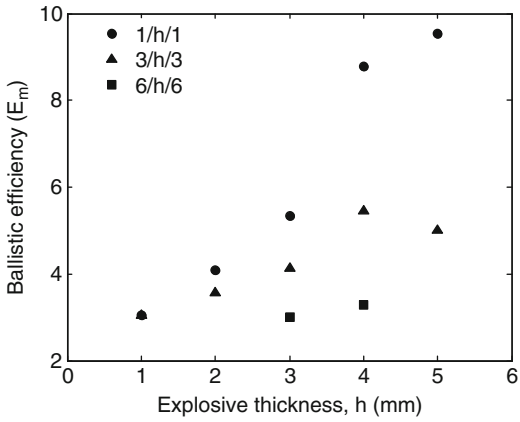

Fig. 7.49 The mass efficiency of different cassettes as a function of explosive thickness

The interaction of the jet with moving plates is a very complex process since it involves many issues such as: the dynamics of hole growth in a thin plate, the grazing interaction of the jet elements with the edge of the hole, the growth of small disturbances along the jet with time and distance, the effect of the explosive products, etc. Obviously, this interaction is too complicated for an analytical treatment, which is the main reason for the scarcity of published models in the open literature. Mayseless (2010) applied a momentum-based analysis in order to account for the efficiency of reactive cassettes. This analysis is based on an earlier model by Mayseless et al. (1984) for the efficiency of a given cassette, in terms of the mass flux ratio between the jet and the plate. The mass flux ratio for a given jet/plate pair is given by:

$$\frac{\dot{m}_p}{\dot{m}_j} = \frac{k}{V_j \tan\alpha / V_p \pm 1/\cos\alpha} \tag{7.19}$$

where the (+) and (−) signs stand for the front and rear plates, respectively. The parameter k includes the jet/plate density ratio as well as the ratio of jet diameter to plate thickness. The efficiency of the cassette according to this model is due mainly to the rear plate, which moves in the direction of the jet. As shown by Mayseless (2010) the calculated efficiency, as defined by this mass-flux ratio, follows the general trend in the results of Held (2006) and Ismail et al. (2004).

The high efficiency of ERA cassettes against shaped charge jets has been demonstrated in many publications by M. Held, who showed that the differential efficiency, as defined by (6.2), of cassettes with a thick explosive layer can reach values of more than twenty, as demonstrated in Held (1999a). The specific cassette which was used in this work consisted of two steel plates, 2.5 mm thick, and a 12 mm thick datasheet explosive. The residual penetration of the jet into a semi-infinite steel target was 143 mm, as compared with a penetration depth of 460 mm without the cassette. Held (1999b) also demonstrated the efficiency of heavy cassettes against long rod penetrators. He notes that a useful cassette should be effective against both shaped charge jets and long rods. Thus, he used a 40/10/25 cassette, with explosive thickness of 10 mm, against long rods and shaped charge jets in full scale experiments. The thick plates in these cassettes were propelled to relatively low velocities in order to prolong their interaction with the long rod, which is much slower than the shaped charge jet. The differential efficiency of the heavy cassette against a large shaped charge jet was about seven, and about 4.5 against a long rod.

One of the main problems concerning the use of reactive cassettes is due to the collateral damage which the flying plates induce to both the protected vehicle and to its surroundings. In order to reduce this damage, Mayseless (2007) proposed the use of ceramic tiles instead of steel plates, realizing that the brittle nature of ceramics should result in their total comminuting upon jet impact. This idea has been followed by Koch and Bianchi (2010) who compared the efficiencies of alumina tiles with those of steel plates for equal weight reactive cassettes. The thicknesses of the alumina tiles were: h = 2.9, 5.9 and 11.8 mm thick, matching the weights of the h = 1, 3 and 6 mm steel plates, respectively. As far as the explosive thickness is

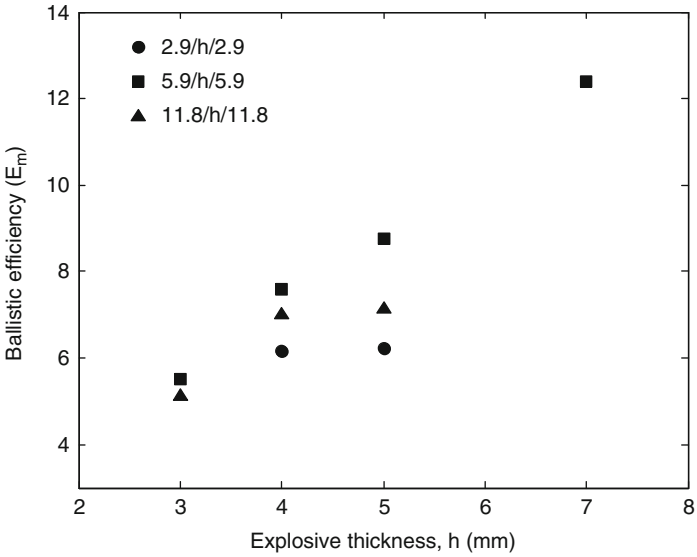

Fig. 7.50 Ballistic efficiencies of alumina-based symmetric cassettes as a function of explosive thickness

concerned, the same general trends in the ballistic efficiency were found for these ceramic-based cassettes, as shown in Fig. 7.50.

Koch and Bianchi (2010) obtained higher efficiencies with the ceramic tiles, as compared with the equal weight steel cassettes. For example, a symmetric steel cassette with 3 mm thick plates and an explosive layer of 5 mm, resulted in an efficiency of $E_m = 5$, as compared with an efficiency of $E_m = 8.8$ for an equal weight ceramic cassette. The difference can be attributed to the smaller hole which the jet opens in the ceramic tile. A smaller hole results in a shorter jet which "escapes" the interaction, as was already demonstrated for the higher strength steel plates. It is also worth noting that these experiments resulted in an enhanced efficiency for asymmetric cassettes with thicker front plates, especially for cassettes with thick explosive layers. In particular, an efficiency of $E_m = 14.3$ was obtained for a cassette with an explosive thickness of 7 mm, a front tile of 11.8 mm, and a 2.9 mm back tile, which was the highest efficiency in this study. Thus, the ceramic tiles showed a clear advantage over the steel plates, as far as mass efficiencies are concerned. In addition, these tiles were pulverized during their early stages of flight, as observed by the x-ray shadowgraphs, resulting in less damage to the surrounding, as expected.

The effect of the explosive products on jet disruption has been investigated by Brown and Finch (1989) in a series of experiments where the jets impacted the cassettes at normal incidence. With this configuration, most of the jet elements are not disturbed by the plates. Thus, any disturbance to the main part of the jet should be attributed to its interaction with the explosive products. The cassettes in this study consisted of mild steel plates with an explosive sheet (type SX2) between them. X-ray shadowgraphs were taken after the whole jet emerged from the

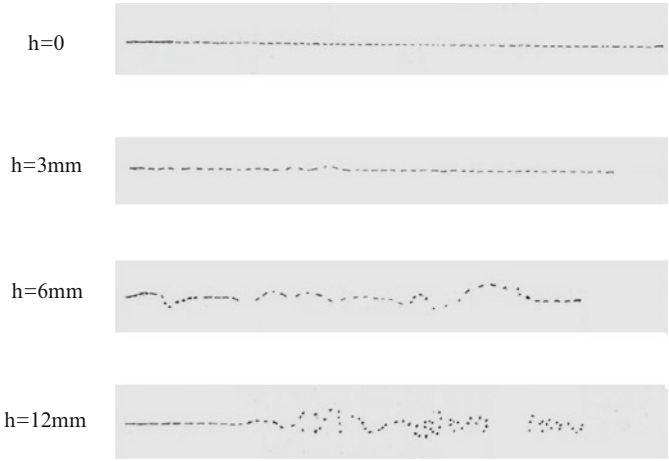

Fig. 7.51 Jet disruption as a function of explosive thickness

interaction with the cassettes. Several results are shown in Fig. 7.51, for 6/h/6 cassettes which consisted of 6 mm plates of mild steel and an explosive layer of varying thickness (h). These shadowgraphs were taken at 152 μs after impacting cassettes with h = 0, 3, 6, and 12 mm. It is clear that a minimal explosive thickness is needed in order to induce a meaningful disruption to the jet.

In order to investigate this disruption process, Rosenberg and Dekel (1999b) performed a series of 2D numerical simulations for similar cassette configurations. The copper jets in these simulations, with a diameter of 3 mm, were given a uniform velocity of 7.0 km/s. The relevant properties of the steel plates and the explosive sheets, from Brown and Finch (1989), were reproduced in the simulations to a reasonable degree. The initiation of the explosive in the simulations was performed through a threshold pressure which resulted in its immediate detonation. The basic disruption mechanism is captured by following the results of one of these simulations as shown in Fig. 7.52, for a 6/6/6 cassette which consists of equal thicknesses (6 mm) for all the layers. During the first few microseconds the jet penetrates the cassette, opens a large hole in the plates, and initiates the explosive. At 15 μs after impact there is a clear indication that the inverted jet material, together with the plate debris and the explosive products, arrived at the symmetry axis, impacted the jet and disrupted its later parts. The disturbance to the jet was related to the timing of this lateral impact at the axis. Thus, the more effective disturbances, resulting in a shorter precursor which "escaped" the interaction, were obtained when the debris arrived earlier at the axis. This part of the jet is denoted as L_{esc} in the figure.

These simulations qualitatively reproduced most of the experimental results from Brown and Finch (1989). For example, replacing the explosive with a stronger one resulted in a shorter precursor in both experiments and simulations. Also the effectiveness of an explosive "pill" inserted in the steel plates, was compared with that of the explosive sheet. Both the experiments of Brown and Finch (1989) and

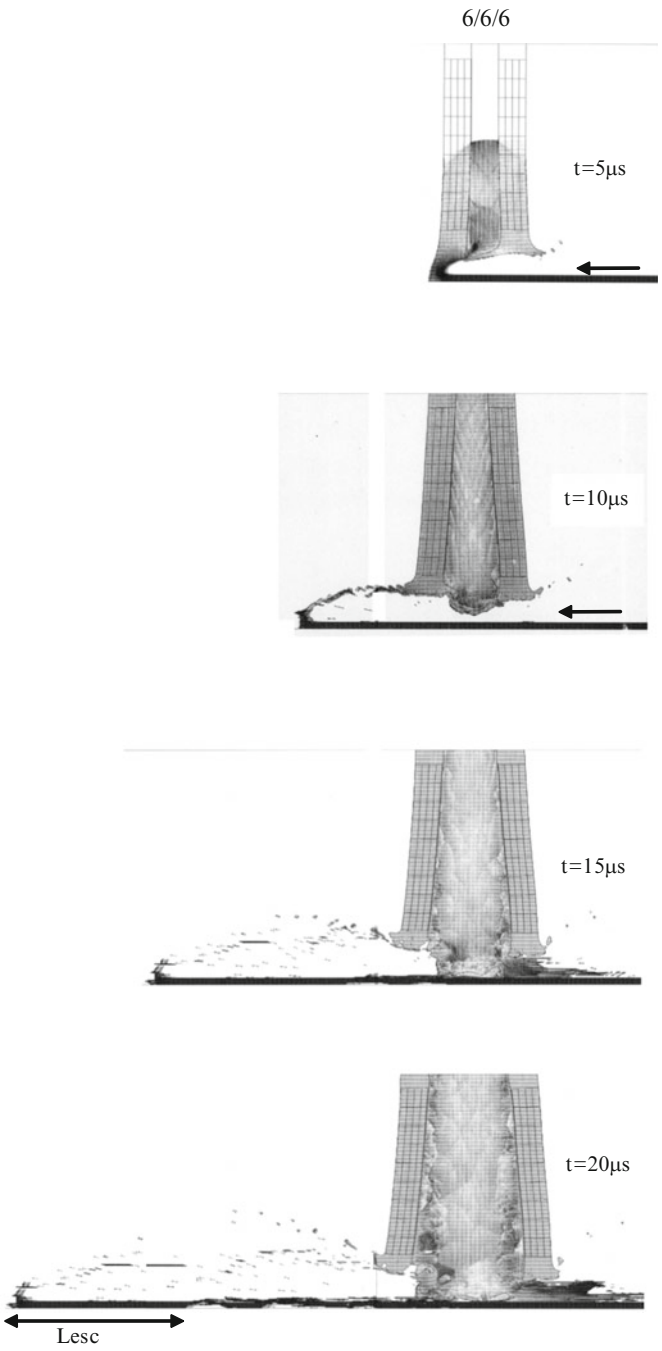

Fig. 7.52 Simulation results for the interaction of a jet with a reactive cassette at normal incidence

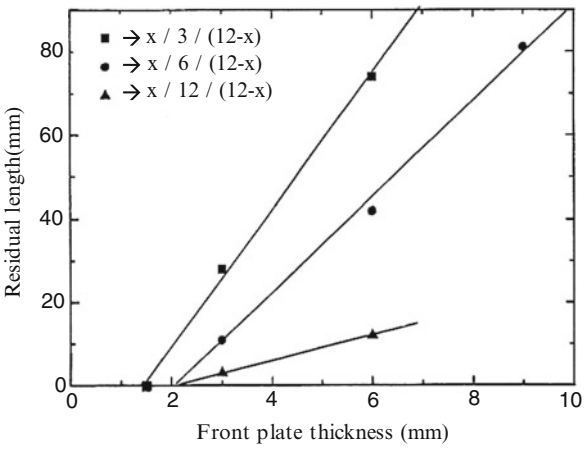

Fig. 7.53 The intact jet length as a function of front plate thickness in constant weight cassettes

the simulations by Rosenberg and Dekel (1999b), showed that these explosive discs induce the same jet disturbances, as those obtained by continuous explosive sheets. Replacing the steel plates with aluminum plates of equal-weight resulted in very similar interactions, which means that the confinement of the explosive layer is important for this interaction. Finally, a set of simulations was performed with a total thickness of 12 mm for the steel plates, varying the respective thicknesses of the front and back plates. These cassettes were also checked for different explosive layers, and the residual lengths of the escaping intact jets are shown in Fig. 7.53. One can clearly see that for the three types of cassettes, with explosive layers of h = 3, 6 and 12 mm, the shortest intact jets are obtained for the cassettes with the thinnest front plates. The extrapolation of these results gives a value of about 2 mm for the front plate thickness which reduces the length of the escaping jet to zero.

One should regard these simulations as a demonstration of their usefulness in following the mechanism responsible for a given defeat process, as well as highlighting the role of material properties in the interaction. These parametric studies are not intended to serve as design tools but they can save a lot of experimental effort for the armor engineer.

7.3.2 Passive Cassettes

The reactive armor cassettes were found to be very effective in disrupting shaped charge jets but they have an inherent disadvantage, which is due to the damage they inflict on their surroundings, as discussed above. A much less violent reaction is obtained if the explosive layer in the cassette is replaced by an inertial material, as was first suggested by Held (1973). These, so called "passive cassettes," consist of a low impedance interlayer between the two steel plates and, obviously, they are less effective than the reactive cassettes. However, with the proper choice of materials the passive cassette can disrupt a major part of the jet, as can be seen in Fig. 7.54.

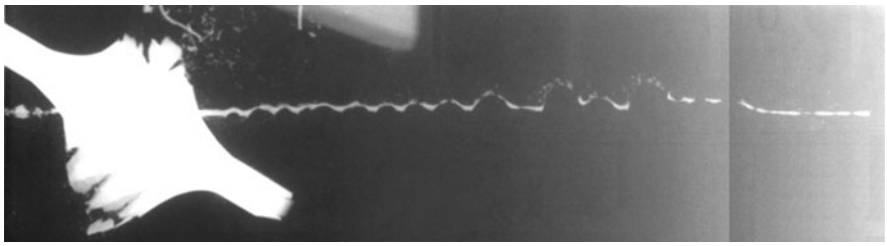

Fig. 7.54 The disruption of a jet by a passive cassette

Their main advantage is the much less collateral damage which they induce, mainly because the steel plates do not acquire high velocities. In fact, the plates do not fly apart during the interaction with the jet, which results in their bulging around the impact point, as is seen in the figure.

The interaction of the jet with the passive cassettes has been investigated by Gov et al. (1992), Thoma et al. (1993), Held (1993) and Yaziv et al. (1995). The basic principle behind this interaction, as outlined by Gov et al. (1992), is based on the bulging of the steel plates around the impact area of the jet. The bulging is due to the high pressures induced in the interlayer material by jet impact, pushing the plates apart in a large area around the penetrating jet. In addition, the rear plate is accelerated by the impact of the jet and its bulging is enhanced, as compared with the front plate. The local motion of the plates results in a continuous interaction with the jet, disrupting it in a similar way to that of the reactive cassette. The main difference between the actions of the two cassettes is in the much shorter time duration which the passive cassette interacts with the jet.

Gov et al. (1992) used 2D numerical simulations to follow the bulging process of the steel plates in a cassette which included a rubber interlayer. Their analysis showed that the process of plate acceleration is insensitive to the obliquity of the impact. Thus, 2D simulations can approximate the actual bulging of inclined plates, as they showed by comparing the bulging in their simulations with the experimental X-ray shadowgraph. Since the impact is at normal incidence in these simulations, the continued interaction between the plates and the jet is not accounted for. Still, these 2D simulations can be very useful for a parametric study of the passive cassette, as was shown by Rosenberg and Dekel (1998b). They followed the relative velocities of the metallic plates, at several locations away from the symmetry axis, and related them to the efficiency of the cassette. The basic assumption is that faster moving plates will induce enhanced disruption to the jet. The three control points, where the relative velocities were determined, were chosen at arbitrary distances from the impact point. The bulging process of a 3/10/3 cassette impacted by a 3.0 mm copper jet at 7.0 km/s, is shown in Fig. 7.55. The 10 mm thick interlayer material in this simulation was Plexiglas with strength of 0.1 GPa. Note the much larger deflection of the back plate which moves in the direction of the jet's motion, as discussed above.

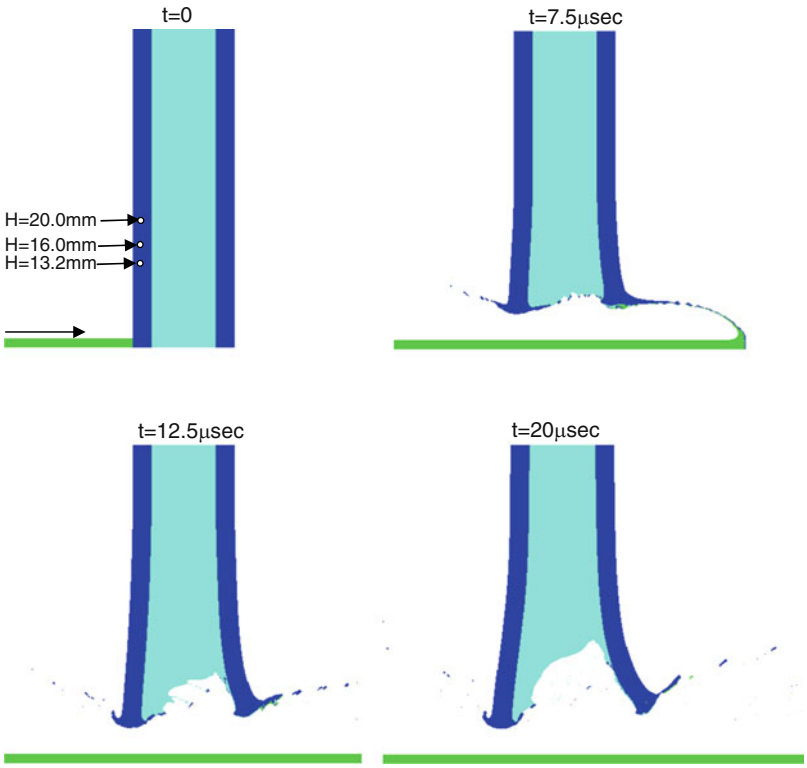

Fig. 7.55 Simulation results for the bulging process of a 3/10/3 passive cassette

The following figures describe some of the results from Rosenberg and Dekel (1998b) in terms of the relative plate velocities as a function of the relevant parameters of the passive cassettes. Figure 7.56 shows the relative velocities of the two plates for 3/h/3 cassettes as a function of the interlayer thickness, at the three locations away from the symmetry axis: H = 13.2, 16 and 20 mm. The thickness of the Plexiglas interlayer was varied between h = 3–16 mm, and it is clear that for a thicknesses of about h = 8.0mm these velocities reach their asymptotic values. Thus, according to these simulations there is no advantage in using a thicker interlayer for this particular setup.

Varying the strength of the Plexiglas interlayer resulted in increased relative velocities with decreasing interlayer strength. On the other hand, these velocities were independent on the strength of the steel plates, as expected. Note that the efficiency of a cassette with stronger steel plates is expected to be higher because the diameter of their holes will be smaller, and they should interact more frequently with the jet.

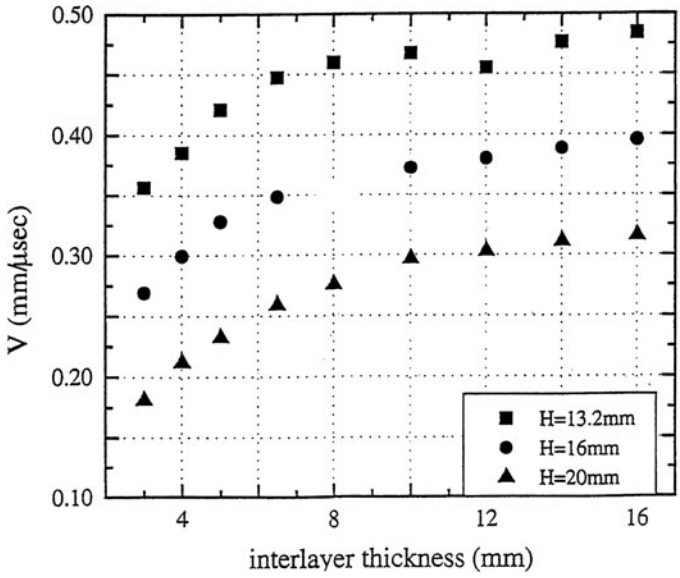

Fig. 7.56 The dependence of the relative plate velocity on interlayer thickness

A set of simulations was performed for constant weight cassettes, where the total thickness of the front and back plates was 6 mm. As seen in Fig. 7.57, the relative velocities of the symmetric cassettes are the lowest, which means that the

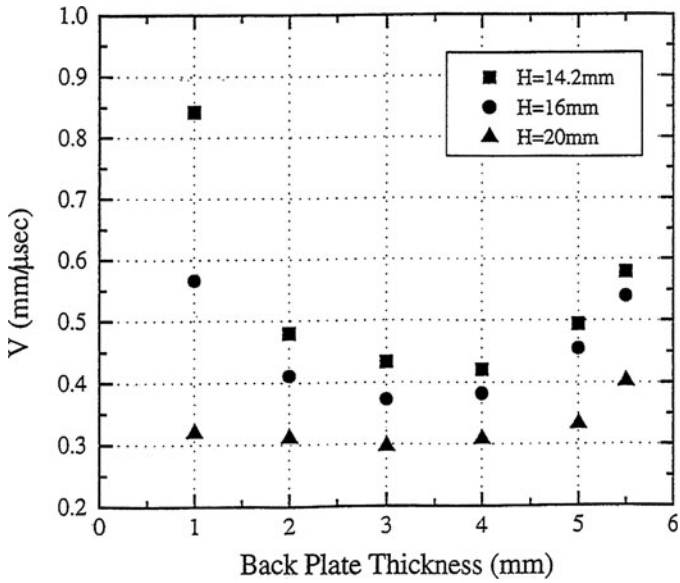

Fig. 7.57 Simulation results for constant weight cassettes with total steel plate thickness of 6 mm

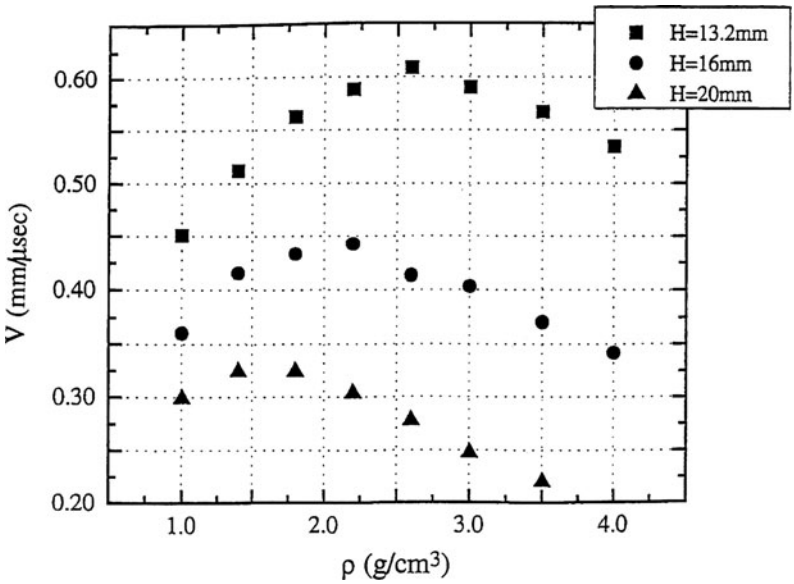

Fig. 7.58 Simulation results for cassettes with a constant interlayer areal density

asymmetric cassettes are expected to perform better. Moreover, according to these simulations, cassettes with thin back plates are expected to perform better than the others, as far as this configuration is concerned.

Finally, the density and thickness of the interlayer cassette were varied in such a way that their product (the areal density) was held constant, at 19 kg/m^2. Figure 7.58 shows the results of this set of simulations and it is evident that the highest plate velocities are obtained for interlayer densities in the range of 2.0–2.5 g/cm^3. We should emphasize, again, that these simulations are not aimed at an actual design of armor systems, but to identify the important parameters and their trend, in order to minimize the experimental work which is needed for such studies.

We have noted above that the lower ballistic efficiency of the passive cassette, as compared with the reactive one, is compensated by the much less damage which it induces to the surrounding. Several laboratories are engaged in developing hybrid cassettes which contain interlayers of energetic materials. Obviously, these cassettes have a reduced efficiency as compared with reactive cassettes. However, they are expected be more effective than the passive cassettes since their interlayer material is undergoing some reaction, pushing the steel plates apart more effectively. Holzwarth and Weimann (2001) examined the performance of such an interlayer, which consisted of a mixture of the energetic binder glycidyl-azide-polymer (GAP) and some other materials, including the RDX explosive. Their reference interlayer material for a 2/X/2 cassette, was rubber with a density of 1.4 g/cm^3. In their tests with different energetic mixtures, they found that a mixture of the GAP binder with 50% RDX resulted in a significant improvement as compared with their reference cassettes.

One of the more important issues which determine the ballistic efficiency, for both reactive and passive cassettes, is related to the growth dynamics and the maximal diameter of the hole which the jet induces in the plate. We have seen that large holes result in an appreciable jet which escapes the interaction with the plate without being disturbed. Thus, the best performing cassettes are those for which the hole diameters are minimal. In order to have an estimate for the parameters which influence the size of these holes, consider the model of Szendrei (1983), who addressed the dynamics of crater enlargement in a semi-infinite target by a high velocity jet. His analysis resulted in the following expression for the maximum diameter which the crater achieves (D_{max}) in terms of the jet's velocity (V), the densities of the jet and the target, and the strength of the target (Y_t):

$$\frac{D_{\max}}{D_j} = \frac{V}{\sqrt{2Y_t}(1/\sqrt{\rho_j} + 1/\sqrt{\rho_t})} \tag{7.20}$$

where D_j is the diameter of the jet. Minor modifications to this expression were suggested by Shinar et al. (1995) and Held (1995), but the basic dependence of D_{max} on the relevant parameters is the same as in (7.20). There is a certain ambiguity about the final expression for the crater diameter and the definition of Y_t in the works of Szendrei (1983) and Shinar et al. (1995) who use $\sigma_t = 2Y_t/\sqrt{3}$ for the strength of the target. Their expression for the maximal crater diameter is:

$$\frac{D_{\max}}{D_j} = \left(1 + \frac{V^2}{2\sigma_t(1/\sqrt{\rho_j} + 1/\sqrt{\rho_t})^2}\right)^{0.5} \tag{7.21}$$

which reduces to that of Szendrei (1983), (7.20), for high impact velocities. In fact, for typical jet velocities of 3–8 km/s the two expressions result in similar values, as was shown by Shinar et al. (1995). One can simplify both equations for cases where copper jets ($\rho_j = 8.9$ g/cm^3) impact steel targets ($\rho_t = 7.85$ g/cm^3) by writing $\rho_t \approx \rho_t = \rho$. Equation (7.20) reduces to the following form:

$$\frac{D_{\max}}{D_j} = \frac{V}{2}\sqrt{\frac{\rho}{2Y_t}} \tag{7.22a}$$

and (7.21) simplifies to:

$$\frac{D_{\max}}{D_j} = \left(1 + \frac{\rho V^2}{8\sigma_t}\right)^{0.5} \tag{7.22b}$$

Naz (1989) performed a set of experiments with L/D = 10, D = 4 mm copper rods, which impacted various steel targets at velocities in the range of 2.5–5.0 km/s. The steel targets had compressive strengths in the range of 0.64–1.4 GPa,. The final

crater diameters were in excellent agreement with the calculated values from (7.22a) and (7.22b), as shown by Shinar et al. (1995). An important consequence from these analyses is that for plates of equal strength, the one with the lower density is expected to result in a smaller cavity diameter. Assuming that a similar analysis also holds for plates with finite thicknesses, we may conclude that a lower density plate, in either reactive or passive cassettes, will have a higher ballistic efficiency against shaped charge jets.

The dynamics of crater growth as a result of jet impact has been also analyzed by Szendrei (1983). His result for the time dependence of the crater diameter, D = D (t), has been verified by several workers who followed this growth process with flash X-ray shadowgraphs, such as in Held and Kozhushko (1999). The analysis of Shinar et al. (1995) for the time dependence of the crater growth resulted in a close agreement with similar experiments, by De-Rosset and Merendino (1984), who followed the crater growth in 6.35 mm steel plates, by using flash x-rays. An analytical model for the interaction between the jet and the moving plates, of either reactive or passive cassettes, will have to be based on these results from the analysis of Szendrei (1983).

References

Abrate S (2011) Impact engineering of composite materials. Springer, Vienna

Alekseevskii VP (1966) Penetration of a rod into a target at high velocity. Combust Explos Shock Waves 2:63–66

Al'tshuler LV (1965) Use of shock waves in high-pressure physics. Sov Phys Uspenskhi 8:52–90

Allen WA, Rogers JW (1961) Penetration of a rod into a semi-infinite target. J Franklin Inst 272:275–284

Allison FE, Vitali R (1963) A new method of computing penetration variables for shaped charge jets. Ballistic Research Laboratories Internal Report, BRL-R-1184

Almohandes AA, AbdelKader MS, Eleiche AM (1996) Experimental investigation of the resistance of steel-fiberglass reinforced polyester laminated plates. Compos Part B Eng 27:447–458

Anderson CE (1987) A review of the theory of hydrocodes. Int J Impact Eng 5:33–59

Anderson CE (2002) Developing an ultra-lightweight armor concept. In: McCauley J et al (eds) Ceramic armor materials by design, ceramics transactions, vol 134. The American Ceramic Society, Westerville, Ohio, pp 485–498

Anderson CE (2003) From fire to ballistics: a historical retrospective. Int J Impact Eng 29:13–67

Anderson CE (2006) A review of computational ceramic armor modeling, advances in ceramic armor II. In: Frank LP (ed) Proceedings of the 30th international conference and explosion on advanced ceramics and composites, vol 27, pp 1–18

Anderson CE, Orphal DL (2008) An examination of deviations from hydrodynamic penetration theory. Int J Impact Eng 35:1386–1392

Anderson CE, Mullin SA (1988) Hypervelocity impact phenomenology: some aspects of debris cloud dynamics. In: Ammann WJ (ed) Effects of fast transient loading. Balkana, Rotterdam, pp 105–122

Anderson CE, Walker JD (1991) An examination of long rod penetration. Int J Impact Eng 11:481–501

Anderson CE, Walker JD (1999) Ceramic dwell and defeat of the 0.30-cal AP projectile. In: Proceedings of the 15th army symposium on solid mechanics, Myrtle Beach, Apr 1999

Anderson CE, Morris BL, Littlefield DL (1992) Penetration mechanics database. SwRI Report 3593/001. Southwest Research Institute, TX

Anderson CE, Mullin SA, Kuhlman CJ (1993) Computer simulation of strain-rate effects in replica scale model penetration experiments. Int J Impact Eng 13:35–52

Anderson CE, Walker JD, Bless J, Sharron TR (1995) On the velocity dependence of the L/D effect for long rod penetrators. Int J Impact Eng 17:13–24

Anderson CE, Walker JD, Bless SP, Partom Y (1996a) On the L/D effect for long rod penetrators. Int J Impact Eng 16:247–264

Z. Rosenberg and E. Dekel, *Terminal Ballistics*,
DOI 10.1007/978-3-642-25305-8, © Springer-Verlag Berlin Heidelberg 2012

Anderson CE, Hohler V, Stilp AJ, Walker JD (1996b) The influence of projectile hardness on ballistic performance. Proceedings of the 16th international symposium on ballistics, San Francisco, pp 277–286

Anderson CE, Walker JD, Hauver GE (1996c) Target resistance for-long rods penetration into semi-infinite targets. Nucl Eng Des 138:93–104

Anderson CE, Hohler V, Walker JD, Stilp AJ (1999) The influence of projectile hardness on ballistic performance. Int J Impact Eng 22:619–632

Asay JR (1997) The use of shock-structure methods for evaluating high-pressure material properties. Int J Impact Eng 20:27–62

Asay JR, Kerley GI (1987) The response of material to dynamic loading. Int J Impact Eng 5:69–100

Asay JR, Lipkin J (1977) A self- consistent technique for estimating the dynamic yield strength of a shock-loaded material. J Appl Phys 49:4242–4247

Ashuach Y (2003) The effect of plate temperatures on their ballistic limit velocities. RAFAEL Report No. 2003/72, Nov 2003

Atkins AG (1988) Scaling in combined plastic flow and fracture. Int J Mech Sci 30:173–191

Atkins AG, Khan MA, Liu JH (1998) Necking and radial cracking around perforations in thin sheets and normal incidence. Int J Impact Eng 21:521–539

Avinadav C, Ashuach Y, Kreif R (2011) Interferometry-based Kolsky bar system. Rev Sci Instr 82:073908

Awerbuch J, Bodner SR (1974) Analysis of the mechanics of perforation of projectiles in metallic plates. Int J Solids Struct 10:671–684

Backman ME (1976) Terminal ballistics. Naval Weapons Center Report NWC-TP-5780. NWC China Lake, CA

Backman ME, Goldsmith W (1978) The mechanics of penetration of projectiles into targets. Int J Eng Sci 16:1–99

Bai YL, Dodd B (1992) Adiabatic shear localization: occurrence, theories and applications. Pergamon Press, Oxford

Bai YL, Johnson W (1982) Plugging: physical understanding and energy absorption. Metal Technol 9:182–190

Barker LM, Hollenbach RE (1964) Interferometer technique for measuring the dynamic mechanical properties of materials. Rev Sci Instr 36:1617–1620

Barsis E, Williams E, Skoog C (1970) Piezoresistivity coefficients in manganin. J Appl Phys 41:5155–5162

Bauer F (1983) PVF_2 polymers: ferroelectric polarization and piezoelectric properties under dynamic pressure and shock wave action. Ferroelectrics 49:213–240

Bauer F (1984) Piezoelectric and electric properties of PVF2 polymers under shock wave action. In: Asay J, Graham RA, Straub GK (eds) Proceedings of the APS conference on shock waves in condensed matter, 1983. Elsevier Science Publ., pp 225–228

Bazhenov SL, Dukhowskii IA, Kovalev PI, Rozhkov AN (2001) The fracture of SVM aramide fibers upon a high velocity transverse impact. Polym Sci Ser A 1:61–71

Bethe HA (1941) An attempt at a theory of armor penetration, Ordnance Laboratory Report R-492, Frankford Arsenal, May 1941

Behner T, Volker V, Anderson CE, Goodlin D (2002) Influence of yaw angle on the penetration of long rods in oblique targets. Proceedings of the 20th international symposium on ballistics, Orlando, Sept 2002, pp 834–841

Behner T, Anderson CE, Holmquist TJ, Wickert M, Tempelton DW (2008) Interface defeat for unconfined SiC tiles. Proceedings of the 24th international symposium on ballistics, Lancaster. vol 1, pp 35–42

Belyakov LV, Vitman FF, Zlatin NA (1964) Collision of deformable bodies and its modeling. Sov Phys Tech Phys 8:736–739

Ben-Dor G, Dubinsky A, Elperin T (2006) Effect of the order of plates on the ballistic resistance of ductile layered shields perforated by non-conical impactors. J Mech Mat Struct 1:1161–1177

Ben-Moshe D, Tarsi Y, Rosenberg G (1986) An armor assembly for armored vehicles. European Patent No. EP 0209221 A1, 13 May 1986
Bernstein D, Godfrey C, Klein A, Shimmin W (1967) Research on manganin pressure transducers. In: Proceedings of the HDP symposium on the behavior of dense media under high dynamic pressures, Paris, Sept 1967, pp 461–467
Bhatanagar A (2006) Lightweight ballistic composites- military and law-enforcement applications. Woodhead Publishing Limited, Cambridge
Bierke TW, Silsby GF, Scheffler DR, Mudd RM (1992) Yawed long-rod armor penetration. Int J Impact Eng 12:281–292
Birkhoff G, MacDougal DP, Pugh EM, Taylor GI (1948) Explosives with lined cavities. J Appl Phys 16:563–582
Bishop R, Hill R, Mott NF (1945) The theory of indentation and hardness tests. Proc R Soc 57:147–159
Bless SJ, Barber JP, Bertke RS, Swift HF (1978) Penetration mechanics of yawed rods. Int J Engng Sci 16:829–834
Bless SJ, Rosenberg Z, Yoon B (1987) Hypervelocity penetration of ceramics. Int J Impact Eng 5:165–171
Bless SJ, Benyami M, Apgar LS, Eylon D (1992) Impenetrable ceramic targets struck by high velocity tungsten long rods. Proceedings of the 2nd international conference on structure under shock and impact, Portsmouth, June 1992, pp. 27–38
Bless SJ, Subramanian R, Normandia M, Campos J (1999) Reverse impact results from yawed long rods perforating oblique plates. Proceedings of the 18th international symposium on ballistics, San Antonio, Nov 1999, pp 693–701
Borvik T, Langseth M, Hopperstad OS, Malo KA (1999) Ballistic penetration of steel plates. Int J Impact Eng 22:885–886
Borvik T, Langseth M, Hopperstad OP, Malo KA (2002) Perforation of 12 mm thick steel plates by 20 mm diameter projectiles with blunt, hemispherical and conical noses. Int J Impact Eng 27:19–35
Borvik T, Hopperstad OS, Langseth M, Malo KA (2003) Effect of target thickness in blunt projectile penetration of Weldox 460-E steel plates. Int J Impact Eng 28:413–464
Borvik T, Clausen AH, Hopperstad OS, Langseth M (2004) Perforation of AA5083-H116 aluminum plates with conical nosed steel projectiles-experimental study. Int J Impact Eng 30:367–384
Borvik T, Forrestal MJ, Hopperstad OS, Warren TL, Langseth M (2009) Perforation of AA5083-H116 aluminum plates with conical-nosed steel projectiles-calculations. Int J Impact Eng 36:426–437
Borvik T, Hopperstad OS, Pederson KO (2010) Quasi-brittle fracture during structural impact of AA7075-T651 aluminum plates. Int J Impact Eng 37:537–551
Bridgman PW (1952) Studies in large plastic flow and fracture. McGraw-Hill, London
Brooks PN (1974) Ballistic impact- the dependence of hydrodynamic transition velocity on projectile tip geometry, Rep. No. DREV 4001/74, Defense Research Establishment Valcartier, Quebec
Brooks PN, Erickson WH (1971) Ballistic evaluation of materials for armor penetrators, Rep. No. DREV R-643/71, Defense Research Establishment Valcartier, Quebec
Brown J, Finch D (1989) The shaped charge jet attack of confined and unconfined sheet explosives. Proceedings of the 11th international symposium on ballistics, Brussels, May 1989, pp 211–223
Bukharev Y, Zhurkov VI (1995) Model of the penetration of metal barrier by a rod projectile with an angle of attack. Combust Explos Shock Waves 31:104–109
Burkins MS, Paige JI, Hansen JS (1996) A ballistic evaluation of Ti/6Al/4V vs. long rod penetrators. Army Research Laboratory Report ARL-TR-1146, July 1996

Cagliostro DJ, Mandell DA, Schwalbe LA, Adams TF, Chapyak EJ (1990) Mesa 3-D calculations of armor penetration by projectiles with combined obliquity and yaw. Int J Impact Eng 10:81–92

Canfield JA, Clator IG (1966) Development of scaling law techniques to investigate penetration in concrete. NWL Report# 2057, Naval Weapon Laboratory, Dahlgren

Cheeseman BA, Bogetti TA (2003) Ballistic impact into fabric and compliant compositie laminates. Comp Struct 61:161–173

Cheeseman BA, Gooch WA, Burkins MS (2008) Ballistic evaluation of aluminum 2139-T8. Proceedings of the 24th international symposium on ballistics, New Orleans, Sept 2008, pp 651–659

Chen XW, Li QM (2002) Deep penetration of a non-deforming projectile with different geometrical characteristics. Int J Impact Eng 27:619–637

Chen YJ, Meyers MA, Nesterenko VF (1999) Spontaneous and forced shear localization in high deformation of tantalum. Mater Sci Eng 70:268

Chhabildas LC (1987) Survey of diagnostic tools used in hypervelocity impacts. Int J Impact Eng 5:201–220

Chocron S, Anderson CE, Walker JD (1998) Long-rod penetration: cylindrical vs. spherical cavity expansion for extent of plastic flow. Proceedings of the 17th international symposium on ballistics, Midrand, Mar 1998, pp 319–326

Chocron S, Grosch DJ, Anderson CE (1999) DOP and V_{50} predictions for the 0.30-cal APM2 projectile. Proceedings of the 18th international symposium on ballistics, San Antonio, Nov 1999, pp 769–776

Chocron S, Anderson CE, Walker JD, Ravid M (2003) A unified model for long-rod penetration in multiple metallic target plates. Int J Impact Eng 28:391–411

Chocron S, Kirchdoerfer T, King N, Freitas CJ (2011) Modeling of fabric impact with high speed imaging and nickel-chromium wires validation. J App Mech 78:051007

Chou PC, Flis WJ (1986) Recent developments in shaped charge technology. Propellants Explos Pyrotechnics 11:99–114

Christman DR, Gehring JW (1966) Analysis of high-velocity projectile penetration mechanics. J Appl Phys 37:1579–1587

Christman DR, Isbell WM, Babcock SG, McMillan AR, Green SJ (1971) Measurements of dynamic properties of materials, vol III-6061-T6 aluminum. General Motors Inc. Report MSL 70-23

Coleau B, Buzaud E, Chapells S (1998) A numerical study of non-normal incidence perforation of 6061-T651 aluminum plates by ogive-nosed projectiles. Proceedings of the 17th international symposium on ballistics, Mildrand, South Africa, Mar 1998,vol 3, pp 367–374

Corbett GG, Reid SR, Johnson W (1996) Impact loading of plates and shells by free-flying projectiles: a review. Int J Impact Eng 18:141–230

Cunniff PM (1992) An analysis of the system effects in woven fabrics under ballistic impact. Textile Res J 62:495–509

Cunniff PM (1996) A semi-empirical model for the ballistic impact performance of textile-based personnel armor. Textile Res J 66:45–59

Cunniff PM (1999a) Decoupled response of textile body armor. Proceedings of the 18th international symposium on ballistics, San Antonio, Nov 1999, pp 814–821

Cunniff PM (1999b) Dimensionless parameters for optimization of textile based body armor systems. Proceedings of the 18th international symposium on ballistics, San Antonio, Nov 1999, pp 1303–1310

Curran DR (1982) Dynamic fracture. In: Zukas JA, Nicholas T, Swift HF, Geszczuk LB, Curran DR (eds) Impact dynamics. John Wiley and Sons Inc., New York, pp 333–366

Curran DR, Seaman L, Cooper T, Shockey DA (1993) Micromechanical model for comminution and granular flow of brittle materials under high strain rate application to penetration of ceramic targets. Int J Impact Eng 13:52–83

Dehn JT (1986) A unified theory of penetration. Ballistic Research Laboratories Technical Report, BRL-TR-2770
Dehn J (1987) A unified theory of penetration. Int J Impact Eng 5:239–248
De-Rosset WS, Merendino AB (1984) Radial hole growth: experiments vs. calculations. Proceedings of the 8th international symposium on ballistics, Orlando, 1984, pp. 1–6
Dey S, Borvik T, Hopperstad OS, Leinum JR, Langseth M (2004) The effect of target strength on the perforation of steel plates using three different projectile nose shapes. Int J Impact Eng 30:10005–1038
Dey S, Borvik T, Teng X, Wierzbicki T, Hopperstad OS (2007) On the ballistic resistance of double layered steel plates: an experimental and numerical investigation. Int J Solids Struct 44:6701–6723
DiPersio R, Simon J, Merendino A (1965) Penetration of shaped charge jets into metallic targets. Ballistic Research Laboratories Internal Report, BRL-R-1296
Duan Y, Keefe M, Bogetti TA, Cheeseman BA, Powers B (2006) A numerical investigation of the influence of friction on energy absorption by a high-strength fabrics subjected to ballistic impact. Int J Impact Eng 32:1299–1312
Eichelberger RJ (1956) Experimental test of the theory of penetration by metallic jets. J Appl Phys 27:63–68
Ernst HJ, Wolf T, Nusing R (1999) Experimental medium-caliber studies with electromagnetic armor against KE and SC threats. Proceedings of the 18th international symposium on ballistics, San Antonio, Nov 1999, pp 861–868
Ernst HJ, Merkel T, Wolf T, Hoog K (2003) High-velocity impact loading of thick GFRP blocks. J Phys IV France 110:633–638
Euler L (1745) Neue Grundsuatze de Artillerie, reprinted as vol 14, ser. II of Euler's Opera Omnia, Teubner, Berlin, 1922
Fair H (1987) Hypervelocity then and now. Int J Impact Eng 5:1–11
Finch DF (1990) The shaped charge jet attack on confined and unconfined glass targets. Proceedings of the 12th international symposium on ballistics, San Antonio, 1990, p 67
Flockhart CJ, Woodward RL, Lam YC, O'Donell RG (1991) The use of velocity discontinuities to define shear failure trajectories in dynamic plastic deformations. Int J Impact Eng 11:93–106
Forrestal MJ, Piekutowski AJ (2000) Penetration experiments with 6061-T6511 aluminum targets and spherical nosed steel projectiles at striking velocities between 0.5 and 3.0 km/s. Int J Impact Eng 24:57–67
Forrestal MJ, Lee LM, Jenrette BD, Setchell RE (1984) Gas gun experiments determine forces on penetrators into geological targets. J App Mech 51:602–607
Forrestal MJ, Rosenberg Z, Luk VK, Bless SJ (1987) Perforation of aluminum plates by conical nosed projectiles. J App Mech 54:230–232
Forrestal MJ, Okajima K, Luk VK (1988) Penetration of 6061-T651 aluminum targets with rigid long rods. J App Mech 55:755–760
Forrestal MJ, Luk VK, Brar NS (1990) Perforation of aluminum armor plates with conical nosed projectiles. Mech Mater 10:97–105
Forrestal MJ, Brar NS, Luk VK (1991) Penetration of strain-hardening targets with rigid spherical nose rods. J App Mech 58:7–10
Forrestal MJ, Luk VK, Rosenberg Z, Brar NS (1992) Penetration of 7075-T651 aluminum targets with ogival-nosed rods. Int J Solids Struct 29:1729–1736
Forrestal MJ, Altman BS, Cargile JD, Hanchak SJ (1994) An empirical equation for penetration depth of ogive nose projectiles into concrete targets. Int J Impact Eng 15:395–405
Forrestal MJ, Frew DJ, Hanchak SJ, Brar NS (1996) Penetration of grout and concrete targets with ogive-nose steel projectiles. Int J Impact Eng 18:465–476
Forrestal MJ, Borvik T, Warren TL (2010) Perforation of 7075-T651 aluminum armor plates with 7.62 mm APM2 bullets. Exp Mech 50:1245–1251
Frank K (1981) Armor-penetration performance measures. Memorandum Report, ARBRL –MR-03097, Ballistic Research Laboratory, Mar 1981

Frew DJ, Hanchak SJ, Green ML, Forrestal MJ (1998) Penetration of concrete targets with ogive-nose steel rods. Int J Impact Eng 21:489–497
Fuller PJA, Price JH (1964) Dynamic pressure measurements to 300 kb with manganin transducers. Br J Appl Phys 15:751–758
Gama BA, Guillespie JW (2011) Finite element modeling of impact, damage evolution and penetration of thick-section composites. Int J Impact Eng 38:181–197
Gee DJ, Littlefield DL (2001) Yaw impact of rod projectiles. Int J Impact Eng 26:211–220
Giovanola JH (1988a) Adiabatic shear banding under pure shear loading. Part I: direct observation of strain localization and energy dissipation measurements. Mech Mater 7:59–71
Giovanola JH (1988b) Adiabatic shear banding under pure shear loading. Part II: fractographic and metallographic observations. Mech Mater 7:73–87
Gogolewski RP, Cunningham BJ, Riddle RA (1996) On the importance of target material interfaces during low speed impact. In: Proceedings of the 16th international symposium on ballistics, San Francisco, vol 3, Sept 1996, pp 751–760
Goldsmith W (1999) Non-ideal projectile impact on targets. Int J Impact Eng 22:95–395
Goldsmith W, Finnegan SA (1971) Penetration and perforation processes in metal targets at and above ballistic limits. Int J Mech Sci 13:843–866
Gooch WA (2002) An overview of ceramic armor applications. In: McCauley JW et al (eds) Ceramic armor material by design. The American Ceramic Society, Westerville, Ohio, pp 3–21
Gooch WA, Burkins MS, Ernst HJ, Wolf T (1995) Ballistic penetration of titanium alloy Ti-6Al-4V. Proceedings of the lightweight armor symposium, Shrivenham, June 1995
Goodier JN (1965) On the mechanics of indentation and cratering in solid targets of strain hardening metals of hard and soft spheres. In: AIAA Proceedings of the 7th symposium on hypervelocity impact, vol III, pp 215–259
Gorham DA, Pope PH, Cox O (1984) Sources of error in very high strain rate compression tests. Inst Phys Conf Ser 70:151–158
Gov N, Kivity Y, Yaziv D (1992) On the interaction of a shaped charge jet with a rubber filled metallic cassettes. Proceedings of the 13th international symposium on ballistics, vol I, Stockholm, Sweden, June 1992, pp 95–102
Grabarek CL (1971) Penetration of armor by steel and high density penetrators. Memorandum Report No. 2134. Ballistic Research Laboratories, Aberdeen
Grace FI (1993) Non-steady penetration of long rods into semi-infinite targets. Int J Impact Eng 14:303–314
Grady DE (1988) The spall strength of condensed matter. J Mech Phys Solids 36:353–384
Gray GT, Bourne NK, Henrie BL (2007) On the influence of loading profile upon tensile failure of stainless steel. J Appl Phys 101:093507
Griffith AA (1920) The phenomena of rupture and flow in solids. Phil Trans R Soc Ser A 221:163–198
Griffith AA (1924) The theory of rupture. In: Biezeno CB, and Burgers JM (eds) Proceedings of the 1st international Congress on Applied Mechanics, Delft, The Netherlands, pp 54–63
Gupta NK, Madhu V (1997) An experimental study of normal and oblique impact of hard-core projectile on single and layered plates. Int J Impact Eng 19:395–414
Gupta NK, Iqbal MA, Sekhon GS (2007) Effects of projectile nose shape, impact velocity and target thickness on deformation behavior of aluminum plates. Int J Solid Struct 44:3411–3439
Gurney R (1943) The initial velocities of fragments from bombs, shells and grenades. Ballistics Research Laboratory, Report No. 405, AII-36218, Sept 1943
Haldar A, Hamieh HA (1984) Local effects of solid missiles on concrete structures. J Struct Div ASCE 110:948–960
Halperson SM, Atkins WW (1962) Observations of hypervelocity impact. Fifth hypervelocity impact symposium, vol 2, part 2, pp 497–505
Hauver GE, Netherwood PH, Benck RF, Gooch WA, Perciballi WJ, Burkins MS (1992) Variation of target resistance during long-rod penetration into ceramics. Proceedings of the 13th international symposium on ballistics, Sundyberg, Sweden, vol 3, pp 257–264

Hauver GE, Netherwood PH, Benck RF, Kecskes IJ (1993) Ballistic performance of ceramic targets. Proceedings of the 13th army symposium on solid mechanics, Plymouth, Aug 1993, pp 23–34

Hauver GE, Netherwood PH, Benck RF, Kecskes IJ (1994) Enhanced ballistic performance of ceramic targets. Proceedings of the 19th Army Science conference, Orlando, June 1994

Hauver GE, Rapacki EJ, Netherwood PH, Benck RF (2005) Interface defeat of long-rod projectiles by ceramic armor. Army Research Laboratory Report, ARL-TR-3590, Sept 2005

Held M (1970) Explosive reactive armor, patent filed on 21.02.1970, Germany, No. 2008156

Held M (1973) Protective device against projectiles, especially shaped charges, German Patent No. 2358277, 22.11.1973

Held M (1993) Armor. Proceedings of the 14th international symposium on ballistics, Quebec city, Canada, 1993, pp 45–57

Held M (1995) Verification of the radial crater growth by shaped charge jet penetration. Int J Impact Eng 17:387–398

Held M (1999a) Effectiveness factors of explosive reactive armor systems. Propell Explos Pyrotech 24:70–75

Held M (1999b) Comparison of explosive reactive armor against different threat level. Propell Explos Pyrotech 24:76–77

Held M (2005) Defeating mechanisms of reactive armor sandwiches. Proceedings of the 22nd international symposium on ballistics, Vancouver, Canada Nov 2005, pp 1001–1007

Held M (2006) Stopping power of ERA sandwiches as a function of explosive layer thickness or plate velocity. Propellants Explosives Pyrotechnics 31:234–238

Held M, Kozhushko AA (1999) Radial crater growing process in different materials with shaped charge jets. Propell Explos Pyrotech 24:339–342

Held M, Mayseless M, Rototaev E (1998) Explosive reactive armor. Proceedings of the 17th international symposium on ballistics, Midrand, South Africa, Mar 1998, pp 33–46

Heritier D, Derassat E, Fonlupt S (2010) Ballistic impact experiments on ultrahigh hard perforated add-on armor. Proceedings of the 25th international symposium on ballistics, Beijing, China, May 2010, pp 1501–1508

Hermann W, Jones AH (1961) Survey of hypervelocity impact information; MIT, Aeroelastic and Structure Research Laboratory Report No. 99-1, Oct 1961

Hermann W, Wilbeck JS (1987) Review of hypervelocity penetration theories. Int J Impact Eng 5:307–322

Hill R (1950) The mathematical theory of plasticity. Oxford University Press, London

Hill R (1980) Cavitation and the influence of headshape in attack of thick targets by non-deforming projectiles. J Mech Phys Solids 28:249–263

Hohler V, Behner T (1999) Influence of the yaw angle on the performance reduction of long rod projectiles. Proceedings of the 18th international symposium on ballistics, San Antonio, Nov 1999, pp 931–938

Hohler V, Stilp A (1975) Terminal ballistics investigation to discover the resistance of two-plate targets of steel. Ernst Mach Institute Report No. E-9/75

Hohler V, Stilp AJ (1987) Hypervelocity impact of rod projectiles with L/D from 1 to 32. Int J Impact Eng 5:323–332

Hohler V, Stilp AJ (1990) Long-rod penetration mechanics. In: Zukas JA (ed) High velocity impact mechanics, Wiley, pp 321–404

Hohler V, Rothenhausler H, Schneider E, Senf H, Stilp AJ, Tham R (1978) Untersuchung der Shockwirkung auf Panzerfahrzeuge. Ernst Mach Institute Report No. V2/78 (in German), Mar 1978

Hohler V, Stilp AJ, Weber K (1995) Penetration of tungsten-alloy rods into alumina. Int J Impact Eng 17:409–418

Holmquist TJ, Johnson GR (2002) A detailed computational analysis of interface defeat, dwell and penetration for a variety of ceramic targets. Proceedings of the 20th international symposium on ballistics, Orlando, Sept 2002, pp 746–753

Holmquist TJ, Anderson CE, Behner T (2005) Design, analysis and testing of an unconfined ceramic target to induce dwell. Proceedings of the 22nd international symposium on ballistics, Vancouver, Nov 2005, pp 860–868

Holmquist TJ, Anderson CE, Behner T (2008) The effect of a copper buffer on interface defeat. Proceedings of the 24th international symposium on ballistics, Lancaster, 2008, pp 721–728

Holsapple KA (1987) The scaling of impact phenomena. Int J Impact Eng 5:343–255

Holzwarth A, Weimann K (2001) Combination of inert and energetic materials in reactive armor against shaped charge jets. Proceedings of the 19th international symposium on ballistics, Interlaken, Switzerland, May 2001, pp 1523–1530

Hopkins HG (1960) Dynamic expansion of spherical cavities in metals. In: Hill R, Sneddon JN (eds) Progress in solid mechanics, vol I. Pergamon Press, Oxford, pp 84–164

Hopperstad OS, Borvik T, Langseth M, Labibes K, Albertini C (2003) On the influence of stress triaxiality and strain rate on the behavior of a structural steel, part I. Experiments. Eur J Mech A/Solids 22:1–13

Hornemann U (1989) The terminal ballistic resistance of glass against shaped charge penetration. Proceedings of the 11th international symposium on ballistics, Brussels, Belgium, vol II, May 1989, pp 381–389

Horz F, Cintala MJ, Bernhard RP, See TH (1994) Dimensionally scaled penetration experiments: aluminum targets and glass projectiles 50 μm to 3.175 mm In diameter. Int J Impact Eng 15:257–280

Inglis CE (1913) Stresses in a plate due to the presence of cracks and sharp corners. Trans Inst Nav Archit London 55:219–241

Irenmonger MJ (1999) Polyethylene composites for protection against high velocity small arms bullets. Proceedings of the 18th international symposium on ballistics, San Antonio, Nov 1999, pp 946–953

Ivanov AG (1994) Dynamic fracture and its scale effects (survey). J App Mech Tech Phys 35:430–442

Ismail MM, Rayad AM, Alwany H, Alshenawy TA (2004) Optimization of performance of explosive reactive armors. In: Proceedings of the 21st international symposium on ballistics, Adelaide, vol 1, pp 227–231

Jacobs MJN, Van Dingenen JLJ (2001) Ballistic protection mechanisms in personal armor. J Mat Sci 36:3137–3142

Jameson JW, Stewart GM, Petterson DR, Odell FA (1962) Dynamic distribution of strain in textile materials under high speed impact: part III, strain-time-position history in yarns. Textile Res J 32:858–860

Johnson W (1972) Impact strength of materials. Edward Arnold, London

Johnson PM, Burgess TJ (1968) Free surface velocity measurements of an impacted projectile by optical Doppler shift, Rev. Sci. Instr. 39:1100–1103

Johnson GR, Cook WH (1983) A constitutive model and data for metals subjected to large strain, high strain rates and high temperatures. Proceedings of the 7th international symposium on ballistics, The Hague, pp 541–547

Johnson GR, Cook WH (1985) Fracture characteristics of three metals subjected to various strains, strain rates, temperatures and pressures. Eng Fract Mech 21:31–48

Johnson GR, Holmquist TJ (1990) A computational constitutive model for brittle materials subjected to large strains, high strain rates and high pressures. In: Meyers MA, Murr LE, Staudhammer KP (eds) Proceedings of the EXPLOMRT conference, San Diego, Aug 1990. Shock Wave and High Pressure Phenomena, Marcel Dekker Inc., pp 1075–1082 (1992)

Johnson GR, Holmquist TJ (1993) An improved computational constitutive model for brittle materials. In: Schmidt SC, Shaner JW, Samara GA, Ross M (eds) Proceedings of the APS conference on high-pressure science and technology, Colorado Springs, June 1993, pp 981–984

Johnson W, Sengupta AK, Ghosh SK (1982) Plasticine modeled high velocity oblique impact and ricochet of long rods. Int J Mech Sci 24:437–455

Jones SE, Rule WK, Jerome DM, Klug RT (1998) On optimal nose geometry for a rigid penetrator. Comp Mech 22:413–417

Jones TL, DeLorme RD, Burkins MS, Gooch WA (2007) Ballistic performances of magnesium alloy AZ31B. In: Proceedings of the 23rd international symposium on ballistics, Tarragona Spain, Apr 2007, pp 989–995

Kanel GI, Vakhitova GG, Dremin AN (1978) Metrological characteristics of manganin pressure pickups under conditions of shock compression and unloading. Combust Explos Shock Waves 14:244–248

Kinard WH, Lambert CH, Schryer DR, Casey FW (1958) Effect of target thickness on cratering and penetration of projectiles impacting at velocities to 13,000 fps, NASA Memorandum 10-18-58L

Kineke JH, Richards LG (1963) Influence of target strength on hypervelocity crater formation in aluminum. Proceedings of the 6th symposium on hypervelocity impact, vol 2, part 2, pp 513–524

Kinslow R (1970) High velocity impact phenomena. Academic Press, New York

Koch A, Bianchi S (2010) Protection efficiency of steel and ceramic confinement plates for explosive reactive armors against shaped charges. Proceedings of the 25th international Symposium on ballistics, Beijing, China, May 2010, pp 1547–1553

Kolsky H (1949) An investigation of the mechanical properties of materials at very high rates of loading. Proc Roy Soc London B62:676–700

Kozhushko AA, Rykova II (1994) On the shortening of the effective length of a shaped charge jet in penetrating ceramic materials. Tech Phys Lett 20:377–378

Kozhushko AA, Rykova II, Sinani AB (1992) Resistance of ceramics to penetration at high interaction velocities. Combust Explos Shock Waves 28:84–86

Kraft JM (1955) Surface friction in ballistic penetration. J Appl Phys 26:1248–1253

Lambert JP (1978) A residual velocity predictive model for long rod penetrators. Ballistic Research Laboratories Report ARBRL-MR-02828

Lambert JP, Jonas GH (1976) Towards standardization in terminal ballistics testing. Ballistic Research Laboratories Report No. 1852 (ADA-021389)

Lampert S, Jeanquartier R (1999) Threat dependent protection efficacy of metal/liner compositions. Proceedings of the 18th international symposium on ballistics, San Antonio, Nov 1999, pp 970–977

Landkof B, Goldsmith W (1985) Petalling of thin metallic plates during penetration by cylindro-conical projectiles. Int J Solids Struct 21:245–266

Lee M, Bless SJ (1996) Cavity dynamics for long rod penetration. Proceedings of the 16th international symposium. on ballistics, San Francisco, Sept 1996, pp 569–578

Lee M, Bless SJ (1998) A discreet impact model for effect of yaw angle on penetration by rod projectiles. Proceedings of the 1997 conference on shock compression of condensed matter, Amherst, MA, July 1997, pp 929–932

Lee W, Lee HJ, Shin H (2002) Ricochet of a tungsten heavy alloy long-rod projectile from deformable steel plates. J Phys D App Phys 35:2676–2696

Leppin S, Woodward RL (1986) Perforation mechanisms in thin titanium alloy targets. Int J Impact Eng 4:107–115

Li QM, Meng H (2003) About the dynamic strength enhancement of concrete and concrete-like materials in a split Hopkinson pressure bar. Int J Solids Struct 40:343–360

Li JR, Yu JL, Wu ZG (2003) Influence of specimen geometry on adiabatic shear instability of tungsten heavy alloys. Int J Impact Eng 28:303

Liden E (2008) How to model fracture behavior in long rod projectile. Proceedings of the 24th international symposium ballistics. New Orleans, LA, 2008, pp 912–919

Liden E, Johannson E, Lundberg B (2006) Effect of thin oblique moving plates on long rod projectiles: a reverse impact study. Int J Impact Eng 32:1696–1720

Liden E, Helte A, Tjernberg A (2008) Multiple cross-wise orientated Nera panels against shaped charge warheads. Proceedings of the 24th international symposium ballistics, New Orleans, Louisiana, 2008, pp 1373–1380

Liss J, Goldsmith W, Kelly JM (1983) A phenomenological penetration model of plates. Int J Impact Eng 1:321–341

Littlefield DL, Anderson CE, Partom Y, Bless SJ (1997) The penetration of steel targets finite in radial extent. Int J Impact Eng 19:49–62

Liu D, Stronge WJ (2000) Ballistic limit of metallic plates struck by blunt deformable missiles: experiments. Int J Solids Struct 37:1403–1423

Lundberg P, Holmberg L, Janzon B (1998) An experimental study of long rod penetration into boron carbide at ordnance and hyper velocities. Proceedings of the 17th international symposium on ballistics. Midrand, South Africa, Mar 1998, vol 3, pp 251–258

Lundberg P, Renstrom R, Lundberg B (2000) Impact of metallic projectiles on ceramic targets: the transition between interface defeat and penetration. Int J Impact Eng 24:259–275

Lundberg P, Renstrom R, Holmbrg L (2001) An experimental investigation of interface defeat at extended interaction time, 2001. Proceedings of the 19th international symposium on ballistics. Interlaken, Switzerland, pp 1463–1469

Maggness LS, Leonard W (1993) Scaling issues for kinetic energy penetrators. Proceedings of the 14th international symposium on ballistics, Quebec, Sept 1993, pp 281–289

Magness LS, Farrand TG (1990) Deformation behavior and its relationship to the penetration performance of high-velocity KE penetrator material. Proceedings of the 1990 Army Science conference, Durham, June 1990, pp 465–479

Malaise F, Collombet F, Tranchet JY (2000) An investigation of ceramic block impenetrability to high velocity long rod impact. J Phys IV France 10:589–594

Marom I, Bodner SR (1979) Projectile perforation of multi-layered beams. Int J Mech Sci 21:489–504

Masri R, Durban D (2005) Dynamic spherical cavity expansion in an elastoplastic compressible Mises solid. J App Mech 72:887–898

Mayseless M (2007) Controlled harm explosive reactive armor, U.S. Patent No. 7299736 B2 (2007)

Mayseless M (2010) Reactive armor: simple modeling. Proceedings of the 25th international symposium on ballistics, Beijing, China, May 2010, pp 1554–1563

Mayseless M, Ehrlich Y, Falcovitz Y, Rosenberg G, Wheis D (1984) Interaction of shaped-charge jets with reactive armor. Proceedings of the 8th international symposium on ballistics, Orlando, vol II, pp 15–20

McCauley JW, Crowson A, Gooch WA, Rajendran AM, Bless SJ, Logan KV, Normandia M, Wax S (2002). Proceedings of the conference on ceramic armor material by design, Wailea, Hawaii, Nov 2001

McClintock FA,Walsh JB (1962) Friction in Griffith cracks in rocks under pressure. Proceedings 4th US National Congress: Applied Mechanism vol II, American Society of Mechanical Engineers, New York, pp 1015–1021

McQueen RG, Marsh SP, Taylor JW, Fritz JN, Carter WJ (1970) The equation of state of solids from shock wave studies. In: Kinslow R (ed) High velocity impact phenomena. Academic Press, New York

Mellgrad I, Holmberg L, Olsson GL (1989) An experimental method to compare the ballistic efficiencies of different ceramics against long rod projectiles. Proceedings of the 11th international symposium on ballistics, Brussels, Belgium, May 1989, pp 323–331

Mescall JF, Tracy CA (1986) Improved modeling of fracture in ceramic armor. Proceedings of the U.S. Army Science conference, June 1986, pp 41–53

Meyers MA (1994) Dynamic behavior of materials. Wiley, New York

Moran B, Glenn LW, Kusubov A (1991) Jet penetration in glass. J Phys IV 1(C3):147–154

Naz P (1989) Penetration and perforation of steel targets by copper rods – measurement of crater diameter. In: Proceedings of the 11th international symposium on ballistics, Brussels, Belgium, May 1989, pp. 233–242

Ogorkiewicz RM (1995) Combat vehicle armor progress, Janes Defence, June 1995, pp 59–67

Ogorodnikov VA, Ivanov AG, Luchinin VI, Khokhlov AA, Tsoi AP (1999) Scaling effect in dynamic fracture spallation of brittle and ductile material. Combust Explos Shock Waves 35:97–102

Orphal DL (1997) Phase three penetration. Int J Impact Eng 20:601–616

Orphal DL, Andeson CE (2003) The dependence of penetration velocity on impact velocity. Int J Impact Eng 33:546–554

Orphal DL, Anderson CE (2006) The dependence of penetration velocity on impact velocity. Int J Impact Eng 33:546–554

Orphal DL, Franzen RR (1989) Penetration mechanics and performance of segmented rods against metal targets. Int J Impact Eng 10:427–438

Orphal DL, Franzen RR (1997) Penetration of confined silicon carbide by tungsten long rods at impact velocities from 1.5 to 4.6 km/s. Int J Impact Eng 19:1–13

Orphal DL, Franzen RR, Piekutowski AJ, Forrestal MJ (1996) Penetration of confined aluminum nitride targets by tungsten long rods at 1.5-4.5 km/s. Int J Impact Eng 18:355–368

Orphal DL, Franzen RR, Charters AC, Menna TL, Piekutowski AJ (1997) Penetration of confined boron carbide targets by long rods at impact velocities from 1.5 to 5.0 km/s. Int J Impact Eng 19:15–29

Pack DC, Evans WM (1951) Penetration by high velocity (Munroe) jets: I. Proc Phys Soc (London) B64:298–302

Paik SH, Kim SJ, Yoo YH, Lee M (2007) Protection performance of dual flying oblick plates against a yawed long-rod penetrators. Int J Impact Eng 34:1413–1422

Paterson MS (1978) Experimental rock deformation – the brittle field. Springer-Verlag, Heidelberg

Perez E (1980) An experimental and theoretical study of the penetration of semi-infinite metallic targets by metallic long rods at impact velocities beyond 2000 m/s. Institute Franco-Allemand de Recherches (ISL). Report No. R/108/80, St. Louis, France

Piekutowski AJ (1996) Formation and description of debris clouds produced by hypervelocity impact. NASA contract report 4707, Feb 1996

Piekutowski AJ, Forrestal MJ, Poormon KL, Warren TL (1996) Perforation of aluminum plates with ogive nosed steel rods at normal and oblique impacts. Int J Impact Eng 18:877–887

Piekutowski AJ, Forrestal MJ, Poormon KL, Warren TL (1999) Penetration of 6061-T6511 aluminum targets by ogive nosed steel projectiles with striking velocities between 0.5 and 3.0 km/s. Int J Impact Eng 23:723–734

Poncelet JV (1835) Rapport sur un memoire de MM Piobert et Morin, Mem. Acad. Sci. 15:55–91

Rajendran AM, Grove DJ (1996) Determination of Rajendran-Grove ceramic constitutive model constants. Int J Impact Eng 18:611–631

Rakhmatulin KA (1966) Strength under high transient loads, Israel Program for Scientific Translation, Jerusalem

Rao MP, DuanY KM, Powers BM, Bogetti TA (2009) Modeling the effects of yarn material properties and friction on the ballistic impact of a plain-weave fabric. Compos Struct 89:556–566

Rapoport L, Rubin MB (2009) Separation and nose velocity dependence of the drag force applied to a rigid ovoid of Rankine nosed projectile penetrating an elastic-perfectly plastic target. Int J Impact Eng 36:1012–1018

Ravid M, Bodner SR (1983) Dynamic perforation of viscoplastic plates by rigid projectiles. Int J Eng Sci 21:577–591

Reaugh JE, Holt AD, Wilkins ML, Cunningham BJ, Hord BL, Kusubov AS (1999) Impact studies of five ceramic materials and Pyrex. Int J Impact Eng 23:771–782

Recht R, Ipson TW (1962) The dynamics of terminal ballistics. Denver Research Institute Report No. AD 274128

Recht R, Ipson TW (1963) Ballistic perforation dynamics. J App Mech 30:384–390

Resal H (1895) Sur la penetration d'un projectile dans les semi-fluides et les solides, Compte Rendus, 120:397–401

Rice JR, Levy N (1969) Local heating by plastic deformation of a crack tip. In: Argon AS (ed) Physics of strength and plasticity. MIT Press, Cambridge, pp 277–293
Rice JR, Tracey DM (1969) On the ductile enlargement of voids in triaxial stress fields. J Mech Phys Solids 17:210–217
Rittel D, Wang ZG, Dorogoy A (2008) Geometrical imperfection and adiabatic shear banding. Int J Impact Eng 35:1280–1292
Robins B (1742) New principles of gunnery. J Nourse, London
Rogers HC (1983) Adiabatic shearing-general nature and material aspects. In: Mescall J, Weiss V (eds) Material behavior under high stresses and ultrahigh loading rates. Plenum Press, New York, pp 101–118
Rosenberg Z (1987) Accounting for the spall strength of ductile metals by the spherical expansion analysis. Mat Sci Eng 93:L17–L18
Rosenberg Z (1993) On the relation between the Hugoniot elastic limit and the yield strength of brittle materials. J Appl Phys 74:752–753
Rosenberg Z, Dekel E (1994a) How large should semi-infinite targets be? Proceedings of the 45th meeting of the aeroballistics range association, Huntsville, Alabama, 10–14 Oct 1994
Rosenberg Z, Dekel E (1994b) A critical examination of the modified Bernoulli equation using two-dimensional simulations of long rod penetrations. Int J Impact Eng 15:711–720
Rosenberg Z, Dekel E (1994c) The relation between the penetration capability of long rods and their length to diameter ratio. Int J Impact Eng 15:125–129
Rosenberg Z, Dekel E, Hohler V, Stilp AJ, Weber K (1998) Penetration of tungsten-alloy rods into composite ceramics: experiments and numerical simulations, In: Proceedings of the APS conference on Shock Waves in Condensed Matter, Amherst, Mass. July 1997, pp. 917–920
Rosenberg Z, Dekel E (1998a) A computational study of the relations between material parameters of long-rod penetrators and their ballistic performance. Int J Impact Eng 21:283–298
Rosenberg Z, Dekel E (1998b) A parametric study of the bulging process in passive cassettes with 2D numerical simulations. Int J Impact Eng 21:297–305
Rosenberg Z, Dekel E (1999a) On the role of nose profile in long-rod penetration. Int J Impact Eng 22:551–577
Rosenberg Z, Dekel E (1999b) On the interaction between shaped charge jets and confined explosives at normal incidence. Int J Impact Eng 23:795–802
Rosenberg Z, Dekel E (2000) Further examination of long rod penetration: the role of penetrator strength at hypervelocity impacts. Int J Impact Eng 24:85–101
Rosenberg Z, Dekel E (2001a) Material similarities in long-rod penetration mechanics. Int J Impact Eng 25:361–372
Rosenberg Z, Dekel E (2001b) More on the secondary penetration of long rods. Int J Impact Eng 26:639–649
Rosenberg Z, Dekel E (2004) On the role of material properties in the terminal ballistics of long rods. Int J Impact Eng 30:835–851
Rosenberg Z, Dekel E (2005) The use of 3D numerical simulations for the interaction of long rods with moving plates. Proceedings of the 2nd international conference on computational ballistics, Cordoba, Spain, WIT Press, pp 53–60
Rosenberg Z, Dekel E (2008) A numerical study of the cavity expansion process and its application to long-rod penetration mechanics. Int J Impact Eng 35:147–154
Rosenberg Z, Dekel E (2009a) The penetration of rigid long rods- revisited. Int J Impact Eng 36:551–564
Rosenberg Z, Dekel E (2009b) On the deep penetration and plate perforation by rigid projectiles. Int J Solids Struct 46:4169–4180
Rosenberg Z, Dekel E (2010a) The deep penetration of concrete targets by rigid rods-revisited. Int J Protect Struct 1:125–144
Rosenberg Z, Dekel E (2010b) On the deep penetration of deforming long rods. Int J Solids Struct 47:238–250

Rosenberg Z, Dekel E (2010c) Revisiting the perforation of ductile plates by sharp-nosed rigid projectiles. Int J Solids Struct 47:3022–3033
Rosenberg Z, Forrestal MJ (1988) Perforation of aluminum plates with conical-nosed rods-additional data and discussion. J App Mech 55:236–237
Rosenberg Z, Partom Y (1982) One-dimensional isentropic compression measurements of multiply loaded PMMA. App Phys Lett 41:921–923
Rosenberg Z, Partom Y (1985) Lateral stress measurement in shock-loaded targets with transverse piezoresistance gauges. J Appl Phys 58:3072–3076
Rosenberg Z, Tsaliah J (1990) Applying Tate's model for the interaction of long-rod projectiles with ceramic targets. Int J Impact Eng 9:247–251
Rosenberg Z, Yeshurun Y (1988) The relation between ballistic efficiency of ceramic tiles and their compressive strengths. Int J Impact Eng 7:357–362
Rosenberg Z, Yaziv D, Partom Y (1980) Calibration of foil-like manganin gauges in planar shock wave experiments. J Appl Phys 51:3702–3705
Rosenberg Z, Partom Y, Yaziv D (1981) The response of manganin gauges shock loaded in the 2-D straining mode. J Appl Phys 52:755–758
Rosenberg Z, Dawicke D, Strader E, Bless SJ (1986) A new technique for heating specimens in split Hopkinson bar experiments using induction coil heaters. Exp Mech 26:275–278
Rosenberg Z, Bless SJ, Yeshurun Y, Okajima K (1987a) A new definition of ballistic efficiency of brittle materials based on the use of thick backing plates. In: Chiem CY, Kunze HD, Meyer LWP (eds) Proceedings of IMPACT 87 symposium, impact loading and dynamic behavior of materials. DCM Informationsgesellschaft Verlag, pp 491–498
Rosenberg Z, Yaziv D, Yeshurun Y, Bless SJ (1987b) Shear strength of shock loaded alumina as determined by longitudinal and transverse manganin gages. J Appl Phys 62:1120
Rosenberg Z, Yeshurun Y, Mayseless M (1989) On the ricochet of long rod projectiles. In: Proceedings of the 11th international symposium on ballistics, Brussels, May 1989, pp 501–506
Rosenberg Z, Marmor E, Mayseless M (1990) On the hydrodynamic theory of long rod penetration. Int J Impact Eng 10:483–486
Rosenberg Z, Brar NS, Bless SJ (1991a) Shear strength of titanium-diboride under shock loading measured by transverse manganin gages, In: Schmidt SC, Dick, RD, Forbes JW, Tasker DG (eds) Proceedings of the 1991 conference on shock waves in condensed matter, Williamsburg, June 1991, pp 471–473
Rosenberg Z, Brar NS, Bless SJ (1991b) Dynamic high-pressure properties of AlN ceramic as determined by flyer plate impact. J Appl Phys 70:167–171
Rosenberg Z, Dekel E, Yeshurun Y, Bar-On E (1995) Experiments and 2-D simulations of high velocity penetration into ceramic tiles. Int J Impact Eng 17:697–706
Rosenberg Z, Berkovitz E, Keese F (1996) Experiments and simulations of impacts on ceramic cylinders. Proceedings of the 16th international symposium on ballistics, San Francisco, Sept 1996, pp 505–513
Rosenberg Z, Kreif R, Dekel E (1997a) A note on the geometric scaling of long-rod penetration. Int J Impact Eng 19:277–283
Rosenberg Z, Dekel E, Hohler V, Stilp AJ, Weber K (1997b) Hypervelocity penetration of tungsten-alloy rods into ceramic tiles: experiments and 2-D simulations. Int J Impact Eng 20:675–683
Rosenberg Z, Dekel E, Hohler V, Stilp AJ, Weber K (1998) Penetration of tungsten alloy rods into composite ceramics: experiments and numerical simulations, In: Proceedings of the APS conference on Shock Waves in Condensed Matter, Amherst, Mass. July. 1997, pp 917–920
Rosenberg Z, Surujon Z, Yeshurun Y, Ashuach Y, Dekel E (2005) Ricochet of 0.3″ AP projectiles from inclined polymeric plates. Int J Impact Eng 31:221–233
Rosenberg Z, Dekel E, Ashuach Y (2006) More on the penetration of yawed rods. J Phys IV France 134:397–402
Rosenberg Z, Ashuach Y, Dekel E (2007) More on the ricochet of eroding long rods-validating the analytical model with 3D simulations. Int J Impact Eng 34:942–857

Rosenberg Z, Ashuach Y, Yeshurun Y, Dekel E (2009) On the main mechanisms for defeating AP projectiles, long rods and shaped charge jets. Int J Impact Eng 36:588–596
Rosenberg Z, Ashuach Y, Kreif R (2010) The effect of specimen dimensions on the propensity to adiabatic shear failure in Kolsky bar experiments. Rev Mater 15:316–324
Roylance D (1977) Ballistics of transversely impacted fibers. Textile Res J 47:679–684
Ruoff AL (1967) Linear shock-velocity-particle-velocity relationships. J Appl Phys 38:4976–4980
Scheffler DR (1997) Modeling the effect of penetrators nose shape on the threshold velocity for thick aluminum targets. Army Research Laboratory report, ARL-TR-1417, July 1997
Senf H (1974) Shattering of hard steel spheres. EMI report E-7/74 (in German)
Senf H, Weimann K (1973) Die wirkung von stahlkugeln auf dural–einfach–und mehrplattenziele. EMI report no. V6-73 (in German)
Senf H, Rothenhauesler H, Scharpf F, Poth A, Pfang W (1981) Experimental and numerical investigation of the ricocheting of projectiles from metallic surfaces. Proceedings of the 6th international symposium on ballistics, Orlando, pp 510–521
Senf H, Strassburger E, Rothenhausler H, Lexow B (1998) The dependency of ballistic mass efficiency of light armor on striking velocity of small caliber projectiles. Proceedings of 17th international symposium on ballistics, Midrand, South Africa, Mar 1998, pp 199–206
Segletes SB (2007) The erosion transition of tungsten-alloy rods into aluminum targets. Int J Solids Struct 44:2168–2191
Shadbolt PJ, Corran RSJ, Ruiz C (1983) A comparison of plate perforation models in the sub-ordnance impact velocity range. Int J Impact Eng 1:23–49
Shim VPW, Tan VBC, Tay TE (1995) Modeling deformation and damage characteristics of woven fabrics under small projectile impact. Int J Impact Eng 16:585–605
Shin H, Yoo YH (2003) Effect of the velocity of a single flying plate on the protection capability against obliquely impacting long-rod penetrators. Combust Explos Shock Waves 39:591–600
Shinar G, Barnea N, Ravid M, Hirsch E (1995) An analytical model for the cratering of metallic targets by hypervelocity long rods. Proceedings of the 15th international symposium on ballistics, Jerusalem, Israel, May 1995, pp 59–66
Shockey DA, Marchand AH, Cort GE, Burkett MW, Parker R (1990) Failure phenomenology of confined ceramic targets and impacting rods. Int J Impact Eng 9:263–275
Shockey DA, Ehrlich DC, Simons JW (1999) Lightweight fragment barriers for commercial aircraft. Proceedings of the 18th international symposium on ballistics, San Antonio, 15–19 Nov 1999, pp 1192–1199
Showalter DD, Gooch WA, Burkins MS, Koch RS (2008) Ballistic testing of SSAB ultra-high hardness steel for armor applications. Proceedings of the 24th international symposium on ballistics, New Orleans, Sept 2008, pp 634–642
Siegel AE (1955) The theory of high speed guns, AGARDograph 91. Advisory Group for Aerospace Research and Development, London
Silsby GF, Rozak RJ, Giglio-Tos L (1983) BRL's 50 mm high pressure powder gun for terminal ballistics – the first year experience. Ballistic Research Laboratory Report No. BRL-MR-03236
Smith JC, McCrackin FL, Scheifer HF (1958) Stress–strain relationships of yarns subjected to rapid impact loading, part V-wave propagation in long textile yarns impacted transversely. Textile Res J 28:288–302
Solve G, Cagnoux J (1990) The behavior of pyrex glass against a shaped charge jet. In: Schmidt SC, Johnson JN, and Davison LW (eds) Proceedings of the APS conference on shock waves in condensed matter, 1989, Elsevier Science Publ., 1990, pp 967–970
Staker MR (1981) The relation between adiabatic shear instability strain and material properties. Acta Metall 29:683–689
Steinberg DJ (1987) Constitutive model used in computer simulation of time-resolved shock wave data. Int J Impact Eng 5:603–611
Sterzelmeier K, Brommer V, Sinniger L, Grasser B (2002) Active armor protection –conception and design of steerable launcher systems fed by modular pulsed-power supply units. Proceedings of the 20th international symposium on Ballistics, Orlando , Sept 2002, pp 1012–1019

Stilp AJ, Hohler V (1990) Experimental methods for terminal ballistics and impact physics. In: Zukas JA (ed) High velocity impact dynamics. John Wiley and Sons, New York, pp 515–592
Stilp AJ, Hohler V (1995) Aeroballistics and impact physics at EMI – an historical overview. Int J Impact Eng 17:785–805
Strand OT, Goosman DR, Martinez C, Whitworth TL, Kuhlow WW (2006) Compact system for high-speed velocimetry using heterodyne techniques. Rev Sci Instr 77:083108
Subramanian R, Bless SJ (1995) Penetration of semi-infinite AD995 alumina targets by tungsten long rod penetrators from 1.5 to 3.5 km/s. Int J Impact Eng 17:807–816
Subramanian R, Bless SJ, Cazamias J, Berry D (1995) Reverse impact experiments against tungsten rods and results for aluminum penetration between 1.5 and 4.2 km/s. Int J Impact Eng 17:817–824
Swift HF (1982) Image forming instruments. In: Zukas JA, Nicholas T, Swift HF, Greszczuk LB, Curran DR (eds) Impact dynamics. John Wiley and Sons, New York, pp 241–275
Szendrei T (1983) Analytical model for crater formation by jet impact and its application to calculation of penetration curves and hole profiles. Proceedings of the 7th international symposium on Ballistics, Den Haag, The Netherlands, Apr 1983, pp 575–583
Tabor D (1951) The hardness of metals. Oxford University Press, London
Tan VBC, Lim CT, Cheong CH (2003) Perforation of high-strength fabric by projectiles of different geometries. Int J Impact Eng 28:207–222
Tate A (1967) A theory for the deceleration of long rods after impact. J Mech Phys Solids 15:387–399
Tate A (1969) Further results in the theory of long rod penetration. J Mech Phys Solids 17:141–150
Tate A (1977) A possible explanation for the hydrodynamic transition in high speed impact. Int J Mech Sci 19:121–123
Tate A (1979) A simple estimate of the minimum target obliquity required for the ricochet of a high speed long rod projectile. J Phys D App Phys 12:1825–1829
Tate A (1986) Long rod penetration models-part 2, extensions to the hydrodynamic theory of penetration. Int J Mech Sci 28:599–612
Tate A (1990) Engineering modeling of some aspects of segmented rod penetration. Int J Impact Eng 9:327–341
Tate A, Green KEB, Chamberlain PG, Baker RG (1978) Model scale experiments on long rod penetrators. Proceedings of the 4th international symposium on ballistics, Monterey, 1978
Taylor GI (1948) The formation and enlargement of a circular hole in a thin plastic plate. Quart J Mech App Math 1:103–124
Teng XQ, Dey S, Borvik T, Wierzbicki T (2007) Protection perforation of double-layered metal shields against projectile impact. J Mech Mater Struct 2:1309–1330
Thoma K, Vinckler D, Kiermeir J, Diesenroth J, Fucke W (1993) Shaped charge jet interaction with highly effective passive sandwich systems – experiments and analysis. Propell Explos Pyrotech 18:275–281
Thomson WT (1955) An approximate theory of armor penetration. J Appl Phys 26:80–82
Timothy SP, Hutchings IM (1985) The structure of adiabatic shear bands in a titanium alloy. Acta Metall 23:667–676
Tuler FR, Butcher BM (1968) A criterion for the time dependence of dynamic fracture. Int J Fract Mech 4:431–437
Van-Gorp EHM, van der Loo LLH, van-Dingenen JLJ (1993) A model for HPPE-based light-weight add-on armor. Proceedings of the 14th international symposium on Ballistics, Quebec, Canada, Sept 1993, pp 701–709
Vantine HC, Erickson LM, Janzen JA (1980) Hysteresis-corrected calibration of manganin under shock loading. J Appl Phys 51:1957–1962
Van-Wegen FTM, EP Carton (2008) New lightweight metals for armors. Proceedings of the 24th international symposium on Ballistics, New Orleans, Sept 2008, pp 830–837
Vural M, Erim Z, Konduk BA, Ucisik AH (2002) Ballistic perforation of alumina ceramic armors. In: McCauley JW et al (eds) Ceramic armor materials by design. The American Ceramic Society, Westerville, Ohio, pp 103–110

Walker JD (1999) An analytical velocity field for back surface bulging. In: Reinecke WG (ed) Proceedings of the 18th international symposium on ballistics, Lancaster, Technomic Publishing Co., vol 2, pp 1239–1246
Walker JD (2001) Ballistic limit of fabrics with resin. Proceedings of the 19th international symposium on ballistics, Interlaken, Switzerland, May 2001, pp 1409–1414
Walker JD (2003) Analytically modeling hypervelocity penetration of thick ceramic targets. Int J Impact Eng 29:747–755
Walker JD, Anderson CE (1995) A time-dependent model for long-rod penetration. Int J Impact Eng 16:19–48
Walker JD, Anderson CE (1996) An analytic model for ceramic- faced light armor. In: Proceedings of the 16th international symposium on ballistics, San Francisco, Sept 1996, vol 3, pp 289–298
Walker JD, Anderson CE, Goodlin DL (2001) Tungsten into steel penetration including velocity, L/D and impact inclination effects. Proceedings of the 19th international symposium on ballistics, Interlaken Switzerland, May 2001, pp 1133–1139
Walters WP (1990) Fundamentals of shaped charges. In: Zukas JA (ed) High velocity impact dynamics. John Wiley & Sons, New York, pp 731–829
Walters WP, Zukas JA (1989) Fundamentals of shaped charge jets. John Wiley and Sons, New York
Warren TL, Poormon KL (2001) Penetration of 6061-T6511 aluminum plates by ogive-nosed VAR 4340 steel projectiles at oblique angles: experiments and simulations. Int J Impact Eng 25:993–1022
Wei ZG, Yu JL, Li JR, Li YC, Hu SS (2001) Influence of stress conditions on adiabatic shear localization of tungsten heavy alloys. Int J Impact Eng 26:843–852
Weimann K (1974) Penetration of steel spheres in aluminum targets. EMI report, E-3/74 (in German)
Wen HM, Jones N (1996) Low velocity perforation of punch impact loaded plates. J Press Vessel Technol 118:181–187
Westerling L, Lundberg P, Lundberg B (2001) Tungsten long-rod penetration into confined cylinders of boron carbide at and above ordnance velocities. Int J Impact Eng 25:703–714
Whipple FL (1947) Meteorites and space travel. Astron J, No. 1161, Feb 1947, p 131
Wierzbicki T (1999) Petalling of plates under explosive and impact loading. Int J Impact Eng 22:935–944
Wilkins ML (1964) Calculations of elastic–plastic flow. In: Adler B, Fernback S, Rotenberg M (eds) Methods of computational physics. Academic Press, New York
Wilkins ML (1968) Third progress report of light armor program. Lawrence Radiation Laboratory, Livermore, UCRL – 50460
Wilkins ML (1978) Mechanics of penetration and perforation. Int J Eng Sci 16:793–807
Wilkins ML, Landingham RL, Honodel CA (1970) Fifth progress report of light armor program. Lawrence Radiation Laboratory, Livermore, UCRL – 50980
Wingrove AL (1973) The influence of projectile geometry on adiabatic shear and target failure. Metall Trans 4:1829–1833
Wollmann E, Sterzelmeir K, Weihrauch G (1996) Electromagnetic active armor. Proceedings of the 16th international symposium on ballistics, San Francisco, Sept 1996, vol I, pp 21–28
Woodward RL (1978) The penetration of metal targets by conical projectiles. Int J Mech Sci 20:349–359
Woodward RL (1987) A structural model for thin plate perforation by normal impact of blunt projectiles. Int J Impact Eng 6:128–140
Woodward RL (1990) Material failure at high strain rates. In: Zukas JA (ed) High velocity impact dynamics. John Wiley and Sons, Inc., New York, pp 65–126
Woodward RL, Cimpoeru SJ (1998) A study of the perforation of aluminum laminate targets. Int J Impact Eng 21:117–131

Woodward RL, De-Morton ME (1976) Penetration of targets by a flat-ended projectile. Int J Mech Sci 18:119–127

Woodward RL, Baxter BJ, Scarlett NV (1984) Mechanics of adiabatic shear plugging in high strength aluminum and titanium alloys. Proceedings of the third conference on the mechanical properties of materials at high rates of strain, Oxford, April 1984, Institute of Physics Conference Series No. 70, pp 525–532

Woolsey P, Mariano S, Dokidko D (1989) Alternative test methodology for ballistic performance ranking of armor ceramics. Presented at the 5th annual TACOM armor coordinating conference, Monterey, Mar 1989

Wright TW, Frank K (1988) Approaches to penetration problems. Ballistics Research Laboratory Technical Report BRL-TR-2957, Dec 1988

Yarin AL, Rubin MB, Roisman IV (1995) Penetration of a rigid projectile into an elastic–plastic target of finite thickness. Int J Impact Eng 16:801–831

Yaziv D, Rosenberg G, Partom Y (1986) Differential ballistic efficiency of appliqué armor. Proceedings of the 10th international symposium on ballistics, Shrivenham, UK, pp 315–319

Yaziv D, Walker JD, Riegel JP (1992) Analytical model of yawed penetration in the 0 to 90 degrees range. Proceedings of the 13th international symposium on ballistics, Stockholm, Sweden, pp 17–23

Yaziv D, Friling S, Kivity Y (1995) The interaction of inert cassettes with shaped charge jets. Proceedings of the 15th international symposium on ballistics, Jerusalem, Israel, May 1995, pp 461–467

Yeshurun Y, Rosenberg Z (1993) AP projectile fracture mechanisms as a result of oblique impact. Proceedings of the 14th international symposium on ballistics, Quebec Canada, pp 537–544

Yeshurun Y, Ziv D (1992) Composite protective armor and its use. U.S. Patent No. 5134725

Yeshurun Y, Ashuach Y, Rosenberg Z, Rozenfeld M (2001) Lightweight armor against firearm projectiles. U.S. Patent No. 7,163,731 B2, filed at 16.07.2001, issued at 16.01.07

Zaera R (2011) Ballistic impacts on polymer matrix composites composite armor, personal armor. In: Abrate S (ed) Impact engineering of composite materials. Springer, Vienna, pp 305–403

Zeldovich YB, Raizer YP (1965) Physics of shock waves and high temperature phenomena. Academic, New York

Zener C, Hollomon JH (1944) Effect of strain rate upon plastic flow of steel. J Appl Phys 15:22–32

Zerilli F, Armstrong R (1987) Dislocation-mechanics-based constitutive relations for material dynamics calculations. J Appl Phys 61:1816–1825

Zhu G, Goldsmith W, Dharan CKH (1992a) Penetration of laminated Kevlar by projectiles–I. Experimental investigation. Int J Solids Struct 29:399–420

Zhu G, Goldsmith W, Dharan CKH (1992b) Penetration of laminated Kevlar by projectiles–II. Analytical model. Int J Solids Struct 29:421–436

Zukas JA (1982) Penetration and perforation of solids. In: Zukas JA, Nicholas T, Swift HF, Grebszczuk LB, Curran DR (eds) Impact dynamics. Wiley, New York, pp 155–214

Zukas JA (1990) Survey of computer codes for impact simulations. In: Zukas JA (ed) High velocity impact dynamics. John Wiley and Sons Inc., New York, pp 693–714